DELHI COLLEGE OF ENGINEERING

LIBRARY

Class No.

Book No.

Accession No.

DELHI COLLEGE OF ENGINEERING

Kashmere Gate, Delhi

LIBRARY

DATE DUE

For each day's delay after the due date a fine of **10** P. per Vol. shall be charged for the first week, and **50** P. per Vol. per day for subsequent day. Text Book Re. **1.00**

Borrower's No.	Date Due	Borrower's No.	Date Due

Applied Scientific Research

An International Journal on the Applications of Fluid Dynamics

VOLUME 49 1992

KLUWER ACADEMIC PUBLISHERS
DORDRECHT BOSTON LONDON

Applied Scientific Research

An International Journal on the Applications of Fluid Dynamics

Editor-in-Chief

F.T.M. Nieuwstadt, Laboratory for Aero- and Hydrodynamics, Technical University of Delft, Rotterdamseweg 145, 2628 AL Delft, The Netherlands.

BITNET: WBAHNIE @ HDETUD1.

Associate Editors

P.C.T. de Boer, Sibley School of Mechanical and Aerospace Engineering, Cornell University, Ithaca, NY 14853, U.S.A.

BITNET: W6YJ @ CORNELLA

A.M. Savill, Department of Engineering, Trumpington Street, Cambridge CB2 1PZ, England

EARN/BITNET: AMS3 @ PHX.CAM.AC.UK

Editorial Board

R.B. Bird, *University of Wisconsin-Madison, Wis., U.S.A.*; **H. Buggisch**, *University of Karlsruhe, Karlsruhe, Germany*; **A.K. Chesters**, *Unilevers Research, Vlaardingen, The Netherlands*; **J.F. Dijksman**, *Philips Lighting, Eindhoven, The Netherlands*; **L. Hesselink**, *Stanford University, Stanford, Calif., U.S.A.*; **T. Kambe**, *University of Tokyo, Tokyo, Japan*; **G.D.C. Kuiken**, *Technical University of Delft, Delft, The Netherlands*; **G.E.A. Meier**, *Max-Planck-Institut für Strömungschforschung, Göttingen, Germany*; **G. Ooms**, *Koninklijke-Shell Exploration and Production Laboratory, Rijswijk, The Netherlands*; **J.K. Platten**, *University of Mons, Mons, Belgium*; **J.A. Steketee**, *Technical University of Delft, Delft, The Netherlands*; **J. Villermaux**, *Laboratoire des Sciences du Génie Chimique de Nancy, Nancy, France*; **L. van Wijngaarden**, *Technical University of Twente, Enschede, The Netherlands*; **J.S. Walker**, *University of Illinois, Urbana, Ill., U.S.A.*.

ISSN 0003-6994

All Rights Reserved
© 1992 Kluwer Academic Publishers

No part of the material protected by this copyright notice may be reproduced or
utilised in any form or by any means, electronic or mechanical,
including photocopying, recording or by any information storage and
retrieval system, without written permission from the copyright owner

Printed in the Netherlands

Applied Scientific Research

Contents of Volume 49 (1992)

Vol. 49 No. 1 January 1992

T.G. Thomas and H.S. Takhar: Turbulent mass transport and attenuation in Stokes waves 1

V.D. Rao, J. Saibabu and P.K. Sarma: Direct contact condensation of vapor on turbulent, falling liquid film 31

T.J. Moon, T.Q. Hua, J.S. Walker and B.F. Picologlou: Liquid metal flow in a simple manifold with a strong transverse magnetic field 49

A.K. Coker, G.V. Jeffreys and C.J. Mumford: Mechanisms of nozzle type reactor operation with gas removal 67

T. Govindarajulu and M.B.K. Moorthy: An approximate solution for free convection flows in a thermally stratified porous medium 83

G.E. Tupholme: Elastoplastic cracks moving in orthotropic crystals 91

Vol. 49 No. 2 April 1992

B.A. Jubran, M.N. Hamdan and B.O. Al Bedoor: Roughness and turbulence intensity effects on the induced flow oscillation of a single cylinder 101

H.I. Andersson and K.L. Tiseth: Leakage effects in laminar duct flow: a numerical study 117

M. Jagannadham, K. Subba Reddi and D. Angirasa: Buoyant plumes due to mass diffusion 135

S.D. Gulwadi and A.F. Elkouh: Unsteady flow in an annulus between two concentric rotating spheres 147

H.C.J. Hoefsloot, H.W. Hoogstraten, L.P.B.M. Janssen and J.W. Knobbe: Growth factors for Marangoni instability in a spherical liquid layer under zero-gravity conditions 161

R. Coene: Flutter of slender bodies under axial stress 175

Vol. 49 No. 3 July 1992

Papers from *Euromech Colloquium 279*
Image analysis as measuring technique in flows
Delft University of Technology, July 2–5, 1991

Preface, by F.T.M. Nieuwstadt 189

R.D. Keane and R.J. Adrian: Theory of cross-correlation analysis of PIV images 191

S.B. Dalziel: Decay of rotating turbulence: some particle-tracking experiments 217

H. Stapountzis, J. Westerweel, J.M. Bessem, A. Westendorp and F.T.M. Nieuwstadt: Measurement of product concentration of two parallel reactive jets using digital image processing 245

H.A. Siller, R.J. Perkins and G. Janke: Image analysis of oil film interferometry – a method of measuring wall shear stress distributions 261

Regular papers

T. Fusegi, J.M. Hyun and K. Kuwahara: Three-dimensional numerical simulation of periodic natural convection in a differentially heated cubical enclosure 271

H.F. Bauer: Response of a viscous annular liquid layer in zero-gravity to different axial excitations of the rigid boundary plates 283

Vol. 49 No. 4 October 1992

H. Knoester and J. van der Zanden: On the stability of multi-layered fluids. Part I: analysis 307

I.A. Hassanien: Flow and heat transfer from a continuous surface in a parallel free stream of viscoelastic second-order fluid 335

M.H. Hamdan and R.M. Barron: Analysis of the squeezing flow of dusty fluids 345

J.B. Aparecido and R.M. Cotta: Laminar thermally developing flow inside right-angularly triangular ducts 355

F. Osterle: On the relationship between Lorentz's theorem for viscous flow and Onsager's reciprocal theorem 369

Reviewers of Applied Scientific Research 1991–1992 377

Euromech Meetings 1993 379

Kluwer LaTeX style file: Instructions to authors 383

Applied Scientific Research **49:** 1–29, 1992.
© 1992 *Kluwer Academic Publishers. Printed in the Netherlands.*

Turbulent mass transport and attenuation in Stokes waves

T.G. THOMAS & H.S. TAKHAR*

*Department of Engineering, University of Manchester, Simon Building, Oxford Road, Manchester M13 9PL, UK (*author for correspondence)*

Received 27 April 1990; accepted 10 May 1990

Abstract. The motion of turbulent Stokes waves on a finite constant depth fluid with a rough bed is considered. First and second order turbulent boundary layer equations are solved numerically for a range of roughness parameters, and from the solutions are calculated the mass transport velocity profiles and attenuation coefficients. A new mechanism of turbulent mass transport is found which predicts a reduction and reversal of drift velocity in shallow water in agreement with experimental observations under turbulent conditions. This transpires because the second order Stokes wave motion, in a turbulent boundary layer, can directly influence the mass transport velocity by mode coupling interactions between different second order Fourier modes of oscillation. It is also found that the Euler contribution due to the radiation stress of the first order motion is reduced to half of it's corresponding laminar value as a consequence of the velocity squared stress law. The attenuation is found to be of inverse algebraic type with the reciprocal wave height varying linearly with either distance or time. The severe wave height restriction applicable to the Longuet-Higgins [4] solution is shown not to apply to progressive waves on a finite constant depth of fluid. The existence of sand bars on sloping beaches exposed to turbulent waves is predicted.

Nomenclature

Latin
a, b = numerical magnitudes introduced in Eq. (24);
a_{im} = particle amplitude;
$c_1, c_2, c\mu$ = empirical constants;
c_f = friction coefficient;
C, C_1, C_2 = phase velocity, perturbations to C;
d = depth;
$D^2, \mathbb{D}$ = operator defined by Eq. (27), rate of deformation tensor;
e = exponential function;
E_m = rate of energy dissipation in boundary layer;
f_w = friction factor;
g, G = acceleration due to gravity, group velocity;
k = turbulent kinetic energy;
H = wave amplitude;
i = $(-1)^{1/2}$;
$\mathbb{I}$ = unit second order tensor;
$\hat{\mathbf{m}}, m_e, m$ = vertical unit vector, attenuation constant, mass flux;
M = number of unsteady terms in Fourier series;
$\hat{\mathbf{n}}$ = unit surface normal vector;
N, N_1, N_2^A, N_2^B = eddy viscosity, inner perturbations of N;
p, p_e, p_a = pressure, excess pressure, atmospheric pressure;
$\mathbf{r}$ = position vector;

Note: Full details of the mathematics involved in this work are in reference [34], a copy of which is lodged with the editors.

$\mathbb{R}$, R = Reynolds stress tensor, Reynolds number $U_0/\nu\beta$;
Re, Im = real part, imaginary part;
$\hat{\mathbf{s}}$, $\bar{s}$, S = unit surface tangent vector, mean surface slope, surface curve;
S_t = Strouhal number $\sigma\delta_1/U_0$;
t, t_D = time, characteristic decay time;
u, v, w = velocity components in the x, y and z directions;
$\mathbf{U}$, U_0, U_τ = velocity vector, typical velocity, shear velocity;
x, y, z = horizontal coordinate in direction of wave propogation, vertical coordinate, horizontal coordinate;
$Z(\delta)$ = $3/(2\sinh\delta)$;
y_0, y_{inf} = two values of y;

Greek

α = $(1/\beta\Lambda)$;
β = $(2\nu/\sigma)^{1/2}$;
δ, δ_1, δ_2, $\delta_{(j)(m)}$ = relative depth d, displacement thickness, boundary layer thickness, Kronecker delta symbol;
$\frac{1}{2}\gamma$, Λ = friction factor, bed roughness size;
$\Delta_{(1)(m)}$, $\Delta^{B}_{(2)(m)}$ = displacement thickness functions;
ε = relative amplitude H/d;
ζ = inner coordinate;
ζ_0, ζ_{inf} = two values of ζ;
η = height of free surface above still water level;
η_1, η_2 = perturbations of η;
θ = phase;
κ = wave number;
ν = kinematic viscosity;
ξ = turbulent dissipation;
ξ_1, ξ_2 = inner perturbations of ξ;
Π_A, Π_B = asymptotes of mass transport velocities $F'^{A}_{(2)(0)}$ and $F'^{B}_{(2)(0)}$;
ρ = density;
σ = angular frequency;
σ_κ, σ_ε = empirical constants;
τ = shear stress R_{xy};
τ_1, τ_2^A, τ_2^B = perturbations to τ;
Φ = turbulent production defined by Eq. (32);
Φ_1, Φ_2^A, Φ_2^B = inner perturbations of Φ;
$\boldsymbol{\kappa}$ = von Karman's constant;
ψ = stream function;
ψ_1, ψ_2 = outer perturbations of ψ;
Ψ_1, Ψ_2^A, Ψ_2^B = inner perturbations of ψ;
Ψ = mass transport stream function defined by Eq. (55);
ϖ = mean pressure gradient in the x direction.

1. Introduction

Irrotational wave motion and the associated particle drift in water waves was first investigated theoretically by Stokes [1] and later by Rayleigh [2]. The steady streaming induced by an oscillating solid object in a viscous fluid was investigated using boundary layer theory by Schlichting [3]. Longuet-Higgins [4] calculated the Stokes drift, and the Euler drift due to both the surface and bed boundary layers, for progressive and standing waves on water. The rapid dispersion of a dye formally taken to indicate turbulence may be interpreted as a laminar phenomenon. The streaming velocity was measured by observing the migration of dye filaments; and intense turbulence would disperse the dye rapidly so as to prevent observation. This point was noted by the experimenters for large waves near to breaking and under highly turbulent conditions. They also noted that when the waves were spilling onto a sloping beach, i.e. under fully turbulent conditions, the streaming velocity in the bed boundary layer was reversed. In the experiment of Bijker, Kalkwijk and Pieters [5], the mass transport velocity measured in the turbulent boundary layer on a rippled sloping beach showed a reduction and reversal in the shallow water outside the breaking zone. In both experiments the effect of bed slope on the laminar results was insignificant, while in the second experiment the reduction began well before the waves broke. This behaviour is predicted by the present analysis, but is not predicted by the Longuet-Higgins [6] theory in which the streaming velocity within the boundary layer is always in the direction of propagation of the wave.

In the present work the method of matched asymptotic expansions is used to derive first and second order boundary layer equations which are solved numerically in terms of a complex Fourier series. The motion in the interior is the well known Stokes wave solution plus a mean second order vorticity representing the Euler drift velocity. The turbulence is modelled by a k–ϵ transport model which has been experimentally tested.

We consider the effects of coupling interactions between different Fourier modes of oscillation of the boundary layer at the same level of approximation, which arise from the non-linear nature of turbulence. These have been neglected through linearisation in previous studies. The interactions allow the second order Stokes wave term to directly drive the Euler mass transport velocity, and thus establish a new contribution to turbulent mass transport. This is found to reduce and reverse the streaming velocity just outside the boundary layer as the relative depth parameter is reduced, and is in agreement with the experimental results of Bijker, Kalkwijk and Pieters [5]; it also leads to a theory of sand bar formation. In addition, that component of the Euler drift associated with the convected first order momentum is reduced to approximately half of it's corresponding laminar value in consequence of the velocity squared stress law. This is completely different from the linearised calculations of Longuet-Higgins [6], Johns [7] and Noda [8], although the latter results may be recovered by suppressing the coupling interactions.

The calculated attenuation coefficients, expressed in terms of a friction factor, are compared with experimental measurements, with which they show good agreement.

2. Mathematical analysis

Equations of motion and boundary conditions

We shall consider steady two-dimensional plane waves propogating on an incompressible fluid of uniform depth as shown in Fig. 1, with no first order mean current.

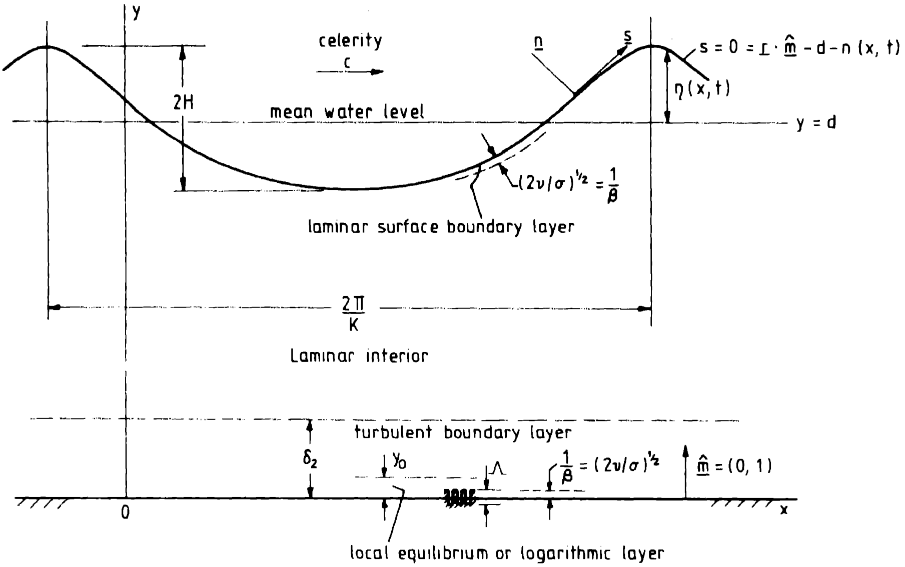

Fig. 1. Definition diagram for turbulent Stokes waves over a rough bed.

The amplitude H is small compared to depth d, so that the relative amplitude $\varepsilon = H/d$ is a small parameter. In the Stokes limit the wavelength $2\pi/\kappa$ and the depth d are of comparable magnitude, thus the relative depth $\delta = \kappa d$ is a parameter of order unity. Since the attenuation is small, the waves are treated as periodic with phase velocity $C = \sigma/\kappa$ such that the ratio C^2/gd is of order unity, where g denotes the acceleration due to gravity and σ the angular frequency. Let U_0 denote a typical velocity, thus $U_0 = \varepsilon C$ and $1/\beta = (2\nu/\sigma)^{1/2}$ denote a viscous length, where ν is the kinematic viscosity. A Reynolds number appropriate to the bed boundary layer is thus $\mathrm{Re} = U_0/\nu\beta$. The boundary layer over the bed on Nikuradse roughness Λ is assumed fully turbulent so that in the range $0.1 \leqslant \beta\Lambda \leqslant 16$ we require the condition (Sleath [9])

$$\mathrm{Re} \geqslant 139(\beta\Lambda)^{-0.29} \tag{1}$$

to be satisfied. For wind waves and swell with periods of 10 s, $1/\beta = 1.78$ mm, so this range corresponds to $0.17\,\mathrm{mm} < \Lambda < 28\,\mathrm{mm}$. The analysis is simplified if we limit ourselves to hydrodynamically rough beds so that $U_\tau\Lambda/\nu \geqslant 100$ (Goldstein [10]), where U_τ is a typical value of the shear velocity, and also if $\Lambda/\delta_2 \ll 1$, where δ_2 denotes the thickness of the boundary layer. In this case the velocity in the neighbourhood of roughness elements will satisfy a logarithmic law, independent of Re, and consistent with a low friction factor f_w, typically 0.01, defined as $\frac{1}{2}f_w$=(maximum of bed stress)/(maximum of near bed velocity)^2. To summarise, we require in addition to (1) and after some rearrangement, the following conditions:

$$\varepsilon \ll 1, \quad \delta = \mathrm{O}(1), \qquad \beta\Lambda f_w^{1/2}\,\mathrm{Re} \geqslant 100, \qquad f_w \ll 1. \tag{2}$$

These are best satisfied by full sized waves in the field.

The instantaneous values of turbulent variables are decomposed by standard methods into the sum of Reynolds averaged values, denoted by an overbar, and fluctuating values, denoted by a prime. The exact equations for the velocity $\mathbf{U} = \bar{\mathbf{U}} + \mathbf{U}'$ and turbulent kinetic energy $k = \frac{1}{2}\overline{|\mathbf{U}'|}$ follow from the Navier–Stokes equations and are

$$\frac{\partial \bar{\mathbf{u}}}{\partial t} + \bar{\mathbf{u}} \cdot \nabla \bar{\mathbf{u}} + \nabla\overline{(p_e/\rho)} = \nu\nabla^2\bar{\mathbf{u}} + \nabla \cdot \mathbb{R}, \tag{3}$$

$$\nabla \cdot \bar{\mathbf{u}} = \nabla \cdot \mathbf{u}' = 0, \tag{4}$$

$$\frac{\partial \mathbf{u}'}{\partial t} + \nabla \cdot (\bar{\mathbf{u}} \otimes \mathbf{u}' + \mathbf{u}' \otimes \bar{\mathbf{u}} + \mathbf{u}' \otimes \mathbf{u}' - \overline{\mathbf{u}' \otimes \mathbf{u}'}) + \nabla \cdot (p_e'/\rho) = \nu\nabla^2\mathbf{u}', \tag{5}$$

$$\frac{\partial k}{\partial t} + \bar{\mathbf{u}} \cdot \nabla k + \nabla \cdot (\overline{\tfrac{1}{2}|\mathbf{u}'|^2\mathbf{u}'} + \overline{(p_e'/\rho)\mathbf{u}'}) = \nu\nabla^2 k + \Phi - \xi, \tag{6}$$

$$k \equiv \tfrac{1}{2}\overline{|\mathbf{u}'|^2} \equiv \tfrac{1}{2} \text{ trace } \mathbb{R}, \tag{7}$$

$$2\bar{\mathbb{D}} = \nabla\bar{\mathbf{u}} + (\nabla\bar{\mathbf{u}})^T, \tag{8}$$

$$\mathbb{R} = -\overline{\mathbf{u}' \otimes \mathbf{u}'}, \tag{9}$$

$$\Phi = \mathbb{R} \cdots \mathbb{D}, \tag{10}$$

$$\xi = \overline{\nu\nabla\mathbf{u}' \cdot\cdot \nabla\mathbf{u}'}, \tag{11}$$

where p_e denotes the excess pressure above hydrostatic, ρ the density, $\mathbb{R}$ the Reynolds stress, $\mathbb{D}$ the deformation rate tensor, and t the time. The symbol $\otimes$ denotes a dyadic product and $\mathbb{A} \cdot\cdot \mathbb{B}$ represents the double contraction of $\mathbb{A}$ and $\mathbb{B}$ defined, in Cartesian components, as $A_{ij}B_{ij}$. The turbulent production Φ is the rate of energy transfer from the averaged motion to the fluctuating motion, and the turbulent dissipation ξ is the rate of energy loss from the fluctuating motion due to viscous dissipation in the small scale eddies. The free surface is defined by the curve $S = 0$ where

$$S = \mathbf{r} \cdot \hat{\mathbf{m}} - d - \eta, \tag{12}$$

and $\mathbf{r}$ denotes position, $\hat{\mathbf{m}}$ a unit vector pointing vertically upwards, and η the height of the surface above mean water level. The surface normal vector $\mathbf{n} = \nabla S$ and a unit tangent sector $\hat{\mathbf{s}}$ satisfies $\mathbf{n}.\ \hat{\mathbf{s}} = 0$. The kinematic free surface conditions on $S = 0$ is written

$$\frac{\partial}{\partial t} S + \bar{\mathbf{u}} \cdot \mathbf{n} = 0. \tag{13}$$

The dynamic surface condition which requires the vanishing of the stress vector on $S = 0$, is written as

$$\mathbf{n}\cdot(\mathbb{R} + 2\nu\bar{\mathbb{D}} - (p_e/\rho)\mathbb{I} + g\eta\mathbb{I}) = \mathbf{0}, \tag{14}$$

where $\mathbb{I}$ denotes a unit tensor. The true pressure is related to the excess pressure p_e and the atmospheric pressure p_a by the relation

$$p = p_a + p_e + \rho g(d - \mathbf{r}\cdot\hat{\mathbf{m}}), \tag{15}$$

which permits the removal of g from the momentum equations (3) and (6). The no slip condition on the bed requires

$$\bar{\mathbf{u}} = \mathbf{u}' = \mathbf{0}. \tag{16}$$

We seek to obtain approximate solutions for the mean flow without resort to calculating $\mathbf{u}'$ and p_e' explicitly, thus expressions for $\overline{\mathbf{u}' \otimes \mathbf{u}'}$, $\overline{\mathbf{u}' \otimes \mathbf{u}' \otimes \mathbf{u}'}$, $\overline{(p_e/\delta)\mathbf{u}'}$ etc. are obtained by manipulation of (5). Unfortunately each expression thus found introduces further, unknown, higher order quantities, and this process extends without end; this is the turbulence closure problem, which to date remains unsolved except in situations with unrealistically high symmetry. Therefore a closure hypothesis is required, and following Launder and Spalding [11] we write, in our notation,

$$\left.\begin{aligned}
&\frac{\partial}{\partial t}(k, \xi) + \bar{\mathbf{u}}\cdot\nabla(k, \xi) = \nabla\cdot((N+\nu)\nabla(\sigma_k^{-1}k, \sigma_\xi^{-1}\xi)) + \left(\Phi - \xi, \frac{\xi}{k}(c_1\Phi - c_2\xi)\right),\\
&\mathbb{R} + \tfrac{2}{3}k\mathbb{I} = 2N\bar{\mathbb{D}},\\
&N = C_\mu k^2/\xi,
\end{aligned}\right\} \tag{17}$$

in which N denotes an eddy viscosity and the empirical constants are $c_\mu = 0.09$, $c_1 = 1.44$, $c_2 = 1.92$, $\sigma_\kappa = 1.0$, $\sigma_\varepsilon = 1.3$. This is based on a gradient diffusion hypothesis and the approximation of the unknown terms in exact equations for k and ξ derived from (6), (7) and (11), see for example Launder, Reece and Rodi [12]. This model has been used to predict a wide range of turbulent shear flows, typical of which are Launder and Spalding [13, 11] and Gosman et al. [14]. Relevant to the present problem is the experimental verification of this model to predict an unsteady turbulent boundary layer in the presence of an oscillating free stream by Cousteix et al. [15] for a Strouhal number, $S_t = \sigma\delta_1/U_0$, of order 10^{-2} and less, where δ_1 is the displacement thickness. Near the bed the turbulence is dominated by the Φ and ξ terms in (7) and is consequently in local equilibrium. Subject to the conditions $u_\tau\Lambda/\nu \geqslant 100$ and $\Lambda/\delta_2 \ll 1$, we can impose the following equations on the surface

$\mathbf{r}\cdot\hat{\mathbf{m}} = y_0$ where $y_0 = 0(\Lambda)$;

$$\bar{\mathbf{u}}\cdot\hat{\mathbf{m}} = 0, \tag{18}$$

$$-\hat{\mathbf{m}}\cdot\mathbb{R}\cdot\hat{\mathbf{u}} = u_\tau^2 = (\tfrac{1}{2}\gamma)|\bar{\mathbf{u}}|\bar{\mathbf{u}}, \tag{19}$$

$$(\tfrac{1}{2}\gamma)^{-1/2} = \frac{1}{\kappa}\ln(y_0/\Lambda) + 8.48, \tag{20}$$

$$(k, \xi) = (0.24^{-1}u_\tau^2, u_\tau^3/\kappa y_0), \tag{21}$$

where von Karmans constant $\kappa = 0.40$, and $\hat{\mathbf{u}}$ is the unit vector of $\bar{\mathbf{U}}$. Equation (20) is due to Nikuradse [16] and the constants in (21) are from Hinze [17] and are used by Launder, Reece and Rodi [12]. The two remaining necessary boundary conditions,

$$\mathbf{n}\cdot\nabla(k, \xi) = (0, 0) \tag{22}$$

are imposed on the surface $S = 0$ and imply no flux of k and ξ over the surface. Henceforth it will be understood that all turbulent variables are to be treated as Reynolds averaged quantities, so the overbar is dropped and it will take on the new definition of averaging over a wave cycle, so that

$$\left.\begin{aligned} \bar{f} &\equiv \frac{1}{T}\int_t^{t+T} f\,\mathrm{d}t, \\ 0 &= \overline{\frac{\partial f}{\partial t}g} + \overline{f\frac{\partial g}{\partial t}} = \overline{\frac{\partial}{\partial t}(fg)} = \frac{1}{T}[fg]_t^{t+T} \end{aligned}\right\} \tag{23}$$

where f and g are periodic functions of t with period T.

Orders of magnitude

We estimate the orders of magnitude of turbulent quantities in a boundary layer of thickness δ_2 by comparing the magnitudes of terms in (3)–(10) and (17) so that, with τ denoting the Reynolds shear stress R_{xy} we find

$$\left.\begin{aligned} \tau &\sim au_0^2 \\ k &\sim abu_0^2 \\ N &\sim au_0\delta_2 \\ \Phi &\sim \xi \sim au_0^3/\delta_2 \\ t_D &\sim k/\xi \sim b\delta_2/u_0 \end{aligned}\right\}, \tag{24}$$

where $b \doteqdot 3$, in agreement with wall turbulence (Hinze [17]). Here a has the interpretation of a friction coefficient which we may estimate using (20) and $\Lambda/y_0 = O(1)$, thus $a \doteqdot 0.01$. Since $a \sim f_w$ the present analysis is centred on $f_w \doteqdot 0.01$. The turbulent kinetic energy can only alter significantly over time scales of order t_D while keeping production and dissipation of comparable magnitude. Thus t_D characterises 'unsteadiness' of the turbulence so that, relative to the time scale $1/\sigma$, the turbulence in the boundary layer is quasi-steady, i.e. in local equilibrium, if $\sigma t_D \ll 1$, and steady state if $\sigma t_D \gg 1$. A typical acceleration is $U_0\sigma = \varepsilon C^2\kappa$, which is required to be comparable to the stress gradient, τ/δ_2, which retards the motion, so noting that $\delta = O(1)$ and using (24) the boundary layer thickness is estimated as $\delta_2/d \sim a\varepsilon \sim f_w\varepsilon$. The ratio of the boundary layer thickness to the wave amplitude of order $f_w \doteqdot 0.01$. We can now rewrite (24) as follows:

$$\left.\begin{aligned} &\tau \sim a\varepsilon^2 C^2 \\ &k \sim ab\varepsilon^2 C^2 \\ &N \sim a^2\varepsilon^2 Cd \\ &\Phi \sim \xi \sim \varepsilon^2 C^3/d \\ &\delta_2 \sim a\varepsilon d \\ &\sigma t_D \sim ab \end{aligned}\right\}, \tag{25}$$

and note that $\sigma t_D \sim 0.03$ indicating unsteady turbulence tending to local equilibrium. We thus expect "unsteadiness' to play a significant but not dominant role. At a distance of order Λ from the bed we use $t_D \sim b\Lambda/U_0$ from (24) with $\Lambda/\delta_2 \ll 1$ to estimate that $\sigma t_D \ll 0.03$. This confirms the existence of a local equilibrium layer of thickness at least of order Λ and justifies the logarithmic wall laws of (18)–(21).

Outside the boundary layer, in the fluid interior and surface boundary layer, the velocity gradients are of order $\varepsilon C/d$, the Reynolds stresses are of order ε^2C^2, the turbulent production Φ and turbulent transport of turbulent kinetic energy k are of order ε^3C^3/d. There is thus no source of energy, either by direct production or by turbulent transport from the bed boundary layer, for the turbulent kinetic energy of order ε^2C^2, which must consequently vanish. Successive application of this argument to higher orders shows, by induction, that the turbulent kinetic energy in the interior vanishes to any order, thus we conclude the interior and surface boundary layer remain laminar. The Strouhal number $S_t = \sigma\delta_1/U_0$ may be estimated using $\delta = O(1)$ and $\delta_1/\delta_2 = O(1)$, thus $S_t = O(f_w)$ and the condition of Cousteix et al. [15] on the experimental verification of (17) is satisfied. The normal velocity just outside the turbulent boundary layer can now be estimated to be of order $\delta_1 U_0/d \doteqdot f_w\varepsilon^2 C$, which is small compared with a typical second order velocity, thus we accept a relative error of order f_w by ignoring the normal velocity and shall take advantage of the resultant mathematical simplifications that follow. The physical basis of this approximation is the one way interaction between the boundary layer and the interior due to the smallness of the boundary layer thickness compared with the wave amplitude. It is well known (see e.g. Lighthill [8]) that the small normal component of velocity just outside the boundary layer determines the wave attenuation by exciting out of phase second order motion in the interior, resulting in a complex frequency or wavenumber. By ignoring this we simplify the analysis but retain the physics of attenuation, using the method of Hunt [19].

Non-dimensional equations

We introduce rectangular cartesian coordinates (x, y, z) fixed with respect to the bed, $y = 0$, with the y axis vertically upwards and the x-axis in the direction of wave propogation. The velocity $\mathbf{u} = (u, v, w)$ is confined to the (x, y) plane so $u = \partial\psi/\partial y$, $v = -\partial\psi/\partial x$, $w = 0$ and the vorticity is $-\nabla^2\psi$ where ψ is the stream function and ∇ the laplacian. Let a set of non-dimensional variables, denoted here by primes, be defined by the transformations

$$\left.\begin{array}{llll} x' = xk, & y' = y/d, & t' = t\sigma, & \eta' = \eta/d, \\ k' = k/C^2, & \xi' = \xi/C^2, & N' = N\sigma/C^2, & \Phi' = \Phi/C^2\sigma, \\ \psi' = \psi/Cd, & p_e' = p_e/C^2, & -D^2\psi' = -\nabla^2\psi\delta/\sigma & \end{array}\right\}, \tag{26}$$

where

$$D^2 \equiv \frac{\partial^2}{\partial y^2} + \delta^2\frac{\partial^2}{\partial x^2}. \tag{27}$$

We shall further need non-dimensional forms of the normal and tangent vectors, and deformation rate tensor, which we define as follows:

$$\mathbb{D}' = \mathbb{D}d/C, \quad \mathbf{n}' = \mathbf{n}/d, \quad \hat{\mathbf{m}}' = \hat{\mathbf{m}}/d, \quad \tilde{\mathbf{s}} = \tilde{\mathbf{s}}/d. \tag{28}$$

Henceforth all primed quantities above will be understood to be non-dimensional quantities, and the primes will be dropped for the sake of clarity.

In non-dimensional variables the governing equations (3), (17), (10) and (9) may now be written

$$\frac{\partial}{\partial t}D^2\psi - \frac{\partial(\psi, D^2\psi)}{\partial(x, y)} = \frac{\alpha}{\delta}D^4\psi + \frac{1}{\delta}\left(\frac{\partial^2}{\partial y^2} - \delta^2\frac{\partial^2}{\partial x^2}\right)R_{xy} + \frac{\partial}{\partial x\,\partial y}(R_{xx}\delta^2 - R_{yy}), \tag{29}$$

$$\frac{\partial k}{\partial t} - \frac{\partial(\psi, k)}{\partial(x, y)} = \frac{1}{\delta}(\sigma_k^{-1}N + \alpha\delta^2)D^2k + \sigma_k^{-1}\left(\frac{\partial N}{\partial x}\frac{\partial k}{\partial x} + \frac{1}{\delta^2}\frac{\partial N}{\partial y}\frac{\partial k}{\partial y}\right) + \Phi - \xi, \tag{30}$$

$$\frac{\partial \xi}{\partial t} - \frac{\partial(\psi, \xi)}{\partial(x, y)} = \frac{1}{\delta}(\sigma_\varepsilon^{-1}N + \alpha\delta^2)D^2\xi + \sigma_\varepsilon^{-1}\left(\frac{\partial N}{\partial x}\frac{\partial \xi}{\partial x} + \frac{1}{\delta^2}\frac{\partial N}{\partial y}\frac{\partial \xi}{\partial y}\right) + \frac{\xi}{k}(c_1\Phi - c_2\xi), \tag{31}$$

where $\alpha(1/\beta d)^2$ the turbulent production Φ and eddy viscosity N are given by

$$\left.\begin{aligned} \Phi &= N\left(\frac{\partial^2\psi}{\partial y^2} - \delta^2\frac{\partial^2\psi}{\partial x^2}\right) + 4N\left(\frac{\partial^2\psi}{\partial x\,\partial y}\right)^2 \\ N &= c_\mu k^2/\xi. \end{aligned}\right\} \tag{32}$$

For 10 s waves on a depth of 5 m $\beta = 1.78$ mm and $\alpha = 1.3 \times 10^{-7}$ The Reynold stress components R_{xx}, $R_{xy} = R_{yx}$ and R_{yy} satisfy

$$\left.\begin{aligned} R_{xy} &= \frac{1}{\delta}(N + \alpha\delta^2)\left(\frac{\partial^2}{\partial y^2} - \delta^2\frac{\partial^2}{\partial x^2}\right)\psi, \\ R_{xx} + \tfrac{2}{3}k &= -\frac{1}{\delta}(N + \alpha\delta^2)\frac{\partial^2\psi}{\partial x\,\partial y}, \\ R_{yy} + \tfrac{2}{3}k &= \frac{1}{\delta}(N + \alpha\delta^2)\frac{\partial^2\psi}{\partial x\,\partial y}. \end{aligned}\right\} \tag{33}$$

The free surface boundary conditions to be evaluated on $y = 1 + \eta(x, t)$ are, with $N = 0$ because the surface layer is laminar,

$$\frac{\partial\eta}{\partial t} + \frac{\partial\psi}{\partial y}\frac{\partial\eta}{\partial x} + \frac{\partial\psi}{\partial x} = 0, \tag{34}$$

$$2\alpha\delta^2\hat{\mathbf{n}}\cdot\mathbb{D}\cdot\hat{\mathbf{n}} - p_e/\rho - (gd/C^2)\eta = 0, \tag{35}$$

$$2\alpha\delta^2\hat{\mathbf{n}}\cdot\mathbb{D}\cdot\hat{\mathbf{s}} = 0, \tag{36}$$

which represent the kinematic condition and the vanishing of the normal and tangential components of the surface stress vector. The near bed boundary conditions evaluated on $y = y_0/d$ are

$$R_{xy} = u_\tau^2 = (\tfrac{1}{2}\gamma)\left|\frac{\partial\psi}{\partial y}\right|\frac{\partial\psi}{\partial y}, \tag{37}$$

$$(k, \xi) = (0.24^{-1}u_\tau^2,\ u_\tau^3 d/xy_0\delta), \tag{38}$$

$$(\tfrac{1}{2}\gamma)^{-1/2} = \frac{1}{x}\ln(\Lambda/y_0) + 8.48, \tag{39}$$

and we replace the tangential velocity condition (18) by putting $\psi = 0$ on $y = 0$ and then evaluating ψ on $y = y_0/d$ by trapezium rule and accept an error of order $\frac{1}{12}y_0\partial^3\psi/\partial y^3$, hence

$$\psi = \tfrac{1}{2}(y_0/d)\frac{\partial\psi}{\partial y} - 0\left(\frac{1}{12}\frac{y_0^3}{d^3}\frac{\partial^3\psi}{\partial y^3}\right). \tag{40}$$

This error is very small because $y_0 \ll \delta_2 \ll d$. The remaining conditions for k, ξ on the surface $S = 0$ are replaced by conditions requiring that there is no flux of k, ξ into the fluid interior, so on $y \gg \delta_2$ we write

$$\frac{\partial k}{\partial y} = 0, \qquad \frac{\partial \xi}{\partial y} = 0. \tag{41}$$

Outer expansions

We now consider the solution in the interior of the fluid, which has been shown to remain laminar. The condition $f_w \ll 1$ allows this solution to be decoupled from the bed boundary layer which we may temporarily ignore.

We expand the solution asymptotically in powers of ε, and ignoring turbulent quantities, write

$$\left.\begin{aligned} \psi &= \varepsilon^2\psi_1 + \varepsilon^3\psi_2 + \cdots, \\ p_e/\rho &= \varepsilon p_1 + \varepsilon^2 p^2 + \cdots, \\ \eta &= \varepsilon\eta_1 + \varepsilon^2\eta_2 + \cdots, \\ c/\sqrt{gd} &= C_0 + \varepsilon C_1 + \cdots. \end{aligned}\right\} \tag{42}$$

Substituting (42) into (29) and collecting equal powers of ε we obtain, from a matching requirement with the turbulent boundary layer section at the bed where Π_A and Π_B are functions only of bed roughness. The solutions, in our notation and where only real parts are implied, are

$$\psi_1 = \frac{\sinh \delta y}{\sinh \delta}\, e^{i\theta}, \tag{43}$$

$$\psi_2 - \bar{\psi}_2 = \frac{3\delta}{4}\,\frac{\sinh 2\delta y}{\sinh^4 \delta}\, e^{i2\theta}, \tag{44}$$

$$\bar{\psi}_2 = \frac{\delta^2}{\sinh^2\delta}\left[\Pi_A y + \frac{3\Pi_B y}{2\sinh^2\delta} - \delta y^2\,\frac{\sinh 2\delta}{2}\right] + \tfrac{1}{6}(y^3 - 3y^2)\varpi\,\frac{2d}{\rho\alpha\varepsilon^2 C^2}, \tag{45}$$

where $\theta = x - t$. The pressure is then determined as

$$p_1 = -\frac{\delta\cosh\delta y}{\sinh\delta}\, e^{i\theta}, \tag{46}$$

$$p_2 = -\frac{\delta^2}{4\sinh^2\delta}\left(1 - 6\,\frac{\cosh 2\delta y}{\sinh^2\delta}\right)e^{i2\theta} - \frac{\delta^2\cosh 2\delta y}{\sinh^2\delta}. \tag{47}$$

The surface elevation is given by

$$\eta_1 = e^{i\theta}, \tag{48}$$

$$\eta_2 = \frac{\delta \cosh \delta}{4 \sinh^3 \delta}(\cosh 2\delta + 2)e^{i2\theta}. \tag{49}$$

The non-dimensional phase velocity $C/\sqrt{gd}$ is given by (42) with

$$C_0 = \left(\frac{\tanh \delta}{\delta}\right)^{1/2}, \qquad C_1 = 0, \tag{50}$$

so that correct to order ε^2 the group velocity $G = \mathrm{d}\sigma/\mathrm{d}\kappa$ is given by

$$G = \tfrac{1}{2}C(1 + 2\delta/\sinh \delta). \tag{51}$$

In the foregoing analysis the second order solution has been split into 2 parts, part A driven by convection of first order solutions and part B driven by Stokes second order wave motion. The fact that these may be obtained independently follows from the linear property of the second perturbation, and it introduces a new Euler drift velocity, $\overline{\partial\psi_2^{(B)}/\partial_y}$, not previously considered in mass transport studies. Since $\overline{\psi_2^{(B)}}$ is driven by a pressure gradient that has a zero mean value, it would vanish in a linear system such as a laminar one or one described by a steady eddy viscosity. It is clear that $\overline{\tau_2^{(B)}} = 0$ and so we can write

$$\overline{N_1}\frac{\partial^2\overline{\Psi_2^{(B)}}}{\partial\zeta^2} + \overline{(N-\overline{N_1})\frac{\partial^2}{\partial\zeta^2}(\Psi_2^{(B)} - \overline{\Psi_2^{(B)}}))} + \overline{N_2^{(B)}\frac{\partial^2\Psi_1}{\partial\zeta^2}} = 0, \tag{52}$$

where we have split the first term into steady and unsteady contributions. It can now be seen that the unsteady part of Ψ_2^B coupled with N_1 may drive $\overline{\Psi_2^B}$ and that second order eddy viscosity N_2^B couples with Ψ_1 to produce a further contribution. Both these effects are new, and cause Euler drift stream function $\overline{\psi_2^B}$ to be non-zero even though the second order mean stress $\overline{\tau_2^B}$ vanishes. The mean stress $\overline{\tau_2^A}$, produced by mean convected first order momentum, is obtained by averaging and noting that $\partial(\partial\Psi_1/\partial\zeta)^2/\mathrm{d}x = 0$. Integrating this with respect to ξ, hence, noting that $\overline{\tau_2^A} \to o$ for large ζ, we obtain

$$\overline{\tau_2^A} = -\overline{\frac{\partial\Psi_1}{\partial x}\frac{\partial\Psi_1}{\partial\zeta}} + \overline{\frac{\partial\Psi_1}{\partial x}\frac{\partial\Psi_1}{\partial\zeta}}\bigg|_{\zeta\to\infty}, \tag{53}$$

and the mean stress $\overline{\tau_2^A}$ on the bed is given by the second term. Equation (53) may be written as

$$\overline{\tau_2^A} = \overline{N_1}\,\frac{\partial^2\overline{\Psi_2^A}}{\partial\zeta^2} + \overline{(N_1-\overline{N_1})\frac{\partial^2}{\partial\zeta^2}(\Psi_2^A-\overline{\Psi_2^A})} + \overline{N_2^A\frac{\partial^2\Psi_1}{\partial\zeta^2}}\,. \tag{54}$$

If N_1 is steady so that $N_1 - \overline{N_1} = 0$ and we set $N_2^A = 0$ we recover the case of Johns [7] for a prescribed eddy viscosity, a function of y only, and if we further set $N_1 = \text{const}$ we recover the Longuet-Higgins [4] solution, equivalent to the laminar solution. In each case $\partial\Psi_2^A/\partial\zeta \to 3/4$ for large ζ. The effect of unsteady N_1 and of $N_2^A \neq o$ will be to modify $\overline{\Psi_2^A}$ relative to previous studies. The effect of the last term in (54) is to reduce the Euler drift velocity by a factor of approximately $\frac{1}{2}$ relative to previous studies so that $\overline{\partial\Psi_2^A/\partial\zeta} \to 3/8$ approximately, for large ζ. This follows because in a fully turbulent flow, where a typical stress is proportional to a typical velocity squared in contrast to the fixed eddy viscosity case, any given velocity perturbation will produce twice the stress caused in a fixed eddy viscosity system. Since (53) gives the stress, it follows that we expect only half the velocity.

3. Mass transport

Following Longuet-Higgins [4], we take the mass transport velocity as the mean migration distance of particles during one wave cycle divided by the wave period. There is no first order mean Euler velocity so that, provided the particle orbits are small compared to the wavelength which requires $\varepsilon \ll 1$, the non-dimensional Lagrangian drift stream function Ψ is related to the non-dimensional Euler stream function ψ by

$$\Psi = \overline{\psi} + \overline{\int \frac{\partial\psi}{\partial y}\,\mathrm{d}t\,\frac{\partial\psi}{\partial x}} + \mathrm{O}(\overline{\psi^3}) + \mathrm{O}(\overline{\psi^4}) + \cdots \tag{55}$$

In terms of outer expansions (42) this is written as

$$\begin{aligned}\Psi &= \varepsilon^2\overline{\psi_2} + \varepsilon^2\overline{\int \frac{\partial\psi_1}{\partial y}\,\mathrm{d}t\,\frac{\partial\psi_1}{\partial x}} + \varepsilon^3\mathrm{O}(\overline{\psi_1^3}, \overline{\psi_1\psi_2}) \\ &\quad + \varepsilon^4\mathrm{O}(\overline{\psi_1^4}, \overline{\psi_1^2\psi_2}, \overline{\psi_2^2}) + \cdots\end{aligned} \tag{56}$$

and in terms of inner expansions it becomes

$$\begin{aligned}\Psi &= \frac{\varepsilon^2\delta^2}{\sinh^3\delta}\overline{\Psi_2^A} + \frac{\varepsilon^2\delta^2}{\sinh^3\delta}\overline{\int \frac{\partial\Psi_1}{\partial\zeta}\,\mathrm{d}t\,\frac{\partial\Psi_1}{\partial x}} \\ &\quad + \frac{3\varepsilon^2\delta^2}{2\sinh^5\delta}\overline{\Psi_2^B} + \varepsilon^3\mathrm{O}(\overline{\Psi_1^3}, \overline{\Psi_1\Psi_2}) + \varepsilon^4\mathrm{O}(\overline{\Psi_1^4}, \overline{\Psi_1^2\Psi_2}, \overline{\Psi_2^2}).\end{aligned} \tag{57}$$

We note that Ψ_1 consists of terms $e^{i\theta}$, $e^{3i\theta}, \ldots$ and Ψ_2 consists of terms in e^0, $e^{i2\theta}$ so that the ε^3 term in (56) vanishes. By similar argument the ε^3 term in (57) also vanishes, thus the next approximation neglected is of order ε^4 in both cases. The mass transport in the interior is evaluated as

$$\Psi = \frac{\varepsilon^2\delta^2}{\sinh^3\delta}\left[\frac{\sinh 2\delta y}{4\delta} + \Pi_A y + \frac{3}{2}\frac{\Pi_B y}{\sinh^2\delta} - \frac{\delta y^2 \sinh 2\delta}{2}\right] + \tfrac{1}{6}(y^3 - 3y^2)\varpi\left(\frac{2d}{\rho\alpha C^2}\right) + O(\varepsilon^4), \tag{58}$$

and the total mass flux m across any vertical surface is thus $\Psi(1)$, which is

$$m = \frac{\varepsilon^2\delta^2}{\sinh^3\delta}\left[\frac{1}{2}\sinh 2\delta\left(\frac{1}{2\delta} - \delta\right) + \Pi_A + \frac{3\Pi_B}{2\sinh^2\delta}\right] - \tfrac{2}{3}\varpi\left(\frac{2d}{\rho\alpha C^2}\right) + O(\varepsilon^4). \tag{59}$$

The mass-transport velocity just outside the boundary layer, on putting $y = 0$, is

$$\frac{\partial\Psi}{\partial y} = \frac{\varepsilon^2\delta^2}{\sinh^2\delta}\left[\frac{1}{2} + \Pi_A + \frac{3\Pi_B}{2\sinh^2\delta}\right] + O(\varepsilon^4). \tag{60}$$

and on putting $\Pi_A = 3/4$ and $\Pi_B = 0$ we recover the results of Longuet-Higgins [4]. To uniquely determine Ψ in the interior, we may put $m = 0$, corresponding to no net mass flux in the x-direction, or put $\varpi = 0$ corresponding to no mean surface slope, typically occurring on an unbounded fluid expanse. Otherwise, we have a relation between m and $\varpi = 0$.

The mass transport in the turbulent boundary layer is evaluated from the Fourier expansions of the inner variables, as

$$\Psi = \frac{\varepsilon^2\delta^2}{\sinh^3\delta}\left[\frac{1}{4}\sum_{n=1}^{M}\frac{d}{d\zeta}(F_{(1)(2n-1)}F^*_{(1)(2n-1)}) + F^A_{(2)(0)} + \frac{3F^B_{(2)(0)}}{2\sinh^2\delta}\right] + O(\varepsilon^4). \tag{61}$$

On using the asymptotic forms of $F_{(1)(2n-1)}$, $F^A_{(2)(0)}$ and $F^B_{(2)(0)}$ for large ζ we note that

$$\frac{1}{4}\sum_{n=1}^{M}\frac{\mathrm{d}}{\mathrm{d}\zeta}(F_{(1)(2n-1)}F^*_{(1)(2n-1)}) \to \tfrac{1}{2}\zeta \tag{62}$$

and differentiating (61) with respect to y, where $y = \varepsilon\zeta/\sinh\delta$, the result smoothly matches (60) outside the boundary layer as required.

The general turbulent expression for the mass transport velocity just outside the boundary layer (not the maximum value which occurs inside the layer) is given by (60) where Π_A and Π_B are functions of the bed roughness, parameterised by a_{i_m}/Λ and hence uniquely related to the friction factor f_w. The presence of fully developed

Table 1. Dependence of the solution on a_{im}/Δ

$\frac{a_{im}}{\Lambda} \times 10^{-3}$	Π_A	Π_B	Re Δ_{11} $\times 10^3$	Im Δ_{11} $\times 10^3$	Re Δ^B_{22} $\times 10^3$	Im Δ^B_{22} $\times 10^3$	f_w $\times 10^3$
5.00	0.378	−0.348	1.16	2.54	0.82	−1.52	5.12
3.33	0.378	−0.348	1.25	2.78	0.87	−1.67	5.63
2.00	0.363	−0.354	1.40	3.15	0.93	−1.87	6.40
1.00	0.363	−0.346	1.65	3.76	1.06	−2.28	7.70
0.50	0.368	−0.349	2.02	4.55	1.25	−2.76	9.40
0.33	0.359	0.354	2.31	5.11	1.39	−3.08	10.64
0.25	0.344	−0.354	2.56	5.57	1.53	−3.37	11.67
0.20	0.329	−0.352	2.79	5.97	1.57	−3.61	12.56
0.125	0.302	−0.326	3.38	6.94	2.08	−4.40	14.77

turbulence in the boundary layer has thus introduced the new third term, which by numerical solution is negative, and has introduced a dependence on a_{im}/Λ and changed Π_A from its laminar value, as given in Table 1. We note also that the result (60) is independent of the pressure gradient ϖ and hence m.

4. Wave attenuation

The attenuation is calculated by a method similar to that of Hunt [19] in which the spatial gradient of the mean wave energy flux is related to the mean energy dissipation in the turbulent boundary layer. The resulting energy equation integrates to yield the attenuation function. We shall suppose that the amplitude, and hence ε, varies slowly with x, and that only turbulent dissipation of energy is significant. The expression for the mean energy flux appropriate to finite amplitude waves is the one used by Longuet-Higgins [20], and the mean energy dissipation follows by integrating Φ over the boundary layer. In non-dimensional variables the resulting energy equation is

$$\delta C^3 \frac{\partial}{\partial x} \overline{\int_0^{1+\eta} \left(\frac{\partial \psi}{\partial y}\right)^2 \mathrm{d}y} + \delta C^3 \int_0^1 \overline{\Phi}\, \mathrm{d}y = 0, \tag{63}$$

where the δC^3 cancel out.

The first term is evaluated using the outer expansions and, after writing the integral as a Taylor series about $y = 1$, is given by

$$\frac{\partial}{\partial x} \overline{\int_0^{1+\eta} \left(\frac{\partial \psi}{\partial y}\right)^2 \mathrm{d}y} = \frac{\partial}{\partial x}\left(\varepsilon^2 \int_0^1 \overline{\left(\frac{\partial \psi_1}{\partial y}\right)^2} \mathrm{d}y + \varepsilon^3 \int_0^1 2\overline{\frac{\partial \psi_1}{\partial y}\frac{\partial \psi_2}{\partial y}}\, \mathrm{d}y \right.$$
$$\left. + \varepsilon^3 \overline{\eta_1 \left(\frac{\partial \psi_1}{\partial y}\right)^2}\right) + \mathrm{O}(\varepsilon^4). \tag{64}$$

Since ψ_1 and η_1 consists of terms in $e^{i\theta}$ and ψ_2 consists of terms in e^0 and $e^{i2\theta}$, the only non-zero term on the right-hand side is the first. Thus the mean wave energy flux is independent, correct to order ε^3, of the effects of finite amplitude and second order drift velocity. Hence we have

$$\frac{\partial}{\partial x}\int_0^{1+\eta}\left(\frac{\partial\psi}{\partial y}\right)^2 \mathrm{d}y = \frac{1}{4}\frac{\delta}{\tanh\delta}\left(1+\frac{2\delta}{\sinh 2\delta}\right)\frac{\partial(\varepsilon^2)}{\partial x} + O(\varepsilon^4). \tag{65}$$

The right-hand term of (55) may be written in terms of inner variables and numerically integrated over the boundary layer, however this integral may be related to the displacement thickness Δ_{11} as follows.

The equation for kinetic energy conservation in a general incompressible fluid motion is,

$$\frac{\partial}{\partial t}(\tfrac{1}{2}|\mathbf{u}|^2) + \nabla\cdot(\tfrac{1}{2}|\mathbf{u}|^2\mathbf{u}) + \Phi = \nabla\cdot(\mathbb{R}\cdot\mathbf{u} - (p_e/\rho)\mathbf{u}), \tag{66}$$

where $\mathbb{R}$ denotes the Reynolds stress tensor, ignoring viscous stress, and $\mathbf{u}$ is the Reynolds averaged velocity. Written in non-dimensional variables and averaged over a period this becomes

$$\begin{aligned}&\overline{\frac{\partial}{\partial t}\left(\frac{1}{2}q^2\right)} + \overline{\frac{\partial}{\partial x}\left(\frac{\partial\psi}{\partial y}\frac{q^2}{2} + \frac{\partial\psi}{\partial y}\left(\frac{p_e}{\rho} - R_{xx}\right) + \frac{\partial\psi}{\partial x}R_{xy}\right)}\\ &\quad + \overline{\frac{\partial}{\partial y}\left(-\frac{\partial\psi}{\partial x}\frac{q^2}{2} - \frac{\partial\psi}{\partial x}\left(\frac{p_e}{\rho} - R_{yy}\right) - \frac{\partial\psi}{\partial y}R_{xy}\right)} + \overline{\Phi} = 0\end{aligned} \tag{67}$$

where $q^2 = (\partial\psi/\partial x)^2 + (\partial\psi/\partial y)^2$.

The first and second terms vanish due to periodicity, and integrating from $y = 0$, where $\partial\psi/\partial x = \partial\psi/\partial y = 0$, to a point y_{inf} just outside the boundary layer, where $R_{xy} \to 0$ and $R_{yy} \to 0$, we find

$$\int_0^{y_{\mathrm{inf}}}\overline{\Phi}\,\mathrm{d}y = \overline{\frac{\partial\psi}{\partial x}\left(\frac{1}{2}q^2 + \frac{p_e}{\rho}\right)}\Bigg|_{y=y_{\mathrm{inf}}}. \tag{68}$$

Since the motion at y_{inf} is irrotational, the pressure satisfies a Bernoulli equation, so that

$$\int_0^{y_{\mathrm{inf}}}\overline{\Phi}\,\mathrm{d}y = \overline{\left(\frac{\partial\psi}{\partial x}\frac{\partial\psi}{\partial y}\right)}_{y=y_{\mathrm{inf}}}. \tag{69}$$

In terms of inner variables this becomes

$$\int_0^{y_{\mathrm{inf}}} \Phi\,\mathrm{d}y = \frac{\varepsilon^2\delta^2}{\sinh^3\delta}\left[\frac{\partial\Psi_1}{\partial x}\frac{\partial\Psi_1}{\partial\zeta} + \frac{\varepsilon\delta}{\sinh\delta}\left(\frac{\partial\Psi_1}{\partial x}\frac{\partial\Psi_2^A}{\partial\zeta} + \frac{\partial\Psi_2^A}{\partial x}\frac{\partial\Psi_1}{\partial\zeta}\right)\right.$$
$$\left. + \frac{3\varepsilon\delta}{2\sinh^3\delta}\left(\frac{\partial\Psi_1}{\partial x}\frac{\partial\Psi_2^B}{\partial\zeta} + \frac{\partial\Psi_2^B}{\partial x}\frac{\partial\Psi_1}{\partial\zeta}\right) + \mathrm{O}(\varepsilon^2)\right]_{\zeta=\zeta_{\mathrm{inf}}}, \tag{70}$$

and noting that ψ_1 consists of odd terms in $e^{i\theta}$, $e^{i3\theta}$ etc., and that Ψ_2^A and Ψ_2^B consists of even terms in e^0, $e^{i2\theta}$ etc. the last two terms vanish. Thus, correct to order ε^4, the mean energy dissipation is given by the first term which is also equal to the mean bed stress $\overline{\tau_2^A}(\zeta_0)$. The asymptotic forms valid for large ζ give this term as

$$\overline{\frac{\partial\Psi_1}{\partial x}\frac{\partial\Psi_1}{\partial\zeta}} = \tfrac{1}{2}\mathrm{Im}(\Delta_{11}), \tag{71}$$

equal to half the imaginary part of the first order displacement thickness Δ_{11} which is tabulated in Table 1 for various values of a_{im}/Λ. Correct to order ε^4 the mean energy dissipation is given by

$$\int_0^{y_{\mathrm{inf}}} \overline{\Phi}\,\mathrm{d}y = \frac{\varepsilon^2\delta^2}{2\sinh^3\delta}\,\mathrm{Im}(\Delta_{11}) + \mathrm{O}(\varepsilon^5), \tag{72}$$

and we note this is of order ε^3 as distinct from the laminar case of order ε^2.

The complete energy equation (63) after differentiating (ε^2) in (65) and substituting (72), is

$$\frac{1}{\varepsilon^2}\frac{\partial\varepsilon}{\partial x} + \frac{2\delta\,\mathrm{Im}(\Delta_{11})}{\sinh\delta(\sinh 2\delta + 2\delta)} = 0 + \mathrm{O}(\varepsilon^2), \tag{73}$$

which integrates to give the inverse algebraic attenuation of

$$\frac{1}{\varepsilon(x_2)} - \frac{1}{\varepsilon(x_1)} = \frac{2\delta\,\mathrm{Im}(\Delta_{11})}{\sinh\delta(\sinh 2\delta + 2\delta)}(x_2 - x_1), \tag{74}$$

where x_1 and x_2 are any two points on the x-axis and $\varepsilon(x_1)$, $\varepsilon(x_2)$ are the relative amplitudes at those points. This can be case in the form of temporal attenuation by replacing $\partial/\partial x$ by $C/G(\partial/\partial t)$, because energy propogates at the group velocity G, and hence obtaining

$$\frac{1}{\varepsilon(t_2)} - \frac{1}{\varepsilon(t_1)} = \frac{\delta\,\mathrm{Im}(\Delta_{11})}{\sinh\delta\,\sinh 2\delta}(t_2 - t_1). \tag{75}$$

The attenuation decreases with increasing δ, and the non-dimensional variables x, t increase by 2π for each wave cycle. The inverse algebraic nature of the attenuation is a direct consequence of total energy dissipation being of order ε^3.

The expression for temporal attenuation (75) is in agreement with Lighthill [18] where the attenuation of a wave motion by a boundary layer is determined by the imaginary part of the displacement thickness $\mathrm{Im}(\delta_1)$ so that

$$\frac{1}{\varepsilon}\frac{\mathrm{d}\varepsilon}{\mathrm{d}t} = \frac{\delta}{\sinh 2\delta}\,\mathrm{Im}\left(\frac{\delta_1}{d}\right). \tag{76}$$

The laminar result follows if $\mathrm{Im}(\delta 1/d) = (2\nu/\sigma)^{1/2}/d$ and the turbulent result (75) follows if $\mathrm{Im}(\delta_1/d) = \varepsilon\,\mathrm{Im}(\Delta_{11})\sinh\delta$.

The boundary layer thickness is proportional to the friction factor f_w, by (25) with $a \sim f_w$, so that $\mathrm{Im}(\Delta_{11}) = 2m_e f_w$ where m_e is a constant which by Table 1, equals 0.24. If this result is compared with the turbulent wave attenuation expression of Putnam and Johnson [21], derived by assuming that the total energy dissipation is due to the bed velocity of an irrotational wave doing work against a bed stress satisfying the quadratic friction law, then we find that

$$\tfrac{1}{2}\mathrm{Im}(\Delta_{11}) = m_e f_w = \frac{2}{3\pi}c_f. \tag{77}$$

The coefficient of friction c_f in the Putnam and Johnson [21] formula is usually taken to be equal to f_w, hence $m_e = 2/3\pi \doteqdot 0.212$, and f_w is determined from an extensive empirical literature relating f_w to a range of bed properties, see for example, Riedel et al. [22] and Kamphuis [23]. Finally, to facilitate comparisons of mean energy dissipation E_m in a turbulent boundary layer inferred by direct measurement, by wave attenuation studies, and by numerical studies, we note that

$$\frac{E_m}{\rho} = \left[\frac{\delta\varepsilon C}{\sinh\delta}\right]^3 \tfrac{1}{2}\,\mathrm{Im}(\Delta_{11}), \tag{78}$$

where the expression in square brackets is the velocity just outside the boundary layer and ρ is the fluid density.

5. Discussion

The numerical solution for $a_{im}/\Lambda = 10^3$ is presented in Figs 2–8 and for reasons of clarity, only solutions up to and including the fourth harmonic are displayed. Figure 2 shows the mass transport velocity functions $F'^{B}_{(2)(0)}$, $F'^{A}_{(2)(0)}$, the Stokes drift velocity, and the result of putting $N_1 = \overline{N_1}$ and $N_2 = 0$ which gives the Euler contribution, according to Longuet-Higgins [6]. For large ζ the functions $F'^{A}_{(2)(0)}$ and $F'^{B}_{(2)(0)}$ tend

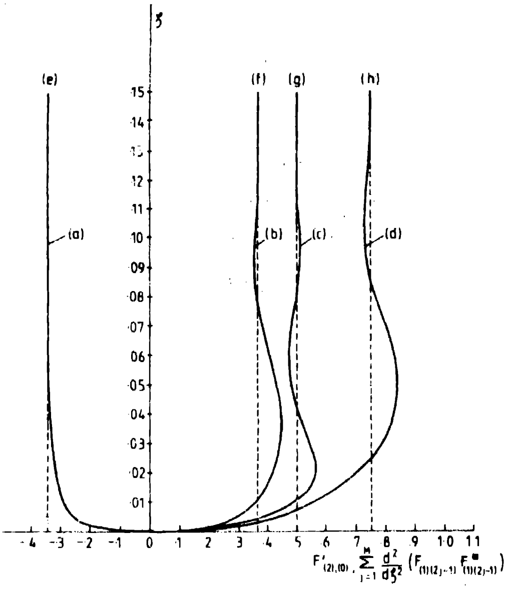

Fig. 2. Mass transport velocity functions and asymptotes for $a_{im}/\Lambda = 10^3$: (a) $F'^{B}_{(2)(0)}$, (b) $F'^{A}_{(2)(0)}$, (c) Stokes drift $\Sigma_{j=1}^{M} d^2/(d\zeta^2)F_{(1)(2j-1)}F^*_{(1)(2j-1)}$, (d) Longuet-Higgins solution obtained by using $N_1 = \overline{N}_1$ and $N_2 = 0$, – – – – asymptotes as $\zeta \to \infty$ equal to (e) −0.34.6, (f) 0.365, (g) 0.50, (h) 0.75.

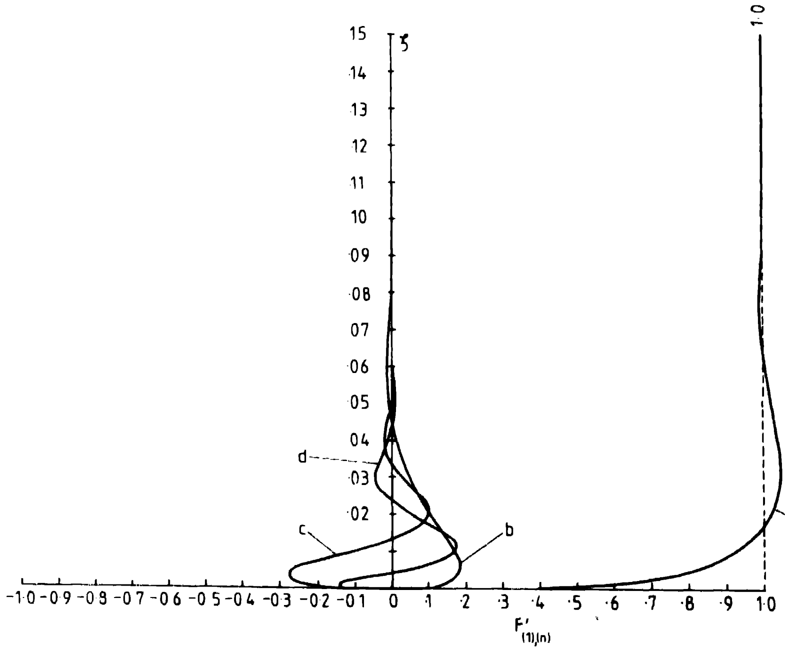

Fig. 3. First order velocity functions and asymptotes for $a_{im}/\Lambda = 10^3$ (a) Re $F'_{(1)(1)}$, (b) Im $F'_{(1)(1)}$, (c) Re $F'_{(1)(3)} \times 10$, (d) Im $F'_{(1)(3)} \times 10$.

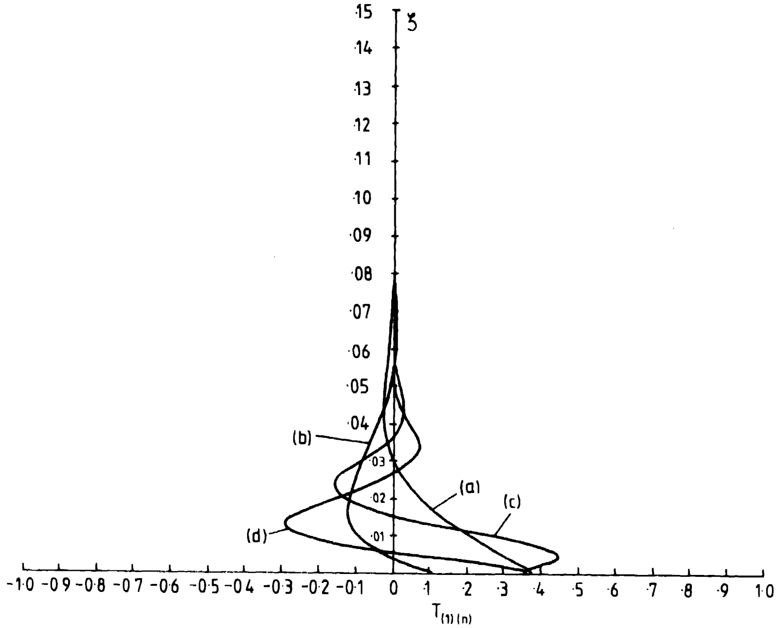

Fig. 4. First order Reynolds stress functions for $a_{im}/\Lambda = 10^3$: (a) Re $\tau_{(1)(1)} \times 10^2$, (b) Im $\tau_{(1)(1)} \times 10^2$, (c) Re $\tau_{(1)(3)} \times 10^3$, (d) Im $\tau_{(1)(3)} \times 10^3$.

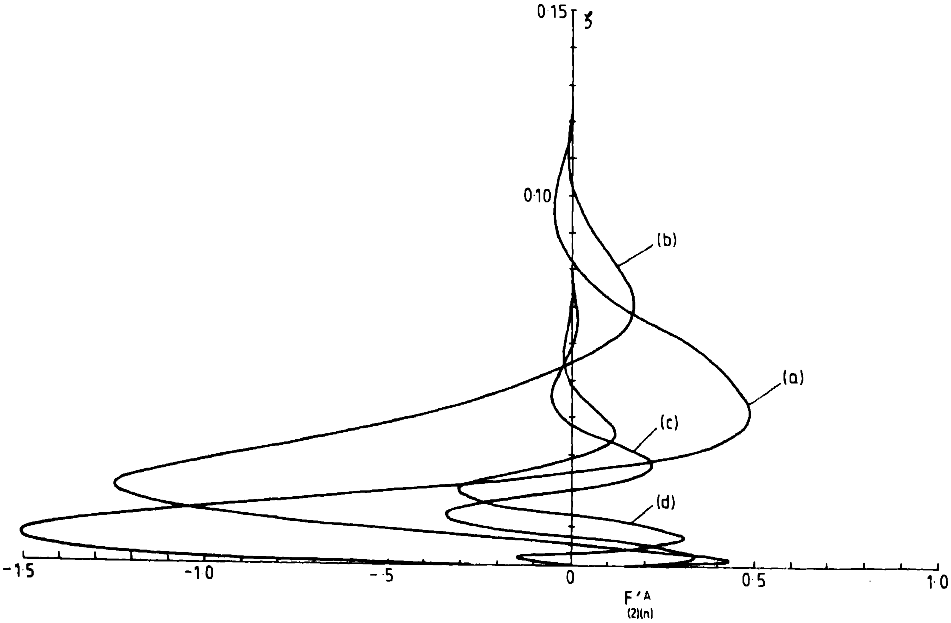

Fig. 5. Second order (A) unsteady velocity functions for $a_{im}/\Lambda = 10^3$: (a) Re $F'^{A}_{(2)(2)} \times 10$, (b) Im $F'^{A}_{(2)(2)} \times 10$, (c) Re $F'^{A}_{(2)(4)} \times 10$, (d) Im $F'^{A}_{(2)(4)} \times 10$.

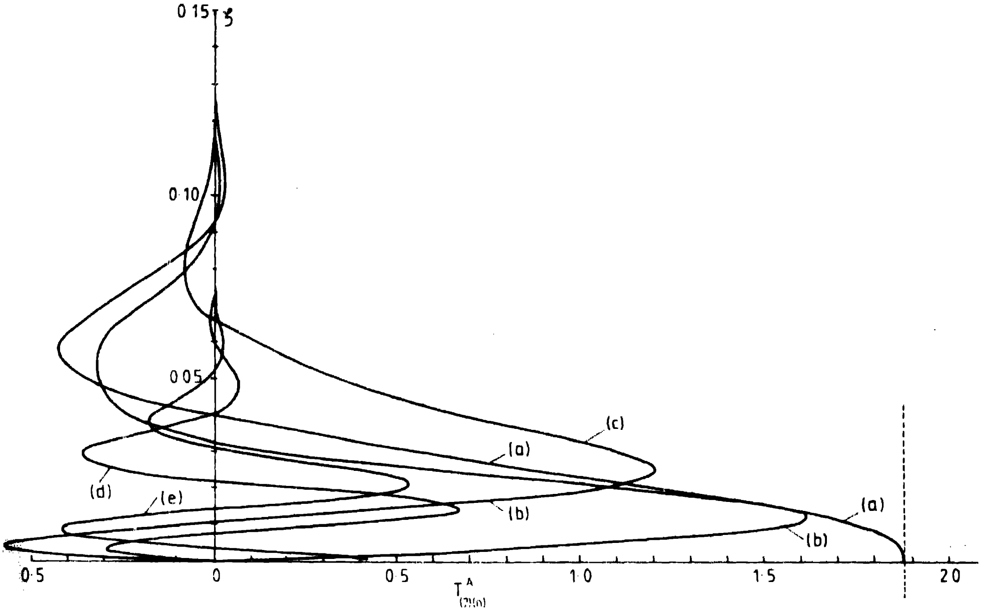

Fig. 6. Second order (*A*) Reynolds stress for $a_{im}/\Lambda = 10^3$: (a) Re $\tau^A_{(2)(0)} \times 10^2$, (b) Re $\tau^A_{(2)(2)} \times 10^3$, (c) Im $\tau^A_{(2)(2)} \times 10^3$, (d) Re $\tau^A_{(2)(4)} \times 10^3$, (e) Im $\tau^A_{(2)(4)} \times 10^3$, - - - - - asymptote of $\tau^A_{(2)(0)} \times 10^3$ as, $\zeta \to \infty$ equal to 0.00188.

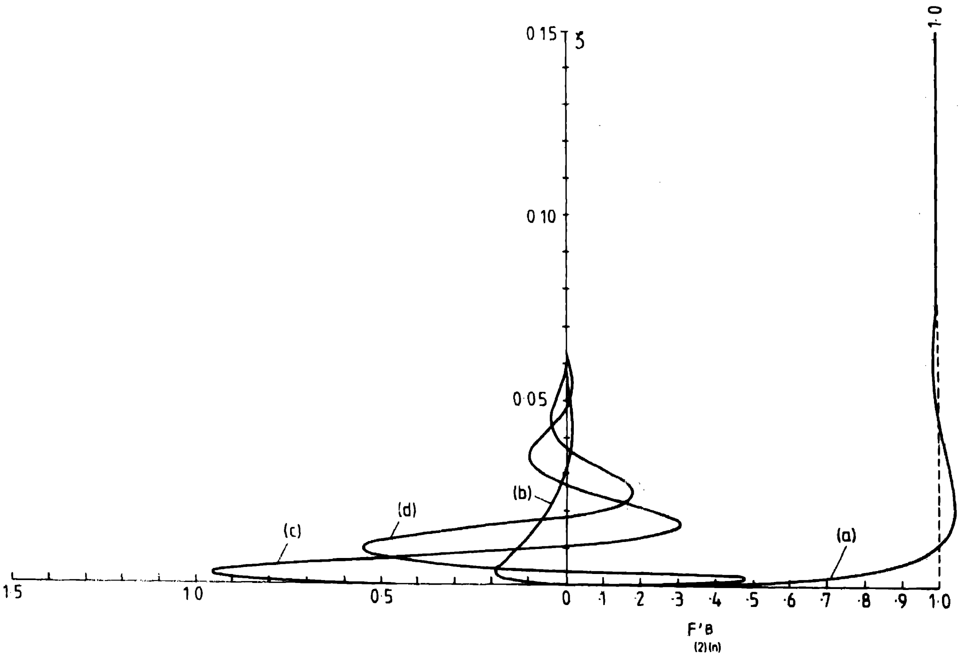

Fig. 7. Second order (*B*) unsteady velocity functions for $a_{im}/\Lambda = 10^3$: (a) Re $F'^B_{(2)(2)}$, (b) Im $F'^B_{(2)(2)}$, (c) Re $F'^B_{(2)(4)} \times 10$, (d) Im $F'^B_{(2)(4)} \times 10$.

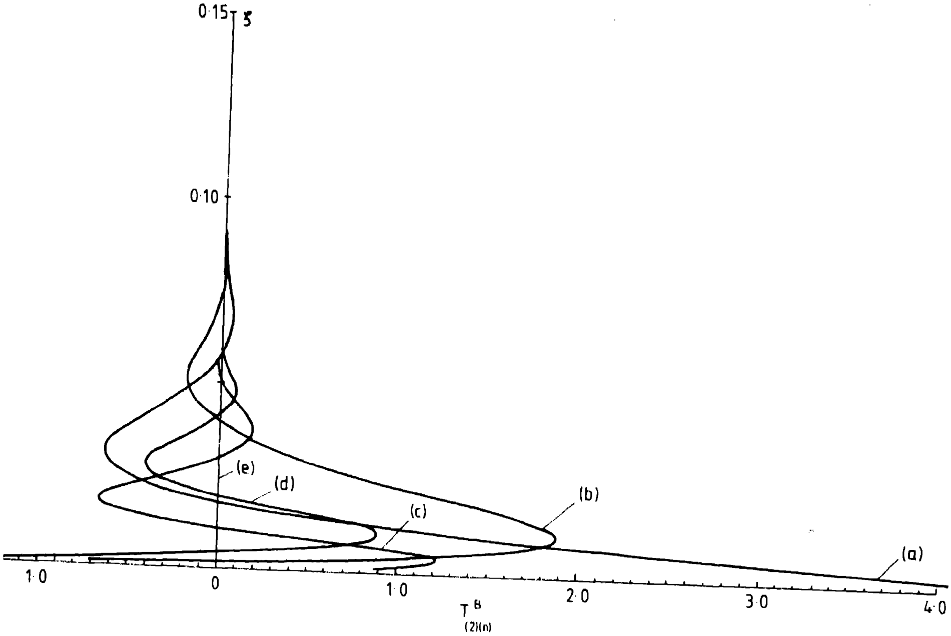

Fig. 8. Second order (B) Reynolds stress for $a_{im}/\Lambda = 10^3$: (a) Re $\tau^B_{(2)(2)} \times 10^3$, (b) Im $\tau^B_{(2)(2)} \times 10^3$, (c) Re $\tau^B_{(2)(4)} \times 10^3$, (d) Im $\tau^B_{(2)(4)} \times 10^3$ and $\tau^B_{(2)(0)} = 0$.

rapidly to constants equal to 0.365 and -0.346 respectively; the Stokes drift contribution tends to 0.5, equal to the theoretical value obtained just outside the boundary layer; and the Euler drift corresponding to a time-independent eddy viscosity tends to 0.75, equal to the theoretical value obtained by Longuet-Higgins [6]. The effect of including the mode coupling interactions in the calculation, equivalent to dropping the conditions $N_1 = \overline{N_1}$ and $N_2 = 0$, is to reduce the Euler drift velocity just outside the boundary layer, due to convected first order momentum, by a factor of approximately one half in agreement with the arguments presented before concerning the square law nature of the turbulent stress. In addition, the second order Stokes wave motion makes a contribution to the Euler drift velocity through the function $F'^B_{(2)(0)}$ which is negative and hence reduces and reverses the total drift velocity as the relative depth parameter δ is reduced. The results $F'^B_{(2)(0)} \neq 0$ and $\tau^B_{(2)(0)} = 0$ are mutually consistent because the second order stresses are not proportional to the second order velocity gradients when the mode coupling interactions are present; in the Longuet-Higgins [6] theory, and in the laminar case, the result $\tau^B_{(2)(0)} = 0$ demands that $F'^B_{(2)(0)} = 0$.

The unsteady part of the boundary layer motion consists of the real part, in phase with the external flow, and the imaginary part which lags by $\pi/2$ radians. The velocity maxima and minima correspond to inflection points on the stress curves, the maxima and minima of which correspond to points where the velocity curves intersect with their respective asymptotes. As expected the higher harmonic modes oscillate and decay away from the bed more rapidly than lower modes.

In Fig. 3 the imaginary part of the first order velocity of the fundamental mode, $\mathrm{Im}\, F'_{(1)(1)}$, is predominantly positive and thus lags $\pi/2$ radians behind the external flow, and contributed work against the pressure force. The area under this curve is equal to $\mathrm{Im}\, \Delta_{11}$ and is proportional to the energy dissipation correct to $O(\varepsilon^3)$ in the boundary layer. In Fig. 7 the function $\mathrm{Im}\, F'^{B}_{(2)(2)}$ is predominantly negative, thus leading the external flow by $\pi/2$. This is quite opposite to the laminar behaviour and is due to the non-proportionality between the second order stress and the second order velocity gradient. In Fig. 6 the mean stress $\tau^{A}_{(2)(0)}$ has a value at the bed of 0.00188, which by equations (53) and (71) is equal to $\frac{1}{2}\mathrm{Im}\, \Delta_{11}$. The stress $\tau^{B}_{(2)(0)}$ in Fig. 8 vanishes because there is no mean forcing by the Stokes second order wave term.

The solutions for other values of a_{im}/Λ are very similar to those discussed above; the trend is for increasing boundary layer thickness for increasing a_{im}/Λ, as indicated in Table 1. The values of Π_A and Π_B show a very weak dependence on the parameter a_{im}/Λ. The friction factor f_w is taken to be equal to $2(\tau_{(1)(1)}\tau^{*}_{(1)(1)})^{1/2}$, thus ignoring the much smaller higher harmonics, and the relation between f_w and a_{im}/Λ is shown in Fig. 10.

The solutions are relatively insensitive to the value of the constants in the turbulence model, such that over the range of values that could reasonably be adopted the solutions varied only by a few percent. This property of insensitivity to the disposable constants in the turbulence model also appears in the calculations of Kajiura [24], Brevik [25] and Dag Myrhaug [26].

The origin of the new Euler contribution to the mass transport in a turbulent oscillating boundary layer is related to the non-linear nature of the turbulent stress, and the consequent appearance of mode coupling interactions between quantities at the same level of approximation. Thus in the second order boundary layer approximation there are forcing terms proportional to $\delta^2/\sinh^2 \delta$ due to convected first order momentum, and forcing terms proportional to $\delta^2/\sinh^4 \delta$ due to the second order Stokes wave motion. Since energy may be exchanged between the second order modes of oscillation of the boundary layer, the mean motion will be described by a linear combination of the two above mentioned terms; the transformations used for the inner equations are thus characteristic of non-linearity in a boundary layer driven by Stokes waves, and are unrelated to the particular turbulence model adopted. Two important conclusions follow; (i) the mass transport velocity outside a boundary layer possessing a non-linear constitutive relation will be given by an equation of the form (60) with Π_A and Π_B chosen appropriately and (ii) any turbulence model which fails to support mode coupling interactions is inappropriate for use in mass transport studies in which second order wave motions occur. This last conclusion applies to the linearised calculations of Longuet-Higgins [6], Johns [7] and Noda [8], in which a time-dependent eddy viscosity formulation was used.

6. Comparison with experiment

Friction factors relating to oscillatory turbulent boundary layers over rough beds have been measured by Riedel, Kamphius and Brebner [22], subsequently reanalysed and corrected by Kamphius [23] and by Jonsson and Carlsen [27]. These results are shown in Fig. 9, expressed as the relation between f_w and a_{im}/Λ, together with the measurements of Bagnold [28], the semi-theoretical relation of Kajiura [24] and the empirical curve of Jonsson [29]. The results of the present analysis are included for the range $10^2 \leqslant a_{im}/\Lambda \leqslant 10^3$. The agreement is good, and this is insensitive to variations of the model constants.

The dissipation of energy in the bed boundary layer is related to the friction factor f_w, and the area under the imaginary part of the first order velocity curve given by $\text{Im}\,\Delta_{11}$ through the equations (77) and (78). The Putnam and Johnson [21] expression for the attenuation is obtained by putting m_e equal to $2/3\pi$, i.e. $m_e = 0.212$. However this result depends on the assumption made about the bed stress; if the instantaneous stress and velocity are related by the friction law, then $m_e = 2/3\sqrt{\pi}$; if the stress and velocity are sinusoidal with a relative phase difference of ϕ, then $m_e = \cos\phi$. The values of m_e obtained from Table 1 using the relation $m_e = \text{Im}\,\Delta_{11}/2f_w$ lie in the range 0.235 for $a_{im}/\Lambda = 125$ to 0.248 for $a_{im}/\Lambda = 5000$. The value of m_e determined by Jonsson [29] from the experimental data of Jonsson and Carlsen [27] is 0.21 for $a_{im}/\Lambda = 124$. The results of the present analysis concerning the wave attenuation and energy dissipation are thus in broad agreement with experimental observations and with field measurements and engineering practice as outlined by Hsiao and Shemdin [30]. Sleath [31, 32] and Justesen [33] have recently reported such comparisons.

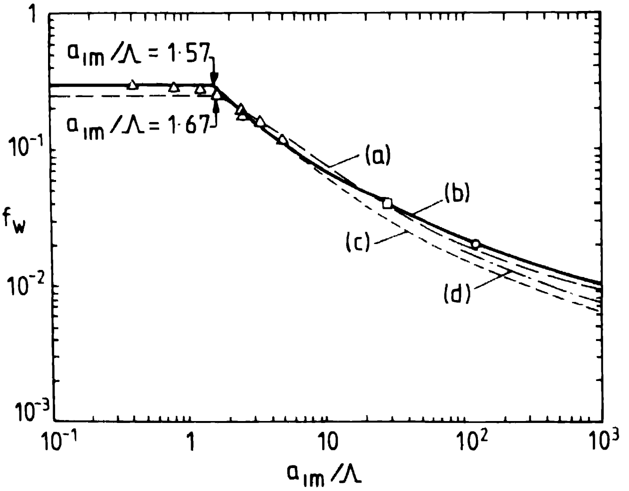

Fig. 9. Comparison of friction factors: (a) ——— Kajiura (1968, theoretical), (b) ——— Jonsson (1980, semiempirical), (c) ----- Kamphius (1975, experimental), (d) — — — — present authors and △ Bagnold (1946, experimental). 0, □ Jonsson and Carlsen (1976) experimental tests No. 1 and No. 2 respectively.

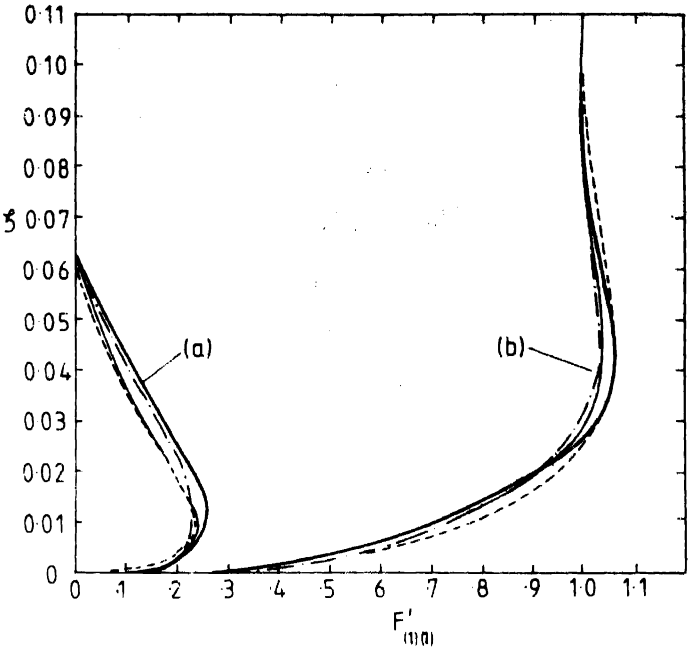

Fig. 10. Comparison of theory with experiment for first order velocity in the boundary layer for $a_{im}/\Lambda = 10^3$: (a) imaginary part, (b) real part; ––– Jonsson and Carlsen (1976) stretched by $\pi/2$, –·–·– Brevik (1981). Dag Myrhaug (1982), ----- Present authors.

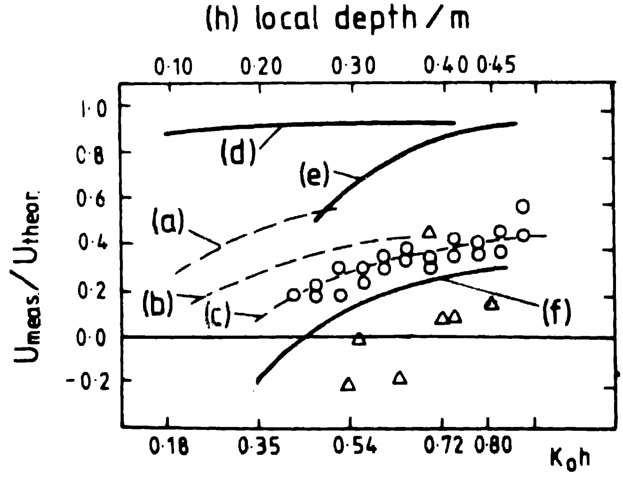

Fig. 11. Mass transport on a sloping beach. (h is the local depth and K_0 is the initial wavenumber, the initial depth is 0.45 m and to the right): (a) $\varepsilon = 0.045$ smooth bed, (b) $\varepsilon = 0.1$ smooth bed, (c) $\varepsilon = 0.178$ smooth bed, showing experimental data denoted o, (d) $\varepsilon = 0.178$ laminar prediction using Longuet-Higgins (1953) theory, (e) $\varepsilon = 0.178$ laminar prediction including influence of local second harmonics by Bijker (1974), (f) $\varepsilon = 0.178$ turbulent prediction by present authors with $\Pi_A = 0.37$ and $\Pi_B = -0.35$ ($\delta_{crit} = 0.71$); $\Delta\varepsilon = 0.178$ rippled bed measurements, Bijker (1974).

The first order oscillatory velocity profile is plotted in Fig. 10 for $a_{im}/\Lambda = 124$, so as to correspond to test No. 1 of Jonsson and Carlsen [27]. Also included are the theoretical results of Brevik [25] and Dag Myrhaug [26] which relate to this experiment. The experiment was performed using a U-tube oscillator with a 10-m long observation section which was 30 cm high and 40 cm wide. The bed profile was of a saw-tooth shape of amplitude 3 mm and wave number 0.37 mm^{-1}, and the viscosity was measured above a trough. The driving mechanisms introduced second harmonic motion, thus breaking the half wave symmetry by about 10%. The velocity measurements were made using a micro-propeller at 24 points within each cycle, and these values were averaged over 50 cycles. The stress was determined by numerical integration of the measured velocity field. The relevant parameters are; period = 8.39; $a_{im} = 285$ cm; $1/\beta = 1.63$ mm; $\beta\Lambda = 4$; $R = 4400$; $S_t = 0.028$ (based on a 8-cm length); $f_w = 0.0193$; $a_{im}/\Lambda = 124$. There is a good concensus amongst the theoretical results including the present analysis, but the experimental boundary layer thickness is over predicted by 57%. This point is less clear in the work of Brevik [25] and Dag Myrhaug [26] because a logarithmic scale is used to make the comparison.

Considering the experiment more closely, we note that the energy dissipation reported implies $m_e f_w = 0.0040$, whereas a measurement of the area under the out-of-phase velocity component, taken from the published profile, gives approximately $\operatorname{Im}\Delta_{11} = 0.0046$, i.e. $m_e f_w = 0.0023$. There is thus some inconsistency in the experiment, and it is interesting to note that if the experimental profile is stretched by a factor of $\pi/2$, then the result, plotted in Fig. 10, shows good agreement with the theoretical calculations. There is a possibility that the experiment contains a flaw. The present analysis gives $\operatorname{Im}\Delta_{11} = 0.00694$, $m_e f_w = 0.00347$ for $a_{im}/\Lambda = 124$.

The principle difference between the present theory and that of Longuet-Higgins [6] is the reduction and reversal of the streaming velocity for small values of the relative depth parameter. Reversed flow occurs just outside the boundary layer when $\delta < \delta_{\text{crit}}$, where

$$\delta_{\text{crit}} = \sinh^{-1}\left(\frac{-3\Pi_B}{2 + 4\Pi_A}\right)^{1/2}. \tag{79}$$

Since the drift velocities converge on the reversal point, we can expect the formation of sand bars on a shoaling beach in the vicinity of δ equal to δ_{crit}. This reversal behaviour is found in the experiments of Bijker, Kalkijk and Pieters [5] with which we shall compare our results. Measurements were made at 20 stations in a 32-m long wave tank of width 0.8 m and depth 0.6 m on beaches with slopes of 1:10, 1:25 and 1:40. The bottom textures investigated were smooth concrete, glued sand grains of diameter between 1.6 mm and 2.0 mm and artificial ripples of amplitude 9 mm and wave number 0.0785 mm^{-1}. Prior to encountering the beach, on a depth of 0.45 m, the waves have a value of δ of O(1) and relative amplitudes of ε equal to 0.045, 0.10, 0.178. The measured streaming velocity just outside the boundary layer, made non-dimensional by dividing by the Longuet-Higgins prediction based on local wave parameters, is shown in Fig. 11 for various cases. The horizontal axis h measures the initial wavenumber multiplied by the local depth at various points on the beach. The curves (a), (b) and (c) are averages for smooth beds for increasing values of ε; the slope dependence was very small. The curves for the rippled bed and relative amplitude of $\varepsilon = 0.178$ are also plotted; (d) represents the Longuet-Higgins [6] prediction; (e) represents the same theory but modified by Bijker et al. [5] to include the effects of local higher harmonics; (f) represents the present theory; the experimental points are depicted by the symbol Δ, and show much scatter especially at the confluence of the two opposing flows. In applying the present theory the local value of δ was calculated using linear wave theory and the values $\Pi_A = 0.37$, $\Pi_B = -0.35$ and hence $\delta_{crit} = 0.53$, were used. For the smooth bed the Reynolds number, based on the length β^{-1}, is of the order 10^2, increasing up the slope, while the value of $\beta\Lambda$ is approximately 180. This last figure is outside the range of Sleath's formula (1), but since the flow would be turbulent for smaller $\beta\Lambda$, we shall suppose the present theory to be applicable. The curve (f) falls between the curve (c) for the smooth bed and the results for the rippled bed; since the present calculation has been made for moderately rough beds, this represents reasonably good agreement, especially when the curves (d) and (e) for the Longuet-Higgins theory are considered. The results for the sand rough bed were not fully reported, although the authors state that these followed similar tendencies to those of the smooth case, but with the velocities at the bottom being somewhat smaller. Although this comparison does not provide conclusive verification of the present theory, this will require more experimental observations under conditions for which the theory is properly applicable, it does indicate that the theory is basically sound, and that mode coupling interactions do play an important role in turbulent boundary layers.

Conclusions

The motion of turbulent Stokes waves on a finite constant depth of fluid with a rough bed has been considered. The turbulence is found to be confined to a thin layer near the bed and the interior and surface boundary layer remain laminar. The attenuation is found to be of inverse algebraic type, where the reciprocal wave height varies linearly with either distance or time, and is in quantitative agreement with semi-empirical prediction methods and experimental observations. The mass transport velocity in the interior satisfies an equation similar to that found by Longuet-Higgins [4] for laminar motion, but modified due to the presence of turbulence in the boundary layer. We have considered the effects of coupling interactions between different second order Fourier modes of oscillation of the boundary layer, which arise due to the non-linear nature of turbulence, and we have identified a new mechanism responsible for turbulent mass transport. The action of mode coupling interactions enables the Stokes second order wave motion to directly drive a component of the Euler mass transport velocity. This new contribution is found to reduce and reverse the mass transport velocity when the relative depth parameter is less than approximately 0.53, thus explaining the experimentally observed reversal of mass transport velocity under waves climbing a sloping beach, under turbulent conditions, and the associated formation of a sand bar. In addition the Euler contribution of mass transport due to the radiation stress of the first order motion is found to be approximately half of its corresponding laminar value, in contradiction to the linearised turbulent calculations of Longuet-Higgins [6], Johns [7] and Noda [8], and in consequence of the velocity squared stress law. The reason why earlier turbulent calculations of mass transport velocity found no significant difference from the laminar case lies with the linearisation of the time invariant eddy viscosity adopted.

Acknowledgements

We are grateful to the referees for making helpful comments on this paper. T.G. Thomas was in receipt of an SERC studentship during the course of this work.

References

1. Stokes, G.G.: On the theory of oscillatory waves. *Trans. Cambridge Philos. Soc.* 8 (1847) 441–455.
2. Rayleigh, J.W.S. (Lord): On the circulation of air observed in Kundt's tubes and some allied acoustical problems. *Phil. Trans. R. Soc. Lond.* 175 (1884) 1–21.
3. Schlichting, H.: Bevechnung ebener periodischer Grenzschichtstromungen. *Phys. Zeit* 33 (1932) 327–335.
4. Longuet-Higgins, M.S.: Mass transport in water waves. *Proc. Roy. Soc.* A245 (1953) 535–581.
5. Bijker, E.W., Kalkwijk, J.P. and Pieters, T.: Mass transport in gravity waves on a sloping bottom. In: ASCE. *Proc. 14th Conf. Coast. Engng.* No. 14 (1974) pp. 447–465.
6. Longuet-Higgins, M.S.: The mechanics of the boundary layer near the bottom in a progressive wave. In: ASCE. *Proc. 6th Conf. Coast. Engng.* C10 (1957) pp. 184–193.
7. Johns, B.: On the mass transport induced by oscillatory flow in a turbulent boundary layer. *J. Fluid Mech.* 43 (1970) 177–185.
8. Noda, H.: On the oscillatory flow in turbulent boundary layers induced by water waves. Bull. Disaster, Prev. Res. Inst., Kyoto Univ., No. 176, 20(3) (1971) 127–144.
9. Sleath, J.F.A.: Stability of laminar flow at the seabed. *J. Waterways Harb. Div. Am. Soc. Civ. Engrs.* 100 (1974) 105–122.
10. Goldstein, S.: *Modern Developments in Fluid Dynamics*, Vols I & II. New York: Dover (1965).
11. Launder, B.E. and Spalding, D.B.: The numerical computation of turbulent flow. *Comp. Maths Appl. Mech. Engng.* 3 (1974) 269.
12. Launder, B.E., Reece, G.J. and Rodi, W.: Progress in the development of a Reynolds stress turbulence closure. *J. Fluid Mech.* 68 (1975) 537.
13. Launder, B.E. and Spalding, D.B.: *Mathematical Models of Turbulence*. London: Academic Press (1972).
14. Gosman, A.D., Khalil, E.E. and Whitelaw, J.H.: The calculation of two-dimensional turbulent recirculating flows. In: F. Durst, B. E. Launder, F. W. Schmidt and J. H. Whitelaw (eds), *Turbulent Shear Flows* I. New York: Springer Verlag (1979) pp. 237–255.
15. Cousteix, J., Desopper, A. and Houdeville, R.: Structure and development of a turbulent boundary layer in an oscillatory external flow. In: F. Durst, B. E. Launder, F. W. Schmidt and J. H. Whitelaw (eds), *Turbulent Shear Flows* I. New York: Springer Verlag (1979) pp. 154–171.

16. Nikuradse, J.: Ver. Deutsch. Ing., Forshungsheft 361 (1933).
17. Hinze, J.O.: *Turbulence*. New York: McGraw-Hill (1959).
18. Lighthill, M.J.: *Waves in Fluids*. Cambridge: Cambridge Univ. Press (1978).
19. Hunt, J.N.: Viscous damping of waves over an inclined bed in a channel of finite width. *La Houille Blanche* 1 (1952) 836–842.
20. Longuet-Higgins, M.S.: Integral properties of periodic gravity waves of finite amplitudes. *Proc. Roy. Soc. Lond.* A342 (1975) 157–174.
21. Putnam, J.A. and Johnson, J.W.: The distribution of wave energy by bottom friction. *Trans. Amer. Geophys. Un.* 30 (1949) 67–74.
22. Riedel, H.P., Kamphius, J.W. and Brebner, A.: Measurement of bed shear stress under waves. In: *Proc. 12th Conf. Coast. Engng.* C31 (1975) pp. 587–603.
23. Kamphius, J.W.: Friction factors under oscillatory waves. *J. Waterways and Harb. Div. Am. Soc. Civ. Engrs.* 101 (1975) 135–144.
24. Kajiura, K.: A model of the bottom boundary layer in water waves. *Bull. Earthq. Res. Inst.* 46 (1968) 75–123.
25. Brevik, I.: Oscillatory rough turbulent boundary layers. *J. Waterways, Port, Coast. Ocean Div. Am. Soc. Civ. Engrs.* 107 (WW3) (1981) 175–188.
26. Myrhaug Dag: On a theoretical model of rough turbulent wave boundary layers. *Ocean Engng.* 9(6) (1982) 547–565.
27. Jonson, I.G. and Carlsen, N.A.: Experimental and theoretical investigations in an oscillatory rough turbulent boundary layer. *J. Hydr. Res.* 14 (1976) 45–60.
28. Bagnold, R.A.: Sand movement by waves: some small-scale experiments with sand of very low density. *J. Inst. Civ. Engrs. Lond* 27 (1947) 447–469.
29. Jonson, I.G.: A new approach to oscillatory rough turbulent boundary layers. *Ocean Engng.* 7 (1980) 109–152.
30. Hsiao, S.V. and Shemdin, O.H.: Bottom dissipation in finite depth water waves. In: ASCE. *Proc. 16th Conf. Coast Engng.* C24 (1978) pp. 434–448.
31. Sleath, J.F.A.: Measurements of mass transport over a rough bed. In: ASCE. *Proc. 19th Conf. Coastal Engng.* C27 (1984) pp. 1149–1160.
32. Sleath, J.F.A.: Turbulent oscillatory flow over rough beds. *J. Fluid Mech.* 182 (1987) 369–409.
33. Justesen, P.: Prediction of turbulent oscillatory flow over rough beds. *Coastal Engineering* 12 (1988) 257–284.
34. Takhar, H.S. and Thomas, T.G.: Turbulent mass transport and attenuation in Stokes waves. University of Manchester, Simon Engineering Laboratories, Report 1985.

Applied Scientific Research **49**: 31–48, 1992.
© 1992 Kluwer Academic Publishers. Printed in the Netherlands.

Direct contact condensation of vapor on turbulent, falling liquid film

V. DHARMA RAO[2], J. SAIBABU[1] & P.K. SARMA[1,*]

*Departments of [1]Mechanical Engineering, and [2]Chemical Engineering, College of Engineering, Andhra University, Visakhapatnam 530003, India (*Author for correspondence)*

Received 28 June 1989; accepted in revised form 11 May 1990

Abstract. The problem of condensation of pure vapor on turbulent falling liquid film of the same species is analytically solved. The gradual change in enthalpy of the coolant liquid film in the flow direction is considered to take place in three successive stages. The study brings out the influence of inlet Reynolds number, Prandtl number and degree of subcooling of the coolant on condensation heat transfer coefficients. The heat transfer coefficients predicted from the theoretical analysis are in reasonable agreement with the experimental data available in literature.

Nomenclature

C_p = specific heat of liquid at constant pressure
F = variable defined in equation (12)
F_t = variable defined in equation (10)
Gr_x = Grashof number, $gx^3(\rho - \rho_v)/(\nu^2\rho)$
g = gravitational constant
h_{fg} = latent heat of condensation
h_x, h_m = local and average condensation heat transfer coefficients respectively
k = thermal conductivity of liquid
L = length of the plate
L^+ = $S\,\mathrm{Gr}_L^{1/3}/\mathrm{Pr}$
$\dot{m}$ = mass flow rate of liquid per unit width of the plate
Nu_x = local Nusselt number, $(h_x/k)[\nu^2\rho/g(\rho - \rho_v)]^{1/3}$
Nu_m = average Nusselt number, $(h_m/k)[\nu^2\rho/g(\rho - \rho_v)]^{1/3}$
Pr = Prandtl number
q = heat flux in y-direction at $x = x$
R = q_w/q_i
Re = local film Reynolds number defined in equation (3)
Re_L = film Reynolds number at the exit on the downstream
$\mathrm{Re}_{c,x}$ = local condensate Reynolds number, $(\mathrm{Re} - \mathrm{Re}_o)$
$\mathrm{Re}_{c,L}$ = condensate Reynolds number at the exit, $(\mathrm{Re}_L - \mathrm{Re}_o)$
Re_t = variable defined in equation (11)
S = subcooling parameter, $C_p(T_s - T_o)/h_{fg}$
T = temperature
T^+ = dimensionless temperature, $k(T - T_o)u^*/(q_i\nu)$
T_s^+ = $k(T_s - T_o)u^*/(q_i\nu)$
u = velocity along the x direction
U^+ = u/u^*
u^* = $(\tau_w/\rho)^{1/2}$
x = downstream distance
X^+ = dimensionless downstream distance, $S\,\mathrm{Gr}_x^{1/3}/\mathrm{Pr}$
x_1 = maximum limiting length as defined in equation (27)
x_2 = maximum limiting length as defined in equation (28)
y = direction normal to the plate
Y^+ = yu^*/ν

Subscripts

0 = inlet at $x = 0$
i = vapor-liquid interface
s = saturation
w = wall
L = exit at $x = L$

Greek symbols

δ = local liquid film thickness
δ^+ = $\delta u^*/\nu$

δ_t = thermal penetration depth
δ_t^+ = $\delta_t u^*/\nu$
ε = eddy viscosity
ν = kinematic viscosity of the liquid
λ = parameter appearing in equation (1a), $g(\rho - \rho_v)\delta/(u^{*2}\rho)$
μ = dynamic viscosity of liquid
ρ = density of liquid
ρ_v = density of vapor
τ = shear stress

Introduction

Direct contact heat transfer has assumed industrial importance in view of certain inherent advantages such as high heat transfer rates, trouble-free maintenance and less initial capital outlay for the manufacture of equipment. Direct contact condensers, which drastically minimise the shutdown period in process industry or in desalination plants, are found to be superior in certain respects due to the absence of scale formation. Classification of direct contact condensers is made based on geometric pattern of the coolant coming in direct contact with vapor. Such demarcation resulted in the investigation of condensation of vapor on spherical droplets, liquid sheets, jets and gravity controlled falling liquid films. Sideman and Moalem-Maron (1982) and Jacobs (1986) summarised the state-of-the-art on direct contact condensation.

In relation to the desalination plants and low pressure regenerative feed water heaters in thermal power plants, film type of condensation with shorter coolant film lengths has been found to give much higher heat transfer coefficients than those predicted from classical Nusselt's analysis. In this context one can find in literature theoretical investigations on hydrodynamic and heat transfer aspects of falling liquid films by Fulford (1964), Hasson (1967), Murthy and Sastry (1973) and Narayanamurthy and Sarma (1973, 1974, 1977, 1978a, 1978b). Wilke (1962), Chun and Seban (1971), Gorla et al. (1986) and Saibabu et al. (1986) considered heat transfer rates from a vertical, diabatic surface to a turbulent falling liquid film. Saibabu et al. (1986) in their analysis on the problem of heating of turbulent falling film, expressed the average thickness of wavy film as a function of Kapitza number. With this correction they found that the theoretically predicted Nusselt numbers are in good agreement with the experimental data available in literature.

The structure of turbulence of the free surface of the film has been the subject of study by many, for example Chu and Dukler (1975), Mudawwar and El-Masri (1986), Shmerler and Mudawwar (1988a, 1988b). The studies in general considered the influence of surface tension forces on the dynamics of the turbulent falling film. According to Mudawwar and El-Masri (1986) these effects are to be taken into account through Kapitza number up to a certain value of film Reynolds number, 10,000. However, for higher film Reynolds numbers they recommended turbulent correlations similar to those used in conventional internal and external flows. Such an observation is consistent with Chu and Dukler (1975) who excluded the existence of capillary waves at high Reynolds numbers. Shmerler and Mudawwar (1988a) also observed that at high Reynolds numbers the effect of wave-induced mixing may not be as pronounced as those caused by thinner wall boundary layer.

In a previous work, Rao and Sarma (1984) considered laminar wave-free flow regimes. Condensation of vapor at the vapor–liquid interface was tackled by integral method of analysis for the thermally developing and developed regimes of the film. However, the Reynolds number characterizes the flow structure as either laminar or turbulent. From the earlier studies, there is a clear indication that direct contact condensation is helpful in scaling down the size of condensers. However, the earlier studies were limited to low coolant Reynolds numbers and the phenomenon of condensation of vapor on turbulent falling film, in spite of its practical significance, has not received due importance.

The present article considers theoretical investigation of the problem of condensation of quiescent vapor on a subcooled turbulent falling liquid film, hereafter termed as "coolant film". The analysis takes into account the process of condensation with simultaneous heating of the liquid film. The heating of the film due to condensation of vapor is assumed to take place in three successive stages, of which the first and second stages correspond to the thermal development of the film and in the third stage the film is thermally developed. The purpose of the present study is to assess the advantages and limitations of direct contact condensation of vapor on a turbulent falling film.

Physical model and formulation

The physical model (see Fig. 1) envisaged in the analysis is a vertical surface on which the coolant liquid film at inlet temperature T_0 is made to flow under the action of gravity with shear resistance at the wall. The wall surface is maintained all along its length under isothermal condition at T_0 and $T_0 < T_s$, where T_s is the saturation temperature of the liquid corresponding to the system pressure. The film Reynolds number is high enough that the regime corresponds to a fully developed turbulent flow. The liquid film is exposed to an ambient medium of pure quiescent vapor of its own species. The condensate and coolant films belong to the same species and hence are completely miscible. The film flow can be characterized by the homogeneous flow model (Sykes and Marchello, 1970). The inertial force term in the equation of conservation of momentum is neglected on the assumption that the dominating forces are viscous and body forces. Since the vapor is quiescent and $\mu_L \gg \mu_v$, the shear at the vapor-liquid interface is of negligible order. Further, the interface is assumed to acquire the saturation temperature, T_s. Thus, under the framework of these assumptions the velocity field in the liquid film can be obtained from the following equation:

$$\mu(1 + \varepsilon/v)\frac{\mathrm{d}u}{\mathrm{d}y} = \tau_w - g(\rho - \rho_v)y. \tag{1}$$

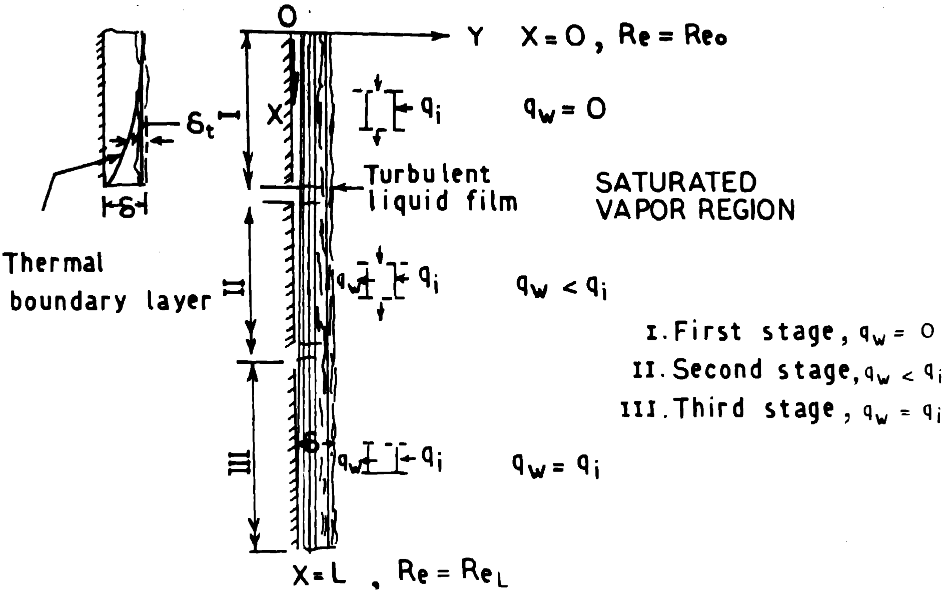

Fig. 1. Physical model: turbulent falling liquid film.

Equation (1) in non-dimensional form is as follows:

$$(1 + \varepsilon/\nu)\frac{\mathrm{d}U}{\mathrm{d}Y} = 1 - \lambda(Y^+/\delta^+), \tag{1a}$$

where $\lambda = g(\rho - \rho_v)\delta/(u^{*2}\rho)$.

The boundary condition is

$$U^+ = 0 \quad \text{at } Y^+ = 0. \tag{2}$$

In the present analysis the value of λ is taken to be unity in view of the assumption of negligible interfacial shear. The local film Reynolds number, Re and the local non-dimensional film thickness, δ^+ are related by the equation

$$\mathrm{Re} = 4\dot{m}/\mu = 4\int_0^{\delta^+} U^+\,\mathrm{d}Y^+, \tag{3}$$

where $\dot{m}$ is the local mass flow rate of the liquid film per unit width of the plate.

At $x = 0$, viz., at the inlet, the liquid film is that of coolant only and the Reynolds number and nondimensional thickness of the film are denoted as Re_o and δ_o^+ respectively. At any $x > 0$, the liquid film contains the condensate in addition to the coolant.

The change in thermal energy of the film, due to condensation of vapor at the film surface, is evaluated by considering three successive stages in flow direction. The heat flow patterns in the three stages, shown in Fig. 1, are explained below:

First stage

The thermal penetration depth, δ_t, starts from a value zero at $x = 0$ and develops further along downstream until δ_t becomes equal to δ, the thickness of the liquid film. During this stage the thermal energy of the liquid film increases due to phase transformation taking place at the vapor–liquid interface. However, q_w, the heat abstracted at the wall, is zero. The equation of conservation of energy in integral form is

$$\frac{\mathrm{d}}{\mathrm{d}x}\int_{\delta - \delta_t}^{\delta} u(T - T_s)\,\mathrm{d}y - (T_s - T_0)\frac{\mathrm{d}}{\mathrm{d}x}\int_0^{\delta - \delta_t} u\,\mathrm{d}y = \frac{q_i}{\rho C_p}, \tag{4}$$

where q_i is the heat flux at the vapor-to-liquid interface.

Second stage

During the second stage, part of q_i is utilized to increase further the thermal energy of liquid film and the rest is dissipated at the wall as q_w. In other words $q_w > 0$, but $q_w < q_i$. Thus, the thermal transport of heat is given by the integral equation as follows:

$$\frac{\mathrm{d}}{\mathrm{d}x}\int_0^{\delta} u(T - T_s)\,\mathrm{d}y = \frac{(q_i - q_w)}{\rho C_p}, \tag{5}$$

where $q_w = q_w(x)$ and $q_i = q_i(x)$.

Third stage

When the temperature field is completely established and is no longer dependent on the downstream distance, the phase transformation at the interface is purely dictated by turbulent thermal conduction in the liquid film. Hence, during this stage $q_w = q_i$. For all stages the process of phase transformation can be described by the integral

$$\frac{\mathrm{d}}{\mathrm{d}x}\int_0^{\delta} u\,\mathrm{d}y = \frac{q_i}{\rho h_{fg}}. \tag{6}$$

Evaluation of the integro-differential equations (4), (5), (6) can be made possible with the velocity and temperature profiles being made known.

Equations (4), (5) and (6) are rendered in dimensionless form respectively as follows:

First stage ($0 < \delta_t^+ < \delta^+$ and $q_w = 0$):

$$\frac{\mathrm{d}(F_t + \mathrm{Re}_t)}{\mathrm{d}X^+} = -\frac{4\delta^{+1/3}}{ST_s^+\lambda^{1/3}}. \tag{7}$$

Second stage ($0 < q_w < q_i$):

$$\frac{\mathrm{d}F}{\mathrm{d}X^+} = -\frac{4\delta^{+1/3}(1 - R)}{ST_s^+\lambda^{1/3}}. \tag{8}$$

Phase transformation (for all three stages):

$$\frac{\mathrm{d}\,\mathrm{Re}}{\mathrm{d}X^+} = \frac{4\delta^{+1/3}}{T_s^+\lambda^{1/3}}. \tag{9}$$

Re appearing in equation (9) is defined as in equation (3). The terms F_t, Re_t and F are defined as follows:

$$F_t = 4\int_{\delta^+ - \delta_t^+}^{\delta^4} U^+(1 - T^+/T_s^+)\,\mathrm{d}Y^+, \tag{10}$$

$$\mathrm{Re}_t = 4\int_0^{\delta^+ - \delta_t^+} U^+\,\mathrm{d}Y^+, \tag{11}$$

$$F = 4\int_0^{\delta^+} U^+(1 - T^+/T_s^+)\,\mathrm{d}Y^+. \tag{12}$$

The dimensionless terms appearing in the above equations are defined as below:

$$T^+ = k(T - T_o)u^*/q_i;\; T_s^+ = k(T_s - T_o)u^*/q_i, \tag{13}$$

$$\left.\begin{aligned} &R = q_w/q_i;\; S = C_p(T_s - T_o)/h_{fg} \\ &\mathrm{Gr}_x = gx^3(\rho - \rho_v)/(\nu^2\rho) \\ &X^+ = S\,\mathrm{Gr}_x^{1/3}/\mathrm{Pr} \end{aligned}\right| . \tag{14}$$

The boundary condition for the differential equations are

$$\text{at } X^+ = 0, \quad \mathrm{Re} = \mathrm{Re}_t = \mathrm{Re}_o \quad \text{and} \quad F_t = 0. \tag{15}$$

Velocity and temperature profiles

The velocity variation across the film at any X^+ is obtained from the solution of equation (1a) corresponding to the value of local δ^+. As already stated, λ appearing in equation (1a) is assumed to be equal to unity. In other words the shear stress at the vapor-to-liquid interface is assumed to be equal to zero. The following equations depict the variation of heat flux across the film during the three successive stages as shown in Fig. 1. The temperature variation across the film in a particular stage is obtained by solving the heat flux equation with appropriate boundary conditions.

First stage ($0 < \delta_t^+ < \delta^+$ and $q_w = 0$):

$$[1 + \Pr(\varepsilon/\nu)]\frac{\partial T^+}{\partial Y^+} = \frac{q}{q_i} = \frac{(Y^+ - \delta^+ + \delta_t^+)}{\delta_t^+} \tag{16}$$

satisfying the boundary conditions

$$\left.\begin{array}{l} Y^+ = \delta^+ - \delta_t^+,\ q = 0 \quad \text{and} \quad T^+ = 0 \\ Y^+ = \delta^+,\ q = q_i \quad \text{and} \quad T^+ = T_s^+ \end{array}\right| . \tag{16a}$$

Second stage ($0 < q_w < q_i$):

$$[1 + \Pr(\varepsilon/\nu)]\frac{\partial T^+}{\partial Y^+} = \frac{q}{q_i} = R + (1 - R)\frac{Y^+}{\delta^+}, \tag{17}$$

where $R = q_w/q_i$.

The boundary conditions are

$$\left.\begin{array}{l} Y^+ = 0,\ q = q_w \quad \text{and} \quad T^+ = 0 \\ Y^+ = \delta^+,\ q = q_i \quad \text{and} \quad T^+ = T_s^+ \end{array}\right| . \tag{17a}$$

Third stage ($q_w = q_i$):

$$[1 + \Pr(\varepsilon/\nu)]\frac{\partial T^+}{\partial Y^+} = 1. \tag{18}$$

The boundary conditions are

$$\text{at } Y^+ = 0,\ T^+ = 0 \quad \text{and} \quad \text{at } Y^+ = \delta^+,\ T^+ = T_s^+. \tag{19}$$

Thus, the first two stages in the formulation correspond to thermally developing region of coolant film and subsequently the developed zone in the third stage.

Local heat transfer coefficient

For design considerations the local and average heat transfer coefficients are very much essential. The local coefficient is defined by the equation

$$q_i(x) = h_x(T_s - T_o). \tag{20}$$

Equation (20) is written in dimensionless form to give the local Nusselt number as

$$\mathrm{Nu}_x = \delta^{+1/3}/(\lambda^{1/3} T_s^{+}), \tag{21}$$

where

$$\mathrm{Nu}_x = \frac{h_x}{k}\left[\frac{v^2\rho}{g(\rho - \rho_v)}\right]^{1/3}.$$

In addition, the necessary length of the plate for an anticipated Reynolds number, Re at the exit can be obtained from equations (9) and (21) as follows:

$$L^+ = 4\int_{\mathrm{Re}_0}^{\mathrm{Re}_L} \mathrm{d(Re)}/\mathrm{Nu}_x, \tag{22}$$

where $L^+ = S\,\mathrm{Gr}_L^{1/3}/\mathrm{Pr}$, $\mathrm{Gr}_L = gL^3(\rho - \rho_v)/(v^2\rho)$.

Further, the average Nusselt number (dimensionless average heat transfer coefficient) is obtained as

$$\mathrm{Nu}_m = \frac{1}{L^+}\int_0^{L^+} \mathrm{Nu}_x\,\mathrm{d}X^+. \tag{23}$$

Choice of expression for eddy viscosity

The formulation of the problem is still incomplete unless an expression for eddy viscosity, i.e., (ε/v), is selected for use in equations (1a), (16), (17) and (18). A survey of literature reveals various expressions for eddy viscosity suggested by different authors. Investigations concerning turbulent falling films are reported in literature for two situations, viz., heating/evaporation of film and absorption/desorption of a gaseous component at the free surface of the film. Most of the effort in modelling turbulent liquid films has been directed towards the choice of proper profile for eddy viscosity across the film. Mudawwar and El-Masri (1986) listed the expressions employed by several investigators. Because of the absence of experimentally measured profiles for eddy viscosity, the Van Driest (1956) expression was modified by Mills and Chung

(1973), Limberg (1973), Hubbard et al. (1976) and Seban and Faghri (1976). The expressions of Mills and Chung (1973) and Mudawwar and El-Masri (1986) give zero magnitude of (ε/ν) at the free surface of the film and thus are more suitable for the situation of free convection. However, Chu and Dukler (1975) found severe turbulent fluctuations at the free surface of the film, indicating that the eddy viscosity at the free surface is not equal to zero, but is of appreciable magnitude. Further, from an examination of these expressions for (ε/ν) it appears that the choice of the expression should depend on the specific problem considered.

The eddy viscosity expressions so far developed by various investigators fall in any one of the three categories, namely (1) monotonically increasing, (2) asymptotic variation and (3) rise and decay.

In view of so many different approaches adopted by various investigators, it is felt that one of the conventional eddy viscosity expressions used for internal and external flows can as well be employed for the present problem. Hence, in the absence of experimental data for (ε/ν) profile for the present case, the expression suggested by Kato et al (1968) is selected, which is as follows:

$$\frac{\varepsilon}{\nu} = 0.4Y^{+}[1 - \exp(-0.0017Y^{+2})]. \tag{24}$$

Results shown in the present paper were obtained with the aid of Eq. (24). For the sake of comparison, other results were obtained with Limberg's model (1973), and shown in Fig 5. This figure depicts a comparison of experimental correlations available in literature

In accordance with the observation of Shmerler and Mudawwar (1988a), the effects of wave-induced mixing and surface tension forces are neglected since the majority of the results involve film Reynolds numbers of the order 5000 or more.

Computational procedure

The numerical procedure used in the estimation of various variables relating to the hydrodynamic and thermal aspects of the coolant film is as follows:

1. At $X^{+} = 0$, Re_o, the inlet Reynolds of the coolant is prescribed for chosen values of the subcooling parameter and Prandtl number. Values of Re_o greater than 2000 are chosen. Equations (1a) and (3) are solved simultaneously by trial and error procedure, in which the guesses for δ^{+}, the liquid film thickness are generated by linear interpolation method. Thus, the velocity field at $X^{+} = 0$ is fixed for a given Re_o. At $X^{+} = 0$, the thermal penetration depth, δ_t^{+} is zero.

First stage

2. A small increment $\Delta\delta^{+} = 0.05$ is given in δ^{+} representing the change in film thickness due to condensation of vapors at the interface over an incremental

length, ΔX^+. Equations (1a) and (3) are solved to establish velocity field and film Reynolds number at a new location, viz., at $X^+ = \Delta X^+ (\Delta X^+$ being still unknown).

3. The temperature field in the film is obtained by solving equation (16) with an initial guess value for δ_t^+. The integrals F_t and Re_t are evaluated from equations (10) and (11) respectively.
4. By combining equations (7) and (9), the independent variable X^+ can be eliminated yielding the expression

$$\mathrm{d}(F_t + \mathrm{Re}_t) = -\mathrm{d}(\mathrm{Re})/S. \tag{25}$$

On the R.H.S. of equation (25) the value of d Re comes from step 2. However, both the values of F_t and Re_t appearing on L.H.S. of equation (25) depend on the guess for δ_t^+. Thus, if L.H.S. of equation (25) is equal to R.H.S., then the guess in δ_t^+ is correct and step 5 in computation is taken up. Otherwise, an iterative procedure is adopted with a new guess in δ_t^+ and steps 3 to 4 are repeated. In other words the purpose of steps 3 and 4 is to obtain the value of T_s^+ with the aid of the equation (25).

5. The increment ΔX^+ for the corresponding change in δ^+ is established with the help of equation (9). Equation (21) fixes the local Nusselt number. Note that T_s^+ is only known after the correct value of δ_t^+ has been established.

Steps 2 through to 5 are repeated until $\delta_t^+ \to \delta^+$. Then the first stage in the analysis ends and the second stage commences.

Second stage

During the second stage the computational procedure is similar, but for the use of equations corresponding to the second stage. The scheme of computation is outlined below:

6. For an increment $\Delta\delta^+$, equations (1a) and (17) are solved with a guess in R.
7. After evaluating F from equation (12), the guess in R is checked using the following equation, which is a manipulated form of equations (8) and (9):

$$\mathrm{d}F = -(1 - R)\,\mathrm{d}(\mathrm{Re})/S. \tag{26}$$

The procedure for obtaining suitable value of R is similar to that in steps 3 and 4 for obtaining δ_t^+ in the first stage. Thus in this step the value of T_s^+ is obtained from steps 6 and 7 with the aid of the condition given by equation (26).

8. The corresponding ΔX^+ and the local Nusselt number are computed from equations (9) and (21) respectively. Steps 6 to 8 are repeated until R approaches unity. Thereafter, the third stage begins.

Third stage

In the third stage the calculation procedure is straightforward without resorting to any iteration.

9. For each successive increment in δ^+, equation (1a) and (18) are solved to obtain the velocity and temperature fields in the film. ΔX^+ and Nu_x are computed from equations (9) and (21). Solutions are obtained until Re becomes equal to Re_L, the expected Reynolds at the exit on the downstream side.

Results and discussion

The set of equations are solved numerically on computer for turbulent regime of the film and the results are shown in Figs 2 through 7. Figure 2 represents the variation of local condensation Nusselt number, Nu_x, as a function of dimensionless downstream distance, X^+ for different values of Re_o in the range $2000 < Re_o < 12000$ for $Pr = 5$ and $S = 0.2$. Evidently at a given location, an increase in inlet Reynolds number Re_o, results in an increase in the heat transfer coefficient at any X^+. However, for a given Re_o, the local Nusselt number decreases during the thermally developing stage of the coolant. Later, in the third stage, the local heat transfer coefficient increases marginally along the length of the plate. Thus, in the third stage the influence

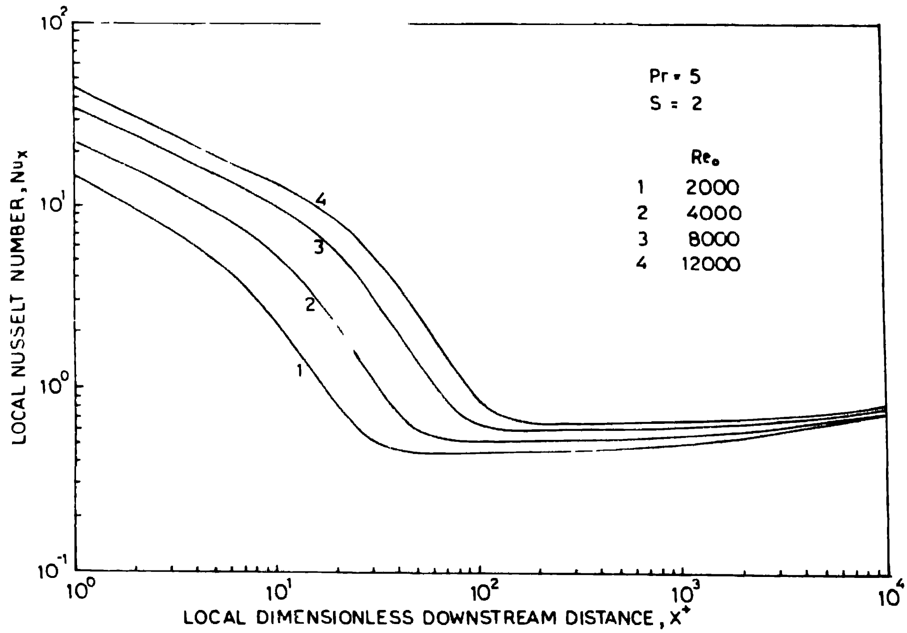

Fig. 2 Effect of Re, inlet film Reynolds number of the coolant on local Nusselt number

of inlet Reynolds of the coolant on heat transfer rates is not so pronounced as in the first and second stages. Figure 3 reveals that the rate of phase transformation is strongly dependent on the coolant Reynolds number, since $\mathrm{Re}_{c,x}$, the local condensate Reynolds number defined by $\mathrm{Re}_{c,x} = \mathrm{Re} - \mathrm{Re}_o$ is found to increase along the downstream. At distances far downstream from the inlet the condensation rates become independent of the inlet Reynolds number of the coolant.

Figure 4 shows the variation of the average Nusselt number with exit condensate Reynolds number as a function of Re_o, the inlet Reynolds number of the coolant. Further, the results of Dukler's (1960) analysis for the conventional turbulent film condensation of vapor on a vertical plate is shown in Fig. 4 by a dotted line. It is evident that direct contact condensation on a coolant film gives substantial augmentation in Nusselt numbers compared to the conventional turbulent film condensation on a vertical plate. However, the improvement in condensation heat transfer is achieved during the first and second stages when the film is thermally developing. In the third stage the advantage obtained is marginal. In other words, condensation on a coolant film is advantageous only for shorter lengths of the coolant film. The loci of the points indicating the end of the first stage and that of second stage are shown encircled. Using the computer results and by regression analysis the following expressions are obtained for Gr_{x_1} and Gr_{x_2} as function of the system parameters Re_o, Pr and S, which are given respectively by equations (27) and (28).

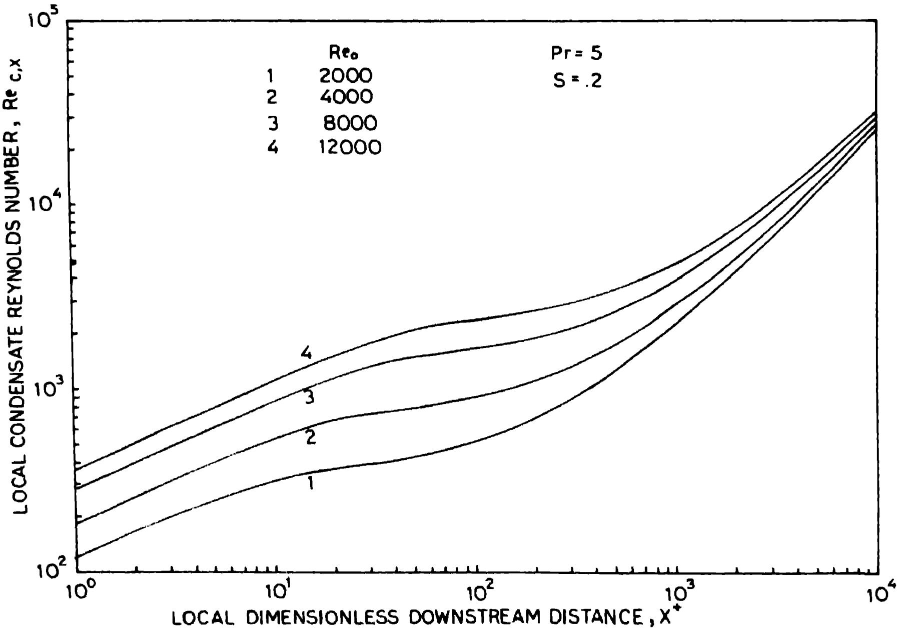

Fig. 3. Variation of Re, the local condensate Reynolds number with the downstream distance – effect of Re.

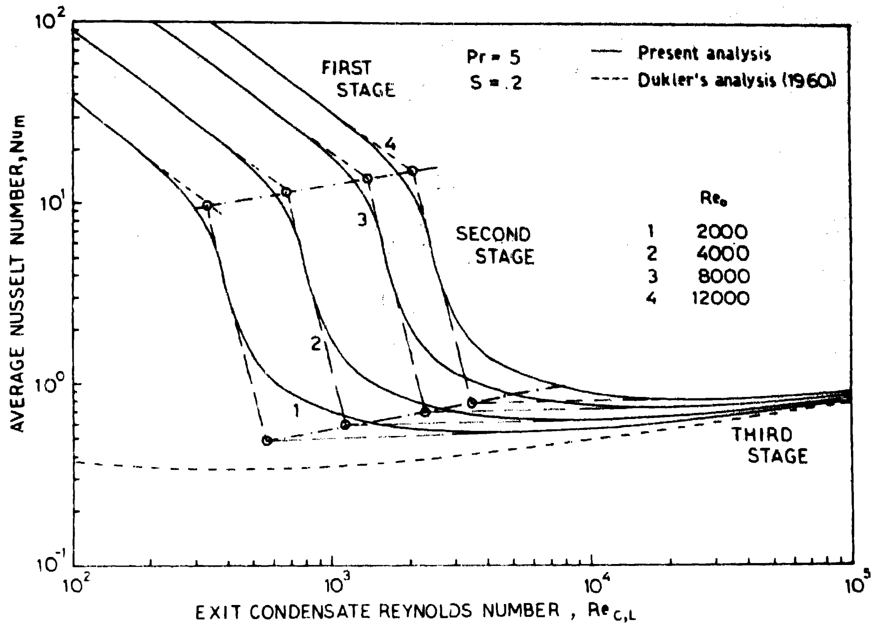

Fig. 4. Effect of Re, inlet film Reynolds number of the coolant on average Nusselt number.

End of first stage at $x = x_1$:

$$Gr_{x_1}^{1/3} = 0.08\, Re_o^{0.8}\, Pr^{2/3}\, S^{-0.04}. \tag{27}$$

End of second stage at $x = x_2$:

$$Gr_{x_2}^{1/3} = 2.62\, Re_o^{0.8}\, Pr^{2/3}\, S^{-0.04}. \tag{28}$$

Gr_{x_1} and Gr_{x_2} represent the dimensionless downstream distance where the first and second stages end.

Also, approximate expressions for average Nusselt numbers are presented in equations (29), (30) and (31) during the first, second and third stages respectively as function of $Re_{C,L}$, Re_o, Pr and S.

During the first stage, $0 < x < x_1$:

$$Nu_m = 0.043\, Re_{C,L}^{-1.1}\, Re_o^{1.349}\, Pr^{0.96}\, S^{0.04}. \tag{29}$$

During the second stage, $x_1 < x < x_2$:

$$Nu_m = 0.0003\, Re_{C,L}^{-5.17}\, Re_o^{5.24}\, Pr^{0.67}\, S^{0.04}. \tag{30}$$

During the third stage, $x > x_2$:

$$\mathrm{Nu}_m = 0.04\ \mathrm{Re}_{C,L}^{0.13}\ \mathrm{Re}_o^{0.108}\ \mathrm{Pr}^{0.45}\ S^{0.04}. \tag{31}$$

Equations (29), (30) and (31) with the aid of equations (27) and (28) are useful to predict the direct contact condensation heat transfer rates for a specified inlet Reynolds number of the coolant.

Figure 5 shows a comparison of the present analysis with the experimental correlation of Krebs and Schlunder (1984). They obtained experimental data for the case of condensation of vapor from a mixture of vapor and non-condensable gas on a cocurrent falling liquid film. The liquid is preheated to its saturation temperature before entering the test section. Their results correspond to the thermally developed zone of the present analysis. The following expression is presented by Krebs and Schlunder (1984) (originally obtained by Blangetti, 1979) for particular case of zero interfacial shear and zero fraction of non-condensable gas:

$$\mathrm{Nu}_m = 0.0051\ \mathrm{Re}_f^{0.382}\ \mathrm{Pr}^{0.5689}, \tag{32}$$

where $\mathrm{Re}_f = \mathrm{Re}_o + \mathrm{Re}_{C,L}$.

A comparison of the present analysis is shown, with the equation (32) for two values of Re_o viz., $\mathrm{Re}_o = 2000$ and $\mathrm{Re}_o = 12000$. It can be observed that the results of the

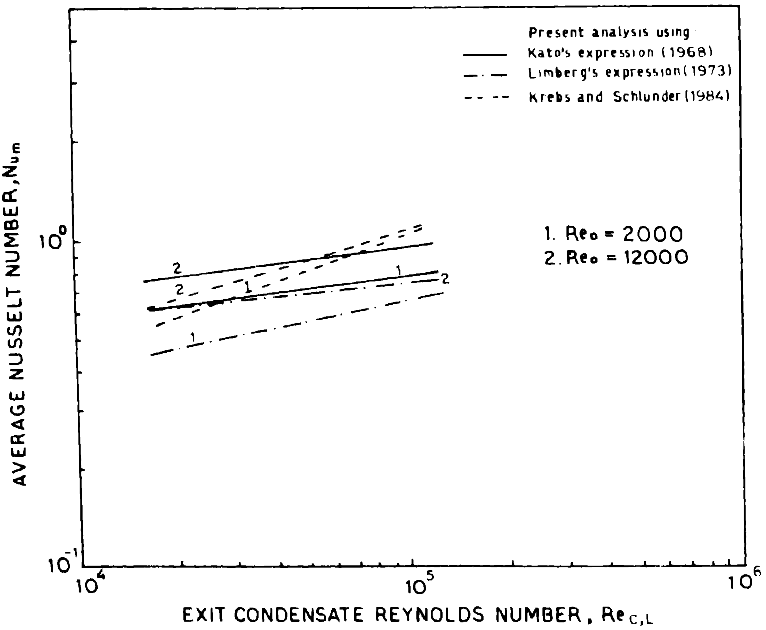

Fig. 5. Comparison with the experimental correlation of Krebs and Schlunder (1984).

present analysis and those of equation (32) agree satisfactorily. Results using Kato's model for eddy viscosity are in better agreement than those resulting from Limberg's model. However, to arrive at a conclusive statement regarding the merits and demerits of the models, more experimental data are needed. Such data are sparse to the best of the knowledge of the authors.

Figure 6 depicts that an increase in the value of the subcooling parameter decreases the local heat transfer coefficients during the thermally developing region. Such a trend is found in the classical Nusselt's analysis as well. However, in the third stage a reverse trend is observed. The effect of the subcooling parameter on average Nusselt numbers, exhibits a similar trend. The effect of Prandtl number on average Nusselt numbers is shown in Fig. 7. As Prandtl number increases the heat transfer coefficients exhibit increasing trend throughout the flow field. Results shown in Fig. 7 indicates that in chemical process industries dealing with high Prandtl fluids, direct contact condensation would be advantageous.

Conclusions

1. The results indicate that in spite of the fact that in the case of direct contact condensation the limitation on the length of the film is dictated by the maximum thermal energy that can be absorbed by the film, still the process can be

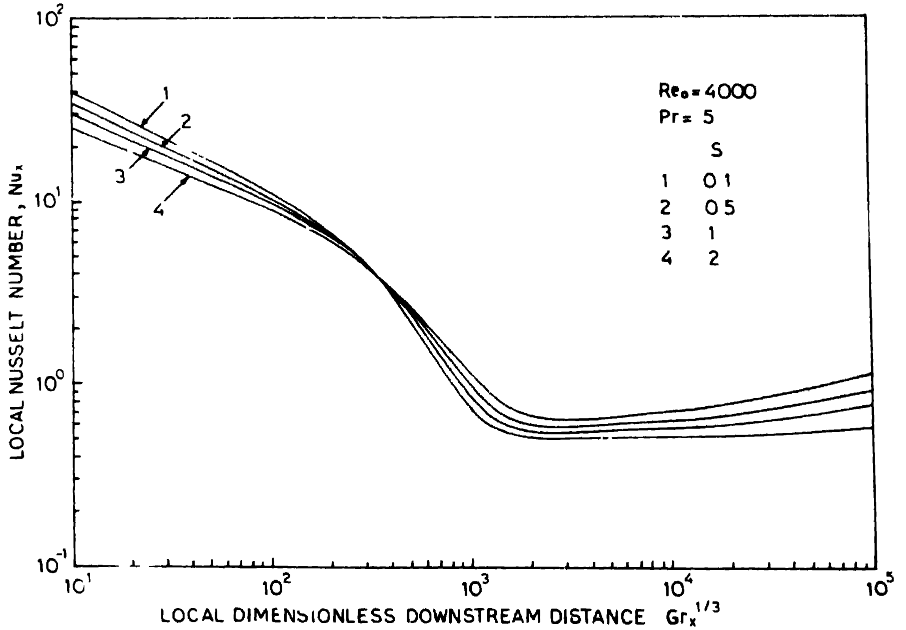

Fig. 6 Effect of S, the subcooling parameter on local Nusselt number.

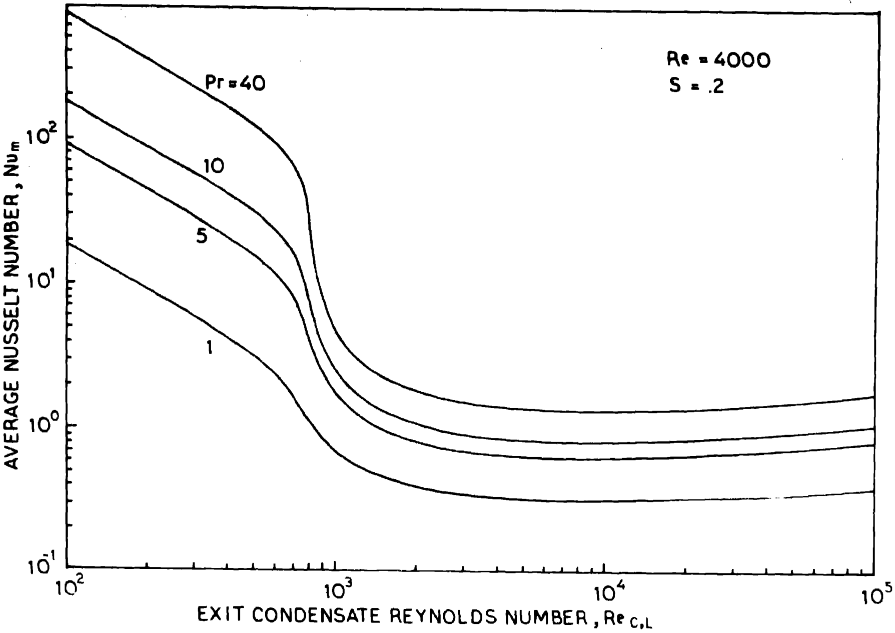

Fig. 7. Effect of Prandtl number on average Nusselt number.

sustained if heat removal is made possible at the solid boundary by maintaining the wall surface under isothermal condition at a value by far less than the saturation temperature. The average heat transfer coefficient is found to be substantially higher than that encountered in the process of turbulent film condensation on a vertical surface.

2. During the thermally developed zone the influence of inlet Reynolds number is not profound. However, results of the first and second stages reveal substantial augmentation in heat transfer coefficients by direct contact condensation of vapor on a coolant film. Hence, direct contact condensation on shorter falling liquid films would be advantageous.
3. The demarcation between different zones or stages can be predicted from equations (27) and (28). The condensation heat transfer coefficients in the three zones can be predicted from equations (29), (30) and (31).

Acknowledgement

This work was performed under the Departmental Research Support Program, Department of Mechanical Engineering, Andhra University, sanctioned by University Grants Commission, New Delhi.

References

Blangetti F Warmeubergang bei der Kondensation mit uberlagerter Konvektion im vertikalen Rohr, Dissertation Univ Karlsruhe Germany (1979)

Chu, J K and Dukler A E Statistical characteristics of thin, wavy films *A I Ch E Journal* 21 (1975) 583 593

Chun, K R and Seban R A Heat transfer to evaporating liquid films *J Heat Transfer, Trans ASME* 96 (1971) 391 396

Dukler, A E Fluid mechanics and heat transfer in vertical falling film systems *Chem Engg Progress Symposium Series* 56(30) (1960) 1 10

Fulford G D *The Flow of Liquid in Thin Films* Advances in Chem Engg Vol 4, Academic Press (1964) pp. 151 236

Gorla, R S Ameri A A and Ponter A B Unsteady heat transfer in falling liquid films *8th Int Heat Transfer Conference* San Fransisco U S A (1986) pp 1943 1947

Hassan N A Laminar flow along a vertical wall *J Applied Mechanics Trans ASME* 34 (1967) 535 537

Hubbard G L Mills A F and Chung D K Heat transfer across turbulent falling film with cocurrent vapor flow *J Heat Transfer Trans ASME* 98 (1976) 319 320

Jacobs H R Direct contact condensers *Heat Exchanger Design Handbook*, Vol 2 New York Hemisphere Publishing Corporation (1986)

Kato H Nishiwaki N and Hirata M On the turbulent heat transfer by free convection from a vertical plate *Int J Heat Mass Transfer* 11 (1968) 1117 1125

Krebs R C and Schlunder E U Condensation with non-condensing gases inside vertical tubes with turbulent gas and film flow *Chem Eng Process* 18 (1984) 341 356

Limberg H Warmeubergang an Turbulente und Laminare Riselfilme *Int J Heat Mass Transfer* 16 (1973) 1691 1702

Mills A F and Chung D K Heat transfer across turbulent falling films *Int J Heat Mass Transfer* 16 (1973) 694 696

Mudawwar I A and El Masri M A Momentum and heat transfer across freely falling turbulent liquid films *Int J Multiphase Flow* 12(5) (1986) 771 790

Murthy N S and Sastry V M K Accelerating laminar film along an inclined wall *Chem Engg Sci* 28 (1973) 869 874

Narayanamurthy V and Sarma P K A note on thin film evaporation prediction of heat transfer rates *J Chem Engg Japan* 6(5) (1973) 457 459

Narayanamurthy V and Sarma P K A note on liquid film thickness under simultaneous action of shear and gravitational forces *Chem Engg Sci* 29 (1974) 1659 1660

Narayanamurthy V and Sarma P K A note on hydrodynamic entrance lengths of non Newtonian laminar falling liquid films *Chem Engg Sci* 32 (1977) 566 567

Narayanamurthy V and Sarma P K Heat transfer to non Newtonian laminar falling liquid film with smooth wave free gas liquid interface *Int J Multiphase Flow* 4 (1978a) 423 425

Narayanamurthy V and Sarma P K Dynamics of developing laminar non Newtonian falling liquid films with free surface *J Applied Mechanics Trans ASME* 45 (1978b) 19 24

Rao V D and Sarma P K Condensation heat transfer on laminar falling films *J Heat Transfer, Trans ASME* 106 (1984) 518 523

Saibabu J Sarma P K Dharma Rao V and Raju G J V J An experimental and theoretical investigation on dynamics and heating of turbulent falling liquid films In *8th Int Heat Transfer Conference San Fransisco U S* Hemisphere Publishing Corporation (1986) pp 1963 1969

Seban R A and Faghri A Evaporation and heating with turbulent falling liquid films *ASME J Heat Transfer* 98 (1976) 315 318

Sideman S and Moalim-Meron D Direct contact condensation *Advances in Heat Transfer* 15 (1982) 228 276

Shmerler J A and Mudawwar I A Local heat transfer coefficient in wavy free-falling turbulent liquid films undergoing uniform sensible heating *Int J Heat Mass Transfer* 31 (1988a) 67–77

Shmerler J A and Mudawwar I A Local evaporative heat transfer coefficient in turbulent free-falling films *Int J Heat Mass Transfer* 31 (1988b) 731 742

Sykes, J.A. and Marchello, J.M.: Condensation of immiscible liquids on a horizontal tube. *Ind. Eng. Ch*
Process Des. Develop. 9 (1970) 63–71.
Van Driest, E.R.: On turbulent flow near a wall. *J. Aeron. Sci.*, 25 (1956) 1007–1011.
Wilke, W.: Warmefibergang and Reiselfilme. *Ver. Deut. Ingr. Forschungsh* 490 (1962).

Applied Scientific Research **49**: 49–65, 1992.
© 1992 *Kluwer Academic Publishers. Printed in the Netherlands.*

Liquid metal flow in a simple manifold with a strong transverse magnetic field

T. J. MOON[1], T. Q. HUA[2], J. S. WALKER[3] & B. F. PICOLOGLOU[2]

[1]*Mechanical Engineering Department, The University of Texas at Austin, Austin, TX 78712-1063, USA*; [2]*Engineering Physics Division, Argonne National Laboratory, Argonne, IL 60439, USA*; [3]*Department of Mechanical and Industrial Engineering, University of Illinois, Urbana, IL 61801, USA*

Accepted 2 June 1990

Abstract. This paper treats a liquid metal flow through a simple manifold connecting one duct to two parallel ducts. The manifold consists of an infinitely long, constant area, rectangular duct with a uniform transverse magnetic field and with a semi-infinite middle wall at the plane of symmetry which is perpendicular to the magnetic field. The magnetic flux density is sufficiently large that inertial effects can be neglected everywhere and that viscous effects are confined to boundary layers and to an interior layer along the magnetic field lines through the end of the middle wall. The purpose of this paper is to illustrate an approach with eigenfunction expansions which will be useful for manifolds with many parallel ducts. In the present simple manifold, the principal three-dimensional effect is a transfer of flow to the inviscid core region from the high velocity jets adjacent to the sides which are parallel to the magnetic field. There is also an important redistribution of flow along magnetic field lines inside the side wall boundary layers.

1. Introduction

Most previous studies of three-dimensional liquid-metal magnetohydrodynamic (MHD) flows treat a single, infinitely long pipe or duct. The three-dimensional disturbance results from a geometric change, such as an expansion, contraction or elbow, or from a change in the magnetic field strength. In a number of technologically important MHD flows, there are a large number of parallel ducts which receive fluid from or deliver fluid to a single duct through a manifold. For example, a liquid-lithium cooling system for a magnetic confinement fusion reactor involves hundreds of parallel ducts in the 'blanket' which surrounds the fusing plasma and which collects the energy from fusion. These many ducts are connected through manifolds to a much smaller number of feeder pipes which are connected to external heat exchangers. Since the manifolds are inside the magnet coils producing the field to confine the plasma, there is a large magnetic field at the manifold, and the liquid-metal flow through a manifold is dominated by MHD effects.

Hua and Picologlou [1] present results for a variable-area manifold between one rectangular feeder duct and nine parallel, electrically connected, rectangular blanket ducts. These results are obtained with a Gauss-Seidel, successive-over-relaxation, finite-difference solution of the appropriate equations. It may not be feasible or practical to extend this finite-difference method to actual fusion-reactor manifolds which connect 50 to 100 parallel ducts to a single feeder duct. There are several variable values at each node, and hundreds of nodes are needed for each parallel duct

Variable gradients can become quite large near the entrance of the parallel ducts or near the walls between ducts, so relatively small grid spacing between nodes is needed in some regions. Since there are several thousand unknowns in each duct, convergence and storage present extraordinary and perhaps insurmountable problems.

Here we present an alternate approach requiring less than a hundred unknowns for each parallel duct, with comparable accuracy. The variables in each duct are given by eigenfunction expansions which satisfy the governing equations, which satisfy all boundary conditions in the cross sections and which approach fully developed flow away from the manifold. The unknown coefficients in each eigenfunction expansion are determined by the matching conditions at the entrance of the parallel ducts. We apply the method of weighted residuals in order to satisfy these matching conditions and to determine the unknown coefficients for each duct.

This approach is only practical if the eigenvalues and eigenfunctions for each duct are independent of all other ducts, so that only the unknown coefficients depend on the coupling of all the ducts. If there are uninsulated metal walls between parallel ducts, then the eigenvalue problems in all the ducts are coupled, and this global eigenvalue problem is intractable for 50 to 100 ducts. Therefore, this approach is only practical when there is some form of electrical insulation between parallel ducts. One alternative is to coat the inside surfaces of all the ducts with an electrical insulator, so that each duct has insulating walls. The eigenvalues and eigenfunctions are then given by the analysis of Walker, Ludford and Hunt [5]. For a fusion reactor blanket, insulating coatings would be ideal because the pressure drops would be several orders of magnitude smaller than those for uninsulated metal walls. Unfortunately there is some doubt that materials scientists will be able to develop an insulating coating which is compatible with hot liquid lithium. Therefore, most current fusion blanket designs assume that there must be metal in contact with the liquid lithium, and the objective is to make the metal as thin as possible in order to reduce the pressure drops. Malang et al. [2] have proposed the use of liners composed of two very thin sheets of metal separated by a thin layer of an electrical insulator. After fabrication, each liner is bent to the shape of a duct and is inserted in order to separate the liquid metal from the metal structural walls. Therefore, the liquid metal is in contact with the inner thin metal sheet of the liner, but each duct is electrically insulated from its neighbors. This is the case we treat, namely, parallel ducts with thin metal walls and with electrical insulators inside the walls between ducts.

The purpose of this paper is to present the eigenfunction expansions and to illustrate the matching by the method of weighted residuals. We treat the simplest possible manifold, namely an infinitely long, constant-area rectangular duct with a uniform transverse magnetic field and with a semi-infinite thin metal plate at the plane of symmetry which is perpendicular to the applied magnetic field. A longitudinal section and a cross section of this simple manifold are sketched in Fig. 1. The x axis coincides with the centerline of the infinitely long duct, the y axis is parallel to the applied magnetic field, and the semi-infinite plate or middle wall lies in the $y = 0$ plane for $x > 0$. The characteristic length L is half the distance between the sides, which are

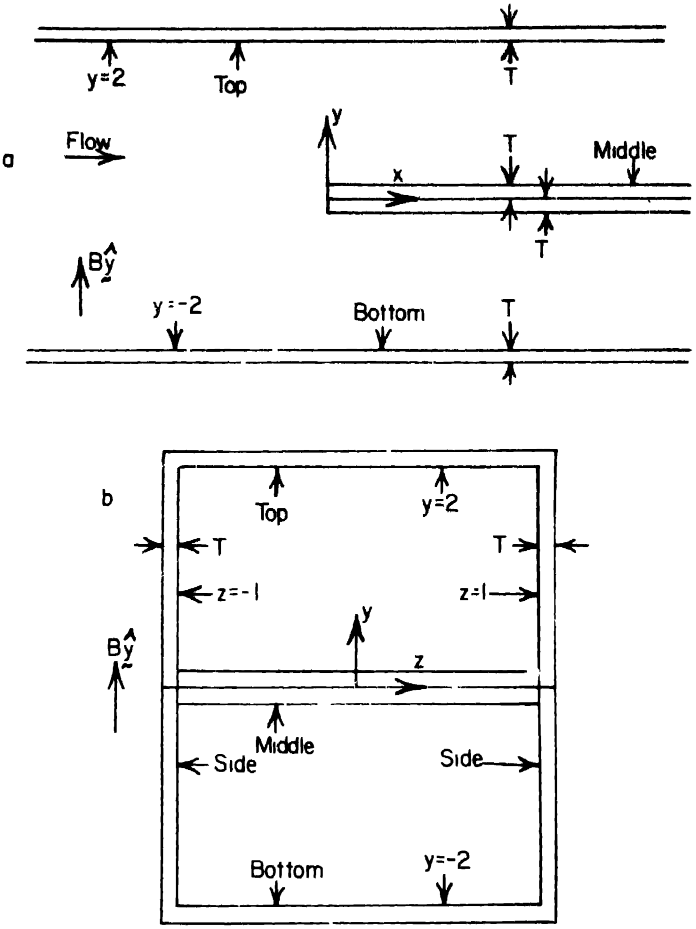

Fig 1 Simple manifold with a semi-infinite middle wall at the plane of symmetry of an infinitely long, constant area rectangular duct with metal walls and with a uniform transverse magnetic field (a) Longitudinal section $z = 0$ and (b) cross section $x = 0$

parallel to the applied magnetic field, so that the sides are at $z = \pm 1$. If the two parallel ducts above and below the middle wall for $x > 0$ have square cross sections, then the top and bottom walls are at $y = \pm 2$

If the magnetic Reynolds number $R_m = \mu_p \sigma U L$ is small, then we can ignore the perturbation of the applied magnetic field due to the electric currents in the liquid metal Here μ_p and σ are the magnetic permeability and electrical conductivity of the liquid metal In addition, the characteristic velocity U is the average axial velocity, so that the integral of u over any cross section must be 8, where u, v and w are the x, y and z components of the dimensionless velocity $\mathbf{v}$. If the magnetic field is sufficiently strong, we can ignore inertial effects everywhere and can ignore viscous effects except inside thin layers with large velocity gradients. There are Hartmann layers with $O(M^{-1})$ thickness adjacent to the top, middle and bottom walls, there are side layers with $O(M^{-1/2})$ thickness adjacent to the sides, and there is an interior layer with $O(M^{-1/2})$ thickness across the duct in the $x = 0$ plane at the end of the middle wall. Here $M = BL(\sigma/\mu)^{1/2}$ is the large Hartmann number, B is the magnetic flux density and μ is the viscosity of the liquid metal.

For fully developed flow in a rectangular duct with thin metal walls and with $M \gg 1$, there is a uniform transverse electric current density j_z in the inviscid core [4]. The body force due to this transverse current and the magnetic field is balanced by the pressure gradient which is driving the flow. The electric current enters the side at $z = 1$, and flows up or down the side to the top or bottom, respectively. The current then flows in the minus z direction inside the top or bottom and down or up the side at $z = -1$, respectively, to complete the electric current circuit. There is no vertical electric current density j_y or vertical electric field E_y in the core. However, the current flow up or down inside the side walls requires a non-zero vertical electric field E_y. Since the tangential component of electric field must be continuous across any interface, there must be a non-zero value of E_y in the liquid metal near the sides. This non-zero E_y is confined to the side layers with $O(M^{-1/2})$ thickness. This E_y produces a j_y inside the side layers and this j_y causes the transverse electric current streamlines to spread apart slightly as they go from the core to the side. Thus the j_z inside a side layer is slightly smaller, by an $O(M^{-1/2})$ amount, than the j_z in the inviscid core. In the core, there is a perfect balance between the driving pressure gradient and the opposing electromagnetic (EM) body force. The pressure gradient is continuous through the side layer, but the EM body force decreases slightly as j_z decreases. The locally unbalanced portion of the pressure gradient accelerates the fluid inside the side layer until viscous stresses restore a force balance. Since the viscous forces are much smaller than the EM forces, the velocity inside the side layer is large, namely $O(M^{1/2})$. Since there is an $O(M^{1/2})$ velocity inside the side layers with $O(M^{-1/2})$ thickness, the flow rate inside the side layers is comparable to that in the core. The electric current in the side is maximum at the top or bottom and decreases linearly to zero at the plane of symmetry as the current feeds into the uniform transverse core current. This implies that E_y inside the sides and the side-layer force imbalance accelerating the flow vary linearly from maxima at the top and bottom to zero at the plane of symmetry. Since the large velocity is zero at the top and bottom, then the high-velocity flow inside each side layer has a parabolic variation with y: zero at the top and bottom and maximum at the plane of symmetry. The fraction of the total flow inside each side layer depends on the aspect ratio of the duct's cross section. For a tall duct, the current must flow a long distance inside the sides. Thus the force imbalance acts over a large height and produces a very large flow inside the side layers. On the other hand, for a wide cross section, there is much less of the total flow inside the side layers.

For the simple manifold shown in Fig. 1, there is a single tall duct upstream, and the side layers in the upstream fully developed flow carry a relatively large fraction of the total flow. On the other hand, there are two square ducts downstream with much less of the total flow inside the side layers. Upstream there is a large parabolic flow distribution in the side layers with a maximum at $y = 0$; downstream we have two smaller parabolic side-layer flow distributions with zero flow at $y = 0$. The three-dimensional disturbance in this simple manifold involves the transfer of flow from the side layers upstream to the core downstream. This transfer involves two elements. The first element is a direct flow from the side layer to the core for finite distances for both positive and negative x. The second element is a transverse flow redistribution within the interior layer at $x = 0$. This interior-layer flow redistribution from the upstream side layer to the downstream core involves $O(M^{1/2})$ values of w inside the interior layer. Since this three-dimensional flow involves high-velocity side and interior layers, the neglect of inertial effects everywhere requires that $M^{1/2} \gg \mathrm{Re} = \rho UL/\mu$, where Re is the Reynolds number and ρ is the liquid metal's density [5].

2. Problem formulation

The dimensionless equations governing the steady, inertialess flow of a liquid metal with constant properties through a uniform magnetic field are

$$0 = -\nabla p + \mathbf{j} \times \hat{\mathbf{y}} + M^{-2}\nabla^2\mathbf{v}, \qquad \nabla \cdot \mathbf{v} = 0, \tag{1a, b}$$

$$\mathbf{j} = -\nabla\phi + \mathbf{v} \times \hat{\mathbf{y}}, \qquad \nabla \cdot \mathbf{j} = 0, \tag{1c, d}$$

where p, $\mathbf{j}$ and ϕ are the pressure, electric current density and electric potential function, normalized by σUB^2L, σUB and UBL, respectively, while the unit vector $\hat{\mathbf{y}}$ represents the dimensionless uniform magnetic field. The duct walls represent the inner metal sheet of the liners proposed by Malang et al. [2], so that the top, bottom and sides have a dimensionless thickness T, while the middle wall is composed of two metal sheets of thickness T which are separated by an insulator. The flow is symmetric in both y and z, so that we only consider one quarter of the cross section, namely $0 \leqslant y \leqslant 2$ and $-1 \leqslant z \leqslant 0$. Since $j_y = 0$ at $y = 0$ by symmetry, we would not need the insulator between the two sheets of the middle wall here, but we would need insulators inside dividing walls for real manifolds in order to apply the present eigenfunction expansions.

If the metal walls are thin, then $T \ll 1$ and the electric potential is constant through each wall, neglecting $O(T^2)$ terms. The tangential electric current densities inside the walls are given by $\mathbf{j} = -(\sigma_w/\sigma)\nabla\phi$, where σ_w is the electrical conductivity of the walls and the same normalizations of $\mathbf{j}$ and ϕ are used. Integration of the conservation law (1d) gives the $O(T)$ normal electric current density inside each wall. Since ϕ and the normal component of current are continuous at the interface between the liquid metal and each wall, the liquid-metal variables must satisfy the thin conducting wall boundary conditions [4],

$$j_z = c\left(\frac{\partial^2\phi_s}{\partial x^2} + \frac{\partial^2\phi_s}{\partial y^2}\right), \qquad \text{at } z = -1, \tag{2a}$$

$$j_y = -c\left(\frac{\partial^2\phi_t}{\partial x^2} + \frac{\partial^2\phi_t}{\partial z^2}\right), \qquad \text{at } y = 2, \tag{2b}$$

$$j_y = c\left(\frac{\partial^2\phi_m}{\partial x^2} + \frac{\partial^2\phi_m}{\partial z^2}\right), \qquad \text{at } y = 0, \text{ for } x > 0. \tag{2c}$$

Here $\phi_s(x, y)$, $\phi_t(x, z)$ and $\phi_m(x, z)$ are the electric potentials of the side wall at $z = -1$, the top wall and the middle wall, respectively, while $c = \sigma_w T/\sigma$ is the wall conductance ratio. The thickness of the middle wall, including liners and structural metal, is considered to be much less than L. In addition, the velocity $\mathbf{v}$ is zero at each wall.

The Hartmann layers with $O(M^{-1})$ thickness adjacent to the top and middle walls have a simple, local, exponential structure and match any tangential velocities in the inviscid core, provided the core velocity satisfy the Hartmann condition

$$v = 0, \quad \text{at } y = 0, \quad \text{and} \quad \text{at } y = 2. \tag{3a, b}$$

The condition (3a) is a Hartmann condition for $x > 0$ and a symmetry condition for $x < 0$. The jumps in j_y and ϕ across a Hartmann layer are $O(M^{-1})$ and $O(M^{-2})$, respectively, so that the conditions (2b) and (2c) can be applied to the inviscid core solutions, neglecting $O(M^{-1})$ terms [5].

The core solution which satisfies the inviscid version of the equations (1), which satisfies the conditions (3) and which matches the top wall potential is

$$j_x = \frac{\partial p}{\partial z}, \qquad j_z = -\frac{\partial p}{\partial x}, \qquad u = \frac{\partial\phi}{\partial z} - \frac{\partial p}{\partial x}, \qquad w = -\frac{\partial\phi}{\partial x} - \frac{\partial p}{\partial z}, \tag{4a–d}$$

$$v = 0, \qquad \phi = \phi_t + (2 - y)j_y, \qquad \frac{\partial^2 p}{\partial x^2} + \frac{\partial^2 p}{\partial z^2} = 0, \tag{4e–g}$$

where $p(x, z)$ and $j_y(x, z)$ are integration functions.

For $x < 0$, symmetry in y gives $j_y(x, z) = 0$, so that the condition (2b) gives the equation

$$\frac{\partial^2\phi_t}{\partial x^2} + \frac{\partial^2\phi_t}{\partial z^2} = 0, \qquad \text{for } x < 0, \tag{5}$$

governing $\phi_t(x, z)$ upstream. For $x > 0$, matching the electric potential of the middle wall gives $j_y = \frac{1}{2}(\phi_m - \phi_t)$. Therefore, the conditions (2b) and (2c) give the equations

$$\frac{\partial^2\phi_t}{\partial x^2} + \frac{\partial^2\phi_t}{\partial z^2} = \frac{1}{2c}(\phi_t - \phi_m), \quad \text{for } x > 0, \tag{6a}$$

$$\frac{\partial^2\phi_m}{\partial x^2} + \frac{\partial^2\phi_m}{\partial z^2} = \frac{1}{2c}(\phi_m - \phi_t), \quad \text{for } x > 0 \tag{6b}$$

governing $\phi_m(x, z)$ and $\phi_t(x, z)$ downstream. Once the equations (4g) and (5) or (6) are solved for p, ϕ_t and ϕ_m, the equations (4a)–(4f) give the other core variables upstream with $j_y = 0$ or downstream with $j_y = \frac{1}{2}(\phi_m - \phi_t)$. The symmetry conditions are

$$\phi_t = \phi_m = \frac{\partial p}{\partial z} = 0, \quad \text{at } z = 0, \tag{7}$$

where the electric potential at the origin is the reference potential.

In the side layer with $O(M^{-1/2})$ thickness adjacent to the side at $z = -1$, the deviation of j_z from the local core value is $O(M^{-1/2})$. This small deviation is important because it produces the local force imbalance which accelerates the side-layer velocity to $O(M^{1/2})$ values, but it is not important in the thin conducting wall condition (2a). This condition and the core solution (4b) give the equation

$$\frac{\partial^2\phi_s}{\partial x^2} + \frac{\partial^2\phi_s}{\partial y^2} = -\frac{1}{c}\frac{\partial p}{\partial x}(x, -1) \tag{8}$$

governing $\phi_s(x, y)$ and neglecting $O(M^{-1/2})$ terms. The electric potential must be continuous where the top or middle wall meet the side. In addition, the electric current in the plus or minus y direction inside the side at $y = 2$ or at $y = 0$ must enter the top or middle wall at $z = -1$, respectively, because the corners with $T \times T$ cross sections are too small to carry any significant axial electric current. Therefore ϕ_s, ϕ_t and ϕ_m satisfy the conditions

$$\phi_s(x, 2) = \phi_t(x, -1), \quad \frac{\partial\phi_s}{\partial y}(x, 2) = \frac{\partial\phi_t}{\partial z}(x, -1), \quad \text{for all } x, \tag{9a, b}$$

$$\frac{\partial\phi_s}{\partial y}(x, 0) = 0, \quad \text{for } x < 0, \tag{9c}$$

$$\phi_s(x, 0) = \phi_m(x, -1), \quad \frac{\partial\phi_s}{\partial y}(x, 0) = -\frac{\partial\phi_m}{\partial z}(x, -1), \quad \text{for } x > 0. \tag{9d, e}$$

The condition (9c) is a symmetry condition.

Inside the side layer at $z = -1$, the z component of Ohm's law (1c) gives the $O(M^{1/2})$ axial velocity, $u = \partial\phi/\partial\zeta$, where $\zeta = M^{1/2}(z + 1)$ is the stretched coordinate normal to the side. Therefore, the dimensionless volumetric flow rate in each Δy of the side layer is given by the local jump in ϕ across the side layer,

$$\int_0^{\alpha} u \, \mathrm{d}\zeta = \phi(x, -1) - \phi_s(x, y), \tag{10}$$

where $\phi(x, -1)$ is the core potential (4f) evaluated at $z = -1$. We can ignore the details of the side-layer solution provided we insure conservation of mass for the entire flow [1]. Since U is the average axial velocity, the integral of u over one quarter of any cross section must equal 2. The O(1) contributions to this integral come from the O(1) core velocity (4c) and the O($M^{1/2}$) side-layer velocity (10). With the symmetry condition (7), the conservation of mass condition becomes

$$\int_0^2 \phi_s \, \mathrm{d}y + \int_{-1}^{0} \frac{\partial p}{\partial x} \, \mathrm{d}z = -1, \tag{11}$$

neglecting O($M^{-1/2}$) terms. The condition (11) is a solubility condition: if ϕ_s and p satisfy this condition, then there exists a unique solution for the side-layer variables which matches the core variables as $\zeta \to \infty$, which satisfies $\mathbf{v} = 0$ and $\phi = \phi_s$ at $\zeta = 0$, which satisfies $v = 0$ and $\phi = \phi_t(x, -1)$ at $y = 2$, which satisfies $v = 0$ and $\partial\phi/\partial y = 0$ ($x < 0$) or $\phi = \phi_m(x, -1)$ ($x > 0$) at $y = 0$, and which gives a local flow rate equal to the potential jump (10). This side-layer solution is presented by Walker [4], but is not repeated here because our only interest is in the total side-layer flow given by the equation (10).

There is an interior layer with O($M^{-1/2}$) thickness across the duct in the $x = 0$ plane at the end of the middle wall. The electric potentials in the top and side must be continuous at $x = 0$. If any O(1) electric current enters the interior layer from the top, middle or side wall, then j_y or j_z would be O($M^{1/2}$) inside the layer, which in turn implies that w or v would be O(M) [4]. This would give an O($M^{1/2}$) volumetric flow rate inside this layer, but no volumetric flow rate can be larger than O(1) with our normalization. Therefore, the interior layer cannot exchange any O(1) current with any wall. The electric potential conditions at $x = 0$ are

$$\phi_t(0^-, z) = \phi_t(0^+, z), \qquad \frac{\partial\phi_t}{\partial x}(0^-, z) = \frac{\partial\phi_t}{\partial x}(0^+, z), \tag{12a, b}$$

$$\phi_s(0^-, y) = \phi_s(0^+, y), \qquad \frac{\partial\phi_s}{\partial x}(0^-, y) = \frac{\partial\phi_s}{\partial x}(0^+, y), \tag{12c, d}$$

$$\frac{\partial\phi_m}{\partial x}(0, z) = 0. \tag{12e}$$

The O(1) j_x must be continuous across this layer for the same reason, so equation (4a) indicates that p is continuous. In a general manifold, $\partial p/\partial x$ can be discontinuous. However, conservation of mass for the interior layer requires that the sums of the individual duct heights times their values of $\partial p/\partial x$ at $x = 0$ must be the same upstream and downstream of the interior layer [1]. In other words, the height-averaged value of $\partial p/\partial x$ must be continuous across the layer. In the present, simple manifold with symmetry in y, this gives continuity of $\partial p/\partial x$. Therefore the pressure conditions at $x = 0$ are

$$p(0^-, z) = p(0^+, z), \qquad \frac{\partial p}{\partial x}(0^-, z) = \frac{\partial p}{\partial x}(0^+, z). \tag{13a, b}$$

Since j_y is discontinuous across the interior layer, the core potential (4f) is also discontinuous. Inside the interior layer, the x component of Ohm's law (1c) gives the $O(M^{1/2})$ transverse velocity, $w = -\partial\phi/\partial\xi$, where $\xi = M^{1/2}x$ is the stretched axial coordinate. Therefore, the total dimensionless volumetric flow in the z direction inside the interior layer at each z position is

$$\int_0^2 \int_{-\infty}^{\infty} w \, d\xi \, dy = \phi_t(0, z) - \phi_m(0, z). \tag{14}$$

Since the jump in ϕ is linear in y, this transverse, interior-layer flow is distributed linearly in y with zero at $y = 2$ and the maximum at $y = 0$. The flow inside the upstream side layer splits as it enters the intersection of the side and interior layers at $x = 0$ and $z = -1$. Part continues into the downstream side layer, but the rest turns to enter the interior layer at $z = -1$. Inside the interior layer, this transverse flow gradually feeds into the downstream core as it progresses toward the $z = 0$ plane. Thus the transverse, interior-layer flow (14) is a maximum at $z = -1$ and decreases to zero as z increases from -1 to 0. In the present, simple manifold, the only O(1) flow inside the interior layer is in the z direction. In a general manifold, $\partial p/\partial x$ may be discontinuous between an individual downstream duct and the upstream core [1]. These discontinuities in $\partial p/\partial x$ correspond to a vertical redistribution of the flow inside the interior layer. Part of the flow entering a section of the interior layer from the upstream core may flow up or down inside the interior layer to enter the downstream duct above or below. The continuity of the height-averaged $\partial p/\partial x$ insures that the sum of all the vertical redistributions is zero. Thus the condition (13b) is a solubility condition for the interior layer which is comparable to the condition (11) for the side layer. Again we can ignore the details of the interior-layer solution because our only interest is in its transverse flow redistribution (14).

The equations (4g), (5), (6) and (8), together with the conditions (7), (9), (11), (12) and (13), constitute a well-posed boundary value problem for p, ϕ_m, ϕ_s and ϕ_t. In the next section, we present upstream and downstream eigenfunction expansions which satisfy all the equations and conditions, except the matching conditions (12) and (13) at $x = 0$. A method of weighted residuals is then used to satisfy these matching conditions and to determine the unknown coefficients in the expansions.

3. Eigenfunction expansions and matching conditions at $x = 0$

The separation-of-variables solutions which satisfy the upstream equations (4g), (5) and (8), and which satisfy the upstream conditions (7), (9a), (9b) and (9c) are

$$p = A_0 - K_u cx + \sum_{n=1}^{\infty} A_n a_n \exp(\alpha_n x)\cos(\alpha_n z), \tag{15a}$$

$$\phi_t = 2K_u z - 2\sum_{n=1}^{\infty} A_n \exp(\alpha_n x)\sin(\alpha_n)\sin(\alpha_n z), \tag{15b}$$

$$\phi_s = K_u(\tfrac{1}{2}y^2 - 4) + \sum_{n=1}^{\infty} A_n \exp(\alpha_n x)\left[\cos(\alpha_n y) - \frac{a_n\cos(\alpha_n)}{c\alpha_n}\right], \tag{15c}$$

$$a_n = c\alpha_n[\cos(\alpha_n) - 3\sin(\alpha_n)\tan(\alpha_n)]. \tag{15d}$$

The terms to the left of each summation represent the upstream fully developed flow for the present duct [4], while A_0 is an arbitrary, additive, constant pressure. The terms to the right of each summation are the eigenfunctions with eigenvalues α_n and with unknown coefficients A_n.

When the solutions (15a) and (15c) are introduced into the volumetric flow rate condition (11), (a) the fully developed flow solution gives the -1 on the right hand side if $K_u = 3/(10 + 3c)$, and (b) each eigenfunction must satisfy the condition (11) with zero on the right hand side. The latter gives a characteristic equation for the eigenvalues α_n,

$$2\alpha_n\cos(3\alpha_n)[c\alpha_n\tan(\alpha_n) - 1] + \sin(2\alpha_n)\cos(\alpha_n) = 0. \tag{16}$$

There are an infinite number of discrete, real values of α_n which satisfy the characteristic equation (16). The double eigenvalue, $\alpha_0 = 0$ corresponds to fully developed flow. For the eigenfunction expansions (15) for $-\infty < x < 0$, we only want the positive eigenvalues. To find the eigenvalues, (a) we first search over all values from 0 to 25 to find the approximate neighborhoods where the expression (16) changes sign, and (b) we locate the eigenvalue in each such neighborhood with an iterative Newton-Raphson scheme. The eigenvalues are numbered in ascending magnitude, corresponding to increasingly rapid spatial decay as x decreases from zero. For $c = 0.1$, the first three eigenvalues are $\alpha_1 = 1.4329$, $\alpha_2 = 1.5708$ and $\alpha_3 = 2.5754$. We truncate the expansions (15) at $n = 31$, which includes all $\alpha_n < 25$.

When we look for solutions for the downstream equations (6), it is obviously easier to deal with the sum and difference of ϕ_t and ϕ_m. In addition, ϕ_s can be split into two parts which are even and odd functions of $Y = (y - 1)$. The sum $(\phi_t + \phi_m)$ is governed by the Laplace equation and is tied to the even part of ϕ_s through the sum of the conditions (9a) and (9d) and through the difference of the conditions (9b) and (9e). The even part of ϕ_s gives a non-zero value for the first integral in the condition (11), so that p is non-zero and gives an inhomogeneous term in the equation (8). The boundary value problem governing p, $(\phi_t + \phi_m)$ and the even part of ϕ_s leads to one family of eigenfunctions with eigenvalues β_n and unknown coefficients B_n. The difference $(\phi_t - \phi_m)$ is governed by the Helmholtz equation and is tied to the odd part of ϕ_s through the difference of the conditions (9a) and (9d) and through the sum of the conditions (9b) and (9e). For the odd part of ϕ_s, the first integral in the condition (11) is zero and the solution of the equation (4g) with a zero integral in the condition (11) is $p = 0$. The boundary value problem governing $(\phi_t - \phi_m)$ and the odd part of ϕ_s leads to a second family of eigenfunctions with eigenvalues γ_n and with unknown coefficients C_n. Therefore the downstream eigenfunction expansions are

$$p = -K_d x + 2c \sum_{n=1}^{\infty} B_n \exp(-\beta_n x)\beta_n \operatorname{ctn}(2\beta_n)\cos(\beta_n z), \tag{17a}$$

$$\phi_t + \phi_m = -2K_d z + 2 \sum_{n=1}^{\infty} B_n \exp(-\beta_n x)\sin(\beta_n z), \tag{17b}$$

$$\phi_t - \phi_m = 2 \sum_{n=1}^{\infty} C_n \exp(-\gamma_n x)\frac{\sin(\lambda_n z)}{\lambda_n}, \tag{17c}$$

$$\begin{aligned}\phi_s = {} & K_d(1 + c - \tfrac{1}{2}y^2) + \sum_{n=1}^{\infty} B_n \exp(-\beta_n x)[2\cos(\beta_n)\operatorname{ctn}(2\beta_n) \\ & - \operatorname{ctn}(\beta_n)\cos(\beta_n Y)] + \sum_{n=1}^{\infty} C_n \exp(-\gamma_n x)\frac{\cos(\lambda_n)\sin(\gamma_n Y)}{\gamma_n \cos(\gamma_n)},\end{aligned} \tag{17d}$$

$$K_d = \frac{3}{4 + 3c}, \qquad \lambda_n = \left(\gamma_n^2 - \frac{1}{c}\right)^{1/2} \tag{17e, f}$$

The first term in each of the solutions (17a), (17b) and (17d) represents the downstream fully developed flow, while the reference pressure has been fixed by setting the arbitrary constant in the solution (17a) equal to zero. The form of the eigenfunction in the solution (17c) is chosen so that $\sin(\lambda_n z)/\lambda_n$ is real for all real γ_n.

The characteristic equations for the two independent families of discrete, real eigenvalues are

$$2\beta_n[c\beta_n \tan(\beta_n) - 1] + \tan(2\beta_n) = 0, \tag{18a}$$

$$\frac{\tan(\gamma_n)}{\gamma_n} + \frac{\tan(\lambda_n)}{\lambda_n} = 0 \tag{18b}$$

The characteristic equation (16) corresponds to modes which are even in y in a duct with its top and bottom at $y = \pm 2$. The equation (18a) corresponds to modes which are even in $Y = y - 1$ in a duct with its top and bottom at $Y = \pm 1$. The upstream odd modes corresponding to the equation (18b) are excluded by symmetry. Because of the form of the expansions (17), we only keep the positive values of β_n and γ_n, which are again numbered by ascending magnitude, corresponding to increasingly rapid spatial decay as x increases from zero. In the solutions (17), we truncate the first series of even modes at $n = 23$ and the second series of odd modes at $n = 15$, again retaining all eigenvalues which are less than 25. For $c = 0.1$, the first three eigenvalues in each family are $\beta_1 = 1.4398$, $\beta_2 = 2.2703$, $\beta_3 = 3.8326$, $\gamma_1 = 2.3280$, $\gamma_2 = 4.0270$, and $\gamma_3 = 5.1981$.

We use a method of weighted residuals to satisfy the remaining conditions (12) and (13) and to determine the unknown coefficients A_n, B_n and C_n in the eigenfunction expansions (15) and (17). The residual is the sum of the integrals of the squares of the errors in the conditions (12) and (13). We introduce weighting factors in order to balance the contributions of the different conditions to the residual. In the x derivatives of the eigenfunctions, each unknown coefficient is multiplied by its eigenvalue. Since the eigenvalues here range from 1.43 to 25, the axial derivatives are weighted more heavily than the values of the functions themselves. If we do not introduce a compensating weighting factor, the method of weighted residuals gives an excellent match of axial derivatives and a very poor match of the functions themselves. Therefore we weigh the functions with a factor W_f relative to axial derivatives. For fusion blanket applications, we are interested in rather small values of c, such as $c = 0.1$. As c decreases, the potentials increase in magnitude slightly, but the pressure decreases roughly in proportion to c. Therefore, for a small value of c, a large relative error in the conditions (13) would make a relatively small contribution to the residual unless we weigh the pressure with a factor W_p relative to the potentials. Therefore the weighted residual is

$$\begin{aligned} R = \int_{-1}^{0} \Bigg\{ & W_p W_f [p(0^-, z) - p(0^+, z)]^2 + W_p \left[\frac{\partial p}{\partial x}(0^-, z) - \frac{\partial p}{\partial x}(0^+, z) \right]^2 \\ & + W_f [\phi_t(0^-, z) - \phi_t(0^+, z)]^2 + \left[\frac{\partial \phi_t}{\partial x}(0^-, z) - \frac{\partial \phi_t}{\partial x}(0^+, z) \right]^2 \\ & + \left[\frac{\partial \phi_m}{\partial x}(0, z) \right]^2 \Bigg\} \mathrm{d}z + \int_0^2 \Bigg\{ W_f [\phi_s(0^-, y) - \phi_s(0^+, y)]^2 \\ & + \left[\frac{\partial \phi_s}{\partial x}(0^-, y) - \frac{\partial \phi_s}{\partial x}(0^+, y) \right]^2 \Bigg\} \mathrm{d}y. \end{aligned} \tag{19}$$

we have arbitrarily chosen $W_f = 10$, which is comparable to the average value of all the eigenvalues, and $W_p = 10$, which is $1/c$ for our case with $c = 0.1$. We have made no attempt to optimize these weighting factors. However, we have run the program with $W_f = W_p = 1$, and these results include rather large discontinuities in p and ϕ_s near the corner at $x = y = 0$ and $z = -1$.

We introduce the eigenfunction expansions (15) and (17) into the residual (19) and we minimize the residual by setting its derivatives with respect to the unknown coefficients equal to zero,

$$\frac{\partial R}{\partial A_0} = 0, \qquad \frac{\partial R}{\partial A_n} = \frac{\partial R}{\partial B_n} = \frac{\partial R}{\partial C_n} = 0, \tag{20}$$

for n from 1 to 31, 23 and 15, respectively. This minimization gives seventy simultaneous, linear, algebraic equations for the seventy unknown coefficients A_0, A_n, B_n and C_n. Sums of integrals of products of the eigenfunctions are the elements in the matrix multiplying the vector of unknowns, and this matrix is full because the eigenfunctions are not orthogonal. Sums of integrals of eigenfunctions times the upstream and downstream fully developed flow solutions are the inhomogeneous terms in the simultaneous equations. The integrals are evaluated analytically and the unknowns are determined by Gauss elimination. Once the equations (20) are solved for the unknown coefficients, then p, ϕ_t, ϕ_m and ϕ_s are given by the eigenfunction expansions (15) and (17), and the other core variables are given by the equations (4a)–(4f).

4. Results for $c = 0.1$

Here we present results for $c = 0.1$, which is a typical wall conductance ratio for fusion reactor blankets. The dimensionless flow rate Q_s inside the side layer at $z = -1$ for $0 \leqslant y \leqslant 2$ is plotted in Fig. 2. The total dimensionless flow rate in one quarter of any cross section is two, so that the core flow rate in each quarter cross section is $(2 - Q_s)$. Far upstream, $Q_s = 0.775$. As the flow approaches the end of the middle wall, fluid leaves the side layer and Q_s decreases from 0.775 for $x < -3$ to 0.57 at $x = 0$. Inside the intersection of the side and interior layers at $x = 0$ and $z = -1$, part of the side-layer flow turns to enter the interior layer and Q_s decreases abruptly from 0.57 at $x = 0$ to 0.42 at $x = 0^+$. Downstream of the function, fluid is flowing back into the side layer, so that Q_s increases from 0.42 at $x = 0^+$ to 0.465 for $x > 2$. Three-dimensional effects are confined to the axial region $-3 < x < 2$.

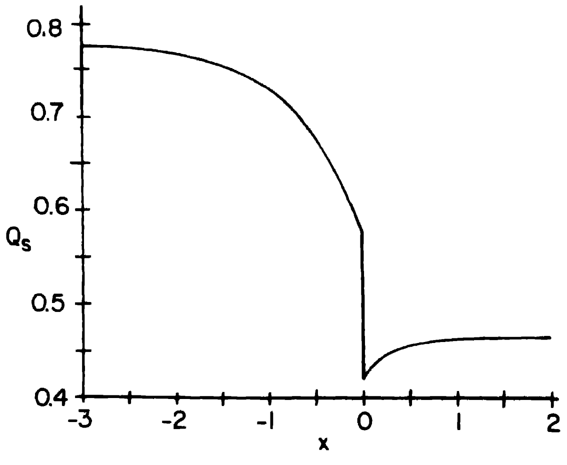

Fig 2 Dimensionless flow rate Q_s in the side layer at $z = -1$ for $0 \leqslant y \leqslant 2$. Flow rate in the core for a quarter cross section is $2 - Q_s$.

The basic flow transfer is from the upstream side layer to the downstream core. However, there is also a vertical redistribution of the flow. Far upstream, the core flow is uniform in y, but the side-layer flow is parabolic in y with zero flow at $y = 2$ and a maximum flow at $y = 0$. Thus the vertical center of the total far upstream flow is at $y = 0.9031$, i.e., at $y = 1$ for the core flow and at $y = 0.75$ for the parabolic side-layer flow. Far downstream, the core is uniform in y and the side-layer flow is parabolic with zero flow at both $y = 0$ and at $y = 2$, and with a maximum flow at $y = 1$. Therefore the vertical center of the total far downstream flow is at $y = 1$, and the three-dimensional flow for $-3 < x < 2$ involves a vertically upward flow redistribution. Since $v = 0$ in both core regions, there is no vertical flow redistribution in either core. Since $\partial p/\partial x$ is continuous across the interior layer, there is no vertical redistribution of the flow inside the interior layer. Therefore, all vertical flow redistribution occurs inside the upstream and downstream side layers.

For $x < 0$, there is no flow in the side layer at $y = 2$, but the flow entering the core from the side layer must be uniform in y since the upstream core u is independent of y. Therefore, the dimensionless flow of 0.205 from the side layer to the core for $-3 < x < 0$ has first been vertically redistributed inside the side layer. There is an additional vertically upward flow redistribution inside the upstream side layer, so that the $Q_s = 0.57$ remaining in the side layer at $x = 0^-$ is distributed at higher levels than the original $Q_s = 0.775$ for $x < -3$. In other words, the vertical center of the side-layer flow has risen from $y = 0.75$ for $x < -3$ to $y = 0.8695$ for the side-layer flow at $x = 0^-$.

Inside the intersection of the side and interior layers at $x = 0$ and $z = -1$, a dimensionless flow rate of 0.150 leaves the side layer, and this flow is distributed linearly in y with zero flow at $y = 2$ and with a maximum flow at $y = 0$. Since this transfer removes flow with a vertical center at $y = 0.667$, the remaining flow of $Q_s = 0.42$ entering the downstream side layer at $x = 0^+$ has a vertical center at $y = 0.942$. The interior layer simply passes flow from the side layer to the downstream core at $x = 0^+$ with no vertical redistribution, so that the flow added by the interior layer is concentrated near the middle wall. The downstream u is linear in y, with larger values at $y = 0$ than at $y = 2$, near $x = 0$. For example, the axial downstream core velocities at $x = 0^+$ and $z = -1$ are $u(0^+, 0, -1) = 1.3176$ and $u(0^+, 2, -1) = 0.6965$. Most of the interior-layer flow enters the core near $z = -1$. Of the flow of 0.150 at $z = -1$, only 0.069 remains inside the interior layer at $z = -0.8$. Therefore the core flow concentration near the middle wall with larger u at $y = 0$ is strongest near $z = -1$. For $x > 0$, there are two flow redistributions. First, the core flow must be redistributed from the concentration near the middle wall near $x = 0^+$ to a uniform flow with u being independent of y for $x > 2$. This redistribution can only be accomplished by passing fluid back to the side layer since $v = 0$ in the core. Second, the vertical center of the side-layer flow must rise from $y = 0.942$ at $x = 0^+$ to $y = 1$ for $x > 2$. For $0 < x < 2$, there is flow from the core to the side layer near $y = 0$ and flow from the side layer to the core near $y = 2$. For example, the transverse core velocities at $x = 0.05$ and $z = -1$ are $w(0.05, 0, -1) = -0.2491$ and $w(0.05,$ 2,

$- 1) = 0.1063$. Here w is also linear in y, so that there is more flow from the core to the side layer near $y = 0$ than from the side layer to the core near $y = 2$. Therefore, the core flow concentration near the middle wall at $x = 0^+$ is redistributed by entering the side layer near $y = 0$ and returning near $y = 2$, but not all the flow returns, so that Q_s increases from 0.42 at $x = 0^+$ to 0.465 for $x > 2$.

The evolution of the side-wall electric potential from its upstream parabola to its different downstream parabola is illustrated in Fig. 3. There is a nearly constant potential at $y = 0.87$. For $0 < y < 0.87$, the potential is increasing as x increases, so that electric current flows in the minus x direction inside this part of the side. For $0.87 < y < 2$, the potential is decreasing as x increases, so that electric currents flow in the plus x direction here. Most of this electric current is simply recirculating in the side, but there is some net current in the minus x direction inside the side at $z = -1$, and this net current completes its electrical circuit either through the core with a j_z which is independent of y or through the top or middle walls.

The core pressures at $z = 0$ and at $z = -1$ are plotted in Fig. 4. The downstream pressure gradient is larger than the upstream one. The basic electric circuit consists of a battery, which is the flow across the magnetic field lines, and a series of resistors, which are the liquid metal, top, bottom and sides. When we add the middle wall, we are adding another resistor in parallel to the top and bottom. The additional resistor in parallel allows more electric current to flow in the liquid metal, and the pressure gradient is proportional to the liquid-metal current. At a given x, the difference between the two pressures in Fig. 4 represents the total axial electric current in one

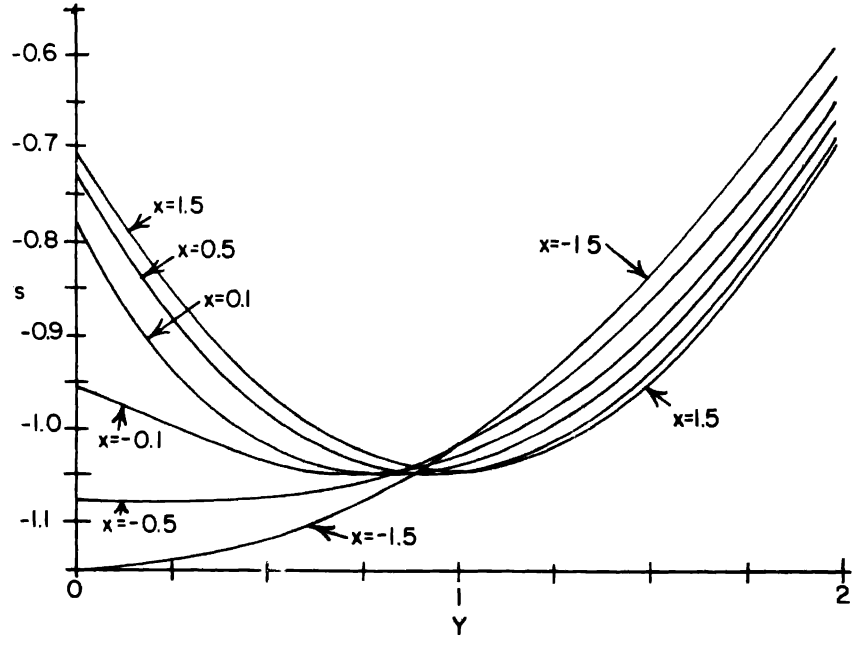

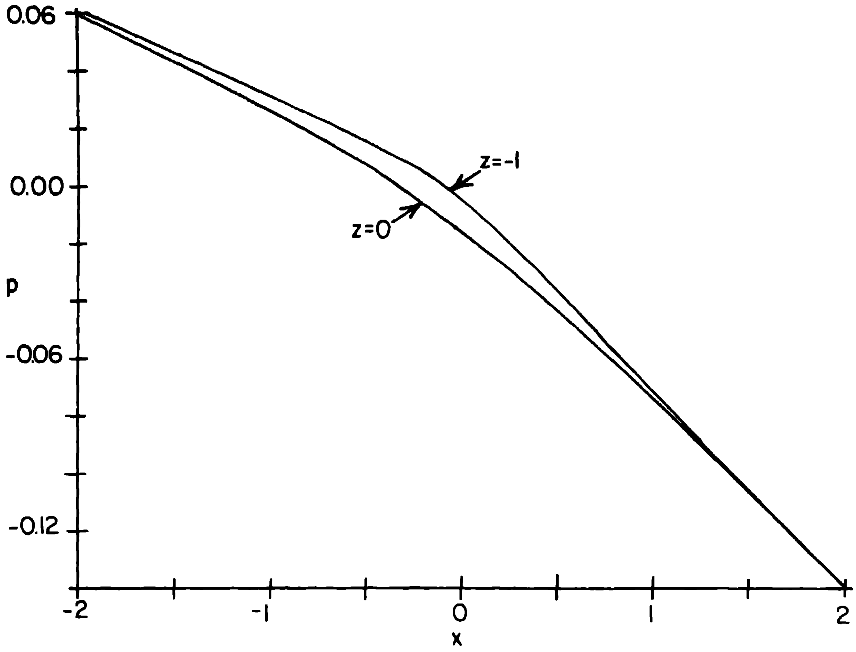

Fig. 4. Core pressures at $z = 0$ and at $z = -1$ for $c = 0.1$.

quarter of this cross section since p acts as a stream function for the electric current, as shown by the equations (4a) and (4b). There is an electric current in the minus x direction in the core for $-1 \leqslant z \leqslant 0$. This three-dimensional current has a maximum at $x = 0$ and decreases exponentially on both sides of the junction. The constant $A_0 = 0.004678$, which represents the three-dimensional pressure drop for this manifold. The three-dimensional pressure drop must be added to the pressure drop for two different fully developed flows for $x < 0$ and $x > 0$.

5. Concluding remarks

Here we have treated flow from a single duct upstream to a pair of ducts downstream. Since inertial effects are negligible and the governing equations are linear, the solution for flow in the opposite direction is obtained by changing the signs of all dependent variables.

The objective of this paper is to illustrate the use of eigenfunction expansions for a liquid-metal flow in a manifold connecting a feeder duct to many parallel ducts which are electrically insulated from each other. Here we treat a very simple manifold with only two parallel ducts downstream, but the advantage of this approach is realized with many parallel ducts. Since the insulator inside the middle wall plays no role here because $j_y = 0$ here by symmetry, the finite-difference solution of Hua and Picologlou

[1] for electrically connected parallel ducts applies as well to this case. This finite-difference code has been run for this case and the results are indistinguishable from the results plotted in Figs 2 4 This comparison provides a check on both approaches and confirms that our choices for the weighting factors in the residual are appropriate. With the eigenfunction expansion, we have only 70 unknowns, while the finite-difference approach has several thousand unknowns for this simple manifold.

In a more realistic manifold with many parallel ducts, there would be an eigenfunction expansion for each parallel downstream duct. For the present simple manifold, the flow is symmetric in z, so we only had two families of modes downstream even modes and odd modes. For a single duct in an array of parallel ducts, the flow is not symmetric in y or z, so that there will be four modes: even in y and even in z, odd in y and even in z, even in y and odd in z, odd in y and odd in z. The first two correspond to the present even and odd (in y) modes. The eigenfunction solutions and characteristic equations for the two new modes which are odd in z represent a straightforward extension of the derivations here.

Acknowledgment

This research was supported by U S. Department of Energy Office of Fusion Energy under Contract No W-31-109-ENG-38

References

1 Hua T Q and Picologlou, B F MHD flow in a manifold and multiple rectangular coolant ducts of self-cooled blankets *Fusion Technology* (1990)

2 Malang, S et al Self cooled liquid-metal blanket concept *Fusion Technology* 14 (1988) 1343

3 Moon T J and Walker, J S Liquid metal flow through a sharp elbow in the plane of a strong magnetic field *J Fluid Mech* 213 (1990) 397 418

4 Walker, J S Magnetohydrodynamic flows in rectangular ducts with thin conducting walls Part 1 Constant-area and variable-area ducts with strong uniform magnetic fields *J de Mecanique* 20 (1981) 79 112

5 Walker, J S, Ludford, G S S and Hunt, J C R Three-dimensional MHD duct flows with strong transverse magnetic fields Part 3 Variable-area rectangular ducts with insulating walls. *J Fluid Mech.* 56 (1972) 121 141

Applied Scientific Research **49**: 67–81, 1992.
© 1992 *Kluwer Academic Publishers. Printed in the Netherlands.*

Mechanisms of nozzle type reactor operation with gas removal

A. K. COKER, G. V. JEFFREYS & C. J. MUMFORD
Aston University, Department of Chemical Engineering and Applied Chemistry, Birmingham B4 7ET, England

Received 28 June 1989; accepted in revised form 13 August 1990

Abstract. A nozzle type reactor with provision for gas removal has been studied for the neutralisation of dodecylbenzene sulphonic acid with sodium carbonate solution. Gas was removed via a central air core so that the product was essentially foam-free. The rate of mixing and the chemical reaction between dodecylbenzene sulphonic acid and sodium carbonate solution, were observed to be much faster than the liquid residence time so complete conversion into the product was achieved within seconds. Some gas bubbles were entrained in the product: however these were negligible compared with the bulk of the gas bubbles expelled at the top of the reactor. The criteria for gas removal was that the time for bubbles to travel to the air core under the prevailing centripetal force was less than the liquid phase residence time in the reactor. Mathematical models were therefore proposed to predict the equilibrium bubble diameter and the time for bubble travel to the core. Predicted times were found to be very much less than the average residence time.

Notation

a = radius of the gas bubble, mm
a_{crit} = critical radius of the gas bubble, mm
A_i = area of the inlet swirl channel, mm^2
b = radius of the nozzle reactor, mm
B = constant (in Bloor and Ingham derivation)
c = radius of top outlet, mm
d_{crit} = critical size of the gas bubble, mm
F_c = centrifugal force, N
F_D = drag force, N
h = thickness of the bubble wall, mm
K'_f = drag coefficient
l = length of the reactor from apex of cone, mm
P = pressure, N/m^2
Q = volumetric flow rate of fluid through the reactor, m^3.s^{-1}
r_{ac} = radius of the air core, mm.
R = radius co-ordinate in cylindrical co-ordinates
Re = Reynolds number
t_i = time, sec.
V_i = average radial velocity, m/s.
V_r = radial velocity of fluid, m/s.
V_z = vertical velocity of fluid, m/s.
V_θ = tangential velocity of fluid, m/s.
X = fractional conversion
z = vertical distance from apex of cone along the axis, mm.

Greek letters

α_* = loss factor (Bloor and Ingham derivation)
α_θ = semi-angle of cone
θ = polar angle
π = constant (3.14159)
Ω = circulation constant, m^2/s.
σ = interfacial tension between liquid and gas bubble, N/m.
μ = viscosity of liquid, mPa.s
ρ = density of liquid, Kg/m^3
ρ' = density of gas, Kg/m^3
ψ = stream function

Introduction

In a number of chemical processes a gas is generated during a reaction between two liquids or between a solid and a liquid. If such a reaction process is undertaken in a conventional C.S.T.R. or tubular reactor, a foam may be produced which is difficult to separate. This difficulty is compounded if the desired product is viscous, or even thixotropic. Therefore a special type of reactor in which the gas bubbles formed are separated as, or before the product is discharged would be desirable. These reactions are generally fast – e.g. neutralisations – the requisite residence time in the reactor is small and the use of a nozzle type reactor, in which the gas bubbles are centrifuged into the air core is therefore appropriate. The separation of the gas and liquid products can be facilitated by imposing a slight vacuum on the air core and withdrawing the gas generated through a liquid entrainment separator installed at the top of the nozzle, so that the reactor functions like a gas-liquid cyclone. This type of reactor has been studied for the neutralisation of dodecylbenzene sulphonic acid with sodium carbonate solution and the results are presented in this paper.

The fluid flow characteristics and the residence time distribution in geometrically-similar laboratory type nozzle reactors have been described elsewhere [1, 2]. A model has also been presented which shows that such a vessel behaves as a series of C.S.T.R.'s and plug flows with a by-pass [3].

Beenackers and Van Swaaij [4] sulphonated liquid benzene with gaseous sulphur trioxide in a gas-liquid cyclone reactor and observed that strong centripetal forces on the gas bubbles caused them to spiral from the wall to the axis which generated high mass transfer coefficients. In the present work, nozzle type reactors were used to neutralise acids with sodium carbonate solution. These reactions are fast and evolve carbon dioxide gas. The product from the reactor must be the completely neutralised salt and be free from foam, and these are the criteria for the assessment of performance. This depends on the effective mixing of the reactants, which is especially important in the case of viscous liquids, and on the generation of sufficient centripetal force to efficiently discharge bubbles of gas, thereby preventing the formation of a foam.

The experimental programme reported here involved the neutralisation of dodecylbenzene sulphonic acid with sodium carbonate solution. A high speed radial flow vortex was created in the reactor and the intense shear forces in the core of the vortex promoted intimate mixing of the liquids. The neutralisation reaction resulted in the formation of carbon dioxide gas bubbles. These were expelled from the liquid into the air core and removed through the top of the reactor; as a result little foam was obtained in the salt product compared with that observed in small-scale batch experiments. The efficiency of gas removal evidently requires that adequate time is available for individual gas bubbles to travel from their loci of generation to reach the air core. Mathematical models were therefore developed to estimate the equilibrium bubble size, and thence the time taken for a typical gas bubble to travel from the wall to the air core for comparison with the liquid phase residence time in the reactor.

Mechanism of reaction

The principal aromatic chemicals used in the synthesis of anionic surfactants are benzene (C_6H_6) and phenol (C_6H_5OH). The former is often used since it can be readily converted by sulphonation of alkylbenzene sulphonic acids. Monoalkyl benzenes in which the side chain contains about C_{10}—C_{15} are commonly referred to as detergent alkylates. However two types of detergent alkylates have been employed as raw materials for the production of anionic surfactants by further processing to alkyl arylsulphonates. The older, branched-chained type which is no longer used, is referred to as hard detergent alkylate. This branch causes persistent foam since it is not amenable to biodegradation of its alkylbenzene sulphonic derivate (ABS) in sewage, disposal systems, rivers and streams.

An alternative to ABS, are alkylbenzene sulphonates produced from the biodegradable "linear detergent alkylates" (LAB or soft detergent alkylates) which are biologically soft. An olefin such as propylene is polymerised from the catalytic cracking process, composed of about 30-50% propylene mixed with 50-70% propane and other light hydrocarbons.

$$\begin{array}{llll} C_3H_6 \xrightarrow[\text{catalyst}]{\text{Polymerised}} & C_{12}H_{24} & \text{or} & C_{15}H_{30} \\ & \text{Dedecene} & & \text{Pentadecene} \\ & \text{Propylene} & & \text{Propylene} \\ & \text{tetramer} & & \text{pentamer} \end{array} \quad (1)$$

The alkylation process is the addition of benzene across the double bond of the olefin in the presence of aluminum chloride ($AlCl_3$) or hydrogen fluoride (HF) as catalyst.

$$\begin{array}{ll} C_{12}H_{24} \text{ or } C_{15}H_{30} + C_6H_6 \xrightarrow{AlCl_3 \text{ or } HF} & C_{12}H_{25}\cdot C_6H_5 \\ & \text{Tetramer-type} \\ & \text{Dodecylbenzene} \\ & \quad\text{or} \\ & C_{15}H_{31}\cdot C_6H_5 \\ & \text{Pentamer-type} \\ & \text{Pentadecylbenzene} \end{array} \quad (2)$$

Alkylbenzenes are sulphonated with oleum (usually 20% SO_3), 100% sulphuric acid or anhydrous sulphur trioxide to give a greater than 95% yield of the sulphonate.

$$\begin{array}{ll} C_{12}H_{25}\cdot C_6H_5 + H_2SO_4 \longrightarrow & C_{12}H_{25}\cdot C_6H_4SO_3H + H_2O \\ \text{Dodecylbenzene} & \text{Dodecylbenzene} \\ & \text{sulphonic acid} \\ & \text{(Dobane JN)} \end{array} \quad (3)$$

The sulphonic acid is usually neutralised with aqueous alkali to give a slurry containing 40–50% of sodium dodecylbenzene sulphonate and 5–6% of sodium sulphate (Na_2SO_4), the mixture being suitable for processing into the majority of finished detergent products.

$$C_{12}H_{25}\cdot C_6H_5SO_3H + NaOH \longrightarrow C_{12}H_{25}\cdot C_6H_5SO_3Na + H_2O \qquad (4)$$

However, sodium carbonate (Na_2CO_3) is a common ingredient of soaps and detergent powders. Its main uses are for pH adjustment in small quantities, to give a desired alkalinity in larger amounts, or other times as a filler.

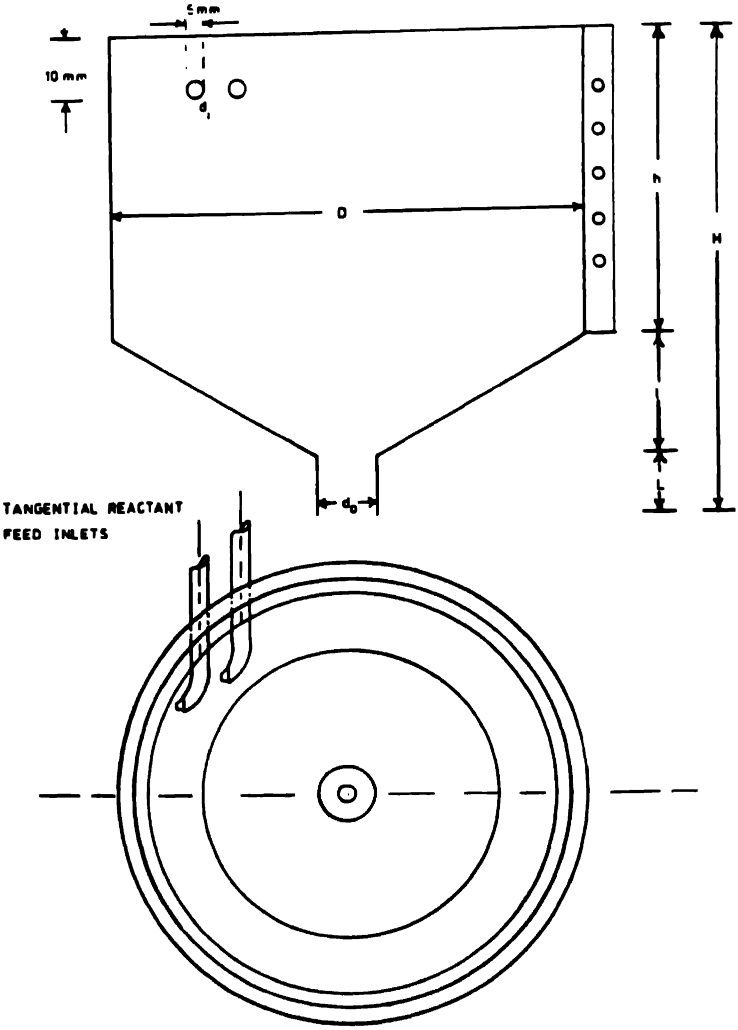

Fig. 1. Plan and elevation of cylindrical nozzle reactor.

The reaction mechanism involving an aqueous solution of Na_2CO_3 and dodecylbenzene sulphonic acid (Dobane JN) is

$$2C_{12}H_{25}\cdot C_6H_4SO_3H + Na_2CO_3 \xrightarrow{\text{Fast}} 2C_{12}H_{25}C_6H_4SO_3Na + H_2O + CO_2 \qquad (5)$$

Experimental

A plan and elevation of the cylindrical nozzle reactor employed are illustrated in Fig. 1; the dimensions are summarised in Table 1. Two reactors with volumes $0.55 \times 10^{-3}\,m^3$ and $1.52 \times 10^{-3}\,m^3$ respectively were fabricated from acrylic perspex rod, machined to fit hollow tubes of the same material. The $5.13 \times 10^{-3}\,m^3$ reactor was constructed to a similar geometry, but was fabricated from polyvinylchloride. Each reactor had two inlet feed points of 6 mm diameter, which projected tangentially into the body of the vessel. Along the side walls there were 4–5 injection ports for inserting tracers or withdrawing samples [1, 2]. A schematic diagram of the apparatus used is shown in Fig. 2.

The reactor was connected to two feed tanks constructed from industrial glass sections, each of 20 litres capacity. Each pipe line from a feed tank to the reactor was connected via a polypropylene Beresford PV 41 pump with a capacity of $5.67 \times 10^{-4}\,m^3 \cdot s^{-1}$, and a pressure gauge capable of recording a maximum pressure of $196.13\,N/m^2$. Each flow rate was controlled by a 19 mm diameter angle-seat valve and measured using a rotameter of $1.42 \times 10^{-4}\,m^3 \cdot s^{-1}$ maximum capacity. A 3-way glass valve was installed in each feed line to control the flow rate, or to divert any flow back to the feed tanks. Effluent flow was measured using a rotameter with a stainless

Table 1 Dimensions of the cylindrical nozzle reactors

Cylindrical nozzle reactor, Material of construction	1 Acrylic	2 Acrylic	3 PVC
Volume of the vessel $10^{-3}\,m^3$	0.55	1.52	5.13
Cylindrical section			
Height of the hollow cylinder h mm	81	114	144
Diameter of the cylinder D mm	85	120	200
Conical section			
Height of the solid cone l mm	38	55	54
Length of the outlet orifice L mm	53	50	72
Diameter of the outlet orifice d_0 mm	10	10	10
Diameter of the inlet orifice d_i mm	6	6	6
Cone angle	96.4	95.0	123.3

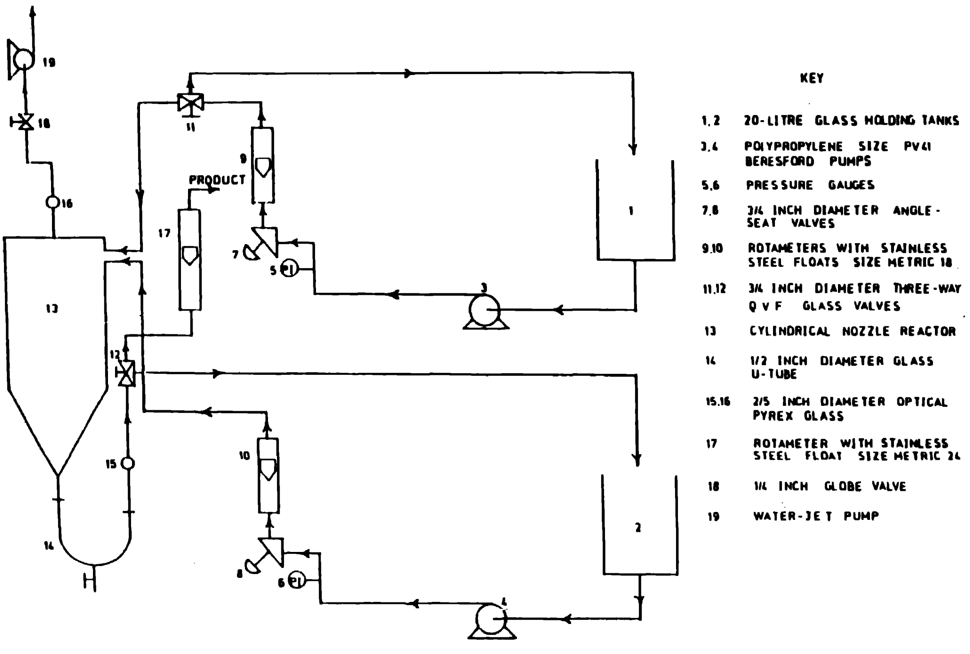
19
18
16
13
PRODUCT
11
9
17
7
5
3
1
12
15
10
14
8
6
4
2
KEY
1, 2 20-LITRE GLASS HOLDING TANKS
3, 4 POLYPROPYLENE SIZE PV41 BERESFORD PUMPS
5, 6 PRESSURE GAUGES
7, 8 3/4 INCH DIAMETER ANGLE-SEAT VALVES
9, 10 ROTAMETERS WITH STAINLESS STEEL FLOATS SIZE METRIC 18
11, 12 3/4 INCH DIAMETER THREE-WAY QVF GLASS VALVES
13 CYLINDRICAL NOZZLE REACTOR
14 1/2 INCH DIAMETER GLASS U-TUBE
15, 16 2/5 INCH DIAMETER OPTICAL PYREX GLASS
17 ROTAMETER WITH STAINLESS STEEL FLOAT SIZE METRIC 24
18 1/4 INCH GLOBE VALVE
19 WATER-JET PUMP

Fig. 2. Flow diagram of the experimental apparatus.

steel float. Finally, a water-jet pump was connected via a 6.35 mm globe valve to a gas-liquid entrainment separator on the top of the reactor.

The viscosity of the dodecylbenzene sulphonic acid ($C_{12}H_{25}C_6H_4SO_3H$) used was determined using a Rotovisco RV 12, Haake viscometer and found to be 1670.7 mPa · s; the pH value was 1.34. The liquid viscosity was subsequently reduced by the addition of 111 trichloroethane to give feeds with viscosities varying in the range 366.27 to 591.17 mPa · s.

At the start of each experiment, 0.5 M sodium carbonate solution was pumped into the reactor in order to fill it. The 3-way valve was used to divert the solution from the outlet orifice to the feed tank. The 3-way valve in the acid line also diverted the flow of acid to the feed tank before entry into the nozzle reactor. After steady hydrodynamic conditions were attained, the dodecylbenzene sulphonic acid mixture was pumped into the sodium carbonate solution already in the vessel. The reaction between the two solutions was very fast to yield a creamy-white slurry of sodium dodecylbenzene sulphonate ($C_{12}H_{25}C_6H_4SO_3 \cdot Na$) or linear alkyl sulphonate (LAS). The carbon dioxide gas formed was transported to the centre of the air core and expelled by a water jet pump. The product LAS was collected and its acidity measured with a Corning pH 119 meter. Analytical tests were carried out on each product sample to determine the percentage of the anionic active detergent (surfactant) and sodium sulphate. Table 2 summarises typical results.

The residence time distribution of the reactants could not be estimated experiment-

Table 2 Summary of neutralization experiments at varying feed rates

Run number	Dobanic acid JN flow rate	Na_2CO_3 $(10^{-3}\,m^3\,s^{-1})$	Product LAS (pH)	Mean residence time *t* (secs)	Critical size of the gas bubble (mm)	Time at whic the gas bubbl travels to the air-core of the vessel (secs)
1	0.0050	0.0458	9.88	10.827	1.042	0.368
2	0.0063	0.0575	9.61	8.621	0.661	0.295
3	0.0098	0.0775	9.80	6.300	0.353	0.201
4	0.0143	0.0917	9.57	5.189	0.239	0.167
5	0.0183	0.1217	9.69	3.929	0.137	0.115
6	0.0273	0.1417	9.44	3.254	0.094	0.096

Av = 9.67
Reactor volume 0.55 × $10^{-3}\,m^3$
Dodecylbenzene sulphonic acid (Dobane JN) 97.0% (w/w)
Na_2CO_3 0.5 M
Viscosity of dobanic acid with 1,1,1 trichloroethane 417.68 mPa s (cp)
pH of dobanic acid with 1,1,1 trichloroethane 0.75

ally because of the opacity of the gas-liquid dispersion. However the rate of mixing and the chemical reaction between dodecylbenzene sulphonic acid and sodium carbonate solution were much faster than the liquid residence time, so complete conversion into the product was achieved within seconds. Some gas bubbles were entrained in the product but were negligible compared with the bulk of the gas bubbles expelled at the top of the reactor. The size of the gas bubbles, and the time required for typical bubbles to travel to the air core of the reactor were therefore evaluated from mathematical models.

A mathematical model for bubble motion in a nozzle reactor

Figure 3 is a schematic diagram of a gas bubble in a nozzle reactor. This reactor is analogous to a cyclone for which the theory relating to the separation of particles has been developed by Ter linden [5], Bradley and Pulling [6] and Kelsall [7]. The theory is based upon the concept of a stability radius, at which centrifugal forces acting on a particle are balanced by the drag forces exerted by the radial flow. Particles attain their stability radius when equilibrium conditions are reached. Particles having a stability radius smaller than the radius of the overflow nozzle are expelled through the overflow, whilst particles with stability radii larger than the overflow nozzle radius are discharged through the base of the nozzle. Rietema [8] proposed a dynamic theory which assumed that particles with a stability radius smaller than the overflow nozzle radius may be collected at the wall before reaching the stability radius.

Bloor and Ingham [9, 10] presented a mathematical model for the flow conditions

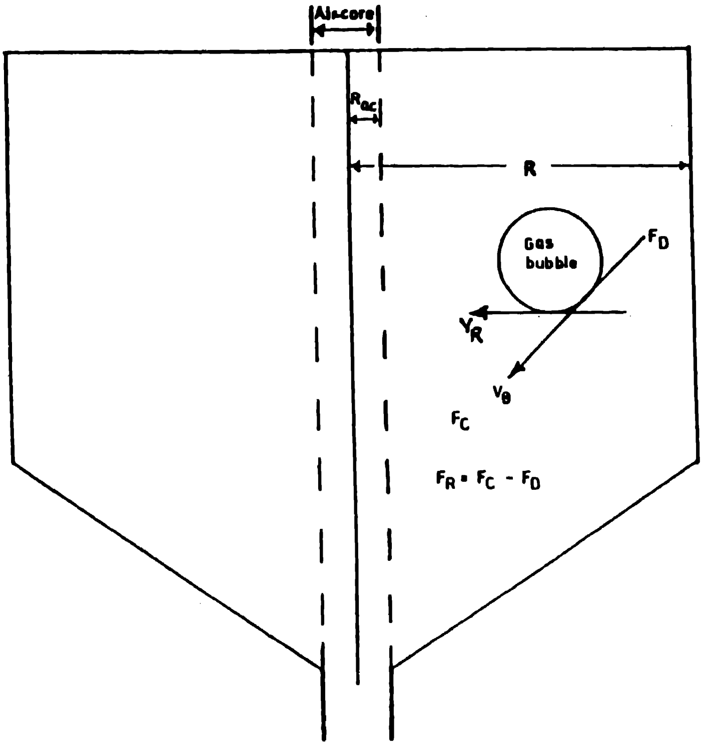

Fig. 3. Schematic diagram of a gas bubble in a nozzle reactor.

in a conical cyclone. On the assumption that the flow of fluid was rotational, they employed a viscous turbulent model based on the Prandtl mixing length theory to show that in a region of viscous flow at the wall, and at the axis of the cyclone, the azimuthal component velocity changes from being a free vortex to "solid body" rotation. The main body of the fluid in a potential core has been taken to be moving only in a free vortex motion with

$$V_\theta = \frac{\Omega}{R}, \tag{6}$$

where Ω is the circulation constant and R is the radial distance from the axis. Due to this free vortex motion a central air core forms within the nozzle [2]. Thus the tangential velocity varies with distance from the nozzle axis; shear is therefore exerted on bubbles resident in the nozzle liquids. This deforms, and fragments the bubbles so that in order to evaluate the bubble residence time it is necessary to be able to estimate the equilibrium bubble size.

Bubble break-up

The mechanism of bubble rupture in a turbulent fluid has been reviewed by Levich [11]. Originally bubble deformation and ultimate break-up were considered to occur when the dynamic pressure ($\rho V^2/2$) in the medium exceeded the capillary pressure (σ/R) inside the bubble [12]. This postulation has been disproved and consequently Levich proposed that the drag of the liquid phase sets up rotational or turbulent motion inside the bubble. This motion creates in turn a dynamic pressure which is directed outward from inside the bubble. Once this dynamic pressure exceeds the capillary pressure, break-up is inevitable. Hence the bubble fragmentation condition is

$$K'\rho'\frac{V_\theta^2}{2} \geqslant \frac{\sigma\pi h^2}{V}, \tag{7}$$

where

$$h = \frac{\sigma}{\Delta P} = \frac{2\cdot\sigma}{\rho V_\theta^2}. \tag{8}$$

h is the thickness of the bubble wall.

$$V = \tfrac{4}{3}\pi a^3, \tag{9}$$

so that

$$K'_f\rho'\frac{V_\theta^2}{2} = \frac{4\cdot\sigma^3\pi}{\rho^2 V_\theta^4\cdot V} \tag{10}$$

$$= \frac{4\cdot\sigma^3\cdot\pi}{\rho^2\cdot V_\theta^4\cdot\frac{4}{3}\cdot\pi a^3}, \tag{11}$$

$$K'_f\rho'\cdot\frac{V_\theta^2}{2} = \frac{3\cdot\sigma^3}{\rho^2\cdot V_\theta^4\cdot a^3}. \tag{12}$$

Hence the critical bubble diameter is

$$K'_f\rho'\cdot\frac{V_\theta^2}{2} = \frac{3\cdot\sigma^3}{\rho^2 V_\theta^4(d^3/8)}, \tag{13}$$

$$d_{\text{crit}}^3 = \frac{48\cdot\sigma^3}{K'_f\rho'\rho^2 V_\theta^6}, \tag{14}$$

$$d_{\text{crit}} = \sqrt[3]{\frac{48}{K'_f}}\cdot\frac{\sigma}{V_\theta^2}\cdot\frac{1}{\sqrt[3]{\rho'\rho^2}}. \tag{15}$$

Therefore the equilibrium bubble diameter, respresenting the largest bubble which can exist, is

$$d_{\text{crit}} = \sqrt[3]{\frac{48}{K_f'} \cdot \frac{\sigma}{\rho V_\theta^2}} \sqrt[3]{\frac{\rho}{\rho'}}. \tag{16}$$

Bubble dynamics

The viscous rotational flow model developed by Bloor and Ingham showed that the velocity components of the fluid in terms of cylindrical polar co-ordinates (r, θ, z) may be expressed as,

$$V_\theta = \frac{\Omega}{R} \tag{17}$$

and

$$V_z = -\frac{1}{2} \cdot BR^{-1/2} \cdot \frac{(3 \cdot \alpha^* - 5R)}{z} \tag{18}$$

where Ω and B are constants, α^* is the semi-angle of the cone. The stream function ψ is expressed by

$$\psi = BR^{3/2}(\alpha^* - R/z) \tag{19}$$

and the constants for any set of experimental conditions,

$$\Omega = \frac{\alpha \cdot bQ}{Ai} \tag{20}$$

and

$$B = \frac{Q}{2 \cdot \pi c^{3/2}(\alpha^* - c/1)}. \tag{21}$$

In this study, c is assumed to be the outer radius of the top outlet and 1 is the distance from the apex to the top of the reactor. The radial velocity of the fluid V_r is towards the axis of the nozzle reactor and is opposed by the centrifugal acceleration. This fluid velocity V_r will tend to transport bubbles into the air core but the actual bubble velocity will depend on the drag forces impeding bubble flow. These drag forces must therefore be assessed in order to estimate the bubble residence time. At the plane of zero vertical velocity, the longitudinal velocity of the fluid V_z is zero and from equation 18,

$$z = \frac{5 \cdot R}{3\alpha^*}. \tag{22}$$

z is the distance along the axis from the apex.

Equations 20–22 were programmed to estimate the radial velocity. This was calculated incrementally along the radial distance from the axis to the wall of the reactor at increments of 0.00425 m. The average radial velocity V_i in the increment along the radius of the reactor was evaluated at a constant step length ($\Delta R = 0.00425$).

Bloor and Ingham [10] considered that in their system the presence of an air core was irrelevant provided the boundary of the air core fell in the region where the flow was approximately "solid body"; that is where there was no shearing stress. In practice, as observed in this work, an air core exists along the axis of the reactor [1, 2]. Hence for a stable flow rate, the air core radius must adjust itself so that the discharge is a maximum and as observed by Binnie and Hookings [13], the condition is when

$$\frac{\partial Q}{\partial h} = 0 \tag{23}$$

which yields

$$r_{\mathrm{ac}}^2 = \frac{\rho}{8P} \{\Omega^2 + (\Omega^4 + 16h^2\Omega^2 p/\rho)^{0.5}\}. \tag{24}$$

A gas bubble travelling from the wall of the reactor under an acceleration V_θ^2/r would exert a centripetal force

$$F_C = m \cdot \frac{V_\theta^2}{r}, \tag{25}$$

where m is the bubble mass

$$F_C = (\rho' - \rho) \cdot \frac{\pi \cdot d_{\mathrm{crit}}^3}{6} \cdot \frac{V_\theta^2}{r}. \tag{26}$$

The drag force exerted by the liquid on the gas bubble is

$$F_D = K_f' \cdot \rho' \cdot A \cdot \frac{V_r^2}{2}, \tag{27}$$

where A is the bubble area.

$$A = \frac{\pi \cdot d_{\text{crit}}^2}{4}, \tag{28}$$

$$F_D = K' \cdot \rho' \cdot \pi \cdot d_{\text{crit}}^2 \cdot \frac{V_r^2}{8}. \tag{29}$$

If $F_C > F_D$, the velocity of the gas bubble could be assumed as the liquid velocity. The time of travel of the gas bubble to the air core was obtained by Newton's Gregory interpolation. Hence, the time taken for the gas to travel to the air core from the wall of the reactor is

$$t_i = \sum \frac{R}{V_i}. \tag{30}$$

Discussion of results

The results of the neutralisation reaction involving dodecylbenzene sulphonic acid mixture at a viscosity of 417.68 mPa · s with sodium carbonate solution are presented in Table 2. Quantitative analyses to determine the percentages of both the anionic active detergent (AD) matter and the inert sodium sulphate (Na_2SO_4) indicated a relatively high percentage of the active detergent, up to 50%, together with a low

Table 3. A typical result for gas bubbles at reactant feed rates of $0.0508 \times 10^{-3}\ m^3 \cdot s^{-1}$

Radial distance (m)	Radial velocity of the gas bubble ($m \cdot s^{-1}$)	Bubble time (s)	Centripetal force (N)	Drag force (N)
0.00425	−0.23564	0.0361	-0.1699×10^{-1}	0.1244×10^{-4}
0.00850	−0.16662	0.0211	-0.2124×10^{-2}	0.6219×10^{-5}
0.01275	−0.13605	0.0281	-0.6294×10^{-3}	0.4146×10^{-5}
0.01700	−0.11782	0.0335	-0.2655×10^{-3}	0.3109×10^{-5}
0.02125	−0.10538	0.0381	-0.1359×10^{-3}	0.2488×10^{-5}
0.02550	−0.09620	0.0422	-0.7867×10^{-4}	0.2073×10^{-5}
0.02975	−0.08906	0.0459	-0.4954×10^{-4}	0.1777×10^{-5}
0.03400	−0.08331	0.0493	-0.3319×10^{-4}	0.1555×10^{-5}
0.03825	−0.07856	0.0525	-0.2331×10^{-4}	0.1382×10^{-5}
0.04250	−0.07452	0.0555	-0.1699×10^{-4}	0.1244×10^{-5}

Reactor volume = $0.55 \times 10^{-3}\ m^3$.
Dodecylbenzene sulphonic acid (dobane JN) = 97.0% (w/w).
Na_2CO_3 = 0.5 M.
Viscosity of dobanic acid with 111 trichloroethane = 417.68 mPa · s (cp).
pH of dobanic acid with 111 trichloroethane = 0.75.

percentage of sodium sulphate, <0.3% in each experiment. This suggested that a substantial amount of dodecylbenzene sulphonic acid had been converted into the product, sodium dodecylbenzene sulphonate (LAS). This was also evident from the high percentage conversion, >99% (1).

The mathematical model was first applied to predict the critical size of the gas bubbles using the physical properties of carbon dioxide gas and the continuous phase. The time necessary for the gas bubbles to travel from the wall of the vessel to the air core before being expelled from the top outlet of the system was then predicted. Table 3 represents a typical result at a feed flow rate of $0.0508 \times 10^{-3} m^3 s^{-1}$.

The results indicated that the effective centripetal force acting on the gas bubble was large compared to the drag force. The bubble velocity could therefore be assumed to approximate to that of the liquid. Figures 3–6 present typical predicted, velocity profiles of gas bubbles along the radial coordinate at varying feed rates. The profiles of the gas bubbles were found to be the same irrespective of the feed rates or the capacities of the nozzle vessel. The predicted time for gas bubbles to travel to the air core of the vessel decreased with an increase in the reactant volumetric rates, but in all cases was very much less than the mean residence time of liquid in the reactor. Hence a substantial amount of the gas evolved as bubbles would be expected to reach the air core, rather than being expelled with the product, with the result that less foam was obtained. The critical size of the gas bubble was in the range of 0.1 mm to 1.0 mm and decreased with an increase in the reactants volumetric flow rates.

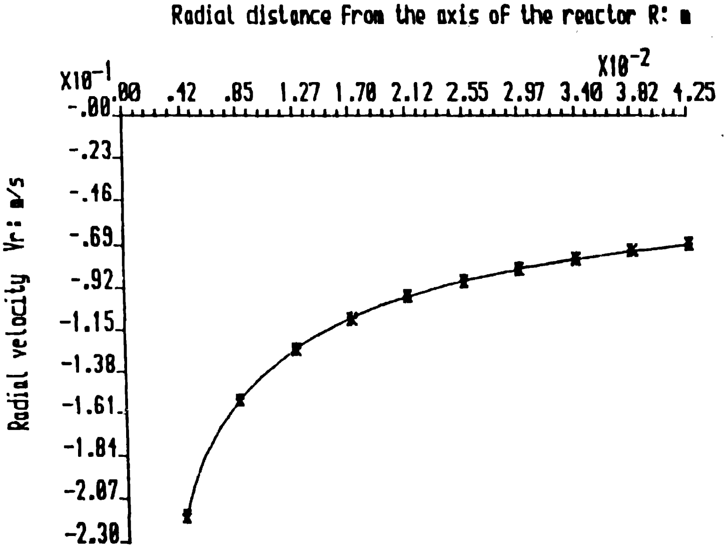

Fig. 4. Radial velocity profile of the gas bubble at reactant feed rates of $0.0508 \times 10^{-3} m^3 \cdot s^{-1}$.

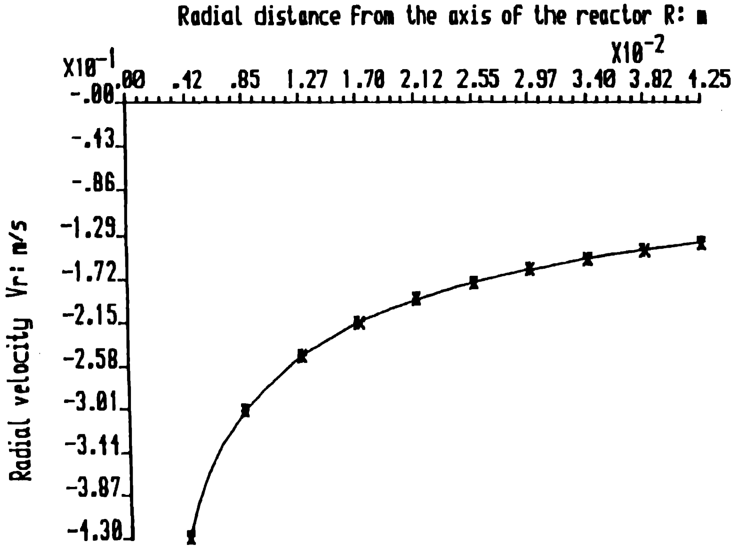

Fig. 5. Radial velocity profile of the gas bubble at reactant feed rates of $0.0873 \times 10^{-3}\,m^3 \cdot s^{-1}$.

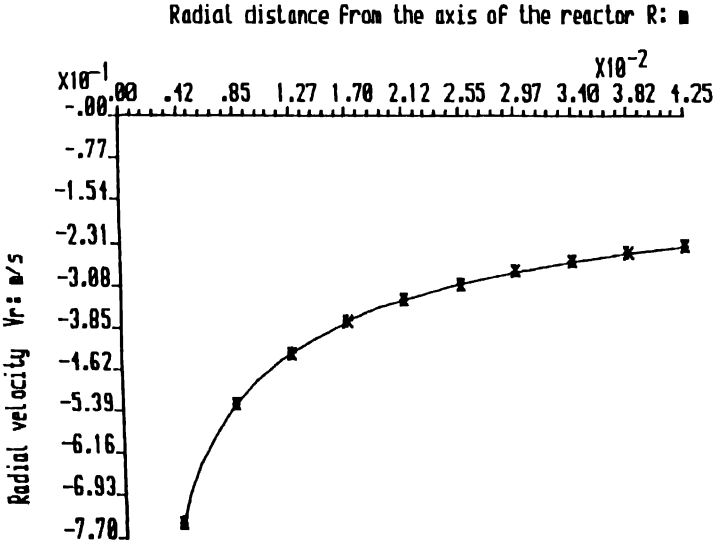

Fig. 6. Radial velocity profile of the gas bubble at reactant feed rates of $0.1690 \times 10^{-3}\,m^3 \cdot s^{-1}$.

Conclusions

Over the range of acid viscosities, and reactants volumetric rates studied, high conversions (>99%) to the segregated product sodium dodecylbenzene sulphonate ($C_{12}H_{25}C_6H_4SO_3Na$) were achieved The product pH values were shown to conform to the range appropriate for commercial use The product LAS was found to have a high percentage of the anionic active detergent

The products contained negligible amounts of foam because the time for gas bubbles to travel to the air core was considerably less than the mean residence time of the reactants The model predictions for the equilibrium bubble sizes in the turbulence were in reasonable agreement with experimental observations This justified the use of these sizes in the second model for bubble velocities and hence wall-to-core travel times

References

1 Coker A K Fast Reactions In Nozzle Type Reactors Ph D Thesis Aston University U K (1985)
2 Coker A K and Jeffreys G V Flow patterns and residence time distributions in nozzle-type reactors *Chem Eng Symp Ser* No 108 Fluid Mixing III
3 Coker A K Jeffreys G V and Mumford C J Characterization of mixing and residence time distributions in nozzle type reactors *Chem Eng Technol* 12 (1989) 2 2 269
4 Beenackers A A C M and Van Swaaij W P M *The Chem Eng J* 15 (1978) 39 53
5 Ter Linden A J *Proc Inst Mech Eng* 160 (1949) 233 240
6 Bradley D and Pulling D J *Trans Instn Chem Engrs* 37 (1959) 34 45
7 Kelsall D F *Trans Inst Chem Engrs* 30 (1952) 87 108
8 Rietema K *Chem Eng Sci* 15 (1961) 310 319
9 Bloor M I G and Ingnam D B *Trans Instn Chem Engrs* 51 (1973) 36 41
10 Bloor M I G and Ingham D B *Trans Instn Chem Engrs* 53 (1975) 1 6
11 Levich V G *Physicochemical Hydrodynamics* Prentice Hall New York (1962) pp 395 471
12 Prandtl L *Applied Hydro and Aeromechanics* McGraw Hill Book Co New York (1934)
13 Binnie A M and Hookings G A *Proc Roy Soc* A 194 (1948) 398 415

Applied Scientific Research **49**: 83–89, 1992.
© 1992 *Kluwer Academic Publishers. Printed in the Netherlands.*

An approximate solution for free convection flows in a thermally stratified porous medium

T. GOVINDARAJULU & M. B. K. MOORTHY
Division of Mathematics, Madras Institute of Technology, Madras 600 044, India

Received 26 June 1990; accepted 24 August 1990

Abstract. A simple and sufficiently accurate method for finding the rate of heat transfer for buoyancy-induced flows over bodies of arbitrary shape embedded in a thermally stratified porous medium is given

Nomenclature

a	parameter used to scale f
b	parameter used to scale η
C	function defined by equation 8(b)
E	residual
I	integral of squared residual
k	thermal conductivity
K	permeability
n	parameter associated with thermal stratification
Nu_x	local Nusselt number
r	function representing wall geometry
Ra_x	local Rayleigh number
T	temperature
u, v	Darcian velocity components
x, y	boundary layer coordinates
α	thermal diffusivity
β	coefficient of thermal expansion
η	similarity variable
	power law index of the surface temperature
ν	kinematic viscosity
ξ	transformed variable in the streamwise direction
ψ	stream function

Subscripts

w	wall
∞	ambient

Introduction

Nakayama and Koyama [1] recently considered the buoyancy-induced flows over a curved surface embedded in a thermally stratified porous medium. By means of a generalised similarity variable they presented similarity solutions for a class of bodies with power-law variations in surface and ambient temperature distributions. In this note, a very simple method, which requires the solution of a quadratic equation, is given to find the heat transfer rates for the problem studied by Nakayama and Koyama

Analysis

Consider the buoyancy flow in a saturated porous medium above a heated body, embedded in a porous medium. The body is either two dimensional or axisymmetric (see Fig. 1). The surface temperature as well as the ambient temperature may vary in the streamwise direction.

With the usual boundary layer approximation, the equations of continuity, the Darcy's law, and energy are given by (see Ref. [1])

$$\frac{\partial}{\partial x}(r^*u) + \frac{\partial}{\partial y}(r^*v) = 0, \tag{1}$$

$$\frac{\partial u}{\partial y} = \frac{K\beta}{\nu} g_x \frac{\partial T}{\partial Y} \tag{2}$$

and

$$u\frac{\partial T}{\partial x} + v\frac{\partial T}{\partial Y} = \alpha\frac{\partial^2 T}{\partial Y^2}, \tag{3}$$

where

$$r^* = \begin{cases} 1: & \text{for plane body,} \\ r(x): & \text{for axisymmetric body,} \end{cases} \tag{4a}$$

and

$$g_x = g\sin\phi, \tag{4b}$$

ϕ being the angle between normal to the body and downward vertical. The other symbols are the same as defined in Ref. [1].

The boundary conditions are

$$\begin{aligned} &y = 0: \quad v = 0, \quad T = T_w(x), \\ &Y \to \infty: \quad u = 0, \quad T = T_\infty(x) = (1-n)T_0 + nT_w(x), \end{aligned} \tag{5a, b}$$

where n is a constant, such that $0 \leqslant n < 1$. The n defined as above is equal to $m/(1+m)$ of Ref. [1]. T_0 is a constant reference temperature say, $T_\infty(0)$. The suffixes w and ∞ denote surface and ambient conditions. The continuity equation can be eliminated using the stream function defined by

$$u = \frac{1}{r^*}\frac{\partial\psi}{\partial y} \quad \text{and} \quad v = -\frac{1}{r^*}\frac{\partial\psi}{\partial x}. \tag{6a, b}$$

We now introduce the following transformations:

$$\psi = \alpha r^*(C\,\mathrm{Ra}_x)^{1/2} f(x, y),$$
$$\eta = \frac{y}{x}\left(\frac{\mathrm{Ra}_x}{C}\right)^{1/2},$$
$$\theta = (T - T_\infty)/\Delta T, \qquad \Delta T = T_w - T_\infty, \tag{7a, b, c}$$

where

$$\mathrm{Ra}_x = \frac{K\beta g_x \Delta T x}{\nu\alpha} \tag{8a}$$

is the modified Rayleigh number and

$$C(x) = \frac{\int_0^x g_x r^{*2}\,\mathrm{d}x}{x g_x r^{*2}} \tag{8b}$$

is a body shape parameter.

Substituting (7) into equation (2) and (3) there results

$$f' = \theta, \tag{9}$$

$$\theta'' + \tfrac{1}{2}[1 + P(\xi)]f\theta' - \left(\frac{n}{1-n} + \theta\right)P(\xi)f' = \xi\left(f'\frac{\partial\theta}{\partial\xi} - \theta'\frac{\partial f}{\partial\xi}\right), \tag{10}$$

where

$$P(\xi) = \frac{\xi}{\Delta T}\frac{d}{d\xi}\Delta T$$

and

$$\xi = \int_0^x g_x r^{*2}\,\mathrm{d}x. \tag{11a, b}$$

Eliminating θ from equations (9) and (10) we get

$$f''' + \tfrac{1}{2}[1 + P(\xi)]ff'' - P(\xi)\left(\frac{n}{1-n} + f'\right)f' = \xi\left(f'\frac{\partial f'}{\partial\xi} - f''\frac{\partial f}{\partial\xi}\right). \tag{12}$$

This is a nonsimilar equation. However as pointed out by Nakayama, this becomes similar for the class of surface temperature variation, $\Delta T \sim \zeta^{\lambda}$, in which case $P(\zeta) = \lambda$. The equation (12) becomes then

$$f''' + \tfrac{1}{2}(1+\lambda)ff'' - \lambda\left(\frac{n}{1-n} + f'\right)f' = 0 \tag{13}$$

with the boundary conditions

$$\begin{aligned} &\eta = 0\colon f = 0,\ f' = 1,\\ &\eta \to \infty\colon f' = 0. \end{aligned} \tag{14a, b}$$

The local surface heat flux q_w may be computed from

$$q_w = -k\left(\frac{\partial T}{\partial Y}\right)_{y=0}, \tag{15}$$

or in the dimensionless form

$$\mathrm{Nu}_x = \frac{xq_w}{\Delta Tk} = -f''(0)\left(\frac{\mathrm{Ra}_x}{C}\right)^{1/2}. \tag{16}$$

Approximate solution

Dey [2] recently presented an efficient method for finding an approximate analytical solution to the Falkner-Skan equation. The method uses a known solution of another equation with exactly the same boundary conditions. The variables in this solution are scaled using a set of parameters. These parameters are then determined by minimizing the squared residual. We note that equation (13) admits of the exact solution for $\lambda = 1$,

$$f = \frac{1}{h}(1 - e^{-h\eta}), \tag{17}$$

where

$$h = (1-n)^{-1/2}. \tag{18}$$

This escaped the notice of Nakayama and Koyama [1]. Take the trial solution

$$f = \frac{a}{h}(1 - e^{-hb\eta}), \tag{19}$$

where a and b are parameters used to scale f and η respectively. However the boundary condition, $f'(0) = 1$ implies

$$ab = 1. \tag{20}$$

Substituting (19) in the equation (13) we get the residual

$$E(\eta, b) = \left[h^2b^2 - \frac{1}{2}(1+\lambda) - \frac{n}{1-n}\lambda\right] e^{-hb\eta} + \frac{1}{2}(1-\lambda)e^{2hb\eta}. \tag{21}$$

Integrating the squared residual from $\eta = 0$ to $\eta = \infty$, we get

$$I = \int_0^\infty E^2\,\mathrm{d}\eta = \frac{1}{hb}\left[\frac{1}{2}(h^2b^2 - p)^2 + \frac{1}{16}(1-\lambda)^2 + \frac{1-\lambda}{3}(h^2b^2 - p)\right], \tag{22}$$

where

$$p = \tfrac{1}{2}[1 + \lambda(1+n)/(1-n)].$$

The parameter b is then determined on minimizing $I(b)$, for which $\partial I/\partial b = 0$. We get a quadratic equation,

$$\begin{aligned} s^2 - \frac{1}{9}\left[1 + \lambda\left(\frac{5+n}{1-n}\right)\right]s - \frac{1}{72}&\left[1 + 2\left(\frac{n+3}{1-n}\right)\lambda\right. \\ &\left.+ \left\{6\left(\frac{1+n}{1-n}\right)^2 + 8\left(\frac{1+n}{1-n}\right) + 3\right\}\lambda^2\right] = 0, \end{aligned} \tag{23}$$

where

$$s = b^2h^2. \tag{24}$$

The positive root is considered for determining the Nusselt number

$$\mathrm{Nu}_x = bh\left(\frac{\mathrm{Ra}_x}{C}\right)^{1/2}. \tag{25}$$

The computed values of $(C/\mathrm{Ra}_x)^{1/2}\mathrm{Nu}_x$ are given in Table 1. For the purpose of comparison the equation (13) together with (14) is integrated numerically using Runge–Kutta–Gill method. The values are also shown in the Table 1. We see from the table that the values as given by (24) are in excellent agreement with the exact values, especially for larger values of n and λ. The maximum error is about 3%. Incidentally equation (23) also gives the exact values of Nu_x for $\lambda = 1$.

Table 1. Values of $-f''(0)$

λ \ n	0	0.25	0.5	0.75	0.9
Exact	0.4438	0.4438	0.4438	0.4438	0.4438
0					
Approximate	0.4311	0.4311	0.4311	0.4311	0.4311
0.25	0.6266	0.6877	0.7973	1.0635	1.6210
	0.6166	0.6801	0.7925	1.0615	1.6204
0.5	0.7704	0.8705	1.0433	1.4442	2.2549
	0.7647	0.8667	1.0412	1.4435	2.2547
0.75	0.8923	1.0223	1.2425	1.7443	2.7463
	0.8899	1.0207	1.2417	1.7441	2.7462
1	1	1.1547	1.4142	2	3.1623
	1	$2/3^{1/2}$	$2^{1/2}$	2	$10^{1/2}$

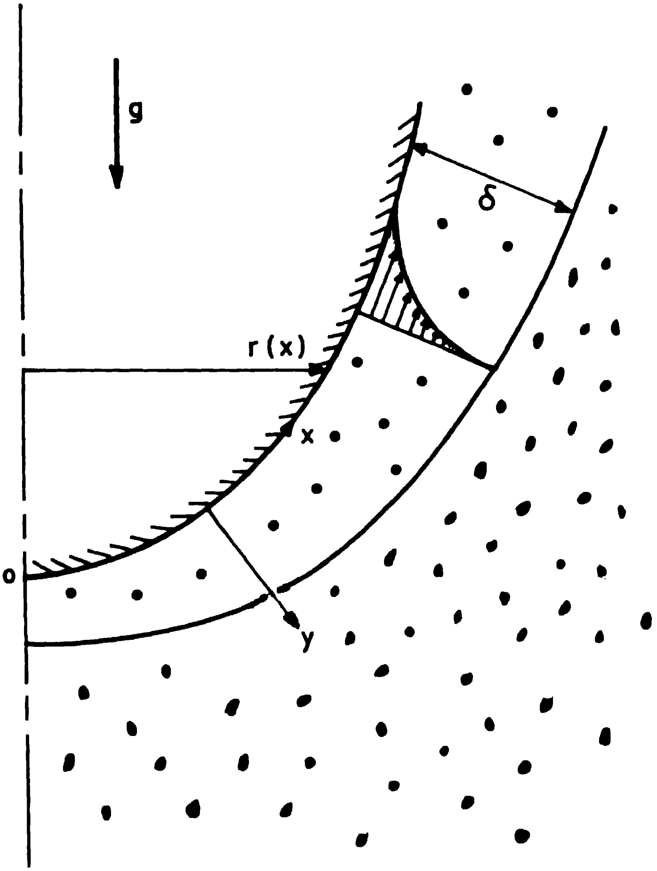

Fig. 1. Physical model and coordinates.

Acknowledgement

The author wishes to thank Dr. N. S. Venkataraman for providing all facilities to undertake this work.

References

1. Nakayama, A. and Koyama, H., Similarity solutions for buoyancy-induced flows over a non-isothermal curved surface in a thermally stratified porous medium. *Appl. Sci. Res.* 46 (1989) 309–322.
2. Dey, J., A simple technique for approximate solutions of the Falkner-Skan Equation. *Acta Mechanica* 77 (1989) 299–305.

Applied Scientific Research **49**: 91–99, 1992.
© 1992 *Kluwer Academic Publishers. Printed in the Netherlands.*

Elastoplastic cracks moving in orthotropic crystals

G. E. TUPHOLME

Department of Mathematics, University of Bradford, Bradford BD7 1DP, England

Received 8 September 1989; accepted in revised form 7 October 1990

Abstract. The stress field, crack-tip plastic zones and total plastic displacement created around an infinite row of collinear elastoplastic constant width Griffith-type strip cracks moving within an orthotropic crystal are considered using the powerful method of dislocation layers. The method is applied with the BCS modelled elastoplastic cracks moving under mode III loading at constant crack-tip velocity, according to the Yoffe model. Simultaneously the analysis provides solutions for a corresponding single crack moving similarly within a finite orthotropic plate and a finite plate containing a surface crack. Analogous results for the corresponding mode I, mode II and purely elastic cracks can be deduced.

1. Introduction

For many years, there has been much technologically motivated interest in undertaking analyses of the effects of cracks within elastic materials. The work of Tait and Moodie [1], Singh, Moodie and Haddow [2], Georgiadis and Theocaris [3] and Boiko and Karpenko [4], for example, has demonstrated that recently renewed attempts have been made to find solutions for various cracked-strip problems. For simplicity much attention has been focussed on isotropic elastic materials using traditional techniques often involving integral transform, complex potential functions and numerical methods, as extensively referenced by, for example, Sneddon and Lowengrub [5] and Sih [6].

However, it is now generally recognised (see, for example, Bilby and Eshelby [7], Lardner [8]) that alternatively the so-called "dislocation layer method", whereby straight cracks can be represented by equivalent continuous distributions of dislocations, can be conveniently utilized. Most importantly, Bilby, Cottrell and Swinden [9] postulated the "BCS model" and thereby showed that this technique can be advantageously extended to an analysis of various stationary elastoplastic cracks within isotropic materials.

The purpose of the present paper is to demonstrate that the dislocation layer method is suitable for giving an investigation of the stress field created around an infinite row of collinear elastoplastic cracks moving uniformly in orthotropic crystals loaded at infinity. This is appropriate for mode III loadings, upon which for brevity we focus here, but, further as discussed in Section 5, the corresponding results for mode I and mode II loaded cracks can be deduced. Moreover, it is shown in Section 5 that our solution not only applies to the situation formulated in Section 2 but, at the same time, we have actually provided the solution to the problem of a single, elastoplastic crack moving within a finite orthotropic plate, or a finite plate initially containing a surface crack.

The BCS model for elastoplastic cracks provides a plausible, manageable simplication of the complexities involved in an analysis of real elastoplastic crack growth. Justification for this is supplied in the antiplane shear case of a single crack by the close agreement of the results with those given classically by Hult and McClintock [10]. The use of such a model in the tensile case is, at first sight, perhaps more difficult to interpret. However this can be made more realistic by involving the tensile stress in the plane of the crack, rather than the shear stress, in the plastic flow criterion. Dugdale [11] was the first to develop such a tensile-yield stress model and it was later extended by Goodier and Field [12]. It is interesting to note that, more generally, Leighton, Champion and Freund [13] have recently re-examined asympotically the crack-tip stress and deformation fields near a model I tensile crack propagating steadily through an elastic-perfectly plastic incompressible material. Here the material is assumed to yield according to the Tresca condition and to deform plastically subject to the associated flow rule.

The foundations of our discussion are provided by detailed information which is available about the stress field around a uniformly moving straight dislocation in such media. The fundamental work of Bullough and Bilby [14] provided the starting point for the more general studies of Teutonico [15, 16] and the special cases of various cubic and hexagonal materials considered by Teutonico [17, 18] and Weertman [19, 20].

In Section 2 the basic mode III problem is formulated, before the singular integral equation governing the density function of the proposed dislocation layers is derived and its solution is given in Sections 3 and 4, respectively. Expressions illustrating the effects of anisotropy and the speed of crack propagation upon the length of the plastic zones and total plastic displacement created at the crack-tips are presented in Section 5. Some low-stress approximations and analogous results for purely elastic cracks are deduced.

2. Basic formulation of the problem

An infinite homogeneous crystal, which is initially everywhere at rest and stress-free in a natural reference state and is orthotropically symmetrical in its linearly elastic response, is supposed to be situated so that the coordinate planes of a system of rectangular Cartesian coordinates x, y, z coincide with its three mutually perpendicular planes of symmetry. The material is considered to contain an infinite periodic array of equal, plane, collinear, Griffith-type, strip cracks of constant width, each of which is assumed to be moving parallel to its axis with uniform velocity in its own plane, based upon Yoffe's model [21].

At time t, the cracks are assumed to be lying on the $y = 0$ plane and centred at $x = vt, vt \pm 2h, vt \pm 4h, \ldots$, in such a way that they occupy the regions

$$I_t = \{(x, y, z): 2nh + vt - c < x < 2nh + vt + c,\ y = 0,\ -\infty < z < \infty\} \qquad (1)$$

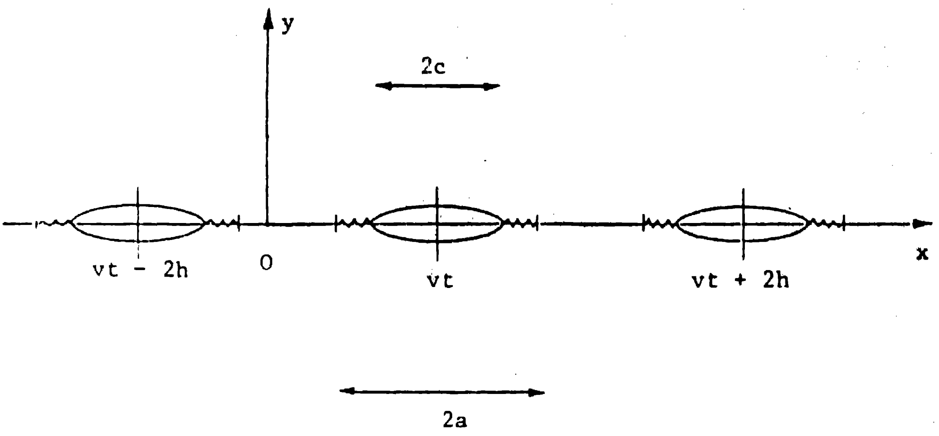

Fig. 1. Infinite row of equal strip cracks and plastic zones moving with constant speed v in the x-direction.

of the $x-z$ plane, with $n = 0, \pm 1, \pm 2, \ldots$. The width of each crack is therefore $2c$ and v is its constant speed of propagation. In the vicinity of the tips of the cracks it is supposed that the material behaves elastoplastically with constant yield stress σ_1 in accordance with the BCS model [9]. The consequent plastic flow is taken to extend over plastic zones of length $a-c$ in the plane of the cracks throughout the regions

$$I_{tp} = \{(x, y, z): c < |x - 2nh - vt| < a,\ y = 0,\ -\infty < z < \infty\} \tag{2}$$

of the $x-z$ plane, with $n = 0, \pm 1, \pm 2, \ldots$. The configuration of the cracks is illustrated in Fig. 1. The medium is considered to be deformed in mode III antiplane strain by an antiplane shear stress applied so that $\sigma_{yz} \to \sigma$ at infinity, where $\sigma(<\sigma_1)$ is a prescribed constant and σ_{yz} is a component of the stress tensor referred to the x, y, z system of coordinates. For an orthotropic material, the relation connecting the components of the stress and strain tensors $\boldsymbol{\sigma}$ and $\boldsymbol{\varepsilon}$, respectively, referred to the x, y, z coordinate system can be written in the form

$$\begin{bmatrix} \sigma_{11} \\ \sigma_{22} \\ \sigma_{33} \\ \sigma_{23} \\ \sigma_{13} \\ \sigma_{12} \end{bmatrix} = \begin{bmatrix} c_{11} & c_{12} & c_{13} & 0 & 0 & 0 \\ c_{12} & c_{22} & c_{23} & 0 & 0 & 0 \\ c_{13} & c_{23} & c_{33} & 0 & 0 & 0 \\ 0 & 0 & 0 & 2c_{44} & 0 & 0 \\ 0 & 0 & 0 & 0 & 2c_{55} & 0 \\ 0 & 0 & 0 & 0 & 0 & 2c_{66} \end{bmatrix} \begin{bmatrix} \varepsilon_{11} \\ \varepsilon_{22} \\ \varepsilon_{33} \\ \varepsilon_{23} \\ \varepsilon_{13} \\ \varepsilon_{12} \end{bmatrix} \tag{3}$$

where the $c_{ij}(i,j = 1, \ldots, 6)$ denote the elastic constants referred to the chosen coordinate system. Especially important classes of orthotropic crystals are those of hexagonal and cubic crystals and Tupholme [22] has given a useful discussion of the necessary modifications which can be made to the representation (3) to provide an analysis directly appropriate to them.

3. Singular integral equation formulation

First, we define a moving coordinate ξ given by

$$\xi = x - vt,$$

and consider a moving screw dislocation whose line and Burgers vector is parallel to the z-axis and with displacement discontinuity given by

$$\mathbf{u}^{\mathrm{III}}(\xi, 0+) - \mathbf{u}^{\mathrm{III}}(\xi, 0-) = (0, 0, -b) \quad \text{for} \quad \xi > 0, \tag{4}$$

where b is a constant and throughout a superfix III is attached to the displacement vector $\mathbf{u}$ and the corresponding components of the stress tensor. The stress field of such a dislocation situated at the origin can be extracted from the analyses of Bullough and Bilby [14] and Teutonico [15] and is found to have non-zero components given by

$$\left.\begin{aligned} \sigma_{xz}^{\mathrm{III}}(\xi, y) &= -\frac{bK_s}{2\pi}\frac{\eta^2\beta_5 y}{\xi^2 + \eta^2\beta_5^2 y^2}, \\ \sigma_{yz}^{\mathrm{III}}(\xi, y) &= \frac{bK_s}{2\pi}\frac{\beta_5 \xi}{\xi^2 + \eta^2\beta_5^2 y^2}, \end{aligned}\right\} \tag{5}$$

where

$$K_s = (c_{44}c_{55})^{1/2}, \ \eta = (c_{55}/c_{44})^{1/2}, \ \beta_5^2 = 1 - \delta_5^2, \ \delta_5^2 = \rho v^2/c_{55}, \tag{6}$$

ρ being the density of the material in the reference state.

The fundamental general technique of the dislocation layer method suggests that strip cracks can be studied by replacing them by an equivalent continuous planar distribution of straight dislocations. For the above row of moving, mode III cracks, it is appropriate to utilize an array of moving screw dislocations of the type specified by equations (4) to (6). In accordance with the BCS model [9], we suppose that these are not blocked at the crack tips, but rather that the plastic zones extending over the regions I_{tp}, defined by equation (2), are also represented by plane distributions of similar dislocations, coplanar with the cracks so as to create the prescribed shear stress throughout them. To the right of each crack the screws are taken to be positive and to the left they are negative, so that the proposed distribution of dislocations is odd in ξ. If the number of dislocations in the interval $(\xi, \xi + \mathrm{d}\xi)$ on $y = 0$ is $f(\xi)\mathrm{d}\xi$, then, using equation (5_2), the corresponding stress component at a point on the ξ-axis is given by

$$\sigma_{yz}(\xi, 0) = \int_{-\infty}^{\infty} \sigma_{yz}^{\mathrm{III}}(\xi - \xi', 0) f(\xi')\,\mathrm{d}\xi' = \frac{bK_s\beta_5}{2\pi} \int_{-\infty}^{\infty} \frac{f(\xi')}{\xi - \xi'}\,\mathrm{d}\xi', \tag{7}$$

where it is clear from the Plemelj formulae that a Cauchy principal value integral interpretation of the integral here must be imposed. The equilibrium equation for the dislocation density function $f(\xi)$ which must be satisfied is therefore

$$\frac{bK_s\beta_5}{2\pi} \int_{-\infty}^{\infty} \frac{f(\xi')}{\xi - \xi'}\,\mathrm{d}\xi' = \begin{cases} -\sigma & \text{in } I_t, \\ -(\sigma - \sigma_1) & \text{in } I_{tp}, \end{cases} \tag{8}$$

since within the plastic zones the resistance to the dislocations' motion is taken to be the constant yield stress σ_1.

The singular integral equation (8) enables not only $f(\xi)$ but also the relationship between c and a to be determined with the values of the physical constants σ and σ_1 prescribed. This then essentially provides a solution to the whole problem, since any of the stress components produced around the cracks can be calculated from the formula

$$\sigma_{ij}(\xi, y) = \int_{-\infty}^{\infty} \sigma_{ij}^{\mathrm{III}}(\xi - \xi', y) f(\xi')\,\mathrm{d}\xi', \tag{9}$$

with the necessary $\sigma_{ij}^{\mathrm{III}}$ given by the corresponding expressions (5) and (6).

4. Solution of integral equation

The infinite integral on the left-hand side of equation (8) can be represented as the sum of contributions from each of the cracks. Then, by noting that $f(\xi) = -f(-\xi)$ and $f(\xi + 2nh) = f(\xi)$, and appealing to the result that

$$\sum_{n=1}^{\infty} \frac{1}{z^2 - n^2} = -\frac{1}{2z^2} + \frac{\pi}{2z} \cot \pi z,$$

it can be rewritten (cf. Leibfried [23]) in the alternative form

$$\frac{bK_s\beta_5}{4h} \int_{-a}^{a} \frac{\cos(\pi\xi'/2h)}{\sin(\pi\xi/2h) - \sin(\pi\xi'/2h)} f(\xi')\,\mathrm{d}\xi.$$

A change of variables, defined by

$$\left.\begin{aligned} \xi_1 &= \sin(\pi\xi/2h), & a_1 &= \sin(\pi a/2h), \\ \xi_1' &= \sin(\pi\xi'/2h), & c_1 &= \sin(\pi c/2h), \end{aligned}\right\} \tag{10}$$

can be introduced to transform the integral equation for $f(\xi)$ into

$$\int_{-a_1}^{a_1} \frac{f_1(\xi_1')}{\xi_1 - \xi_1'}\, d\xi_1' = \frac{2\pi}{bK_s\beta_5} \begin{cases} -\sigma, & |\xi_1| < c_1, \\ -(\sigma - \sigma_1), & c_1 < |\xi_1| < a_1, \end{cases} \tag{11}$$

with $f_1(\xi_1) = f_1(\sin(\pi\xi/2h)) \equiv f(\xi)$.

This is now of a well-known type and bears a close affinity to that derived by Bilby, Cottrell and Swinden [9] and subsequently by Bilby, Cottrell, Smith and Swinden [24] in the corresponding stationary isotropic case. For brevity, the details of the derivation of its solution by adaptation of the technique discussed by Muskhelishvili [25] and Gakhov [26], for example, are omitted here.

The requirement that the solution for $f_1(\xi_1)$ must be bounded at $\xi_1 = \pm a_1$, because there are no barriers there, leads to the condition

$$\int_{-c_1}^{c_1} \frac{\sigma}{(a_1^2 - \xi_1'^2)^{1/2}}\, d\xi_1' + \left\{ \int_{-a_1}^{-c_1} + \int_{c_1}^{a_1} \right\} \frac{(\sigma - \sigma_1)}{(a_1^2 - \xi_1'^2)^{1/2}}\, d\xi_1' = 0, \tag{12}$$

subject to which the appropriate solution of equation (8) can be most neatly written as

$$f_1(\xi_1) = f(\xi) = \frac{2\sigma_1}{\pi b K_s \beta_5} \ln \left| \frac{\xi_1(a_1^2 - c_1^2)^{1/2} + c_1(a_1^2 - \xi_1^2)^{1/2}}{\xi_1(a_1^2 - c_1^2)^{1/2} - c_1(a_1^2 - \xi_1^2)^{1/2}} \right|. \tag{13}$$

This together with the representation (9) yields the stress at any point in the medium.

5. Discussion of implications

Before analyzing our solution further, it is appropriate to observe that it should be borne in mind that in fact we have, as a bonus, at the same time also solved two further problems in addition to the situation formulated in Section 2.

The stress distribution around a single moving crack, which initially occupies the region $-c < x < c$ in a finite plate, $-h < x < h$, of orthotropic material with stress-free surfaces $x = \pm h$, is supplied by that around the infinite row of cracks. This is because the stress component σ_{xz} is zero on the planes $x = \pm h$ as a consequence of the antisymmetry of the distribution of dislocations. Furthermore, an initial edge crack, $0 < x < c$, which moves into an orthotropic finite plate $0 < x < h$ will also have been analyzed, since the distribution is also odd about $x = 0$.

The maximum extent of the plastic zones in front of the cracks and the total plastic displacement at the moving crack tips are the two quantities which frequently attract the most interest. The restriction (12) can be manipulated into the form

$$\frac{c_1}{a_1} = \frac{\sin(\pi c/2h)}{\sin(\pi a/2h)} = \cos\left(\frac{\pi\sigma}{2\sigma_1}\right), \tag{14}$$

from which the length, $a - c$, of the plastic zones is determined as a function of the applied stress. Interestingly, this is observed to be independent of not only the anisotropy of the crystal but also the speed of propagation of the cracks. On the other hand, the plastic displacement at the moving crack tip is defined by

$$\Phi_0^{\mathrm{III}}(v) = \int_c^a bf(\xi)\,\mathrm{d}\xi \tag{15}$$

and it follows therefore that its ratio, $\Phi_0^{\mathrm{III}}(v)/\Phi_0^{\mathrm{III}}(0)$, to that for a stationary crack is given by

$$\frac{\Phi_0^{\mathrm{III}}(v)}{\Phi_0^{\mathrm{III}}(0)} = \frac{1}{\beta_5}, \tag{16}$$

β_5 being given by equation (6_3). The corresponding ratio, $\Phi_i^{\mathrm{III}}(v)/\Phi_i^{\mathrm{III}}(0)$, for a crack moving within an isotropic material of shear modulus μ, which has also not been investigated previously, is found, by letting $c_{55} \to \mu$, to be given by

$$\frac{\Phi_i^{\mathrm{III}}(v)}{\Phi_i^{\mathrm{III}}(0)} = \frac{1}{\beta_2}, \tag{17}$$

where

$$\beta_2^2 = 1 - \rho\frac{v^2}{\mu}. \tag{18}$$

Both the ratios (16) and (17) are 1 when $v = 0$ and become infinite as the Rayleigh speed is approached. For comparison, the ratio

$$\frac{\Phi_0^{\mathrm{III}}(v)}{\Phi_i^{\mathrm{III}}(v)} = \frac{\mu\beta_2}{K_s\beta_5}, \tag{19}$$

demonstrates the effect of the anisotropy.

A discussion similar to that given by Lardner and Tupholme [27] for a single crack in isotropic media applies regarding the possible implications for ductile crack growth.

In the cases of small stress ($\sigma \ll \sigma_1$), it can be shown from equations (13), (14) and (15) that

$$\frac{a-c}{c} \approx \frac{\pi^2\sigma^2}{8\sigma_1^2}\,\frac{\tan(\pi c/2h)}{\pi c/2h}, \quad \Phi_0^{\mathrm{III}}(v) \approx \frac{\sigma^2}{\beta_5 K_s \sigma_1}\, h\tan(\pi c/2h), \tag{20}$$

which in the limit $h \to \infty$ agree with the results predicted by Tupholme [28] for a single crack in an infinite plate. By letting $\sigma_1 \to \infty$, the results for a purely elastic orthotropic material can be deduced. The shear stress directly in front of a crack can be shown, in this limit, from equations (9) and (13) to be

$$\sigma_{yz}(\xi, 0) = \frac{\sigma\sin(\pi\xi/2h)}{\{\sin^2(\pi\xi/2h) - \sin^2(\pi c/2h)\}^{1/2}}. \tag{21}$$

Consequently, the low-stress approximations for elastoplastic cracks can be compactly written in terms of the resulting stress-intensity factor, K_{III}, as

$$a - c \approx \pi^2 K_{\mathrm{III}}^2/4\sigma_1^2, \quad \Phi_0^{\mathrm{III}}(v) \approx \pi K_{\mathrm{III}}^2/\beta_5 K_s \sigma_1, \tag{22}$$

where, as usual,

$$K_{\mathrm{III}} = \sigma\left\{\frac{h}{\pi}\tan\left(\frac{\pi c}{2h}\right)\right\}^{1/2}, \tag{23}$$

with the dependence upon the speed, v, contained entirely within β_5.

Similar results to the above are found for elastoplastic cracks subjected to mode I and II loadings by making appropriate changes to the elastic constants, using the fields summarized by Tupholme [28] for straight edge moving dislocations. However, since for edge dislocations the image constructions do not leave the planes $x = vt \pm nh$ stress-free, the solutions of the ancillary problems in a finite plate are not deducible in these cases.

Acknowledgement

The author would like to take this opportunity to thank Professor R. W. Lardner for introducing him to "the dislocation layer method" and he is indebted to a referee for drawing reference [13] to his attention.

References

1. Tait, R. J. and Moodie, T. B., Complex variable methods and closed form solutions to dynamic crack and punch problems in the classical theory of elasticity. *Int. J. Engng. Sci.* 19 (1981) 221–229.
2. Singh, B. M., Moodie, T. B. and Haddow, J. B., Closed-form solutions for finite length crack moving in a strip under anti-plane shear stress. *Acta Mech.* 38 (1981) 99–109.
3. Georgiadis, H. G. and Theocaris, P. S., The Keldysh-Sedov method for a closed-form elastodynamic solution of the cracked strip under anti-plane shear. *Int. J. Engng. Sci.* 24 (1986) 1135–1140.
4. Boiko, A. V. and Karpenko, L. N., On an integral equation of the problem for an elastic strip with a slit. *P.M.M. U.S.S.R.* 51 (1987) 797–802.
5. Sneddon, I. N. and Lowengrub, M., *Crack Problems in the Classical Theory of Elasticity*. New York: Wiley (1969).
6. Sih, G. C. (ed.), *Mechanics of Fracture, Vol. 1, Methods of Analysis and Solutions of Crack Problems*. Leyden: Noordhoff Int. Pub. (1973).
7. Bilby, B. A. and Eshelby, J. D., Dislocations and the theory of fracture. In: Liebowitz, H. (ed.), *Fracture*, Vol. 1. New York: Academic Press (1968) pp. 99–182.
8. Lardner, R. W., *Mathematical Theory of Dislocations and Fracture*. University of Toronto Press (1974).
9. Bilby, B. A., Cottrell, A. H. and Swinden, K. H., The spread of plastic yield from a notch. *Proc. Roy. Soc.* A, 272 (1963) 304–314.
10. Hult, J. A. H. and McClintock, F. A., Elastic-plastic stress and strain distributions around sharp notches under repeated shear. *Proc. 9th Int. Congress on Applied Mechs, Brussels* 8 (1957) 51–58.
11. Dugdale, D. S., Yielding of steel sheets containing slits. *J. Mech. Phys. Solids* 8 (1960) 100–104.
12. Goodier, J. N. and Field, F. A., Plastic energy dissipation in crack propagation. In: Drucker, D. C. and Gilman, J. J. (eds), *Fracture of Solids*. New York: Wiley (1963) pp. 103–118.
13. Leighton, J. T., Champion, C. R. and Freund, L. B., Asymptotic analysis of steady dynamic crack growth in an elastic-plastic material. *J. Mech. Phys. Solids* 35 (1987) 541–563.
14. Bullough, R. and Bilby, B. A., Uniformly moving dislocations in anisotropic media. *Phys. Soc. London* 67B (1954) 615–626.
15. Teutonico, L. J., Dynamical behaviour of dislocations in anisotropic media. *Phys. Rev.* 124 (1961) 1039–1045.
16. Teutonico, L. J., Uniformly moving dislocations of arbitrary orientation in anisotropic media. *Phys. Rev.* 127 (1962) 413–418.
17. Teutonico, L. J., Moving edge dislocations in cubic and hexagonal materials. *Phys. Rev.* 125 (1962) 1530–1533.
18. Teutonico, L. J., Dynamical behaviour of dislocations in the primary slip systems of body-centered cubic crystals. *J. App. Phys.* 34 (1963) 950–955.
19. Weertman, J., Fast moving edge dislocations on the (110) plane in anisotropic body-centered—cubic crystals. *Phil. Mag.* 7 (1962) 617–631.
20. Weertman, J., Fast moving edge dislocations on the (111) plane in anisotropic face-centered—cubic crystals. *J. App. Phys.* 33 (1962) 1631–1637.
21. Yoffe, E. H., The moving Griffith crack. *Phil. Mag.* 42 (1951) 739–750.
22. Tupholme, G. E., A study of cracks in orthotropic crystals using dislocation layers. *J. Eng. Math.* 8 (1974) 57–69.
23. Leibfried, G., Verteilung von versetzungen in statischen gleichgewicht. *Z. Phys.* 130 (1951) 214–226.
24. Bilby, B. A., Cottrell, A. H., Smith, E. and Swinden, K. H., Plastic yielding from sharp notches. *Proc Roy. Soc.* A, 279 (1964) 1–9.
25. Muskhelishvili, N. I., *Singular Integral Equations*. Leyden: Noordhoff Int. Pub. (1953).
26. Gakhov, F. D., *Boundary Value Problems*. Oxford: Pergamon (1966).
27. Lardner, R. W. and Tupholme, G. E., Dislocation layers applied to moving crack problems. *Int. J. Frac.* 10 (1974) 113–119.
28. Tupholme, G. E., Dislocation layers applied to moving cracks in orthotropic crystals. *J. Elast.* 4 (1974) 187–200.

Applied Scientific Research **49**: 101–115, 1992.
© 1992 *Kluwer Academic Publishers. Printed in the Netherlands.*

Roughness and turbulence intensity effects on the induced flow oscillation of a single cylinder

B. A. JUBRAN, M. N. HAMDAN & B. O. AL BEDOOR
Mechanical Engineering Department, University of Jordan, Amman-Jordan

Received 27 November 1989; accepted in revised form 7 October 1990

Abstract. The effects of the surface roughness and the turbulence intensity on the dynamic characteristics of the flow induced oscillations of an elastically supported single circular cylinder in a cross flow in the vortex shedding and fluid elastic regions were experimentally investigated. The results of these experiments indicate that, for the vortex shedding region, increasing the surface roughness results in a reduction of the amplitude of oscillation, while in the fluid elastic region, increasing the surface roughness tends to enhance the oscillations. A similar trend for the dynamic response of the cylinder in the vortex shedding region was also observed when the free stream turbulence intensity was varied, while in the fluid elastic region variations in the free stream turbulence intensity were observed to have no drastic effect on the dynamic response of the cylinder

1. Introduction

Flow induced vibration is often identified as a major cause of failure in various engineering systems, such as tall tower, tubes in heat exchangers, and power transmission cables. It is generally known that as the flow separates from either side of cylinder vortices are shed alternately resulting in an oscillating external force which causes the cylinder to oscillate in a direction normal to the flow. When the frequency of the vortex shedding is equal to the natural frequency of the oscillating cylinder, resonance is reached which is characterized by a large amplitude of oscillation, the magnitude of which depends upon the dynamic parameters of the system, and the flow characteristics.

An extensive bibliography of numerous experimental investigations on flow induced oscillations of an elastically supported single circular cylinder have been presented by Blevins [1], Parkinson [2] and Blake [3]. Following the review of Blake [3] it seems that there is a lack of systematic investigations regarding the effect of turbulence intensity and surface roughness on the dynamic response of a single cylinder. It is generally known that resonance occurs when the frequency of vortex shedding is equal to the natural frequency of the cylinder. Also it is known that there exists a reduced velocity U_r range, ($U_r = U/fD$, U = free stream velocity, f = natural frequency, D = cylinder diameter), wherein the so called "lock-in" phenomena occurs which is characterized by a constant frequency of oscillation equal to the fundamental natural frequency of the system in the vertical direction. The effects of various system parameters such as damping and natural frequency on the stability of induced oscillation have been reported in [1–6]. The results of these investigations agree with those presented by Blevins [1] in that they show the existence of a single resonance peak in the lock-in region. However, they disagree with regard to the width of the lock-in region and the value of the reduced velocity at which the peak occurs.

Penzin [7] observed a second resonance peak in the frequency response curve beyond the lock-in region and at a frequency equal to about 3 times the natural frequency of the oscillating cylinder. A similar observation was also reported by Durgin et al. [8]. Shiriakashi et al. [9] used a similar arrangement to the experimental set up used here, and noted that the second resonance may be attributed to the end effects or to the rotation mode of oscillation. A single peak response with a hysteresis like behavior was recently reported Gowda et al. [10] indicating a nonlinear behavior in the response curve. Gerrard [11] conducted an experimental investigation to study the order of magnitude of the oscillating properties of the flow past circular cylinder in the Reynolds number range 2×10^3 to 5×10^4. It was found that in this range these properties are highly susceptible to small disturbance of the frequency of the transition waves which just precede turbulence in the shear layers just downstream of the cylinder and this susceptibility is responsible for the different coefficient values measured by various workers.

It appears from the aforementioned investigations that most attention has been paid to the characteristics of flow induced vibration in the reduced velocity range corresponding to the vortex shedding region. Furthermore there seems to be a lack of data on the effect of surface roughness and turbulence intensity on the stability of these induced oscillations. It also appears from the above that there is a disagreement on the exact characteristics of the dynamic response curve of a smooth single cylinder over the most frequently considered reduced velocity ranges.

The aim of the present study is to extend the data available on flow induced vibration over a single cylinder to the fluid elastic region other than those frequently considered in the literature, as well as to explore the effects of surface roughness, turbulence intensity and their combined effect on the stability of those induced oscillations, as these parameters have practical significance. The results are discussed and compared with earlier investigations whenever it is possible.

2. Experimental setup

The experiments were conducted on an aluminum tube with circular cross section of outer diameter $D = 20\,\text{mm}$, wall thickness $t = 1$ mm and a length of $l = 480\,\text{mm}$. This combination yields an aspects ratio l/D of 15 and mass per unit length $\bar{m}$ of 0.239 kg/m.

The cylinder was suspended by two clamped plate springs at its two ends, Fig. 1(a–b), similar to the mounting used by Shiriakashi et al. [9]. The cylinder passed through two slots of (4 cm in height and 3 cm in width) on the side walls of the wind tunnel. The plate springs were placed outside the test section of the wind tunnel to avoid interference with the flow. This experimental end mountings for the cylinder was adopted to minimize the mode coupling effects which may arise from the streamwise

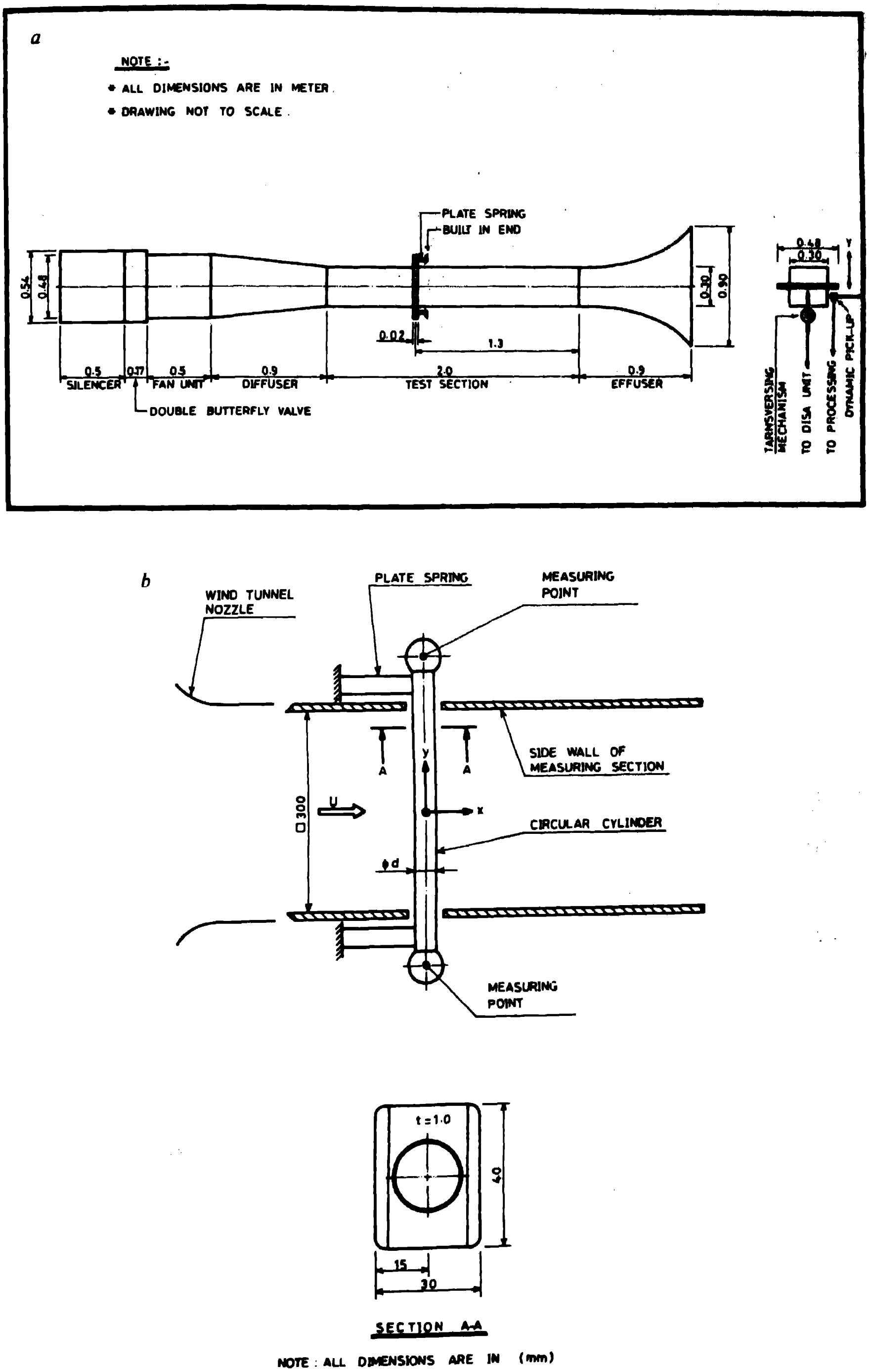

Fig. 1. General view of the wind tunnel and the experimental rig.

and rotational motions. Note that the streamwise motion is difficult to excite in this case since the plates axial rigidity is much higher than its rigidity in the vertical direction and the torsional mode is eliminated by carefully adjusting the overhang length of each plate spring so that equivalent stiffness at each end is obtained. Note that careful considerations were given to ensure the two dimensionality of the vortex wake. This was achieved by making the height of the slots at the two sides of the wind tunnel to be less than nearly four times the diameter of the test cylinder, as was recommended by Graham [12]. This was confirmed by preliminary tests. It should be noted that an initial attempt was made to mount the cylinder by four linear springs of equal stiffness, two at each end, similar to the arrangement used by Gowda and Prabhu [10]. However, it was found necessary to discard this arrangement, since it was felt that such mounting may lead to mode coupling and it is difficult to obtain a single degree of freedom behavior for this test cylinder.

An open suction type wind tunnel was used with a square cross section of (300 mm × 300 mm) and of length equal to (2m). The wind tunnel is capable of producing a free stream velocity range of (5 to 35 m/sec), with a free stream turbulence intensity level of (0.2%). The test cylinder was located at 1.3 m from the inlet of the test section where the flow was found to be fully developed. The resulting Reynolds number range was about $(6 \times 10^3 - 4.6 \times 10^4)$.

The amplitude of vibration was measured by placing a contactless vibration pick up (B&K MM0002) underneath the end of the cylinder, the output signal was simultaneously fed to a digital frequency analyzer (B&K 2131) and to a tunable band pass filter (B&K 1621) and then the signal from the tunable filter was also simultaneously fed to a measuring amplifier (B&K 2616) and to a digital storage oscilloscope (OS 4100). Using this arrangement, it was possible to measure the RMS value and to monitor the signal on both frequency and time domain, a schematic diagram of this measuring arrangement is shown in Fig. 2. The signal from the storage oscilloscope was recorded using an $X - Y$ recorder (WX 4402).

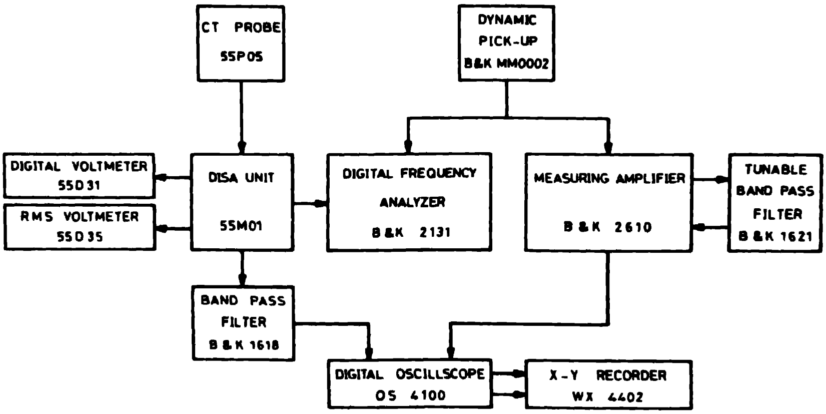

Fig. 2. Signals processing diagram.

The natural frequency (f) and the logarithmic decrement (δ) of the test cylinder were determined by an impulsive test, wherein the cylinder was set into the vibration by slightly tapping its center.

The free stream velocity and turbulence intensity were measured using a constant temperature hot wire anemometer type (DISA 55M01). The frequency spectrum and the wave form of the velocity fluctuation in the wake of the oscillating cylinder, which yield the vortex shedding frequency were monitored by simultaneously feeding the signal from the hot wire probe placed at 1 D in the horizontal direction and 2 D in the vertical direction from the static equilibrium position of the middle of the oscillating cylinder, to the frequency analyzer and to a digital oscilloscope.

Standard sand papers with known roughness were glued and wrapped to obtain various values for the surface roughness of the test cylinder. Three grits of sand papers with equivalent roughness (k/D) of 0.0215, 0.011 and 0.00575 were used respectively.

In order to investigate the effects of freestream turbulence intensity on the flow-induced vibrations of circular smooth and rough cylinders, three different "wood" turbulence generating grids were designed and used in the present experiments. The turbulence grid was located at 1 m upstream the test section. The specifications of the grids as well as the turbulence intensity obtained at the position of the test cylinder are presented in Table 1. The location of the grids was found to produce a homogeneous turbulence at the position of the test cylinder by means of monitoring the turbulence signals in the test section by a digital frequency analyzer.

3. Results and discussion

Reduced velocity values within the vortex shedding region were obtained by tuning the natural frequency of the test cylinder to about 85 Hz, for which the logarithmic decrement was found to be about 0.018 as shown in the impulsive test results in Fig. 3.

3.1. Smooth cylinder

The variation of the nondimensional RMS vibration amplitude divided by the diameter (A/D) with the reduced velocity for the smooth cylinder is shown in Fig. 4. It can be seen from this figure that the lock-in region starts at a reduced velocity of about

Table 1. Turbulence grids characteristics

Grid no.	Rod shape	Rod size	Mesh size	Open ratio	Turbulence level
no	—	—	—	100%	0.2%
1	Circular	1 cm	7.5 cm	90%	4.2%
2	Circular	1 cm	5.0 cm	83%	3.5%
3	Square	5 cm	2.7 cm	83%	2.8%

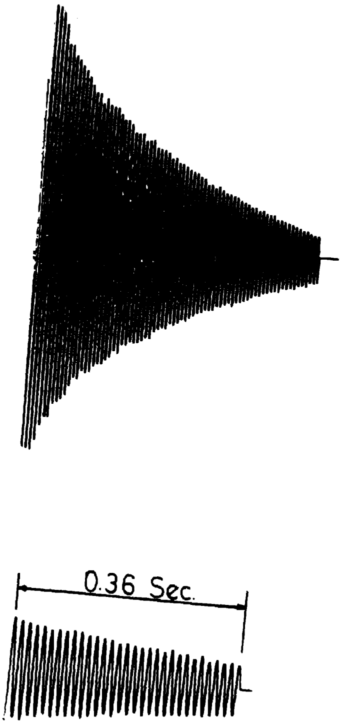

Fig. 3. Typical impulsive test, $f = 85\,Hz$ and $\delta = 0.018$.

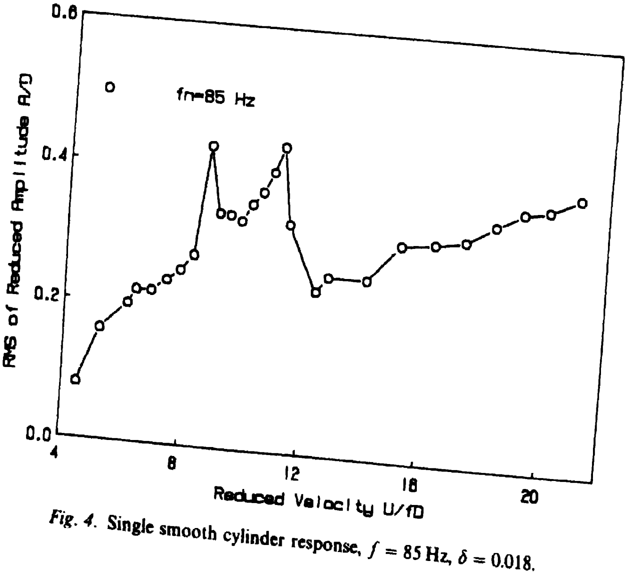

Fig. 4. Single smooth cylinder response, $f = 85$ Hz, $\delta = 0.018$.

5 which is in agreement with Gowda and Prabhu [10], and in disagreement with results of other investigators who have shown the lock-in region to start at a lower reduced velocity, i.e. Zdravkovich [13] has shown the lock-in to start at a reduced velocity of about 3.81. In the present investigation two distinct sharp "resonance hills" of nearly equal peak are clearly observed. This is similar to the results presented by Shiriakashi et al. [9], Durgin et al [8] and Penzin [7], however Gowda and Prabhu [10] and Feng [5] results show a single flat resonance hill in the lock-in region. It could be argued that the second peak may be related to the free end effects. It was found in the present investigation that when two end plates were fitted to the cylinder the dynamic response of the cylinder still exhibits two distinct response peaks which means that the spanwise correlation of the vortices may not be the only reason responsible for the presence of the two peaks in the response curve.

It is interesting to note that the vibration signal waveform for both filtered and unfiltered signal over the entire lock-in region were observed to be nearly pure harmonic at a frequency equal to the free vibration frequency of the cylinder as shown in Fig. 5, which was confirmed by the frequency spectrum of the signals which shows a distinct peak of center frequency near the natural frequency of the cylinder Fig. 6. Reduced velocities in the range (18–160) corresponding to the fluid elastic region were obtained by tuning the natural frequency of the cylinder to about 12.5 Hz, for which the logarithmic decrement was found to be 0.04. Fig. 7, shows measurements for reduced velocities higher than those usually found in the literature which were made to explore the dynamic characteristics of the flow induced vibration in that range.

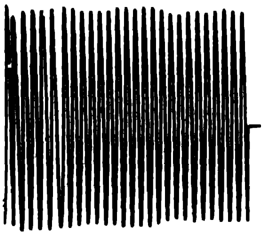

(b) $U/fD = 9.41$

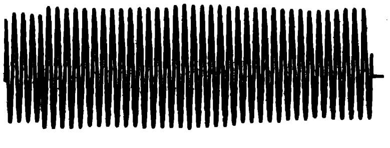

(a) $U/fD = 8$

Fig. 5. Oscillation signals in the lock-in region.

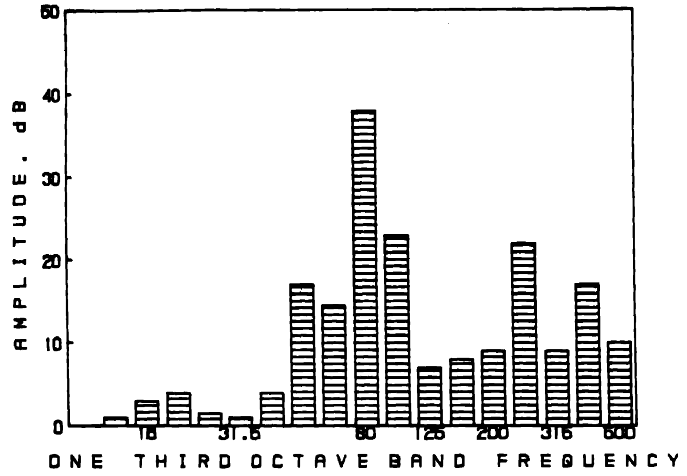

Fig. 6. Frequency spectrum of oscillation signal in the lock-in region [1 Reduced Amplitude = 100 dB].

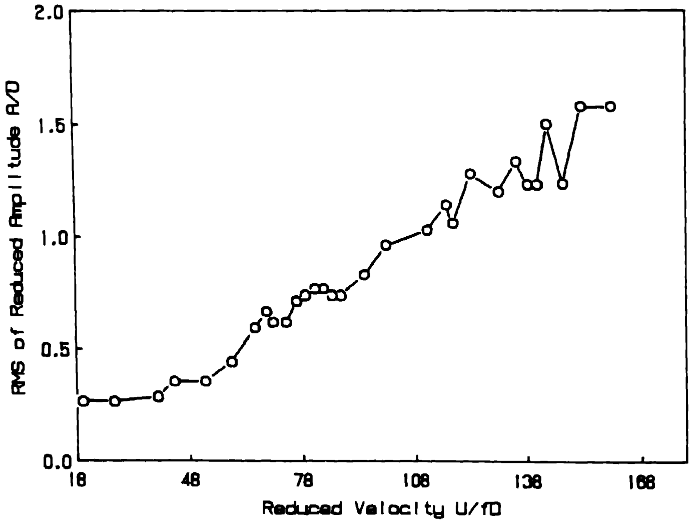

Fig. 7. Smooth cylinder response, $f = 12.5$ Hz, $\delta = 0.04$.

These results show a continuous increase in the dimensionless amplitude of vibration with the increase in the reduced velocity. However, outside the lock-in region, the vibration signal waveform shows a random like behavior of variable strength indicating a nonlinear behavior for the vibrating system, with no distinct dominant peak in the frequency spectrum, Fig. 8.

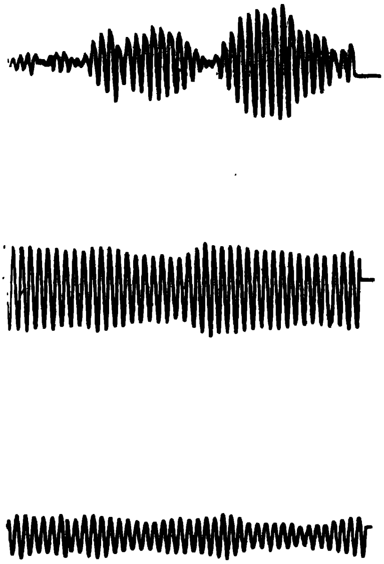

Fig. 8. Oscillation signals in the fluid elastic excitation region.

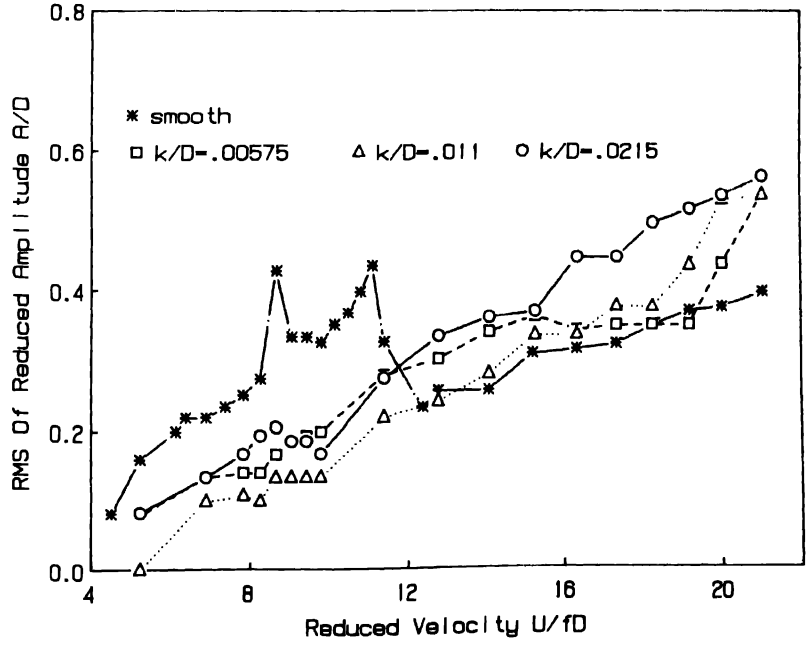

Fig. 9. Effect of surface roughness on the flow induced vibrations of a single cylinder.

3.2. Rough cylinder

The variation of vibration amplitude (A/D) with the reduced velocity for cylinders of various surface roughness of ($k/D = 0.011$, and 0.0215) together with those of smooth cylinder is shown in Fig. 9. The variation of the dimensionless vibration amplitude with surface roughness is shown in Fig. 10 for reduced velocities of 9 and 16 corresponding to vortex shedding and fluid-elastic excitation respectively. It can be seen from these figures that the surface roughness has two main effects on the flow reduced oscillation over a single cylinder.

1. Increasing the surface roughness tends to reduce oscillating amplitude for reduced velocities $\leqslant 12.5$ corresponding to the upper limit of the smooth cylinder.
2. In the fluid-elastic region increasing the surface roughness increases the vibration amplitude.

The above observed behavior for the response amplitude for rough cylinder in the vortex-shedding region may be attributed to the prevention of separation bubbles formation phenomena leading to the reduction of the lift coefficient, Zdravkovich [14], and increase in the drag coefficients. On the other hand the mechanism responsible for the increase in the amplitude of oscillations is not clear and require further investigations. This mechanism may arise from the complex interaction between the flow and the motion of the cylinder and leads to non-linear negative damping.

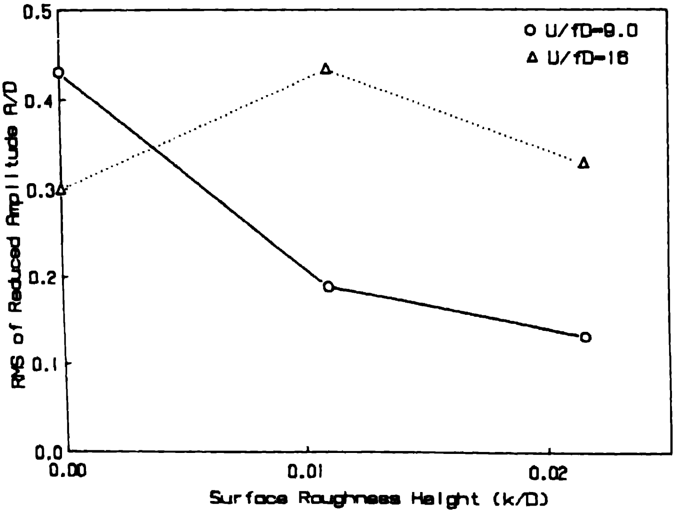

Fig. 10. Reduced vibration amplitude with roughness height (k/D) in both vortex shedding and fluid elastic excitation regions.

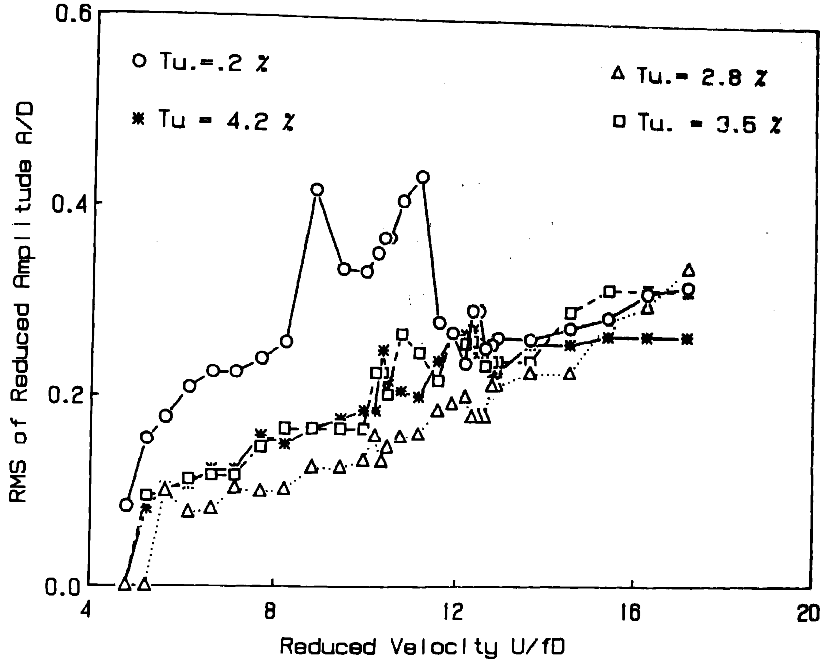

Fig. 11. Effect of free stream turbulence intensity on the flow induced vibrations of a single cylinder, $f = 85$ Hz, $\delta = 0.018$.

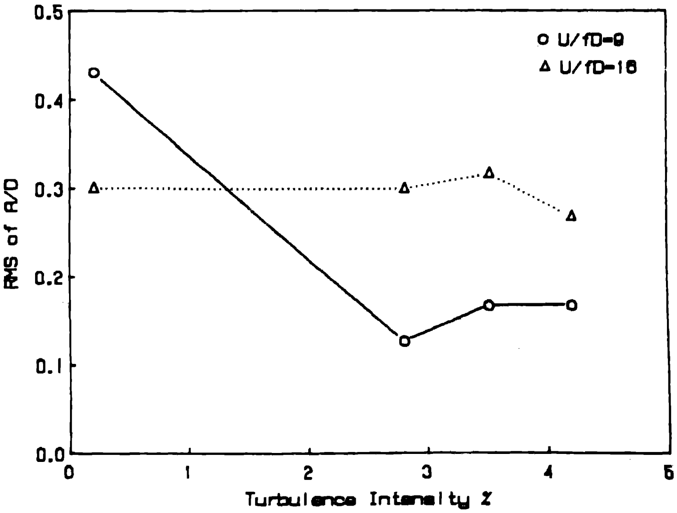

Fig. 12. Variation of reduced vibration amplitude with free stream turbulence intensity in vortex shedding and fluid elastic excitation regions.

3.3. Effect of turbulence intensity

The effect of the variation of the free stream turbulence intensity on the vibration amplitude is shown in Figs. 11 and 12. At free stream turbulence intensity (Tu) of 2.8% a significant drop in the vibration is observed, furthermore no lock-in oscillation were observed (e.g. no simple harmonic oscillations for the vibration amplitude were observed.). However, as the turbulence intensity is increased above 2.8%, the vibration amplitude in the lock-in region corresponding to a low turbulence intensity starts to increase and appears to approach a limiting value equal to about 50% of that of the low turbulence intensity, for a turbulence intensity of about 4.2%. For reduced velocity above 12.5% which corresponds to the end of the lock-in region of the low turbulence response, increasing the free stream turbulence seems to have no drastic effect on the response amplitude as show in Fig. 12.

The variation of the dimensionless RMS amplitude of vibration with reduced velocity for a rough cylinder ($k/D = 0.011$), with various values of turbulence intensity (Tu = 0.2%, 2.8%, and 4.2%) are shown in Figs 13 and 14. It can be seen that increasing the turbulence intensity to 2.8% resulted in a decrease in the vibration amplitude (A/D), while, as the turbulence intensity is further increased (4.2%), the vibration amplitude was increased. Furthermore no distinct regions of lock-in were observed as the oscillation were observed to be nonlinear over the entire reduced velocity range

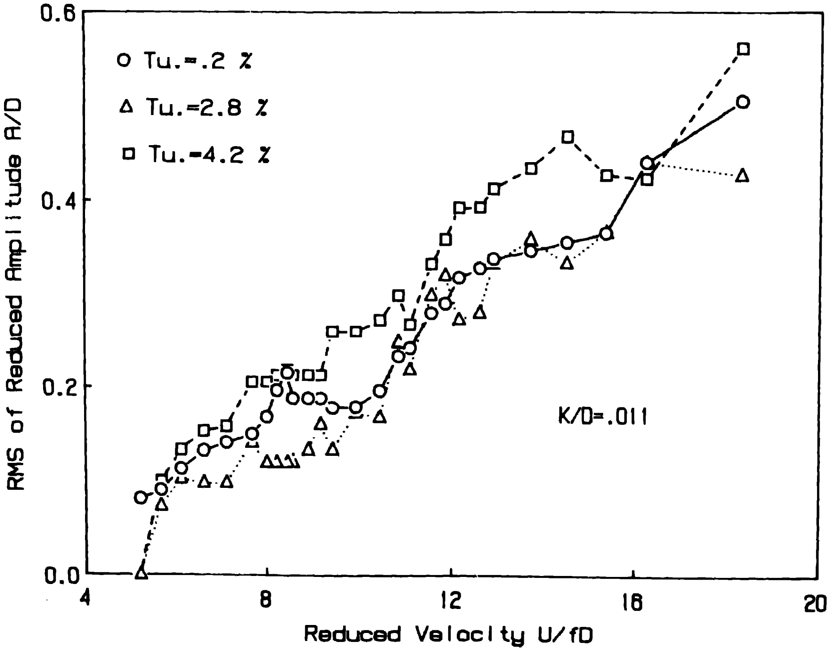

Fig. 13. Effect of free stream turbulence intensity on the flow induced vibrations of rough circular cylinder ($k/D = .011$) in vortex shedding and fluid elastic excitation regions.

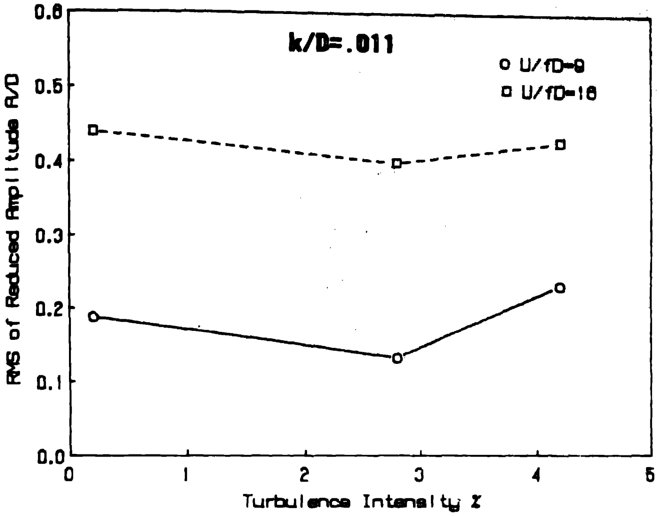

Fig. 14. Variation of reduced vibration amplitude with free stream turbulence intensity for rough cylinder in vortex shedding and fluid elastic excitation regions.

considered. It may be noted that by comparing Fig. 11 and Fig. 13, increasing the surface roughness to ($k/D = 0.011$), the vibration amplitude increases significantly over that of the smooth cylinder.

Note that increasing the turbulence intensity seems to have a similar effect as increasing the surface roughness as can be concluded from Figs 11 and 12 (e.g. increasing the turbulence intensity seems to suppress the lock-in region or as the turbulence intensity is increased the fluid elastic tends to dominate the oscillations even for the low reduced velocity range and tends to increase the vibration amplitude. This is to be expected and may be explained by the fact that turbulence intensity and surface roughness have a similar effect in that both lead to a reduced separation [15–18] and nonuniform vortex streets which result in a nonlinear forcing mechanism.

No comparison is established due to what appears to be lack of data regarding the effect of free stream turbulence intensity and surface roughness on the dimensionless amplitude.

4. Conclusion

The main conclusions deduced from this investigation are as follow:

4.1. Smooth cylinder

1. The lock-in region is characterized by two distinct resonance hills of nearly equal peaks, this is similar to the result presented by Shiriakashi et al [9] and Penzin [7] and in disagreement with Gowda and Prabhu [10] and Feng [5].

2. The waveform of the vibration signal in the lock-in region is nearly sinusoidal of a frequency equal to the free vibration frequency.
3. In the lock-in region increasing the free stream turbulence intensity tends to decrease the vibration amplitude, while, in the fluid elastic region, increasing the turbulence intensity tends to increase the vibration amplitude.

4.2. Rough cylinder

1. Increasing the surface roughness tends to reduce the width of the lock-in region and to reduce the vibration amplitude.
2. In the fluid elastic region increasing the surface roughness tends to increase the vibration amplitude.
3. Increasing the turbulence intensity to 2.8% leads to a decrease in the vibration amplitude, while, a further increase in the turbulence intensity to 4.2% results in an increase in the vibration amplitude.

References

1. Blevins, R. D., *Flow-Induced Vibration.* New York: Van Nostran (1977).
2. Parkinson, G., Phenomena and modelling of flow-induced vibrations of bluff bodies. *Prog. Aerospace Sci.* 26 (1989) 169–244.
3. Blake, W. K., *Mechanics of flow-induced sound and vibration*, Vol. 1. New York: Academic Press (1986).
4. Iwan W. D., The vortex induced oscillations of elastic structural elements. *Trans. ASME, J. of Engineering For Industry* (1975) 1378–1382.
5. Feng, C. C., The measurements of vortex induced effects in flow past stationary and oscillating circular cylinders and D-section cylinders, MSc thesis, University of British Colombia (1968).
6. Kwok, K. C. S and Melbourne, W. H., Cross-wind response of structure due to displacement dependent lock-in excitation. In: *Proc. Fifth Int. Con. Wind Engg., Fort Collins, Colorado, U.S.A.*, Vol. 2. (1979) pp. 699–708.
7. Penzin, J., Wind induced vibration of circular structures. *J. Fluid Mechanics, ASCE*, paper 1141 (1957) 1–17.
8. Durgin, W. W., March, P. A. and Lefbare, P. J., Lower mode response of circular cylinder in cross flow. *Trans. ASME, J. Fluids Engg.* 102 (1980) 183–190.
9. Shiriakashi, M., Ishida, Y. and Wakiya, S., Higher velocity resonance of circular cylinders in cross flow. *Trans. ASME, J. Fluids Engg.* 107 (1985) 392–396.
10. Gowda, B. H. L. and Prabhu, D. R., Interference effects on the flow induced vibration of a circular cylinders. *J. of Sound and Vibration* 112(3) (1987) 487–502.
11. Gerrard, J. H., A disturbance-sensitive Reynolds number range of the flow past a circular cylinder. *Fluid Mechanics* 22(1) (1969) 187–196.
12. Graham, J. M., The effect of end plates on the two dimensionality of a vortex wake. *The Aeronautical Quarterly* (1969) 237–247.
13. Zdravkovich, M. M., Flow-induced vibration of two interference circular cylinders. *J. Sound and Vibration* 101(4) (1985) 511–521.
14. Zdravkovich, M. M., Aerodynamics of two parallel circular cylinders of finite height at simulated high Reynolds number. *J. Wind Engg. and Industrial Aerodynamics* 6 (1980) 59–71.
15. Guven, O., Funel, C. and Patel, V., Surface roughness effects on the near flow past a circular cylinder. *J. Fluid Mechanics* 125(4) (1980) 673–701.

16. Nakamure, Y. and Tomonari, Y., The effects of surface roughness on the flow past circular cylinders, at high Reynolds number. *J. Fluid Mechanics* 123 (1982) 363–378.
17. Nakamure, Y., Ohya Y, and Ozone, S., The effects of turbulence intensity on bluff body near flow. *J. Wind Engg. and Ind. Aerodynamics* 28 (1988) 251–259.
18. Sakamoto, H. and Hanin, H., Effect of free stream turbulence intensity on characteristics of fluctuating forces acting on two square prism in tandem arrangement. *Trans. ASME., J. Fluid Engg.* 110 (1988) 140–146.

Applied Scientific Research **49**: 117–134, 1992.
© 1992 *Kluwer Academic Publishers. Printed in the Netherlands.*

Leakage effects in laminar duct flow: a numerical study

HELGE I. ANDERSSON & KNUT L. TISETH[1]

Division of Applied Mechanics, The Norwegian Institute of Technology, N-7034 Trondheim, Norway;
[1]Present address: OECD Halden Reactor Project, P.O. Box 173, N-1751 Halden, Norway

Received 21 February 1990; accepted in revised form 7 October 1990

Abstract. The influence of transverse leakage into a pressure-driven laminar flow in an infinitely long square duct is investigated. By a simple decomposition of the resulting three-dimensional pressure field, the leakage-induced secondary flow problem decouples from the primary flow problem. The numerical study reveals that two qualitatively different secondary flow patterns may occur, depending on the leakage flow rate. For a given streamwise pressure gradient it is observed that the axial mass flow rate may reduce by about 30 percent under certain leakage conditions, accompanied by a corresponding 50 percent increase in the Darcy-Weisbach friction factor.

Nomenclature

D = duct height and width
D_h = hydraulic diameter
$D_{i,j}$ = cell divergence
F = dimensionless pressure force
h = dimensionless slit height, H/D
H = slit height
i, j = indices
K = streamwise kinematic pressure gradient
n = summation index, time level
p = dimensionless pressure
δp = pressure increment
P = pressure
$\tilde{P}$ = cross-sectional pressure variation
q = dimensionless volumetric axial flow rate
Q = leakage flow rate in m^2/s
Re = leakage Reynolds number, $U_0 D/\nu$
Re_q = primary flow Reynolds number
δt = time increment
x, y = dimensionless cross-sectional coordinates
$\delta x, \delta y$ = cell widths
X, Y = cross-sectional coordinates
z = dimensionless axial coordinate
Z = axial coordinate
u, v, w = dimensionless velocity components
U, V, W = velocity components
U_0 = leakage velocity, Q/H
V = cross-sectional average velocity
W_0 = dummy velocity scale

Greek letters

ρ = density
ν = kinematic viscosity
ω = overrelaxation factor

1. Introduction

In various applications of industrial interest a primary flow field is significantly modified by a secondary fluid motion induced by a sidewise leakage into the main flow. Among the many engineering examples are the flows in single-screw extruders and in labyrinth and visco seals, as well as the flow between the adjustable guide vanes in hydraulic turbines.

A great variety of materials, like metals, polymers and foodstuffs, are formed through extrusion processes. The single-screw extruder which is the most common type of extruder used in the polymer industry, consists of an extruder screw rotating in a barrel [7, 14]. The material situated in the helical screw channel between the barrel and the screw surface is conveyed by frictional and pressure forces. The leakage flow through the clearance between the flight and the barrel is negligible under normal design conditions [11, 14]. If, on the other hand, the screw and/or barrel is subject to wear, the actual clearance can increase substantially and cause considerable reduction in output [14]. An explicit analytical expression for the total volumetric output including the effect of leakage, based on several simplifying assumptions, is given in Ref. [14].

The visco seal is a rotating device which develops an axial pressure gradient in the fluid annulus around the rotating shaft by means of a helical groove located either on the shaft or on the sleeve [3]. Although the working fluid in this device is a gas rather than a liquid, the fundamental flow principles are basically the same as in the single-screw extruder.

Labyrinth seals, which have no pumping capabilities, are frequently used in high performance turbomachinery equipment. A labyrinth seal can be composed of a series of generic annular cavities or grooves on a rotating shaft [8, 15, 17]. This may thus be considered a special case of the visco seal in which the helix angle is zero. Unlike the single-screw extruder and the visco seal the only passage for axial flow in the labyrinth seal is through the small annular clearances between the teeth and the stator housing. Under turbulent flow conditions numerical predictions [8, 17] have demonstrated that the flow pattern inside the seal cavity depends crucially upon the rotation rate. Moreover, the alteration of the flow field in the cavity results in a substantial increase in the pressure drop across it.

The leakage flow underneath the adjustable guide vanes has an important effect on the efficiency of Francis type water turbines [5, 6]. For a prototype turbine, for instance, the loss in efficiency has been measured to about 1.5% at best efficiency point. It is conjectured [5] that the leakage through the clearance gaps underneath the guide vanes is creating vortices in the main flow, which subsequently cause severe disturbancies in the flow through the runner.

Although the flow in a Francis turbine is clearly turbulent, the study of leakage-induced secondary flow phenomena in pressure-driven laminar flows may recover salient features of the leakage effects. The objective of the present investigation is therefore to study the effects of transverse leakages on the laminar Poiseuille flow in an infinitely long square duct (see Fig. 1). As in the aforesaid technological applications, the leakage flows into and out of the duct are both equal in magnitude. The axial flow rate thus remains the same throughout. The two-dimensional leakage flow problem (i.e. without axial flow) has recently been treated numerically in the low Reynolds number (Stokes flow) limit [4]. In the present study laminar flows at moderate Reynolds numbers are considered, for which the nonlinear convection

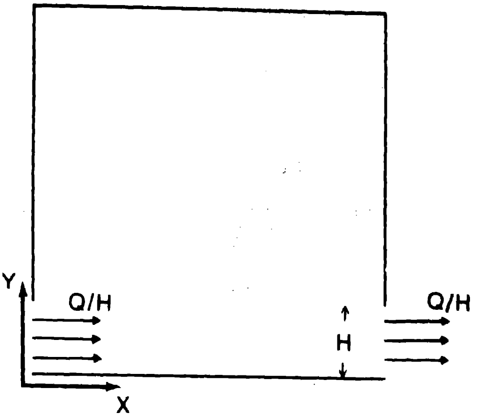

Fig. 1. Cross-sectional view of the square duct and the coordinate system.

cannot be neglected. Then, after having solved the leakage-induced secondary flow problem, the axial flow field is obtained as the solution of a Poisson-type equation.

It should also be emphasized that the model problem depicted in Fig. 1 is a special case of the flow in a single-screw extruder. The helical screw channel may be unwrapped into a straight rectangular duct, and the leakage flow of fluid across the top of the flight land from one screw channel to another results from the pressure difference on the two sides of the land. Then, if the relative motion of the barrel surface to the screw during rotation is neglected, the flow through the screw channel is driven solely by pressure differences.

2. Physical model and governing equations

We consider the laminar flow of an incompressible Newtonian fluid in a straight duct with square cross-section. The height and the width of the duct are denoted by D, as indicated in Fig. 1. Although the main flow is in the axial Z-direction, a secondary fluid motion may be induced by a uniform leakage/drainage through streamwise slits of height H at the bottom of the two vertical side walls of the duct. Here, we assume that the leakage volume Q per second and per unit streamwise length into the duct through one slit exactly equals the drainage through the slit along the opposite wall. Thus, the volumetric flowrate in the streamwise direction remains the same throughout the duct. The resulting three-dimensional viscous flow is assumed to be steady as well as fully developed in the axial direction. Thus, the velocity components U, V and W vary only across the cross-sectional (X, Y) plane. The governing Navier-Stokes equations for the three-dimensional fluid motion therefore reduce to:

$$\frac{\partial U}{\partial X}+\frac{\partial V}{\partial Y}=0, \tag{1}$$

$$U\frac{\partial U}{\partial X}+V\frac{\partial U}{\partial Y}=-\frac{1}{\rho}\frac{\partial P}{\partial X}+\nu\left(\frac{\partial^2 U}{\partial X^2}+\frac{\partial^2 U}{\partial Y^2}\right), \tag{2}$$

$$U\frac{\partial V}{\partial X}+V\frac{\partial V}{\partial Y}=-\frac{1}{\rho}\frac{\partial P}{\partial Y}+\nu\left(\frac{\partial^2 V}{\partial X^2}+\frac{\partial^2 V}{\partial Y^2}\right), \tag{3}$$

$$U\frac{\partial W}{\partial X}+V\frac{\partial W}{\partial Y}=-\frac{1}{\rho}\frac{\partial P}{\partial Z}+\nu\left(\frac{\partial^2 W}{\partial X^2}+\frac{\partial^2 W}{\partial Y^2}\right), \tag{4}$$

Here, equation (1) is the continuity or mass conservation equation, while equations (2)–(4) are the components of the momentum equation in the X, Y and Z-directions, respectively. ρ and ν denote density and kinematic viscosity of the fluid.

It is important to notice that although the Z-derivatives of the velocity components vanish in the present case, the axial pressure gradient is retained. $\partial P/\partial Z$ is, in fact, the driving force in the actual problem. However, differentiation of the momentum equations (2)–(4) with respect to Z reveals that

$$\frac{\partial}{\partial X}\left(\frac{\partial P}{\partial Z}\right)=\frac{\partial}{\partial Y}\left(\frac{\partial P}{\partial Z}\right)=\frac{\partial}{\partial Z}\left(\frac{\partial P}{\partial Z}\right)=0, \tag{5}$$

i.e. the axial pressure gradient is a constant:

$$\frac{\partial P}{\partial Z}=-\rho K, \tag{6}$$

where $K > 0$ if the main flow is in the positive Z-direction. The pressure field $P(X, Y, Z)$ can therefore be expressed as

$$P=-\rho KZ+\tilde{P}. \tag{7}$$

Here, the first term on the right hand side accounts for the axial variation of P according to equation (6), while $\tilde{P}=\tilde{P}(X, Y)$ takes care of the cross-sectional pressure variation.

3. Dimensionless model problem

We now introduce the dimensionless coordinates

$$x = X/D,\ y = Y/D \tag{8}$$

and the dimensionless dependent variables

$$u = U/U_0,\ v = V/U_0,\ w = W/W_0,\ p = \tilde{P}/\rho U_0^2. \tag{9}$$

While the leakage velocity $U_0 \equiv Q/H$ is used as velocity scale for both the secondary velocity components U and V, the axial velocity W is scaled against the dummy scaling velocity W_0. After substitution of eq. (7) and the dimensionless variables (8) and (9), the governing equations (1)–(4) become

$$\frac{\partial u}{\partial x} + \frac{\partial v}{\partial y} = 0, \tag{10}$$

$$u\frac{\partial u}{\partial x} + v\frac{\partial u}{\partial y} = -\frac{\partial p}{\partial x} + \mathrm{Re}^{-1}\left(\frac{\partial^2 u}{\partial x^2} + \frac{\partial^2 u}{\partial y^2}\right), \tag{11}$$

$$u\frac{\partial v}{\partial x} + v\frac{\partial v}{\partial y} = -\frac{\partial p}{\partial y} + \mathrm{Re}^{-1}\left(\frac{\partial^2 v}{\partial x^2} + \frac{\partial^2 v}{\partial y^2}\right), \tag{12}$$

$$u\frac{\partial w}{\partial x} + v\frac{\partial w}{\partial y} = +F\cdot\mathrm{Re}^{-1} + \mathrm{Re}^{-1}\left(\frac{\partial^2 w}{\partial x^2} + \frac{\partial^2 w}{\partial y^2}\right), \tag{13}$$

where the two dimensionless groups F and Re are defined as

$$F \equiv \frac{KD^2}{\nu W_0},\ \mathrm{Re} \equiv \frac{U_0 D}{\nu}. \tag{14}$$

Thus, F is a dimensionless driving pressure force in the axial direction, while Re is a leakage Reynolds number.

It is readily observed that without any leakage, i.e. if $u = v = \mathrm{Re} = 0$, the streamwise momentum equation (13) reduces to the Poisson-equation

$$\frac{\partial^2 w}{\partial x^2} + \frac{\partial^2 w}{\partial y^2} = -F, \tag{15}$$

which should be solved subject to Dirichlet boundary conditions.

In the general case with leakage/drainage through the slits we assume that the velocity components u, v, and w vanish along the boundary of the calculation domain $0 \leqslant x \leqslant 1$, $0 \leqslant y \leqslant 1$. The u-component, however, should account for the leakage/drainage; and we therefore require that

$$u = 1 \quad \text{at} \quad x = 0, 0 \leqslant y \leqslant h, \tag{16a}$$

$$u = 1 \quad \text{at} \quad x = 1, 0 \leqslant y \leqslant h, \tag{16b}$$

where h is the dimensionless slit height H/D. This assures that the leakage at $x = 0$ equals the drainage at $x = 1$.

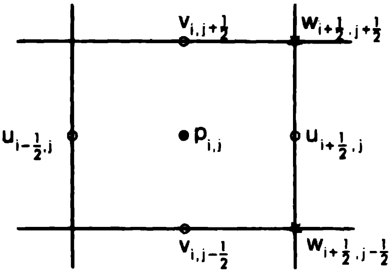

Fig. 2. Staggered arrangement of the discrete variables in a typical SOLA cell.

4. Solution strategy

While the axial velocity component w obviously depends on the secondary velocity field according to equation (13), it is readily observed that the secondary velocity components u and v governed by equations (10)–(12) are independent of w. We therefore adopt the following solution procedure:

1. Solve the secondary flow problem governed by equations (10)–(12) for given slit height h and leakage Reynolds number Re.
2. Solve the primary flow governed by equation (13) for a given pressure gradient parameter F and the secondary velocity field as obtained from step 1.
3. The dimensionless volumetric flow rate in the axial direction

$$q = \int_0^1 \int_0^1 w \, dx \, dy \tag{17}$$

is finally obtained by numerically integrating w over the duct cross-section.

To accomplish the *first step* of the proposed solution strategy we resort to a modified version of the SOLA algorithm [10]. SOLA solves the basic time-dependent differential equations directly for the primitive variables by advancing the solution explicitly in time. The finite-difference mesh consists of equal-sized rectangular cells with edge lengths δx and δy, and the velocity components and the pressure are located at staggered cell positions, as shown in Fig. 2. Tentative velocity components u^* and v^* at the new time level are computed from explicit difference equations, using the pressure and velocity fields from the previous time level:

$$u^*_{i+1/2,j} = u^n_{i+1/2,j} - \delta t\left[\frac{1}{\delta x}(p^n_{i+1,j} - p^n_{i,j}) + FUX + FUY - VUX - VUY\right], \tag{18}$$

$$v^*_{i,j+1/2} = v^n_{i,j+1/2} - \delta t\left[\frac{1}{\delta y}(p^n_{i,j+1} - p^n_{i,j}) + FVX + FVY - VVX - VVY\right]. \tag{19}$$

Here, the convective and viscous terms are represented by the following finite-difference approximations:

$$FUX = \frac{1}{4\delta x}[(u_{i+3/2,j} + u_{i+1/2,j})^2 - (u_{i+1/2,j} + u_{i-1/2,j})^2],$$

$$FUY = \frac{1}{4\delta y}[(u_{i+1/2,j+1} + u_{i+1/2,j})(v_{i+1,j+1/2} + v_{i,j+1/2})$$

$$-(u_{i+1/2,j} + u_{i+1/2,j-1})(v_{i+1,j-1/2} + v_{i,j-1/2})],$$

$$VUX = \frac{1}{\mathrm{Re}(\delta x)^2}[u_{i+3/2,j} - 2u_{i+1/2,j} + u_{i-1/2,j}],$$

$$VUY = \frac{1}{\mathrm{Re}(\delta y)^2}[u_{i+1/2,j+1} - 2u_{i+1/2,j} + u_{i+1/2,j-1}],$$

$$FVX = \frac{1}{4\delta x}[(u_{i+1/2,j+1} + u_{i+1/2,j})(v_{i+1,j+1/2} + v_{i,j+1/2})$$

$$-(u_{i-1/2,j+1} + u_{i-1/2,j})(v_{i,j+1/2} + v_{i-1,j+1/2})],$$

$$FVY = \frac{1}{4\delta y}[(v_{i,j+3/2} + v_{i,j+1/2})^2 - (v_{i,j+1/2} - v_{i,j-1/2})^2],$$

$$VVX = \frac{1}{\mathrm{Re}(\delta x)^2}[v_{i+1,j+1/2} - 2v_{i,j+1/2} + v_{i-1,j+1/2}],$$

$$VVY = \frac{1}{\mathrm{Re}(\delta y)^2}[v_{i,j+3/2} - 2v_{i,j+1/2} + v_{i,j-1/2}].$$

It should be noticed that the convective flux terms in equations (11) and (12) have been rewritten in conservative form prior to discretization.

The new velocity field u^* and v^* computed according to equations (18) and (19) contains the correct vorticity, but has generally nonzero divergence. For the cell (i, j) in Fig. 2, for example, the velocity divergence is

$$D_{i,j} \equiv \frac{1}{\delta x}(u_{i+1/2,j} - u_{i-1/2,j}) + \frac{1}{\delta y}(v_{i,j+1/2} - v_{i,j-1/2}). \tag{20}$$

The tentative velocity field, together with the old pressure field, are to be modified in such a way as to bring the local cell divergence to zero, while preserving the vorticity. For each cell the cell pressure and the edge velocities are simultaneously updated according to the computed cell divergence:

$$\delta p_{i,j} = -\frac{\omega D_{i,j}}{2\delta t}\left(\frac{1}{(\delta x)^2} + \frac{1}{(\delta y)^2}\right)^{-1}, \tag{21}$$

$$p_{i,j} \to p_{i,j} + \delta p_{i,j}, \tag{22a}$$

$$u_{i\pm 1/2,j} \to u_{i\pm 1/2,j} \pm \delta t \cdot \delta p_{i,j}/\delta x, \tag{22b}$$

$$v_{i,j\pm 1/2} \to v_{i,j\pm 1/2} \pm \delta t \cdot \delta p_{i,j}/\delta y. \tag{22c}$$

In this manner the velocity divergence is driven to zero by sweeping iteratively through the mesh. The ultimate steady state solution is then approached asymptotically after a certain number of time steps.

Boundary conditions, according to the last paragraph of Section 3, were imposed numerically at each particular time level during the pseudo-transient sequence of time-steps. For a left boundary coinciding with the left edge of the cell (i, j) shown schematically in Fig. 2, it is required that:

$$u_{i-1/2,j} = 1 \quad \text{for} \quad 0 \leqslant y \leqslant h, \tag{23a}$$

$$u_{i-1/2,j} = 0 \quad \text{for} \quad h < y \leqslant 1, \tag{23b}$$

$$v_{i-1,j+1/2} = -v_{i,j+1/2} \quad \text{for} \quad 0 \leqslant y \leqslant 1. \tag{24}$$

It should be noticed that the discrete form (24) of the boundary condition for the tangential velocity component v involves fictitious boundary cells immediately outside the flow region. The condition (23) for the normal velocity u reflects whether the cell (i, j) is adjacent to the slit (23a) or the rigid wall (23b).

The original SOLA algorithm, as introduced by Hirt et al. [7], uses an explicit first-order Euler-scheme in time, central-difference approximations to the viscous terms and a combined central and donor-cell (upstream) differencing for the convective fluxes. The upstream differencing was introduced in SOLA to suppress numerical instabilities arising from the central form, see e.g. [9]. However, the partial upwind differencing introduces an artificial diffusion in the numerical scheme, so that the resulting solution contains more diffusion than provided by the physics [18]. In the present investigation we have therefore resorted to purely second-order accurate central-difference approximations for all spatial derivatives. With this simple, but yet important, modification, we have recently applied the SOLA-algorithm to some two-dimensional [1, 2] and three-dimensional [12] laminar flow problems.

The *second step* of the solution strategy is to solve equation (13) for w subject to the Dirichlet boundary condition $w = 0$ imposed along the walls of the duct. Equation (13) is discretized using second-order accurate central-difference approximations to all derivatives. The discrete values of w are evaluated at the nodes of the SOLA-mesh, as shown in Fig. 2. Since SOLA provides values of the secondary velocity components at the centers of the cell surfaces, the required values for u and v at the nodes are calculated as simple averages over neighbouring grid points. The resulting *linear* system of algebraic difference equations

$$\begin{aligned} w_{i+1/2,j+1/2} = {} & \frac{1}{4}(w_{i+3/2,j+1/2} + w_{i-1/2,j+1/2} + w_{i+1/2,j+3/2} + w_{i+1/2,j-1/2}) \\ & - \frac{\delta x}{16} \mathrm{Re}^{-1} [(u_{i+1/2,j+1} + u_{i+1/2,j})(w_{i+3/2,j+1/2} - w_{i-1/2,j+1/2})] \\ & - \frac{\delta x}{16} \mathrm{Re}^{-1} [(v_{i+1,j+1/2} + v_{i,j+1/2})(w_{i+1/2,j+3/2} - w_{i+1/2,j-1/2})] \\ & + \frac{(\delta x)^2}{4} F \cdot \mathrm{Re}^{-1} \end{aligned} \tag{25}$$

is then solved iteratively by the Gauss-Seidel method (see, e.g. [13]). For the sake of simplicity equation (25) has been written for the special case with $\delta x = \delta y$.

Finally, as a *third step*, the dimensionless volumetric flow rate q is obtained by straightforward numerical integration of the discrete values of w resulting from step two. First, the axial velocity is evaluated at the center of each cell (i, j) as a simple average:

$$w_{i,j} = \frac{1}{4}(w_{i+1/2,j+1/2} + w_{i+1/2,j-1/2} + w_{i-1/2,j+1/2} + w_{i-1/2,j-1/2}). \tag{26}$$

Then, the extended midpoint rule (see, e.g. [13]) is used for integrating $w_{i,j}$ over the cross-section according to equation (17).

5. Results and discussions

5.1. Secondary flow problem

As the first step in the solution procedure, the partial differential equations (10), (11) and (12) are solved for the secondary velocity components u and v and the cross-sectional pressure variation p. The solutions were calculated on a uniform grid with 20 × 20 grid points. Some different leakage Reynolds numbers in the range 0.1 –200 were considered for the slit heights 0.05, 0.10 and 0.20.

For Re = 100 the computed streamlines are shown in Figs 3–5 for the three different slit heights. It is observed from Fig. 3 that for $h = 0.05$ the leakage flow penetrates far into the duct cross-section before the fluid is drained at the lower right-hand corner of the duct. For the larger slit openings $h = 0.10$ and $h = 0.20$, the leakage flow remains in the lower half of the duct. However, a secondary shear driven vortex is observed in the upper part of the duct in Figs. 4 and 5.

The present calculations indicated that the secondary vortex appears for the higher values of Re and h. The open symbols in the lower left-hand side of Fig. 6 represent calculated flow patterns similar to that in Fig. 3, while the filled symbols in the upper right-hand corner, on the other hand, indicate the formation of a secondary vortex. The line $h = 8/\mathrm{Re}$, which is drawn by chance in the flow pattern map in Fig. 6, approximates the borderline between the two distinct flow pattern regimes.

The numerical solutions for the smallest slit opening $h = 0.05$ are certainly questionable. In these cases the slit has the same size as the grid cell, and it could therefore be argued that the resulting flow pattern is due to the coarse grid resolution rather than to real physical mechanisms. To settle this issue calculations on a refined grid with 40 × 40 cells were compared with the 20 × 20 grid solutions for Reynolds number Re = 1 and 100. Although a slight grid dependence is observed, the resulting streamline pattern remains fairly unaffected. The existence of the two qualitatively different secondary flow regimes, as indicated in the flow pattern map in Fig. 6, has thus been verified.

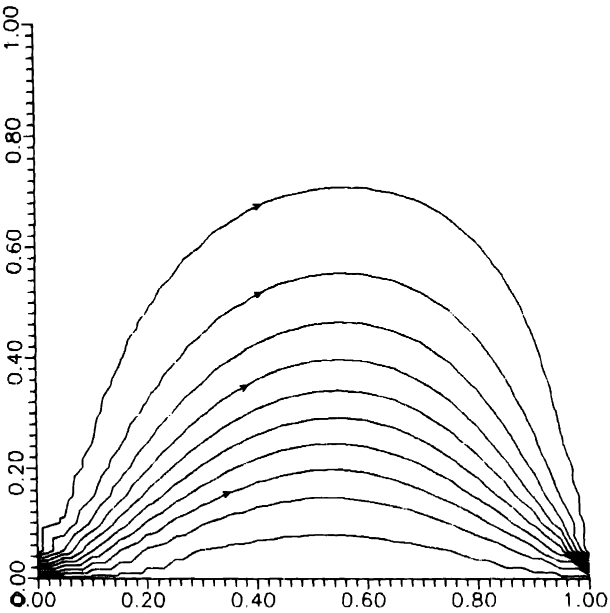

Fig. 3. Streamline pattern of the secondary flow. Re = 100 and $h = 0.05$.

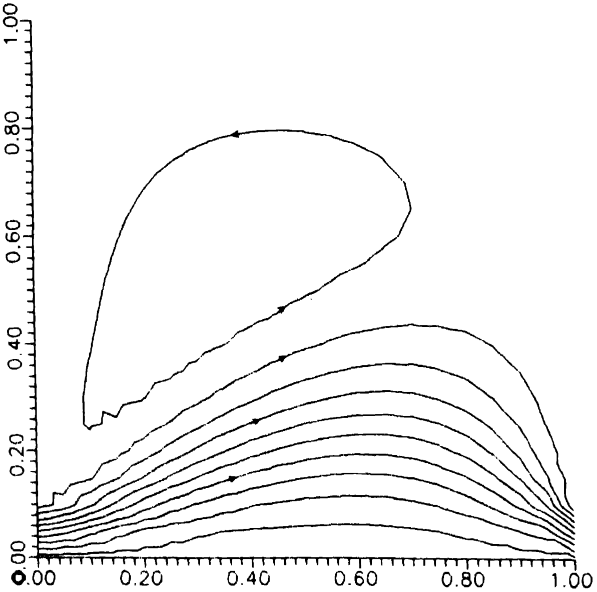

Fig. 4. Streamline pattern of the secondary flow. Re = 100 and $h = 0.10$.

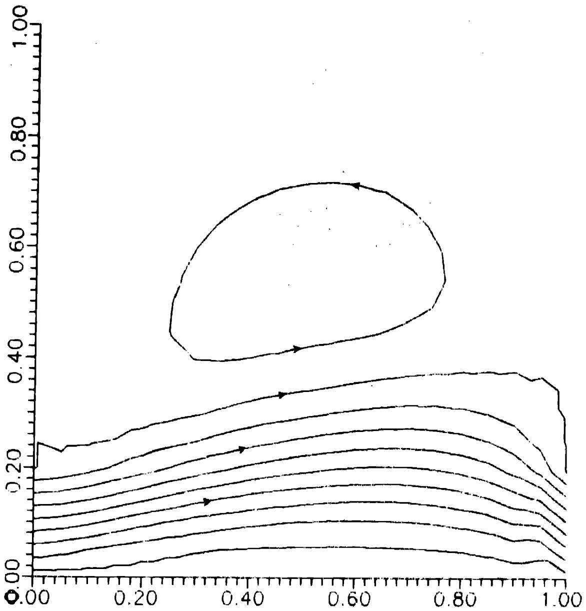

Fig. 5. Streamline pattern of the secondary flow. Re = 100 and $h = 0.20$.

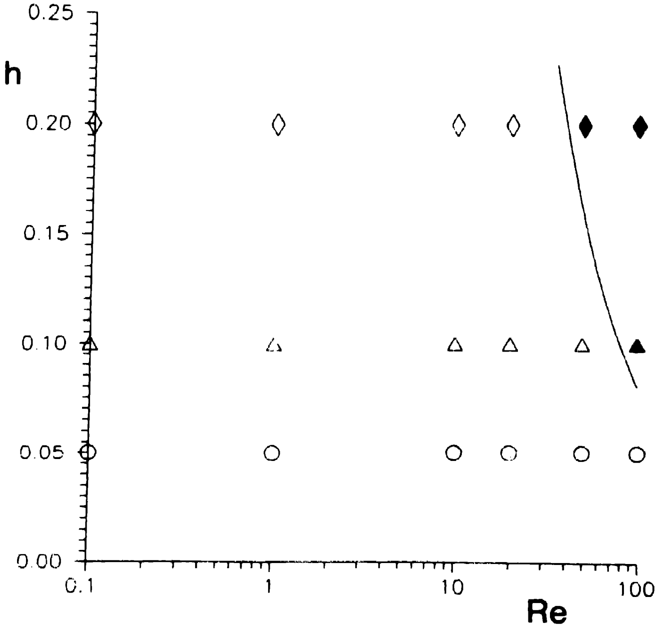

Fig. 6. Flow pattern map in the h – Re plane. The filled symbols identify secondary flow patterns with a secondary vortex. The solid line is given by $h = 8/\text{Re}$.

Along with the solution of the secondary velocity field u, v, the cross-sectional pressure field p is also obtained. For prescribed leakage conditions Re and h, the predicted difference between inlet pressure p_{in} and exit pressure p_{out} is shown in Fig. 7. It is observed that $p_{in} - p_{out}$ is approximately proportional to 1/Re. Thus, for a given fluid (ν) in a given duct (D) the dimensionless pressure difference is inversely proportional to the leakage velocity U_0. For a given leakage Reynolds number Re, on the other hand, the pressure difference $p_{in} - p_{out}$ decreases slightly with increasing slit height h.

5.2. Primary flow problem

The flow rate in the axial direction is solely made up of contributions from the velocity component w in the z-direction (see equation (17)). According to the axial momentum equation (13), w depends on the dimensionless axial pressure force F and the secondary velocity components u and v. The dimensionless axial flow rate q therefore depends on the three dimensionless parameters F, h and Re.

For a given secondary flow field, the primary velocity component w is obtained numerically from eq. (13). A 20 × 20 finite difference grid is used in order to ensure that the primary flow is obtained with the same accuracy as the secondary flow field.

For the particular case Re = 0, i.e. no leakage flow, the axial momentum equation (13) reduces to the simpler equation (15). With no-slip conditions $w = 0$ imposed

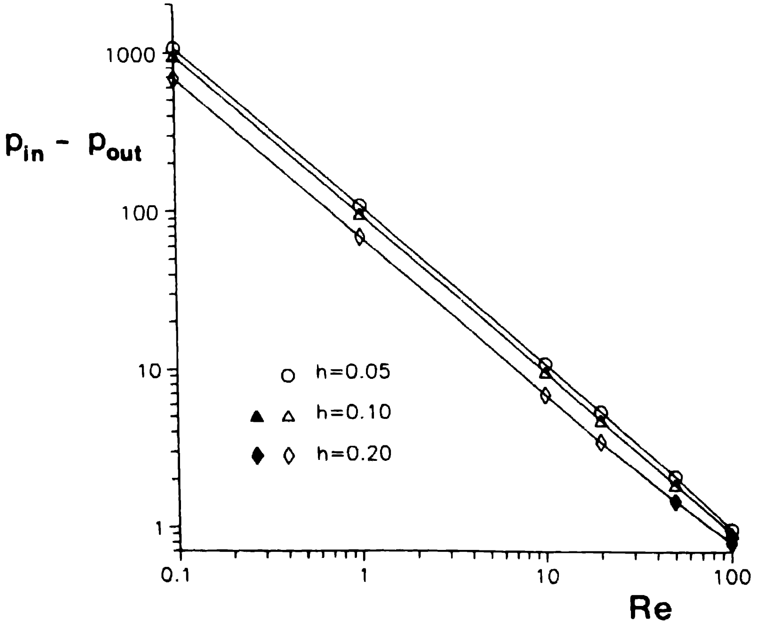

Fig. 7. Dimensionless pressure difference between inlet and outlet.

along the duct walls, eq. (15) has been solved analytically for some different cross-sectional geometries, see e.g. [16], [19]. For the square duct considered in the present investigation, the exact solution becomes

$$w(x, y) = \frac{4F}{\pi^3} \sum_{n=1,3,5\ldots}^{\infty} \frac{1}{n^3}(-1)^{(n-1)/2}\left[1 - \frac{\cosh[n\pi(x - 1/2)]}{\cosh[n\pi/2]}\right]\cdot\cos[n\pi(y - 1/2)]. \tag{27}$$

An exact expression for the dimensionless volumetric flow rate in equation (17) is then obtained by straightforward integration of equation (27):

$$q = \frac{F}{12}\cdot\left[1 - \frac{192}{\pi^5} \sum_{n=1,3,\ldots}^{\infty} \frac{1}{n^5} \tanh(n\pi/2)\right]. \tag{28}$$

By carrying out the infinite summation in equation (28), we obtain the *exact* result

$$q_{\text{exact}} = 0.03514F. \tag{29}$$

The corresponding *approximate* result

$$q = 0.03486F \tag{30}$$

has been obtained numerically by invoking the solution strategy proposed in Section 4. Thus, for Re = 0, the numerically predicted flow rate q in equation (30) is 0.8 percent below the exact flow rate (29).

The axial flow field $w(x, y)$ in equation (27), i.e. without leakage, is symmetric with respect to the center of the duct $x = 1/2$, $y = 1/2$. When leakage occurs, however, the presence of the convective terms on the left-hand side of equation (13) makes the primary flow asymmetric. This distortion is clearly exhibited in Figs 8–10 for the slit heights 0.05, 0.10 and 0.20, respectively. The leakage Reynolds number is kept equal to 100.

It is observed from Fig. 8 that the position of maximum axial velocity is shifted towards the sink, while the position of maximum velocity in Figs 9 and 10 has been shifted upwards. The different behaviour in the two latter cases may be ascribed to the occurence of the secondary vortex in the corresponding leakage flow patterns in Figs 4 and 5.

Since equation (13) is a linear equation for w with source term proportional to the driving pressure force F, the axial flow rate q becomes proportional to F for any leakage conditions. The constant of proportionality, however, depends on the leakage flow, and the exact value 0.03514 in equation (29) applies only for Re = 0.

Fig. 11 demonstrates how the axial flow rate q depends on the leakage parameters h and Re. The predicted flow rate q for a prescribed F has been scaled against q_{exact} in

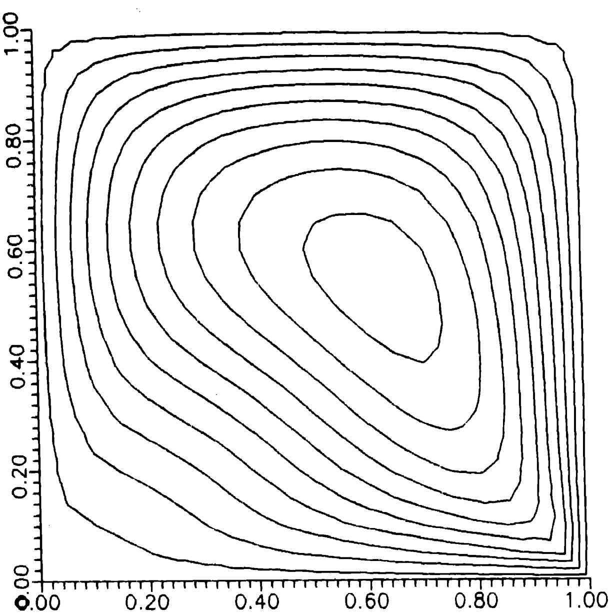

Fig. 8. Isolines for the primary velocity component w. Re = 100 and $h = 0.05$.

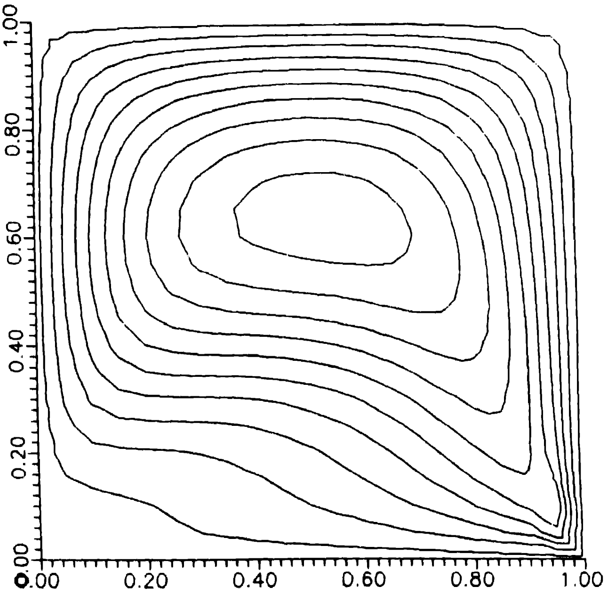

Fig. 9. Isolines for the primary velocity component w. Re = 100 and $h = 0.10$.

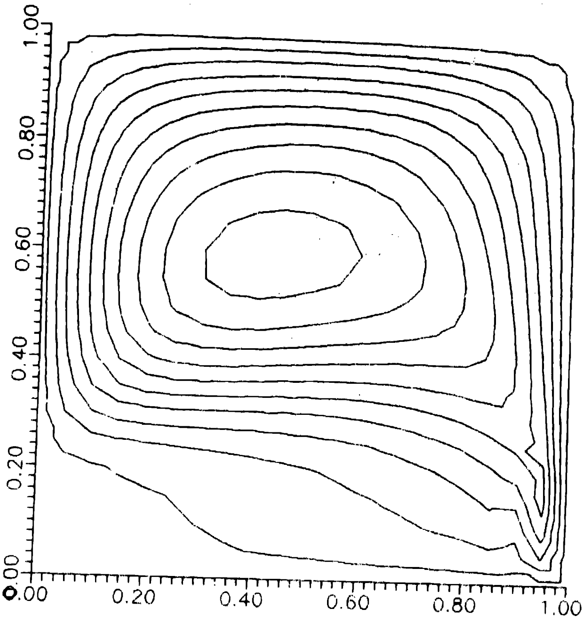

Fig. 10. Isolines for the primary velocity component w. Re = 100 and h = 0.20.

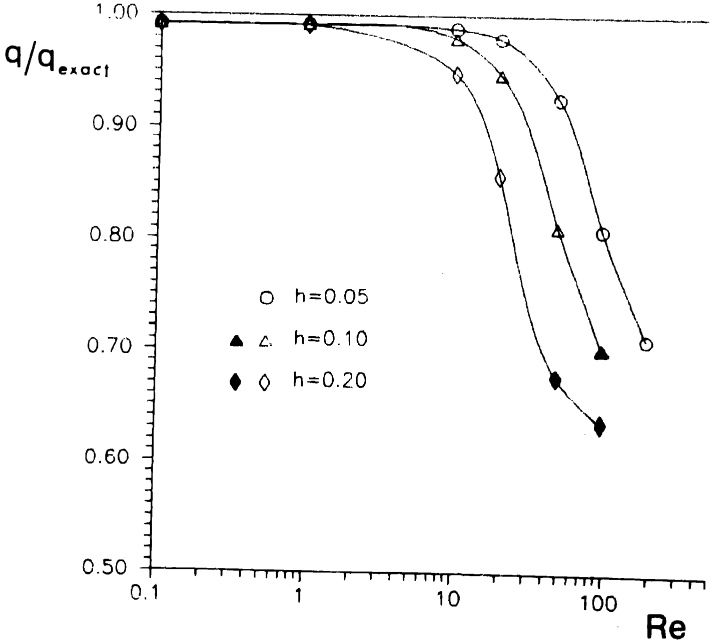

Fig. 11. Variation of primary (axial) flow rate with Re and h.

equation (29). Thus, q/q_{exact} becomes independent of F. As Re tends to zero, q/q_{exact} becomes close to unity. Due to discretization errors, however, the highest obtained value on the 20 × 20 grid is 0.992 rather than 1.

It is observed from Fig. 11 that the axial flow rate decreases with increasing leakage velocity U_0. For a given leakage velocity, say Re = 100, the greatest reductions in flow rate are obtained for the greatest slit heights.

5.3. *The friction factor*

In engineering flow analysis the dimensionless friction factor f in the Darcy-Weisbach equation

$$\frac{\Delta p}{L} = \frac{f}{D_h} \cdot 1/2 \rho V^2 \tag{31}$$

plays a crucial role. In the present context the pressure drop Δp over the duct length L is equal to $\rho K L$, while the cross-sectional average velocity V equals qW_0. For a square duct the hydraulic diameter D_h is equal to the width D of the duct. By introducing the dimensionless pressure force F defined in equation (14) the Darcy-Weisbach equation (31) becomes:

$$f \cdot \mathrm{Re}_q = 2\frac{F}{q}, \tag{32}$$

where

$$\mathrm{Re}_q \equiv \frac{VD}{\nu} = \frac{qW_0 D}{\nu} \tag{33}$$

is the primary flow Reynolds number.

Now, with the ratio between q and F as obtained in the preceeding section, the variation of the friction factor f with the leakage flow parameters h and Re is displayed in Fig. 12. Here, $h \cdot \mathrm{Re}$ represents the Reynolds number Q/ν based on the leakage flow rate Q.

In the leakage Reynolds number range Re < 1, the calculated values for $f \cdot \mathrm{Re}_q$ are approximately constant and exceed only slightly the exact result 56.91 for Re = 0. For leakage Reynolds numbers greater than unity, on the other hand, $f \cdot \mathrm{Re}_q$ increases nearly linearly with log Q/ν. By increasing Q/ν from 1 to 10, for instance, the friction factor $f \cdot \mathrm{Re}_q$ increases by some 40 per cent. It is also interesting to notice that the predictions in Fig. 12 nearly correlate on one single curve for any slit opening h when plotted versus the leakage flow rate Reynolds number $h \cdot \mathrm{Re} = Q/\nu$.

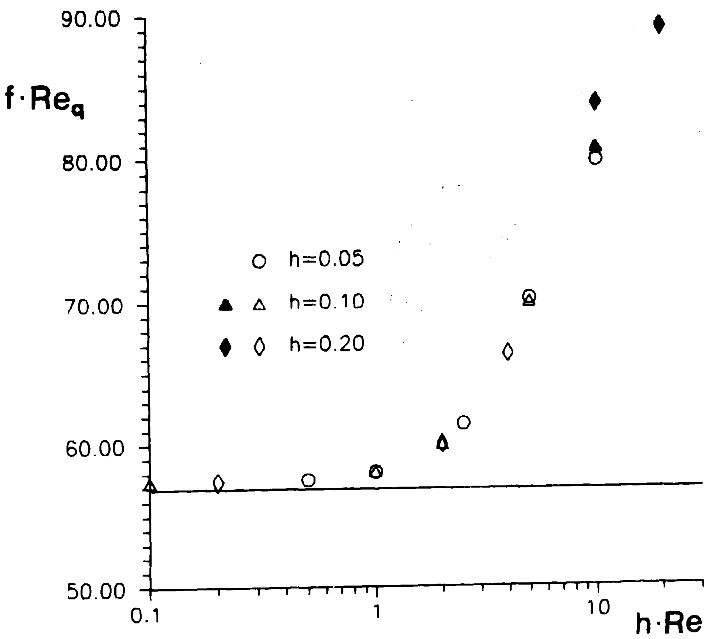

Fig. 12. Variation of the Darcy-Weisbach friction factor with $h \cdot \text{Re}$. The solid lines indicate the exact friction factor without leakage.

6. Conclusions

Based on some simplifying assumptions a decomposition of the pressure has been devised, which decouples the secondary leakage flow problem from the primary flow equation. The 3D flow induced by the leakage has thus been investigated by solving first a 2D elliptic flow problem, followed by the numerical solution of a 2D Poisson-equation.

Two qualitatively different secondary flow patterns have been observed, a secondary vortex being observed if $h \cdot \text{Re} = Q/\nu$ exceeds about 8. It has also been found that the wall friction $f \cdot \text{Re}_q$ increases monotonically with increasing leakage flow rate Reynolds number Q/ν, while the axial flow rate q being correspondingly reduced due to the leakage effects.

The present approach is applicable also to laminar flow situations with $\text{Re} > 200$ or $h < 0.05$. The numerical method should then be modified to allow for grid refinement in the vicinity of the slits. Moreover, a better discretization scheme for the convective fluxes (e.g. QUICK) should be implemented to alleviate the convergence problems observed for the highest Reynolds numbers considered in the present investigation.

Acknowledgement

The assistance of Mr R. Kristoffersen is gratefully acknowledged. The authors are indebted to Professor H. Brekke for stimulating discussions on the guide vane leakage-flow problem in Francis turbines. The authors would also like to extend their thanks to an anonymous referee for his or her constructive comments and criticism.

References

1. Andersson, H. I. and Kristoffersen, R., Numerical simulation of unsteady viscous flow. *Arch. Mech.* 41 (1989) 207–223.
2. Andersson, H. I. and Kristoffersen, R., Start-up of laminar pipe flow. *Proc. AIAA/ASME/SIAM/APS 1st National Fluid Dynamics Congress*, Cincinnati. Washington: AIAA (1988) pp. 1356–1363.
3. Anwar, I., Evaluation of seal concepts for advanced flywheel systems. *Energy Conservation Through Fluid Film Lubrication Technology: Frontiers in Research and Design.* New York: ASME (1979) pp. 147–167.
4. Bayada, G. and Chambat, M., Asymptotic behaviour of a thin film flow in junction with a cavity. In: R. Gruber, J. Periaux and R. P. Shaw (eds), *Proc. 5th International Symposium on Numerical Methods in Engineering*, Vol. 1. Berlin/Heidelberg: Springer Verlag (1989) pp. 737–742.
5. Brekke, H., The influence from the guide vane clearance gap on efficiency and scale effect for Francis turbines. *Proc. 14th IAHR Symposium on Progress within Large and High-Specific Energy Units.* Trondheim: Tapir Publishers (1988) pp. 825–837.
6. Brekke, H., Schanke, P. and Haugen, J. O., The influence of the guide vane clearance gap on efficiency and scale effect. *Proc. 15th IAHR Symposium on Modern Technology in Hydraulic Energy Production*, Paper B3. Belgrade (1990).
7. Cheremisinoff, N. P., Principles of polymer mixing and extrusion. In: N. P. Cheremisinoff (ed.), *Encyclopedia of Fluid Mechanics*, Vol. 7, Rheology and Non-Newtonian Flows. Houston: Gulf Publishing Company (1988) pp. 761–865.
8. Demko, J. A., Morrison, G. L. and Rhode, D. L., Effect of shaft rotation on the incompressible flow in a labyrinth seal. In: C. Taylor, W. G. Habashi and M. M. Hafez (eds), *Proc. 5th International Conference on Numerical Methods in Laminar and Turbulent Flow.* Swansea: Pineridge Press (1987) pp. 509–520.
9. Hirt, C. W., Heuristic stability theory for finite-difference equations. *J. Comp. Phys.* 2 (1968) 339–355.
10. Hirt, C. W., Nichols, B. D. and Romero, N. C., SOLA-A numerical solution algorithm for transient fluid flows. Los Alamos Scientific Laboratory Report LA-5852 (1975).
11. Kalyon, D. M., Mixing in continuous processors. In: N. P. Cheremisinoff (ed.), *Encyclopedia of Fluid Mechanics*, Vol. 7, Rheology and Non-Newtonian Flows. Houston: Gulf Publishing Company (1988) pp. 887–926.
12. Kristoffersen, R., Billdal, J. T. and Andersson, H. I., The three-dimensional lid-driven cavity flow as test case for numerical solution algorithms. In: C. Taylor, P. M. Gresho and R. L. Sani (eds), *Proc. 6th International Conference on Numerical Methods in Laminar and Turbulent Flow.* Swansea: Pineridge Press (1989) pp. 133–143.
13. Press, W. H., Flannery, B. P., Teukolsky, S. A. and Vetterling, W. T., *Numerical Recipes.* Cambridge: Cambridge University Press (1986).
14. Rauwendaal, C., *Polymer Extrusion.* Munich: Hanser Publishers (1986).
15. Rhode, D. L., Demko, J. A., Traegner, U. K., Morrison, G. L. and Sobolik, S. R., Prediction of incompressible flow in labyrinth seals. *ASME J. Fluids Engrg.* 108 (1986) 19–25.
16. Shah, R. K. and London, A. L., *Laminar Flow Forced Convection in Ducts.* New York: Academic Press (1978).
17. Stoff, H., Incompressible flow in a labyrinth seal. *J. Fluid Mech.* 100 (1980) 817–829.
18. Timin, T. and Esmail, M. N., A comparative study of central and upwind difference schemes using the primitive variables. *Int. J. Num. Meth. Fluids* 3 (1983) 295–305.
19. White, F. M., *Viscous Fluid Flow.* New York: McGraw-Hill (1974).

Applied Scientific Research **49**: 135–146, 1992.
© 1992 *Kluwer Academic Publishers. Printed in the Netherlands.*

Buoyant plumes due to mass diffusion

M. JAGANNADHAM[1], K. SUBBA REDDI[2] & D. ANGIRASA[3,*]

[1]*Department of Mechanical Engineering, S.R.K.R. Engineering College, Bhimavaram 534 202, Andhra Pradesh, India;* [2]*Department of Marine Engineering, Andhra University, Visakhapatnam 530 003, India;* [3]*Faculty of Applied Physics, Delft University of Technology, P.O. Box 5046, 2600 GA Delft, The Netherlands (*author for correspondence)*

Received 20 March 1989; accepted in revised form 7 October 1990

Abstract. This paper presents the results of a numerical study of laminar axisymmetric plumes that emanate from a point source of mass diffusion. Various flow configurations that arise in mass diffusion plumes are identified. In the ambient, the cases of constant concentration and stable density stratification are considered. The governing conservation equations of mass, momentum, and species diffusion are cast in finite-difference form using an explicit scheme. Boundary layer and Boussinesq approximations are incorporated. Upwind-differencing is employed for convective terms. Velocity and concentration fields are obtained for various values of Schmidt number, and concentration stratification levels in the ambient. The results are explained in terms of the basic physical mechanisms that govern these flows. The complex interactions between the buoyancy and the Schmidt number, and the stratification parameter are discussed.

Nomenclature

c = concentration of diffusing species
C = concentration excess ratio, $(c - c_{\infty,x})/(c_0 - c_{\infty,0})$
C^* = concentration excess ratio based on centerline concentration, $(c - c_{\infty,x})/(c_c - c_{\infty,x})$
D = diffusion coefficient
g = gravitational acceleration
p = pressure
S^* = concentration stratification parameter, $1/\Delta C_0 \, \mathrm{d}c_{\infty,x}/\mathrm{d}X$
t = temperature
u, v = velocity components
U, V = non-dimensional velocity components
x, r = axial and radial space coordinates
X, R = non-dimensional space coordinates

Greek letters

β^* = coefficient of expansion with concentration, $1/\rho(\partial\rho/\partial c)_{t,p}$
ρ = density
τ = time
τ^* = non-dimensional time
ν = kinematic viscosity

Dimensionless parameter

Sc = Schmidt number, ν/D

Subscripts

∞ = location indicating far away from the axis of the plume
o = location indicating the source
c = location indicating centerline
x = location along X-axis

1. Introduction

Plumes are a part of a broader fluid flow classification called free boundary flows. These are characterized by an absence of rigid walls in the region of flow as, for example, smoke rising in air. If the flow occurs because of a source of buoyancy alone, it is called a plume, while if it is entirely due to an input of momentum, it is classified as a jet. The simultaneous presence of buoyancy and momentum results in a type of free boundary flow called a buoyant jet or a forced plume. In this paper, we are concerned with plumes, in which the only force to cause flow is buoyancy.

Plumes originating due to thermal buoyancy alone have been widely studied. Jaluria [1] reviewed these type of flows. There has not been much work on plumes due to multiple buoyant forces, or plumes from sources of mass diffusion. Multiple buoyant forces result if, for instance, in addition to thermal energy diffusion, mass diffusion is present. It may also be due to the presence of suspended particulate matter in the flow. Recently, some work (Angirasa and Sarma [2], Angirasa and Srinivasan [3], and Srinivasan and Angirasa [4]) has been reported on laminar axisymmetric plumes due to the combined buoyancies of heat and mass diffusion. There is a fundamental difference between thermal plumes and plumes due to mass diffusion. If the temperature of a thermal source is higher than the surrounding, the plume invariably rises upwards since the density of almost all fluids in the range of temperatures commonly encountered decreases with an increase in the temperature. Now consider a plume generated from a point source of mass diffusion. The concentration of the diffusing species at the source is c_0 and in the ambient c_∞ (Fig. 1). The direction of flow depends on the contribution of the diffusing species to the density of the medium. We define a volumetric coefficient due to concentration as

$$\beta^* = \frac{1}{\rho}\left(\frac{\partial \rho}{\partial c}\right)_{t,p}. \tag{1}$$

When $\beta^* < 0$, the diffusing species cause a buoyancy-induced flow upwards (Fig. 1a), and when $\beta^* > 0$, the flow is downwards (Fig. 1b). We also consider a stable density stratification in the ambient. Stable stratification corresponds to a decrease in density with height in the gravity field. The flow configurations for this case are represented in Figs 1(c) and 1(d). Stable ambient density stratification is attained through vertical variation in the concentration of the species.

The aim of the present numerical study is to understand the basic physical mechanisms of the axisymmetric plumes originating from a point source of mass diffusion. Attention here is restricted to thin layer or boundary layer flows. Then, in the flow region of our consideration, the centerline concentration is always greater than that of the ambient. This is particularly relevant to flows in stratified media. If the density stratification of the surrounding fluid is strong, i.e., steep variation of density with height or depth (x), the concentration of the surrounding medium may exceed the plume centerline concentration at some location of x. In such a situation, the flow will reverse beyond this location of x. The flow then is not a boundary layer phenomenon, and cannot be represented by the present analysis. This is discussed further in reference [4].

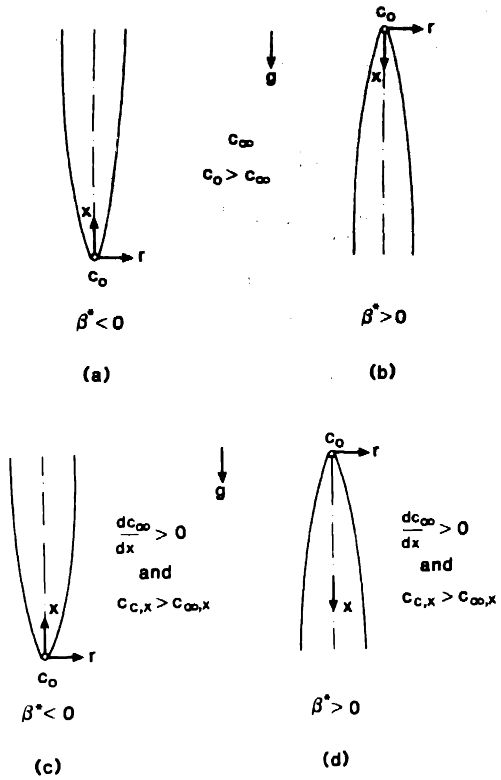

Fig. 1. Various physical configurations of the plumes, and the coordinate system.

2. Analysis and numerical procedure

The governing equations of mass, momentum, and species conservation for laminar, axisymmetric, incompressible buoyancy-induced flows under consideration are

$$\frac{\partial(ru)}{\partial x} + \frac{\partial(rv)}{\partial r} = 0, \tag{2}$$

$$\frac{\partial u}{\partial \tau} + u\frac{\partial u}{\partial x} + v\frac{\partial u}{\partial r} = v\frac{1}{r}\frac{\partial}{\partial r}\left(r\frac{\partial u}{\partial r}\right) \pm g\beta^*(c - c_{\infty,x}), \tag{3}$$

$$\frac{\partial c}{\partial \tau} + u\frac{\partial c}{\partial x} + v\frac{\partial c}{\partial r} = D\frac{1}{r}\frac{\partial}{\partial r}\left(r\frac{\partial c}{\partial r}\right). \tag{4}$$

In the above equations, Boussinesq and boundary layer approximations are incorporated. We also assume that the species concentration levels are small.

Boundary layer approximations are known to be valid for plumes from point as well as line sources (see, for example, Fujii [5]). The plume can be considered to be a thin layer rising vertically upwards or downwards (Fig. 1). In the axial direction, convection is predominant over diffusion. Hence, in the equations (3) and (4) diffusion terms in the axial direction are neglected. The sign before the buoyancy term in the momentum equation (3) is determined by the sign of β^*. For instance, if $\beta^* < 0$, a negative sign is inserted to make it positive.

We define the following dimensionless variables:

$$X = x\left(\frac{g\beta^*\Delta c_0}{\nu^2}\right)^{1/3}, \; R = r\left(\frac{g\beta^*\Delta c_0}{\nu^2}\right)^{1/3}, \; \tau^* = \frac{\tau}{\nu^{1/3}}(g\beta^*\Delta c_0)^{2/3},$$

$$U = \frac{u}{(\nu g\beta^*\Delta c_0)^{1/3}}, \; V = \frac{v}{(\nu g\beta^*\Delta c_0)^{1/3}}, \; C = \frac{c - c_{\infty,x}}{c_0 - c_{\infty,0}}. \tag{5}$$

In the above definitions, $\Delta c_0 = (c_0 - c_{\infty,0})$. In stratified media, the concentration in the ambient varies with x, with $c_{\infty,0}$ as the ambient concentration at $x = 0$. For a constant density medium, $c_{\infty,x} = c_{\infty,0} = c_\infty$.

The nondimensional conservation equations then are obtained as

$$\frac{\partial U}{\partial X} + \frac{\partial V}{\partial R} + \frac{V}{R} = 0, \tag{6}$$

$$\frac{\partial U}{\partial \tau^*} + U\frac{\partial U}{\partial X} + V\frac{\partial U}{\partial R} = \frac{1}{R}\frac{\partial U}{\partial R} + \frac{\partial^2 U}{\partial R^2} + C, \tag{7}$$

$$\frac{\partial C}{\partial \tau^*} + U\frac{\partial C}{\partial X} + V\frac{\partial C}{\partial R} + S^* U = \frac{1}{\mathrm{Sc}}\left(\frac{1}{R}\frac{\partial C}{\partial R} + \frac{\partial^2 C}{\partial R^2}\right), \tag{8}$$

where

$$S^* = \frac{1}{\Delta c_0}\frac{\mathrm{d}c_{\infty,x}}{\mathrm{d}X}$$

is defined as the concentration stratification parameter. For a constant density medium, $S^* = 0$, and for linear density distribution, which is of practical occurrence and which we consider, S^* is constant.

We prescribe the following nondimensional boundary and initial conditions:

$$\tau^* > 0$$

$$X > 0$$

$$R = 0, \frac{\partial U}{\partial R} = 0; \frac{\partial C}{\partial R} = 0; V = 0,$$

$$R \to \infty, U = 0; C = 0,$$

$$
\begin{aligned}
&\quad X = 0,\\
&\quad R = 0,\ C = 1.0,\\
&\quad R > 0,\ U = 0;\ C = 0.\\
&\tau^* = 0\\
&\quad U = 0,\ V = 0;\ C = 0 \text{ for all } X \text{ and } R.
\end{aligned}
\tag{9}
$$

The centerline quantities of U and C have to be obtained as a part of the solution. $R = 0$ corresponds to the centerline position and for this, some of the terms in the governing equations (6–8) become indeterminate. We obtain separate equations for the centerline by making use of L' Hospital's rule and the boundary conditions. The nondimensional centerline equations can be written as

$$\frac{\partial U}{\partial \tau^*} + U\frac{\partial U}{\partial X} = 2\left.\frac{\partial^2 U}{\partial R^2}\right|_{R=0} + C, \tag{7(a)}$$

$$\frac{\partial C}{\partial \tau^*} + U\frac{\partial C}{\partial X} + S^*U = \frac{1}{\mathrm{Sc}}\left(2\frac{\partial^2 C}{\partial R^2}\right)_{R=0}. \tag{8(a)}$$

Yang et al. [10] have shown that it is not possible to obtain similarity solutions for buoyancy induced flows in stably stratified media. Even for flows in constant density media, similarity solutions exist only if we make assumptions regarding the axial variation of the centerline quantities (temperature, concentration etc.), for instance, power-law and exponential variations (see, Mollendorf and Gebhart [11]). Such assumptions may not be valid for the case of stably stratified media.

Equations (6–8) with the initial and boundary conditions (9) are solved using one time-step forward explicit numerical scheme. The numerical procedures employed are essentially the same as those described by Angirasa and Sarma [2], and Himasekhar and Jaluria [7]. In the latter work results for thermal plumes in unstratified media are compared with similarity solutions, and the agreement was found to be good. Details of the numerical procedure and its stability analyses are presented by Roache [12]. Upwind-differencing was employed for convective terms, and central-differencing for diffusive terms. We observe that the cell Reynolds number, Re_c, define as $|U\Delta X/(1/\mathrm{Sc})|$, is higher than 2. Hence, upwind-differencing is required for stability (see Roache [12]).

An explicit scheme has restrictions on the time step due to stability considerations, as discussed by Roache [12]. We varied the grid size from 10 × 10 to 50 × 50. For a grid size finer than 30 × 30, the error due to grid-spacing was less than 1%. The grid-size chosen for the presentation of results was 40 × 40. The convergence criterion employed is of the form $|\theta_{ij}^{n+1} - \theta_{ij}^{n}|_{\max} \leqslant \varepsilon$, where n refers to time level, and i and j to space. The value of ε was chosen to be 10^{-4}. An arbitrary initial velocity field was chosen to start the solution. We varied it to check that it had no influence on the converged solution.

3. Results and discussion

Results are presented for various values of Schmidt number in an unstratified medium, and for Sc = 1 with different levels of ambient concentration stratification. In Table 1, we present data related to various fluids.

In Fig. 2 vertical velocity profiles for a constant density medium are shown (refer to Figs 1a and b). With increasing values of Schmidt number, we observe that velocity at the core increases while away from the core, it decreases. At a higher value of Sc, species diffusion takes place at a slower rate. Hence, there is higher buoyancy and consequent higher velocity at the core. For a fluid with lower Sc, buoyancy at the core decreases because of the higher rate of the species diffusion, and hence velocity levels fall. Away from the core, the higher diffusion rates induce more buoyancy and hence increase the velocities. As the plume moves downstream, it entrains the fluid from the ambient. The horizontal velocity components at a particular axial location indicate the fluid entrainment at that level. In Fig. 3, we observe that horizontal velocities are higher at the core with increasing values of Sc. This is due to higher acceleration of the fluid in the core for larger values of Sc. For very low values of Sc (for instance, 0.2), the horizontal velocities away from the core are also relatively low. This may be attributed to departure from boundary layer flow due to very low rate of momentum diffusion.

Concentration excess ratio profiles at $X = 100$ and for the same range of Sc are

Table 1. Schmidt number and buoyancy parameter for various species at low concentration in air and in water at approximately 25°C and one atmosphere. (Taken from reference [6])

	Sc ν/D	$\rho\beta^*$ $\left(\frac{\partial\rho}{\partial c}\right)_{t,p}$	$D \times 10^5$ cm^2/s
In air			
Ammonia	0.78	−1.07	
Carbon dioxide	0.94	+0.34	
Hydrogen	0.22	−13.4	
Oxygen	0.75	+0.094	
Water	0.6	−0.61	
Benzene	1.76	+0.63	
Ether	1.66	+0.61	
Methanol	0.97	+0.095	
Ethyl alcohol	1.30	+0.37	
In water			
Ammonia	445	+0.5	2.0
Carbon dioxide	453		1.96
Nitrogen	468		1.9
Sulphur dioxide	523		1.7
Methanol	556	+0.17	1.6

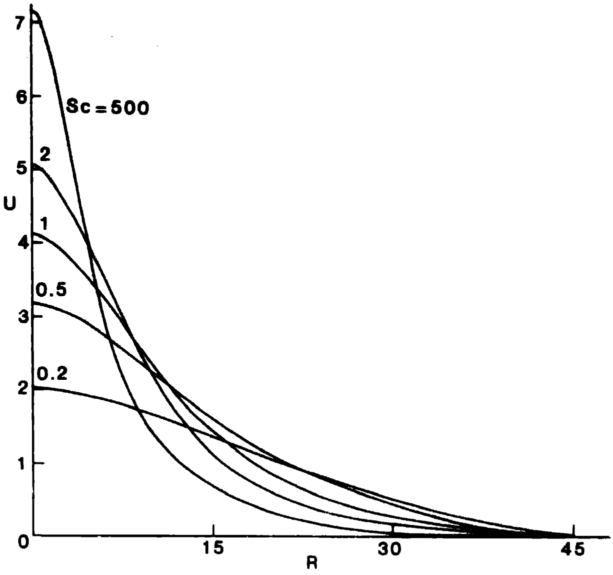

Fig. 2. Vertical velocity profiles at $X = 100$, for various values of the Schmidt number, Sc, and $S^* = 0$.

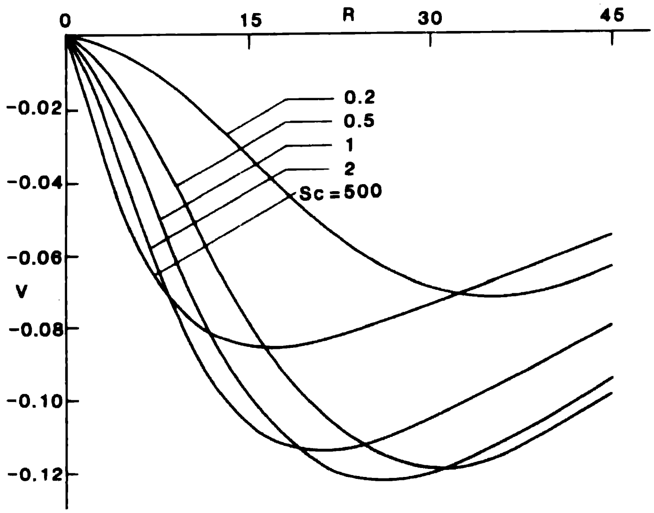

Fig. 3. Horizontal velocity profiles at $X = 100$, for various values of the Schmidt number, Sc, and $S^* = 0$.

presented in Fig. 4. The trends are similar to those obtained by Angirasa and Sarma [2] for multi-component plumes. For Sc = 0.2, the boundary layer thickness is relatively large, and the flow has shown a tendency to depart from boundary layer.

In the study of free boundary flows, the axial variation of centerline physical quantities is of particular interest, since these indicate the distance to which the flow will rise or sink. In Fig. 5, we present the axial variation of centerline velocity in a constant density medium. For all the values of Sc considered, there is a sharp acceleration in the centerline velocity near the origin of the plume. For fluids with higher values of Sc, the flow continues to accelerate at the core for larger distances. The low radial dispersion of the species at higher Sc is responsible for maintaining larger buoyancy at the core over a long distance. As the value of Sc is lowered, the

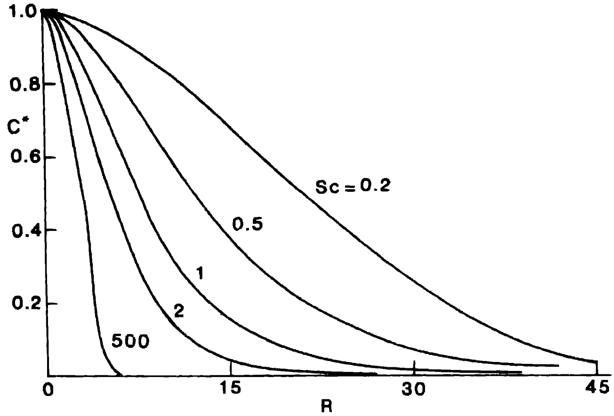

Fig. 4. Concentration profiles at $X = 100$ for various values of the Schmidt number, Sc, and $S^* = 0$.

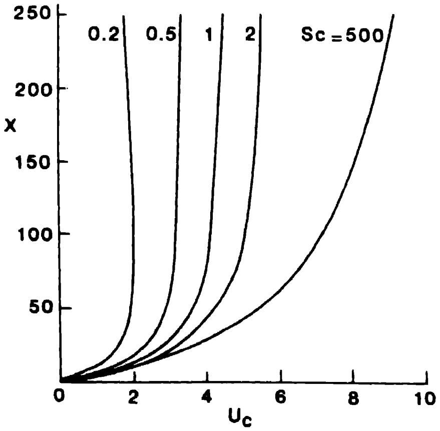

Fig. 5. Centerline variation of velocity for various values of the Schmidt number, Sc, and $S^* = 0$.

centerline velocity, after initial acceleration, reaches a constant value. At this stage, the buoyant and diffusion mechanisms are in balance. For Sc = 0.2, we observe that the centerline velocity has begun to decelerate at a relatively shorter distance. The large diffusion rate drains the species, and hence the buoyancy from the core. The centerline variation of concentration (Fig. 6) further explains these concepts. For Sc = 500, there is high level of centerline species concentration over long distances, and for Sc = 0.2, it nearly reaches zero over a shorter distance. Thus Figs 2–6 are inter-related and together they explain the intricate interaction among the buoyancy, the diffusion rates, the concentration levels, and the plume spread.

We have so far considered plumes in a constant density environment. In buoyancy-induced flows the ambient medium can be often density-stratified. We are concerned with stable stratification, in which the density decreases with height in gravity field. Thermal plumes in a thermally stratified medium were considered by Himasekhar and Jaluria [7], and Wirtz and Chiu [8]. A numerical study of plumes due to combined buoyancies of heat and mass diffusion in a thermally stratified environment was presented by Srinivasan and Angirasa [4]. Various types of density-stratification are discussed in detail by Ostrach [9]. The physical configuration corresponding to the present discussion is given in Figs 1(c) and (d).

Figure 7 presents the velocity profiles at $X = 100$ for Sc = 1, and for different levels of ambient concentration stratification indicated by the value of S^*. Increasing values of S^* decrease the local buoyancy level and hence the velocities fall. We have not observed significant changes in the boundary layer thickness for the range of S^* considered. In Fig. 8, we observe that for all values of S^*, there is a sharp acceleration in centerline velocity near the origin. As the flow proceeds downstream, i.e., with increasing x, the net concentration difference $(c_{c,x} - c_{\infty,x})$ that contributes to the driving buoyant force, decreases. This results in the deceleration of U_c with X. Here we

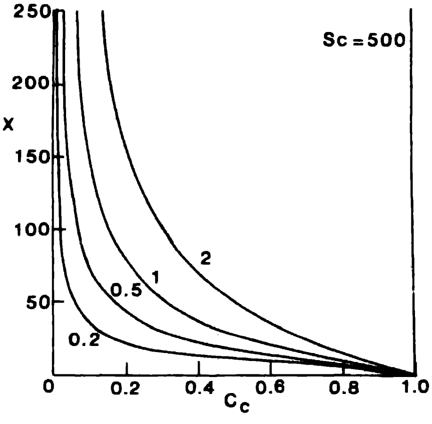

Fig. 6. Centerline variation of concentration excess ratio of the diffusing species for various values of the Schmidt number, Sc, and $S^* = 0$.

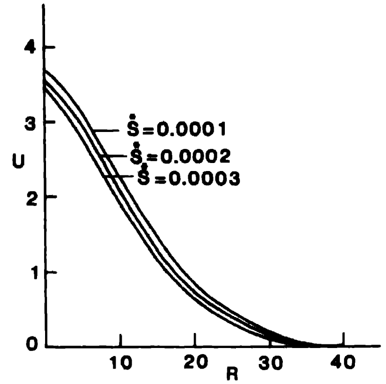

Fig. 7. Velocity profiles at $X = 100$, for various values of the concentration stratification parameter, S^*, and Sc = 1.

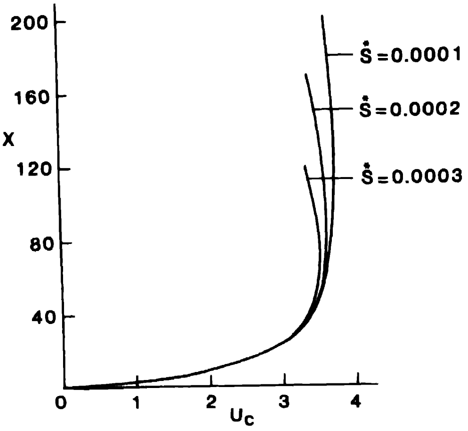

Fig. 8. Centerline variation of velocity for various values of the concentration stratification parameter, S^*, and Sc = 1.

draw attention to the values of the stratification parameter, S^*. For higher values of S^*, the plume levels off at shorter height/depth, X. In contrast to the modeling of Himasekhar and Jaluria [7], boundary layer analysis is not valid in these regions of flow, since the flow decelerates sharply over a short distance.

In Figs 9 and 10, the corresponding concentration profiles and centerline variation of concentration are shown for Sc = 1. With increasing value of S^*, local concentration difference, $\Delta C(=c_c - c_{\infty,x})$ decreases. The fall in concentration levels is physically anticipated. For $S^* = 0.0003$, we observe negative values of concentration in the "wing" of the profile (Fig. 9). At higher ambient stratification level, the concentration in the boundary layer can lag behind the ambient concentration, hence

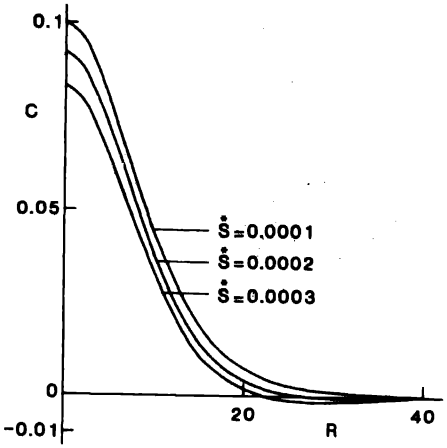

Fig. 9. Concentration excess ratio profiles at $X = 100$ for various values of the concentration stratification parameter, S^*, and Sc = 1.

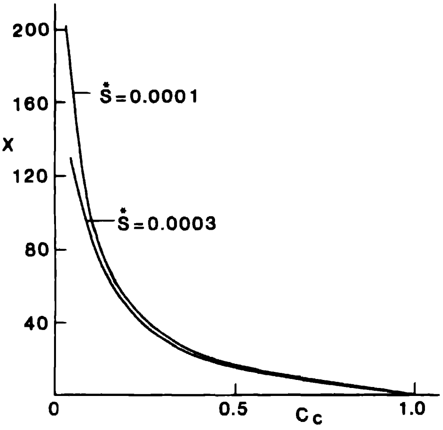

Fig. 10. Centerline variation of concentration excess ratio with concentration stratification parameter, S^*, and Sc = 1.

the negative values. Centerline variation of concentration (Fig. 10) clearly demonstrates that with increasing S^*, the plume travels to a shorter distance before the flow reverses, or levels off.

4. Concluding remarks

In the present numerical study, we considered boundary layer analysis of laminar axisymmetric plumes due to mass diffusion. At high levels of concentration stratifica-

tion in the ambient, and also at low values of Sc, boundary layer flows are not possible. In the former case there are regions of flow reversal and spreading for which the full Navier-Stokes equations have to be solved.

References

1. Jaluria, Y., *Natural Convection Heat and Mass Transfer*. Oxford: Pergamon (1980).
2. Angirasa, D. and Sarma, P. K., A numerical study of laminar axisymmetric plumes due to the combined buoyancy of heat and mass diffusion. *Applied Scientific Research* 45 (1988) 339–352.
3. Angirasa, D. and Srinivasan, J., Axisymmetric free boundary layer flows due to combined thermal and concentration buoyancy in isothermal and stratified media. In: *Proc. 9th National Heat and Mass Transfer Conference, Bangalore, India*, Dec. 1987.
4. Srinivasan, J. and Angirasa, D., Laminar axisymmetric multicomponent buoyant plumes in a thermally stratified medium. *International Journal of Heat and Mass Transfer* 33 (1990) 1751–1757.
5. Fujii, T., Theory of steady laminar convection above a horizontal line source and a point heat source. *International Journal of Heat and Mass Transfer* 6 (1963) 597–606.
6. Gebhart, B. and Pera, L., The nature of vertical natural convection flows resulting from the combined buoyancy effects of thermal and mass diffusion. *International Journal of Heat and Mass Transfer* 14 (1971) 2025–2050.
7. Himasekhar, K. and Jaluria, Y., Laminar buoyancy-induced axisymmetric free boundary flows in a thermally stratified medium. *International Journal of Heat and Mass Transfer* 25 (1982) 213–221.
8. Wirtz, R. H. and Chiu, C. M., Laminar thermal plume rise in a thermally stratified environment. *International Journal of Heat and Mass Transfer* 17 (1974) 323–329.
9. Ostrach, S., Natural convection with combined driving forces. *Physico Chemical Hydrodynamics* 1 (1980) 233–247.
10. Yang, K. T., Novotny, J. L. and Cheng, Y. S., Laminar free convection from a nonisothermal plate immersed in a temperature stratified medium. *International Journal of Heat and Mass Transfer* 15 (1972) 1097–1109.
11. Mollendorf, J. C. and Gebhart, B., Axisymmetric natural convection flows resulting from the combined buoyancy effects of thermal and mass diffusion. In: *Proc. 5th Int. Heat Transfer Conference*, Vol. V, 10–14 (1974).
12. Roache, P. J., *Computational Fluid Dynamics*. Albuquerqe, N.M.: Hermosa (1976).

Applied Scientific Research **49**: 147–159, 1992.
© 1992 *Kluwer Academic Publishers. Printed in the Netherlands.*

Unsteady flow in an annulus between two concentric rotating spheres

S. D. GULWADI & A. F. ELKOUH
Dept. of Mechanical and Industrial Engineering, Marquette University, Milwaukee, WI 53233, USA

Received 18 January 1990; accepted in revised form 18 October 1990

Abstract. An analysis is presented for the unsteady laminar flow of an incompressible Newtonian fluid in an annulus between two concentric spheres rotating about a common axis of symmetry. A solution of the Navier-Stokes equations is obtained by employing an iterative technique. The solution is valid for small values of Reynolds numbers and acceleration parameters of the spheres. In applying the results of this analysis to a rotationally accelerating sphere, a virtual moment of inertia is introduced to account for the local inertia of the fluid.

Nomenclature

R_i = radius of the inner sphere
R_o = radius of the outer sphere
$\bar{r}$ = radial coordinate
r = dimensionless radial coordinate, $\bar{r}/R_i$
θ = meridional coordinate
ϕ = azimuthal coordinate
$\bar{t}$ = time
t = dimensionless time, $\bar{t}\nu/R_i^2$
Re_i = instantaneous Reynolds number of the inner sphere, $\omega_i R_i^2/\nu$
Re_o = instantaneous Reynolds number of the outer sphere, $\omega_o R_o^2/\nu$
$\bar{V}_r$ = radial velocity component
V_r = dimensionless radial velocity component, $\bar{V}_r R_i/\nu$
$\bar{V}_\theta$ = meridional velocity component
V_θ = dimensionless meridional velocity component, $\bar{V}_\theta R_i/\nu$
$\bar{V}_\phi$ = azimuthal velocity component
V_ϕ = dimensionless azimuthal velocity component, $\bar{V}_\phi R_i/\nu$
$\bar{T}$ = viscous torque
T = dimensionless viscous torque, $3\bar{T}/8\pi\mu\nu R_i$
$\bar{T}_i$ = viscous torque at surface of inner sphere
T_i = dimensionless viscous torque at surface of inner sphere, $3\bar{T}_i/8\pi\mu\nu R_i$
$\bar{T}_o$ = viscous torque at surface of outer sphere
T_o = dimensionless viscous torque at surface of outer sphere, $3\bar{T}_o/8\pi\mu\nu R_i$
$\bar{T}_{p,i}$ = externally applied torque on inner sphere
$T_{p,i}$ = dimensionless applied torque on inner sphere, $3\bar{T}_{p,i}/8\pi\mu\nu R_i$
$\bar{Z}_i$ = moment of inertia of inner sphere
Z_i = dimensionless moment of inertia of inner sphere, $3\bar{Z}_i/8\pi\rho R_i^5$
$\bar{Z}_{i,v}$ = virtual moment of inertia of inner sphere
$Z_{i,v}$ = dimensionless virtual moment of inertia of inner sphere, $3\bar{Z}_{i,v}/8\pi\rho R_i^5$
$\bar{Z}_{o,v}$ = virtual moment of inertia of outer sphere
ω_i = instantaneous angular velocity of the inner sphere
ω_o = instantaneous angular velocity of the outer sphere
ρ = density of fluid
μ = viscosity of fluid
ν = kinematic viscosity of fluid, μ/ρ
λ = radius ratio, R_i/R_o
$\bar{\Omega}$ = swirl function, $\bar{V}_\phi \bar{r}\sin\theta$
Ω = dimensionless swirl function, $\bar{\Omega}/\nu$
$\bar{\psi}$ = stream function
ψ = dimensionless stream function, $\bar{\psi}/R_i\nu$
γ_i = acceleration parameter for the inner sphere, $(R_i^4/\nu^2)\mathrm{d}\omega_i/\mathrm{d}\bar{t} = \mathrm{d}/\mathrm{d}t(\mathrm{Re}_i)$
γ_o = acceleration parameter for the outer sphere, $(R_o^4/\nu^2)\mathrm{d}\omega_o/\mathrm{d}\bar{t}$
$\bar{\tau}_{r\phi}$ = shear stress
$\tau_{r\phi}$ = dimensionless shear stress, $\bar{\tau}_{r\phi} R_i^2/\mu\nu$

Introduction

Fluid motion about a rotating sphere or in the annulus between two concentric rotating spheres has received considerable attention due to its practical significance in many areas of engineering and applied science, e.g. meteorology, geophysics and rheology. Due to the large number of studies published, only those relevant to this study are mentioned.

Solutions for steady laminar flow of a Newtonian fluid have been obtained by Haberman [1], Kendall [2], and Munson and Joseph [3]. Haberman [1] studied the secondary flow between two co-axial rotating spheres. Kendall [2] obtained a first correction to the viscous torque by employing a regular perturbation technique; while Munson and Joseph [3] used both perturbation, and a Galerkin type procedure to extend the solution to higher Reynolds numbers. Numerical solution for steady flow in an annulus between rotating spheres has recently been obtained by Schwengels, Schultz, and Shay [4].

Closed-form solutions for flow produced by torsional oscillations of spherical boundaries were obtained by Kanwal [5], Carrier and DiPrima [6], and Munson and Douglass [7]. Kanwal [5], and Carrier and DiPrima [6] considered the flow about a sphere performing small sinusoidal displacements in an infinite medium; while Munson and Douglass [7] dealt primarily with the secondary flow generated when both spherical surfaces oscillated with the same amplitude and frequency. Numerical studies of time-dependent laminar flow of a Newtonian fluid between rotating spheres were performed by Pearson [8], Krause and Bartels [9], and more recently by Yang et. al. [10].

In this study, a solution of the unsteady Navier-Stokes equations is obtained by employing an iterative technique. Expressions valid for all values of λ and containing both local and convective inertia corrections are obtained for the velocity and viscous torque. These expressions are suitable for arbitrary rotation of the spheres, and are valid for small values of Reynolds numbers and acceleration parameters of the spheres. The upper limits for the Reynolds numbers for which these expressions are valid are considered to be below their critical values, above which the flow becomes unstable with formations of Taylor vortices in the region near the equator [11].

In applying the results of this analysis to a rotationally accelerating sphere, a virtual moment of inertia is introduced to account for the local inertia of the fluid. To test the validity of the solution, the motion of a sphere accelerating by a constant torque is compared with the motion obtained numerically by the simultaneous solution of the unsteady Navier-Stokes equations and the equation of motion of the sphere.

Basic equations and their solutions

The unsteady motion of an incompressible Newtonian fluid in the annulus between two concentric rigid spheres is considered (Fig. 1). The inner sphere of radius R_i and

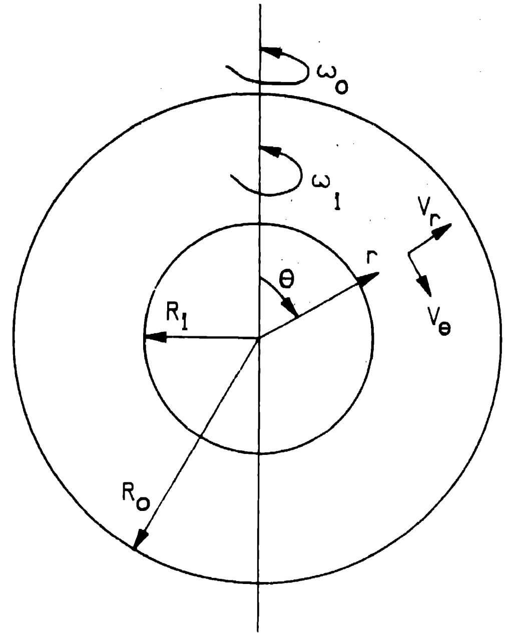

Fig. 1. Notation for flow in spherical annulus.

the outer sphere R_o rotate about a common axis with time-dependent angular velocities ω_i and ω_o, respectively. The dimensionless equation of continuity is satisfied by defining a dimensionless stream function ψ, such that

$$V_r = \frac{1}{r^2 \sin\theta}\frac{\partial\psi}{\partial\theta}, \quad \text{and} \quad V_\theta = -\frac{1}{r\sin\theta}\frac{\partial\psi}{\partial r}. \tag{1}$$

Using the definition of ψ given in equation (1), and introducing the swirl function Ω such that $V_\phi = \Omega/r\sin\theta$, the dimensionless Navier-Stokes equations are

$$\begin{aligned}\frac{\partial(D^2\psi)}{\partial t} &+ \frac{2\Omega}{r^2\sin^2\theta}\left(\frac{\partial\Omega}{\partial r}\cos\theta - \frac{1}{r}\frac{\partial\Omega}{\partial\theta}\sin\theta\right)\\ &- \frac{1}{r^2\sin\theta}\frac{\partial(\psi, D^2\psi)}{\partial(r,\theta)} + \frac{2D^2\psi}{r^2\sin^2\theta}\left(\frac{\partial\psi}{\partial r}\cos\theta - \frac{1}{r}\frac{\partial\psi}{\partial\theta}\sin\theta\right) = D^4\psi,\end{aligned} \tag{2}$$

and

$$\frac{\partial\Omega}{\partial t} - \frac{1}{r^2\sin\theta}\left(\frac{\partial\psi}{\partial r}\frac{\partial\Omega}{\partial\theta} - \frac{\partial\psi}{\partial\theta}\frac{\partial\Omega}{\partial r}\right) = D^2\Omega, \tag{3}$$

where:

$$D^2 \equiv \left(\frac{\partial^2}{\partial r^2} + \frac{1}{r^2}\frac{\partial^2}{\partial \theta^2} - \frac{\cot\theta}{r^2}\frac{\partial}{\partial \theta}\right), \quad \text{and} \quad D^4 \equiv D^2(D^2).$$

The boundary conditions on ψ and Ω are:

$$\Omega(1, \theta, t) = \mathrm{Re}_i \sin^2\theta \tag{4a}$$

$$\Omega(1/\lambda, \theta, t) = \mathrm{Re}_o \sin^2\theta \tag{4b}$$

$$\psi(1, \theta, t) = \psi(1/\lambda, \theta, t) = 0 \tag{4c}$$

$$\frac{\partial \psi}{\partial r}(1, \theta, t) = \frac{\partial \psi}{\partial r}(1/\lambda, \theta, t) = 0 \tag{4d}$$

The creeping-flow solution for the swirl function is obtained by neglecting all acceleration terms on the left-hand-side of equation (3), integrating, and using the boundary conditions on Ω from equations (4a) and (4b). The solution thus obtained is given by

$$\Omega = f_1^0(r, t)\sin^2\theta, \tag{5}$$

where $f_1^0(r, t)$ can be obtained from [1]. The solution for Ω given by equation (5) represents the quasi-steady shearing motion, which sets up a centrifugal force field that drives the secondary flow in the annulus.

A first approximation of the dimensionless stream function for the secondary flow is obtained by neglecting all the inertia terms on the left-hand-side of equation (2) with the exception of those containing Ω, which constitute the centripetal acceleration. Substituting for Ω from equation (5) into the remaining inertia terms, integrating, and using the boundary conditions on ψ and it's derivative from equations (4c) and (4d), the expression for the first approximation of the stream function is

$$\psi = \left[Ar^2 + \frac{B}{r} + C + \frac{D}{r^2} + Er^3 + Fr^5\right]\sin^2\theta\cos\theta, \tag{6}$$

where the coefficients A, B, C, D, E, and F are dependent on λ, Re_i^2, $\mathrm{Re}_i\mathrm{Re}_o$, and Re_o^2. Expressions for these coefficients are available in [1].

The corrected expression for the swirl function is obtained by substituting for Ω and ψ from equations (5) and (6) into the left-hand-side of equation (3), integrating, and using the boundary conditions on Ω given in equations (4a) and (4b). The corrected expression for Ω, which includes both local and convective inertia contributions, is given by

$$\Omega = [f_1^0(r, t)\sin^2\theta] + [f_1^t(r, t)\sin^2\theta] + [f_1^c(r, t)\sin^2\theta + f_2(r, t)\sin^2\theta\cos^2\theta]. \tag{7}$$

The first term on the right-hand side of equation (7) is the inertialess solution given by equation (5), the second term is the local inertia correction, while the third term is the convective inertia correction.

The local inertia correction function, $f_1^t(r, t)$, is given by

$$f_1^t(r, t) = \frac{\alpha_{11}^t}{r} + \alpha_{12}^t r^2 + \alpha_6^t r + \alpha_8^t r^4, \tag{8}$$

where:

$$\alpha_6^t = \left[\frac{-1}{2(1-\lambda^3)}\right]\gamma_i + \left[\frac{\lambda^4}{2(1-\lambda^3)}\right]\gamma_o,$$

$$\alpha_8^t = \left[\frac{-\lambda^3}{10(1-\lambda^3)}\right]\gamma_i + \left[\frac{\lambda^4}{10(1-\lambda^3)}\right]\gamma_o,$$

$$\alpha_{11}^t = \left[\frac{(5-6\lambda+\lambda^3)}{10(1-\lambda^3)^2}\right]\gamma_i + \left[\frac{(5\lambda^5-6\lambda^4+\lambda^2)}{10(1-\lambda^3)^2}\right]\gamma_o,$$

and

$$\alpha_{12}^t = \left[\frac{(6\lambda-5\lambda^3-\lambda^6)}{10(1-\lambda^3)^2}\right]\gamma_i + \left[\frac{(6\lambda^7-5\lambda^5-\lambda^2)}{10(1-\lambda^3)^2}\right]\gamma_o.$$

The dimensionless quantities γ_i and γ_o are the acceleration parameters for the inner and outer spheres, respectively, and are given by

$$\gamma_i = \left(\frac{R_i^4}{\nu^2}\right)\frac{\mathrm{d}\omega_i}{\mathrm{d}\bar{t}}, \quad \text{and} \quad \gamma_o = \left(\frac{R_o^4}{\nu^2}\right)\frac{\mathrm{d}\omega_o}{\mathrm{d}\bar{t}}.$$

The correction functions $f_1^c(r, t)$ and $f_2(r, t)$ are given by

$$f_1^c(r, t) = \frac{\alpha_{11}^c}{r} + \alpha_{12}^c r^2 + \frac{\alpha_1^c}{r^4} + \frac{\alpha_2^c}{r^3} + \alpha_5^c + \alpha_6^c r + \alpha_7^c r^3 + \alpha_8^c r^4 + \alpha_9^c r^6 + \alpha_{10}^c \frac{\ln(r)}{r^3}, \tag{9}$$

and

$$f_2(r, t) = Hr^4 + \frac{I}{r^3} + \frac{J}{r^4} + K\frac{\ln(r)}{r^3} + \frac{L}{r^2} + \frac{M}{r} + N + Qr + Sr^3 + Pr^6. \tag{10}$$

The coefficients α_1^c, α_2^c, α_5^c, α_6^c, α_7^c, α_8^c, α_9^c, α_{10}^c, α_{11}^c, α_{12}^c, H, I, J, K, L, M, N, P, Q, and S are dependent on λ, Re_i^3, $\mathrm{Re}_i\mathrm{Re}_o^2$, $\mathrm{Re}_i^2\mathrm{Re}_o$, and Re_o^3. Expressions for these coefficients can be obtained from [2].

Results and discussions

Due to symmetry about the axis of rotation, the component $\tau_{r\phi}$ of the stress tensor is given by

$$\tau_{r\phi} = -r\frac{\partial}{\partial r}\left(\frac{V_\phi}{r}\right), \tag{11}$$

where:

$$V_\phi = \Omega/(r\sin\theta).$$

Using equations (7), (8), (9) and (10), the expression for the dimensionless shear stress, $\tau_{r\phi}$, can be obtained. The dimensionless viscous torque at any radius r is given by

$$T = \frac{\bar{T}}{(8\pi/3\mu\nu R_i)} = \frac{3}{2}r^3\int_0^{\pi/2}\tau_{r\phi}\sin^2\theta\,\mathrm{d}\theta. \tag{12}$$

Using the expressions for $\tau_{r\phi}$ at the inner and outer radii, the expressions for the dimensionless viscous torque can be written as

$$T_i = T_i^0 + T_i^c + T_i^t, \tag{13}$$

and

$$T_o = T_o^0 + T_o^c + T_o^t, \tag{14}$$

where (T_i^0, T_o^0) are the creeping-flow viscous torques; while (T_i^c, T_o^c) and (T_i^t, T_o^t) are the convective and local inertia corrections, respectively.

The creeping-flow viscous torques at the inner and outer radii are given by

$$T_i^0 = T_o^0 = \frac{3(\mathrm{Re}_i - \lambda^2\mathrm{Re}_o)}{(1-\lambda^3)}. \tag{15}$$

The convective inertia corrections for the viscous torques at the inner and outer radii are

$$T_i^c = T_o^c = (\mathrm{Re}_i^3)(V_a) + (\mathrm{Re}_o^3)(V_b) + (\mathrm{Re}_i\,\mathrm{Re}_o^2)(V_c) + (\mathrm{Re}_i^2\,\mathrm{Re}_o)(V_d), \tag{16}$$

where:

$$V_a = \frac{1}{\Delta_1}[-1+140\lambda^3-675\lambda^4+1143\lambda^5-55\lambda^6-2475\lambda^7+2970\lambda^8+550\lambda^9$$

$$-4158\lambda^{10}+3510\lambda^{11}-275\lambda^{12}-1485\lambda^{13}+1125\lambda^{14}-359\lambda^{15}+45\lambda^{16}],$$

$$V_b = \frac{1}{\Delta_1}[45\lambda^5-359\lambda^6+1125\lambda^7-1485\lambda^8-275\lambda^9+3510\lambda^{10}-4158\lambda^{11}+550\lambda^{12}$$

$$+2970\lambda^{13}-2475^{14}-55\lambda^{15}+1143\lambda^{16}-675\lambda^{17}+140\lambda^{18}-\lambda^{21}],$$

$$V_c = \frac{1}{\Delta_1}[-45\lambda^3+397\lambda^4-1350\lambda^5+1755\lambda^6+1480\lambda^7-8235\lambda^8+10494\lambda^9$$

$$-1925\lambda^{10}-8910\lambda^{11}+8415\lambda^{12}+1430\lambda^{13}-7479\lambda^{14}+5400\lambda^{15}$$

$$-1345\lambda^{16}-270\lambda^{17}+225\lambda^{18}-37\lambda^{19}],$$

$$V_d = \frac{1}{\Delta_1}[-37\lambda^2+225\lambda^3-270\lambda^4-1345\lambda^5+5400\lambda^6-7479\lambda^7+1430\lambda^8$$

$$+8415\lambda^9-8910\lambda^{10}-1925\lambda^{11}+10494\lambda^{12}-8235\lambda^{13}+1480\lambda^{14}$$

$$+1755\lambda^{15}-1350\lambda^{16}+397\lambda^{17}-45\lambda^{18}],$$

and

$$\Delta_1 = 100(1-\lambda^3)^4(-4+25\lambda^3-42\lambda^5+25\lambda^7-4\lambda^{10}).$$

Values of the coefficients V_a, V_b, V_c, and V_d for various values of λ are presented graphically in Fig. 2.

The sum of the creeping-flow viscous torque and the convective inertia correction provides an approximate expression for the viscous torque in steady flow, and in this study it is considered as the quasi-steady viscous torque. Table 1 provides a comparison of the quasi-steady viscous torque with the viscous torque obtained from the numerical solution of the Navier-Stokes equations by Yang et al., [10]. From Table 1, it is shown that the accuracy of the expression for the quasi-steady torque, $(T_i^0 + T_i^c = T_o^0 + T_o^c)$, is improved with increasing values of λ, and that for $\lambda = 0.5$ the expression is reasonably accurate for $\mathrm{Re}_i = 25$ and $\mathrm{Re}_o = 100$, approximately.

The local inertia corrections for the viscous torques at the inner and outer radii are given by

$$T_i^l = (G_{1,i})\gamma_i + (G_{2,i})\gamma_o, \tag{17}$$

and

$$T_o^l = (G_{1,o})\gamma_i + (G_{2,o})\gamma_o, \tag{18}$$

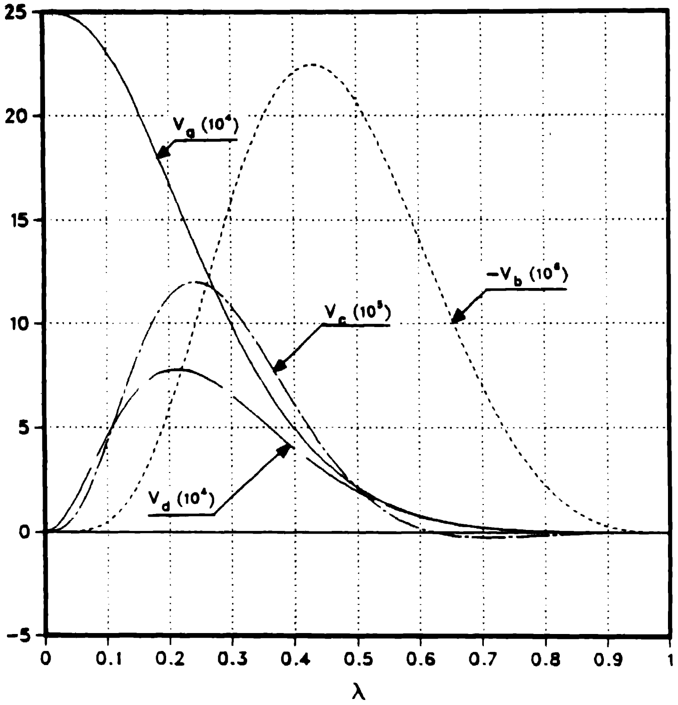

Fig. 2. Convective inertia coefficients.

where:

$$G_{1,i} = \frac{(10 - 18\lambda + 10\lambda^3 - 2\lambda^6)}{10(1 - \lambda^3)^2},$$

$$G_{2,i} = \frac{(3\lambda^2 - 15\lambda^4 + 15\lambda^5 - 3\lambda^7)}{10(1 - \lambda^3)^2},$$

$$G_{1,o} = \frac{(3\lambda^6 - 15\lambda^4 + 15\lambda^3 - 3\lambda)}{10\lambda^3(1 - \lambda^3)^2},$$

and

$$G_{2,o} = \frac{(10\lambda^8 - 18\lambda^7 + 10\lambda^5 - 2\lambda^2)}{10\lambda^3(1 - \lambda^3)^2}.$$

Values of the functions $G_{1,i}$, $G_{2,i}$, $G_{1,o}$, and $G_{2,o}$ for various values of λ are presented graphically in Fig. 3. When one of the spheres only accelerates, the local inertia correction for the resisting torque can be introduced in the equation of motion of the

Table 1. Comparison with steady-flow numerical solution

	Yang [10]		Present study	
Case	$\lvert T_i\rvert$	$\lvert T_o\rvert$	$\lvert T_i^0 + T_i^c\rvert$	$\lvert T_o^0 + T_o^c\rvert$
$\mathrm{Re}_i = 4$, $\mathrm{Re}_o = 0$, $\lambda = 0.2$	12.2	12.2	12.205	12.205
$\mathrm{Re}_i = 0$, $\mathrm{Re}_o = 10$, $\lambda = 0.2$	1.21	1.205	1.216	1.216
$\mathrm{Re}_i = 0$, $\mathrm{Re}_o = 100$, $\lambda = 0.2$	13.45	13.6	17.95	17.95
$\mathrm{Re}_i = 2.5$, $\mathrm{Re}_o = 0$, $\lambda = 0.5$	8.574	8.574	8.575	8.575
$\mathrm{Re}_i = 25$, $\mathrm{Re}_o = 0$, $\lambda = 0.5$	89.26	89.22	89.05	89.05
$\mathrm{Re}_i = 0$, $\mathrm{Re}_o = 10$, $\lambda = 0.5$	8.59	8.59	8.59	8.59
$\mathrm{Re}_i = 0$, $\mathrm{Re}_o = 100$, $\lambda = 0.5$	99.72	99.8	106.38	106.38
$\mathrm{Re}_i = 81$, $\mathrm{Re}_o = 0$, $\lambda = 0.9$	896.90	896.89	896.90	896.90
$\mathrm{Re}_i = 0$, $\mathrm{Re}_o = 10$, $\lambda = 0.9$	89.67	89.66	89.67	89.67
$\mathrm{Re}_i = 0$, $\mathrm{Re}_o = 100$, $\lambda = 0.9$	896.97	896.95	896.97	896.97

sphere as a virtual (or added) inertia. The virtual moment of inertia due to acceleration of the inner sphere, $\bar{Z}_{i,v}$, is

$$\bar{Z}_{i,v} = \left(\frac{8\pi}{3}\rho R_i^5\right)\left(G_{1,i}\right), \tag{19}$$

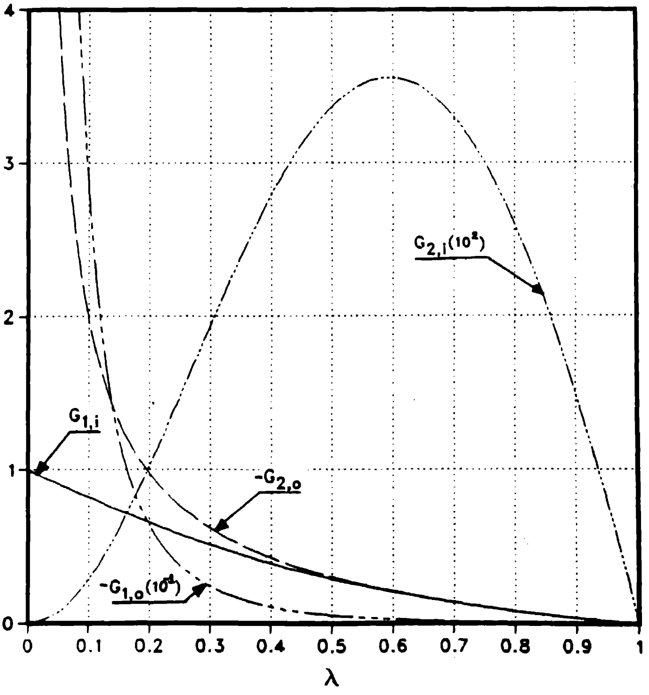

Fig. 3. Local inertia coefficients.

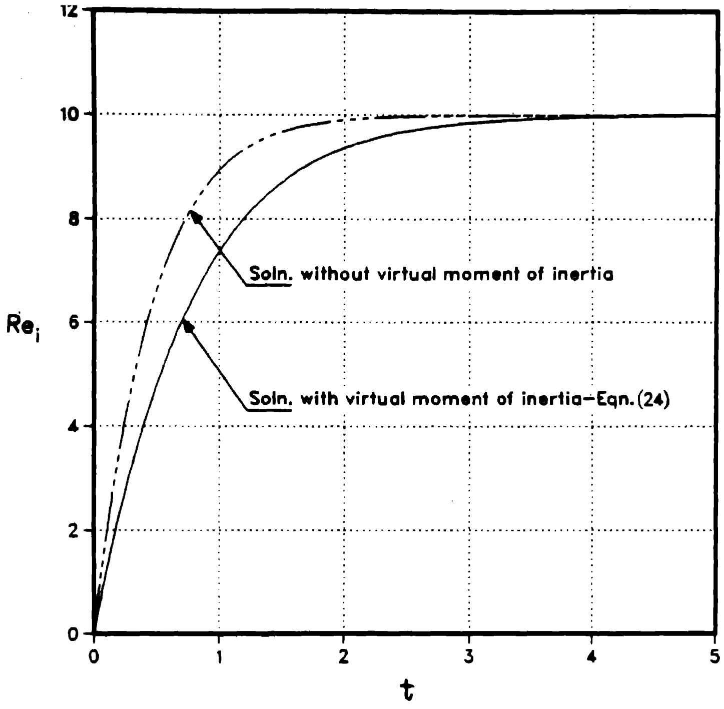

Fig. 4. Motion of an accelerated sphere in an infinite medium when $T_{p,i} = 32.5$, and $Z_i = 1.55284$.

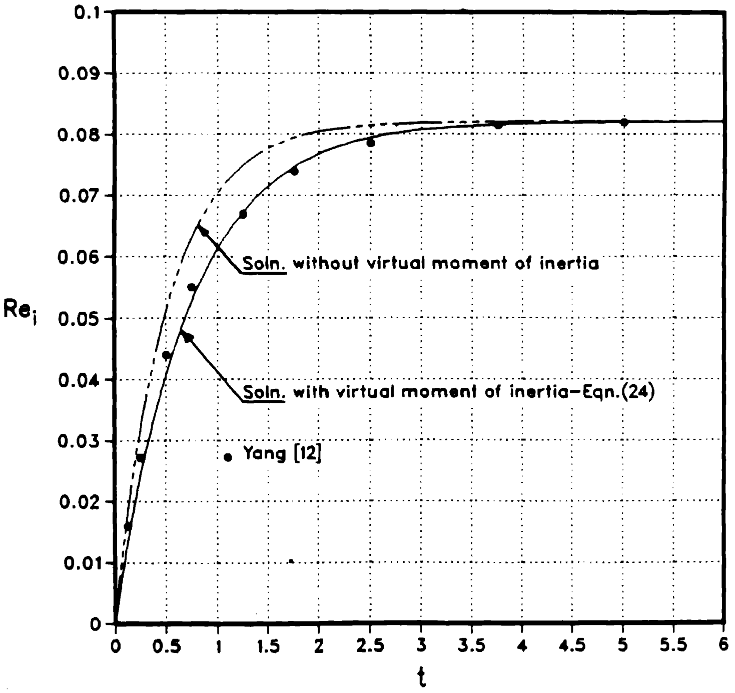

Fig. 5. Motion of an accelerated inner sphere when $T_{p,i} = 0.2485$, $Z_i = 1.55284$, and $\lambda = 0.2$.

while the virtual moment of inertia due to acceleration of the outer sphere, $\bar{Z}_{o,v}$, is

$$\bar{Z}_{0,v} = \left(-\frac{8\pi}{3}\rho R_o^5\right)\left(\lambda G_{2,o}\right). \tag{20}$$

Inspection of the expressions for $(G_{1,i})$ and $(G_{2,o})$ show that $(G_{1,i}) \to 1$ and $(\lambda G_{2,o}) \to -1/5$ as $\lambda \to 0$. Thus, the virtual moment of inertia due to the rotational acceleration of a sphere in an infinite medium stationary at infinity is given by

$$(\bar{Z}_{i,v})_{\lambda\to 0} = \left(\frac{8\pi}{3}\rho R_i^5\right), \tag{21}$$

and that due to the rotational acceleration of a spherical cavity is

$$(\bar{Z}_{o,v})_{\lambda\to 0} = \left(\frac{8\pi}{15}\rho R_o^5\right), \tag{22}$$

which is the rotational moment of inertia of a fluid sphere of radius R_o.

To test the validity of the unsteady torque expression developed herein, we consider the case when the inner sphere accelerates from rest under the influence of a constant applied torque, $\bar{T}_{p,i}$, while the outer sphere is stationary. The dimensionless equation of motion of the sphere is

$$[Z_i + Z_{i,v}]\frac{\mathrm{d}}{\mathrm{d}t}(\mathrm{Re}_i) = T_{p,i} - (T_i^0 + T_i^c). \tag{23}$$

Using equations (15), (16) and (19) the dimensionless equation of motion for the inner sphere is

$$[Z_i + G_{1,i}]\frac{\mathrm{d}}{\mathrm{d}t}(\mathrm{Re}_i) = T_{p,i} - \frac{3}{(1-\lambda^3)}\mathrm{Re}_i - (V_a)\mathrm{Re}_i^3, \tag{24}$$

where $G_{1,i}$ is the dimensionless virtual moment of inertia.

Numerical solutions of equation (24) subject to the initial condition $\mathrm{Re}_i = 0$ are presented in Figs 4, 5, 6 and 7 for $\lambda = 0$, $\lambda = 0.2$, $\lambda = 0.5$, and $\lambda = 0.9$, respectively. Figure 4 represents the motion of a sphere in an infinite medium stationary at infinity for $T_{p,i} = 32.5$ and $Z_i = 1.55284$ (e.g. solid steel sphere in water). The solution obtained by neglecting the virtual inertia term in equation (24) is also shown for comparison. Since the moment of inertia of the sphere and the virtual moment of nertia are of comparable magnitudes for this case, a noticable difference in the nstantaneous Reynolds number is observed. Figures 5, 6 and 7 show that for the same value of Z_i, the relative effect of virtual fluid inertia decreases with increasing λ and

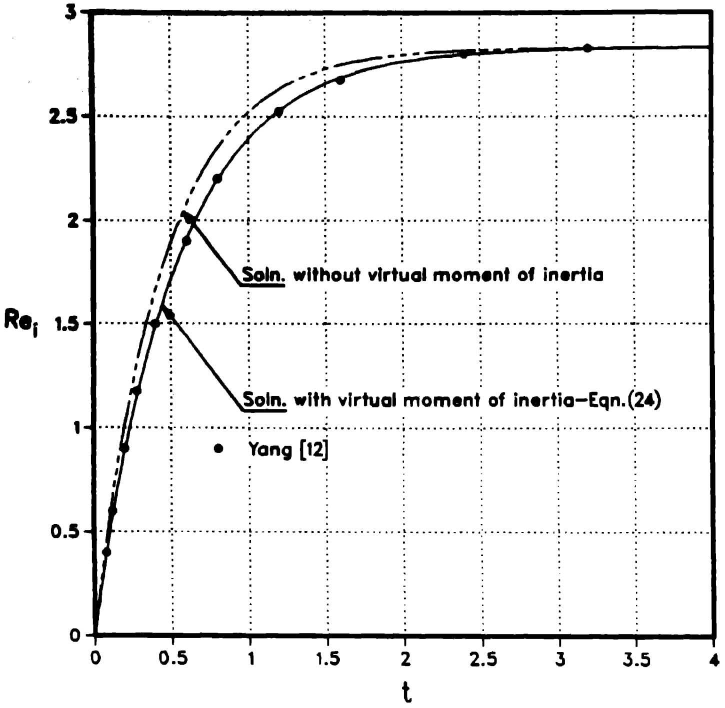

Fig. 6. Motion of an accelerated inner sphere when $T_{p,i} = 9.706$, $Z_i = 1.55284$, and $\lambda = 0.5$.

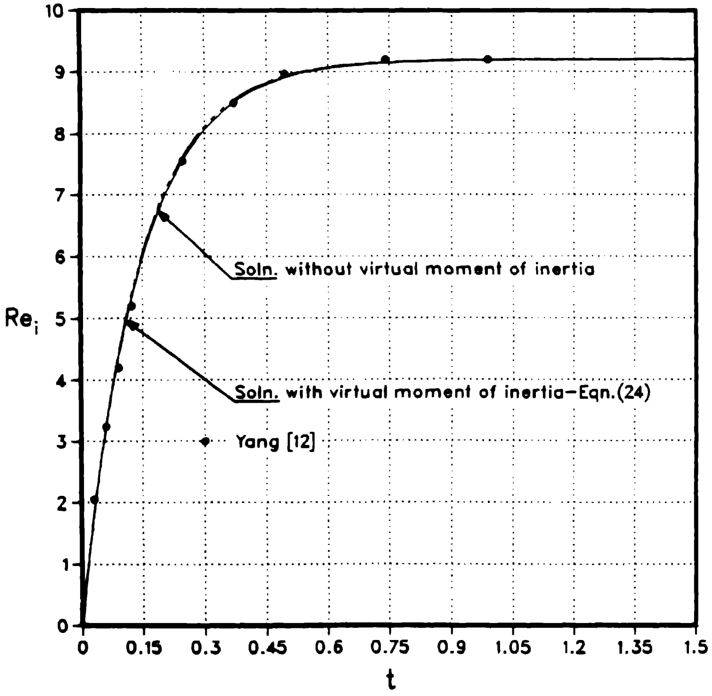

***Fig. 7.* Motion of an accelerated inner sphere for $T_{p,i} = 101.88$, $Z_i = 1.55284$, and $\lambda = 0.9$.**

becomes negligible for values of $\lambda \gtrsim 0.9$. Results obtained numerically by Yang [12], by solving the Navier-Stokes equations simultaneously with the equation of motion of the inner sphere, show excellent agreement with the results from this study (Figs 5, 6 and 7).

References

1. Haberman, W. C., Secondary flow about a sphere rotating in a viscous fluid inside a coaxially rotating spherical container. *Physics of Fluids* 5 (1962) 625–626.
2. Kendall, W. M., Correction to the retarding torque experienced by two rotating concentric spheres. *Physics of Fluids* 19 (1976) 1420–1421.
3. Munson, B. R. and Joseph, D. D., Viscous incompressible flow between concentric rotating spheres. Part 1. Basic Flow. *Journal of Fluid Mechanics* 49 (1971) 289–303.
4. Schwengels, S., Schultz, D. and Shay, W., Second-order finite difference solutions for the flow between rotating concentric spheres. *International Journal For Numerical Methods In Fluids* 9 (1989) 1099–1111.
5. Kanwal, R. P., Rotatory and longitudinal oscillations of axi-symmetric bodies in a viscous fluid. *Quarterly Journal of Mechanics and Applied Mathematics* 8(2) (1955) 146–163.
6. Carrier, G. F. and Di Prima, R. C., On the torsional oscillations of a solid sphere in a viscous fluid. *Journal of Applied Mechanics* 23 (1956) 601–605.
7. Munson, B. R. and Douglass, R. W., Viscous flow in oscillatory spherical annuli. *Physics of Fluids* 22(2) (1979) 205–208.
8. Pearson, C. E., A numerical study of the time dependent viscous flow between two rotating spheres. *Journal of Fluid Mechanics* 28 (1967) 323–336.
9. Krause, E. and Bartels, F., Finite-difference solution of the Navier-Stokes equations for axially symmetric flows in spherical gaps. *Lecture Notes in Mathematics* 771 (1979) 313–322.
10. Yang, J. K., Nigro, N. J., Elkouh, A. F. and Gagliardi, J. C., Numerical study of the axially symmetric motion of an incompressible viscous fluid in an annulus between two concentric rotating spheres. *International Journal For Numerical Methods In Fluids* 9 (1989) 689–712.
11. Bühler, K., Symmetric and asymmetric Taylor vortex flow in spherical gaps. *Acta Mechanica* 81 (1990) 3–38.
12. Yang, J. K., Numerical study of axially symmetric motion of an incompressible viscous fluid in an annulus between two concentric rotating spheres. *Ph.D. Dissertation* Marquette University, February (1987).

Applied Scientific Research **49**: 161–173, 1992.
© 1992 *Kluwer Academic Publishers. Printed in the Netherlands.*

Growth factors for Marangoni instability in a spherical liquid layer under zero-gravity conditions

H.C.J. HOEFSLOOT[1,†], H.W. HOOGSTRATEN[2,*], L.P.B.M. JANSSEN[1] & J.W. KNOBBE[2]

*Departments of [1]Chemical Engineering and [2]Mathematics, University of Groningen, Groningen, The Netherlands (*author for correspondence)*

Received 15 March 1991; accepted 22 May 1991

Abstract. The neutral-stability analysis presented by Hoefsloot et al. [3] is completed by computing the growth factors β for the normal modes and by showing that the neutral states ($\mathrm{Re}(\beta) = 0$) are stationary ($\mathrm{Im}(\beta) = 0$) rather than oscillatory ($\mathrm{Im}(\beta) \neq 0$).

1. Introduction

Hoefsloot et al. [3] studied the onset of surface-tension-driven convective flows (Marangoni instability) for a spherical liquid layer under zero-gravity conditions. The layer contains a solute that can evaporate at the inner surface (a spherical gas/liquid interface) and the outer sphere is taken to be a rigid solid surface. Initially the solute concentration is uniformly equal to c_0. Two separate cases are distinguished: the outer surface is impervious (case 1) and the solute concentration has the constant value c_0 at the outer surface (case 2). By use of a linear normal-mode analysis neutral (or marginal) stability conditions have been computed in [3] for concentration profiles created by diffusion in the motionless liquid, which profiles were 'frozen' at a certain point in time. Neutral stability was investigated by putting the growth factor (β) equal to zero. This leads to an eigenvalue problem yielding for each mode the neutral-stability value of the Marangoni number Ma. The so-called critical Marangoni number (Ma_c) is equal to the smallest of the Ma-values belonging to all possible modes; the corresponding wavenumber (α_c) is called the critical wavenumber. If Ma exceeds slightly the neutral-stability value of a particular mode, this mode will grow in time, the initial rate of growth being determined by β. The principal purpose of the present paper is to compute the growth factors β for the stability problems treated in [3].

In the analysis of [3], and also in the related paper [2], it has been assumed that the so-called 'principle of exchange of stability' holds, that is, if $\mathrm{Re}(\beta) = 0$ then automatically $\mathrm{Im}(\beta) = 0$. This means that the neutral states are stationary rather than oscillatory ($\mathrm{Im}(\beta) \neq 0$). Vidal and Acrivos [4] have shown that this principle is valid for certain systems with a *flat* interface in which surface-tension effects are solely

---

[†] Present address: Department of Chemical Engineering, University of Amsterdam, Amsterdam, The Netherlands

responsible for instability. The only cases for which oscillatory neutral states have been found, appear to possess two competing instability mechanisms. It is also the purpose of this paper to show, by numerical means, that no oscillatory neutral modes exist for the spherical systems under consideration.

2. The eigenvalue problem for the growth factors β

First, we recapitulate the mathematical formulation of the stability problem [3]. Throughout the present paper we adhere to the definitions, notations and non-dimensionalization introduced in [3] and for a discussion of the assumptions underlying the mathematical model we also refer to that paper. For the spherical liquid layer (inner radius a, layer thickness H), the two non-dimensional equations in spherical coordinates (r, θ, φ) governing the perturbation of a given motionless basic concentration profile $c_b(r)$ are [3]:

$$\nabla^2 \left(\mathrm{Pr}^{-1} \frac{\partial}{\partial t} - \nabla^2\right)(ru) = 0, \tag{2.1}$$

$$\left(\frac{\partial}{\partial t} - \nabla^2\right) c = -u \frac{\mathrm{d}c_b}{\mathrm{d}r}, \tag{2.2}$$

where

$$\nabla^2 = \frac{1}{r^2}\frac{\partial}{\partial r}\left(r^2 \frac{\partial}{\partial r}\right) - \frac{1}{r^2}\mathfrak{L}^2, \quad \mathfrak{L}^2 = \frac{-1}{\sin\theta}\frac{\partial}{\partial\theta}\left(\sin\theta\frac{\partial}{\partial\theta}\right) - \frac{1}{\sin^2\theta}\frac{\partial^2}{\partial\varphi^2}.$$

In these equations, u denotes the radial liquid velocity, c is the perturbation solute concentration, t is the time variable, and Pr is the Prandtl number. The boundary conditions at the gas/liquid interface $r = a/H$ are

$$u = 0, \qquad \frac{\partial c}{\partial r} = \mathrm{Bi}\, c, \qquad \frac{\partial^2 (ru)}{\partial r^2} = \frac{1}{r}\mathrm{Ma}\ \mathfrak{L}^2 c, \tag{2.3}$$

where Bi and Ma denote the Biot and Marangoni number, respectively. At the solid boundary $r = 1 + a/H$ we have the conditions

$$u = \frac{\partial u}{\partial r} = 0, \qquad \frac{\partial c}{\partial r} = 0 \text{ (case 1)} \quad \text{or} \quad c = 0 \text{ (case 2)}. \tag{2.4}$$

The solution of the boundary-value problem (2.1)–(2.4) is now written in separated form (normal modes):

$$ru(r,\theta,\varphi,t)=(U(r)+i\mu(r))Y_n^m(\theta,\varphi)\mathrm{e}^{\beta t},$$
$$c(r,\theta,\varphi,t)=(C(r)+i\gamma(r))Y_n^m(\theta,\varphi)\mathrm{e}^{\beta t},\quad m,n=1,2,3,\ldots,\tag{2.5}$$

where $Y_n^m(\theta,\varphi)$ are spherical surface harmonics of the first kind [1], $U+i\mu$ and $C+i\gamma$ denote the complex amplitude of the radial velocity and concentration perturbation, and $\beta=p+iq$ is the complex growth factor of the mode (m,n). Instability is characterized by $p>0$, neutral stability by $p=0$ and stability by $p<0$. If $q\neq 0$ for $p=0$, we have an oscillatory neutral state.

After substitution of (2.5) in problems (2.2)–(2.4) and subsequently separating real and imaginary parts, we obtain four ordinary differential equations for $U(r)$, $\mu(r)$, $C(r)$ and $\gamma(r)$,

$$(\mathfrak{D}-\mathrm{Pr}^{-1}p)\mathfrak{D}U(r)+\mathrm{Pr}^{-1}q\mathfrak{D}\mu(r)=0,\tag{2.6}$$

$$(\mathfrak{D}-\mathrm{Pr}^{-1}p)\mathfrak{D}\mu(r)-\mathrm{Pr}^{-1}q\mathfrak{D}U(r)=0,\tag{2.7}$$

$$(\mathfrak{D}-p)C(r)+q\gamma(r)=\frac{U(r)}{r}\frac{\mathrm{d}c_b}{\mathrm{d}r},\tag{2.8}$$

$$(\mathfrak{D}-p)\gamma(r)-qC(r)=\frac{\mu(r)}{r}\frac{\mathrm{d}c_b}{\mathrm{d}r},\tag{2.9}$$

with

$$\mathfrak{D}=\frac{\mathrm{d}^2}{\mathrm{d}r^2}+\frac{2}{r}\frac{\mathrm{d}}{\mathrm{d}r}-\frac{n(n+1)}{r^2}$$

and boundary conditions at $r=a/H$:

$$U=\mu=0,\qquad \frac{\mathrm{d}C}{\mathrm{d}r}=\mathrm{Bi}\,C,\qquad \frac{\mathrm{d}\gamma}{\mathrm{d}r}=\mathrm{Bi}\,\gamma,$$
$$\frac{\mathrm{d}^2U}{\mathrm{d}r^2}=\mathrm{Ma}\frac{n(n+1)}{r}C,\qquad \frac{\mathrm{d}^2\mu}{\mathrm{d}r^2}=\mathrm{Ma}\frac{n(n+1)}{r}\gamma\tag{2.10}$$

and at $r=1+a/H$

$$U=\frac{\mathrm{d}U}{\mathrm{d}r}=0,\qquad \mu=\frac{\mathrm{d}\mu}{\mathrm{d}r}=0,\tag{2.11}$$

$$\frac{\mathrm{d}C}{\mathrm{d}r}=\frac{\mathrm{d}\gamma}{\mathrm{d}r}=0\text{ (case 1)}\quad\text{or}\quad C=\gamma=0\text{ (case 2)}.\tag{2.12}$$

Notice that m, the wavenumber in the φ-direction, has vanished from the problem; only the θ-wavenumber n plays a role.

Boundary-value problem (2.6)–(2.12), with $c_b(r)$, a/H, n, Bi, Pr and Ma given, is a linear eigenvalue problem for the eigenvalues $\beta = p + iq$ and the eigensolutions $U + i\mu$ and $C + i\gamma$. We shall assume that there exists an infinite denumerable sequence of eigenvalues β_j which can be ordered such that $\mathrm{Re}(\beta_{j+1}) < \mathrm{Re}(\beta_j)$, $j = 0, 1, 2, \ldots$. This assumption turns out to be supported by our numerical results.

3. Numerical solutions of the eigenvalue problem

The eigenvalue problem consisting of equations (2.6)–(2.9) and boundary conditions (2.10)–(2.12) has been solved numerically with a shooting technique. First, the basic concentration profile $c_b(r)$ is computed for given values of a/H and Bi and the desired time t at which the diffusion process in the motionless liquid is frozen. Details of this computation can be found in [3]. Next, for given values of n and Ma and an *estimated* value of the growth factor $\beta = p + iq$, the general solution of the following pair of initial-value problems A and B is determined:

—problem A for (U, μ) consists of equations (2.6), (2.7) and initial conditions (2.11) at the solid boundary $r = 1 + a/H$;

—problem B for (C, γ) consists of equations (2.8), (2.9) together with initial conditions (2.12) at $r = 1 + a/H$.

The general solution of problem A can be written as

$$(U, \mu) = \sum_{j=1}^{4} B_j(U_j, \mu_j), \tag{3.1}$$

where $B_1, \ldots, B_4$ are integration constants and U_j and μ_j satisfy the additional initial conditions

$$(U_j'', U_j''', \mu_j'', \mu_j''') = \mathbf{e}_j \quad (j = 1, \ldots, 4) \text{ at } r = 1 + a/H$$

where $\mathbf{e}_j$ denotes the jth unit vector in $\mathbb{R}^4$ (or, in other words, the jth row of the 4×4 unit matrix). Likewise, the general solution of problem B is given by

$$(C, \gamma) = \sum_{j=1}^{4} B_j(C_j, \gamma_j) + B_5(C_5, \gamma_5) + B_6(C_6, \gamma_6), \tag{3.2}$$

where the summation term represents a particular solution of (2.8)–(2.9) in which (C_j, γ_j), $j = 1, \ldots, 4$, satisfies the initial conditions at $r = 1 + a/H$:

$$(C_j, C_j', \gamma_j, \gamma_j') = (0, 0, 0, 0).$$

The last two terms at the right of (3.2) involve the integration constants B_5 and B_6 accompanied by the two homogeneous solutions (C_j, γ_j), $j = 5, 6$, of equations (2.8), (2.9) satisfying the initial conditions at $r = 1 + a/H$:

$$(C_j, C_j', \gamma_j, \gamma_j') = \begin{cases} (1, 0, 0, 0) \text{ for } j = 5 \\ (0, 0, 1, 0) \text{ for } j = 6 \end{cases} \quad \text{(case 1)},$$

or

$$(C_j, C_j', \gamma_j, \gamma_j') = \begin{cases} (0, 1, 0, 0) \text{ for } j = 5 \\ (0, 0, 0, 1) \text{ for } j = 6 \end{cases} \quad \text{(case 2)}.$$

The fundamental solutions (U_j, μ_j), $j = 1, \dots, 4$ and (C_j, γ_j), $j = 1, \dots, 6$, have been computed with a fourth-order Runge–Kutta method.

Substituting the combined general solution (3.1), (3.2) of problems A and B in the remaining six boundary conditions (2.10) at the gas/liquid interface $r = a/H$, we obtain a set of six homogeneous linear algebraic equations for the integration constants $B_1, \dots, B_6$. The coefficient determinant D of this set of equations depends on the value of β. If $D(\beta) = 0$, then β is an eigenvalue; if not, then the estimate for β has to be improved successively until $D(\beta)$ becomes sufficiently small.

Numerical computation of $D(\beta)$ for a number of cases shows that $D(\beta)$ will not vanish unless $\mathrm{Im}(\beta) = q = 0$ (see next section). So, in the subsequent computation of the growth factors β and eigensolutions (U,C), it is allowed to take β real $(q = 0)$ and, without loss of generality, to consider only real eigensolutions, that is, to put $\gamma(r) = \mu(r) = 0$. Accordingly, the shooting method described above simplifies considerably. The combined general solution of problems A and B now consists of five fundamental solutions accompanied by only three integration constants (analogous to the shooting method used in [3]):

$$\begin{aligned} U(r) &= B_1 U_1(r) + B_2 U_2(r), \\ C(r) &= B_1 C_1(r) + B_2 C_2(r) + B_5 C_5(r). \end{aligned} \tag{3.3}$$

The eigenvalue equation for β follows from the equating to zero of a 3×3 coefficient determinant and the zeros of this equation have been computed by use of the Regula Falsi method.

The eigenvalue problem turns out to possess a denumerably infinite number of eigenvalues. We are mainly interested in the largest eigenvalue, β_0, because this value determines the stability behaviour of the particular mode under consideration. In order to decide whether a computed eigenvalue is indeed the largest one, the corresponding eigensolution $(U(r), C(r))$ is computed; U and C are found as particular linear combinations of the form (3.3). Typically, the eigensolution belonging to the largest eigenvalue β_0 possesses no zeros in the *interior* of the interval $a/H \leqslant$

$r \leqslant 1 + a/H$. So the search for zeros of $D(\beta)$ is continued until the one is found for which $(U(r), C(r))$ has no zeros in the open interval $(a/H, 1 + a/H)$.

4. Numerical results and discussion

The possible occurrence of oscillatory neutral states has been investigated by performing a series of computations in which the coefficient determinant $D(\beta)$ has been determined under the assumption that β is purely imaginary ($\beta = iq$, $p = 0$). Figure 1 is a typical result for case 1. It shows D as a function of q for various values of Ma (and fixed parameter values $\mathrm{Pr} = 787$, $a/H = 10$, $\mathrm{Bi} = 20$, $t = 0.001$) for the mode with wavenumber $\alpha = 9$ ($\alpha = nH/a$ is the number of waves in the θ-direction per unit length along the interface $r = a/H$). This mode is the critical one with regard to neutral stability for this particular set of parameter values [3] with corresponding $\mathrm{Ma}_c = 1058$. It is seen that D is an even function of q, as can be shown easily by observing that, if $(U, \mu, C, \gamma, p, q)$ satisfies boundary-value problem (2.6)–(2.12), then also $(\mu, U, \gamma, C, p, -q)$ is a solution. Figure 1 shows that D does not vanish unless Ma has its critical value and, furthermore, if D vanishes, then $q = 0$. Figure 2 presents analogous results for case 2. The general pattern of Figs 1 and 2 has also been found for a large number of other sets of parameter values. On the basis of these findings it can be concluded that there are no oscillatory neutral states and, hence, that the principle of exchange of stability holds for the spherical systems under consideration.

The question of the possibility of oscillatory growth ($p > 0, q \neq 0$) has also been addressed. Figures 3 and 4 show typical results for case 1 and case 2, respectively. Here D has been plotted as a function of p for several values of q for fixed values of Pr, a/H,

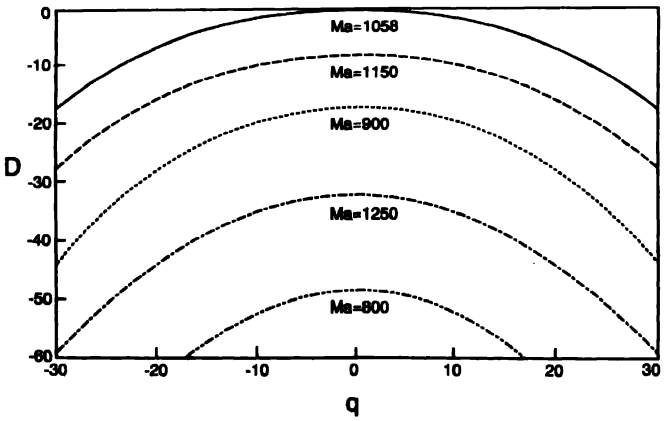

Fig. 1. Determinant D for case 1 as a function of $q(=\mathrm{Im}(\beta))$ for various values of Marangoni number Ma. Parameter values: $\mathrm{Pr} = 787$, $a/H = 10$, $\alpha = 9$, $\mathrm{Bi} = 20$, $t = 0.001$, $p(=\mathrm{Re}(\beta)) = 0$. The corresponding critical values are $\mathrm{Ma}_c = 1058$ and $\alpha_c = 9$.

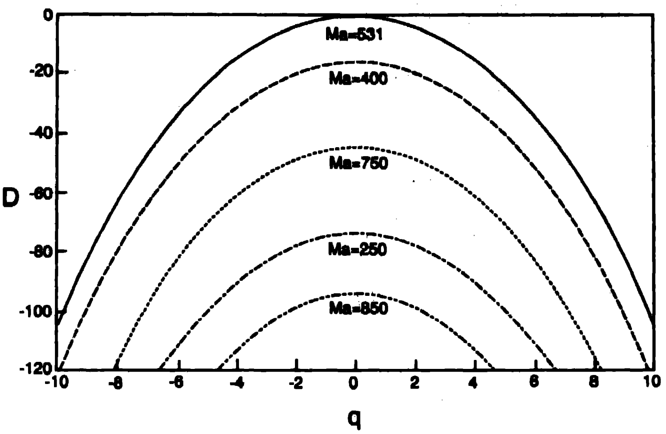

Fig. 2. Determinant D for case 2 as a function of $q(=\text{Im}(\beta))$ for various values of Marangoni number Ma. Parameter values: $\text{Pr}=1$, $a/H=1$, $\alpha=4$, $\text{Bi}=20$, $t=0.1$, $p(=\text{Re}(\beta))=0$. Here, $\text{Ma}_c=531$ and $\alpha_c=4$.

α, Bi and t. The Marangoni number has been chosen as $\text{Ma}=1200$, which is slightly above the critical value for both cases and it leads to at least one mode growing in time. In both figures it is seen that D does not vanish for $p>0$ unless $q=0$ with corresponding real growth factor $p=\beta_0>0$. So the growth of the modes under unstable circumstances is governed by a real exponential function of time, rather than a complex exponential, the latter of which would imply oscillatory growth in time with exponentially increasing amplitude.

The numerical results discussed so far show that in the subsequent computations, the results of which will be presented below, we can restrict ourselves to the case of

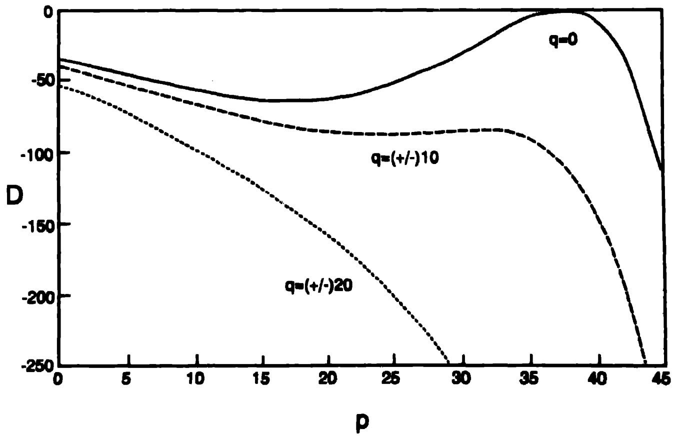

Fig. 3. Determinant D for case 1 as a function of $p(=\text{Re}(\beta))$ for various values of $q(=\text{Im}(\beta))$. Parameter values: $\text{Pr}=787$, $a/H=10$, $\alpha=9$, $\text{Bi}=20$, $\text{Ma}=1200$, $t=0.001$. ($\text{Ma}_c=1058$ and $\alpha_c=9$.)

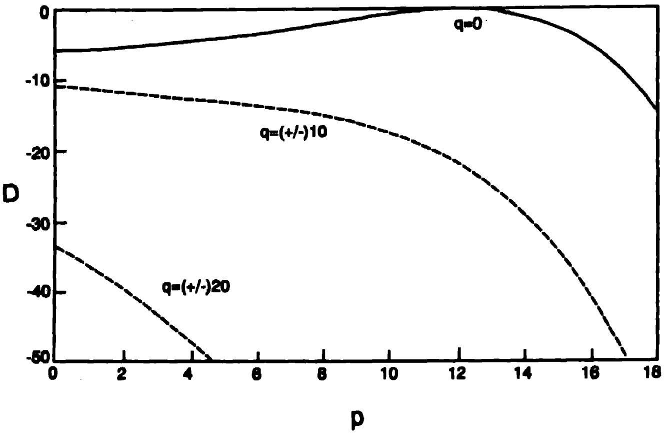

Fig. 4. Determinant D for case 2 as a function of $p(=\mathrm{Re}(\beta))$ for various values of $q(=\mathrm{Im}(\beta))$. Parameter values: $\mathrm{Pr}=1$, $a/H=1$, $\alpha=4$, $\mathrm{Bi}=40$, $\mathrm{Ma}=1200$, $t=1.0$ ($\mathrm{Ma}_c=1115$ and $\alpha_c=4$.)

real growth factors β with corresponding real eigensolutions pairs $(U(r), C(r))$. As explained in Section 3, this means a considerable simplification of the numerical shooting method.

Figures 5 and 6 show the growth factor β_0 for cases 1 and 2, respectively, as a function of the wavenumber α for several values of the 'freezing' time t at which the

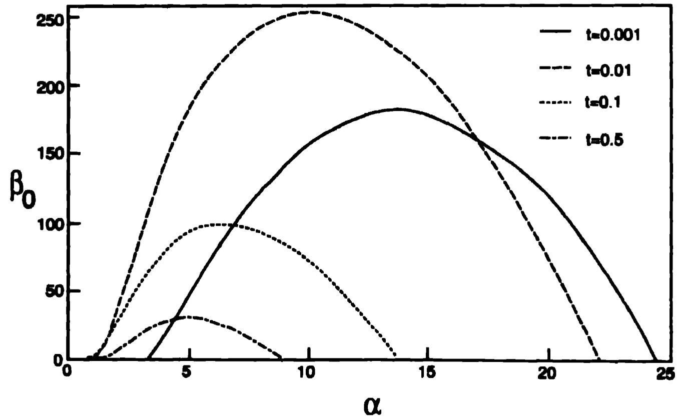

Fig. 5. Growth factor β_0 for case 1 as a function of wavenumber α for various values of time t. Parameter values: $\mathrm{Pr}=787$, $a/H=1$, $\mathrm{Bi}=20$, $\mathrm{Ma}=1600$. The critical values are as follows:

t	0.001	0.01	0.1	0.5
Ma_c	1071	505	516	830
α_c	9	5	4	3

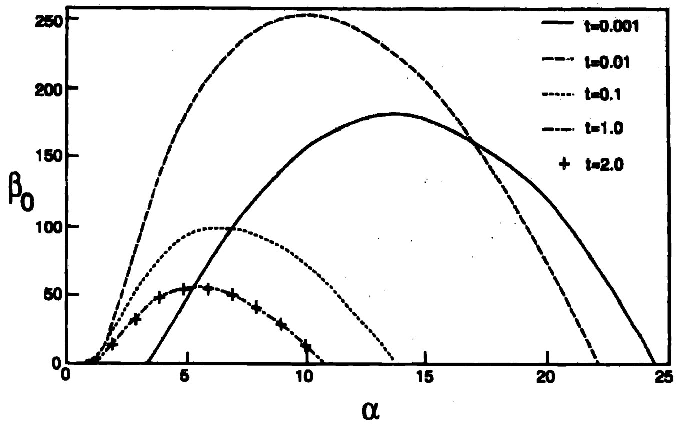

Fig. 6. Growth factor β_0 for case 2 as a function of wavenumber α for various values of time t. Parameter values: Pr = 787, $a/H = 1$, Bi = 20, Ma = 1600. The critical values are as follows:

t	0.001	0.01	0.1	1.0	2.0
Ma_c	1071	508	531	649	649
α_c	9	5	4	4	4

basic motionless concentration profile $c_b(r)$ has been obtained. In both cases the chosen Marangoni number (Ma = 1600) is larger than the values of Ma_c belonging to the various times involved, so there is always growth ($\beta_0 > 0$) for some interval of α-values at each time instant for which the graphs have been presented. It is seen that the maximum growth factor increases initially and decreases for later times. In case 1 there will be no positive values of β_0 after some finite time, when Ma_c has become larger than 1600. In case 2 the graphs tend to a limit graph which has been reached almost completely for $t = 1$; this corresponds to the non-zero limit concentration profile being reached for $t \to \infty$ in this case. For small times the graphs for cases 1 and 2 are nearly identical, since for these times the difference in the boundary condition at the solid outer surface is not yet noticeable in the basic concentration profile $c_b(r)$. The wavenumber α at which β_0 reaches its maximum value decreases in time. This is due to the increasing penetration depth of the motionless diffusion process as time increases, allowing for larger wavelengths of the normal modes. These α-values are always larger than the corresponding values of α_c at each time.

Table 1 shows the strong dependence of β_0 on the curvature parameter a/H and Biot number Bi for fixed time $t = 0.01$, wavenumber $\alpha = 5$, Prandtl number Pr = 787 and various values of Ma. For fixed Bi and Ma the largest curvature ($a/H = 0.1$) shows the lowest value of β_0. Increasing the value of a/H from 1 to 10 leads in most cases to an increase of β_0 for Bi = 1 and 20, and to a decrease of β_0 for Bi = 40 and Bi = 60.

Table 1. Results for case 1: growth factor β_0 as a function of a/H for Bi = 1, 20, 40, 60 and various values of Ma. Parameter values: Pr = 787, $\alpha = 5$, $t = 0.01$

	Bi = 1			Bi = 20		
a/H	Ma = 1100	Ma = 2000	Ma = 3000	Ma = 600	Ma = 2000	Ma = 3000
0.1	−1.4	−1.4	−1.2	−1.3	53.0	160.7
1	1.8	37.8	80.5	12.3	254.8	430.0
10	9.0	50.1	96.0	14.8	254.1	490.3

	Bi = 40			Bi = 60		
a/H	Ma = 800	Ma = 1400	Ma = 2000	Ma = 1100	Ma = 1500	Ma = 2000
0.1	−1.3	0.3	27.9	−1.3	−0.7	6.1
1	3.9	76.3	160.8	5.3	40.6	92.9
10	3.3	75.3	155.9	3.7	38.7	88.6

Table 2. Values of β_0, β_1, β_2 and β_3 for case 1 for various values of Pr. Parameter values: $a/H = 10$, $\alpha = 9$, Bi = 20, Ma = 1200, $t = 0.001$ ($\mathrm{Ma}_c = 1058$, $\alpha_c = 9$)

Pr			β_2	β_3
0.1	3.1	−9.4	−14.7	−22.3
1	16.3	−73.7	−91.9	−99.8
787	34.9	−73.8	−101.1	−149.2

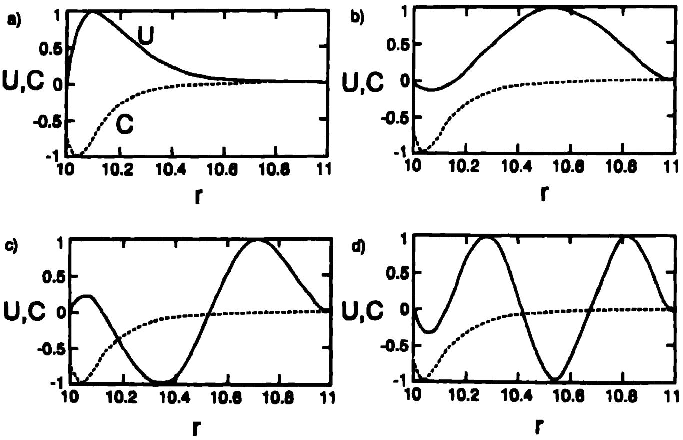

Fig. 7. Eigensolutions U and C for case 1 as a function of the radial coordinate r, corresponding to the eigenvalues β_0, β_1, β_2 and β_3. Parameter values: Pr = 0.1, $a/H = 10$, $\alpha = 9$, Bi = 20, Ma = 1200, $t = 0.001$ ($\mathrm{Ma}_c = 1058$, $\alpha_c = 9$). Figure (a): (U_0, C_0), (b): (U_1, C_1), (c): (U_2, C_2), (d): (U_3, C_3).

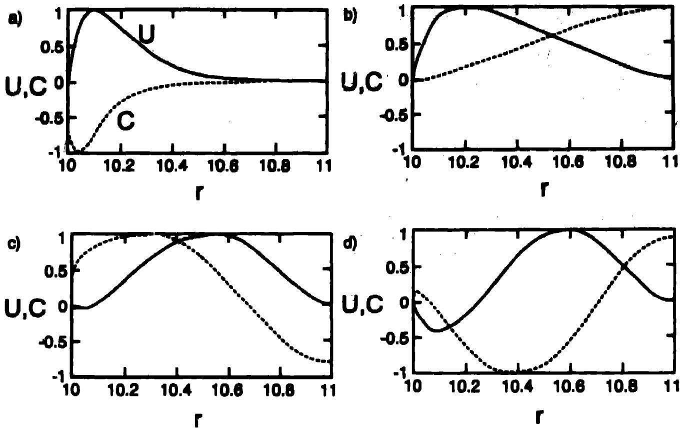

Fig. 8. As for Fig. 7 with Pr = 1.

The dependence of the first four eigenvalues β_0, β_1, β_2 and β_3 on the Prandtl number Pr for fixed values of a/H, α, Bi, Ma and t is shown in Table 2 for case 1. Increasing values of Pr are seen to yield increasing values of $|\beta_i|$, $i = 0, 1, 2, 3$.

For the same parameter values as in Table 2, Figures 7, 8 and 9 show for case 1 the dependence of the first four eigensolution pairs (U_i, C_i), $i = 0, 1, 2, 3$, on Pr. It is remarkable that for Pr small (large) the eigensolution $C_i(U_i)$ has about the same shape for $i = 0, 1, 2, 3$. A nice property of the computed eigensolution pairs is seen to be that U_i and C_i together possess precisely i zeros in the open interval $a/H < r < 1 + a/H$.

The increase of the penetration depth of the diffusion process as time progresses is clearly demonstrated by the graphs of U_0 and C_0 for various times t for case 1 (see Fig. 10).

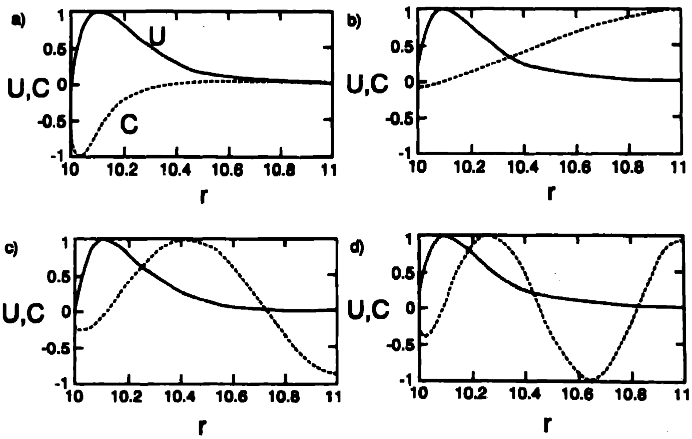

Fig. 9. As for Fig. 7 with Pr = 787.

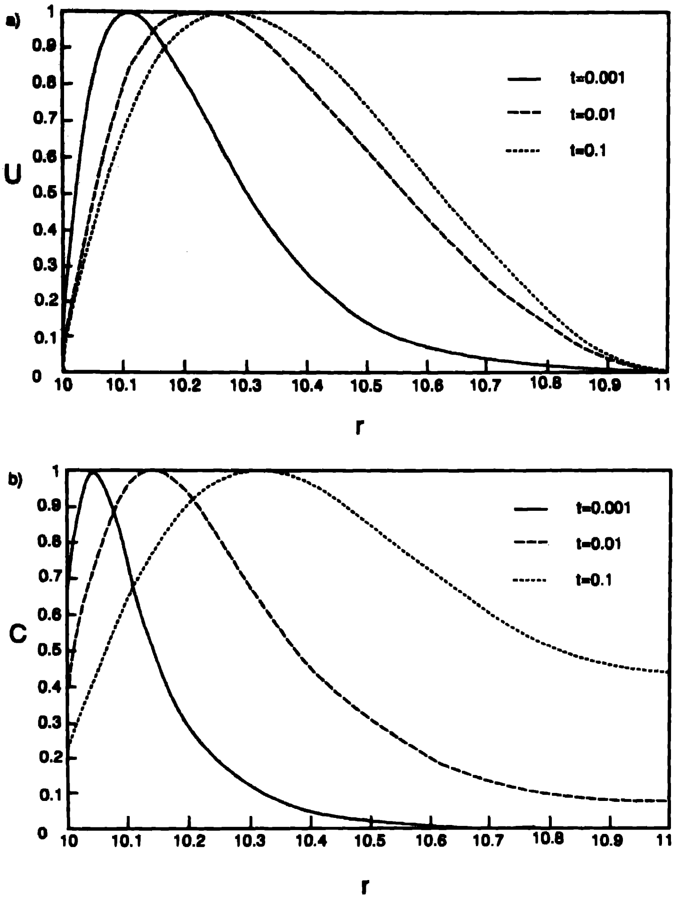

Fig. 10. Eigenfunctions U_0 (Fig. 10(a)) and C_0 (Fig. 10(b)) for case 1 as functions of r for $t = 0.001$, 0.01 and 0.1. Parameter values: $\mathrm{Pr} = 787$, $a/H = 10$, $\mathrm{Bi} = 20$. Ma and α (and corresponding value of the growth factor β_0) are as indicated in the table below:

t	Ma	α	β_0
0.001	1070	9.0	2.9
0.01	500	4.3	1.1
0.1	540	3.0	0.5

5. Concluding remarks

For the linear stability problem governing the onset of Marangoni convection in a spherical liquid layer under zero-gravity conditions, it has been shown that no oscillatory neutral modes exist. The only possible neutral modes are stationary.

Further, the initial growth in time of the modes under unstable circumstances is shown to be monotone rather than oscillatory with increasing amplitude.

The maximum of the growth factor, taken over all possible modes at a certain 'freezing' time t, is an increasing function of t for sufficiently small t and it decreases again for later times. Apart from the obvious dependence of the growth factor for a particular mode on the Marangoni number Ma, this growth factor also turns out to depend quite strongly on the Prandtl number Pr, the Biot number Bi and the curvature parameter a/H.

References

1. Abramowitz, M. and Stegun, I.A., *Handbook of Mathematical Functions.* New York: Dover Publications (1965).
2. Hoefsloot, H.C.J., Hoogstraten, H.W., Hoven, A. and Janssen, L.P.B.M., Marangoni instability in a liquid layer bounded by two coaxial cylinder surfaces. *Applied Sci. Research* 47 (1990) 1–21.
3. Hoefsloot, H.C.J., Hoogstraten, H.W. and Janssen, L.P.B.M., Marangoni instability in a liquid layer confined between two concentric spherical surfaces under zero-gravity conditions. *Applied Sci. Research* 47 (1990) 357–377.
4. Vidal, A. and Acrivos, A., Nature of the neutral state in surface tension driven convection. *Phys. Fluids* 9 (1966) 615–616.

Applied Scientific Research **49**: 175–187, 1992
© 1992 *Kluwer Academic Publishers. Printed in the Netherlands.*

Flutter of slender bodies under axial stress

R. COENE

Department of Aerospace Engineering, Delft University of Technology, Delft, The Netherlands

Received 18 June 1990; accepted in revised form 27 May 1991

Abstract. The equations of motion of flexible slender bodies with constant body sections immersed in a uniform axial flow are discussed and used to derive some simple results for the divergence speed and the flutter speed. The results are compared with a classical waving flag result in two-dimensional flow. The slender body result for the flutter speed is compared with values obtained from wind tunnel experiments for some low budget paper strips.

1. Introduction

In Milne-Thomson's book 'Theoretical Hydrodynamics' [1] the problem of a two dimensional flapping flag is formulated in two examples, 18 and 19, in chapter XV as follows:

> '18. Two portions of a large uniform stream of liquid of density ρ, flowing with velocity U, are separated by a plane boundary of perfectly flexible fabric, of mass m per unit area, and subject to a tension T, the boundary being parallel to the stream. Show that waves of length λ can be propagated along the fabric, in the direction of the stream, with a velocity V given by
>
> $$mV^2 - T + \frac{\lambda\rho}{\pi}(U - V)^2 = 0, \tag{1.1}$$
>
> provided that
>
> $$T\left(1 + \frac{m\pi}{\lambda\rho}\right) > mU^2. \tag{1.2}$$
>
> 19. Explain, giving the necessary theory, why a flag flaps in a breeze'.

In this paper the slender body problem corresponding to the waving flag problem referred to above is treated. Solutions corresponding to (1.1) and (1.2) will be derived for flexible slender bodies with arbitrary cross-sections which are invariable in the streamwise direction. For cases with nearly neutral buoyancy (i.e. with the density of the body nearly equal to the density of the surrounding fluid) the results are relevant to the readily observed wavy motions of weeds in a river. We also obtain some results for the divergence and flutter of a beam supported at both ends. Here divergence is the steady state aeroelastic instability and the term flutter is used for the oscillatory instability in a potential flow which involves no separation.

In the present context some general remarks on slender body theory are in order. Here a body is called slender if the local thickness in all directions perpendicular to the stream, is small with respect to the length in the direction of the undisturbed stream. A body whose local thickness is small in one direction only is called thin. Thus a line is the limit of a slender body as the thickness tends to zero, while the limit of a thin body is a surface. Whenever a slender body is laterally compressed the body may be both thin and slender, the result being a slender wing.

An essential feature of the slender body-approximation is that the velocity potential which describes the flow outside the boundary layer satisfies the two-dimensional Laplace equation in the near field. (In the far field the flow is dominated by a three-dimensional dipole). Satisfying certain conditions of smoothness in the streamwise direction solutions are readily obtained for many flow regimes of practical interest. The idea to use the concept of virtual momentum of a lateral section is due to Munk [2]. The same method is also applicable to unsteady flow problems. An interesting example of such an application is due to Lighthill [3] who explains the swimming of slender fish. The theory indicates that efficient propulsion can be generated by a wave of increasing amplitude which passes down the body at a phase velocity V slightly larger than the swimming speed U. At the sharp trailing edge a weak Joukowski condition, which allows for a finite pressure jump, is being satisfied while vorticity is being shed into the wake. Positive thrust can only be generated at a positive rate of working by the body. Conversely, a negative rate of working by the body is associated with drag. This case, of course, is related to 'flutter' and instability of motion.

In [4] and [5] the dynamics and the stability of towed flexible cylinders is discussed. Modes of oscillation are obtained for neutrally buoyant cylinders allowing for viscous effects and a variable tension in the bodies, keeping the nose of the body fixed in a steady stream. Surprisingly no reference is made in [4] and [5] to the fundamental results (1.1) and (1.2) or their slender body counterparts.

The stability problem and the voluntary swimming problem, where the body experiences a propulsive force by actively generating a wave passing down the body, are not the only ones which may lead to waves in a body.

As shown in [6] a wavy stream leads to a passive recoil mode with a phase velocity equal to the phase velocity of the oncoming waves when there is no tension in the body. Another example is a flag waving in the von Karman vortex street of the mast, where the wave velocity is dictated by the phase velocity at which the alternating vortices are convected downstream. In this paper, however, we consider the stability problem of slender bodies with constant tension and invariable body sections to derive the slender body counterpart of (1.1) and (1.2). Some experimental values for the flutter speeds [7] of three strips of paper will be compared with the slender body results.

2. The equations of motion

We consider a flexible slender body in a uniform oncoming flow. A Cartesian coordinate system (x, y, z) which is an inertial system has its x-axis aligned with the oncoming flow velocity U. The body has length l and lateral dimensions which are small with respect to l (Fig. 2.1).

The cross-sections may perform displacements $h(x, t)$ in the vertical z-direction. Moreover, the z-x plane is a plane of symmetry of the body (Fig. 2.2). Therefore the flow is also symmetrical and there will be no torsional moments. The z-axis is a principal axis of the body sections and we assume a bending stiffness EI. We neglect deformations due to shear.

For the lateral (z-component) force exerted by the fluid on the body per unit length in the x-direction we use the classical slender body result [3]:

$$L(x, t) = -\rho\left(\frac{\partial}{\partial t} + U\frac{\partial}{\partial x}\right)(wA), \tag{2.1}$$

where ρ is the density of the fluid, and w is the resultant cross-flow with

$$w = \frac{\partial h}{\partial t} + U\frac{\partial h}{\partial x}. \tag{2.2}$$

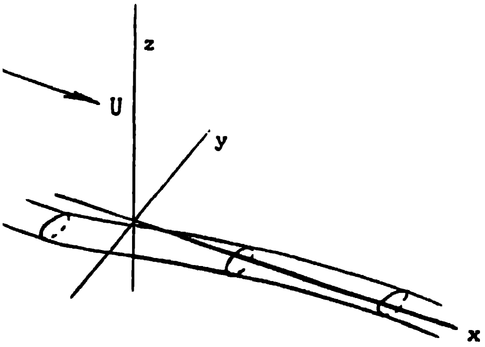

Fig. 2.1. The coordinate system.

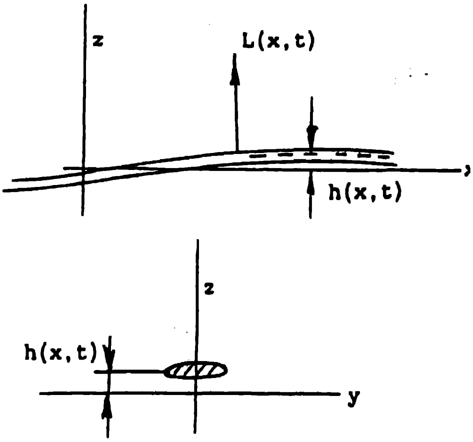

Fig. 2.2. The lateral displacements and the lateral force.

ρA is the virtual mass of the cross-sections for motions in the z-direction. The virtual mass (per unit length in the x-direction) is defined by

$$\rho A = \rho \oint_x \phi \, \mathrm{d}y, \tag{2.3}$$

where ϕ is the velocity potential of the two-dimensional cross-flow when the cross-section moves at unit velocity in the z-direction. This quantity can be obtained from complex-variable theory of two-dimensional irrotational flow. For an elliptic section, of any excentricity, with axes a and b, moving in the direction of the a axis, one obtains

$$A = \frac{\pi}{4} b^2, \tag{2.4}$$

which is independent of a and therefore also valid for a flat plate with $a = 0$. For $a = b$, (2.4) is equal to the cross-sectional area of the circular cross-section. One may also observe that for $a < b$, A is given by the cross-sectional area of the smallest possible circular cylinder which circumscribes the section.

The differential operator $(\partial/\partial t + U(\partial/\partial x))$ appearing in (2.1) and (2.2) is the linearized approximation of the material derivative; i.e. a time derivative following a particle. Thus the right-hand side of (2.1) stands for the material time derivative of the z-component of momentum of a slice of fluid of unit thickness in the x-direction. One may write, neglecting the x-component of the velocity perturbations with respect to U:

$$\frac{D}{Dt} = \frac{\partial}{\partial t} + U\frac{\partial}{\partial x}, \tag{2.5}$$

for the time derivative in a coordinate system travelling at speed U in the positive x-direction with respect to the body. Obviously this coordinate system is fixed with respect to the fluid which is undisturbed far from the body. Equation (2.1) is valid for smooth variations in the x-direction and by virtue of the physical significance of (2.5) it is obvious that both w and A may depend on x and t. In this paper, however, only w is dependent on x and t while A is assumed to be constant. This restriction is not important for the validity of (2.1) but it is relevant to what follows. It implies that the expression on the right-hand side of (2.1) involves only second derivatives of $h(x, t)$ with respect to x and t and this, in turn, leads to the possibility of simple solutions which exhibit some interesting features.

By virtue of (2.1) the differential equation for $h(x, t)$, equating the rate of change of lateral momentum to the forces, becomes

$$(\rho_b S)\frac{\partial^2 h}{\partial t^2} = \frac{\partial}{\partial x}\left(T\frac{\partial h}{\partial x}\right) - \frac{\partial^2}{\partial x^2}\left(EI\frac{\partial^2 h}{\partial x^2}\right) - \left(\frac{\partial}{\partial t} + U\frac{\partial}{\partial x}\right)(\rho w A), \tag{2.6}$$

where the first three terms are the usual contributions for a vibrating beam, with

ρ_b the mass density of the body;
S the area of the cross-sections;
T the axial tension;
EI the flexural rigidity.

Assuming constant $\rho_b S = \sigma$, constant EI, constant T and constant $\rho A = \alpha$, equation (2.6) simplifies to

$$\sigma \frac{\partial^2 h}{\partial t^2} = T \frac{\partial^2 h}{\partial x^2} - EI \frac{\partial^4 h}{\partial x^4} - \alpha \left(\frac{\partial}{\partial t} + U \frac{\partial}{\partial x} \right)^2 h. \tag{2.7}$$

This is a fourth order linear equation for $h(x, t)$ involving only second and fourth order derivatives. This opens the way for wave solutions of exponential growth.

3. Exponentially growing wave solutions

Equation (2.7) has solutions of the form

$$h(x, t) = a\,e^{i(kx - \omega t)}, \tag{3.1}$$

where a is the amplitude in the steady oscillation case and the wavenumber k is related to the wavelength by $k = 2\pi/\lambda$; ω is the circular frequency.

Substitution of (3.1) into (2.7) yields a quadratic equation for ω (with $a \neq 0$):

$$-\sigma\omega^2 = -Tk^2 - EIk^4 - \alpha(-\omega^2 - U^2k^2 + 2\omega Uk), \tag{3.2}$$

which is solved by

$$\omega_{1,2} = \frac{k}{\alpha + \sigma}\left(\alpha U \pm \sqrt{(T + k^2 EI)(\alpha + \sigma) - \alpha\sigma U^2}\right). \tag{3.3}$$

Equating the discriminant in (3.3) to zero yields the critical situation:

$$T + k^2 EI - \frac{\alpha\sigma}{\alpha + \sigma} U^2 = 0. \tag{3.4}$$

If the left-hand side in (3.4) is positive one has the possibility of steady oscillations. If it is negative one has the possibility of exponential growth, i.e. flutter.

Starting from the critical situation (3.4) we distinguish three cases:

(a) In the absence of external flow, with $U = 0$, (3.4) cannot be satisfied with positive values of T. In what follows we shall come back to the case with negative values of T.

(b) Putting $T = 0$ in (3.4) yields a unique wavelength ($\lambda = 2\pi/k$):

$$\lambda = \frac{2\pi}{U}\sqrt{\frac{\alpha+\sigma}{\alpha\sigma}EI}, \tag{3.5}$$

and the corresponding frequency

$$\omega = \frac{\alpha U^2}{\alpha+\sigma}\sqrt{\frac{\alpha\sigma}{\alpha+\sigma}\frac{1}{EI}}, \tag{3.6}$$

and wavespeed

$$V = \frac{\omega}{k} = \frac{\alpha U}{\alpha+\sigma} < U. \tag{3.7}$$

(c) For a body with negligible rigidity, of perfectly flexible fabric, but also in the limit $k \to 0$, one obtains a unique flutter speed, U_{cr}, for given T with

$$U_{\mathrm{cr}}^2 = \frac{\alpha+\sigma}{\alpha\sigma}T, \tag{3.8i}$$

or alternatively, a critical tension T_{cr} for given U,

$$T_{\mathrm{cr}} = \frac{\alpha\sigma}{\alpha+\sigma}U^2. \tag{3.8ii}$$

We note that in this case the wave speed is also given by (3.7):

$$V = \frac{\omega}{k} = \frac{\alpha U}{\alpha+\sigma} < U, \tag{3.8iii}$$

but λ and ω are indeterminate.

For a waving weed with a circular cross-section and neutral buoyancy ($\alpha = \sigma$) in a river the wave speed which follows from (3.7) is one half the flow speed: $V = \frac{1}{2}U$. Obviously, the present analysis does not apply to the behaviour of the weeds after the onset of actual flutter, nor to large amplitude waves with variable stress and viscous effects but personal observations suggest that $V = \frac{1}{2}U$ might not be too far off.

The results (3.8) explain why the trailing part of a banner towed by an aircraft will generally be unstable. Adding a drag device behind the banner which increases the tension above the value (3.8ii) would stabilize the banner and increase its lifetime. The added drag due to the extra device is not a pure loss since a flapping banner with $V < U$ has a larger drag than a quiescent banner. The results (3.8) can be obtained in a slightly different way which sheds some light on the physical background. Putting $EI = 0$ in (2.7) and thereby retaining only the second order derivatives, equation (2.7) can be expressed as

$$\left(\frac{\partial}{\partial t} + c_1 \frac{\partial}{\partial x}\right)\left(\frac{\partial}{\partial t} + c_2 \frac{\partial}{\partial x}\right) h = 0, \tag{3.9}$$

with

$$c_1 c_2 = -\frac{T - \alpha U^2}{\alpha + \sigma}, \tag{3.10}$$

and

$$c_1 + c_2 = \frac{2\alpha U}{\alpha + \sigma}. \tag{3.11}$$

From (3.10) and (3.11) one readily obtains

$$c_{1,2} = \frac{\alpha U}{\alpha + \sigma} \pm \sqrt{\left(\frac{\alpha U}{\alpha + \sigma}\right)^2 + \frac{T - \alpha U^2}{\alpha + \sigma}}. \tag{3.12}$$

The discriminant in (3.12) vanishes with

$$T = \frac{\alpha\sigma}{\alpha + \sigma} U^2, \tag{3.13}$$

and the two phase velocities are then equal:

$$c_1 = c_2 = \frac{\alpha U}{\alpha + \sigma}. \tag{3.14}$$

The flutter speed which follows from (3.13) is the same as obtained before, in (3.8), and arises when two waves have the same phase velocity (3.14). From (3.10) we note that with

$$T = \alpha U^2, \tag{3.15}$$

which is larger than the critical value (3.8ii), one of the phase velocities, say c_1, vanishes and one finds:

$$c_1 = 0 \quad \text{and} \quad c_2 = \frac{2\alpha U}{\alpha + \sigma}. \tag{3.16}$$

At the special value (3.15) for the tension, a steady deformation $h(x)$, with $\partial h/\partial t = 0$, of arbitrary shape is possible. Thus, from (3.15) we obtain a divergence speed given by

$$U_{\text{div}}^2 = \frac{T}{\alpha}. \tag{3.17}$$

We note that this divergence speed is smaller than the flutter speed given by (3.8i) since

$$U_{\text{cr}}^2 = \frac{\alpha + \sigma}{\sigma} U_{\text{div}}^2 \quad \text{and} \quad \frac{\alpha + \sigma}{\sigma} > 1,$$

although for $\alpha \ll \sigma$ the two will be close together.

It is easily verified that equations (3.15) and (3.17) can be derived directly from equation (2.7) by putting the time derivatives equal to zero. Retaining the flexural rigidity then yields, with $T = -P$,

$$(P + \alpha U^2) \frac{\partial^2 h}{\partial x^2} + EI \frac{\partial^4 h}{\partial x^4} = 0. \tag{3.18}$$

Thus, e.g. Euler's buckling formula for a doubly pinned beam of length l ($l = \lambda/2$) can be supplemented with an apparent mass effect for exterior flow as

$$P_{\text{cr}} = \frac{\pi^2 EI}{l^2} - \alpha U^2. \tag{3.19i}$$

For a given value of the compression force one also obtains the divergence speed given by

$$\alpha U_{\text{div}}^2 = \frac{\pi^2 EI}{l^2} - P. \tag{3.19ii}$$

4. The two dimensional analogy

In the two dimensional case, referred to in the introduction, we start from a wave potential in the form

$$\phi^+ = -ac\,e^{-kz}\cos[k\{x-(U+c)t\}]. \tag{4.1}$$

It is easily verified that (4.1) satisfies the two dimensional Laplace equation and vanishes for $z \to +\infty$ where we have uniform flow at speed U in the x-direction.

The + indicating the upperside of the flag. At the lower side one has $\phi^- = -\phi^+$. $(U+c)$ is the phase speed of the wave and k is, again, the wavenumber, related to the wavelength λ by $k = 2\pi/\lambda$.

At $z = 0^+$, the boundary condition becomes

$$w = \frac{\partial h}{\partial t} + U\frac{\partial h}{\partial x} = \left(\frac{\partial \phi}{\partial z}\right)_{(z=0)} = -k\phi^+_{(z=0)}. \tag{4.2}$$

For the lateral force per unit surface we have from the linearized Bernoulli equation:

$$L(x, t) = -2p^+_{(z=0)} = 2\rho\left(\frac{\partial}{\partial t} + U\frac{\partial}{\partial x}\right)\phi^+_{(z=0)} = -2\rho ac^2 k\sin[k\{x-(U+c)t\}]. \tag{4.3}$$

From (4.2) and (4.3) we obtain

$$\left(\frac{\partial}{\partial t} + U\frac{\partial}{\partial x}\right)^2 h = -k\left(\frac{\partial}{\partial t} + U\frac{\partial}{\partial x}\right)\phi^+_{(z=0)} = -\frac{kL}{2\rho}. \tag{4.4}$$

With $k = 2\pi/\lambda$, the lateral force may be expressed in terms of the wavelength:

$$L(x, t) = -\frac{\lambda\rho}{\pi}\left(\frac{\partial}{\partial t} + U\frac{\partial}{\partial x}\right)^2 h. \tag{4.5}$$

Equating the rate of change of vertical momentum to the vertical component of the force, this leads to an equation of motion analogous to (2.7) with $EI = 0$,

$$m\frac{\partial^2 h}{\partial t^2} = T\frac{\partial^2 h}{\partial x^2} - \frac{\lambda\rho}{\pi}\left(\frac{\partial}{\partial t} + U\frac{\partial}{\partial x}\right)^2 h, \tag{4.6}$$

where m is the mass per unit area of the fabric, as in (1.1).

With

$$\alpha = \frac{\lambda\rho}{\pi}, \tag{4.7}$$

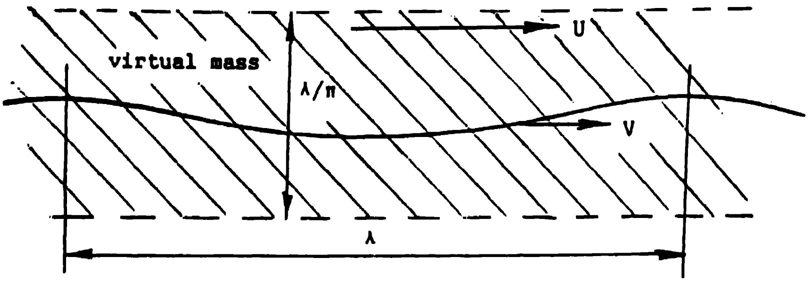

Fig. 4.1. The virtual mass in the two dimensional case.

the analogy with the slender body case is established. This leads to an interpretation of the coefficient $\lambda\rho/\pi$ in the two dimensional case which is somewhat unusual. Apparently the term $\lambda\rho/\pi$ plays the role of a virtual mass. A layer of fluid with thickness λ/π is effectively involved in the two dimensional flag case, see Fig. 4.1. In contrast with the slender body case this term is wavelength dependent.

Neglecting the flexural rigidity in equation (3.2) and putting $\omega/k = V$, we obtain

$$\sigma V^2 - T + \alpha(U - V)^2 = 0. \tag{4.8}$$

By virtue of (4.7) equation (4.8) is equivalent to (1.1) and (1.2) is implied. We note that the slender body results of Section 3 are more general than the two dimensional result in the sense that the cross-sections of the slender bodies need only be symmetrical with respect to the z-x plane, while there is no need for them to be laterally compressed, or 'thin'.

Moreover, we note that in the two dimensional case there are no unique speeds. The wave speed, the divergence speed and the flutter speed are wavelength-dependent, while the wavelength is indeterminate. In the slender body case these three speeds are uniquely determined but the wavelength and the corresponding frequency, being inversely proportional are also indeterminate in the free-free problems for a perfectly flexible body or foil.

5. Experimental results

The results (3.8) for the flutter speed and the critical tension will be compared with some experimental results for three strips of paper with different spans. These strips were mounted in the M-tunnel of the Aerospace Department in Delft, as indicated in Fig. 5.1. The test section of the M-tunnel is $0.40 \times 0.40\,\mathrm{m}^2$ and the speed range used was from 7 m/s to 16 m/s.

The end conditions for the strips were of the free-free type; the cable mountings restrained the strips only in the streamwise direction. The weights attached to the trailing edges were used to vary the tension in the strips. The tensions applied were

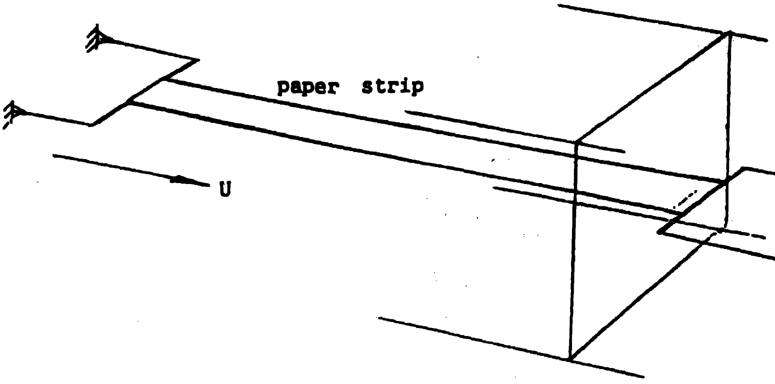

Fig. 5.1. The experimental set up.

sufficiently large with respect to the variations due to viscosity to justify the assumption of constancy of the tension. The length of the paper strips was 0.96 m. Three spans, 0.25 m, 0.165 m and 0.085 m were used. The mass density of the paper was $1.31 \times 10^3\ \mathrm{kg\,m^{-3}}$. The flexural rigidity was considered negligible, the thickness being 0.10×10^{-3} m. The tension applied went up to 2.6 N for the strip of largest span.

The following procedure was followed: weights were installed to adjust the tension. Then the wind tunnel speed was increased to the point where instability was observed. Then the tension and the corresponding dynamic pressures were plotted.

The results are given in Figs 5.2 and 5.3. In the latter the appropriate theoretical values are compared with the experimental values in terms of a referential tension defined by

$$T^* = U^2 \frac{\eta^2 \alpha_0 \sigma_0}{\eta \alpha_0 + \sigma_0}, \tag{5.1}$$

where η defines the span of a strip with respect to the span $b_0 = 0.085$ m of strip 3:

$$b = \eta b_0. \tag{5.2}$$

For α_0, the apparent mass per unit length of the reference strip, we have the mass of air enclosed by the circumscribed circular cylinder:

$$\alpha_0 = \rho \frac{\pi}{4} b_0^2 = 7.32 \times 10^{-3}\ \mathrm{kg/m},$$

and for σ_0 one has

$$\sigma_0 = 1.13 \times 10^{-2}\ \mathrm{kg/m}.$$

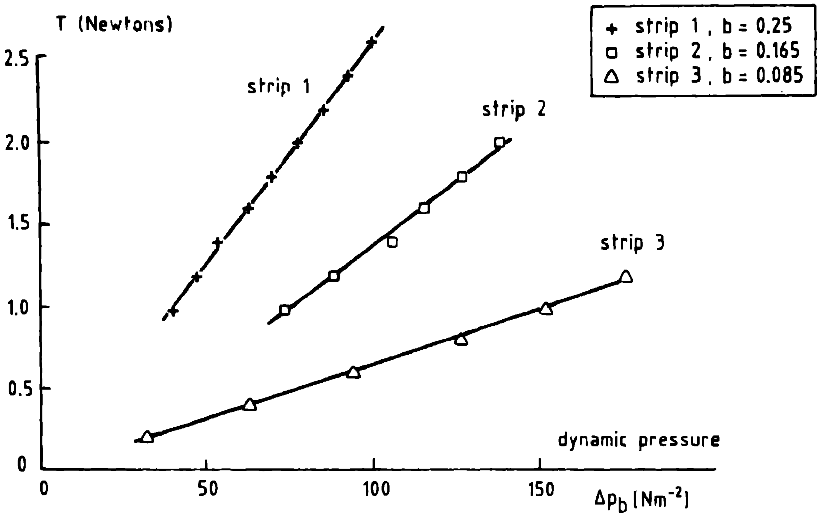

Fig. 5.2. The experimental results for the relation between the dynamic pressure $\Delta p_b = \frac{1}{2}\rho U^2$ and the tension in the strips at the trailing edge.

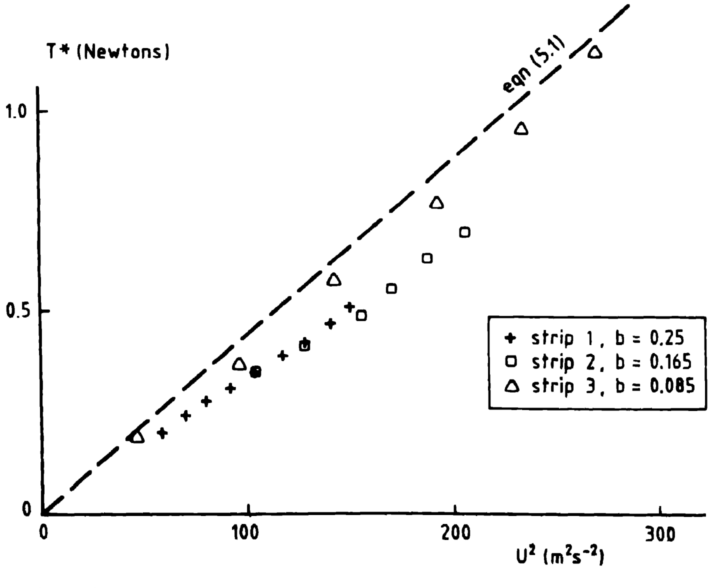

Fig. 5.3. Comparison of the theoretical T^* (equation 5.1) and the experiments with three strips. In fact, only strip 3 ($b/l = 0.09$) is 'slender'.

We note that the experimental results for strip 3 (span $b = 0.085$ m are closest to the theoretical prediction. Clearly strip 3 is 'more slender' than the other two.

6. Concluding remarks

From Fig. 5.2 it can be seen that the agreement of theory with experiment for strip 3, with aspect ratio $b/l = 0.09$, is satisfactory. The other strips, with $b/l = 0.17$ and 0.27, are not so slender and the agreement is less satisfactory. In all cases the critical speed is (safely) underpredicted. One reason is probably the neglect of viscous effects in the theory. In the experiments the tension due to the weights applied is only a minimum value at the trailing edge. The actual tension will slowly increase to some higher value (larger by the amount of the drag of the strip) at the leading edge. Thus one would expect the trailing part to be more unstable than the leading part. This however, could not be observed. Whenever flutter set in, the strip moved violently along the whole length.

Equation (3.8i) indicates that underpredicting U_{cr} may be due not only to underestimating T but also to overprediction of α. Strictly speaking, the value $\pi b^2/4$ (2.4) for the thin strip should be considered as an upper limit for l and λ tending to infinity. It may be noted that in the short wave limit, $\lambda/b \to 0$, the virtual mass α is given by (4.7) which vanishes with λ, rather than by (2.4). Obviously, only a more complete three dimensional lifting surface theory could match and incorporate both limits.

Acknowledgment

The experiments were carried out by two students, R.Y.C.M. Poland and A.J.J. Raayman, to whom the author expresses his gratitude.

References

1. Milne-Thomson, L.M., *Theoretical Hydrodynamics*, 5th edn. London: MacMillan (1968).
2. Munk, M.M., The aerodynamic forces on airship hulls. Report 184 (1923) NACA, pp. 451–468.
3. Lighthill, M.J., Note on the swimming of slender fish, *J. Fluid Mech.* 9 (1960) 305–317.
4. Paidoussis, M.P., Dynamics of flexible slender cylinders in axial flow, *J. Fluid Mech.* 26 (1966) 717–751.
5. Pao, H.P., Dynamical stability of a towed thin flexible cylinder, *J. Hydronautics* (1971) 144–150.
6. Coene, R., The swimming of flexible slender bodies in waves, *J. Fluid Mech.* 72 (1975) 289–303.
7. Raayman, A.J.J., Unpublished Report of the Department of Aerospace Engineering of the Delft University of Technology, TZ verslag TUD (1987).

PREFACE
Image analysis as measuring technique in flows

Progress in fluid mechanics depends heavily on the availability of good experimental data which can inspire new ideas and concepts but which are also necessary to check and validate theories and numerical calculations. The usual experimental probes, such as the pitot tube, the hot wire but also the more advanced laser-doppler equipment, can be characterized as point measurements, i.e. they only give us information in a single spatial point in the flow field. Although useful, such information is at the same time quite limited especially when flow phenomena are dominated by spatial structures. A primary example of the latter case is turbulent flow. One may even venture to say that these limitations of experimental tools have hampered the progress in this field.

With the advent of new recording and image analysis techniques new and promising experimental methods in fluid flows have presented themselves which are able to obtain spatial information. In some aspects these techniques are almost old-fashioned because they use the well established methods of flow visualization. However, the progress lies in the fact that now we are able to obtain quantitative information from these visualizations by applying the methods of image analysis. Examples are the rather newly developed techniques such as particle tracking velocimetry (PTV), particle image velocimetry (PIV) and laser induced fluorescence (LIF).

Within the regular series of Euromech colloquia a meeting was organized to discuss the rapid developments in this new field of the application of image analysis techniques to flow measurements. The meeting was held at the Delft University of Technology from July 2 until July 5, 1991 under the title Euromech 279, Image Analysis as Measuring Technique in Flows.

At this colloquium invited lectures were given by experts in the field on various specific topics. In addition shorter presentations were given by the participants on their recent results. We feel that some of these presentations are interesting for a wider audience, because they offer up to date information on this rapidly developing new experimental field. Therefore, participants at the colloquium were invited to submit their presentations for publication.

All submissions were subjected to the usual reviewing procedure. As an outcome of this procedure four papers have been selected to be published in this issue of *Applied Scientific Research.* These papers are also thought to represent characteristic examples of various techniques. The other papers, which certainly contain interesting and new material on various aspects of image analysis, have been collected in a proceedings. In this proceedings the four articles mentioned above have also been reprinted so that a rather complete overview is given of the present state of the art on the use of image analysis techniques in flow measurements.

The table of contents of the proceedings reads:

R. D. Keane and R. J. Adrian:
Theory of cross-correlation analysis of PIV images
S. B. Dalziel:
Decay of rotating turbulence: Some particle tracking experiments
H. Stapountzis, J. Westerweel, J. M. Bessem, A. Westendorp and F. T. M. Nieuwstadt:
Measurements of product concentrations of two parallel reactive jets using digital image processing
H. A. Siller, R. J. Perkins and G. Janke:
Image analysis of oil film interferometry—a method of measuring wall shear stress distributions
L. Lourenco:
Recent advances in LSV, PIV and PTV
P. Guibert, Q. C. Duan, M. Murat, J. Julien:
Development of particle image velocimetry: a new computation method with directional resolution
A. Chavez and F. Mayinger:
Algorithms for automatic measurements of size and velocity of spray droplets from holography reconstructions
J. Massons, Jna. Gavalda, J. Escoda, X. Ruiz and F. Diaz
Characterization of Savonius rotor wake using image analysis processing techniques
V. Baier, W. Bechteler and S. Hartmann
An application of image processing methods to determine the critical shear stress in sewer systems
M. P. Arroyo and C. A. Greated:
A three dimensional particle image velocimetry system and its application to the measurement of acoustic streaming
C. Hugi and A. Mueller:
A camera for measuring density, size and velocity of rising air bubbles and water velocity in a bubble plume
D. R. McCluskey, C. Elgaard, W. J. Easson and C. A. Greated:
The application of PIV to turbulent two-phase flow
P. A. Quinn, D. J. Skyner, C. Gray, C. A. Greated and W. J. Easson
A critical analysis of the particle image velocimetry technique as applied to waves
J. Stefanini, G. Cognet, J. C. Vila, B. Merite, Y. Brenier:
A colored method for PIV technique
A. K. Hind:
Digital PIV applied to flows around artificial heart valves: analysis by autocorrelation

Euromech Colloquium 279
Delft University of Technology
July 2–5, 1991

F.T.M. NIEUWSTADT
Editor

Applied Scientific Research **49**: 191–215, 1992.
© 1992 *Kluwer Academic Publishers. Printed in the Netherlands.*

Theory of cross-correlation analysis of PIV images

RICHARD D. KEANE & RONALD J. ADRIAN

Department of Theoretical and Applied Mechanics, University of Illinois at Urbana-Champaign, 216 Talbot Lab., 104 S. Wright Street, Urbana, IL61801-1793, U.S.A.

Abstract. To improve the performance of particle image velocimetry in measuring instantaneous velocity fields, direct cross-correlation of image fields can be used in place of auto-correlation methods of interrogation of double- or multiple-exposure recordings. With improved speed of photographic recording and increased resolution of video array detectors, cross-correlation methods of interrogation of successive single-exposure frames can be used to measure the separation of pairs of particle images between successive frames. By knowing the extent of image shifting used in a multiple-exposure and by *a priori* knowledge of the mean flow-field, the cross-correlation of different sized interrogation spots with known separation can be optimized in terms of spatial resolution, detection rate, accuracy and reliability.

For the direct cross-correlation method of single-exposure, double-frame systems which model video array detector interrogation and of double-exposure single-frame systems which generalize earlier direct auto-correlation methods of interrogation of photographic recordings, optimal system parameters are recommended for a range of velocity fields in order to eliminate signal bias and to minimize loss of signal strength. The signal bias resulting from velocity gradients in auto-correlation analysis can be eliminated in cross-correlation interrogation by appropriate choice of the optimal parameters. Resolution, detection rate, accuracy and reliability are compared with direct auto-correlation methods for double- and multiple-pulsed systems.

Key words: PIV, cross-correlation, auto-correlation

1. Introduction

Particle Image Velocimetry (PIV) uses images of marker particles in a fluid flow to measure instantaneous velocity fields in experimental fluid mechanics. In general, the particles are illuminated by pulsed sheets of light at precise time intervals to produce images that are recorded on photographic film or on a video camera array. The analysis of these images to measure the particles displacements is a key element in the PIV technique and many approaches have been proposed and explored experimentally. In the high image density case, the concentration of particles is large so that it is natural to measure the average displacement of *local groups of particles*, as opposed to tracking individual particles. This case will be the principal topic of the present work. The preferred forms of analysis of high image density images are based on correlation techniques that are performed numerically on digitized image data, numerically on the digitized Young's fringe patterns that result from optical Fourier transforming of the image data, or in a purely optical correlation processor. Each of these methods is basically similar so it suffices to discuss the first of the three.

In previous work, two variations of the PIV technique have been studied theoretically and by numerical simulation. Adrian [1] and Keane and Adrian [6] analyzed double-exposure single-frame PIV, in which an individual frame of photographic film or of a video camera array is exposed to a double light pulse. This is the most commonly used PIV recording technique. Keane and Adrian [7] analyzed autocorrelation of multiple exposures on a single frame. Examples of this approach are the experiments on fluid flow behind an impulsively started circular cylinder by Lourenco and Krothapalli [11] and Meynart, Simpkins and Dudderar's [12] study of an unsteady descending plume in a convection cell. More recently, Cenedese and Paglialunga [4] used multiple exposures to study vertical structures in a mixer and Arroyo, Yonte, Quintanilla and Saviron [3] investigated Rayleigh-Benard convection using a number of exposures ranging from 13 to 40.

An alternative to single frame recording using either double or multiple pulses is to record images on multiple frames using video cameras or high speed cinematography. Although cinematic recording offers higher resolution than digitized video camera data recording, the precision needed for frame registration and the relative ease of video camera recording have made video recording an attractive alternative. Other methods of obtaining single images include the use of two different laser wavelengths and two color recording of consecutive exposures of a double-pulsed system onto color film and the subsequent use of color filters to retrieve first and second images [5]. Adrian and Zoltani [2] obtained separate image frames on adjacent halves of a single video array by changing the polarization of successive illuminating light sheets and using a polarization sensitive prism assembly to separate the image fields. In these cases, it is natural to evaluate the image displacement between pairs of frames by *cross-correlation*. Spatial cross-correlations of pairs of single-exposure frames have been used by Kimura and Takemori [9] to analyze flow around a circular cylinder, and Willert and Gharib [15] have applied a similar procedure to analysis of a vortex ring experiment. Goss et al. [5] also used cross-correlation of pairs of frames of color-filtered images to study a jet diffusion flame.

Furthermore, cross-correlation can be applied with some advantage to the analysis of double- or multiple-exposure single-frame images by cross-correlating two different regions on the same frame. Turbulent open channel flow has been investigated using this approach by Utami et al. [14].

In multiple-exposure, single-frame photographic recording, a number of pulsed illuminating beams forms light sheets of variable center and thickness within the flow field in order to record multiple images of the particles in the light sheets, on a single photographic recording. Knowledge of the flow field enables the locations and thicknesses of the illuminating sheets to be chosen to enhance successive particle image recording. In a study of the turbulent characteristics of droplets injected into a pipe flow, Lee et al. [10] located multiple illuminating light sheets perpendicular to the direction of mean flow with spatial separations based on the axial velocity of the droplets in order to record multiple droplet images on a single exposure. The interrogation is then carried out by illuminating two small interrogation spots on the single frame, centered at $\mathbf{X}_1$ and $\mathbf{X}_2$ and with diameters d_1 and d_2, with interrogation beams of intensity $I_{I1}(\mathbf{X})$ and $I_{I2}(\mathbf{X})$ respectively as shown in Fig. 1. With single-exposure multiple-frame PIV, the images of seeded particles within successive light sheets are recorded on each frame. The interrogation spots, identical in location and

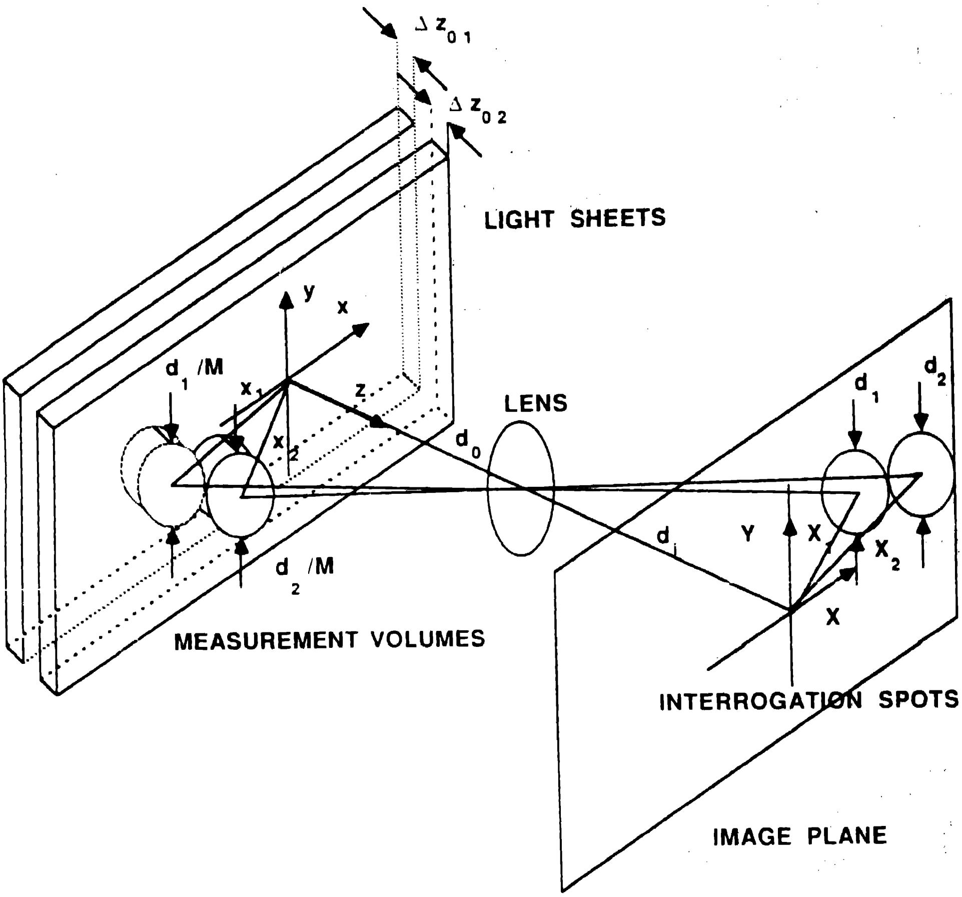

Fig. 1. Light sheets and image recording system for planar pulsed laser velocimetry.

size to those above, are then illuminated by interrogation beams. The displacement of the particle image $\Delta\mathbf{X}(\mathbf{X}_1)$ is determined and scanning $\mathbf{X}_1$ and $\mathbf{X}_2$ over each frame produces displacements over the entire image plane.

If the images are recorded on a digitized video detector array, instead of a photograph, the interrogation spots can be defined by choosing digital window functions with shapes corresponding to I_{I1} and I_{I2}, to multiply the data in the array detector. The image displacements then yield the measured in-plane velocity for each interrogation spot centered at $\mathbf{X}_1$.

The present work is an extension of that reported by Keane et al. [8] and Keane and Adrian [7]. Its purposes are, firstly, to develop a theoretical description of the mean value of the cross-correlation function of particle image fields for the case of locally linear fluid velocity variation. Secondly, the properties of the cross-correlation function as a means of estimating the particle image displacement are explored using Monte Carlo simulation. As with earlier auto-correlation methods, the performance of this PIV method is determined by the spatial resolution, the detection probability and the accuracy of the in-plane velocity measurements. Unlike auto-correlation analysis, the spatial resolution is limited by the maximum spatial separation of recorded particle images as well as the size of the first interrogation spot and is assumed here to be the greater of these two values. The detection probability is defined as the fraction of interrogation spots that produce velocity measurements that satisfy certain interrogation criteria; and the accuracy is defined as the error of all detections that satisfy the interrogation criteria, whether they are valid or not, with respect to the true velocity field. These three parameters are affected by the experimental configuration, the recording medium, the interrogation procedure and its detection criteria so that optimization of PIV performance necessitates an understanding of all these facets of the technique. Finally, the cross-correlation procedure is compared to the auto-correlation procedure for double-pulsed and multiple-pulsed single-exposure recording.

2. Interrogation by spatial cross-correlation

Following the notation and theory developed by Adrian [1], the transmissivity of a distortion-free nearly paraxial photographic recording of a single exposed flow field with illuminating light sheet intensity $I_{01}(\mathbf{x})$, sampled at time t is

$$\tau_1(\mathbf{X}) = \sum_i I_{01}(\mathbf{x}_i)\tau_0(\mathbf{X} - M\mathbf{x}_i(t)), \tag{1}$$

where τ_0 is the transmissivity of a particle image and where $\mathbf{x}_i(t)$ is the location of the ith particle in the flow field at time t. The transmitted light of the photograph after interrogation by a light beam of intensity $I_{I1}(\mathbf{X} - \mathbf{X}_1)$ centered at $\mathbf{X}_1$ with diameter d_1 is

$$I_1(\mathbf{X}) = I_{I1}(\mathbf{X} - \mathbf{X}_1)\tau_1(\mathbf{X}). \tag{2}$$

Similarly, for a second recording of the flow field sampled at time $t + \Delta t$, we have

$$\tau_2(\mathbf{X}) = \sum_i I_{02}(\mathbf{x}_i)\tau_0(\mathbf{X} - M\mathbf{x}_i(t + \Delta t)) \tag{3}$$

and

$$I_2(\mathbf{X}) = I_{I2}(\mathbf{X} - \mathbf{X}_2)\tau_2(\mathbf{X}). \tag{4}$$

For a double exposure of the flow field, with linear, unsaturated recording, the transmissivity of the photographic recording is additive:

$$\tau(\mathbf{X}) = \tau_1(\mathbf{X}) + \tau_2(\mathbf{X}). \tag{5}$$

Then the transmitted light intensities after interrogation, $I_1(\mathbf{X}), I_2(\mathbf{X})$, are given by equations (2) and (4) with τ replacing τ_1 and τ_2 respectively.

In PIV the two-dimensional spatial convolution of I_1 and I_2 with separation vector s

$$R(\mathbf{s}) = \int I_1(\mathbf{X}) I_2(\mathbf{X} + \mathbf{s})\, d\mathbf{X} \tag{6}$$

is used to determine the image displacement. It approximates a true spatial cross-correlation to the extent that the area integral corresponds to the ensemble average of $I_1(\mathbf{X})I_2(\mathbf{X} + \mathbf{s})$. For brevity, it is conventional to refer to the estimator in (6) as the cross-correlation, and we shall continue that practice here.

If the images are recorded on a video detector array instead of a photograph, the interrogation spots can be defined by choosing digital window functions, with shapes corresponding to I_{I1} and I_{I2} to multiply the data in the detector arrays. Thus, the formula defined above applies to both photographic recording and to video detector array recording.

Following previous work [1, 6], it is convenient to decompose the estimator for cross-correlation of single-exposure frames into three components

$$R(\mathbf{s}) = R_C(\mathbf{s}) + R_D(\mathbf{s}) + R_F(\mathbf{s}), \tag{7}$$

where R_C is the convolution of the mean intensities, R_F is the fluctuating noise component of the correlation estimator and R_D is the displacement correlation which gives the image displacement. The equations for these components are presented in the Appendix. In contrast, either the cross-correlation estimator or the auto-correlation estimator of double-exposure frames consist of five components: $R_C, R_F, R_{D^+}, R_{D^-}$ and R_P where R_{D^+} and R_{D^-} are displacement peaks which are reflectionally symmetric for auto-correlation analysis and R_P is the self-correlation peak or "pedestal" (Adrian [1]). When using cross-correlation of single-exposure frames there is no necessity to employ image shifting to resolve directional ambiguity, and there is no correlation of particle images in either exposure with themselves. Thus the R_P component which occurs in the correlation of multiple-exposure frames is absent from (7). The dynamic range of the cross-correlation estimator of single-exposure frames is larger than that of the auto-correlation estimator if the latter is formed without image shifting. Furthermore, as this cross-correlation estimator does not include any contribution from particle images in a given frame correlating with other images in the same frame, the number of random noise peaks in cross-correlation analysis from $(R_C + R_F)$ in single-exposure frames is approximately half of the number of peaks produced in cross-correlation and auto-correlation analysis of double-exposure frames.

The components of the spatial cross-correlation function for a pair of single-exposure interrogation spots with $I_{01} = I_{02}, I_{I1} = I_{I2}, \mathbf{X}_1 = \mathbf{X}_2$ and $d_I = d_1 = d_2$ are

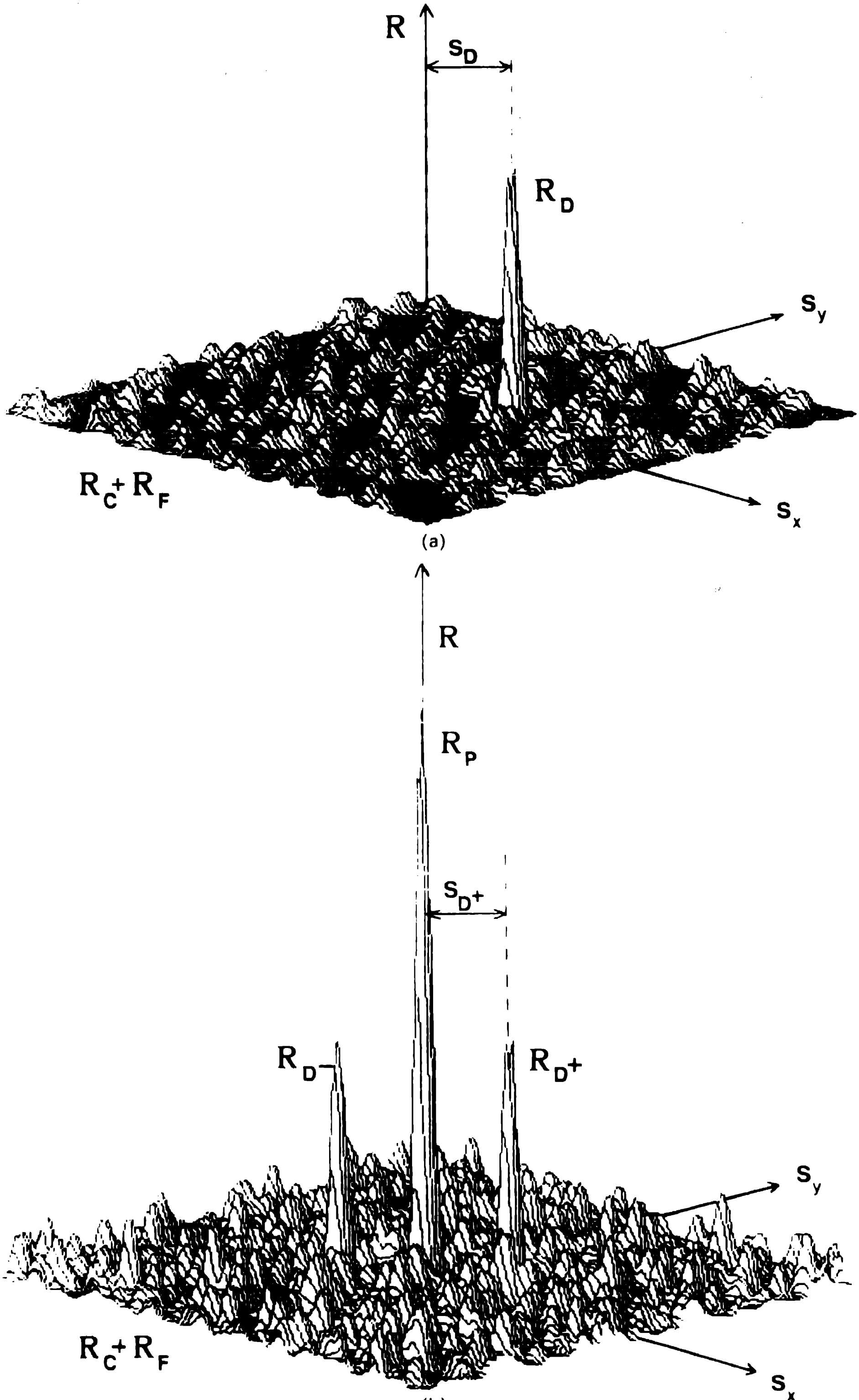

(a)

(b)

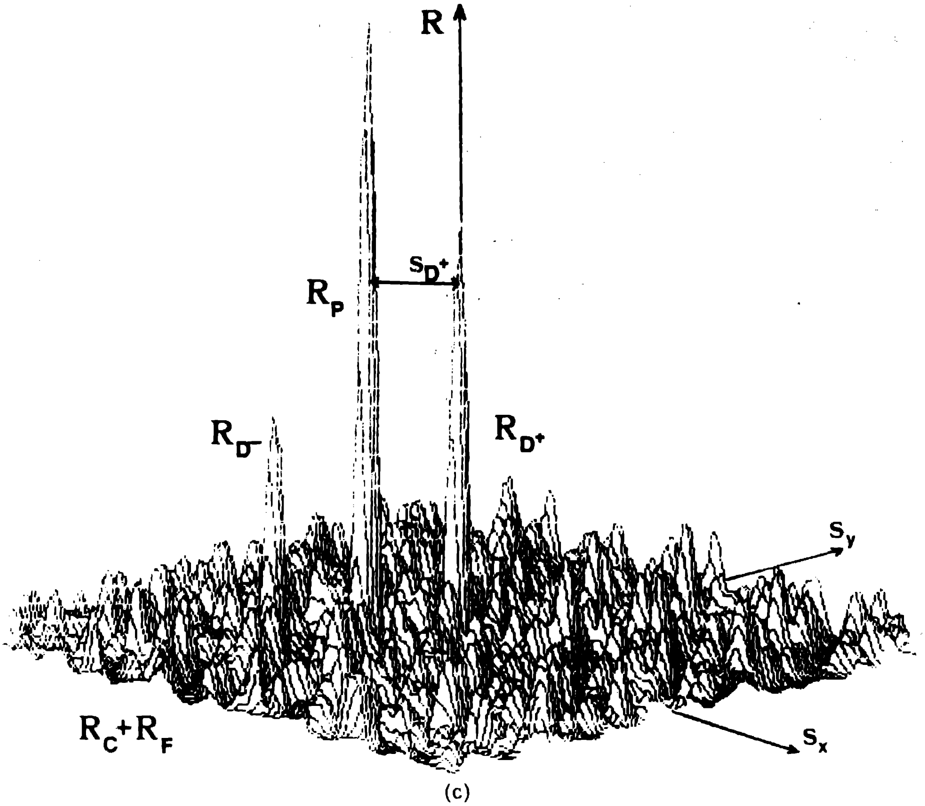

Fig. 2. (a) Cross-correlation function R of image transmissivity $I(\mathbf{X})$ for single-exposure frames where $N_I = 15$, $\Delta\mathbf{X}/d_I = (0.10, 0.10)$. (b) Auto-correlation function R of image transmissivity $I(\mathbf{X})$ where $N_I = 15$, $\Delta\mathbf{X}/d_I = (0.10, 0.10)$. (c) Cross-correlation function R of image transmissivity $I(\mathbf{X})$ for double-exposure frames with optimal window displacement $\Delta\mathbf{X} = \mathbf{X}_2 - \mathbf{X}_1$ where $N_I = 15$, $\Delta\mathbf{X}/d_I = (0.10, 0.10)$.

illustrated in Fig 2a for a constant in-plane velocity field and for which each interrogation spot contains randomly located particles for which $N_I = 15$. For the corresponding double-pulsed exposure, the auto-correlation function and the cross-correlation function with $\mathbf{X}_2 = \mathbf{X}_1 + \Delta\mathbf{X}$ are illustrated in Figs 2b and 2c, respectively.

As for auto-correlation function analysis, the mean image displacement across a given interrogation spot is determined by locating the centroid of R_D, namely

$$\mu_D = \frac{\int \mathbf{s}R_D(\mathbf{s})\,d\mathbf{s}}{\int R_D(\mathbf{s})\,d\mathbf{s}}, \tag{8}$$

from which the mean velocity is estimated as $\mu_D/M\Delta t$, (M is the magnification).

It can be seen from Fig. 2 that the approximation of locating the peak in $R_D(\mathbf{s})$ by locating the peak of R in the s-plane of the cross-correlation function of single-exposure frames will be more accurate than a similar procedure for the auto-correlation function as the random noise peaks from $(R_C + R_F)$ are approximately halved in single-exposure analysis and R_P is absent there also. In addition, the cross-correlation function for the double-exposure frames contains a taller peak of R_{D^+} than auto-correlation when the displacement between frames is optimized, as in Fig. 2c.

3. Mean cross-correlation

To compare the cross-correlation function R for single-exposure double-pulsed systems with the auto-correlation functions for both double- and multiple-exposure systems which have been analyzed in earlier works [6, 7], the statistical properties of the cross-correlation function need to be determined. An ensemble of pairs of single-exposure recordings and corresponding double-exposure recordings of identical velocity fields is used in which each realization contains different sets of randomly located particles. For a given velocity field $\mathbf{u}(\mathbf{x})$, the conditional average $\langle R(\mathbf{s})|\mathbf{u}\rangle$ calculated over random particle locations measures the mean behavior of R and its components, given the flow field $\mathbf{u}$.

The conditional average of R for single-exposure systems is determined by conditionally averaging equation (7). It has the form

$$\langle R(\mathbf{s})|\mathbf{u}\rangle = \langle R_C(\mathbf{s})|\mathbf{u}\rangle + \langle R_D(\mathbf{s})|\mathbf{u}\rangle. \tag{9}$$

The form of the conditional average for the cross-correlation function for double-exposure systems is identical to that for autocorrelation, namely

$$\langle R(\mathbf{s})|\mathbf{u}\rangle = \langle R_C(\mathbf{s})|\mathbf{u}\rangle + \langle R_P(\mathbf{s})|\mathbf{u}\rangle + \langle R_{D^+}(\mathbf{s})|\mathbf{u}\rangle + \langle R_{D^-}(\mathbf{s})|\mathbf{u}\rangle. \tag{10}$$

In each case $\langle R_F(\mathbf{s})|\mathbf{u}\rangle = 0$.

To facilitate the study of the important parameters of $\langle R(\mathbf{s})|\mathbf{u}\rangle$ and to compare the behavior of these parameters to those of double- and multiple-pulsed systems using auto-correlation, identical specific models of transmissivity functions, light intensities and particle image properties have been chosen. Thus, the intensities of the light sheet pulses I_{oi} are modelled as either top hat functions equal to I_0 within the light sheets and zero outside of them, or as Gaussian functions centered on the light sheets with width Δz_{oi} measured at the e^{-2} points. The interrogation beam intensities are modelled as Gaussian functions centered at $\mathbf{X}_1$ and $\mathbf{X}_2$ with diameters d_1 and d_2 respectively, while all particle image transmissivities are Gaussian functions centered at the image center with image diameter d_τ. Thus we have

$$I_{oi}(z - z_{oi}) = \begin{matrix} I_0 & |z - z_{oi}| < \Delta z_{oi}/2 \text{ or } I_0 \exp(-8(z - z_{oi})^2/\Delta z_{oi}^2), \\ 0 & \text{otherwise} \end{matrix} \tag{11}$$

$$I_{I1}(\mathbf{X}-\mathbf{X}_1) = A_1 \exp(-8|\mathbf{X}-\mathbf{X}_1|^2/d_1^2), \tag{12}$$

$$I_{I2}(\mathbf{X}-\mathbf{X}_2) = A_2 \exp(-8|\mathbf{X}-\mathbf{X}_2|^2/d_2^2) \tag{13}$$

and

$$\tau_0(\mathbf{X}) = \frac{8\tau_{00}}{\pi d_\tau^2} \exp(-8|\mathbf{X}|^2/d_\tau^2), \tag{14}$$

where $\tau_{00} = \int \tau_0\, d\mathbf{X}$ is determined by the photographic process and the development process.

The components of the cross-correlation of single-exposure images in (9) for a general displacement field $\Delta\mathbf{x}(\mathbf{x}, t)$ become

$$\langle R_C(\mathbf{s})|\mathbf{u}\rangle = \frac{1}{\pi} I_0^2 A_1 A_2 \tau_{00}^2 \frac{(N_I^*)^2}{d_*^2} \exp\left(-\frac{4}{d_*^2}|\mathbf{s}+\mathbf{X}_1-\mathbf{X}_2|^2\right), \tag{15}$$

$$\begin{aligned}\langle R_D(\mathbf{s})|\mathbf{u}\rangle = C \int d\mathbf{x}\, I_{01}(z) I_{02}(z+\Delta z) \int d\mathbf{X}\, A_1 A_2 \exp(-8|\mathbf{X}-\mathbf{X}_1|^2/d_1^2)\\ \times \exp(-8|\mathbf{X}-\mathbf{X}_2+\mathbf{s}|^2/d_2^2) \times \left(\frac{8\tau_{00}}{\pi d_\tau^2}\right)^2 \exp(-8|\mathbf{X}-M\mathbf{x}|^2/d_\tau^2)\\ \times \exp(-8|\mathbf{X}-M\mathbf{x}+\mathbf{s}-M\Delta\mathbf{x}|^2/d_\tau^2).\end{aligned} \tag{16}$$

For the cross-correlation of a double-exposure image, the components in (10) are

$$\langle R_C(\mathbf{s})|\mathbf{u}\rangle = \frac{1}{\pi} I_0^2 (A_1+A_2)^2 \tau_{00}^2 \frac{(N_I^*)^2}{d_*^2} \exp\left(-\frac{4}{d_*^2}|\mathbf{s}+\mathbf{X}_1-\mathbf{X}_2|^2\right), \tag{17}$$

$$\langle R_{D^+}(\mathbf{s})|\rangle = \langle R_D(\mathbf{s})|\mathbf{u}\rangle, \tag{18}$$

$$\langle R_P(\mathbf{s})|\mathbf{u}\rangle = \frac{2}{\pi} I_0^2 A_1 A_2 \tau_{00}^2 \frac{N_I^*}{d_\tau^2} \exp(-4|\mathbf{s}|^2/d_\tau^2) \exp(-8|\mathbf{s}+\mathbf{X}_1-\mathbf{X}_2|^2/(d_1^2+d_2^2)). \tag{19}$$

The average interrogation spot size d_* is defined by

$$1/d_*^2 = \frac{1}{2}(1/d_1^2 + 1/d_2^2) \tag{20}$$

and the average particle image density N_I^* is defined consequently as a weighted average of the image densities in each window, $(N_I)_1$, $(N_I)_2$,

$$N_I^* = C\pi\Delta z_0/4M^2 \cdot d_*^2 \tag{21}$$

assuming circular interrogation spots

These results are valid for arbitrary velocity field $\mathbf{u}$ through the displacements $\Delta\mathbf{x}$, and they generalize earlier results on the auto-correlation function for double-pulsed PIV in [6]. From these earlier results on double-pulsed PIV, [6], it can be seen that the mean intensity correlation, $\langle R_C(\mathbf{s})|\mathbf{u}\rangle$ in equation (15) is one quarter of the corresponding mean intensity correlation for auto-correlation of double-exposure images and the displacement correlation, $\langle R_D(\mathbf{s})|\mathbf{u}\rangle$ in equation (16) is identical to that for auto-correlation of double-exposure images for arbitrary velocity vector fields $\mathbf{u}$ where $A_1 = A_2 = I_{I0}$, $d_1 = d_2 = d_I$ and $\mathbf{X}_1 = \mathbf{X}_2$. Thus, with identical interrogation spots for comparison, spatial cross-correlation of single-exposure double-frame PIV, like auto-correlation analysis of double-exposure single-frame PIV, will be limited in signal strength by loss-of-pairs effects due to in-plane and out-of-plane motion. However, as seen in Fig. 2, the height of the spurious noise correlation peak in single-exposure double-frame PIV is approximately half that in double-exposure single-frame PIV. In general, the mean intensity correlation is a poor estimator for the peak of the noise correlation, being too low for the seeding densities considered here.

In the presence of a velocity field which varies sufficiently slowly that it can be approximated by a locally constant velocity field within an interrogation spot, the mean displacement component of both single- and double-exposure cross-correlation functions can be written more simply as

$$\begin{aligned}\langle R_D(\mathbf{s})|\mathbf{u}\rangle &= \frac{1}{\pi} A_1 A_2 I_0^2 \frac{\tau_{00}^2}{d_\tau^2} \{N_I^* F_0(\Delta z) \exp(-8|\mathbf{s}-(\mathbf{X}_2-\mathbf{X}_1)|^2/(d_1^2+d_2^2))\} \\ &\quad \times \exp\{-4|\mathbf{s} - M\Delta\mathbf{x}|^2/d_\tau^2\} \\ &= \frac{1}{\pi} A_1 A_2 I_0^2 \frac{\tau_{00}^2}{d_\tau^2} \{N_I^* F_0(\Delta z) F_I(\mathbf{s})\} \exp\{-4|\mathbf{s} - M\Delta\mathbf{x}|^2/d_\tau^2\},\end{aligned} \tag{23}$$

where F_I is the normalized correlation of the interrogation intensity across the interrogation spots, generalized from Adrian [1], namely

$$F_I(\mathbf{s}) = \int I_{I1}(\mathbf{X}-\mathbf{X}_1) I_{I2}(\mathbf{X}-\mathbf{X}_2+\mathbf{s})\, d\mathbf{X} \bigg/ \int I_{I1}(\mathbf{X}) I_{I2}(\mathbf{X})\, d\mathbf{X}. \tag{24}$$

Likewise, $F_0(\Delta z)$ is the normalized correlation of the intensities of two successive light pulses in terms of the out-of-plane displacement Δz between successive pulses,

$$F_0(\Delta z) = \int I_{01}(z - z_{01}) I_{02}(z - z_{02} + \Delta z)\, dz \bigg/ \int I_{01}(z) I_{02}(z)\, dz. \tag{25}$$

These terms reduce $\langle R_D(\mathbf{s})\rangle$ due to loss-of-pairs as a consequence of in-plane motion and out-of-plane motion, respectively. $N_I^* F_I F_0$ represents the mean number of particle image pairs, weighted by the light intensity distribution and is the mean effective particle image density contributing to $\langle R_D(\mathbf{s})|\mathbf{u}\rangle$.

In order to minimize the loss-of-pairs effect, the interrogation spot shift, $\mathbf{X}_2 - \mathbf{X}_1$, can be chosen so that $\mathbf{X}_2 - \mathbf{X}_1 = M\Delta\mathbf{x}$, and the second light sheet thickness, Δz_{02}, and relative position $(z_{02} - z_{01})$, can be chosen to ensure that all particles whose first images lie in the first light sheet will have second images in the second light sheet. In addition, by selecting d_2 sufficiently larger than d_1 all particles with images in the first spot have images again in the second spot so that $F_0 = F_I = 1$ and the effective image density becomes N_I^* with the signal strength maximized to be

$$\langle R_D(\mathbf{s})|\mathbf{u}\rangle = \frac{1}{\pi} A_1 A_2 I_0^2 \frac{\tau_{00}^2}{d_\tau^2} N_I^* \tag{26}$$

when $\mathbf{s} = M\Delta\mathbf{x}$, as illustrated for cross-correlation of a double-exposure system in Fig. 2c.

In the case where the velocity field varies sufficiently rapidly that velocity variations within the interrogation volume cannot be ignored, spatial cross-correlation analysis of single-exposure and double-exposure double-pulse PIV can reduce and eliminate gradient bias, which, in previous double- and multiple-pulse PIV systems, biased the location of the centroid of $\langle R_D\rangle$ towards the displacement of lower speed particles. Choosing adequate size and reasonably correct relative displacement of the second interrogation window ensures that all first images are captured again in the second window, and it eliminates in-plane gradient bias because no images of more rapidly moving particles are lost. However, the distribution of image displacements reduces the amplitude and increases the width of the displacement correlation peak reducing the probability of a valid measurement by producing more undetectable peaks in regions of large velocity gradient. This detection bias is independent of the size or relative displacement of the second interrogation window and reduces the apparent velocity gradient for a given realization by measuring noise peaks in $R_C + R_F$ rather than true correlation peaks. The detection bias depends upon the random instantaneous noise peaks in $R_C + R_F$ which, in single-exposure systems, have less than half the amplitude of those in comparable double-exposure PIV systems that use either cross-correlation or auto-correlation methods.

Thus gradient bias can be eliminated by appropriate selection of interrogation windows and detection bias occurs less frequently in spatial cross-correlation analysis of single-exposure PIV as will be shown in the next section when individual realizations are examined to compare possible PIV alternative systems.

4. Comparative cross-correlation performance

4.1. Procedure

The comparative performance of the spatial cross-correlation interrogation method of measuring image displacements for a single-exposure or a double-exposure double-pulse PIV system as an alternative to auto-correlation analysis of double or multiple-pulsed systems is measured in terms of three criteria, which were developed previously. These are the spatial resolution, the detection probability and the accuracy of the velocity measurements that are considered to be valid. Random fluctuations of the spatial cross-correlation function for specified dimensionless parameters listed above affect the performance of the interrogation method. Specific details of the interrogation procedure will similarly affect the method's performance.

The interrogation procedure for a single-exposure double-frame PIV system is identical to that of double- and multiple-pulsed systems using auto-correlation methods, but it is more simple as there is no self-correlation component R_P to consider. It locates the highest peak in $R(\mathbf{s})$ and, in assuming this peak corresponds to R_D, compares it to the second tallest peak, thereby determining the detectability, D, as the ratio of the tallest peak to the second tallest peak. As there is no self correlation component, R_P, in the cross-correlation function and as there is an arbitrary displacement, $\mathbf{X}_2 - \mathbf{X}_1$, between interrogation windows, the peak search is conducted over the whole cross-correlation plane. On the other hand, although the cross-correlation function for a double-exposure may contain a self-correlation component R_P, the peak location of R_P is known to be $\mathbf{X}_1 - \mathbf{X}_2$ and the peak search is then conducted over the plane to the right of $(\mathbf{X}_1 - \mathbf{X}_2)$. The centroid of the cross-correlation peak is determined by integrating a small area around the peak, as described in [6] in order to calculate the measured velocity.

4.2. Monte Carlo simulation

As the analysis of the mean cross-correlation function does not directly address questions concerning probabilities of measurement and the fluctuation in the statistics of individual velocity measurements, the numerical simulation of the PIV image field and the interrogation analysis by cross-correlation methods of both single-exposure and double-exposure double-pulse systems have been modified from the multiple-pulse system. The details of the simulation can be found in [6]. The simulation has been performed for three dimensional velocity fields over a range of velocity gradients. Figure 3 shows a simulated region of two interrogation frames in which a constant velocity causes a mean particle displacement with $M\Delta\mathbf{x}/d_1 = (0.10, 0.10, 0.10)$ where $\mathbf{X}_2 = \mathbf{X}_1 + M\Delta\mathbf{x}, (N_I)_1 = 12$ and d_2 is chosen larger than d_1 to ensure no loss-of pairs due to in-plane motion. Although d_2 need be no larger than d_1 in this example which illustrates an optimal relative displacement and a constant velocity field, in general, lack of precise *a priori* knowledge of the velocity field and its gradients necessitates larger second spots to ensure that all particles with first images possess second images in the second spot. Out-of-plane motion within the flow field reduces the number of paired images within the light sheet, as shown. In general, the location and thickness of the light sheets and the size and relative displacement of the interrogation frames can be optimized to ensure that no such loss of paired images will occur.

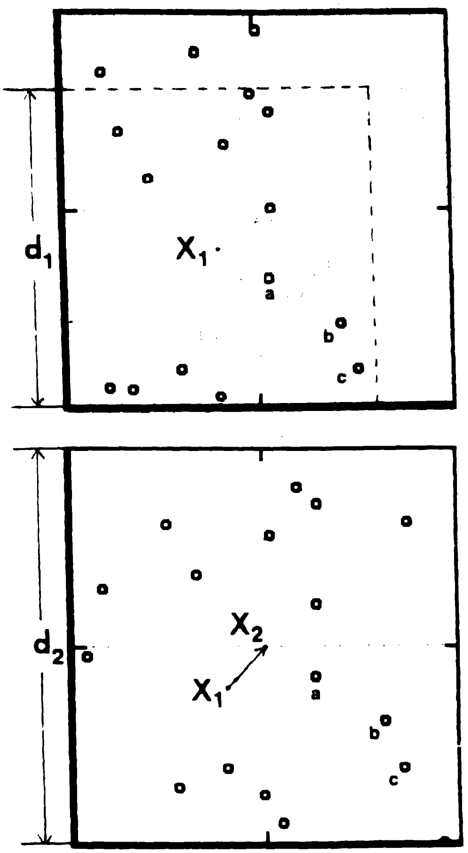

Fig. 3. A simulated pair of interrogation frames for a single-exposure double-frame system in which $(N_I)_1 = 12$, $M\Delta\mathbf{x}/d_1 = (0.1, 0.1, 0.1)$, $\mathbf{X}_2 = \mathbf{X}_1 + M\Delta\mathbf{x}$ and $F_I = 1$.

The detection probability and the valid detection probability for a given ensemble of realizations of experimental parameters are defined in [6].

4.3. Comparative performance

Comparisons of the mean cross-correlation function to previous results for double-pulsed and multiple-pulsed systems, show that the detection probability can be related to the mean effective number of particle image pairs within a pair of interrogation spots, namely $N_I^* F_I F_0$ for cross-correlation analysis and $N_P F_I F_0$ for multiple-pulse auto-correlation analysis, where $N_P = (n - 1)N_I$ for an n-pulse system.

For the case of a constant velocity field, it can be seen from equation (22) that if the interrogation spots are chosen so that their relative separation, $\mathbf{X}_2 - \mathbf{X}_1$, satisfies

$$\mathbf{s} = (\mathbf{X}_2 - \mathbf{X}_1) = M\Delta\mathbf{x} \tag{27}$$

then $F_I = 1$ from equation (24) and there is no loss-of-pairs due to in-plane displacements. Similarly by choosing appropriate light sheet thicknesses and relative positions, out-of-plane pair losses can be eliminated and $F_0 = 1$. This technique has been used for example by Lee et al. [10]. In this case, for a given particle seeding density in the fluid C, the strength of the displacement correlation peak is maximized.

More generally, in the case of a constant or variable velocity field, loss-of-pairs due to in-plane displacements can be eliminated by choosing the relative separation, $\mathbf{X}_2 - \mathbf{X}_1$, to be approximately equal to the local mean image displacement and then choosing d_2 sufficiently larger than d_1 so that all particles with images in the first window have images in the second window. In this case, $F_I = 1$. Out-of-plane pair losses can be eliminated in a similar way to ensure $F_0 = 1$ as well. That is, the second light sheet can be made thicker than the first so as to capture all particles illuminated by the first light pulse. Thus, the effective particle image density is determined by the number of particles in the first window, $(N_I)_1 = N_I = N_I F_I F_0$. The larger second window ensures optimal use of the chosen seeding density.

A comparison of the valid detection probability as a function of the mean effective number of particle image pairs can be made for the cross-correlation analysis of single-exposure and double-exposure images and for the auto-correlation analysis of double-pulse and triple-pulse systems considered in previous work ([6], [7]) using a detectability criterion of $D_0 = 1.2$, for a range of image displacements $|\Delta \mathbf{X}|/d_I$ of constant three-dimensional velocity fields.

In addition to cross-correlation analysis using identical interrogation windows initially and image displacements considered in earlier work, a more general range of larger image displacements, $|\Delta \mathbf{X}|/d_1$, has been used in the cross-correlation analysis, as the relative window separation, $\mathbf{X}_2 - \mathbf{X}_1$, and d_2 have been chosen then to ensure that there is no aliasing of the measurements and no loss-of-pairs, due to in-plane motion. From Figs 2a, b, c and from [7], it can be seen that the non-signal noise peak for cross-correlation analysis of single-exposure systems is generally about half of the corresponding peak for cross-correlation and auto-correlation analysis of double-exposure systems. Furthermore, increasing the second interrogation spot diameter d_2 relative to d_1 within reasonable limits does not increase the non-signal noise peak enough to affect the valid detection probability when $D_0 = 1.2$. A range of (d_2/d_1) from 1.0 to 4.0 was chosen to analyze the effect of superfluous noise peaks, but there was no significant decrease in valid detection probability for the latter case (figures 4a, b). However, a choice of d_2 which is unnecessarily large will reduce the pixel resolution of the first window in the digitization process leading to bias errors as discussed in Prasad et al. [13].

Figure 4 shows the relationship between valid detection probability and the mean effective number of particle image pairs in the interrogation spot for cross-correlation analysis of single-exposure and double-exposure images and auto-correlation analysis of double- and triple-pulse systems. To ensure a 95% valid detection rate for cross-correlation of single-exposure and double-exposure images, it is sufficient to choose

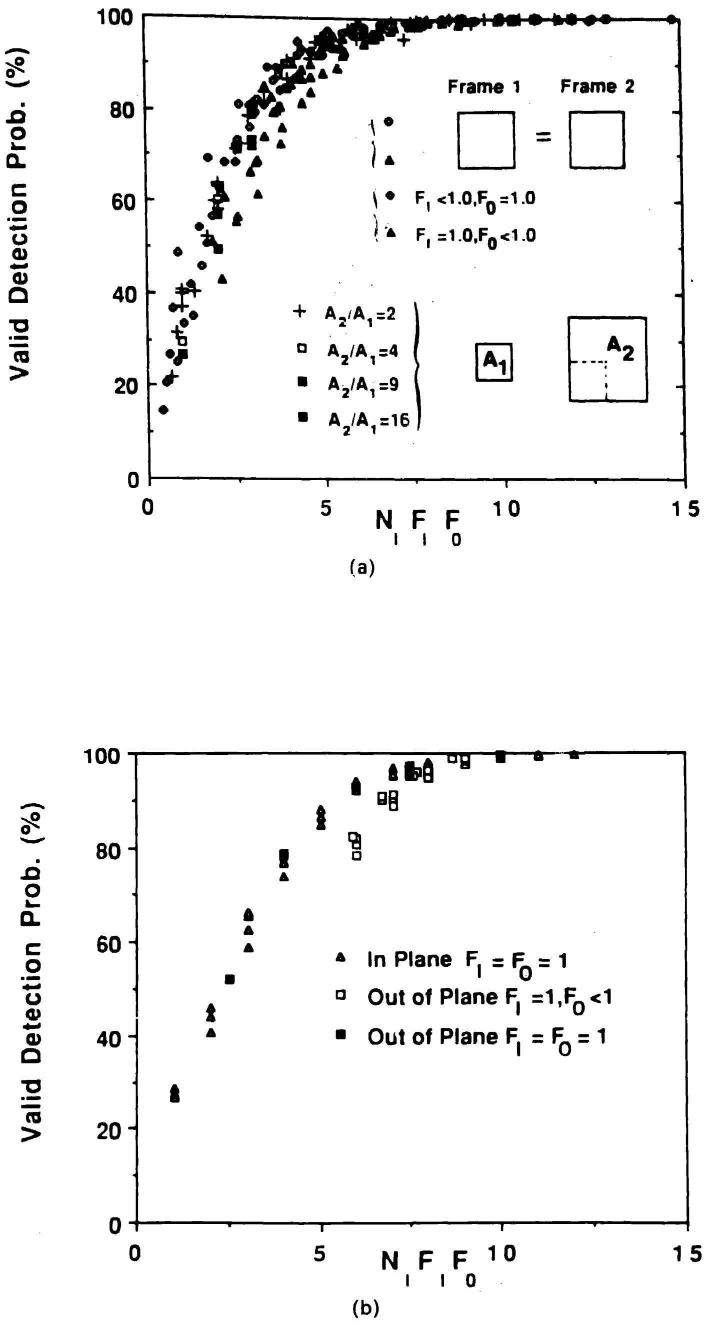

(a)

(b)

Fig. 4. Comparison of valid detection probability for (a) single-exposure double-frame cross-correlation analysis, (b) double-exposure single-frame cross-correlation analysis, (c) double-pulse autocorrelation analysis and (d) triple-pulse auto-correlation analysis as a function of effective particle image density, $N_I F_I F_O$, where $D_0 = 1.2$.

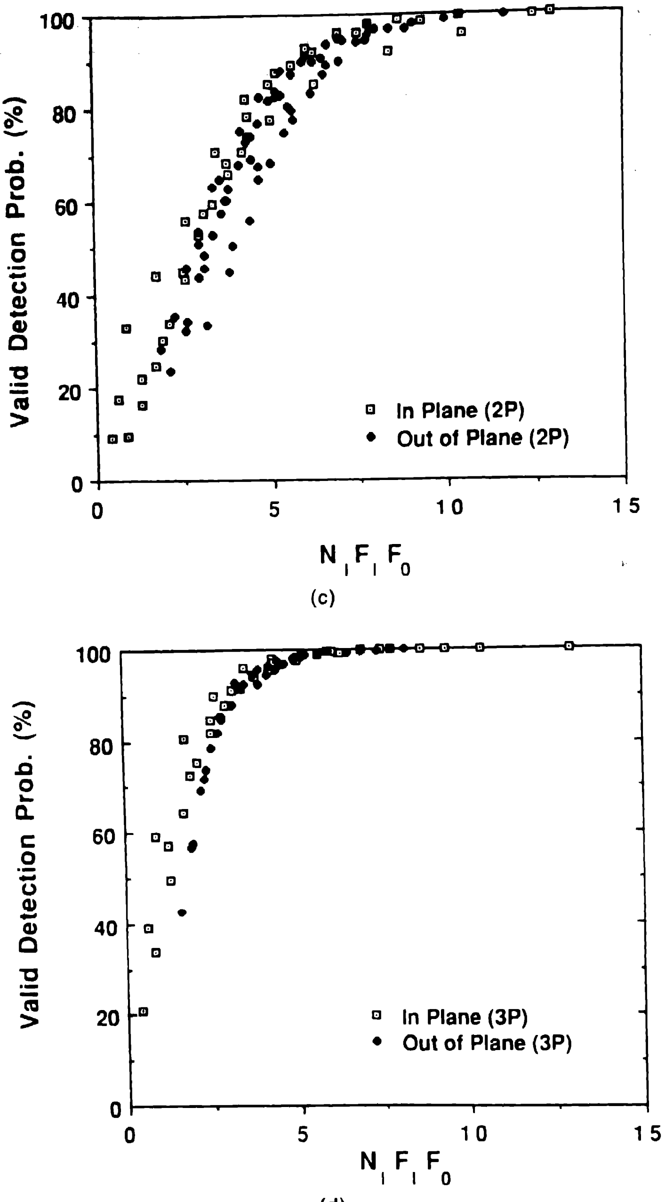

(d)

Fig. 4 (Continued)

$(N_I)_1 > 6$ and $(N_I)_1 > 8$ respectively, and then select the relative displacement $\mathbf{X}_2 - \mathbf{X}_1$ and d_2 to ensure that there is no loss-of-pairs. It is no longer necessary therefore to restrict $|\Delta \mathbf{X}|$ to be less than $0.30\, d_1$ as $F_I = 1$ and $(N_I)_1$ becomes the main parameter for constant velocity flow fields. This result for single-exposure images is a significant improvement over auto-correlation of a double-pulse system as shown earlier [6] where $N_I F_I F_0 > 8$ requires $N_I > 15$ for a reasonable range of image displacements to ensure a 95% valid detection probability. Further, it is a moderate improvement over the method of auto-correlation of triple-pulsed systems for which it is necessary to have $N_I > 8$ in order to ensure $N_I F_I F_0 > 4$ for an acceptable range of in-plane and out-of-plane displacements to obtain a 95% valid detection probability. The mean effective pair density, $N_P F_I F_0$ for this triple-pulse system then satisfies $N_P F_I F_0 > 8$. However, quadruple-pulse systems, interrogated by auto-correlation methods, require $N_I \geqslant 5$ to maintain a 95% valid detection probability over a range of image displacements [7]. They provide an alternative to single- and double-pulse systems using cross-correlation methods when the seeding density is low and velocity gradients are small.

The result, $(N_I)_1 > 8$, for double-exposure images is very similar to that obtained earlier [6] for auto-correlation methods with small improvements caused by reductions in peak noise correlation when optimal use of image pairs enables smaller first interrogation windows to be used for a given seeding density, C. Thus, although the mean effective pair density is not significantly decreased for cross-correlation analysis compared to auto-correlation analysis, the elimination of image pair losses allows lower seeding densities while maintaining acceptable detection probabilities. Alternatively, for a given seeding density, C, this more efficient use of particle image pairs permits a higher spatial resolution by reducing the size of the first interrogation spot needed to achieve a required number of effective image pairs. The spatial resolution is limited by the spot size to obtain this number of effective pairs and by the smallest scales of recorded images.

In the limit of small N_I, the probability of detection is equal to the probability of finding precisely one image for a given particle within each interrogation spot. In both auto-correlation of double-pulsed systems and cross-correlation of single-exposure and double-exposure systems, this probability is that of finding one particle in that portion of the interrogation volume from which the particle could be displaced and still remain within the interrogation volume at the time of the second exposure. From the arguments above, the average number of effective image pairs is $N_I F_I F_0$, and from a Poisson distribution it follows that

$$P\{\text{exactly one pair of images}\} = N_I F_I F_0 \exp(-N_I F_I F_0)\exp(-2N_I F_0(1 - F_I)). \tag{28}$$

Figure 5 confirms the correlation between detection probability and the single parameter, $N_I F_I F_0$ when the image density is small and shows that equation (28) is valid for $N_I F_I F_0$ less than about 0.3. Comparative results are shown for double- and triple-pulsed systems using auto-correlation analysis for a range of image displacements as well as a similar model for a triple-pulsed system. Although these results are independent of D_0 due to the lack of noise peaks in $R(\mathbf{s})$ for very low $N_I F_I F_0 < 0.3$, it can be seen that triple-pulse analysis, with twice as many image pairs, is superior to cross-correlation analysis of single exposures. The latter, in turn, is superior to double-

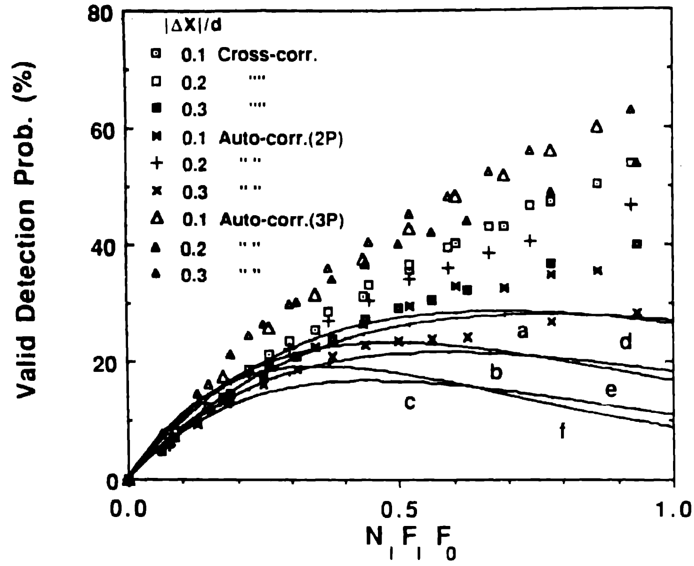

Fig. 5. Valid detection probability for low image density interrogation windows in terms of the effective image density $N_I F_I F_0$ for detectability $D_0 = 1.0$. Full curves (a), (b), (c) illustrate equation (20) for double-pulse auto-correlation and cross-correlation analysis while (d), (e), (f) model triple-pulse auto-correlation.

pulse auto-correlation analysis as there are fewer noise peaks and the choice of interrogation windows can ensure $F_I = 1.0$. In these low image density cases, alternative simpler methods such as one dimensional orthogonal image compression [16] can be used as the valid detection probability depends principally upon the probability of finding a true pair of images.

While the above comparative performance is based upon constant velocity fields, the presence of a velocity gradient in the flow field determines both the size of the two interrogation windows and their separation. Velocity gradients diminish and broaden the mean cross-correlation peak $\langle R_D \rangle$ necessitating higher particle image densities to overcome peak splintering in individual realizations. However, gradient bias in the location of the mean cross-correlation peak $\langle R_D \rangle$ can be eliminated by selection of d_1, d_2 and $X_2 - X_1$ to guarantee no loss of pairs due to in-plane motion and by selection of Δz_{01} and Δz_{02} to guarantee no loss of pairs due to out-of-plane motion.

In order to compare the cross-correlation method with auto-correlation analysis of double- and multiple-pulsed systems, the simplest case of a velocity gradient in which $(\partial u/\partial y) \neq 0$ has been examined for variable interrogation window sizes. This determines the effect of velocity gradient upon valid detection probability by peak spreading, upon gradient bias due to loss of image pairs and upon individual realization variation in measured velocities, due to random particle locations within an interrogation spot.

The dimensionless velocity variations, such as $M \Delta u_y \Delta t / d_\tau$ in the case of simple shear, affect the amplitude of $\langle R_D \rangle$ and the detection probability because the degree of peak spreading due to velocity variation must be measured in terms of particle image diameters. However, in cross-correlation analysis of velocity fields with a velocity gradient, smaller interrogation windows can be chosen than for auto-correlation for a given seeding density C due to the maximum utilization of images pairs in cross-correlation. Then, in order to compare cross-correlation with varying window sizes with auto-correlation methods, more useful non-dimensional velocity variations to consider are of the form $M\Delta u_y \Delta t/d_1$. These variations are independent of the window size d_1 or d_I for a given velocity gradient, as $\Delta u_y = (\partial u/\partial y).(d_1/2)$.

With a constant seeding density for cross-correlation and auto-correlation chosen to yield $N_I = 15$ from earlier work, Fig. 6 shows that for single-exposure cross-correlation the first interrogation spot can be halved in area in cross-correlation to maintain no loss-of-pairs with $(N_I)_1 = 7.5$ and achieve an acceptable valid detection probability of 95% provided that $M|\Delta \mathbf{u}|\Delta t/d_1 < 3\%$. For a given velocity gradient, a range of first interrogation spot sizes is considered as $M\Delta u_y \Delta t/d_1$ is constant for a fixed **u**. This is an improvement over auto-correlation methods as the spatial resolution can be increased for a given seeding density of a varying velocity field without loss of detection probability. However, the valid detection probability can become unacceptably low, if the effective image density is reduced by further increases in the spatial resolution. Figure 6 illustrates this loss of detection probability when the first interrogation spot is halved in area again yielding $(N_I)_1 = 3.75$.

However, in comparing cross-correlation analysis of single-exposure frames and

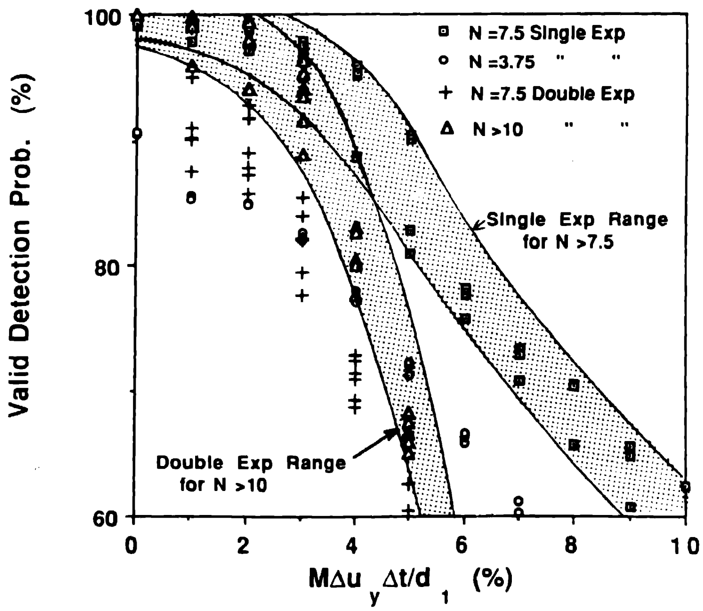

Fig. 6. Comparison of valid detection probability for a plane shearing velocity in terms of relative variation of image displacements, $M\Delta u_y \Delta t/d_I$, in cross-correlation analysis for both single-exposure and double-exposure imaging.

double-exposure frames, Fig. 6 also shows that for double-exposure frames cross-correlation analysis requires a higher particle image density to achieve an acceptable valid detection probability of 95% for a given velocity gradient, due to the doubling of noise peaks from a single-exposure analysis to a double-exposure analysis of the same realization. For the latter case, $(N_I)_1$ must be larger than 10 to achieve the same acceptable valid detection probability of 95% with the same velocity gradient and an identical range of first interrogation spot sizes. Thus, there is less spatial resolution possible with a double-exposure image for a given seeded fluid flow as the interrogation spot sizes cannot be reduced to the same extent as above for cross-correlation of single-exposure frames.

For the above parameters in cross-correlation analysis, velocity gradient bias, which is present in all correlation analysis when loss-of-pairs occurs, can be removed by choosing d_2 sufficiently large that $F_I = 1$. Figure 7 shows that in-plane velocity gradient bias is substantially reduced and finally eliminated whenever loss-of-pairs is reduced and similarly eliminated by choosing $d_2 > d_1$. This is compared to the theoretical result from auto-correlation methods in which the velocity gradient bias was shown to be a linear function of the velocity variation tensor, $d_{ij} = \partial u_i/\partial x_j$, in equation (35) from [7].

Finally, as for double- and multiple-pulsed systems, the random particle locations in individual realizations of a variable velocity field cause the centroid of $R_D(s)$ to be located over a finite range of displacements, causing random variations in valid measurements. Figure 8 shows that variation in measured velocity in terms of the

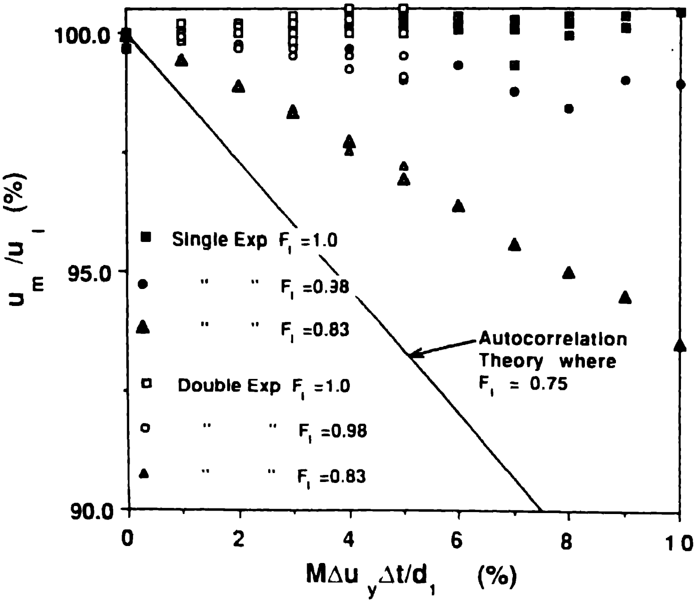

Fig. 7. Relative measured mean velocity in terms of relative variation of image displacements illustrating no velocity gradient bias for optimal choice of cross-correlation parameters.

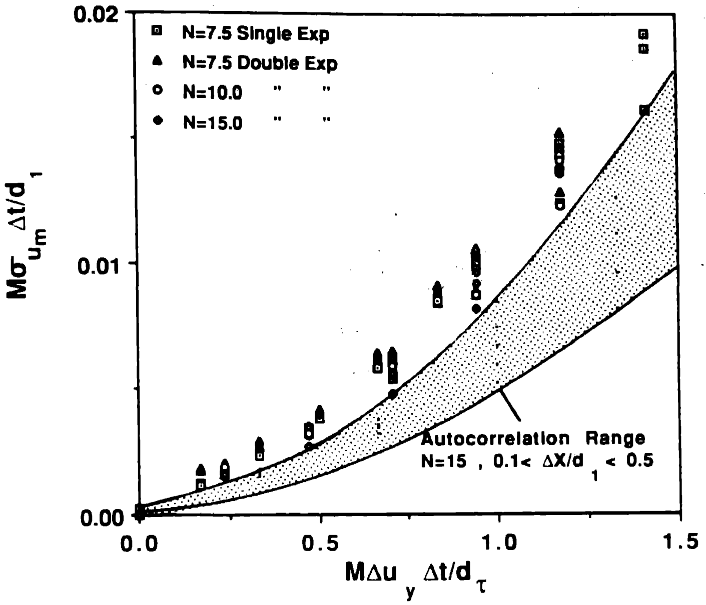

Fig. 8. Variation in measured velocity for a plane shearing velocity in terms of the relative image displacement variation $M\Delta u_y \Delta t/d_\tau$ for both single-exposure and double-exposure cross-correlation analysis.

relative image displacement variation $M\Delta u_y \Delta t/d_\tau$ is higher than that obtained from auto-correlation analysis of double- or multiple-pulsed systems and is independent of the mean image displacement. The variation is greater because the choice of interrogation windows guarantees no loss of image pairs whereas in auto-correlation analysis, the variation is restricted by the loss of larger displacement pairs. In order to restrict this variation to 1% and obtain an acceptably high detection probability, the velocity gradient must satisfy $M\Delta u_y \Delta t/d_\tau < 1$ and $M\Delta u_y \Delta t/d_1 < 3\%$.

Thus, in single exposure, double-frame systems using cross-correlation methods, the choices of d_1 and Δt are determined with criteria for adequate spatial resolution, valid detection probability and variation in velocity measurement about a measured mean. The maximum velocity variation, $|\Delta \mathbf{u}|$ that can be tolerated for successful interrogation is no longer dependent upon $\mathbf{u}$ but is bounded by the above restrictions for valid detection probability and acceptable variation in velocity measurements.

5. Summary and conclusions

Cross-correlation methods of interrogation of single-exposure and double-exposure double-pulse PIV systems have been studied as alternatives to auto-correlation analysis of double- or multiple-pulse PIV systems. Theoretical analysis of full 2-D spatial cross-correlation demonstrates the similarity and versatility of the method compared to that of auto-correlation of double- or multiple-pulse systems.

Both single-exposure and double-exposure double-pulse PIV systems which use cross-correlation methods of interrogation are superior to double-pulse PIV systems using auto-correlation analysis for a range of velocity fields for a number of reasons. The versatility in selecting the size and location of successive interrogation spots permits a higher level of spatial resolution by more efficient pairing of particle images. As there are ideally no pair losses in the optimal implementation of the cross-correlation method, the spatial resolution can be improved or the seeding density can be reduced while maintaining acceptable detection probabilities. Furthermore, in cross-correlation of single-exposure systems, image shifting is not required to resolve directional ambiguity. Without this need for image shifting the dynamic range of velocity measurements is doubled. (Other researchers have claimed much greater increases in dynamic range from cross-correlation but this is not the case when image shifting is implemented in auto-correlation.)

In experimental fluid flows where high seeding densities are not possible, multiple-pulse PIV systems with $n \geqslant 4$ can maintain acceptable detection probabilities at lower seeding densities than single- or double-exposure PIV systems using cross-correlation methods. Triple-pulse systems, on the other hand, while being superior to double-exposure PIV systems using cross-correlation analysis require a higher image density than single-exposure images to yield acceptable detection probabilities.

In fluid flows which have significant velocity gradients, the above choice of interrogation spots and light sheet thicknesses in the cross-correlation method removes the gradient bias in velocity measurements which occurs in auto-correlation methods. It has been shown that the size of the second interrogation window is not critical provided that there is no loss-of-pairs from in-plane motion as the strength of the noise does not vary significantly as the size of the second window increases. In-plane loss of pairs is avoided if the second interrogation window is sufficiently large to contain all particle images that were in the first window. The penalties for using a large second window include longer computation time and reduced pixel resolution in the first window. Out-of-plane loss of pairs is avoided by using a sufficiently thick second light sheet. The penalty associated with this procedure is the increased energy requirement for the second sheet. Detection bias caused by low seeding density is not present because the lower more efficient seeding levels of the procedure ensure 95% valid detection probability.

An extended range of velocity fields has been utilized in this analysis and in a Monte Carlo simulation of the cross-correlation method to reveal the critical dimensionless parameters of the mean cross-correlation function and its fluctuations. These parameters are an extension of those used for multiple-pulse systems, namely $(N_I)_1$, D_0, $|\mathbf{X}_2 - \mathbf{X}_1|/d_1$, $|\Delta\mathbf{X}|/d_1$, d_2/d_1, $M|\Delta\mathbf{u}|\Delta t/d_\tau$, d_τ/d_1, $|w|\Delta t/\Delta z_{01}$ and $\Delta z_{02}/\Delta z_{01}$.

To optimize the system performance, the following broad criteria, similar to those used in auto-correlation analysis of double- and multiple-pulse systems, are recommended. For single-exposure images, choose

(a) $(N_I)_1 > 7$ and $F_0 = F_I = 1$;

(b) $M|\Delta\mathbf{u}|\Delta t/d_1 < 0.03$;
(c) $M|\Delta\mathbf{u}|\Delta t/d_\tau < 1$;
(d) $1.0 < D_0 < 1.2$.

For double-exposure images, the particle image density must be higher as the noise peaks are doubled so we must choose (a) $(N_I)_1 > 10$ and $F_0 = F_I = 1$. The remaining criteria are identical to those above, (b)–(d).

In these cases, proper selection of the light sheet thickness, the interrogation spot sizes and separation can ensure that there is no loss-of-pairs due to either in-plane or out-of-plane motion with pulse separation selected to provide sufficient spatial resolution by maintaining adequate image displacements. While these criteria are a good general combination, more precise values can be used for a particular experimental flow field by reference to the appropriate figures.

To achieve optimal operation, some *a priori* knowledge of the flow field must be used to estimate the bounds of in-plane and out-of-plane motion and the extent of variation in the velocity field caused by velocity gradients. For flow fields which do not have appreciable velocity gradients, choose the seeding density C, d_1 and Δz_{01} to ensure adequate spatial resolution and Δt to maintain adequate image displacements and then choose d_2 and Δz_{02} to eliminate loss-of-pairs and to obtain a satisfactory valid detection probability.

In the presence of significant velocity gradients, conditions (b) and (c) above place a physical limit on the extent of the velocity variation that can be tolerated in designing an optimal group of parameters. In this case both d_1 and Δt must be chosen to satisfy these constraints with the seeding density C to be determined to enable $(N_I)_1 > 7$ for single-exposure analysis or $(N_I)_1 > 10$ for double-exposure analysis. The remaining parameters can then be chosen to ensure that there is no loss-of-pairs.

Appendix

To develop mathematical expressions for the components of $R(\mathbf{s})$ in equation (7), it is useful to reformulate the expression for the transmissivity of a distortion free nearly paraxial photographic recording of a single exposure flow field in equation (1) as follows:

$$\tau_1(\mathbf{X}) = \int I_{01}(\mathbf{x})g(\mathbf{x},t)\tau_0(\mathbf{X} - M\mathbf{x})\,d\mathbf{x}, \tag{A-1}$$

where

$$g(\mathbf{x},t) = \sum_i \delta(\mathbf{x} - \mathbf{x}_i(t)) \tag{A-2}$$

indicates the locations of the particles in the flow at time t. A similar expression can be used for equation (3). It is convenient to decompose $g(\mathbf{x}, t)$ into mean and fluctuating parts

$$g(\mathbf{x}, t) = C(\mathbf{x}, t) + \Delta g(\mathbf{x}, t), \tag{A-3}$$

where $C(\mathbf{x})$ is the mean number of particles per unit volume and is assumed to be time independent and $\langle \Delta g \rangle = 0$.

Substituting (A-1) and (A-3) and similar expressions into earlier expressions for $I_1(\mathbf{X})$ and $I_2(\mathbf{X})$ in equations (2) and (4) respectively, shows that R consists of three components as shown in equation (7). They are

$$\begin{aligned} R_C(\mathbf{s}) = &\int d\mathbf{X} I_{I1}(\mathbf{X} - \mathbf{X}_1) I_{I2}(\mathbf{X} - \mathbf{X}_2 + \mathbf{s}) \int d\mathbf{x} I_{01} C \tau_0(\mathbf{X} - M\mathbf{x}) \\ &\times \int d\mathbf{x}' I'_{02} C' \tau_0(\mathbf{X} - M\mathbf{x}' + \mathbf{s}), \end{aligned} \tag{A-4}$$

$$\begin{aligned} R_D(\mathbf{s}) = &\int d\mathbf{X} I_{I1}(\mathbf{X} - \mathbf{X}_1) I_{I2}(\mathbf{X} - \mathbf{X}_2 + \mathbf{s}) \int\int d\mathbf{x}\, d\mathbf{x}' \tau_0(\mathbf{X} - M\mathbf{x}) \tau_0(\mathbf{X} - M\mathbf{x}' + \mathbf{s}) \\ &\times I_{01} I'_{02} \Delta g(\mathbf{x}, t) \Delta g(\mathbf{x}', t + \Delta t), \end{aligned} \tag{A-5}$$

$$\begin{aligned} R_F(\mathbf{s}) = &\int d\mathbf{X} I_{I1}(\mathbf{X} - \mathbf{X}_1) I_{I2}(\mathbf{X} - \mathbf{X}_2 + \mathbf{s}) \int\int d\mathbf{x}\, d\mathbf{x}' \tau_0(\mathbf{X} - M\mathbf{x}) \tau_0(\mathbf{X} - M\mathbf{x}' + \mathbf{s}) \\ &\times I_{01} I'_{02} \{ C \Delta g(\mathbf{x}', t + \Delta t) + C' \Delta g(\mathbf{x}, t) \}. \end{aligned} \tag{A-6}$$

The conditional average for each component of R can be determined by using the equation for $\langle \Delta g \Delta g' | u \rangle$ from Adrian [1], namely;

$$\langle \Delta g(\mathbf{x}, t) \Delta g(\mathbf{x}', t + \Delta t) | \mathbf{u} \rangle = C(\mathbf{x}, t) \delta(\mathbf{x}' - \mathbf{x} - \mathbf{u}(\mathbf{x}, t) \Delta t). \tag{A-7}$$

Acknowledgment

This material is based on work supported by the National Science Foundation under Grant No. ATM 89-20605.

References

1. Adrian, R. J., Statistical properties of particle image velocimetry measurements in turbulent flow. *Laser Anemometry in Fluid Mechanics*, Vol. III. LADOAN Institute Superior Tecnico, Lisbon, Portugal (1988) pp. 115–129.
2. Adrian, R. J. and Zoltani, C., Measurement of particulate motion using a high resolution solid-state camera and high speed electro-optic double framing. *Abstract* ICALEO (1990).

3. Arroyo, M. P., Yonte, T., Quintanilla, M. and Savirón, J. M., Particle image velocimetry in Rayleigh-Bénard convection: Photographs with high number of exposures. *Optics and Lasers in Engineering* 9 (1988) 295–316.
4. Cenedese, A. and Paglialunga, A., Digital direct analysis of a multi-exposed photograph in PIV. *Experiments in Fluids* 8 (1990) 273–280.
5. Goss, L. P., Post, M. E., Trump, D. D. and Sarka, B., Two color particle velocimetry. *Proc.* ICALEO, LIA 68 (1989) pp. 101—111.
6. Keane, R. D. and Adrian, R. J., Optimization of particle image velocimeters. Part I: Double-pulsed systems. *Measurement Science and Technology* 1 (1990) 1202–1215.
7. Keane, R. D. and Adrian, R. J., Optimization of particle image velocimeters. Part II: Multiple-pulsed systems. *Measurement Science and Technology* 2 (1991) 963–974.
8. Keane, R. D., Adrian, R. J. and Ford, D. K., Single exposure double frame particle image velocimeters. *Proc.* ICALEO 72 (1990) 91–110.
9. Kimura, I. and Takamori, T., Image processing of flow around a circular cylinder by using correlation techniques. In: Veret, C. (ed.), *Flow Visualization IV.* Washington, D.C.: Hemisphere Publishing Corp (1986) pp. 221–226.
10. Lee, M. M., Hanratty, T. J. and Adrian, R. J., An axial viewing photographic technique to study turbulence characteristics of particles. *Int. J. Multiphase Flow* 15 (1989) 787–802.
11. Lourenco, L. M. and Krothapalli, A., The role of photographic parameters in laser speckle or particle image displacement velocimetry. *Experiments in Fluids* 5 (1987) 29–32.
12. Meynart, R., Simpkins, P. G. and Dudderar, T. D., Speckle measurements of convection in a liquid cooled from above. *J. Fluid Mech* 182 (1987) 235–254.
13. Prasad, A. K., Adrian, R. J., Landreth, C. C. and Offutt, P. W., Effect of resolution on the speed and accuracy of particle image velocimetry interrogation. *Experiments in Fluids* 13 (1992) 105–116.
14. Utami, T., Blackwelder, R. F. and Ueno, T., A cross-correlation technique for velocity field extraction from particulate visualization. *Experiments in Fluids* 10 (1991) 213–223.
15. Willert, C E. and Gharib, M., Digital particle image velocimetry. *Experiments in Fluids* 10 (1991) 181–193.
16. Yao, C. S. and Adrian, R. J., Orthogonal compression and 1-D analysis technique for measurement of particle displacements in pulsed laser velocimetry. *Applied Optics* 23 (1984) 1687–1689.

Applied Scientific Research **49**: 217–244, 1992.
© 1992 *Kluwer Academic Publishers. Printed in the Netherlands.*

Decay of rotating turbulence: some particle tracking experiments

STUART B. DALZIEL

Department of Applied Mathematics and Theoretical Physics, University of Cambridge, Silver Street, Cambridge, CB3 9EW, U.K.

Key words: rotating turbulence, particle tracking, experiments, inertial waves

Abstract. Recent development of measurement techniques based on particle image velocimetry (PIV) are enabling more detailed measurements to be made over extended regions of a flow than have been previously possible. These techniques are of particular value for turbulent flows where the structures present within such flows are incompletely understood and are not readily accessible to traditional measurement techniques. Unfortunately the considerable processing time and specialised equipment required with most PIV techniques limits their applicability when ensemble statistics are required for an evolving turbulent flow. This paper reports on the development and application of an efficient, fully automated particle tracking system. The system was developed as part of a study of the decay of turbulence in a rotating environment. Ensemble descriptions of the temporally evolving flow were required over an extended measurement domain. For each set of parameters particles were tracked with a sampling frequency of 12.5Hz over 60 seconds for 25 realisations. Typically 350 particles were identified and tracked at each time step. Processing speeds in the region ten to fifteen sample images per minute were achieved using a PC/AT compatible computer. The results of the experiments were found to be in broad agreement with previous investigations. However it was found that the method of generating the initial turbulent flow had a profound affect on the subsequent evolution due to the forcing of a strong, large scale systematic flow.

1. Introduction

Turbulence is widely considered one of the most difficult problems in fluid dynamics. Except in special cases, theoretical advancements are hampered by an inability to find exact solutions to the Navier-Stokes equations; approximations to these equations using closure models has met with only limited success. The range of scales involved in a turbulent flow means that only relatively low Reynolds number flows are accessible numerically to the present generation of computers. As a result experimental work continues to play a major role in developments, the scope being limited by our ability to measure and understand what is happening, rather than the use of approximate fluid dynamics. The quantity of primary interest in such experiments is the fluid velocity as a function of both space and time.

Over recent years the velocity measurement techniques available have advanced significantly. Starting from flow visualisation and hand-eye digitization, hot wire/film anenometry and then laser doppler anenometry were able to yield accurate point measurements of the flow. Fuelled by modern image processing technology there is renewed interest in flow visualisation as it now offers accurate quantitative information about a two or three dimensional region of the flow rather than just a single point. A wide range of image processing techniques have been developed to measure the fluid velocity. The key feature in common with most these techniques is the seeding of the flow with particles: it is the motion of these particles which is actually measured. A thorough review of particle image velocimetry (PIV) techniques may be found in Adrian [1] and elsewhere in this volume.

In this paper we describe a simple, efficient method for measuring velocity by tracking a large number of individual particles. This method was developed as part of a study of the temporal decay of rotating turbulence, but has subsequently been used to measure a variety of other flows (turbulence near a stress-free surface, turbulent plumes and jets, two dimensional turbulence in a stratified environment, Rayleigh-Taylor instability, baroclinic instability and baroclinic vortex interaction). The particle tracking forms a part of a wide ranging image processing package, DigImage, developed for analysing fluid flows. In this paper we illustrate the particle tracking (PT) as it was applied to the rotating turbulence problem.

Considering its importance to a range of fields (e.g. meteorology, oceanography and turbo machinery), turbulence in rotating systems has been the subject of relatively few experimental studies. Part of this is due to experimental difficulties in generating and measuring such turbulence, and part due to the as yet incomplete understanding of the classical nonrotating problem. As a consequence there are very few data sets available for comparison with theoretical and numerical results. The results which are in the literature fall into two broad categories: inhomogeneous turbulence (typically produced by an oscillating grid – we shall comment on these briefly in the final section), and decaying homogeneous turbulence (typically produced by a single pass of a grid or flow past a grid). The work reported in this paper falls into the second category: the temporal decay of grid generated turbulence with a zero mean flow.

The majority of early work on classical turbulence has been undertaken in wind tunnels looking at the evolution of turbulence generated by a uniform flow past a grid. It is generally accepted that ensemble statistics may be replaced by their temporal equivalents in this set up. The space-time transformation and Taylor's frozen field hypothesis suggest point measurements are equivalent to a one dimensional transect in the direction of the mean flow. Such grid generated turbulence may be considered homogeneous and isotropic to a reasonable approximation. Unfortunately it is not practical to rotate a sufficiently large wind tunnel at adequate rotation rates to study the effect of rotation, particularly if we are interested in the later stages of decay. Instead we must consider an ensemble of experiments in which the turbulence exhibits a temporal evolution. The requirement for ensemble statistics means that a large number of experiments must be processed, and so the processing time was a fundamental design consideration during the development of the particle tracking.

Ibbetson and Tritton [11] were the first to make detailed measurements of the temporal decay of rotating turbulence. The turbulent flow was generated in air by pulling two grids apart vertically within a shallow rotating annulus, and measurements were made by sweeping a hot wire probe around the annulus. Their primary concern was to determine whether rotation produced an increase or decrease in the decay rate: they found it to increase, but concluded this was due to inertial wave dissipation in the viscous bondary layers on the tank top and bottom.

The most recent work is by Jacquin et al. [12] who considered a tube rotating rapidly about its axis. Air was blown down this tube at up to 20 ms^{-1}. The air passed through a suitable diffuser to bring it into solid body rotation and a grid to generate the turbulence. The decay downstream of the grid was then observed using hot wire probes. The main conclusion that rotation slows the decay is consistent with present thinking. As with Ibbetson and Tritton, Jacquin et al. found a strong anisotropy develop in the length scales parallel with and perpendicular to the rotation axis. In contrast very little change in anisotropy in the corresponding velocity fluctuations was observed.

In section 2 we detail the experimental set up, and in section 3 outline the particle tracking technique employed. We present classical and rotating results in sections 4 and 5 (respectively), before concluding in section 6.

2. Experimental apparatus

Figure 1 sketches the tank in which all the experiments were performed. The tank measures 1.2 m long (x direction), 0.25 m wide (y direction) and 0.6 m deep (z direction). The tank is positioned on a precision rotating table capable of rotation rates of up to 2π radians per second about the vertical z axis. The basic experiment

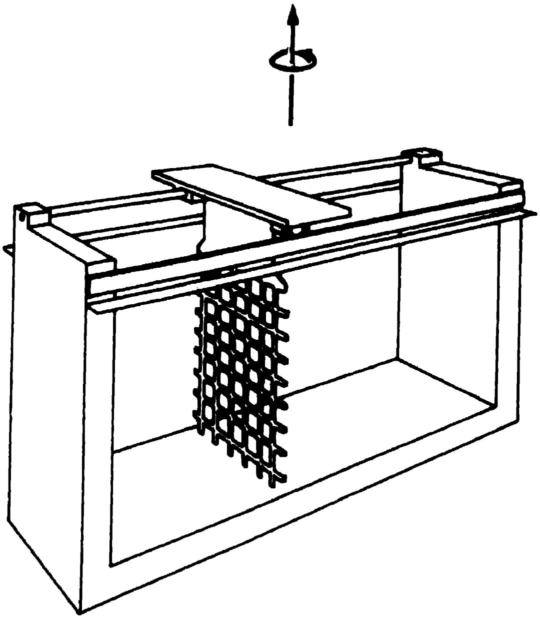

Fig. 1. Sketch of experimental setup showing tank, traversing mechanism and grid.

consists of a grid being towed down the length of the tank filled with water. The grid is machined from a single sheet of aluminium to give a square mesh consisting of 6.35 mm square bars at $M = 31.75$ mm centres. The grid is towed along the length of the tank at up to $U = 0.24\,\mathrm{ms}^{-1}$ by means of a traversing carriage located on the top of the tank. The grid Reynolds number ($\mathrm{Re}_M = UM/\nu$, where ν is the kinematic viscosity of water) is constant at $\mathrm{Re}_M \approx 7500$ over most of the length of the tank. The carriage and other associated equipment are controlled by means of a small microcomputer mounted on the rotating table, which in turn communicates with a terminal in the laboratory via a set of slip rings.

The design and construction of the tank and traversing mechanism included the ability to traverse a conventional hot film probe for velocity measurement. However the vibration in the traversing mechanism proved too great for reliable turbulence measurements. The development of the particle tracking system described in this paper grew out of the need to measure the flow field and the inability to utilise hot film anenometry (the project did not have access to an LDA system at the time).

The optical arrangement used in the particle tracking experiments is sketched in figure 2. The need to keep the effective diameter of the table relatively small (less than 1 m) forced all imaging to be indirected through a front silvered mirror. Reference points for image registration during the analysis were provided by fluorescent strip lights, covered in aluminium foil and painted matt black. The individual points were

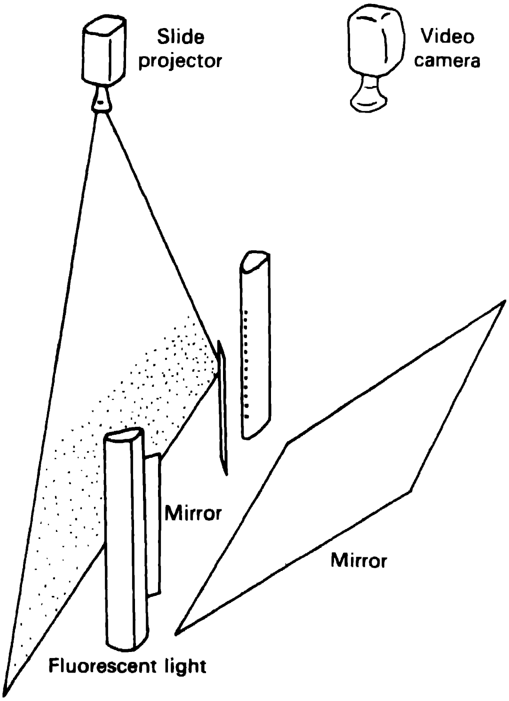

Fig. 2. Sketch of optical arrangement for experiments. The three mirrors are all front-silvered.

produced by piercing the foil against the glass tube with a sharp needle. This technique provides diffuse reference points (so the angle at which they are viewed is not critical) with an easily adjusted size. The points were superimposed as a row down each side of the image through the use of front silvered mirrors. The fluorescent lights were positioned so that the reference points lay in the in-focus plane of the camera.

The flow was illuminated using a sheet of light approximately 7 mm thick (δy) provided by a 250 W quartz halogen slide projector mounted above the tank. The light rays were approximately parallel to the rotation (z) axis with the sheet cutting along the length of the tank (x) at the centre line ($y = y_0$). The flow was imaged using a medium cost single CCD Super VHS camera (625 lines, 50 Hz field rate), fitted with a zoom lens (f1.6, focal length 10.5 mm to 126 mm), feeding through slip rings to a Super VHS video tape recorder. While the camera produced a Y/C colour signal, only the luminance (Y) component was passed through the slip rings to be recorded. This arrangement provided approximately 400 lines horizontal (intensity) resolution. Electronic shutter speeds of 1/50 s and 1/120 s were employed. At the higher shutter speed it was necessary to utilise the camera's automatic gain circuitry. The minimum useful illumination is quoted as 7 lux at f1.4 in the camera documentation: the camera was typically operating close to this limit. The signal noise due to the recording medium was generally less than that due to the camera at the relatively low light levels. The signal to noise ratio on playback remained adequate, allowing successful particle tracking even when the automatic gain was necessary. The equipment utilised to track the particles after the experiment was completed will be described in conjunction with the tracking process in the next section.

The particles used were produced by crushing and seiving pliolite (a resin used in the manufacture of white paint) to obtain sizes in the range 150 μm to 250 μm. The very small particles and dust remaining after the seiving were removed by a decanting process after suspension in fresh water. Photographic wetting agent was used to prevent the particles adhering to the free surface, and around 3 wt% salt used to adjust the water density so that the particles were approximately neutrally buoyant. While the particles were of irregular geometry, they were sufficiently small and close to spherical for their precise geometry to be of little importance.

3. Particle tracking

In this section we describe the particle tracking approach to PIV used in this study. The underlying philosophy is one of simplicity and computational efficiency. Efficiency is of particular concern with the need for ensemble statistics in this evolving turbulent flow.

The particle tracking process may be divided into a number of distinct tasks: experimentation, image acquisition and enhancement, particle location, particle pairing and subsequent analysis. Generally, due to the volume of data involved, it is desirable to combine some of these tasks into a single phase. Here we shall consider the tracking phase which consists of the acquisition, location and pairing tasks. The end product is six bytes of data per particle per time step, describing the particle positions, characteristics and relationships.

3.1. Image acquisition

Images are acquired from Super VHS video tape recorder (VTR) with a resolution of 512 × 512 pixels at 256 grey levels using a Data Translation DT-2862 arithmetic frame grabber. Due to the nature of video tape technology, it is not possible to acquire suitable high quality images from a "paused" VTR. A combination of the VTR's internal frame strobe, markers on the audio channel and interrupt driven routines on the host computer allowed efficient, reliable control of tape transport and acquisition of the exact frame required while in "play" mode.

During the tracking process, images are acquired as a sequence of four frames (not necessarily adjacent) from the playing VTR. The tape is then repositioned as a background task while the subsequent processing is undertaken. If desired, a *background* image is subtracted from the incoming signal to enable the subsequent application of uniform thresholds. If the particles are moving more than a small fraction of their diameter between each video field (1/50 s – each frame consists of two interlaced fields), it is necessary to remove half the information contained on the interlaced frame to ensure that a given particle appears at only one location on a given sample image. This also provides the possibility of sampling at the 50 Hz field rate, provided the small vertical displacement between the two fields is not important (the video camera may be modified so that it always produces only the odd or the even lines).

The fluorescent reference points are located and used to generate a mapping from the current pixel coordinate system to a reference pixel coordinate system using a least squares routine. In the majority of cases only a simple translation is required. The root mean square (rms) error in this mapping is calculated from the residuals and used as a check on the quality of the image. If the rms error exceeds a preset limit, then a further attempt will be made to acquire the image in the hope of improving its quality. The reference point mapping is used in conjunction with a pixel to world transformation to obtain the true world coordinates from the current pixel system.

3.2. Particle location

To locate a particle the image is first searched for a point satisfying a spatially uniform threshold condition (the optional subtraction of the background image during acquisition means that this threshold may be spatially varying relative to the raw image). The region of the image satisfying the threshold and connected to this first pixel is fathomed, and statistics are collected describing this region or *blob*. The shape, size and intensity characteristics of the blob are then checked against the allowable limits to determine if the blob represents a valid particle. The location of the particle is determined from the volume (mass) centroid of the region satisfying the threshold and the position transformed to the world coordinate system. This strategy produces good estimates of the relative position of a given particle in a sequence of images, provided the particles are sufficiently close to spherical that any rotation of the particle is of no concern. As an estimate of their absolute position, the volume centroid is less accurate, but the small errors in this are much less important. More complex and computationally expensive models such as those assuming a Gaussian intensity profile (e.g. Perkins and Hunt [14]) are not appropriate for the current method of illumination and are not expected to yield significantly better results.

Particles less than one pixel in size may only be located with pixel accuracy. However, for particles occupying more than one pixel in each direction the volume centroid gives subpixel accuracy, the error being related to the area A occupied by the particle through

$$\sigma_x \leqslant a(\sigma_i\bar{i})A^{-1/2}, \qquad (1)$$

where σ_x is some measure of the error in estimating the position of the particle, $\sigma_i\bar{i}$ is a measure of the relative intensity variations within a pixel (which may include both the unresolved portion of the intensity signal and the noise introduced by camera, recording medium and the digitizing process), and a is some constant. Experience shows that particles extending at least three pixels in each direction may typically be located to an accuracy of better than 0.2 pixels (typically 0.1 pixels) relative to the same particle at some other position.

In practice we search for particles in an image twice. The second pass utilises less stringent threshold requirements than the first and is used to pick up blobs which we are less certain about. As will be explained in section 3.4, this second set of particles is handled somewhat more cautiously.

3.3. Particle pairing

A wide variety of methods have been used to pair the particle images between two successive image samples (see Adrian [1]). Here we develop an efficient pairing algorithm based on the *transportation algorithm* [9], a graph theory technique frequently used in operations research for determining optimal associations between two sets. With careful coding the computational time for this method increases only slightly more rapidly than the number of particles (in many cases the matching process is faster than the particle location).

The basic idea is to minimise some objective function ζ which is linear in the associations it includes between the two sets. Here one set is the particle images $P = \{p_{[i]}$ for $i = 1, M\}$ at the *old* time, $t_{[n]}$ (say), and the other the particle images $Q = \{q_{[j]}$ for $j = 1, N\}$ at the *new* time, $t_{[n+1]}$. We define a set of variables α_{ij} recording the set of particle pairings: if $\alpha_{ij} = 1$, then particle image $p_{[i]}$ at $t_{[n]}$ is considered to be the same particle as the image $q_{[j]}$ at $t_{[n+1]}$. If $p_{[i]}$ and $q_{[j]}$ are considered as different physical particles, then $\alpha_{ij} = 0$. We express the objective function ζ as the linear combination

$$\zeta = \sum_i \sum_j \alpha_{ij} c_{ij}, \tag{2}$$

where c_{ij} is the *cost* for the association α_{ij} to be included in the pairings. The subscript i is summed from 0 to M, where M is the number of particle images at $t_{[n]}$. The value $i = 0$ is reserved for all particles outside the set of particles P found at $t_{[n]}$ (i.e. all particles outside the viewing region plus those obscured within the viewing region). Similarly, subscript j is summed from 0 to N, where N is the number of particle images at $t_{[n+1]}$ and $j = 0$ represents all particles outside the set of particles Q found at $t_{[n+1]}$. We shall discuss how to assign the costs c_{ij} in the next subsection. Before that we shall consider in more depth the structure of the problem and how to solve it.

The constraints on α_{ij} arise from a physical particle only being able to be in one location at a given time. Thus, for any $i = K \neq 0$, there must be one and only one j in $[0, N]$ for which $\alpha_{Kj} = 1$. Similarly, for any $j = L \neq 0$, there must be one and only one i in $[0, M]$ for which $\alpha_{iL} = 1$. An association of the form $\alpha_{ij} = 1$ for $i, j \neq 0$ represents a pairing between images in the two sets of particles, while $\alpha_{0j} = 1$ indicates that $q_{[j]}$ was not in the set P. Similarly $\alpha_{i0} = 1$ indicates that $p_{[i]}$ is no longer in the set Q of physical particles we have located at $t_{[n+1]}$. Note that there may be many values of i and j giving $\alpha_{0j} = 1$ or $\alpha_{i0} = 1$ as there can be many particles entering or leaving our viewing region and hence associated with the special index 0. In general α_{00} will not be zero as some of the particles not in the set P will also not be in the set Q. However the value of α_{00} is of no concern and so we assign it a zero cost.

The transportation problem differs from our present particle pairing problem in that the former does not have the possibility of associations outside the sets P and Q (i.e. $i = 1, M$ and $j = 1, N$). Nevertheless the structure of our present problem is very similar to the transportation problem. Both may be written as a linear program of the form $\mathbf{B}\boldsymbol{\alpha} = \boldsymbol{\xi}$ with $\zeta = \min \mathbf{c}^T\boldsymbol{\alpha}$, where all the coefficients of the $\mathbf{B}$ matrix are either 0 or 1 and are arranged in such a way that $\mathbf{B}$ is totally unimodular. For our present problem the right hand side $\boldsymbol{\xi}$ is integer, so that the only solutions for $\boldsymbol{\alpha} = \alpha_{ij}$ are also integer. The differences lie in that the present problem includes a set of constraints for the associations with $i = 0$ or $j = 0$ (particles external to P or Q, respectively). While these constraints follow the simple block identity structure of the transportation problem they are inequality constraints and so require the introduction of artificial variables (these artificial variables do not have the same block identity structure). With $\boldsymbol{\xi} = \mathbf{1}$ all the variables, except α_{00}, are constrained to be either zero or one. The variable α_{00} may be any nonnegative integer, depending on the total number of particles in the flow. However, as we have already stated, the value of α_{00} is of no consequence.

Solution of the particle pairing problem can be tackled in the same manner as the graph theory approach to the transportation problem. We consider α_{ij} and c_{ij} as two dimensional tables and define the relational index $I(j)$ as the value of i, for given $j \geqslant 1$, for which $\alpha_{ij} = 1$. Similarly we define $J(i)$ as the value of j, for given $i \geqslant 1$, for which $\alpha_{ij} = 1$. Note that $I(J(i)) = i$ and $J(I(j)) = j$, provided the corresponding association is between particles in the two sets P and Q. In the transportation problem, this identity means that only one of $I(j)$ and $J(i)$ are needed. However, for the particle pairing problem, $I(0)$ and $J(0)$ can not be defined uniquely, hence the need for both relational indices.

The solution process starts by assigning some arbitrary set of associations which satisfy the physical constraints on particles. Careful choice of this initial assignment of $I(j)$ and $J(i)$ will lead to the optimal solution being attained much more rapidly. Suppose some association α_{kl} is currently not in the set of associations. If we were to allow the α_{kl} pairing to be made, then for the constraints on the $p_{[k]}$ and $q_{[l]}$ particle images to remain satisfied, the associations $\alpha_{I(l)l}$ and $\alpha_{kJ(k)}$ must leave the set of pairings. Further, to maintain the constraints on the $p_{[I(l)]}$ and $q_{[J(k)]}$ particle images, we must introduce the association $\alpha_{I(l)J(k)}$. Now the change in the overall cost (*reduced cost*) associated with this change over is

$$rc_{kl} = (c_{kl} + c_{I(l)J(k)}) - (c_{I(l)l} + c_{kJ(k)}). \tag{3}$$

If rc_{kl} is negative, then entry of α_{kl} into the set of pairings is favourable.

The reduced cost is calculated for all $\alpha_{kl} = 0$ with $k \geqslant 1$ and $l \geqslant 1$, although if it has already been evaluated for $rc_{I(l)J(k)}$ it need not be evaluated again for rc_{kl}. Note that associations to the $i = 0$ and $j = 0$ sets may still be made through the $\alpha_{I(l)J(k)}$ variable in such a way that does not violate the inequality constraints on these variables. The k, l pair which yields the most negative value of rc_{kl} will be allowed to enter the set of pairings along with $\alpha_{I(l)J(k)}$. The $\alpha_{I(l)l}$ and $\alpha_{kJ(k)}$ associations must leave the set of pairings. These changes may be reflected by simultaneously updating the relational indices

$$I(l) := k,\ J(k) := l,\ I(J(k)) := J(I(l)),\ J(I(l)) := I(J(k)). \tag{4}$$

This process is repeated until no association has a negative value of rc_{kl}. The linear nature of ζ ensures that this solution has the minimum value for the objective function and corresponds to the optimal set of associations. (In principle this optimal set as defined by c_{ij} may not be unique, but in practice this situation rarely arises.)

3.4. *Costing associations*

The only algorithmic restriction on the assignment of costs c_{ij} is that they may not include information on the state of α_{ij} for the current time step. If information about α_{ij} were used in c_{ij} then the objective function would be nonlinear and a more sophisticated algorithm (e.g. simulated annealing) would be required to determine the optimal solution. Each cost may include information about the positions of $p_{[i]}$ and

$q_{[j]}$, the velocity history (normally only of $p_{[i]}$, but may include other particles at $t_{[n]}$), their geometric properties (e.g. shape), intensity, colour, fluid dynamics or a wide variety of other possible factors. However, experience has shown that a relatively simple costing strategy is all that is required in the majority of cases. In this subsection we outline the strategy we have employed for the current set of experiments. While we have utilised more sophisticated strategies in other flows (e.g. flows containing dye as a tracer), they are beyond the scope of this paper.

The basic method of costing an association α_{ij} is a modification to looking for the nearest neighbour. We define the basic cost of the association as

$$b_{ij} = |\mathbf{x}_{[i]} + \gamma \mathbf{u}_{[i]}\delta t - \mathbf{x}_{[j]}|^m, \tag{5}$$

where $\mathbf{x}_{[i]}$ and $\mathbf{x}_{[j]}$ are the locations of $p_{[i]}$ and $q_{[j]}$ (respectively) projected onto the $y = y_0$ plane, $\mathbf{u}_{[i]}$ is some estimate of the velocity (in the y_0 plane) of $p_{[i]}$ at $t_{[n]}$, γ is some weighting function (typically unity), $\delta t = t_{[n+1]} - t_{[n]}$ is the time step, and m is some positive value (typically $m = 2$). If $\gamma = 0$ and $m = 1$, then b_{ij} forms the basis for a nearest neighbour solution. For $\gamma = 1$ and $m = 1$ we are applying a minimum acceleration criterion, while $\gamma = 1$ and $m = 2$ may be viewed as minimising the rate of work on the fluid elements containing the particles.

To overcome difficulties which arise when considering associations with $i = 0$ or $j = 0$, the possibility of multiple particles casting a single image, or with other anomalous behaviour, we utilise a number of functions or modifiers in conjunction with the basic cost. The cost of an association α_{ij} is written as

$$c_{ij} = C(b_{ij}\eta_i\varepsilon_j\mathscr{D}_j\tau_j), \tag{6}$$

where the modifier functions η_i, ε_j, $\mathscr{D}_j$ and τ_j are typically step functions acting as price premiums or discounts. The purpose of these functions is explained below.

The function $C(\cdot)$ controls the maximum cost, $c_{\max}$ (say), an association is allowed to have. If the expression inside $C(\cdot)$ yields a result larger than $c_{\max}$, then $C(\cdot)$ will set the resultant value of c_{ij} to infinity. The pairing algorithm outlined in the previous section may be modified to ensure that associations with infinite costs are never in the solution. The associations α_{i0} and α_{0j} are costed either on the cost of associating with a particle lying just outside the physical boundaries of the image, or at the maximum cost $c_{\max}$, whichever is smaller. Thus the maximum cost effectively places a limit on how far a particle may be from its predicted position; this is equivalent to a bound on the apparent acceleration or rate of work.

The use of infinite costs in place of $c_{ij} > c_{\max}$ greatly improves computational efficiency as we need not evaluate costs for associations between well separated particles, nor worry about such associations in the pairing algorithm. The number of finite values of c_{ij} will be greater than or equal to $\mathrm{Max}(M, N)$ but much less than $(M + 1)(N + 1)$.

One of the difficulties with basic cost function b_{ij} is the need to have an estimate for the velocity $\mathbf{u}_{[i]}$. If a pairing was made for $p_{[i]}$ at the previous time step, then we may use this to estimate $\mathbf{u}_{[i]}$. However, if we have no history for $p_{[i]}$ then we must make a reasonable guess at $\mathbf{u}_{[i]}$ but make an allowance for the guess being wrong. This guess could be based on a knowledge of the flow or the behaviour of other particles in the neighbourhood of $p_{[i]}$. For thin light sheets or flows where there are no appreciable velocity gradients parallel to the viewing direction within the illuminated region, the local mean velocity is a good predictor of $\mathbf{u}_{[i]}$. For thick light sheets in three dimensional flows we may be able to do no better than predict $\mathbf{u}_{[i]}$ as some constant. Regardless of how we predict $\mathbf{u}_{[i]}$ where it is not known from the particle history, we shall increase the maximum distance between the predicted position of $p_{[i]}$ and any paired image $q_{[j]}$ by reducing the cost of any such association by multiplying by some factor $\eta_i \leqslant 1$ (we may wish to prevent matches on large, small or elliptical particles when $\mathbf{u}_{[i]}$ is not known by setting $\eta_i = \infty$ for such particles). Typically this discount factor will be derived from some estimate of the maximum error in the estimated value of $\mathbf{u}_{[i]}$. If η_i is set too large, then only particles conforming very closely to the predicted $\mathbf{u}_{[i]}$ will be able to enter the tracking process. If too small, then initial matchings may be made over unaceptable distances. However, provided $c_{\max}$ is sufficiently small, any erroneous pairings introduced by a value of η_i which is too small will not persist past the frame pair at which they entered the problem: $\mathbf{u}_{[i]}$ at the next step will not predict the particle's position with sufficient accuracy. For particles $p_{[i]}$ which were matched at the previous time step we know $\mathbf{u}_{[i]}$ so offer no discount and set $\eta_i = 1$.

We utilise a number of ways of detecting and using particles which appear at almost the same location at $t_{[n+1]}$. The first is based on the shape of a particle: if a blob appears very elliptical, then it may represent two particles close together. We assign to the elliptical blob one ordinary particle with the modifier $\varepsilon_j = 1$, and a possible second particle with ε_j set to some constant greater than one. Associations with the ordinary particle proceed as normal. Associations with the second particle are costed higher by the factor ε_j. If ε_j is sufficiently large, and $c_{\max}$ sufficiently small, then an association with this second particle will only be made if we predict two particles should be there on the basis of the information at $t_{[n]}$. Note that particles with no velocity history are prohibited from matching with such particles.

The modifier $\mathscr{D}_j$ operates in much the same manner as ε_j except that it is based on the overall area of the particle rather than the shape. Particles smaller than a preset limit have $\mathscr{D}_j = 1$, while those larger are treated as two, the second with a price premium of $\mathscr{D}_j \geqslant 1$.

As noted in subsection 3.2, we locate particles using two different thresholds. Particles satisfying the more stringent threshold criteria are assigned a modifier value of $\tau_j = 1$, while those satisfying only the less stringent threshold suffer a premium set by $\tau_j \geqslant 1$, restricting the size of the error between their predicted and actual locations at $t_{[n+1]}$.

Extensive use of this costing and pairing strategy in a variety of different flows suggests only a very weak dependence on the ε_j, $\mathscr{D}_j$ and τ_j modifiers. It is for this reason, combined with simplicity, that we have adopted step rather than continuous functions. Only η_i and $c_{\max}$ have a marked effect on the tracking process.

3.5. Implementation

The tracking algorithm we have outlined in the previous four subsections has been implimented on a PC/AT compatible micro computer using a Data Translation DT-2862 arithmetic frame grabber. All software has been written by the author in a combination of assembler and Fortran in such a manner as to allow fully automated tracking. To improve computational efficiency the association costs c_{ij} are evaluated only once and stored after rescaling to a single byte integer value. The cost matrix c_{ij} requires $(M + 1)(N + 1)$ bytes of memory limiting this simple implementation to 511 particles in each sample (c_{ij} is 256 Kbytes). An alternative implementation of the algorithm making use of the fact that many c_{ij} are infinite allows up to 4095 particles to be tracked by the PC/AT. Practical considerations limit the number of particles to around 2000. (When the experimental work reported in this paper was undertaken only 511 particle could be tracked.)

The speed of operation depends on the number of particles and quality of the images. When tracking a relatively small number of particles, the execution speed is limited to around 25 frame pairs per minute by the need to acquire images in groups of four samples from a playing video tape. When tracking more than around 200 particles the computations for the location and pairing of particles becomes important. With approximately 400 particles the processing rate varies from six (20 MHz 80386) to fifteen (25 MHz 80486) frame pairs per minute depending on the speed of the computer.

For each time step the pairing algorithm is executed twice. The first pass operates on $p_{[i]}$ and $q_{[j]}$ at $t_{[n]}$ and $t_{[n+1]}$, respectively. Any particles at $t_{[n]}$ which are not matched are stored away for later use. Particles at $t_{[n+1]}$ which were not matched are then compared with particles a $t_{[n-1]}$ which were also left unmatched, to determine if any further pairings may be made. This second pairing operation increases the number of matches made by between 1% and 10%. The number of matches made at any time step depends primarily on the velocity component normal to the light sheet and the thickness of the light sheet.

3.6. Velocities

There are a number of different methods of estimating the velocities from the positions of a particle along a path. The simplest and arguably most effective of these fit a surface to the positions of a given particle in $\mathbf{x}, t$ space. In practice we fit a straight line to the x, t and z, t data sets over some time interval $s\delta t$ during which the change in velocity is relatively small. The slope of the fitted lines may then be used to estimate the velocity. In the limit of $s = 1$ this degenerates to the simple finite difference approach. The fitting process should utilise all the information in $s\delta t$, suggesting either a least squares fit or a Chebeshev polynomial. Both these strategies are in some sense optimal and in practice yield very similar results. The results presented in this paper employ the least squares approach.

With the least squares fit the error in the estimated velocity σ_u is given by the standard error in the slope of the line which may be expressed as

$$\sigma_u = \left\{\frac{12}{(s+2)(s+1)s}\right\}^{1/2}\frac{\sigma_x}{\delta t}. \tag{7}$$

With the values used in this paper ($\sigma_x < 0.2, s = 5, \delta t = 0.08$s) we have a velocity error $\sigma_u < 0.24\,\mathrm{mms}^{-1}$. Typically the error is less than half this value.

We should note that the particle tracking process and the method of calculating velocities over paths with $s > 1$ leads to a sampling bias in favour of regions of the flow in which the velocity normal to the light sheet is relatively small. This arises through the need for particles to remain in the light sheet over $s + 1$ samples. The value $s = 5$ has been chosen so that relatively few particles will ever cross the 7 mm light sheet in less than $s\delta t = 0.4$ s. In the present experiments this bias is only significant in the very early stages of the decay process and will not affect the discussion in the following sections.

4. Nonrotating turbulence

We shall consider first the nonrotating ($f = 0$) limit as the behaviour of this well known flow will show any major problems with our experimental apparatus or measurement method. There are a wide range of methods of characterising such a flow. For the present we will confine our attention to relatively simple velocity statistics.

We define the spatial-ensemble mean velocity for the illuminated region as

$$\bar{\mathbf{u}}_{se}(t_{[n]}) = \sum_r \sum_i \mathbf{u}_{[i][r]}(t_{[n]}) \Big/ \sum_r M_{[r]}(t_{[n]}), \tag{8}$$

where $u_{[i][r]}(t_{[n]})$ is the velocity for particle i in realisation r at time $t_{[n]}$ in the light sheet. There are $M_{[r]}(t_{[n]})$ particles for which the velocity is known in realisation r at time $t_{[n]}$. The summation is over all particles located in each realisation (approximately 350 particles) and all realisations (typically $R = 25$ realisations) at the specified time. As our tank represents a closed system the flow must have a zero mean velocity. Therefore we might expect (8), which is a sample of the global mean velocity, to evaluate to zero. However, as we can see from Fig. 3, $\bar{\mathbf{u}}_{se}$ does not vanish as expected. Two features are readily apparent in the horizontal component of $\bar{\mathbf{u}}_{se}$: an oscillation with a period of approximately 1.25 s ($Ut/M \approx 9.5$), and an exponentially decaying mean value. The first of these has the correct frequency for deep water waves in the

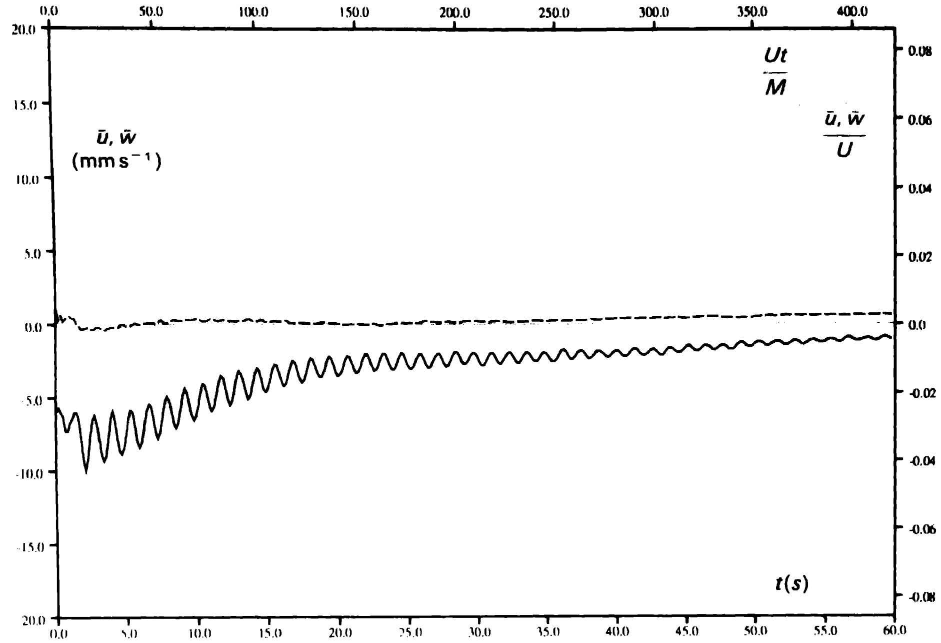

Fig. 3. Evolution of the mean velocity within the light sheet for $f = 0$. The solid line is for the horizontal component, and the dashed line for the vertical component.

tank. These waves are initiated by the passage of the grid. The mechanics of driving the grid prevented a rigid lid from being used. While slats were fitted between the bars of the grid to reduce the effect of the free surface, a significant wave component still exists.

The origin of the decaying flow in Fig. 3 is also due to the passage of the grid. Careful observations show that the passage of the grid sets up a significant large scale circulation within the tank. This motion is predominantly in the direction of the grid near the centre of the tank, with return flow near the boundaries. Increasing the solidity of the grid near the walls and making a double pass with the grid reduced the size of this circulation, but it did not prove possible to eliminate it. The embarrassing existence of the systematic flow is not unique to the apparatus used in these experiments (Maxworthy, personal communication) although much longer tanks do not seem to suffer this problem (e.g. Britter et al. [4]). However, most studies do not address the issue, partly due to the difficulty with measuring and allowing for such a flow, especially using traditional techniques. The majority of experiments on homogeneous turbulence have been in wind tunnels where the problem is much less severe with a much large ratio of mesh length to tunnel width (giving a much better separation of scales). A similar phenomenon is known to exist in oscillating grid experiments with the production of a larger scale systematic flow (e.g. McDougall [13]). In both cases the scale of the systematic flow is set by the overall tank geometry and not the mesh size.

Due to the existence of spatial structure in the surface waves and in the systematic circulation, statistics should be evaluated relative to a spatially varying ensemble mean, $\bar{\mathbf{u}}_e$, say. In practice the mean is evaluated for each time step by distributing the particle velocities onto a regular grid (using a local weighted least squares fit) and averaging the grid over all realisations. Figure 4a plots the evolution of the turbulent fluctuations relative to this mean. If the initial turbulence field is approximately homogeneous and isotropic then during the initial stages of decay, starting some time $t > t_0$ after the passage of the grid, and extending until Ut/M is greater than around 200, the turbulence intensities are then found to follow the power law

$$\frac{\bar{u}^2}{U^2} = A\left[\frac{U(t - t_0)}{M}\right]^{-\beta}, \tag{9}$$

where A and β are constants and t_0 is the virtual origin at which the fluctuations would be infinite. Batchelor's [2] initial period decay law gives $\beta = 1$ for the type of grid used in these experiments. More extensive data sets suggest a value of β between 1.2 and 1.4 (e.g. Comte-Bellot and Corrsin [5]). As is frequently the situation with power laws, the exponent β for the optimal fit is sensitive to location of the virtual origin t_0. Typically the virtual origin is found to be located at Ut_0/M between 1 and 6, with the initial period, during which the power law applies, starting some ten to twenty grid time scales (M/U) later.

Figure 4b reproduces the fluctuation data in a log-log format. Between approximately 10 and 75 grid time scales after the passage of the grid the energy decays following a power law with $\beta \approx 1$. The size of the ensemble is not sufficiently large to pin down β more precisely as the value of t_0 is also unknown. The initial much flatter curve is due to a combination of the behaviour immediately behind the grid and the conditional sampling provided by the particle tracking ($v < \delta y/(s\delta t)$). The bias due to the conditional sampling is significant only in the very early stages of the decay. The other notable feature of this plot is the marked decrease in the decay rate at times larger than $Ut/M \approx 75$ ($t \approx 10$ s). The decay does not follow a power law after this point and cannot be attributed to the normally increased decay during the final period. Rather it would appear as though the largest turbulent scales are starting to interact with the large scale systematic flow set up by the initial passage of the grid. Moreover, as this circulation is on the same scale as the dimensions of the tank, the overall experimental geometry will be playing a significant role. A power-law decay appears to establish again after $Ut/M \approx 250$ once the scales of the systematic flow are fully incorporated into the decay process. The decay rate after this point will be influenced by the geometry of the tank but is again with $\beta \approx 1$.

Clearly the large scale circulation imposed by the initial passage of the grid imposes severe experimental difficulties. A variety of methods were tried to minimise its generation, the results presented in this section representing the best alternative. As will be seen in the next section, rotation compounds the difficulties with the generation of inertial waves.

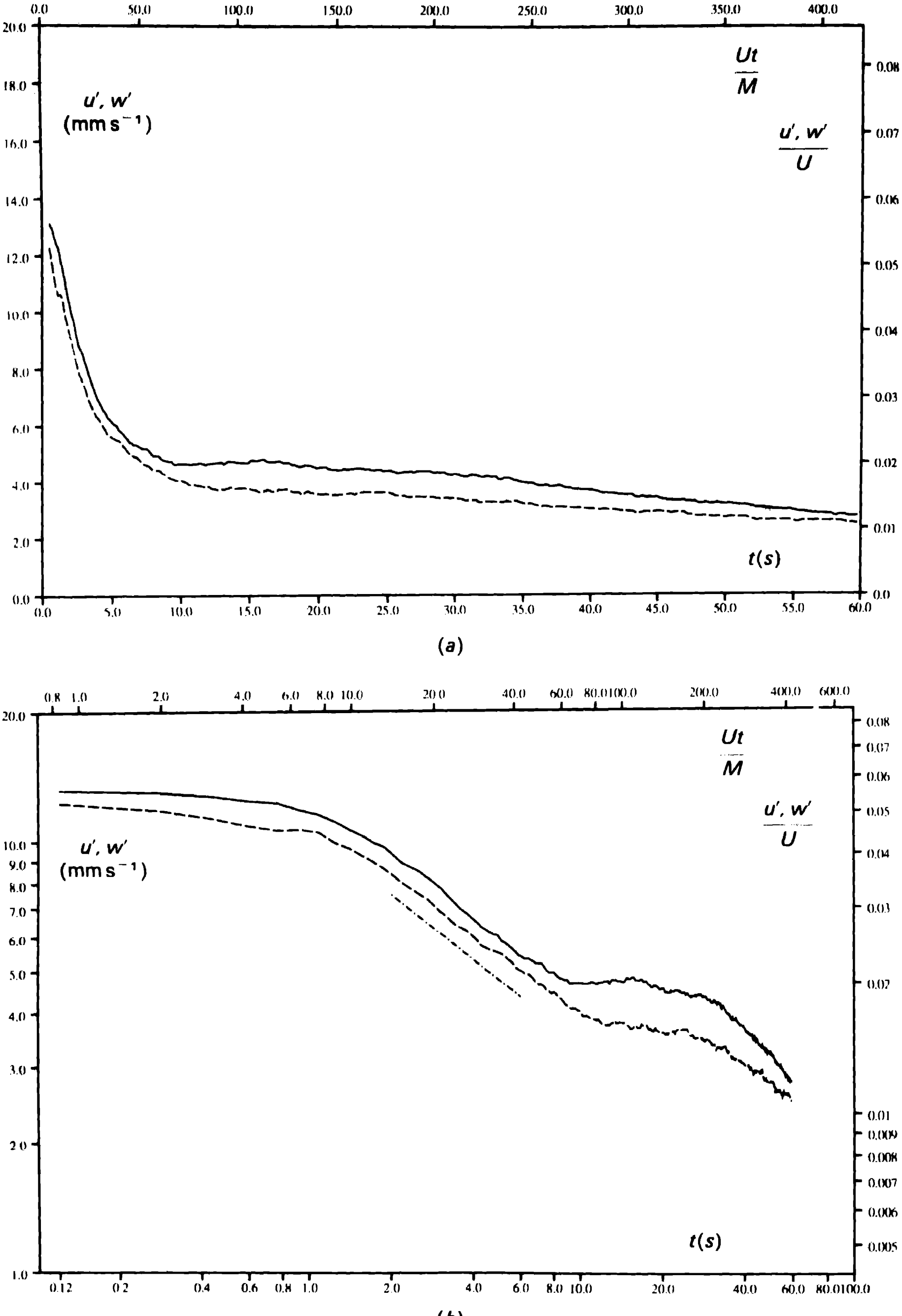

(a)

(b)

Fig. 4. Evolution of the turbulent velocity fluctuations about the spatially varying ensemble mean flow for $f = 0$. Plot (a) has a linear scale while (b) a logarithmic scale showing the power law behaviour of the decay ($t_0 = 0.4s$). Solid lines indicate the along-tank horizontal component, while dashed lines denote the vertical component. The initial period decay law with $\beta = 1$ is shown as a dot-dash line in (b).

5. The effect of rotation

In the interior of the tank, rotation affects the motion through the Coriolis force acting primarily on large scales and low velocities (i.e. small Rossby number). The systematic flow found for nonrotating turbulence has both these features and will hence be affected by the rotation from a very early stage. Figure 5 shows the evolution of the $\bar{u}_{se}$ mean velocity at a rotation rate of $\Omega = f/2 = 0.5\,\text{rad. s}^{-1}$ (for the sake of brevity we shall present results only for this rotation rate). The relatively short period ($\sim 1.25\,\text{s}$) free surface waves (now Kelvin waves) are still present. In addition, we are able to see two (or more) relatively large amplitude inertial wave modes in place of the simple mean flow found in the previous section.

Plane inertial waves in a rotating system may be shown to have the velocities obeying

$$\begin{aligned} u &= \pm(k_2\lambda_3 - k_3\lambda_2)\cos(\kappa(k_1x + k_3z) \mp k_3ft) - \lambda_1 \sin(\kappa(k_1x + k_3z) \mp k_3ft), \\ w &= \pm(k_1\lambda_2 - k_2\lambda_1)\cos(\kappa(k_1x + k_3z) \mp k_3ft) - \lambda_3 \sin(\kappa(k_1x + k_3z) \mp k_3ft), \end{aligned} \tag{10}$$

in the plane of the light sheet (e.g. Greenspan [8]). The magnitude of the wave number is given by κ and the orientation by the unit vector $\mathbf{k}$. The amplitude vector $\boldsymbol{\lambda}$ may be

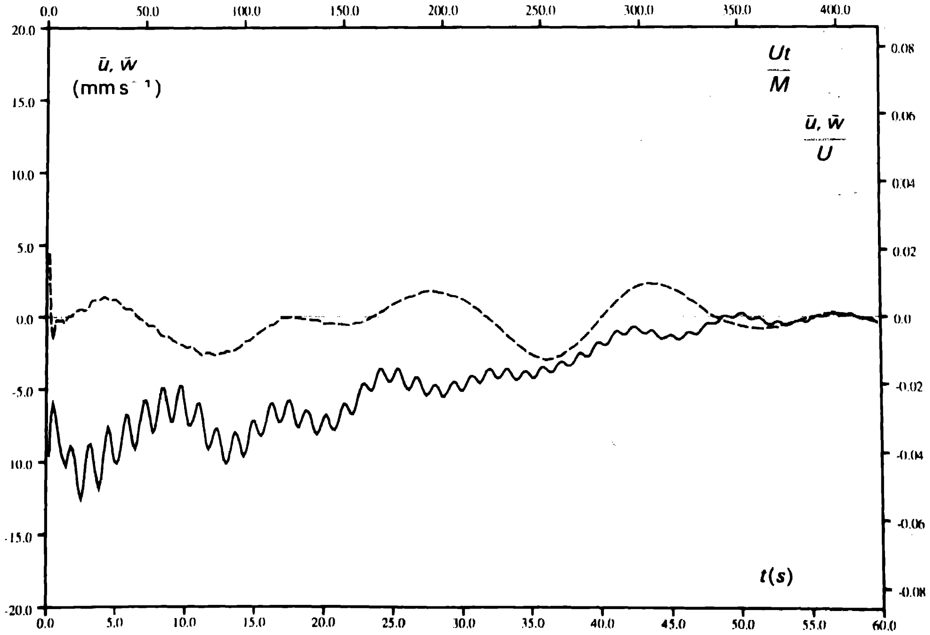

Fig. 5. Evolution of the mean velocity within the light sheet for $f = 1$ rad/s. The solid line is for the horizontal component and the dashed line for the vertical.

any vector perpendicular to **k**. Subscripts indicate the components in the three axis directions. The frequency ω of these plane waves is related to the angle between the rotation axis and the unit wave number vector by

$$\omega = k_3 f. \tag{11}$$

The solution given by (10) satisfies both the linear and nonlinear intertial wave equations. Note, however, that superposition of modes is not possible in the latter case.

While the inertial waves in this flow are likely to be nonliner, we may make some progress by assuming a degree of superposition is possible. As noted above, Fig. 5 shows evidence of two inertial wave modes. Experiments at different rotation rates have shown the relative amplitude of these modes appears to depend on the rotation rate, presumably the result of variations in the ratio of the time to traverse the grid and the rotation period. By considering the vertical mean velocity we can see a mode with $\omega \approx 0.4f$, implying the wave number vector is inclined at an angle of approximately 66° to the rotation axis. In addition to this $\omega \approx 0.4f$ mode, the horizontal mean velocity shows a response at $\omega = f$. The frequency and absence of vertical motion at this frequency are consistent with the wave number vector parallel to the rotation axis.

As with the nonrotating flow in the previous section, we may determine the spatio-temporal structure of the mean flow and utilise it when evaluating the statistics of the turbulence. Figure 6a plots the evolution of the fluctuations about the varying ensemble mean flow. Figure 6b plots the same data on logarithmic axes from which we see the existence of a power law giving a somewhat lower decay rate than observed for $f = 0$. While the value of β is not known for either case, overlay in the two plots allows a direct comparison to be made if we assume t_0 is the same for both cases. The decay process does not show the abrupt change in behaviour found for $f = 0$, suggesting that interaction between the inertial waves is generating turbulence at relatively large scales preventing an initial scale separation between the inertial waves and the turbulence (we had such a scale separation in the nonrotating flow in the previous section). Note that the energy contained in the inertial wave field is significantly larger than the systematic flow in the $f = 0$ limit.

A series of four plots showing the spatial structure and temporal evolution of the ensemble mean velocity field is given in Fig. 7. This series has been chosen to show the spatial structure of the inertial waves and the relatively rapid changes it undergoes. Note that the standard error in this spatially varying ensemble mean is proportional to $\bar{\mathbf{u}}'_e/R^{1/2}$, where $\bar{\mathbf{u}}'_e$ are the fluctuations about $\bar{\mathbf{u}}_e$ and R is the number of realisations (25 for the present experiments). While this represents a relatively small degree of uncertainty, statistics for a much larger ensemble would be desirable.

The degree of anisotropy between the horizontal and vertical components is illustrated by the structure function

$$K = (\bar{u}'_e - \bar{w}'_e)/(\bar{u}'_e + \bar{w}'_e), \tag{12}$$

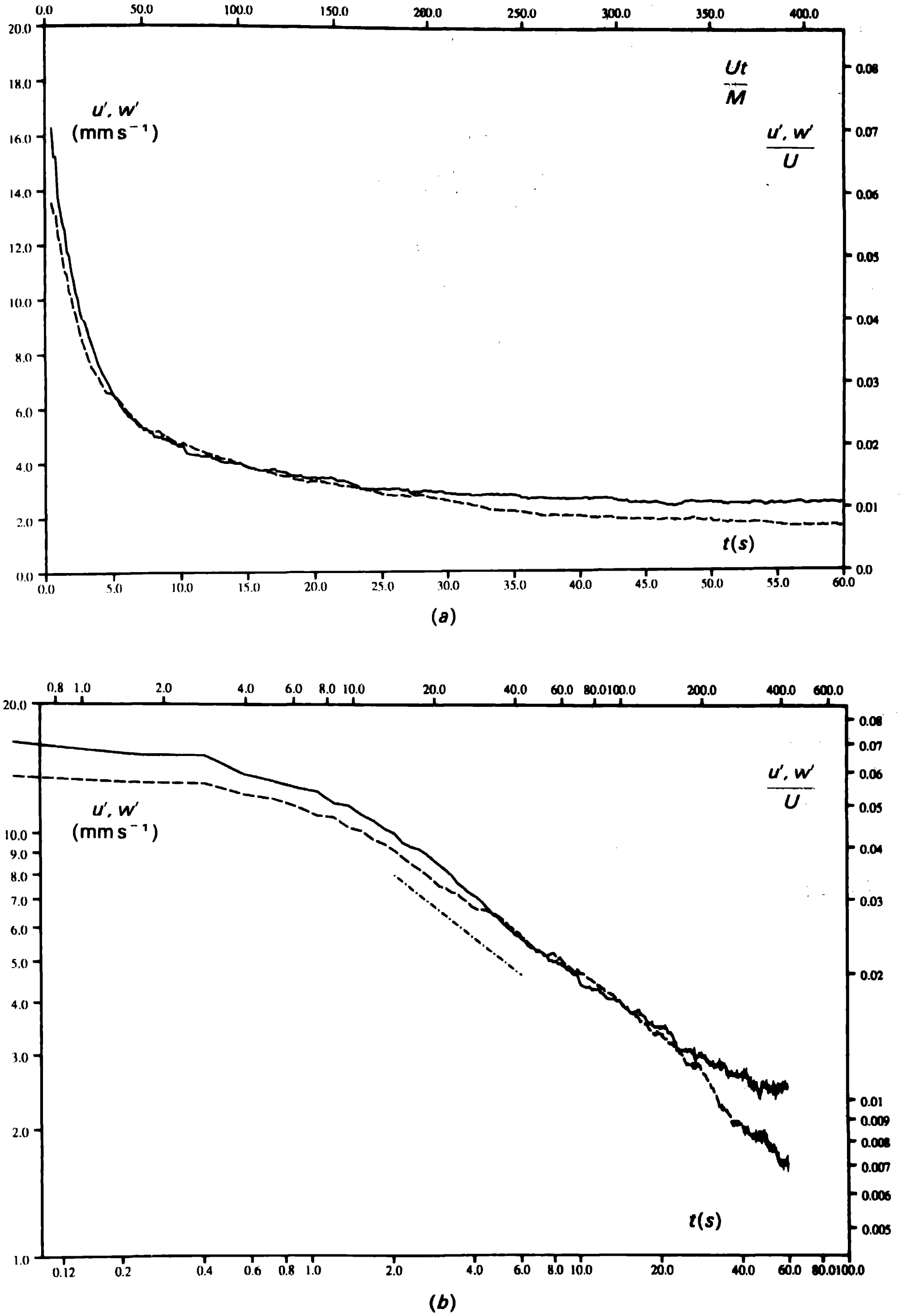

Fig. 6. Evolution of the turbulent velocity fluctuations about the spatially varying ensemble mean flow for $f = 1$ rad/s. Plot (a) has a linear scale while (b) a logarithmic scale showing the power law behaviour of the decay ($t_0 = 0.4s$). Solid lines indicate the along-tank horizontal component, while dashed lines denote the vertical component. The initial period decay law with $\beta = 1$ is shown as a dot-dash line in (b).

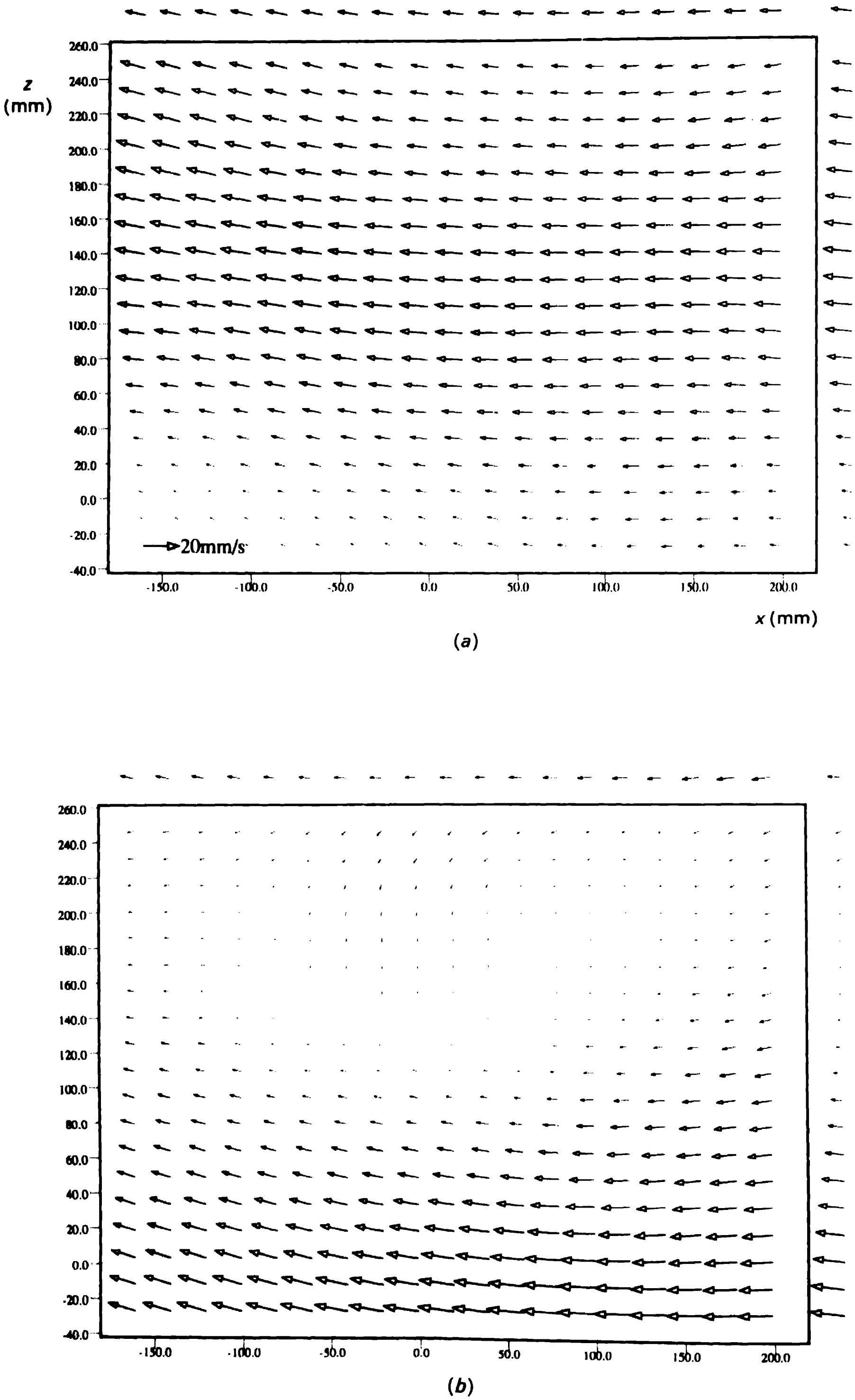
z (mm)
260.0
240.0
220.0
200.0
180.0
160.0
140.0
120.0
100.0
80.0
60.0
40.0
20.0
0.0
-20.0
-40.0
20mm/s
-150.0
-100.0
-50.0
0.0
50.0
100.0
150.0
200.0
x (mm)

(a)

(b)

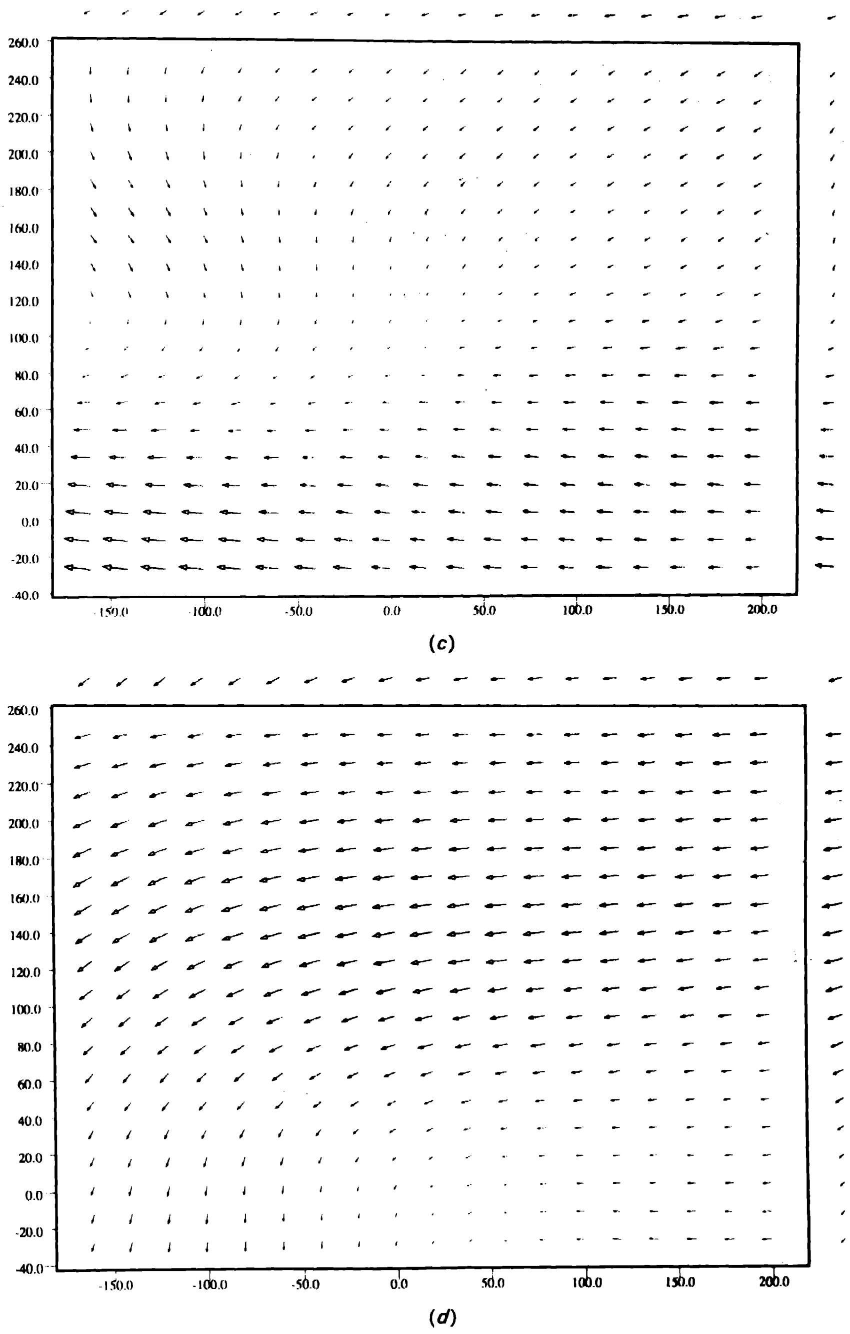

Fig. 7. Series of plots showing the evolution of the spatially varying ensemble mean motion for $f = 1$ rad/s. The passage of a wave crest through the series is clearly visible. The velocity scale is indicated on the first figure. The times corresponding to these plots are (a) $4s(Ut/M = 29)$, (b) $6.24s(Ut/M = 46)$, (c) $8.48s(Ut/M = 62)$, (d) $10.72s(Ut/M = 79)$. The arrows at the top and right-hand extremes of the plots are the averages for the corresponding column or row.

which is plotted in Fig. 8 for both the $f = 0$ rad/s and $f = 1$ rad/s cases. In the absence of rotation we see a persistent 10% anisotropy, a figure consistent with previous investigators for classical turbulence. For $f = 1$ rad/s contamination from the systematic flow yields a smaller degree of anisotropy at early stages. As the decay rate of vertical fluctuations is greater than for horizontal fluctuations, there is a gradual increase in the anisotropy.

The dominant effect of rotation on the flow is in the growth of the associated length scales. We define the two-point correlation functions

$$R_{ij}(\Delta\mathbf{x}, t = t_c) = \frac{\Sigma\,\Sigma\,(u_i'(\mathbf{x})u_j'(\mathbf{x} + \Delta\mathbf{x}) - \bar{u}_i'\bar{u}_j')}{\bar{u}_i'\bar{u}_j'}, \tag{13}$$

where $\Delta\mathbf{x}$ is the separation (in the $y = y_0$ plane) between the points at which the two velocity components (projected onto the $y = y_0$ plane) are evaluated. Subscripts are used here to represent different velocity components rather than different times. The summation is over all particle pairs with the appropriate separation, falling in the specified time interval ($t_c \pm \Delta t_c$), and over all realisations. Note that the finite thickness of the light sheet (δy) means that the correlation functions defined by R_{ij} will in general be slightly smaller (numerically) than the true correlation functions for velocities lying in the $y = y_0$ plane. This will not be significant, however, for $|\Delta\mathbf{x}| \gg \delta y$.

Figure 9 shows the $R_{uu} = R_{11}$ and $R_{ww} = R_{33}$ two-point correlation functions

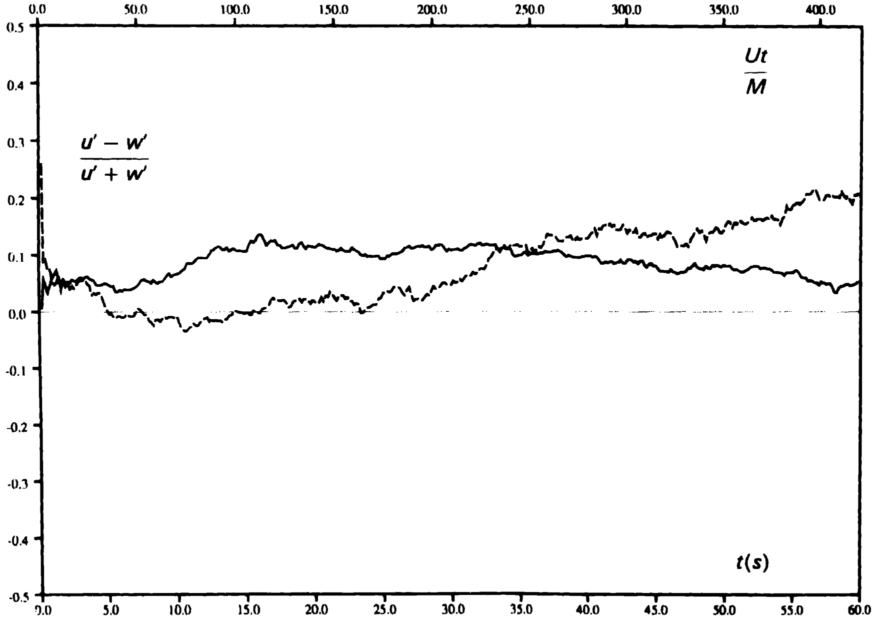

Fig. 8. Evolution of the structure function $K = (\bar{u}_e - \bar{w}_e)/(\bar{u}_e + \bar{w}_e)$ for the classical (solid line) and rotating (dashed line) flows.

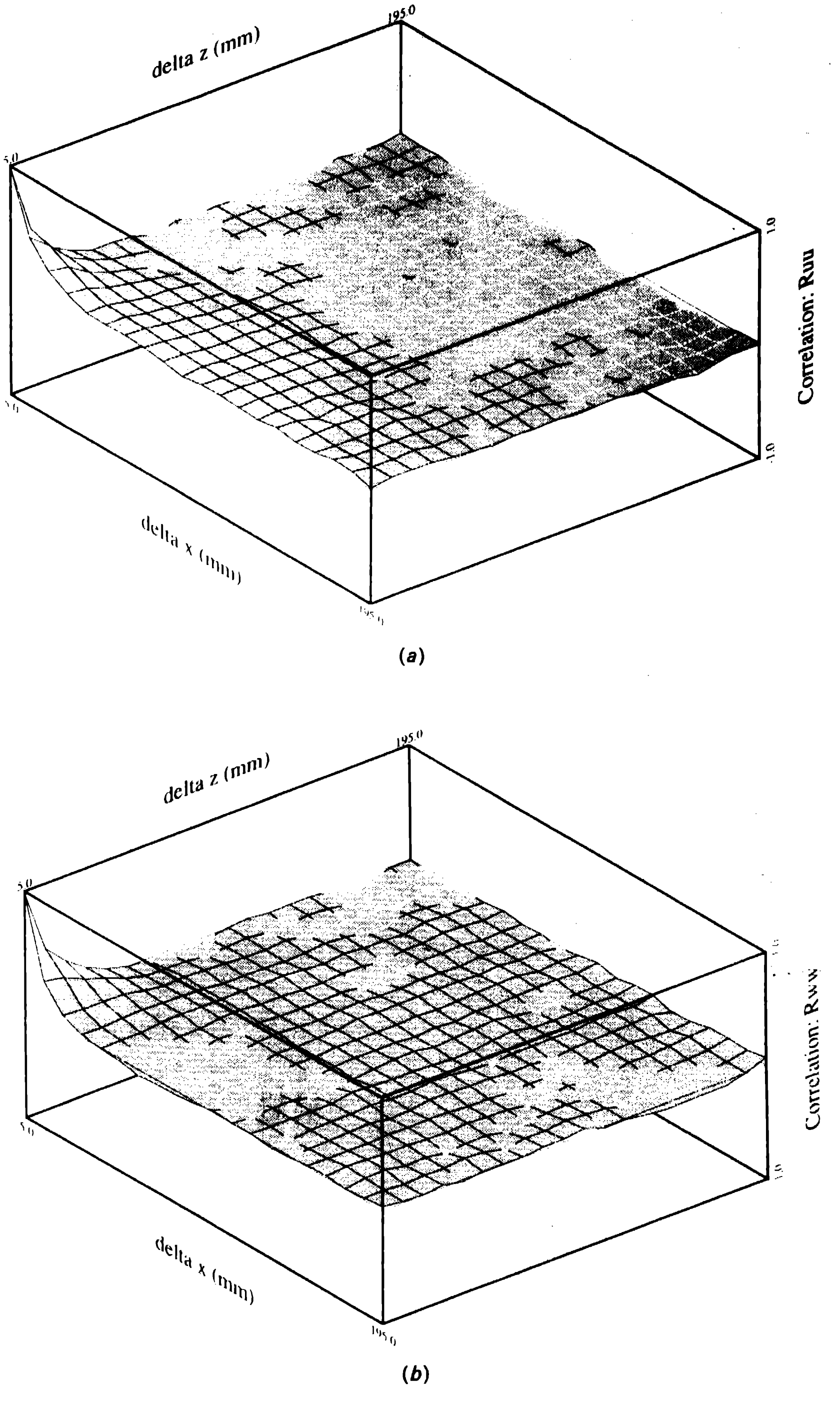

Fig. 9. Two-point correlation functions for the $f = 1$ rad/s ensemble. (a) $R_{uu} = R_{11}$ and (b) $R_{ww} = R_{33}$ at $t = 3s$ ($Ut/M = 22$); (c) $R_{uu} = R_{11}$ and (d) $R_{ww} = R_{33}$ at $t = 20s$ ($Ut/M = 147$).

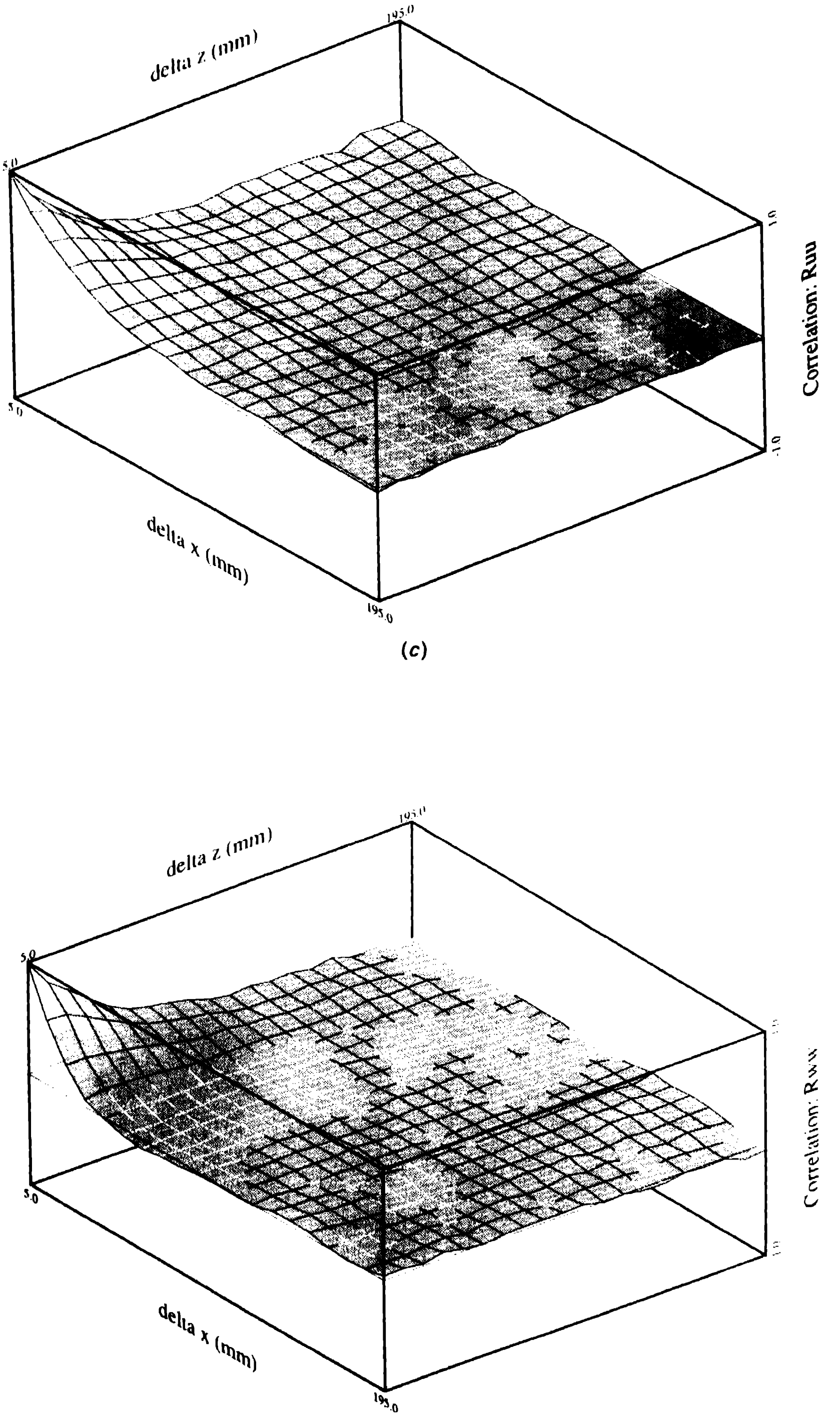

(c)

(d)

Fig. 9 (Continued)

evaluated at two different times. The first pair of plots is evaluated relatively early at $t = 3s$ ($Ut/M = 22$) before the effects of rotation are dominant. The behaviour as a function of spatial separation follows the normal form of correlations between velocities parallel to the separation remaining positive, while those perpendicular pass through zero. The $R_{uv} = R_{13}$ correlation function (not plotted) is approximately zero for all separations, as would be expected. The integral length scales evaluated from these correlations are $L_{uux} = 0.69\,M = 22\,\text{mm}$ for horizontal velocities and separations, and $L_{wwz} = 0.50\,M = 15\,\text{mm}$ for vertical velocities and separations. The inequality of these two length scales reflects the growing anisotropy introduced by rotation in addition to the weak anisotropy inherent in grid turbulence and contamination from the systematic flow. For isotropic turbulence, the length scales with the velocity and separation perpendicular should be half the value of that when the velocity and separation are parallel. Here we find they slightly exceed this relationship ($L_{uuz} = 12\,\text{mm}$ and $L_{wwx} = 10\,\text{mm}$), an affect probably due to the anisotropy introduced by rotation and the systematic flow.

The correlation functions at $t = 20s\,(Ut/M = 147)$ show clearly the enhanced vertical correlation of the velocities, and so will yield larger values for the vertical integral length scale. However, the systematic flow set up by the initial passage of the grid contaminates these figures to a significant degree, with the correlation functions *increasing* with vertical separation for larger separations. This makes evaluation of the integral length scales from these statistics very difficult. Further discussion on these length scales and how they are affected by rotation and the systematic flow are beyond the scope of this paper.

One of the strengths of particle tracking is the ability to obtain Lagrangian statistics much more efficiently than the manual digitization. Figure 10 plots the Lagrangian autocorrelation functions for particles in the light sheet at $t = 5s\,(Ut/M = 37)$. Due to the relatively thin light sheet we are considering there is a strong bias at longer times to particles with small velocities normal to the sheet. The number of particles used in this calculation is also plotted in the figure, and can be seen to decline approximately exponentially, as would be expected for a random distribution of cross-sheet velocities. Caution should be used when interpreting this plot as the turbulence is decaying with time; this is also a feature of comparable Lagrangian statistics in wind tunnel experiments (e.g. Snyder and Lumley [15]). The present results, however, are also contaminated by the systematic flow. The fluctuations in the trace apparent for separations greater than around 2 seconds are due to the free surface Kelvin waves: our Eulerian method of correcting the velocities for the systematic flow is not appropriate for Lagrangian autocorrelations (further discussion is beyond the scope of this paper). Note also that there are too few particles in the sample for separations exceeding 4 seconds.

6. Conclusions

In this paper we have outlined a simple, efficient PIV method of automatically tracking individual particles in a fluid flow. The method has been implemented on a

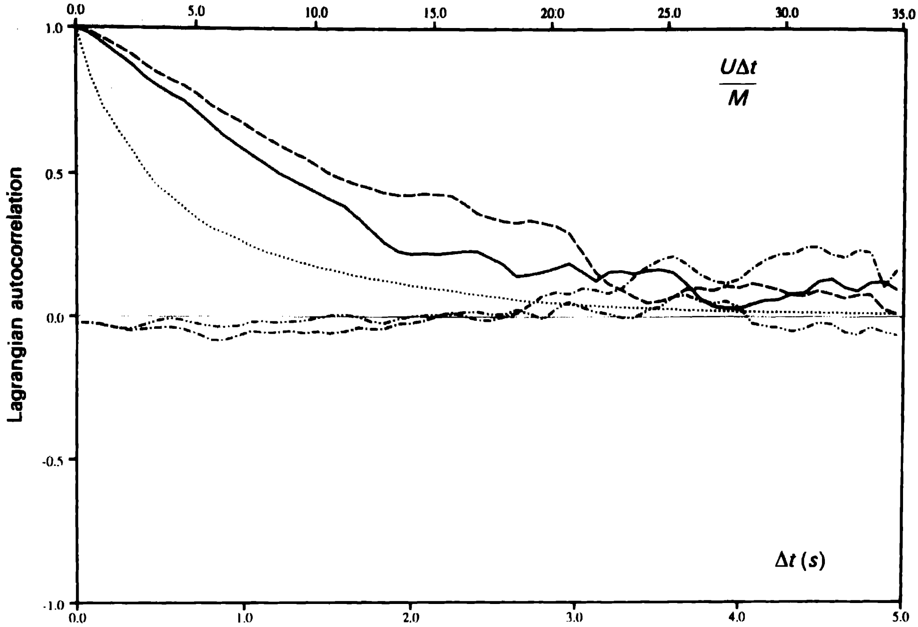

Fig. 10. Autocorrelation functions with $f = 1$ rad/s for particles tracked from $t = 5s$ ($Ut/M = 37$). The $u - u$ component is plotted as a solid line, $w - w$ as dashes, $u - w$ as dot-dash, and $w - u$ as dot-dot-dash. The relative number of particles belonging to the original set still illuminated by the light sheet is also plotted as a dotted line. Note that at large time separations the number of particles becomes too low for the autocorrelations to be meaningful.

PC/AT compatible micro computer utilising a medium cost frame grabber and Super VHS video tape recorder. While the algorithm described in this paper has been implemented to allow up to 4095 particles to be tracked simultaneously, practical considerations impose a limit of approximately 2000 particles. The experiments described in this paper utilised an early version of the particle tracking system following typically 350 particles. The high throughput (up to 25 frame pairs per minute in some situations) makes this method ideal when ensemble statistics of a temporally varying flow are required. Both Eulerian and Lagrangian views of the flow may be obtained from the particle paths.

The particle tracking technique has been applied to a wide range of flows and is illustrated here as part of a study of the decay of rotating turbulence. In addition to being a convenient method for measuring the velocities in this zero mean flow experiment, the ability to gather information over a two dimensional region has proved invaluable in analysing the systematic flow contaminating the experiment.

Severe limitations in the experimental set up have been discovered. The initial passage of the grid is found to set up a large scale systematic flow. In the absence of rotation this flow is predominantly in the direction of the grid near the centre of the tank, with the return flow near the boundaries. Multiple passes of the grid and increased solidity near the walls reduced this effect but did not prove possible to eliminate it. When the system is rotating, the systematic flow breaks up into a large scale inertial wave field in the order of an inertial period. The wave field appears to consist of the superposition of two modes, one with the wave number vector parallel to the rotation axis, and the other with it inclined at approximately 66°. This wave field has a high degree of coherency throughout an ensemble of 25 realisations. The spatially and temporally varying structure of this wave field is established from the ensemble flow, and used as the basis of a correction to establish the turbulent component of the flow. The separation in length scales did not prove sufficient for this technique to be entirely effective.

The generation of such a strong systematic flow during the passage of the grid is of deep concern in the rotating system. Earlier investigators have not reported such difficulties, primarily as a result of such information being less accessible to traditional measurement techniques. The problem may be expected to be less severe with the symmetric grid arrangement of Ibbetson and Tritton [11] as the velocity component of the large scale flow introduced by the passage by the grid will be parallel to the rotation axis over most of the tank. However, at the initial mid-height position of the two grids and at the top and bottom of their annulus we would expect a significant radial component which may be strongly affected by the Coriolis force. The experiments of Jacquin et al. [12] will be less affected due to the mean flow parallel to the rotation axis and the absence of boundaries perpendicular to that axis. Moreover, as our present difficulties are the result of initial transients, the statistically steady flow in their tube does not have the same form of forcing function.

The oscillating grid experiments of Bretherton and Turner [3], Hopfinger et al. [10], Dickenson and Long [6] and Fluery et al. [7] may also be adversely influenced by the existence of a large scale systematic flow. Experiments by McDougall [13] show that in the absence of rotation such oscillating grids generate a systematic flow with an amplitude comparable to the fluctuations. This flow will interact with the Coriolis force in regions of the tank remote from the grid. This feature is being investigated further by Drayton (personal communication) using the present particle tracking technique. The advection of smaller scale turbulence by this flow may well lead to the formation of the intense vortices and rapid spatial change from three dimensional to nearly two dimensional motion characteristic of such experiments.

Despite the experimental limitations, rotation has been found to decrease slightly the rate of decay of turbulent fluctuations. In addition to a small increase in the anisotropy as the decay progresses, rotation leads to a marked increase in the integral length scales. These findings are in broad agreement with those of other authors.

References

1. Adrian, R. J., Particle-image techniques for experimental fluid mechanics. *Annu. Rev. Fluid Mech.* 23 (1991) 261–304.
2. Batchelor, G. K.: *The Theory of Homogeneous Turbulence.* Cambridge University Press (1953).

3. Bretherton, F. P. and Turner, J. S., On the mixing of angular momentum in a stirred rotating fluid. *J. Fluid Mech.* 32 (1968) 449–464.
4. Britter, R. E., Hunt, J. C. R., Marsh, G. L. and Snyder, W. H., The effects of stable stratification on turbulent diffusion and the decay of grid turbulence. *J. Fluid Mech.* 127 (1983) 27–44.
5. Comte-Bellot, G. and Corrsin, S., The use of a contraction to improve the isotropy of grid-generated turbulence. *J. Fluid Mech.* 25 (1966) 657–682.
6. Dickinson, S. C. and Long, R. R., Oscillating-grid turbulence including effects of rotation. *J. Fluid Mech.* 126 (1983) 315–333.
7. Fluery, M., Mory, M., Hopfinger, E. J. and Auchere, D., Effects of rotation on turbulent mixing across a density interface. *J. Fluid Mech.* 223 (1990) 165–191.
8. Greenspan, H. P., *The Theory of Rotating Fluids*. Cambridge University Press (1968).
9. Hichcock, F. L., The distribution of a product from several sources to numerous localities. *J. Math. Phys.* 20 (1941) 224.
10. Hopfinger, E. J., Browand, F. K. and Gagne, Y., Turbulence and waves in a rotating tank. *J. Fluid Mech.* 125 (1982) 505–534.
11. Ibbetson, A. and Tritton, D. J., Experiments on turbulence in a rotating fluid. *J. Fluid Mech.* 68 (1975) 639–672.
12. Jacquin, L., Leuchter, O., Cambon, C. and Mathieu, J., Homogeneous turbulence in the presence of rotation. *J. Fluid Mech.* 220 (1990) 1–52.
13. McDougall, T. J., Measurements of turbulence in a zero-mean-shear mixed layer. *J. Fluid Mech.* 94 (1979) 409–431.
14. Perkins, R. J. and Hunt, J. C. R., Particle tracking in turbulent flows. In Fernholz, H.-H. and Fielder, H. E. (eds), *Advances in Turbulence*, Vol. 2. Springer-Verlag (1979) pp. 286–291.
15. Snyder, W. H. and Lumley, J. L., Some measurements of particle velocity autocorrelation functions in a turbulent flow. *J. Fluid Mech.* 48 (1971) 41–71.

Applied Scientific Research **49**: 245–259, 1992.
© 1992 *Kluwer Academic Publishers. Printed in the Netherlands.*

Measurement of product concentration of two parallel reactive jets using digital image processing

H. STAPOUNTZIS[1], J. WESTERWEEL[2], J. M. BESSEM[2],
A. WESTENDORP[2] & F.T.M. NIEUWSTADT[2]

[1]*University of Thessaloniki, Dept. of Mechanical Engineering, Box 443, Thessaloniki 54006, Greece*
[2]*Delft University of Technology, Faculty of Mechanical Engineering and Marine Technology, Laboratory of Aero- and Hydrodynamics, 2628 AL Delft, The Netherlands*

Key words: jet flows, mixing, concentration fluctuations, LIF techniques, digital image processing

Abstract. The chemically sensitive LIF technique [9] is employed to study the mixing of two reactive axisymmetric jets, one of which carries fluorescein, in an ambient quiescent fluid. The degree of mixing depends on the jet spacing and the axial position downstream of the jets and power laws are found to hold for some concentration characteristics. Unlike the far velocity field of dual plane jets, self preservation laws are not found to hold in general for the concentration field.

1. Introduction

The interaction and mixing of separate jets is a fundamental problem of turbulent shear flow and it is used in a wide variety of engineering applications such as burners and combustion chambers, chemical reactors, propulsion, thrust augmenting ejectors for V/STOL aircraft and fluidics. Both the near or far fields of the jets may be of interest as in the recirculation regions of confined jets and the far field of acoustic noise.

There is little information on dual-jet velocity and pressure fields available in literature and hardly any work on the concentration field of two mixing jets. The conclusions drawn from the study of the interaction of two parallel plane jets [1–6] can be summarized as follows (see Fig. 1): Initially, in region (A), extending 15 to 20 jet diameters, *d*, from the nozzles and for nozzle distances less than about 30 d, the two jets converge towards the centerline between the nozzles. Reversed flow and two counter rotating vortices are observed inside this region. In the merging region, (B), further downstream a stagnation point exists, whose position scales almost linearly with the transverse distance between the jets, l. Finally in the combined flow region, (C), the flow characteristics are resembling those of a single jet. Self preservation for the mean velocity is observed in the regions (A) and (C), and the effect of the Re number is significant. The region (B) is highly anisotropic, with the centerplane longitudinal velocity fluctuation, $\overline{u^2}$, reaching a minimum, the transverse, $\overline{v^2}$ normal to the jet centerplane reaching a maximum and $\overline{w^2}$ showing little change. The intensities there are ordered in value as $\overline{v^2} > \overline{u^2} > \overline{w^2}$. It is anticipated that the commencing of mixing and reaction (for chemically reactive jets) should occur in this regime. It is not

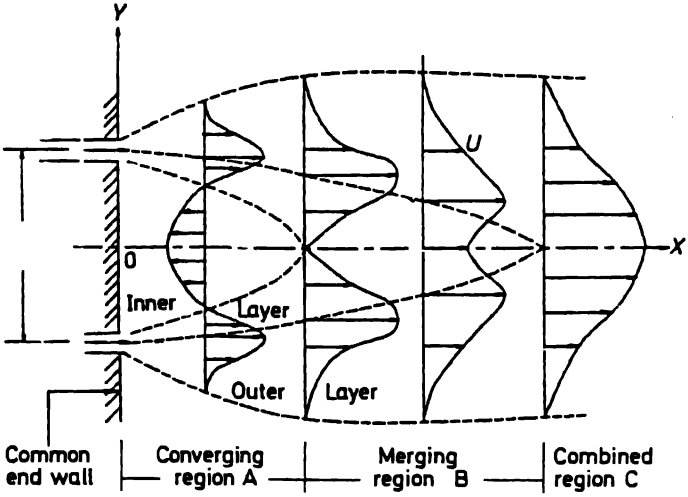

Fig. 1. Mean velocity profiles for plane dual jet flow [6].

known what the position and extent of the merging region would be in dual axisymmetric jets. However, data for axisymmetric dual coflowing reactive jets [7] indicate that it should lie much further downstream from the jet nozzles compared to the dual plane jet position.

The lack of experimental data is partly due to the difficulty in describing mixing in turbulent flow and especially in the measurement of instantaneous concentrations of rapidly reacting species [8].

A useful technique which enables one to distinguish fluid that has been molecularly mixed from that which has been merely stirred, is that of chemically sensitive Laser Induced Fluorescence [9, 10]. This method exploits the pH-sensitive characteristics of a fluorescent dye excited by a laser light beam (or plane sheet) in conjunction with a nearly isothermal (for low concentrations) reaction between a base and an acid into which liquids (in both or in either of them) the dye has been dissolved. With the advent in the development of fast data acquisition and image processing systems, this method can be used to measure the time dependent overall character of entrainment and mixing and the detection of coherent structures, information which cannot be obtained from the statistically averaged concentration field. On the other hand, one aspect of jet mixing which can be directly obtained by this technique is the axial distance, M, required to molecularly mix the jets to at least a given mass ratio. As an extension, the technique may be used to determine the locations of the upper and lower flammability limits, when a flame mixture is being studied.

The purpose of this paper is to apply the chemically sensitive LIF non-intrusive technique together with digital image processing in order to study the mixing of two parallel axisymmetric jets.

2. Experimental set-up

The measurements described were carried out in a tapered vertical water tank 1.4 m high with upper rectangular cross section 0.21 × 0.21 m and lower rectangular cross section 0.25 × 0.32 m, see Fig. 2. The tank had glass windows on all four side walls and the floor. The jets issued vertically downwards into the tank via two parallel stainless steel tubes of internal diameter $d = 5$ mm and outside diameter $D \doteq 6$ mm. The distance between the centers of the tubes, l, was varied between $l = 1.2d$ to $8.2d$. The

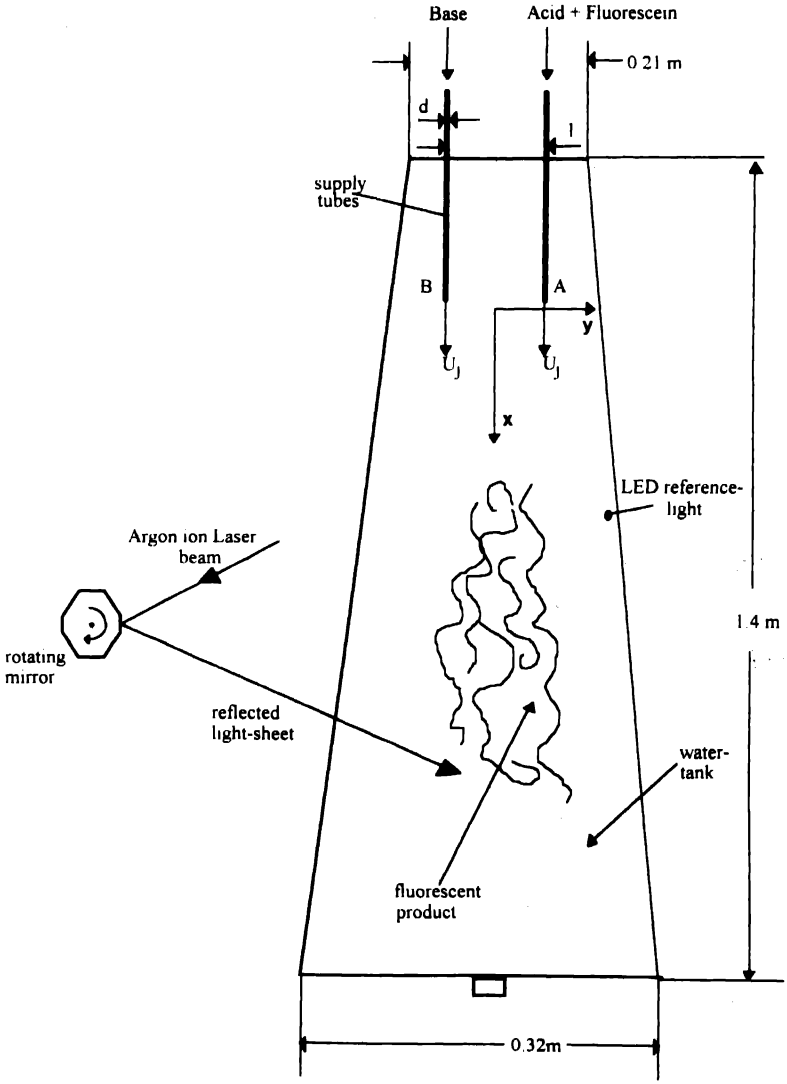

Fig. 2. Experimental setup.

upper value of l was dictated by the size of the tank to avoid interference from the side walls and bottom of the tank. The jet Re number based on the mean exit speed U_j (approximately 1.9 m/s), the diameter d and the kinematic viscosity of water was Re $\approx$ 9000. The reactants used were Nitric Acid and Sodium Hydroxide. Different tests were made with initial acid or base concentrations between 0.1 N and 1 N. Even at the high concentrations the density differences from that of water were small and the jets could be considered as momentum driven [11].

The laser light sheet was produced by a rotating (1000 rpm) polygonal mirror exposed to a 0.8 W Laser Argon ion beam (488 nm) via a fiber optic probe. The sheet was in the plane defined by the centerlines of the jets (x, y plane), its thickness was approximately 1 mm and its vertical extent about 0.65 m. In this present work measurements were taken only at that plane.

A CCD video camera recorded the fluorescence on the $x-y$ plane in a square array of $512*512$ pixels. If the jets were not interfering, the minimum and maximum Kolmogorov microscales under the present conditions would be about 25 μm and 210 μm respectively [12], meaning that not all of the smallest scales of turbulence might be resolved. Similarly, the temporal resolution for the smallest time scales should be at least 1 ms as opposed to the 40 ms frame rate of the CCD camera. Therefore, no detailed investigation of the structure of the concentration field was sought in these experiments. Rather, attention was focused on the mean and rms concentration fluctuations obtained from the intensity of fluorescence.

3. LIF technique

One of the jet fluids consisted of an aqueous acid solution of HNO_3 homogeneously mixed with a small amount of the pH-sensitive fluorescent dye, fluorescein. The other jet fluid was an aqueous solution of NaOH. The concentrations of the acid and base tried in the experiments ranged from 0.1 N to 1 N and the concentrations of the dye from 10^{-6} to 5×10^{-6} moles/lt of acid solution. The fluid carrying the fluorescein is only visible (i.e. it fluoresces) when it reacts with the base or when it is diluted with the ambient water until the local pH of the solution crosses a certain threshold value.

Preliminary tests were performed in a small cubic glass container ($100 \times 100 \times 100$ mm internal dimensions), placed inside the tank, and in the working tank itself. The purpose of these tests was to check: (a) the absorption and scattering of the laser light sheet, (b) the effect of temperature on fluorescence, (c) the homogeneity of the laser light sheet over the area of interest and (d) the dependence of fluorescence intensity on the base–acid concentrations. The procedure was to mix thoroughly acid + fluorescein and base solutions, wait until large scale motions have died out and then use the video camera and the image processing system, in situ, to acquire the data. The small container was used to save on chemicals, when used at high concentrations (1 N). The most severe case for absorption and scattering was to use 1 N concentrations of acid and base and the maximum fluorescein concentration. The base–acid reaction is exothermal and for the aforementioned concentrations the overall temperature rise was less than 7.5°C, after reaction and mixing were completed. Reacted solutions of 16°C and 36°C were tested ($\Delta T = 20°C$), the latter solution being artificially heated to this temperature level.

Figure 3 shows the variation of the intensity of fluorescence on a horizontal cut between the two parallel vertical walls of the container. A mild exponential decay of fluorescence with distance is observed and an overall drop of about 20% due to the temperature rise of $\Delta T = 20°C$. Tests with more dilute solutions in the working tank indicated a fluorescence decay of almost linear type. A vertical cut in the tank (i.e. in the streamwise, x, direction) midway between the tubes, showed good uniformity of fluorescence over the area of interest (0 to 80 d) with some attenuation on both sides due to the longer optical path of the light beams.

The effect of scattering at 488 nm was tested by placing a band pass optical filter in front of the video camera. The sensed wavelength was thus centered at 514 nm (the wavelength of fluorescence). The shapes of the fluorescence-distance curves were similar with and without the filter, a sign that elastic scattering was small. However, the filter attenuated the overall fluorescence intensity by 60%, rendering the measurement of low levels of fluorescence inaccurate. Care was taken to allow for the release of the small air bubbles present in the water tank and the solutions in order to keep the light scattering to a minimum.

The main experimental results presented here were not corrected, at this stage, for the above mentioned effects, because at relatively high concentrations the extent of the reaction zone was small (compared to the size of the test container) and thus the absorption was small, while far downstream, where the reaction zone is wider the reactant concentrations were very low. In support of this, was the recovery, using the

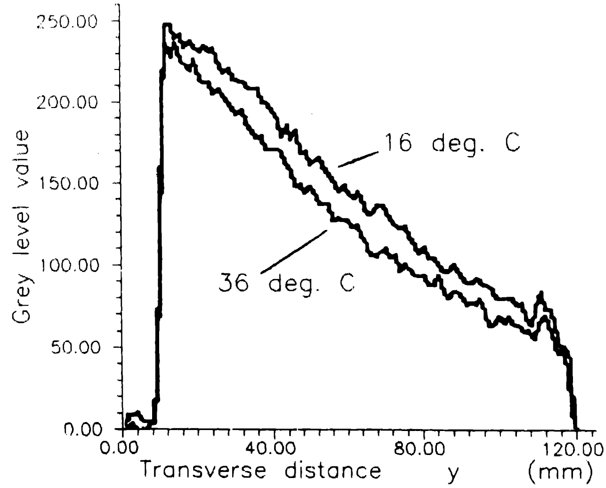

Fig. 3. Variation of fluorescence intensity across the calibration container (normal to the jet flow).

present method, of the concentration decay characteristics of a single, non-reacting jet of water and fluorescein issuing into the water tank.

Depending on the strength and nature of the acid–base solutions, the pH range over which the dye undergoes fluorescence transition, can be crossed in a very narrow range of mixture ratio, ([9], strong base-acid solutions, $\text{pH}_{\text{threshold}} \approx 4.5$) or in a wider range ([8], mild base-acid solutions, $\text{pH}_{\text{threshold}} \approx 7.0$). In the latter case the relationship between fluorescence intensity, I_f, and the acid volume fraction is not linear because of the gradual change of I_f, and the acid volume fraction is not linear because of the gradual change of I_f. For strong reactants, I_f suddenly rises from almost zero, to its maximum value $I_{f\max}$ at the threshold mixture ratio of the acid-base and thereafter it changes linearly with that ratio (so that the dye is merely diluted by the base). This is shown in Fig. 4 which presents data obtained in the small glass container. If C_p is defined as the concentration of the molecularly (dye-bearing) fluid whose local pH is above the fluorescence threshold then,

$$C_p/C_{p\max} = I_f/I_{f\max}. \tag{1}$$

The threshold mixture ratio, also called stoichiometric ratio, defined as the mass ratio of the base fluid to the acid fluid can be determined by gradually adding some known base solution to some known acid solution and marking the relative acid–base concentrations when fluorescence suddenly starts. Since the fluorescence transition across the threshold is reversible and occurs on a very short time scale, the dye

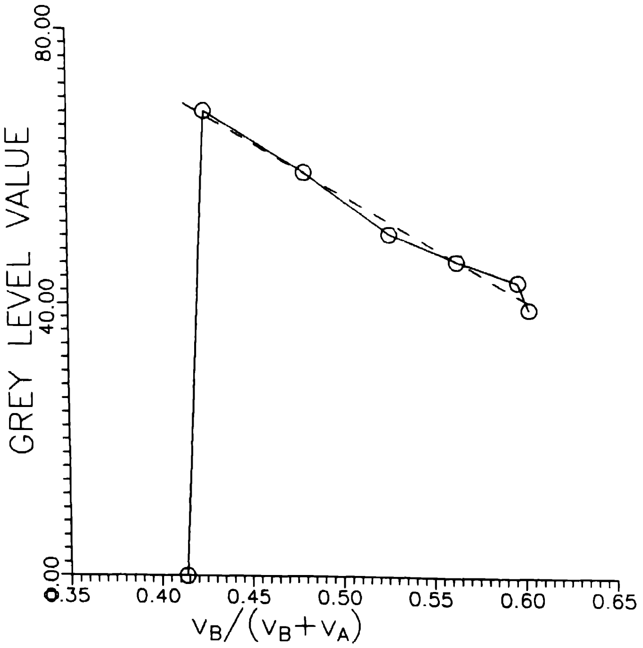

Fig. 4. Fluorescence intensity against base volume fraction. Initial concentration of reactants is 1N.

fluorescence determines directly if the instantaneous local extent of molecular mixing between the jets has crossed this threshold.

The present experimental conditions are however different and more complicated than those of previous workers, in the sense that fluorescence could also be excited by the mixing of the acid jet fluid with the ambient water in the tank, a process which also raises the pH of the mixture. For this reason, strong acid–base solutions were selected for most of the runs and experiments with acid-dye solutions in different ambient fluid environments were planned in order to ascertain the overall effect of ambient fluid mixing. Equation (1) was therefore assumed to be approximately valid, at least in the central area between the jets.

4. Image analysis technique

For the image processing the PC-SEMPER software was used, on a HP-Vectra RS/20 PC-AT equipped with a DT2851 frame grabber and a DT2858 auxiliary frame processor. The image processing software was extended with additional commands for image alignment and image averaging.

Runs at different transverse jet spacings l/d, were recorded in the non-interlaced mode on a video tape (duration approximately 12 s) and were processed later on a workstation. Each frame was grabbed manually, but the subsequent processing was automated. Only half frames were processed, i.e. those containing the "odd" or "even" lines of the field. The resulting image consisted of 256 rows parallel to the streamwise, x, direction and 512 columns in the transverse, y, direction, i.e. a total of 256 × 512 pixels of grey level intensity 0 to 255. This scale sets also the best accuracy in measuring the relative intensity of fluorescence (product concentration). An LED light positioned at the lower right hand side of the tank during the experiments, served as a reference point for the alignment and superposition of the individual frames for statistical averaging. This was accomplished by computing the cross correlation function in a small interrogation area round the reference light for every two consecutive frames. Knowing the relative displacement vector of these frames, of the order of a few pixels (which might have been caused by vibration of the tubes, camera movement etc.), it was easy to align the individual images and perform statistical operations on them to obtain the mean and rms of the concentration fluctuations. With the existing system up to 50 frames were analyzed due to storage limitations. Work is now in progress to enable sequential grabbing of up to 200 frames and subsequent processing on an HP 9000 computer with a much faster software.

5. Experimental results and discussion

Figure 5 shows an example of image grey level representation for the mean and rms product concentration averaged over 25 frames for acid–base solutions of 1N. Higher

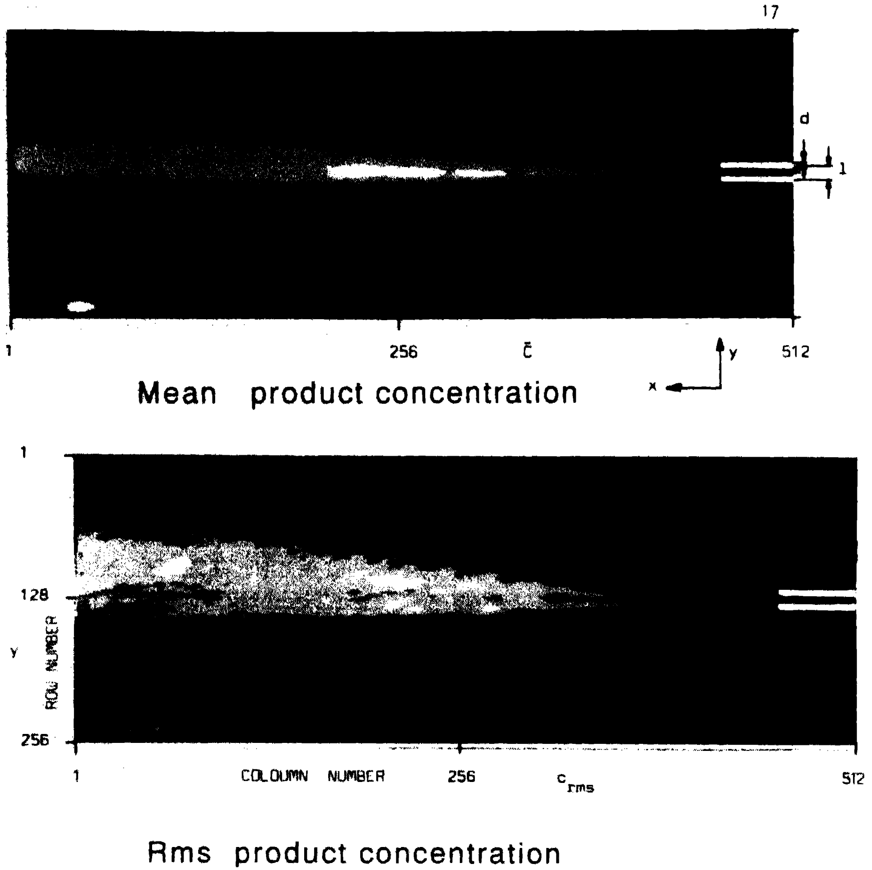

Fig. 5. Grey level representation of the mean and rms concentration fluctuations for two parallel reactive jets. Rows are parallel to jet axes, columns are normal. There are 256 rows and 512 columns. $l/d = 2.2$, 25 frames.

mean product concentration (fluorescence intensity) is observed in the central region between the jets and higher fluctuations outside this central region. This is also what one would expect for a dual plane jet, where both the mean and the fluctuating velocities peak off-centerline till the far downstream self preserving region is reached [3, 5, 6]. Of course the instantaneous composition of mixed fluid cannot be represented by the mean. Figure 6 contains plots of the concentration averaged over 1, 10 and 30 frames and shows that there could be large regions across the combined jet flow where the "instantaneous" composition of mixed fluid may be uniform, that is regions of rather well mixed flow.

The distribution of product is not symmetric with respect to the dual jet centerline. This is more clear in Fig. 7, where averaged profiles of mean concentration, $\bar{c}$, are plotted versus the transverse coordinate for various streamwise locations. The profiles are sharper on the acid side because of the sharp fluorescence transition in a still acidic environment. The gradual dilution of the product on the base side is responsible for

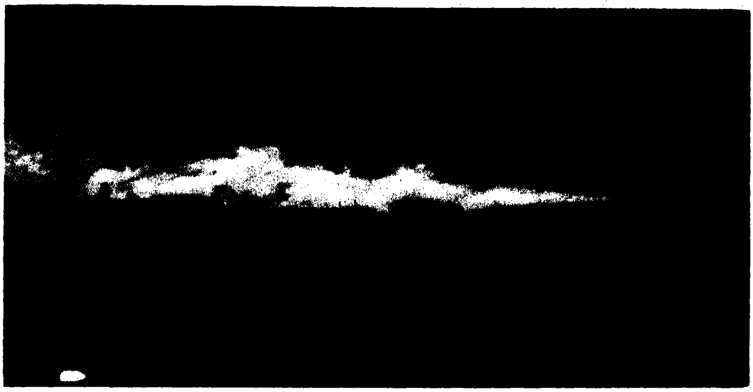

Fig. 6(a).

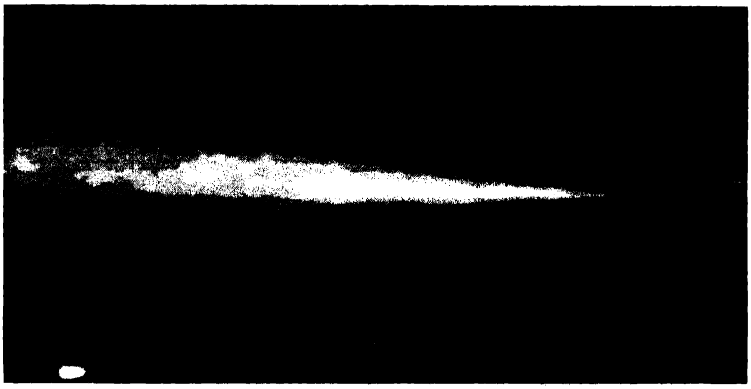

Fig. 6(b).

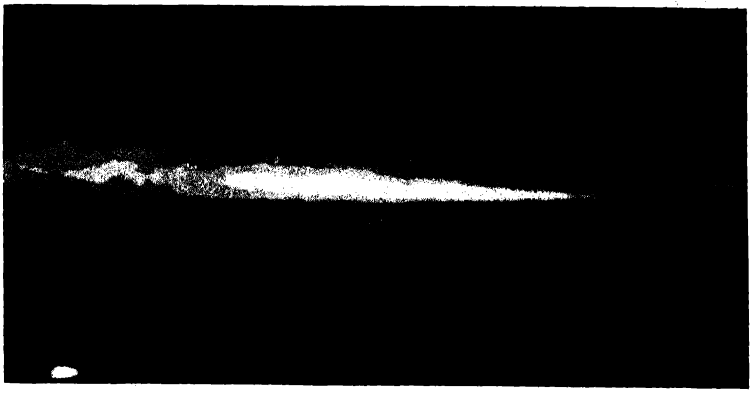

Fig. 6(c).

Fig. 6. Effect of number of averages on image statistics. Mean concentration, $l/d = 1.2$. (a) 1 frame; (b) 10 frames; (c) 30 frames.

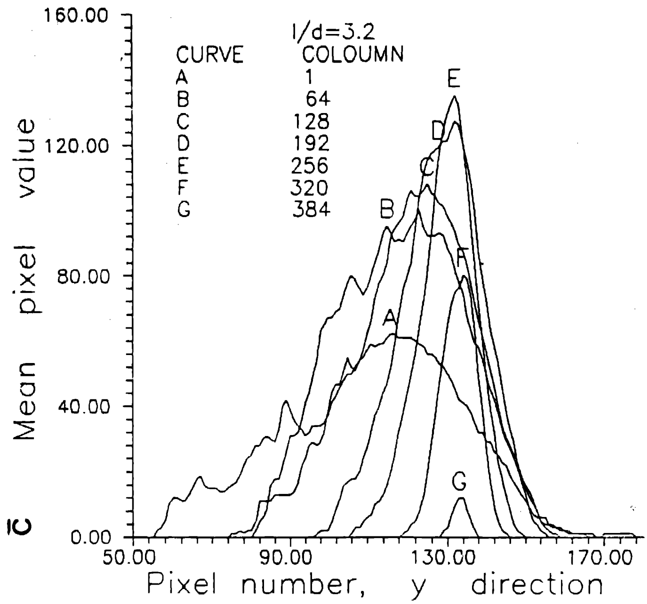

Fig. 7. Development of mean product concentration profiles in the streamwise, x, direction. $l/d = 3.2$. For column position refer to Fig. 5.

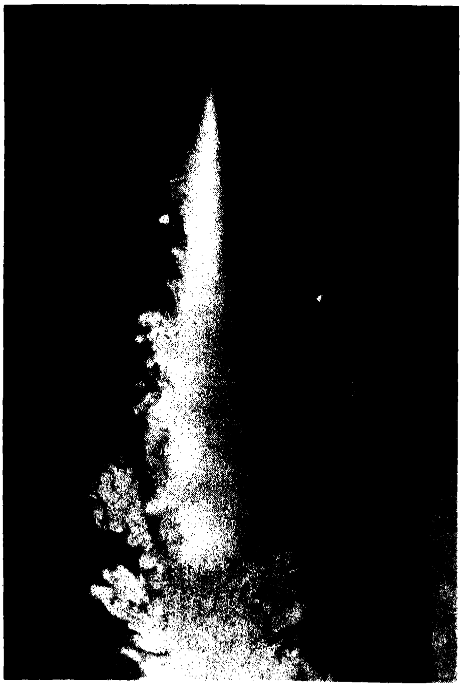

Plate 1. Laser induced fluorescence in the mixing region of two parallel reactive jets. Acid with fluorescein is carried on the right hand side stream, base on the left hand side. $l/d = 1.2$.

the "skewed" shape of $\bar{C}$ in Fig. 7, see also Plate 1. The shift in the maxima of $\bar{C}$ is also attributed to this behavior.

The development of the mean maximum product concentration, C_{max}, with downstream distance x/d, is shown in Fig. 8. Significant mixing and reaction signalled by fluorescence "turn-on" occurs after certain distance, x_s, downstream of the nozzles, depending on their spacing, l/d. In a similar configuration of coflowing jets [7], with $U_j/U_0 = 54$ (U_0 is the ambient coflow speed), mixing appears to start much later, but at large jet spacings this difference diminishes. In the same figure, (i.e. Fig. 9) appears

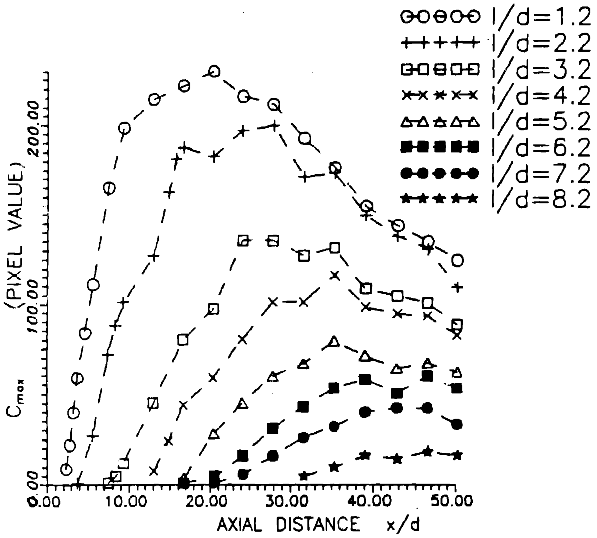

Fig. 8. Maximum product concentration in the streamwise direction.

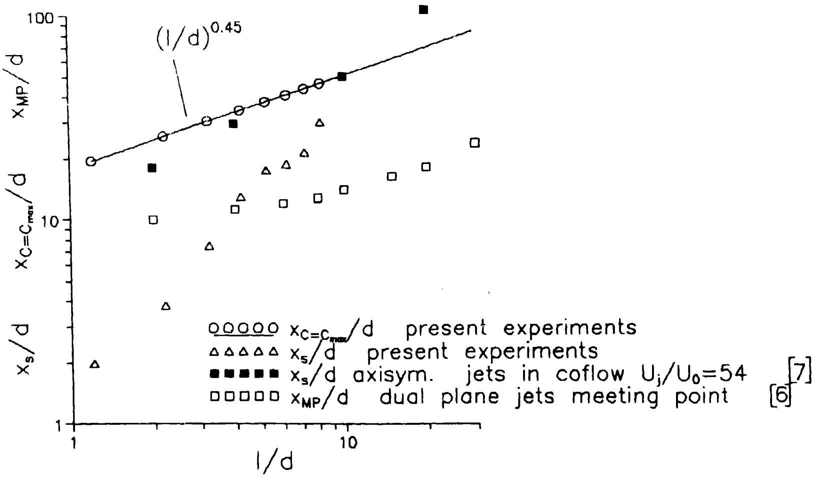

Fig. 9. Streamwise position on centerline of jets where mean concentration is max., $x_{\bar{C}=C_{max}}$, reaction is initiated, x_s, or jets first meet, x_{MP}.

the position, x_{MP}, where the two plane jets meet [6], and which it was thought that it could bring some relevance to the mixing. For $l/d > 4$ the plane jets meet at a streamwise location much shorter than the one it takes for axisymmetric jets to mix. This could be partly due to the greater dilution of the (three dimensional) axisymmetric jets.

Figure 9 shows that the mean concentration reaches a maximum at streamwise location, $x_{\bar{C}=C\max}$, which is also a function of the jet spacing l/d. A corresponding quantity for two parallel nonreactive plumes from line sources A, B is the "interference coefficient" $r = \overline{c_A c_B}/(c_{A\mathrm{rms}} c_{B\mathrm{rms}})$ [15, 16]. In that case as well, it is found that the amount of turbulent mixing midway between the plumes depends on the spacing of the plumes. In Fig. 9, $x_{\bar{C}=C\max}$ is plotted against l/d and it is found that it grows according to a power law, approximately as $(l/d)^{0.45}$. If the two jets were not interfering with each other, then using the known results for the concentration field of single jets [14], one finds that $x_{\bar{C}=C\max}$ should grow linearly with l/d. Therefore, although it is claimed that in the far field the combined jet behaves as a single jet from an appropriate virtual origin [1], there could still be characteristics of the concentrations on which the initial conditions have a persistent influence. There is not sufficient length of working section in the present work to estimate the downstream position where fluorescence becomes very weak.

The effect of jet spacing on the maximum concentration is shown in Fig. 10. In general, the maximum concentration decreases with l/d since the two jets entrain more ambient fluid as l/d increases. Data from a dual plane jet [3], pertaining to the decay of mean maximum velocity, $U_{\max}$ are included in Fig. 10. This maximum velocity is seen to be related to the jet spacing by an approximately $(l/d)^{-0.5}$ power law. $U_{\max}$

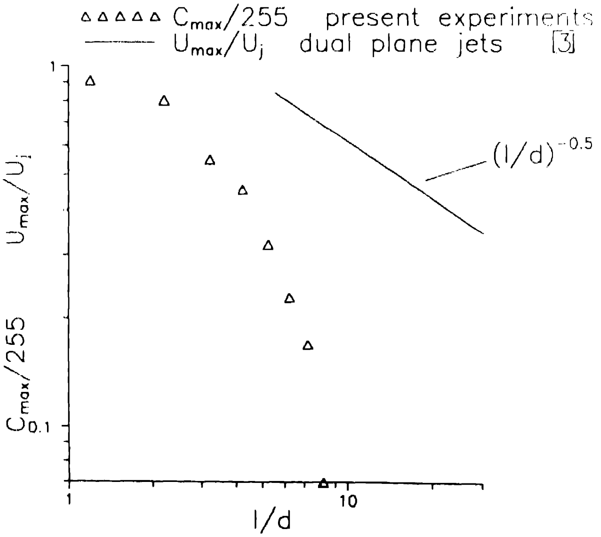

Fig. 10. Maximum concentration and maximum velocity on the center plane of dual jets. Concentration is non-dimensionalized by max. pixel intensity and velocity by the mean exit velocity.

occurs prior to the combined self preserving region of the two jets (region "C" in the introduction) and appears to control the development of this region. In turn, U_{max} depends on $x_{MP}^{-1/2}$, where x_{MP} is the distance from the nozzles to the meeting point of the two jets. Again, it is observed that some characteristics of the concentration field of the axisymmetric dual jets are not self preserving.

Figure 11 shows the variation of the maximum product concentration with x/d at spacing $l/d = 3.2$. It is found, though not shown systematically here (except for the plot of Fig. 5b), that for small l/d there are two maxima off the center-line of the jets. For l/d above approximately 5.2 the maxima move closer to the center-line form with a tendency to disappear. For every l/d, an absolute maximum is found and the position where this maximum occurs, $x_{c_{rms}=c_{rmsmax}}$, is plotted against l/d in Fig. 12.

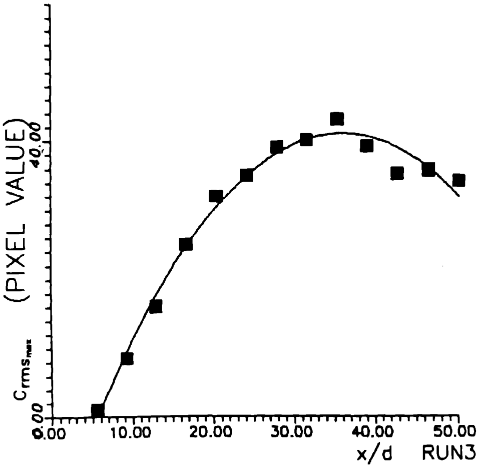

Fig. 11. Maximum rms product concentration, $l/d = 3.2$ in the streamwise direction.

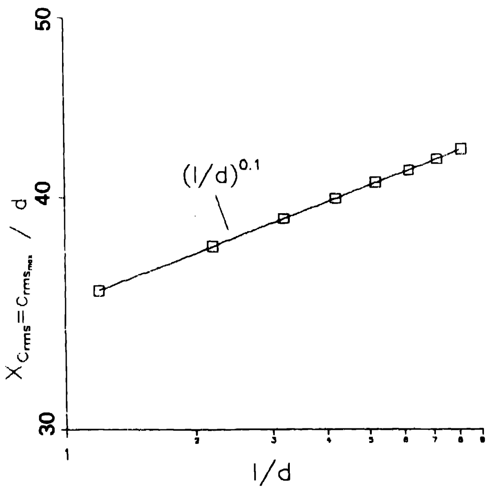

Fig. 12. Streamwise position where rms concentration is maximum.

This quantity, as opposed to the corresponding one for the mean concentration, increases very slowly with l/d. The ratio $c_{\mathrm{rmsmax}}/C_{\max}$ is roughly equal to 0.3 for the range of values l/d considered in this experiment. In single jets this ratio is in the range of 0.25 [10, 11].

6. Conclusions

The degree of mixing between two axisymmetric parallel jets, monitored down to the molecular scale by means of the chemically sensitive LIF technique, was found to depend on the axial distance from the nozzles and their spacing. The closer the jets, the higher the maximum mean product concentration and the earlier it appears along the jet center-line. This position is related with a power law to the jet spacing. The RMS product concentration shows a similar behavior but the maxima occur off the jet center-line and their axial position, although following again a power law, is not as strongly dependent on the jet spacing. The velocity field of interfering dual plane jets is known to be self preserving at large axial distances, but there is evidence that this is not always the case for the concentration field of dual axisymmetric jets.

The LIF technique is proved to be a useful and powerful technique but care should be exercised when dealing with more than two mixing species.

Acknowledgments

The authors would like to thank Mr C. Gerritsen and Mr W. Kracht for their assistance in setting up this experiment.

References

1. Miller, D.R. and Comings, E.W., Force-momentum fields in a dual-jet flow. *Journ. Fl. Mech.* 7 (1960) 237–256.
2. Tanaka, E., The interference of two dimensional parallel jets. *Trans. Bull. of the JSME* 13 (1970) 272–280.
3. Tanaka, E.: The interference of two dimensional parallel jets. *Trans. Bull. of the JSME* 17 (1974) 920–927.
4. Krothapali, A., Baganoff, D. and Karamcheti, K., Development and structure of a rectangular jet in a multiple jet configuration. *AIAA Journ.* 18 (1980) 945–950.
5. Elbanna, H. Gahin, S. and Rashed, M.I.I.: Investigation of two plane parallel jets. *AIAA Journ.* 21 (1983) 986–991.
6. Lin, Y.F. and Sheu, M.J.: Investigation of two plane parallel unventilated jets. *Exp. in Fluids* 10 (1990) 17–22.
7. Stapountzis, H., Tzavellas, P. and Moros, T.: Effects of turbulence on the mixing and chemical reaction for cross flow and coflowing jets. In: Johansson, A.V. and Alfredsson, P.H. (eds), *Advances in Turbulence* 3, Springer Verlag (1991) pp. 300–311.
8. Komori, S. Kanzaki, T. and Murakami, Y.: Simultaneous measurements of instantaneous concen-

trations of two reacting species in turbulent flow with a rapid reaction. *Phys. Fluids A* 3(4) (1991) 507–510.

9. Koochesfahani, M.M. and Dimotakis, P.E.: Mixing and chemical reactions in a turbulent liquid mixing layer. *Journ. Fluid Mech.* vol. 170 (1986) 83–112.
10. Dahm, W.J.A. and Dimotakis, P.E., Measurements of Entrainment and mixing in turbulent jets. *AIAA Journ.* 25 (1987) 1216–1223.
11. Papanicolaou, P.N. and List, E.J.: Investigations of round vertical turbulent buoyant jets. *Journ. Fluid Mech.* 195 (1988) 341–391.
12. Miller, P.L. and Dimotakis, P.E.: Reynolds number dependence of scalar fluctuations in a high Schmidt number turbulent jet. *AIAA Phys. Fluids A* 3(5) (1991) 1156–1163.
13. Shy, S.S. and Breidenthal, R.E.: Turbulent Stratified interfaces. *Phys. Fluids A* E(5) (1991) 1278–1285.
14. Blevins, R.D.: *Applied Fluid Dynamics Handbook*. Van Nostrand Reinhold (1984) p. 243.
15. Stapountzis, H.: Covariance and mixing of temperature fluctuations from line sources in grid turbulence. In: Hirata, M. and Kasagi, N (eds), *2nd Int. Symp. on Transport phenomena, Tokyo* Hemisphere (1988).
16. Warhaft, Z.: The interference of thermal fields from line sources in grid turbulence. *Journ. Fluid Mech.* 144 (1984) 363–387.

Applied Scientific Research **49**: 261–270, 1992
© 1992 *Kluwer Academic Publishers. Printed in the Netherlands.*

Image analysis of oil film interferometry – a method of measuring wall shear stress distributions

HENRI A. SILLER[1], RICHARD J. PERKINS[2] & GERD JANKE[1]

[1]*Hermann Föttinger Institut für Thermo- und Fluiddynamik, Müller-Breslaustrasse 8, DW-1000 Berlin 12, Germany*

[2]*Department of Applied Mathematics and Theoretical Physics, University of Cambridge, Cambridge, U.K.*

Key words: interferometry, shear stress measurement, image processing, fringe patterns

Abstract. A method is described of measuring a wall shear stress distribution that varies in the direction of the flow. Variations in the height of a very thin oil film moving under the boundary layer generate interference fringes, which are recorded and digitised using image processing equipment.

The evolution of the film surface in space and time can be reconstructed from the interference fringe patterns and used to calculate the shear stress field. This reconstruction is achieved by comparing the picture data with images that were calculated for prescribed heights that are adjusted iteratively, until the calculated intensities match the data.

The method is applied to a flow approaching a step, and the results are compared with pulsed-wire measurements.

1. Introduction

The first theoretical analysis of the oil film technique for surface stream line visualisation was developed by Squire [7]. Tanner and Blows [8] introduced oil film interferometry as a method of measuring wall shear stress. The method was then developed further [9, 5, 4], but apart from Tanner's original work the later methods only made point measurements. Using image processing technology, the oil film interferometry technique can be extended to measure shear stress at many locations simultaneously.

Oil film interferometry is based on observing the changing height of a thin oil film moving under a boundary layer: it will spread out, and its surface height will change with time, influenced primarily by the local shear stress, the pressure gradient and gravity.

The height of the oil film is typically of the order of micrometres and is very difficult to measure directly, but changes in height can be visualised by interferometry. On a reflecting surface that is illuminated by monochromatic light, interference fringes are visible in the oil film, and lines of constant light intensity are lines of constant height. By observing the changes in the fringe pattern, it is possible to obtain information on the local film height and its derivatives.

The advantages of oil film interferometry are that it is a direct method that does not have to be calibrated against a reference device, and that it is not dependent on the flow properties – unlike, for example, a Preston tube, where the law of the wall has to be satisfied. Of course, the temperature dependence of the oil's viscosity needs to be known.

This paper describes a new way of acquiring and processing data from oil film interferometric experiments that allows the measurement of shear stress distributions that vary in the direction of the mean flow. During the experiment, the changing fringe pattern along a line parallel to the flow is recorded in an x-t-diagram. When the data is processed, the unknown height distribution in the x-t-diagram is approximated by trying to find a known height distribution that produces a matching fringe pattern. The shear stress distribution can be calculated from these heights.

The technique is illustrated with two sets of experimental data from a flow approaching a step, and the results are compared with measurements from a pulsed wire probe.

2. The motion of a thin oil film under a boundary layer

In order to obtain the relationship between wall shear stress and oil film thickness, we make the following assumptions:

- The presence of a very thin oil film does not change the conditions in the boundary layer.
- The shear stress is constant across the air-oil interface [7]. This is valid provided the slopes of the oil film are small.
- The curvature of the oil film is small, so surface tension effects can be neglected and the pressure is continuous across the oil-air interface.

In a two-dimensional flow on a horizontal surface, the oil film changes its shape under the influence of the local shear stress τ, the external pressure gradient $\partial p/\partial x$, and gravity g [6].

$$\frac{\partial h}{\partial t} = \frac{\partial}{\partial x}\left(\left(\frac{\partial p}{\partial x} - \rho g \frac{\partial h}{\partial x}\right)\frac{h^3}{3\eta} - \tau \frac{h^2}{2\eta}\right), \tag{2.1}$$

where η stands for the viscosity and ρ for the density of the oil.

In order to obtain the shear stress, this equation can be integrated, starting from the edge of the oil film where $h = 0$, if $h(x, t)$, its derivatives with respect to x and t, and the pressure gradient are known:

$$\tau(x) = -\frac{2\eta}{h^2}\int_0^x \frac{\partial h}{\partial t}\mathrm{d}x + \frac{2}{3}h\frac{\partial p}{\partial x} - \frac{2}{3}h\rho g\frac{\partial h}{\partial x}. \tag{2.2}$$

The first term on the right-hand side dominates over the pressure gradient term and the gravity term, except in the vicinity of a separation point. We neglect these terms

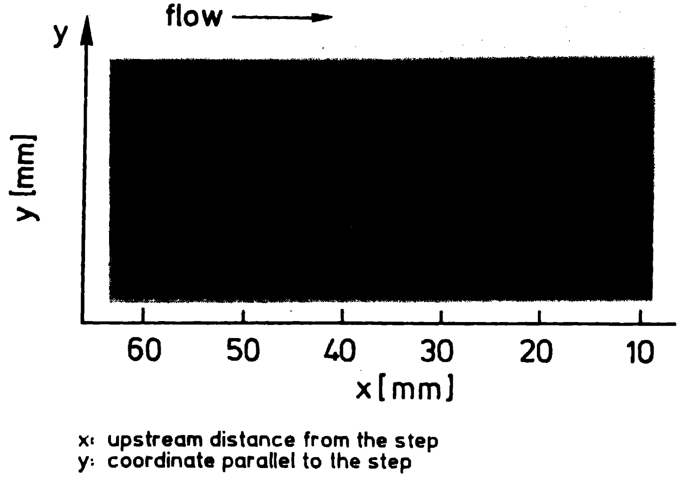
flow
y
y [mm]
60
50
40
30
20
10
x [mm]
x: upstream distance from the step
y: coordinate parallel to the step

Fig. 1. Video picture of interference fringes in the oil film.

because in areas where they become large, the slopes of the oil film will be too steep to produce a visible fringe pattern.

3. Interference and fringe patterns in a thin oil film

In a thin oil film on a reflecting surface that is illuminated by a diffuse background of monochromatic light, interference between rays of light reflected from the upper and the lower surfaces of the film produces a pattern of fringes (Fig. 1).

The fringes are lines of equal height and the relation between the reflected light intensity I and the film height $h(x)$ is

$$I - I_o \propto \cos\left(\frac{4\pi}{\lambda} nh \cos\theta\right), \tag{3.1}$$

where I_o is an offset intensity, λ the wavelength, n the refractive index of the oil, and θ the angle of the light rays in the oil film. This angle is determined by the refractive index of the oil n and the angle of the camera θ' following Snell's law:

$$n = \frac{\sin\theta'}{\sin\theta}.$$

The difference in height between two neighbouring minima of intensity (dark fringes) is

$$\Delta h = \frac{\lambda}{2n} \frac{1}{\cos\theta} \tag{3.2}$$

and is 0.213 μm in these experiments. Note that (3.1) maps a multitude of heights ont the same intensity. It is therefore not possible to invert the height to intensity mappin directly.

4. The method

To calculate the shear stress distribution $\tau(x)$ that generated a given pattern c interference fringes, it is necessary to know the evolution of the height of the oil film i x and t. Unfortunately,

- a pattern of interference fringes only contains information on height differences, no on the heights themselves;
- it is impossible to determine whether the change in height between two fringes i positive or negative.

One way of analysing the interference pattern is with a line-following algorithm, sinc lines of equal intensity correspond to contours of equal height. It was expected tha this approach would be sensitive to small scale disturbances in the fringe pattern an that it would only use a small amount of the data in the picture. Instead, we hav developed a surface fitting method because

- surface fitting algorithms can exploit physical limitations on the surface curvatur
- surface fitting algorithms integrate over larger areas and are therefore much les sensitive to noise than line following algorithms which differentiate to find minim and maxima of the intensity.

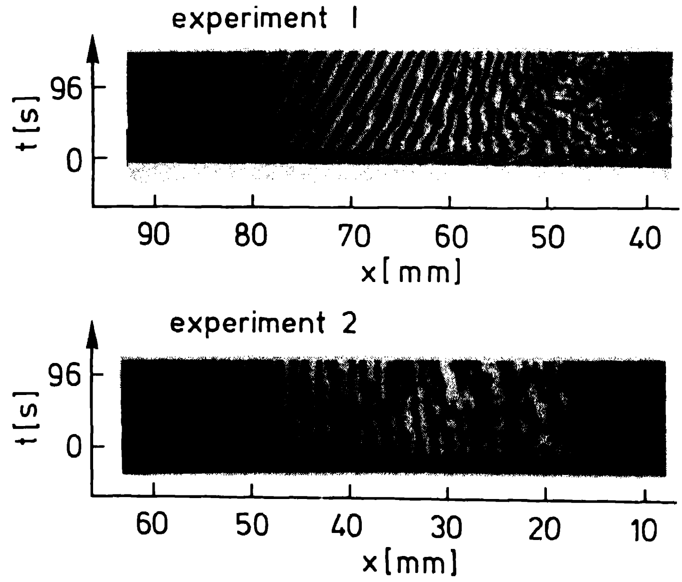

Fig. 2. x-t-diagrams from experiments 1 and 2.

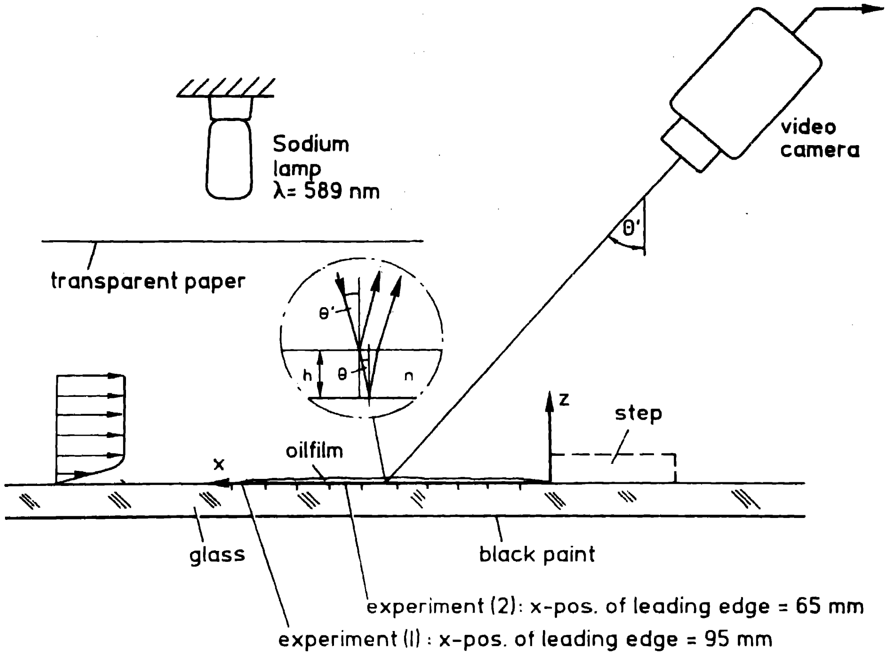
Sodium
lamp
λ= 589 nm
transparent paper
video
camera
θ'
θ'
h
θ
n
z
step
x
oilfilm
glass
black paint
experiment (2): x-pos. of leading edge = 65 mm
experiment (I) : x-pos. of leading edge = 95 mm

Fig. 3. Experimental setup.

This approach has the advantage of being very general and possibly useful for the extension of the method towards the measurement of two-dimensional shear stress distributions.

The method was developed using a numerical model to simulate the evolution of oil film heights under a prescribed shear stress distribution. The computed height distribution was then used to synthesise appropriate images. (Full details of this are given in [6].) This approach was important in the development of techniques for enhancing real images, and it enabled us to investigate the sensitivity of the method to noise in the image data.

The method consists of:

—acquiring picture data from an oil film experiment (Fig. 3);
—arranging the data in an x-t-diagram (Fig. 2);
—preparing that data using image processing techniques;
—calculating an approximation for the surface heights;
—calculating the shear stress from the height data.

4.1. *The experimental procedure*

The technique is illustrated using measurements made in a separating flow in front of a small step in a wall jet facility (Fig. 3). The data presented in this paper were acquired in two experiments. In experiment 1, the leading edge of the oil film was located 95 mm upstream of the position of the step, and in experiment 2 this distance was reduced to 65 mm. The mean flow velocity at the nozzle was approximately 14 m/s for both experiments. The plate was made of glass, its underside was painted black. The light-source was a sodium lamp behind a paper screen. This setup provides an extended light-source, thus our fringes are *localised* [1]. Light reflected off the back surface only adds an offset to the light intensity but does not alter the fringe pattern. The step was 31.2 mm high, 80 mm long in the streamwise direction, 370 mm wide, and it could be removed from the plate. A video camera was fixed overhead and connected to an image processing unit.

The later approximation of the oil film heights required that the heights of the oil film were known at one point in time. For this reason, the experiments were conducted as follows:

- the video camera was positioned, the camera angle θ' and the size of the area seen by the camera were determined;
- the oil was applied in a line perpendicular to the direction of the flow;
- the wind tunnel was turned on and reached its final velocity after approximately 35 seconds;
- under the influence of the flow, the oil spread out into a thin film, forming a ramp with constant slope (this shape is typical of flows with spatially constant shear stress distributions, the heights can be determined from (3.2) by counting fringes);
- a line in the streamwise direction where the oil film was relatively free of disturbances from dust particles was selected and data acquisition began (the choice of the line does not have great effect on the result because disturbances from dust are only local and do not convect);
- the step was placed onto the plate to introduce a shear stress distribution that varied in the streamwise direction.

4.2. Representation of data in x-t-diagrams

For a two-dimensional flow, all the information from the observation of the interference fringes can be expressed in a very compact form, by arranging the data in an x-t-diagram. These diagrams contain the information on the deformation of the interference fringes with time in a narrow region of the oil film along the x-axis and are constructed by

- extracting one line from the video picture parallel to the flow at each time step, typically every 1.5 seconds;
- placing all these lines next to each other in the x-t-diagram.

Figure 1 shows a typical video image and Fig. 2 the two x-t-diagrams (containing 512×64 pixels each) from experiments 1 and 2. Figure 1 shows irregularities in the fringe pattern about 50 mm upstream from the step. They are caused by dust on the plate and have only local effects, because they do not convect.

4.3. Image processing

The aim of the image analysis is to determine the most probable height distribution $h(x, t)$ which would generate the observed fringe pattern $I(x, t)$. Fringe patterns can be calculated for arbitrary heights, camera angles, and refractive indices using (3.1). By iteratively changing the heights, calculating the corresponding intensities for the given camera angle and oil, and comparing them with the given data, the heights can be made to converge towards the height distribution that most probably underlies the intensities in the experimental data.

Before the observed fringe pattern can be compared with patterns calculated from (3.1) using an assumed height distribution, it is necessary to improve the image quality, to remove noise and large scale distortions, and increase the dynamic range of the image.

First, the variations in background intensity are removed by determining the mean intensity variation in the x-direction of the image and subtracting it.

Then, to increase the dynamic range of the image, the intensity histogram is modified using a direct histogram specification, as described in [3]. The model intensity histogram is calculated from the intensity histogram that would be generated by an oil film with constant slope (which is the same as that generated by a random set of heights). Tests with intensity distributions calculated from (3.1) with arbitrary heights showed that the histograms of even complicated fringe patterns always resembled this histogram.

Finally, the picture was smoothed along all the rows with a moving average over three pixels.

4.4. Finding the surface height from the intensity data

In order to calculate the shear stress distribution it is necessary to compute the oil film heights throughout the x-t-plane. It is assumed that the oil film thickness increases linearly with x along the line $t = 0$ and that the height at the leading edge of the oil film remains zero. The problem is then to determine a surface which is consistent with these boundary conditions and with the observed fringe pattern.

4.4.1. A model for the surface

The surface height is modelled by dividing the picture into rectangular patches (Fig. 4), where the height in each patch is defined by bilinear interpolation between its four corner points. The accuracy of this model depends on the relation between the surface slopes and the size of the patches:

- — regions with low surface curvature are well modelled by larger patches;
- — regions with high curvature can only be fitted by smaller patches.

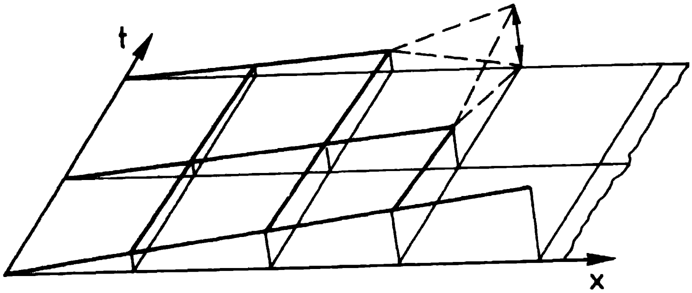

Fig. 4. Calculation of the surface height by surface patches.

4.4.2. Approximating the height over one surface patch

For each surface patch the heights at three of the corners are known from the initial conditions or previous calculations. To determine the height at the fourth corner, an initial height is assumed, the corresponding fringe pattern is calculated using (3.1), and the sum of the squared differences between the calculated and observed intensities is computed. The height at the fourth corner is varied iteratively, so as to minimise the sum of the squared differences.

4.4.3. Approximating the height over a larger area

To approximate the surface height distribution over an x-t-diagram containing 512 × 64 pixels, the area is divided into 8 boxes of 64 × 64 pixels. Knowing the heights along the axes of the area, the heights in the upper right hand corner of each box can be calculated by stepping from box to box from left to right and using the result from one box as input value for the upper left hand corner's height of the next box.

If the height approximation algorithm fails to find the height over a box of 64 × 64 pixels, it will split this box into four sub-boxes and try to minimize over these consecutively, starting with the box at the lower left. This algorithm is applied recursively, the minimum box-size being 4 × 4 pixels.

4.4.4. Assigning the heights along the axes

The initial height distribution along the x-axis is obtained by taking a Fourier transform along the line in the picture that represents the initial condition. The dominant frequency is a measure of the number of fringes along that line and the phase angle a measure of the height at the first pixel. From the data of the Fourier analysis, we can construct a model height distribution which gives a fringe pattern that closely resembles the original.

4.5. Calculating the shear stress

To calculate the shear stress according to equation (2.2), it is not necessary to know the height over the whole picture. In theory, data from two consecutive lines parallel to the x-axis would be sufficient to calculate $\partial h/\partial t$ for each point. In practice, however, it may be necessary to average over several lines to obtain a good result.

The height approximation over the 64 lines of the picture yields the heights on a rectangular grid with a spacing of 4 pixels. To obtain a smooth surface and the derivatives and integrals in an analytical form, we use a cubic b-spline approximation of the surface.

5. Results

The diagram in Fig. 5 shows the shear stress values calculated from the x-t-diagrams in Fig. 2 in comparison with pulsed wire measurements. The shear stress cannot be calculated for the whole length of the x-t-diagrams, because the height approximation breaks down on the far right hand side, where the fringe pattern becomes too irregular. It does so because in this region of the pictures the oil film is higher, due to the Initial height distribution when the film was formed. Small relative changes in the film height have more dramatic effects on the fringe pattern here than in regions where the film is very thin. The data from experiment 2 were obtained in the area around the separation line, where the shear stress and its gradient are very low. A wave develops and travels upstream towards the separation line. The algorithm fails on the steep slopes of the wave.

Near the upstream edge of the oil film, (2.2) produces large errors because both h and $\partial h/\partial t$ approach zero. Apart from these effects, the results from both experiments are consistent and they agree with measurements taken with a wall pulsed wire probe (for more information on this technique see e.g. [2]).

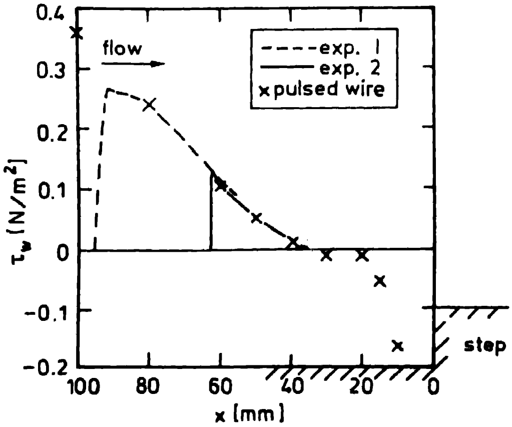

Fig. 5. Resulting shear stress distributions for experiments 1 and 2 compared with pulsed wire data.

6. Conclusions

This paper describes a method of measuring wall shear stress distributions that vary in the direction of the main flow. It is based on interferometric visualisation of changes in height of a thin oil film and the reconstruction of the surface height in the x-t-plane by a surface approximation method.

Applied to a separating flow in front of a step, the surface approximation produces good results as long as the fringe pattern does not become too complicated and the shear stress results agree with those of wall pulsed wire measurements.

Since the method provides an entirely general way of determining a surface from a fringe pattern, given a few boundary conditions, it should be possible to extend it to the measurement of surface shear stress distributions in a plane.

Acknowledgements

We gratefully acknowledge financial support from the British Council and the Deutscher Akademischer Austauschdienst. R. Perkins was funded by the Wolfson Foundation. H. Siller was funded by the Technische Universität Berlin, Corpus Christi College Cambridge, and under the Erasmus scheme.

References

1. Born, M. and Wolf, E., *Principles of Optics*, 6th edn. Oxford: Pergamon Press (1980) p. 291.
2. Castro, I.P., Dianat M. and Bradbury, L.J.S.: The measurement of fluctuating skin friction with a pulsed wire wall probe. In: *Turbulent Shear Flows* 5 New York, Berlin, Heidelberg: Springer (1987).
3. Gonzales, R.C. and Wintz, P.: *Digital Image Processing*. Reading Massachusetts: Addison-Wesley (1987) pp. 152–158.
4. Kim, K.-S. and Settles, G. S.: Skin-friction measurements by laser interferometry. *AGARDograph* 315 (1988), Chapter 3.
5. Monson, D.J. and Higuchi, H.: Skin friction measurements by a dual-laser-beam interferometer technique. *AIAA Journal* 19 (1981) 739–744.
6. Siller, H.A.: An optical method of measuring wall shear stress using oil film interferometry and image processing techniques. A dissertation submitted to the University of Cambridge for the Certificate of Postgraduate Study (1991).
7. Squire, L.C.: The motion of a thin oil sheet under the steady boundary layer on a body. *Journal of Fluid Mechanics* 11 (1961) 161–179.
8. Tanner, L.H. and Blows, L.G.: A study of the motion of oil films on surfaces in air flow, with application to the measurement of skin friction. *J. Phys. E: Sci. Instrum.* 9 (1976) 194–202.
9. Tanner, L.H., A skin friction meter using the viscosity balance principle, suitable for use with flat or curved metal surfaces. *J. Phys. E: Sci. Instrum.* 10 (1977) 278–283.

Applied Scientific Research **49**: 271–282, 1992
© 1992 *Kluwer Academic Publishers. Printed in the Netherlands.*

Three-dimensional numerical simulation of periodic natural convection in a differentially heated cubical enclosure

TORU FUSEGI[1,*], JAE MIN HYUN[2] & KUNIO KUWAHARA[3]

[1]*Institute of Computational Fluid Dynamics, 1-22-3 Haramachi, Meguro, Tokyo 152, Japan*
[2]*Department of Mechanical Engineering, Korea Advanced Institute of Science and Technology, Chong Ryang, Seoul 131, Korea*
[3]*Institute of Space and Astronautical Science, 3-1-1 Yoshinodai, Sagamihara, Kanagawa 229, Japan*

Received 16 July 1990; accepted in revised form 23 December 1990

Abstract. A high-resolution, finite-difference numerical study is carried out of three-dimensional unsteady periodic natural convection of air in a cubical enclosure at the Rayleigh number of 8.5×10^6. The enclosure is subjected to differential heating at the two vertical side walls. The other vertical walls are insulated. A linear temperature profile is specified at the thermally-conducting horizontal walls. Flow details in the three-dimensional field are captured by elaborate post-processing of the computational results, for which the state-of-the-art numerical visualization techniques are utilized. The three-dimensionality of the mean flow fields is observed to be confined into narrow regions near the end walls. The time-dependent solutions clearly indicate the periodic nature of the flow. The oscillation frequency is in close agreement with the previous experimental measurements reported in the literature.

Nomenclature

c_p = specific heat at constant pressure
Fr = Froude number, u_0^2/g^*L_0
f_{ND} = normalized frequency, f^*/N where f^* is the dimensional frequency
g = gravitational acceleration
k = thermal conductivity
L_0 = reference length (enclosure height)
N = Brunt-Väisälä frequency, $[g^*\beta^*(T_H - T_C)/L_0]^{1/2}$
p = pressure
p_0 = reference pressure (hydrostatic pressure)
Pr = Prandtl number, $c_p^*\mu^*/k^*$
Ra = Rayleigh number, $g^*\beta^*c_p^*\rho^{*2}L_0^3(T_H - T_C)/\mu^*k^*$
Re = Reynolds number, $\rho^*u_0L_0/\mu^*$
t = time
T = temperature
T_0 = reference temperature, $(T_C + T_H)/2$
T_C, T_H = cooled and heated side wall temperatures
u_0 = reference velocity, $[g^*\beta^*L_0(T_H - T_C)]^{1/2}$
u, v, w = velocity components in the x, y and z directions
x, y, z = Cartesian coordinates

Greek symbols

β = thermal expansion coefficient
δ = overheat ratio, $(T_H - T_C)/T_0$
μ = viscosity
ρ = density

Superscript

$*$ = dimensional quantities

Introduction

Natural convection in a rectangular enclosure, for which one vertical wall is heated and the opposing side cooled, is a basic model for a variety of thermal engineering systems. These include solar energy collectors, electronic device cooling and compartment fire problems. Analyses on differentially heated enclosures with a square cross section are numerous; numerical studies have been performed for two-dimensional geometries (square channels) [1–5] and for a three-dimensional box [6–8], to cite a few. Experiments have been conducted for media with a Prandtl number in the range from 0.7 (air) to 6000 (glycerin) [9–14].

---

*Toru Fusegi is presently at Heat Transfer and Fluid Dynamics, Energy Technology Research Institute, Tokyo Gas Co. Ltd., 1-16-25 Shibaura, Minato, Tokyo 105, Japan.

It is important to note that, in the majority of the preceding works, the horizontal walls were assumed to be thermally insulated. However, this idealized condition does not faithfully represent the realistic engineering systems; also, it is difficult to reproduce this condition in experiments. Although much effort is usually spent to insulate the horizontal walls, heat transfer through the system boundary walls is unavoidable in actual experimental situations (see, for example, [9, 10, 12]).

There can be several possible thermal boundary conditions at the thermally-conducting horizontal walls. However, one of the most physically meaningful situations is the case in which the temperature at the horizontal wall varies linearly between the temperatures of the cooled and heated vertical walls. This can be approximated with relative ease in the laboratory; if the horizontal walls are made of a thin metallic plate of high thermal conductivity, the resulting temperature distribution at the horizontal walls will be close to the linear profile. Consequently, the cases of a linearly-varying temperature profile at the horizontal walls have attracted attention of several researchers [4, 5, 11, 13]. In what follows, the term "conducting horizontal walls" is used to refer to the cases of a linear temperature profile at the horizontal surfaces, as described above.

It has been observed that, for slender cavities of aspect ratios less than 10, if the horizontal walls are conducting, the flow is destablized at lower Rayleigh numbers than for the cases of the perfectly insulated walls [4, 5]. A stability diagram was obtained for two-dimensional air-filled rectangular enclosures for the aspect ratio range between 1 and 10 [4]. For a two-dimensional square enclosure, in the case of conducting horizontal walls, the critical Rayleigh number, beyond which periodic regular oscillations appeared in the fields, was found to be 2.2×10^6 for air [4, 5]. This value was determined by numerically solving the unsteady Navier-Stokes equations. The period of oscillation was in good agreement with the result based on the lowest Hopf bifurcation point, which was deduced by a two-dimensional linear stability analysis [15]. However, oscillations in the case of insulated horizontal walls for a square cavity first appeared at a much higher Rayleigh number of about 2×10^8 [5, 16].

A series of experiments of considerable physical insight was documented [11, 13]. A cubical enclosure of aspect ratio close to unity was fabricated [11] and this was fitted with conducting horizontal walls. By use of laser Doppler techniques, it was asserted that, in the large-time limit, periodic oscillations were observed in the Rayleigh number range of $2.5 \times 10^6 \leqslant \mathrm{Ra} \leqslant 1.2 \times 10^7$. Further quantitative examinations were made [13] by using Schlieren temperature field measurements. Parallel two-

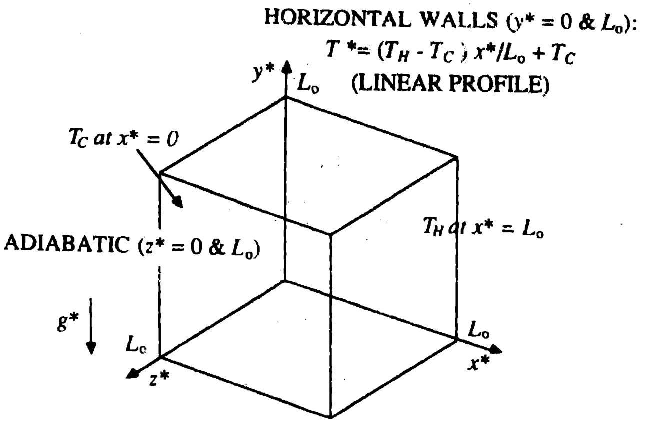
HORIZONTAL WALLS ($y^* = 0$ & L_0):
$T^* = (T_H - T_C)\, x^*/L_0 + T_C$
(LINEAR PROFILE)
y^*
L_0
T_C at $x^* = 0$
T_H at $x^* = L_0$
ADIABATIC ($z^* = 0$ & L_0)
g^*
L_0
z^*
L_0
x^*

Fig. 1. The flow geometry and the boundary conditions of the cubical enclosure.

dimensional calculations were performed for selected Rayleigh numbers [13]. The frequencies obtainable from these two-dimensional computations were consistent with the experimental findings.

It should be stressed that the above-stated experiments [11, 13] were conducted in a cubical box. The measurement data on the mid-symmetry plane ($z = 0.5$) were utilized for the post-processings. However, these experimental data and the results of the parallel two-dimensional computations illustrated some discrepancies [13]: the critical Rayleigh number, at which periodic oscillations appear, was higher in the computation, and the principal local dynamic characteristics such as maximum velocities of the flows were different. These discrepancies were attributed to some hitherto-unexplored three-dimensional effects that are inherent to the experiments. The outstanding issues regarding the flows in a differentially heated enclosure, with conducting horizontal walls, can be better illuminated by full-dress three-dimensional, time-dependent numerical simulations.

In the present paper, the results of a numerical study are reported on three-dimensional natural convection in a cubical enclosure. The thermal boundary conditions are identical to those employed in [11, 13]. As shown in Figure 1, the length of the cube is L_0, and the temperatures of the right and left vertical walls are maintained at T_H and T_C, respectively ($T_H > T_C$). At the horizontal walls, the linear temperature profile is imposed. The planes located at $z^* = 0$ and L_0 (hereafter referred to as the *end walls*) are considered to be thermally insulated. Computations are made for air at the Prandtl number of 0.71.

The primary objective of this paper is to demonstrate that a complete three-dimensional numerical solution at a high Rayleigh number has been successfully accomplished. This exemplary calculation, with the number of grid points of 62^3, consumed an enormous amount of computing time (about 40 hours on a supercomputer). The impetus is placed on ascertaining that fully three-dimensional computations with very high resolution are now feasible. It is also noteworthy that the state-of-the-art computer graphics capabilities have been efficiently incorporated in this study to render three-dimensional numerical flow visualizations. The results of the present three-dimensional simulation were checked against the experimental data [11].

Mathematical model

The flow is governed by the unsteady, incompressible Navier-Stokes and energy equations. The Boussinesq approximation is invoked for the fluid properties. The non-dimensionalized form of the governing equations can be expressed in tensor notation as

$$\frac{\partial u_j}{\partial x_j} = 0, \tag{1}$$

$$\frac{\partial u_i}{\partial t} + \frac{\partial}{\partial x_j}(u_j u_i) = -\frac{\partial p}{\partial x_i} + \frac{1}{\mathrm{Re}}\frac{\partial^2 u_i}{\partial x_j \partial x_j} + \delta_{i2}\frac{T-1}{\mathrm{Fr}}, \tag{2}$$

$$\frac{\partial T}{\partial t} + \frac{\partial}{\partial x_j}(u_j T) = \frac{1}{\mathrm{Re}\,\mathrm{Pr}}\frac{\partial^2 T}{\partial x_j \partial x_j}, \tag{3}$$

where δ_{ij} is the Kronecker delta ($\delta_{ij} = 1$ if $i = j$, and $\delta_{ij} = 0$ otherwise). The viscous dissipation and the pressure work terms are neglected in the energy equation.

The physical quantities are non-dimensionalized in the following manner:

$$(x, y, z) = (x^*, y^*, z^*)/L_0,\ (u, v, w) = (u^*, v^*, w^*)/u_0,$$

$$t = t^* u_0/L_0,\ p = (p^* - p_0)/\rho^* u_0^2,\ T = T^*/T_0$$

where the asterisk (*) denotes dimensional values. The reference scales for length, velocity, time, pressure and temperature are the enclosure height (L_0), a buoyant convective velocity ($u_0 = [g^*\beta^* L_0(T_H - T_C)]^{1/2}$), the convective time ($t_0 = [g^*\beta^*(T_H - T_C)/L_0]^{-1/2} = N^{-1}$, where N is the Brunt-Väisälä frequency), the hydrostatic pressure (p_0) and the film temperature ($T_0 = (T_C + T_H)/2$), respectively.

The flow parameters are shown to be related as $\mathrm{Ra} = \mathrm{Re}^2\,\mathrm{Pr}$ through the selected definition of the reference velocity, u_0. It can be also seen that, by the use of the ideal gas law, the Froude number, Fr, is reduced to the overheat ratio, δ. The overheat ratio is set equal to 0.1 in the present study in order to closely simulate the experimental conditions of [11, 13].

In accordance with the problem statement, the following boundary conditions are specified:

$$u = v = w = 0 \quad \text{on all the solid walls} \tag{4}$$

$$T = (2 - \delta)/2 \quad \text{at } x = 0, \qquad T = (2 + \delta)/2 \quad \text{at } x = 1,$$

$$T = (x - 1/2)\delta + 1 \quad \text{at } y = 0 \text{ and } 1,$$

$$\text{and } \partial T/\partial z = 0 \quad \text{at } z = 0 \text{ and } 1 \tag{5}$$

Solution method

A discretized form of the system of the governing equations (1)–(5) is secured by way of a control-volume based finite difference procedure. The equations are linearized by substituting the most recently available values for the convective velocities in the non-linear terms. An iterative and sequential solution method is adopted: The energy equation (3) is first solved at each iteration level in order to update the temperature. The incompressible Navier-Stokes equations (1) and (2) are dealt with by the well-known SIMPLE (*S*emi-*I*mplicit *M*ethod for *P*ressure-*L*inked *E*quations) algorithm [17]. In conjunction with this technique, a staggered mesh system is introduced for the velocity components, while the remaining variables (i.e., pressure and temperature) are stored in the main grid points.

Numerical solutions to the algebraic finite-difference equations are acquired by the *S*trongly *I*m*p*licit Scheme [18]. SIP can be regarded as a variation of the direct method of the LU-decomposition type, where L and U denote the lower and upper diagonal matrices, respectively. The standard value of the under-relaxation factor for non-linear equations is utilized [18]. SIP is applied to the planes of constant z in order to determine simultaneously dependent variables in the x and y directions on each plane. This multi-dimensional determination technique is found to accelerate convergence characteristics of the solutions comparing with the conventional pointwise or line-by-line methods.

The convection terms in the momentum equation (2) are treated by the QUICK (*Q*uadratic *U*pstream *I*nterpolation for *C*onvective *K*inematics) methodology modified for non-uniform grids [19]. The QUICK scheme is a higher-order upwind differencing which possesses the stability of the first-order upwind formula and is free from substantial numerical diffusion experienced with the usual first-order techniques. A second order extrapolation is adopted for calculating values of outer-wall grid points, which arise in applications of this five-point scheme to a finite difference control-volumes at the solid walls. A hybrid scheme [17] is used for the convection terms in the energy equation (3).

The entire enclosure constitutes the full computational domain. The number of grid points for computations is 62 in each coordinate direction. This considerably large value appears to be the minimum requirement to properly predict the oscillatory behavior of the flow to be presented. Variable grid spacing was introduced to resolve steep gradients of the velocity and the temperature near the walls. The configuration of the non-uniform grid system is the same as that of the prior three-dimensional computations, which considered the thermally insulated horizontal walls [20]. Changes less than 2% and 0.2% of the peak velocity and the overall Nusselt number, respectively, took place when the number of the grid points was doubled in the x-direction. The minimum grid distance is approximately 0.015 in the non-dimensional length unit.

A fully implicit scheme is adopted for marching in time. The method is the conventional forward differencing with respect to time and of the first-order accuracy. The non-dimensional time step is set equal to 0.01, which is sufficiently small compared to the period of oscillations in the fields. In the parallel two-dimensional calculations, this value is found to be necessary to capture oscillation frequencies independent of time increments.

Convergence of computations at each time step is declared when the following convergence criterion is satisfied:

$$\frac{|\phi_n - \phi_{n-1}|}{|\phi_n|_{\text{maximum}}} \leq 10^{-4} \text{ for all } \phi \tag{6}$$

where ϕ denotes any dependent variable, and n indicates the value of ϕ at the n-th iteration level. In each iteration level, the z-momentum equation for the w-velocity component is found to reach convergence last, due to overall smaller magnitudes of velocities in that direction.

The computer program is fully vectorized for execution on vector-processors of a supercomputer.

For the initial condition for the present study, an instantaneous solution of the two-dimensional computation at the same Rayleigh number is utilized. Starting from this state, the three-dimensional calculation is continued far beyond a specific time instant, at which the impact of the initial condition on the results becomes negligible.

Results and discussion

Computations were performed on a HITACHI S-820/80 supercomputer system at the Institute of Computational Fluid Dynamics (ICFD) in Tokyo, Japan. The system has a maximum CPU speed of 3 GFLOPS and a maximum incore memory of 512 MB. The total CPU time for the three-dimensional computation was approximately 44 hours with 16000 time steps and 100 MB of the memory.

In the present study, the Rayleigh number was set at 8.5×10^6. The computational results clearly disclosed that regular periodic oscillations were evident. The results of the last 40 oscillation periods were analyzed for the present discussion. For these results, the influence of the initial condition was extremely small. First, the characteristics of the time-averaged fields will be examined to describe the global field structure. The fluctuating field characteristics will be scrutinized next; a comparison of the present numerical results with the measurements [11] as well as the two-dimensional numerical computations [4, 5, 13] will then be illustrated.

The characteristics of the time-averaged fields

The field data are averaged over an interval of 20 oscillation periods, which is sufficiently large compared to the dominant time scale of the flow. Figure 2 displays perspective three-dimensional views of the mean fields, represented by the isothermal surfaces and the isosurfaces of the absolute values of vorticity. The fields exhibit centro-symmetry with respect to the center ($x = y = z = 0.5$) and symmetry with respect to the plane of $z = 0.5$ (hereafter referred to as the *symmetry plane*). At this high Rayleigh number, the fields can be characterized by the boundary layer-stagnant core structure; thin thermal and hydrodynamic boundary layers are formed near the isothermal walls, while the flow is nearly stagnant in the central region of the enclosure. The temperature field is stratified in the near-stagnant core. As a result of the (externally-imposed) linear-temperature distribution at the horizontal walls, the temperature gradients are very steep in the y-direction in the close proximity of the

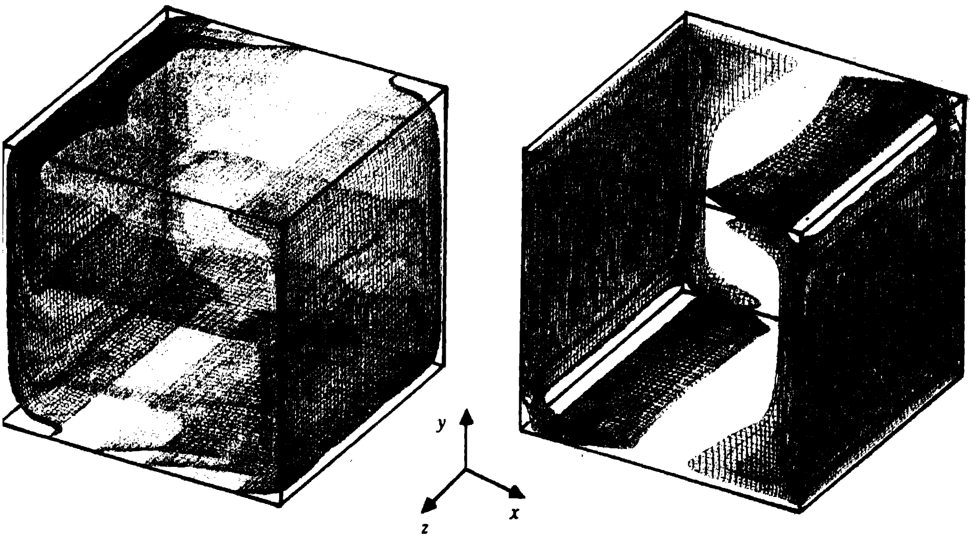

(a) ISOTHERMS (b) ISOVORTICITY SURFACES

Fig. 2. The time-averaged isothermal surfaces and isosurfaces of the absolute values of vorticity [contour levels: (a), 0.9667 (purple), 0.9833 (blue), 1.0 (green), 1.017 (yellow), 1.033 (red); (b), 5 (purple), 10 (blue), 15 (green), 20 (yellow), 25 (red)].

horizontal walls. An interesting behavior in the isotherm surfaces is the presence of a dent of appreciable size in some specific regions. These regions are close to the cooled side wall at the mid-plane ($z = 0.5$). Inspection of the instantaneous isotherm patterns reveals that a pair of these dents is formed symmetrically with respect to the mid-plane ($z = 0.5$). These dents move symmetrically in the z-direction as mirror images, and they merge into one on the mid-plane. Similar behavior of the dents is discernible near the heated side wall. However, it is pointed out that the time scale of the behavior of these isotherm dents appears to be much larger than the characteristic time of the quasi-steady oscillatory flow patterns. No description was given concerning this three-dimensional behavior of the temperature field in the preceding experimental investigations [11, 13].

In the bulk of the enclosure, the temperature fields are fairly uniform in the z-direction, suggesting that the two-dimensional assumption is largely valid. The vorticity is mostly concentrated within very narrow regions adjacent to the isothermal side walls. The time-averaged flow field can be approximated by the two-dimensional structure in much of the enclosure; only in narrow strips near the end walls, the three-dimensionality is appreciable. The three-dimensional numerical visualization plots were produced by an interactive graphic software [21], which ran on a FUJITSU VP-200 supercomputer system at the ICFD.

In order to examine in further detail the three-dimensionality of the time-averaged flow field structure, the velocity profiles near the horizontal and vertical walls are presented in Figure 3. The results of the parallel two-dimensional computation of the present study are also shown for comparison. The velocity distribution in the symmetry mid-plane ($z = 0.5$) displays consistency with the two-dimensional case. Both the locations and the magnitudes of the peak values of the velocities are in close agreement. As remarked earlier, the velocity profiles obtained by the three-dimensional computation are substantially uniform in the z-direction in the main body of the flow field.

The characteristics of the fluctuating fields

The salient features of the periodic fluctuations of the fields are discussed in this subsection. Figure 4(a) demonstrates the temporal variations of the temperature at a representative internal point and, Figure 4(b) gives the temporal behavior of the overall Nusselt number at the cooled wall ($x = 0$), which is defined as

$$Nu_{\text{mean}}(z) = \int_0^1 \left.\frac{\partial T(y, z)}{\partial x}\right|_{x=0} \mathrm{d}y \left(= \int_0^1 Nu_{\text{local}}(y, z)\,\mathrm{d}y \right) \tag{7}$$

$$Nu_{\text{overall}} = \int_0^1 Nu_{\text{mean}}(z)\,\mathrm{d}z \tag{8}$$

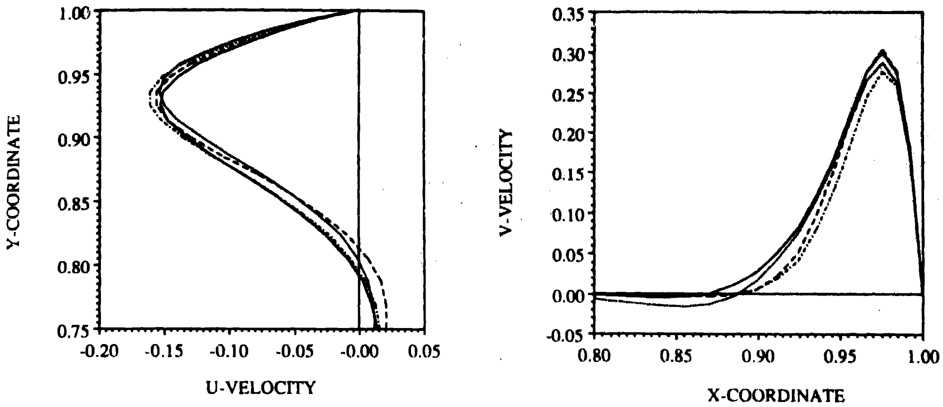

(a) HORIZONTAL VELOCITY AT x = 0.5

(b) VERTICAL VELOCITY AT y = 0.5

Fig. 3. Time-averaged velocity profiles in the planes of z = constant [——, at $z = 0.5$; — — —, $z = 0.3$; ······, $z = 0.1$; - - - - -, two-dimensional results].

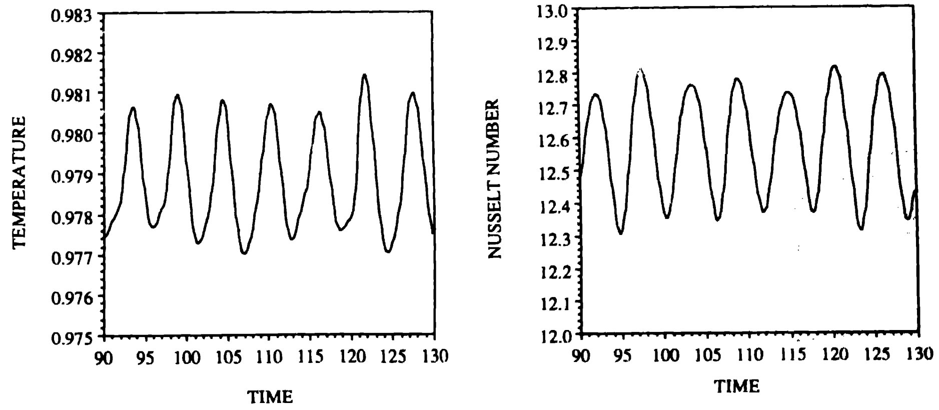

(a) TEMPERATURE AT
(x, y, z) = (0.186, 0.082, 0.5)

(b) OVERALL NUSSELT NUMBER
AT THE COOLED WALL

Fig. 4. Periodic fluctuations of the local temperature and of the overall Nusselt number.

Careful inspection of Figures 4(a) and (b) leads to a conclusion that the frequencies detected in these two plots are identical within the accuracy of the numerical processing of the present data, giving $f_{ND} = 0.33$. It also has to be pointed out that the velocity fluctuations at the same internal measurement point are of the same frequency and in phase with the temperature plot. In the experiments [11], at this

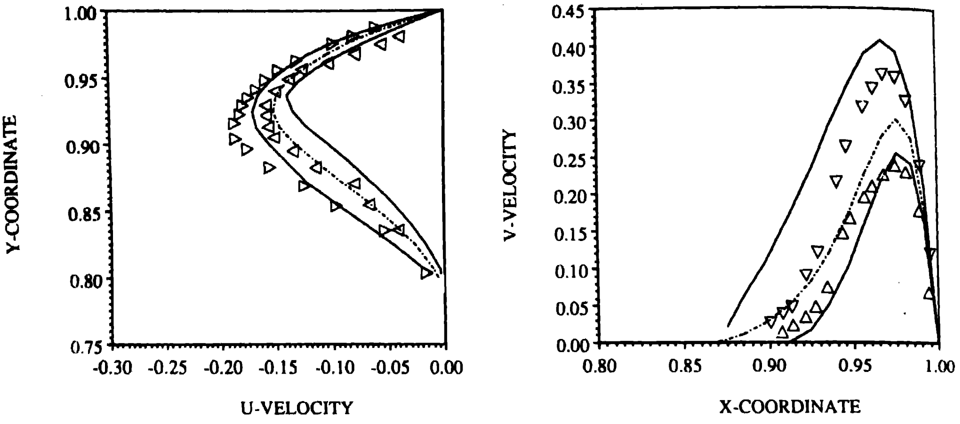

(a) HORIZONTAL VELOCITY AT x = 0.5 (b) VERTICAL VELOCITY AT y = 0.5

Fig. 5. Velocity envelopes in the symmetry plane ($z = 0.5$) [——, the minimum and maximum velocity profiles obtainable from the instantaneous flow fields; — - —, time-averaged velocity profiles; symbols denote the velocity envelopes by the experiment [11]].

Rayleigh number (Ra $= 8.5 \times 10^6$) two frequencies were possible: $f_{ND} = 0.25$ and 0.321. The latter value is within 5% of the frequency detected by the present three-dimensional computation. In a two-dimensional calculation at Ra $= 9 \times 10^6$, the predicted f_{ND} was 0.32 [13], which agreed well with their own measurements [11]. The value obtained by the parallel two-dimensional computations performed in the present study was very close to these data. Independent two-dimensional numerical analyses [4, 5] reported f_{ND} to be around 0.25 at Ra $= 2.2 \times 10^6$, which is also in good agreement with the experimental data [11].

The instantaneous velocity profiles in the symmetry plane ($z = 0.5$) are plotted in Figure 5 as the velocity envelopes. The experimental measurements [11] are also included in the figure. As to the locations of the peak values of the velocity profiles, both the experiments and the present computations provide consistent results. The distinct boundary layers and near-stagnant interior core structure are inferred from the figure (note that only parts of the x and y coordinates are shown in the figure).

Conclusions

High-resolution three-dimensional natural convection in a differentially heated cubical enclosure with the conducting horizontal walls is investigated numerically at the Rayleigh number of 8.5×10^6. The present computations predict successfully periodic oscillations in the fields. The period of the oscillations is consistent with the experimental measurements [11, 13] and the previous two-dimensional computations

[4, 5, 13]. This result is supportive of the two-dimensional assumption that has been invoked in these prior investigations. In particular, the two-dimensional assumption appears to be reasonable to portray the gross features of the time-averaged fields.

According to the experiments [11, 13], two oscillation periods were obtained at this Rayleigh number, depending on whether the particular Ra was approached from lower or higher values. In the present computation, the higher frequency was captured. Because of the limitation of the available CPU time, it was not possible to study the complete and specific effects of the initial condition on the final three-dimensional solutions. This also prevents one carrying out a more detailed examination of the dent structure, that is clearly observed in the temperature field. Detailed investigations on the characteristics of this three-dimensional phenomenon, such as oscillation period, its large time behavior and sources of dent generation, are left as future analysis.

References

1. G. de Vahl Davis, Natural convection of air in a square cavity: a bench mark numerical solution. *Int. J. Numer Methods Fluids* 3 (1983) 249–264.
2. N. C. Markatos and K. A. Pericleous, Laminar and turbulent natural convection in an enclosed cavity. *Int. J. Heat Mass Transfer* 27 (1984) 755–772.
3. H. Ozoe, A. Mouri, M. Ohmura, S. W. Churchill and N. Lior, Numerical calculations of laminar and turbulent natural convection in water in rectangular channels heated and cooled isothermally on the opposing vertical walls. *Int. J. Heat Mass Transfer* 28 (1985) 125–138.
4. P. Le Quere and T. Alziary de Roquefort, Transition to unsteady natural convection of air in differentially heated vertical cavities. In: *Significant Questions in Buoyancy Affected Enclosure or Cavity Flows*, ASME HTD-Vol. 60 (1986) pp. 29–36.
5. R. A. W. M. Henkes and C. J. Hoogendoorn, On the stability of the natural convection flow in a square cavity heated from the side. *Appl. Sci. Res.* 47 (1990) 195–220.
6. G. D. Mallinson and G. de Vahl Davis, Three-dimensional natural convection in a box: a numerical study. *J. Fluid Mech.* 83 (1977) 1–31.
7. A. M. Lankhorst and C. J. Hoodendoorn, Three-dimensional numerical calculations of high Rayleigh number natural convective flows in enclosed cavities. In: *Proc. 1988 Nat. Heat Transfer Conf.* ASME HTD-96, Vol. 3 (1988) pp. 463–470.
8. T. S. Lee, G. H. Son and J. S. Lee, Numerical predictions of three-dimensional natural convection in a box. In: *Proc. 1st KSME-JSME Thermal and Fluids Engineering Conf.* Vol. 2 (1988) pp. 278–283.
9. S. M. Bajorek and J. R. Lloyd, Experimental investigation of natural convection in partitioned enclosures. *J. Heat Transfer* 104 (1982) 527–532.
10. R. J. Krane and J. Jessee, Some detailed field measurements for a natural convection flow in a vertical square enclosure. In: *Proc. 1st ASME-JSME Thermal Engineering Joint Conf.* Vol. 1 (1983) pp. 323–329.
11. D. G. Briggs and D. N. Jones, Two-dimensional periodic natural convection in a rectangular enclosure of aspect ratio one. *J. Heat Transfer* 107 (1985) 850–854.
12. S. M. Bilski, J. R. Lloyd and K. T. Yang, An experimental investigation of the laminar natural convection velocity in square and partitioned enclosures. In: *Proc. 8th Int. Heat Transfer Conf.* Vol. 4 (1986) pp. 1513–1518.
13. D. N. Jones and D. G. Briggs, Periodic two-dimensional cavity flow: effect of linear horizontal thermal boundary condition. *J. Heat Transfer* 111 (1989) 86–91.

14. W. J. Hiller, S. Koch, T. A. Kowalewski, G. de Vahl Davis and M. Behnia: Experimental and numerical investigation of natural convection in a cube with two heated side walls. In: *Proc. Int. Union Theoretical and Applied Mechanics Symp.* (1990) pp. 717–726.
15. K. H. Winters, Hopf bifurcation in the double-glazing problem with conducting boundaries. *J. Heat Transfer* 109 (1987) 894–898.
16. S. Paolucci and D. R. Chenoweth, Transition to chaos in a differentially heated vertical cavity. *J. Fluid Mech.* 201 (1989) 379–410.
17. S. V. Patankar, *Numerical Heat Transfer and Fluid Flow*: Hemisphere Publishing Corp. (1980) Chap. 6.
18. H. L. Stone, Iterative solution of implicit approximations of multi-dimensional partial differential equations. *J. Numer. Analy.* 5 (1968) 530–558.
19. C. J. Freitas, R. L. Street, A. N. Findikakis and J. R. Koseff, Numerical simulation of three-dimensional flow in a cavity. *Int. J. Numer. Methods Fluids* 5 (1985) 561–575.
20. T. Fusegi, J. M. Hyun, K. Kuwahara and B. Farouk, A numerical study of 3-D natural convection in differentially heated cubical enclosure. *Int. J. Heat Mass Transfer* 34 (1991) 1543–1557.
21. S. Shirayama and K. Kuwahara: Patterns of three-dimensional boundary layer separation. *25th Aerospace Sciences Meeting* (1987) AIAA Paper 87-0461.

Applied Scientific Research **49**: 283–305, 1992
© 1992 *Kluwer Academic Publishers. Printed in the Netherlands.*

Response of a viscous annular liquid layer in zero-gravity to different axial excitations of the rigid boundary plates

HELMUT F. BAUER

Institut für Raumfahrttechnik, Universität der Bundeswehr München, Werner-Heisenberg-Weg 39, D-8014 Neubiberg, Germany

Received 16 August 1990; accepted in revised form 30 January 1991

Abstract. A cylindrical annular liquid layer between two plates and around a rigid center-core consisting of incompressible and viscous liquid is subjected to different axial excitations, such as one-sided, counter-directional and double-sided unequal excitations. The response of the free liquid surface, the velocity- and pressure-distribution has been determined.

Zusammenfassung. Eine zylindrische Flüssigkeitsschicht bestehend aus inkompressibler und viskoser Flüssigkeit wurde verschiedenen harmonischen Anregungsformen ausgesetzt. Dabei wurden die Fälle einseitiger, doppelseitiger entgegengesetzter und ungleicher doppelseitiger Anregung mit Phase behandelt. Die Vergrößerungsfunktionen für die freie Flüssigkeitsoberfläche, für die Geschwindigkeits- und Druckverteilung wurden bestimmt.

Key words: response annular liquid layer, viscous liquid, different harmonic axial excitations

List of symbols

a = radius of liquid layer

b = radius of inner cylindrical core

$(a-b)$ = thickness of layer

$\mathbf{e}_r, \mathbf{e}_\varphi, \mathbf{k}$ = unit vectors in the radial, angular and axial direction resp.

h = length of layer

I_m, K_m = modified Bessel functions of first and second kind and order m

$k = \frac{b}{a}$ = diameter ratio

p = pressure

$q = \frac{2n\pi a}{h}$,

$q^* = \frac{n\pi a}{h}$

r, φ, z = cylindrical coordinates

$s = \bar{\sigma} + i\bar{\omega}$ = complex frequency

$S \equiv \frac{sa^2}{\nu}$

t = time

u, w = velocity components in the radial- and axial direction

$\bar{z}_0$ = excitation amplitude

$\bar{Z} \equiv \frac{\bar{z}_0 \nu}{h/a}$ = abbreviation

$\sigma^* \equiv \frac{\sigma a}{\rho \nu^2}$ = surface tension parameter

σ = surface tension

η = dynamic viscosity

$\nu = \frac{\eta}{\rho}$ = kinematic viscosity

ρ = density of liquid

ζ = free liquid surface elevation

$\tau \equiv \frac{t\nu}{a^2}$ = dimensionless time

τ_{rz} = shear stress

$\bar{\Omega} = \frac{\Omega a^2}{\nu}$ = "reduced" forcing frequency

Ω = forcing frequency

Ψ = stream function

ω_{mn} = natural frequency of non-viscous liquid

1. Introduction

The vibrational behavior of cylindrical liquid bridges under micro- or even zero-gravity conditions has recently become of quite some interest and importance in manufacturing processes in space. The favored geometry is the cylindrical liquid column and liquid layer around a rigid center-core. If such a liquid bridge is disturbed, it will perform oscillations which usually have detrimental effects on experiments and on products of a manufacturing process. Due to the lack of gravity the liquid bridge is held together by surface tension, which also acts in case of disturbances as the restoring force. The knowledge of the magnitude of the natural frequencies and of the decay motion, as well as the response of the liquid bridge to harmonic axial excitations is of quite some interest to the experimenter and payload specialist in an orbiting space laboratory. An experiment shall be performed on the second German Spacemission under the title "Liquid Column Resonances" (LICORE), in order to establish experimentally the natural frequencies, the damped natural frequencies and the response of the liquid bridge to several axial excitations. To support these experiments the necessary theoretical knowledge of the behavior of the liquid, as well as pilot experiments with small aspect ratio bridges on earth shall be performed previous to any flight experiments in orbit. Only this way useful, efficient and conclusive results may be obtained from experiments in orbit. The natural frequencies for frictionless liquid, viscous and visco-elastic liquids have been investigated by numerous researchers [1–9]. It was found that the liquid becomes unstable, if the wave length in axial direction for the axisymmetric mode $m = 0$ is equal or larger than the circumference of the liquid column, a result valid for frictionless, viscous and visco-elastic liquid. For viscous liquid there exists, however, a range of axial wave-length, for which (depending on the surface tension parameter $\sigma a/\rho\nu^2$) no damped oscillation occurs anymore, which means, that only an aperiodic decay motion takes place [10]. The response of a liquid bridge consisting of incompressible and frictionless or viscous liquid has been treated extensively by the author for axial- and pitching excitation [11–16]. Since the experimental set-up may partly fail during the experiment in orbit, i.e. if a counter-directional excitation may deteriorate into a one sided excitation or into an excitation mode, where top- and bottom excitation are out of phase, the following investigations have been performed to cover some of these possible cases. This has been performed for a liquid column [17] and shall be done here for an annular liquid layer of thickness $(a - b)$. First we investigate the response of the viscous liquid layer to counter-directional excitation, then to one-sided excitation and finally we treat an excitation, where the top- and bottom wall of the liquid bridge perform different excitation amplitudes with different forcing frequencies and are in addition out of phase. Since viscous liquid columns [10] and annular layers [18] exhibit a quite different vibrational behavior, the results for frictionless liquid, which show always undamped oscillatory behavior, are no longer representative. Motion identification charts are presented [18] and show that damped oscillatory-

and pure aperiodic liquid behavior may occur for some axial wave lengths, depending on the magnitude of the surface tension parameter $\sigma a/\rho v^2$ and the thickness of the layer $a\,(1 - k)$. The thinner the annular liquid layer, the more the system shall exhibit aperiodic motion behavior over an extended axial wave-length-range. The same cases were treated for frictionless liquid column in [12, 13, 14] and for an annular liquid layer in [19]. The results for frictionless liquid show a sharply tuned first resonance peak, which may easily be missed in a sweeping experiment. In addition, of course, the response at the natural frequencies is due to the lack of liquid damping infinite. Thinner liquid layers exhibit decreased resonance frequencies and show responses that are more sharply tuned than those of thicker layers. The response of the free surface displacement and that of the velocity distributions shall be obtained. In addition the pressure distribution at the top- or bottom wall is presented in analytical form.

2. Basic equations

A liquid layer of finite length h and thickness $(a - b)$ consists of incompressible and viscous liquid and is placed between two walls (Fig. 1) in a zero gravity environment. If the layer is disturbed it will perform a damped oscillation, in which the free liquid surface tension acts as the restoring force, thus performing free oscillations or an aperiodic decay, depending on the axial wave length, the diameter ratio k and the magnitude of the surface tension parameter $\sigma a/\rho v^2$ [18]. If one or both of the walls are subjected to axial harmonic excitation, the liquid column shall exhibit a certain response. To determine such a response for free surface displacement $\zeta(z, t)$ and the velocity distribution $u(r,\ z,\ t)$ and $w(r, z, t)$, the Navier-Stokes equations have to be

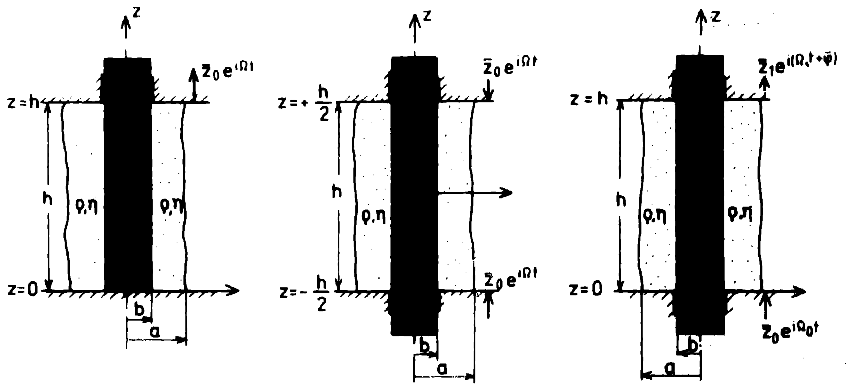

one-sided excitation

counter-excited

"phase"-excited

Fig. 1. Liquid layer and coordinate systems.

solved together with the continuity equation and the appropriate boundary conditions. Assuming small velocities and also small free liquid surface displacements, the basic equations may be linearized and are with the velocity $\mathbf{v} = u\mathbf{e}_r + w\mathbf{k}$ given by the Stokes equation

$$\frac{\partial \mathbf{v}}{\partial t} + \frac{1}{\rho} \operatorname{grad} p + \nu \operatorname{curl} \operatorname{curl} \mathbf{v} = 0 \tag{1}$$

and the continuity equation

$$\operatorname{div} \mathbf{v} = 0. \tag{2}$$

In component writing this yields the expressions

$$\frac{\partial u}{\partial t} + \frac{1}{\rho}\frac{\partial p}{\partial r} = \nu \left[\frac{\partial^2 u}{\partial r^2} + \frac{1}{r}\frac{\partial u}{\partial r} - \frac{u}{r^2} + \frac{\partial^2 u}{\partial z^2}\right], \tag{3a}$$

$$\frac{\partial w}{\partial t} + \frac{1}{\rho}\frac{\partial p}{\partial z} = \nu \left[\frac{\partial^2 w}{\partial r^2} + \frac{1}{r}\frac{\partial w}{\partial r} + \frac{\partial^2 w}{\partial z^2}\right] \tag{3b}$$

and

$$\frac{\partial u}{\partial r} + \frac{u}{r} + \frac{\partial w}{\partial z} = 0. \tag{4}$$

The free surface condition is given by the *kinematic* condition

$$u = \frac{\partial \zeta}{\partial t} \quad \text{at } r = a \tag{5a}$$

and the *dynamic* condition

$$p - 2\eta \frac{\partial u}{\partial r} + \frac{\sigma}{a^2}\left[\zeta + a^2 \frac{\partial^2 \zeta}{\partial z^2}\right] = \frac{\sigma}{a} \quad \text{at } r = a \tag{5b}$$

which combined yield

$$\frac{\partial p}{\partial t} - 2\eta \frac{\partial^2 u}{\partial r \partial t} + \frac{\sigma}{a^2}\left[u + a^2 \frac{\partial^2 u}{\partial z^2}\right] = 0 \quad \text{at } r = a. \tag{6}$$

The shear stress τ_{rz} vanishes at the free surface, i.e.

$$\frac{\partial w}{\partial r} + \frac{\partial u}{\partial z} = 0 \quad \text{at } r = a. \tag{7}$$

At the wall $r = b$ (center-core) the boundary condition is

$$u = w = 0 \quad \text{at } r = b \tag{8a}$$

while at the top- and bottom wall the velocities

$$u = 0 \quad \text{and} \quad w = w(t). \tag{8b}$$

Applying the vector operation "divergence" upon equation (1) yields the Laplace equation for the pressure

$$\frac{\partial^2 p}{\partial r^2} + \frac{1}{r}\frac{\partial p}{\partial r} + \frac{\partial^2 p}{\partial z^2} = 0. \tag{8c}$$

3. Method of solution

Since we treat the linearized behavior of the liquid due to axial excitation, the liquid shall respond in its axisymmetric mode $m = 0$.

3.1. Harmonic counter-excitation

For this excitation modus the excitation of the upper wall will be exactly out of phase by π to the excitation of the lower wall $\bar{z}_0 e^{i\Omega t}$, where $\bar{z}_0$ is the excitation amplitude and Ω the forcing frequency. The upper wall and lower wall boundary condition is therefore with slipping in radial direction $\tau_{rz} = 0$ at $z = \pm h/2$ (instead of no-slip):

$$w = \mp i\Omega \bar{z}_0 e^{i\Omega t} \quad \text{at} \quad z = \pm\frac{h}{2}. \tag{9}$$

Actually the radial velocity u should also vanish there. To obtain, however, an analytic solution the no-slip condition has been abandoned and has been substituted by $\tau_{rz} = 0$ at $z = \pm h/2$. We assume for the pressure- and velocity distribution the following expressions

$$p(r, z, t) = e^{i\Omega t}\left\{\bar{z}_0\bar{P}_0 + \bar{z}_0\bar{P}_1\left[\frac{1}{2}\left(\frac{r}{a}\right)^2 - k^2 \ln\frac{r}{a}\right] + \bar{z}_0\bar{P}_2\frac{z^2}{h^2} + \right.$$

$$\left. + \sum_{n=1}^{\infty} P_{2n}(r)\cos\left(\frac{2n\pi z}{h}\right)\right\} \tag{10a}$$

$$u(r, z, t) = e^{i\Omega t}\left\{\bar{z}_0 U_0\left(\frac{r}{a} - \frac{k^2}{r/a}\right) + \sum_{n=1}^{\infty} U_{2n}(r)\cos\left(\frac{2n\pi z}{h}\right)\right\} \tag{10b}$$

$$w(r, z, t) = e^{i\Omega t}\left\{-2i\Omega\bar{z}_0\frac{z}{h} + \sum_{n=1}^{\infty} W_{2n}(r)\sin\left(\frac{2n\pi z}{h}\right)\right\} \tag{10c}$$

where w satisfies the boundary conditions (9). Introducing these solutions into equations (3a), (3b), (4) and (8) yields for the unknowns

$$U_0 = \frac{i\Omega a}{h}, \qquad \bar{P}_1 = \frac{\rho a^2\Omega^2}{h} \quad \text{and} \quad \bar{P}_2 = -\rho\Omega^2 h. \tag{11}$$

Expanding

$$\frac{z^2}{h^2} = \frac{1}{12} + \frac{1}{2\pi^2}\sum_{n=1}^{\infty}\frac{(-1)^{n-1}}{n^2}\cos\left(\frac{2n\pi z}{h}\right) \tag{12}$$

into a Fourier series and introducing it into the free surface condition (6) yields

$$\bar{P}_0 = \frac{2i\eta\Omega}{h}(1 + k^2) - \frac{\sigma}{ah}(1 - k^2) + \frac{\rho h\Omega^2}{2}\left(\frac{1}{6} - \frac{a^2}{h^2}\right) \tag{13}$$

and the system

$$\frac{i\Omega}{\nu}U_{2n} + \frac{1}{\eta}\frac{dP_{2n}}{dr} = \frac{d^2U_{2n}}{dr^{22}} + \frac{1}{r}\frac{dU_{2n}}{dr} - \frac{U_{2n}}{r^2} - \frac{4n^2\pi^2}{h^2}U_{2n} \tag{14a}$$

$$\frac{i\Omega}{\nu}W_{2n} - \frac{2n\pi}{\eta h}P_{2n} = \frac{d^2W_{2n}}{dr^2} + \frac{1}{r}\frac{dW_{2n}}{dr} - \frac{4\pi^2n^2}{h^2}W_{2n} \tag{14b}$$

$$\frac{dU_{2n}}{dr} + \frac{U_{2n}}{r} + \frac{2n\pi}{h}W_{2n} = 0 \tag{14c}$$

with the boundary conditions

$$\frac{\mathrm{d}W_{2n}}{\mathrm{d}r} - \frac{2n\pi}{h} U_{2n} = 0 \quad \text{at } r = a \tag{15a}$$

$$i\Omega P_{2n} - 2i\eta\Omega \frac{\mathrm{d}U_{2n}}{\mathrm{d}r} - \frac{\sigma}{a^2}\left[\frac{4n^2\pi^2a^2}{h^2} - 1\right] U_{2n} = \frac{i\Omega^3 \bar{z}_0 \rho h(-1)^{n-1}}{2\pi^2 n^2} \quad \text{at } r = a \tag{15b}$$

$$U_{2n} = 0 \quad \text{at } r = b \tag{15c}$$

and with the sine-expansion

$$\frac{z}{h} = \sum_{n=1}^{\infty} \frac{(-1)^{n-1}}{n\pi} \sin\left(\frac{2n\pi z}{h}\right)$$

the boundary condition (8a) yields

$$W_{2n} = \frac{2i\Omega\bar{z}_0}{n\pi}(-1)^{n-1} \quad \text{at } r = b. \tag{15d}$$

Introducing the stream function $\Psi_{2n}(r, z)$ satisfying with

$$U_{2n} = -\frac{2n\pi}{hr}\Psi_{2n} \quad \text{and} \quad W_{2n} = \frac{1}{r}\frac{\partial \Psi_{2n}}{\partial r} \tag{16}$$

the continuity equation identically, we obtain with

$$\Psi(r, z) = \sum_{n=1}^{\infty} \Psi_{2n}(r) \sin\left(\frac{2n\pi z}{h}\right) \tag{17a}$$

the ordinary differential equation

$$\bar{\Delta}\left[\bar{\Delta}\Psi_{2n} - \frac{i\Omega}{\nu}\Psi_{2n}\right] = 0 \tag{17b}$$

where the operator

$$\bar{\Delta} \equiv \frac{\mathrm{d}^2}{\mathrm{d}r^2} - \frac{1}{r}\frac{\mathrm{d}}{\mathrm{d}r} - \frac{4n^2\pi^2}{h^2}.$$

The solution of this equation is given with

$$q \equiv \frac{2n\pi a}{h}$$

and

$$\bar{q}^2 = \frac{4n^2\pi^2 a^2}{h^2} + \frac{i\Omega a^2}{\nu}$$

by the expression

$$\begin{aligned}\Psi(r, z) = \sum_{n=1}^{\infty} \Big\{ & A_{2n}\frac{r}{a} I_1\left(\bar{q}\frac{r}{a}\right) + B_{2n}\frac{r}{a} K_1\left(\bar{q}\frac{r}{a}\right) + \frac{i\nu}{\Omega} C_{2n}\frac{r}{a} I_1\left(q\frac{r}{a}\right) + \\ & + \frac{i\nu}{\Omega} D_{2n}\frac{r}{a} K_1\left(q\frac{r}{a}\right)\Big\} \sin\left(\frac{2n\pi z}{h}\right). \end{aligned} \tag{18}$$

The appearing integration "constants" A_{2n}, B_{2n}, C_{2n} and D_{2n} are functions of the forcing frequency Ω. We obtain thus with (16) for $U_{2n}(r)$ and $W_{2n}(r)$ the expressions

$$\begin{aligned}U_{2n}(r) = -\frac{2n\pi}{ha}\Big[& A_{2n} I_1\left(\bar{q}\frac{r}{a}\right) + B_{2n} K_1\left(\bar{q}\frac{r}{a}\right) + \frac{i\nu}{\Omega} C_{2n} I_1\left(q\frac{r}{a}\right) + \\ & + \frac{i\nu}{\Omega} D_{2n} K_1\left(q\frac{r}{a}\right)\Big] \end{aligned} \tag{19}$$

and

$$\begin{aligned}W_{2n}(r) = \frac{1}{a^2}\Big[& A_{2n}\bar{q} I_0\left(\bar{q}\frac{r}{a}\right) - B_{2n}\bar{q} K_0\left(\bar{q}\frac{r}{a}\right) + \frac{i\nu}{\Omega} C_{2n} q I_0\left(q\frac{r}{a}\right) - \\ & - \frac{i\nu}{\Omega} D_{2n} q K_0\left(q\frac{r}{a}\right)\Big]. \end{aligned} \tag{20}$$

The velocity distribution is then given by

$$\begin{aligned}u(r, z, t) = \mathrm{e}^{i\Omega t}\Big\{ & \frac{\bar{z}_0 i\Omega}{h/a}\left(\frac{r}{a} - \frac{k^2}{r/a}\right) - \sum_{n=1}^{\infty} \frac{2n\pi}{ha} \\ & \times \Big[A_{2n} I_1\left(\bar{q}\frac{r}{a}\right) + B_{2n} K_1\left(\bar{q}\frac{r}{a}\right) + \frac{i\nu}{\Omega} C_{2n} I_1\left(q\frac{r}{a}\right) + \\ & + \frac{i\nu}{\Omega} D_{2n} K_1\left(q\frac{r}{a}\right)\Big] \cos\left(\frac{2n\pi z}{h}\right)\Big\} \end{aligned} \tag{21a}$$

in radial directions and

$$w(r, z, t) = \mathrm{e}^{i\Omega t}\left\{-2i\Omega\bar{z}_0\left(\frac{z}{h}\right) + \frac{1}{a^2}\sum_{n=1}^{\infty}\left[A_{2n}\bar{q}I_0\left(\bar{q}\frac{r}{a}\right) - B_{2n}\bar{q}K_0\left(\bar{q}\frac{r}{a}\right) + \right.\right.$$

$$\left.\left. + \frac{i\nu}{\Omega}C_{2n}qI_0\left(q\frac{r}{a}\right) - \frac{i\nu}{\Omega}D_{2n}qK_0\left(q\frac{r}{a}\right)\right]\sin\left(\frac{2n\pi z}{h}\right)\right\} \tag{21b}$$

in axial direction.

The pressure distribution is obtained from equation (8), i.e.

$$\frac{\mathrm{d}^2P_{2n}}{\mathrm{d}r^2} + \frac{1}{r}\frac{\mathrm{d}P_{2n}}{\mathrm{d}r} - \frac{4n^2\pi^2}{h^2}P_{2n} = 0$$

and yields with (10a), (11), (13) the expression:

$$p(r, z, t) = \mathrm{e}^{i\Omega t}\left\{\bar{z}_0\left[\frac{2i\eta\Omega}{h}(1 + k^2) - \frac{\sigma}{ah}(1 - k^2) + \frac{\rho h\Omega^2}{2}\left(\frac{1}{6} - \frac{a^2}{h^2}\right)\right] + \right.$$

$$+ \frac{\bar{z}_0\rho a^2\Omega^2}{h}\left[\frac{1}{2}\frac{r^2}{a^2} - k^2\ln\frac{r}{a}\right] - \bar{z}_0\rho h\Omega^2\left(\frac{z^2}{h^2}\right) +$$

$$\left. + \sum_{n=1}^{\infty}\left[\frac{\eta}{a}C_{2n}I_0\left(q\frac{r}{a}\right) + \frac{\eta}{a}D_{2n}K_0\left(q\frac{r}{a}\right)\right]\cos\left(\frac{2n\pi z}{h}\right)\right\}. \tag{21c}$$

The values A_{2n}, B_{2n}, C_{2n} and D_{2n} are obtained from the boundary conditions (15a, b, c, d), which yield four algebraic equations:

$$A_{2n}I_1(\bar{q})\left[\bar{q}^2 + \frac{4n^2\pi^2a^2}{h^2}\right] + B_{2n}K_1(\bar{q})\left[\frac{4n^2\pi^2a^2}{h^2} + \bar{q}^2\right] +$$

$$+ C_{2n}a^2\cdot iI_1(q)\left[q^2 + \frac{4n^2\pi^2a^2}{h^2}\right]\Big/\left(\frac{\Omega a^2}{\nu}\right) +$$

$$+ D_{2n}a^2iK_1(q)\left[\frac{4n^2\pi^2a^2}{h^2} + q^2\right]\Big/\left(\frac{\Omega a^2}{\nu}\right) = 0 \tag{22a}$$

$$A_{2n}I_1(k\bar{q}) + B_{2n}K_1(k\bar{q}) + C_{2n}a^2\frac{i}{(\Omega a^2/\nu)}I_1(kq) + D_{2n}a^2\frac{i}{(\Omega a^2/\nu)}K_1(kq) = 0 \tag{22b}$$

$$A_{2n}\bar{q}I_0(k\bar{q}) - B_{2n}\bar{q}K_0(k\bar{q}) + C_{2n}a^2\frac{i}{(\Omega a^2/\nu)}qI_0(kq) - D_{2n}a^2\frac{i}{(\Omega a^2/\nu)}qK_0(kq)$$

$$= 2i\left(\frac{\Omega a^2}{\nu}\right)\frac{(-1)^{n-1}}{n\pi a/h}\left(\frac{\bar{z}_0\nu}{h/a}\right) \tag{22c}$$

$$\begin{aligned}
&A_{2n}\Bigl\{\frac{4n\pi a}{h}\bar{q}I_1'(\bar{q}) - i\frac{\sigma a}{\rho\nu^2}\Bigl[\frac{4n^2\pi^2a^2}{h^2}-1\Bigr]\frac{2n\pi a}{h}\frac{1}{(\Omega a^2/\nu)}I_1(\bar{q})\Bigr\}+\\
&+B_{2n}\Bigl\{\frac{4n\pi a}{h}\bar{q}K_1'(\bar{q}) - i\frac{\sigma a}{\rho\nu^2}\Bigl[\frac{4n^2\pi^2a^2}{h^2}-1\Bigr]\frac{2n\pi a}{h}\frac{1}{(\Omega a^2/\nu)}K_1(\bar{q})\Bigr\}+\\
&+C_{2n}a^2\Bigl\{I_0(q)+\frac{4n\pi a}{h}q\frac{i}{(\Omega a^2/\nu)}I_1'(q)+\frac{\sigma a}{\rho\nu^2}\Bigl[\frac{4n^2\pi^2a^2}{h^2}-1\Bigr]\frac{2n\pi a}{h}\\
&\times\frac{1}{(\Omega a^2/\nu)^2}I_1(q)\Bigr\}+D_{2n}a^2\Bigl\{K_0(q)+\frac{4n\pi a}{h}q\frac{i}{(\Omega a^2/\nu)}K_1'(q)+\\
&+\frac{\sigma a^2}{\rho\nu}\Bigl[\frac{4n^2\pi^2a^2}{h^2}-1\Bigr]\frac{2n\pi a}{h}\frac{1}{(\Omega a^2/\nu)^2}K_1(q)\Bigr\}=\frac{z_0\nu}{h/a}\frac{(-1)^{n-1}}{\frac{2n^2\pi^2a^2}{h^2}}\left(\frac{\Omega a^2}{\nu}\right)^2.
\end{aligned} \tag{22d}$$

If we replace $i\Omega a^2/\nu$ by $S \equiv sa^2/\nu$ with the complex frequency $s = \bar{\sigma} + i\bar{\omega}$, then the coefficient determinant represents the frequency equation for the determination of the damped natural frequencies, i.e. for the axisymmetric frequencies $m = 0$ and $2n$, yielding $\bar{\sigma}_{02n} + i\bar{\omega}_{02n}$ [18]. The problem of the stability of annular liquid columns has been treated there and can also be found for cylindrical columns in [7, 8, 9].

3.2. Response to one-sided axial excitation

For the excitation of the top wall at $z = h$ (Fig. 1) the boundary condition is given by

$$u = w = 0 \quad \text{at} \quad z = 0 \quad \text{and} \quad u = 0, \quad w = i\Omega z_0 e^{i\Omega t} \quad \text{at } z = h. \tag{23}$$

Abandoning again the no-slip condition for the radial velocity, the velocity distribution and the pressure may then be written as:

$$u(r, z, t) = e^{i\Omega t}\left\{\bar{z}_0 U_0\left(\frac{r}{a} - \frac{k^2}{r/a}\right) + \sum_{n=1}^{\infty} U_n(r)\cos\left(\frac{n\pi z}{h}\right)\right\} \tag{24a}$$

$$w(r, z, t) = e^{i\Omega t}\left\{i\Omega\bar{z}_0\left(\frac{z}{h}\right) + \sum_{n=1}^{\infty} W_n(r)\sin\left(\frac{n\pi z}{h}\right)\right\} \tag{24b}$$

and

$$\begin{aligned}
p(r, z, t) = e^{i\Omega t}\Bigl\{&\bar{z}_0\bar{P}_0 + \bar{z}_0\bar{P}_1\left[\frac{1}{2}\left(\frac{r}{a}\right)^2 - k^2\ln\frac{r}{a}\right] +\\
&+ \bar{z}_0\bar{P}_2\frac{z^2}{h^2} + \sum_{n=1}^{\infty} P_n(r)\cos\left(\frac{n\pi z}{h}\right)\Bigr\}
\end{aligned} \tag{24c}$$

where

$$U_0 = -\frac{i\Omega a}{2h}, \qquad \bar{P}_1 = -\frac{\rho a^2 \Omega^2}{2h}, \qquad \bar{P}_2 = \frac{1}{2}\rho\Omega^2 h \tag{25}$$

In addition we obtain

$$\bar{P}_0 = \frac{\sigma}{2ah}(1-k^2) - \frac{i\Omega\eta}{h}(1+k^2) + \frac{\rho h \Omega^2}{12}\left(\frac{3a^2}{h^2} - 2\right). \tag{26}$$

With a similar procedure as above the stream function is given by

$$\Psi(r, z) = \sum_{n=1}^{\infty}\left\{A_n \frac{r}{a} I_1\left(\bar{q}^* \frac{r}{a}\right) + B_n \frac{r}{a} K_1\left(\bar{q}^* \frac{r}{a}\right) + \right.$$
$$\left. + \frac{i\nu}{\Omega} C_n \frac{r}{a} I_1\left(q^* \frac{r}{a}\right) + \frac{i\nu}{\Omega} D_n \frac{r}{a} K_1\left(q^* \frac{r}{a}\right)\right\} \sin\left(\frac{n\pi z}{h}\right) \tag{27}$$

where $\bar{q}^* = q^{*2} + i\Omega a^2/\nu$ and $q^* = n\pi a/h$. With the boundary conditions we obtain four algebraic equations for the determination of $A_n(\Omega)$, $B_n(\Omega)$, $C_n(\Omega)$ and $D_n(\Omega)$. They are given by

$$A_n\left[\bar{q}^{*2} + \frac{n^2\pi^2 a^2}{h^2}\right] I_1(\bar{q}^*) + B_n\left[\bar{q}^* + \frac{n^2\pi^2 a^2}{h^2}\right] K_1(\bar{q}^*) +$$
$$+ C_n a^2 i\left[q^{*2} + \frac{n^2\pi^2 a^2}{h^2}\right] I_1(q^*) \Big/ \left(\frac{\Omega a^2}{\nu}\right) +$$
$$+ D_n a^2 i\left[q^{*2} + \frac{n^2\pi^2 a^2}{h^2}\right] K_1(q^*) \Big/ \left(\frac{\Omega a^2}{\nu}\right) = 0 \tag{28a}$$

$$A_n I_1(k\bar{q}^*) + B_n K_1(k\bar{q}^*) + C_n a^2 \frac{i}{(\Omega a^2/\nu)} I_1(kq^*) + D_n a^2 \frac{i}{(\Omega a^2/\nu)} K_1(kq^*) = 0 \tag{28b}$$

$$A_n \bar{q}^* I_0(k\bar{q}^*) - B_n \bar{q}^* K_0(k\bar{q}) + C_n a^2 \frac{i}{(\Omega a^2/\nu)} q^* I_0(kq^*) - D_n a^2 \frac{i}{(\Omega a^2/\nu)} q^* K_0(kq^*)$$
$$= 2i\left(\frac{\Omega a^2}{\nu}\right)\frac{(-1)^n}{n\pi a/h}\left(\frac{\bar{z}_0 \nu}{h/a}\right) \tag{28c}$$

and

$$A_n \left\{ 2q^*\bar{q}^* I_1'(\bar{q}^*) - \frac{i\sigma a}{\rho\nu^2} \frac{1}{(\Omega a^2/\nu)} q^*(q^{*2} - 1) I_1(\bar{q}^*) \right\} +$$

$$+ B_n \left\{ 2q^*\bar{q}^* K_1'(\bar{q}^*) - \frac{i\sigma a}{\rho\nu^2} \frac{1}{(\Omega a^2/\nu)} q^*(q^{*2} - 1) K_1(\bar{q}^*) \right\} +$$

$$+ a^2 C_n \left\{ \frac{2iq^{*2}}{(\Omega a^2/\nu)} I_1'(q^*) + \frac{\sigma a}{\rho\nu^2} q^*(q^{*2} - 1) I_1(q^*) \Big/ \left(\frac{\Omega a^2}{\nu}\right)^2 + I_0(q^*) \right\} +$$

$$+ a^2 D_n \left\{ \frac{2iq^{*2}}{(\Omega a^2/\nu)} K_1'(q^*) + \frac{\sigma a}{\rho\nu^2} q^*(q^{*2} - 1) K_1(q^*) \Big/ \left(\frac{\Omega a^2}{\nu}\right)^2 + K_0(q^*) \right\}$$

$$= \frac{2(-1)^{n-1}}{q^{*2}} \left(\frac{\Omega a^2}{\nu}\right)^2 \left(\frac{\bar{z}\nu}{h/a}\right). \tag{28d}$$

The coefficient determinant represents again the frequency equation for the free damped oscillation case and renders if set equal to zero the damped natural frequencies, if $i\Omega a^2/\nu$ is replaced by $S \equiv sa^2/\nu$, yielding $\sigma_{0n} + i\omega_{0n}$ [18].

3.3. Response to unequal axial excitations

If the top wall of the liquid layer is excited harmonically by $z(t) = \bar{z}_2 e^{i(\Omega_2 t + \varphi)}$ and the bottom wall by $z(t) = \bar{z}_1 e^{i\Omega_1 t}$ where Ω_1, Ω_2 are forcing frequencies and $\bar{z}_1$, $\bar{z}_2$ are the excitation amplitudes (φ is a phase angle), then the boundary conditions are

$$w_1 = i\Omega_1 \bar{z}_1 e^{i\Omega_1 t} \quad \text{at } z = 0, \qquad w_1 = 0 \quad \text{at } z = h$$

and

$$w_2 = 0 \quad \text{at} \quad z = 0,\ w_2 = i\Omega_2 \bar{z}_2 e^{i(\Omega_2 t + \varphi)} \text{ at } z = h.$$

The response of the liquid may be obtained without any difficulties from the previous section by replacing the proper values and performing the necessary transformation of the z-range.

4. Numerical evaluations and conclusions

Some of the analytically received results have been evaluated numerically and are presented in the following figures as response functions of the "reduced" (dimensionless) forcing frequency $\bar{\Omega} \equiv \Omega a^2/\nu$ for an aspect ratio $h/a = 2.0$ of the liquid layer and different diameter ratios $k = b/a = 0.01$ and 0.5. Three different surface tension parameters $\sigma^* = \sigma a/\rho\nu^2 = 400$ and 100 (or Ohnsorg numbers 1/400 and 1/100) have been chosen and different locations $r = a$ (on the free liquid surface) and z/h have been observed.

4.1. Counter-directional excitation

For a counter-directional excitation with the excitation amplitude $\bar{z}_0$ and the forcing frequency Ω the response of the radial velocity $|u(r, z, \tau)/\bar{Z}\bar{\Omega}e^{i\bar{\Omega}\tau/a^2}|$, which at the location $r = a$ is the free surface displacement $|\zeta\nu/\bar{z}e^{i\bar{\Omega}\tau}|$ (as obtained from the kinematic condition), is presented for various parameters in Figs 2*a* to 2*d*. The value $\tau = t\nu/a^2$ is the dimensionless time, while $\bar{Z} \equiv \bar{z}_0\nu/h/a$. The velocity u is shown at the free liquid surface $r = a$ and that the location $z/h = 0.5$, 0.25 and 0.125. It may be noticed, that according to the analytical structure of the expression u some resonance peaks do not appear, since at such a location a nodal plane may show up. There also is symmetry in the velocity distribution. The diameter ratio $k = 0.01$, i.e. a very thin center-core or thick layer, was chosen to compare the numerical results with previous results [17] for a circular cylindrical liquid column. It may be noticed that due to $n \cos(2n\pi z)/h$ the (even) resonance $2n = 2$ disappears for $a/h = 1/4$ and for $2n = 4$ at $z/h = 1/8$. Figure 2*a* shows the response for $\sigma^* = 400$. At $\Omega \to 0$ we notice the value of the radial velocity due to the show change of the cylindrical free surface as a whole due to the geometry change of the layer. With increasing mode number $2n$ the resonance peaks flattens out. For $k = 0.5$ the response is presented in Fig. 2*b*, where the magnitude of the resonance peaks are reduced in comparison of the results for $k = 0.01$.

Results for $k = 0.8$, i.e. a thinner layer, where the peaks flatten out considerably, or for an even thinner layer $k = 0.99$, where the response is completely flat may be found in [19]. This is due to the fact, that in such a case there does not exist a damped natural frequency, exhibiting a decaying oscillation in case of a free oscillation, but that only an aperiodic motion is possible [18]. For $\sigma^* = 100$ the radial velocity response is presented in Figs 2*c* and 2*d*, where similar behavior may be observed as in the previous case. The axial velocity distribution $|wa^2/\bar{\Omega}\bar{z}e^{i\bar{\Omega}\tau}|$ is presented for a liquid column of aspect ratio $h/a = 2$ at the location $r = a$ and $z/h = 0.125$ (——) and 0.25 (- - -) for $\sigma^* \equiv (\sigma a)/(\rho\nu^2) = 400$ for various diameter ratios $k = 0.01$ and 0.5, in Figs 3*a* and 3*b*. With the increase of the diameter-ratio k or the decrease of the layer's thickness the peaks flatten out and disappear for very thin layers. For increasing forcing frequency $\bar{\Omega} \equiv \Omega a^2/\nu$ the resonance peaks disappear, while for decreased surface tension parameter $\sigma^* = 100$ the result of the axial velocity response is shown in Figs 3*c* and 3*d*. They exhibit decreased resonance peak magnitudes.

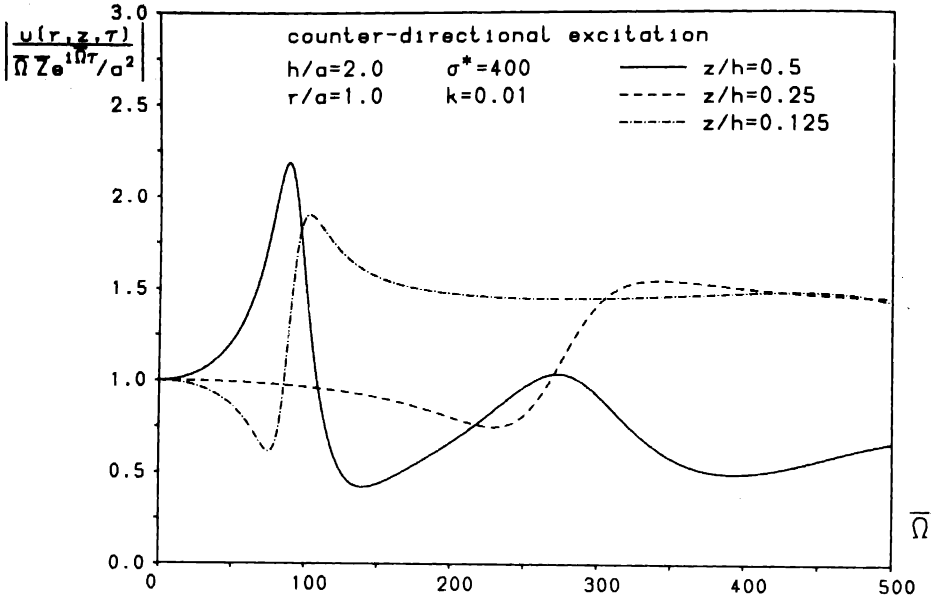
$\left|\frac{u(r,z,\tau)}{\bar{\Omega}\bar{Z}e^{i\bar{\Omega}\tau}/a^2}\right|$
counter-directional excitation
h/a=2.0
r/a=1.0
σ*=400
k=0.01
z/h=0.5
z/h=0.25
z/h=0.125
$\bar{\Omega}$
0.0
0.5
1.0
1.5
2.0
2.5
3.0
0
100
200
300
400
500

(*a*)

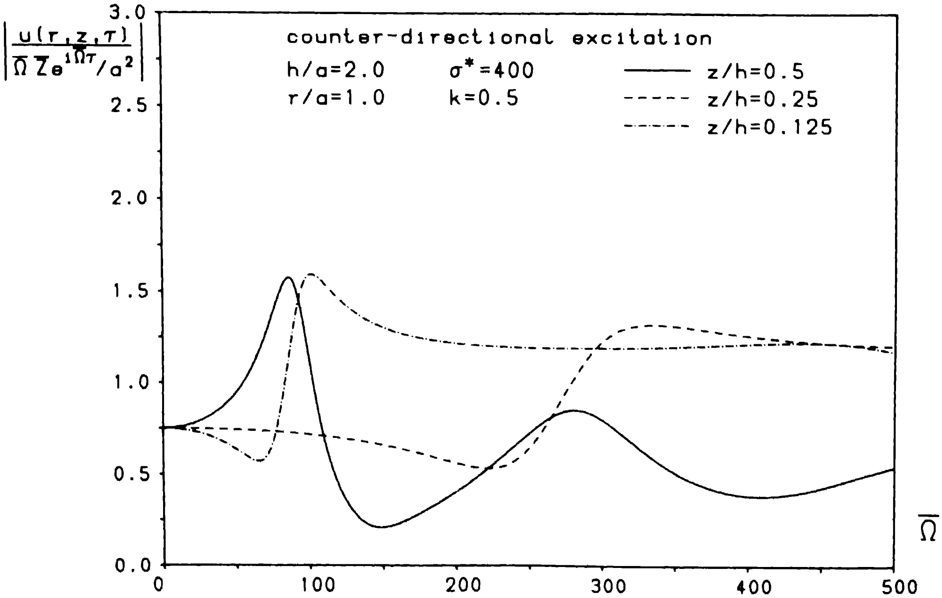
$\left|\frac{u(r,z,\tau)}{\bar{\Omega}\bar{Z}e^{i\bar{\Omega}\tau}/a^2}\right|$
counter-directional excitation
h/a=2.0
r/a=1.0
σ*=400
k=0.5
z/h=0.5
z/h=0.25
z/h=0.125
$\bar{\Omega}$
0.0
0.5
1.0
1.5
2.0
2.5
3.0
0
100
200
300
400
500

(*b*)

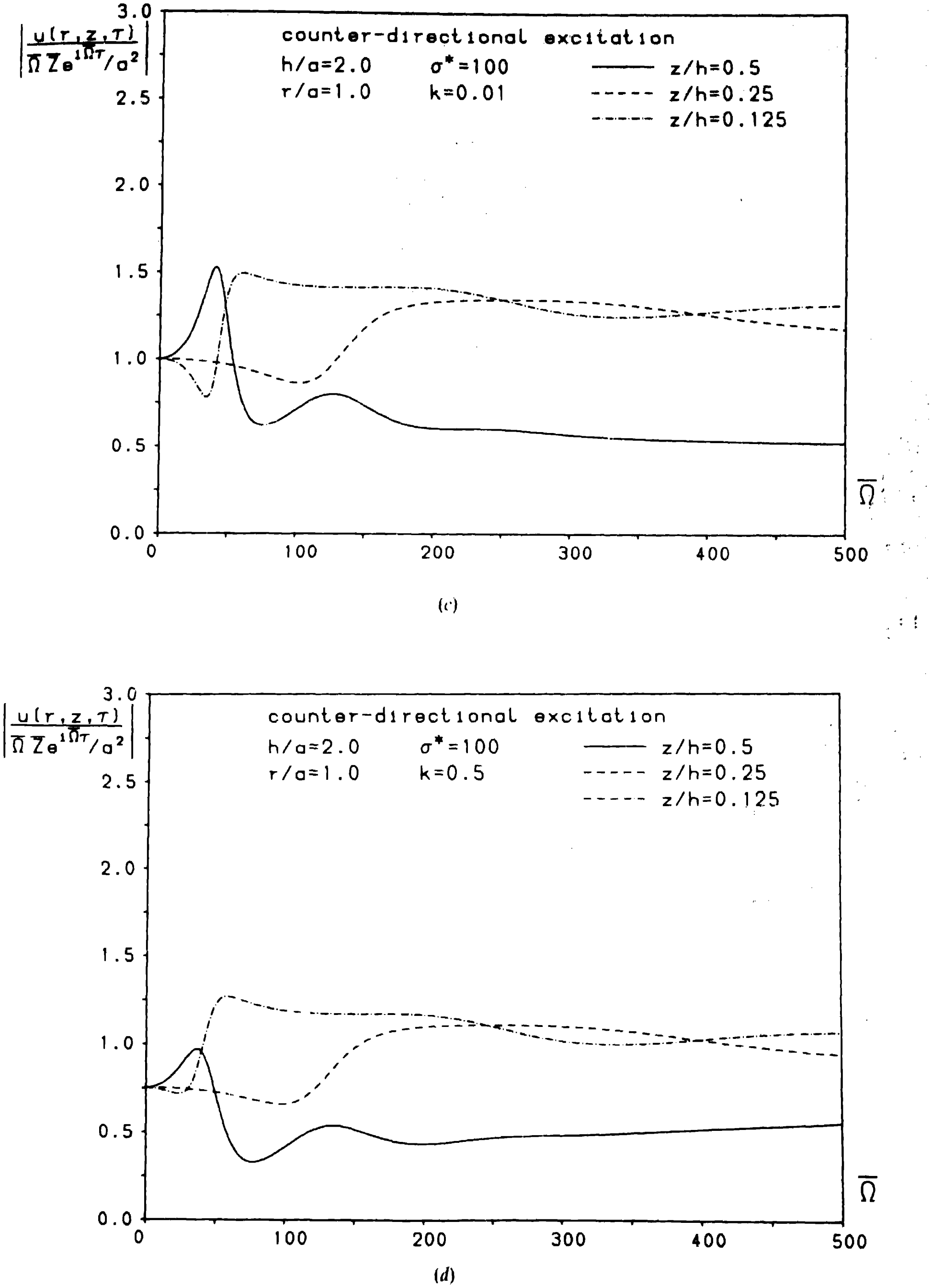

(c)

(d)

Fig. 2. Response of radial velocity distribution for counter-excited excitation.

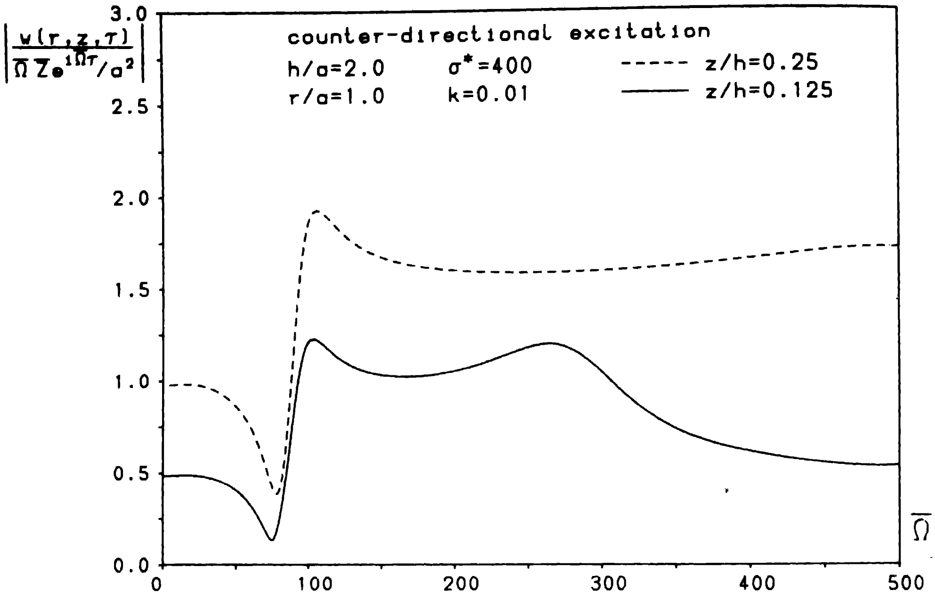
$\left|\frac{w(r,z,\tau)}{\bar{\Omega}\bar{Z}e^{i\bar{\Omega}\tau}/a^2}\right|$
counter-directional excitation
h/a=2.0
r/a=1.0
σ*=400
k=0.01
z/h=0.25
z/h=0.125
$\bar{\Omega}$
0.0
0.5
1.0
1.5
2.0
2.5
3.0
0
100
200
300
400
500

(*a*)

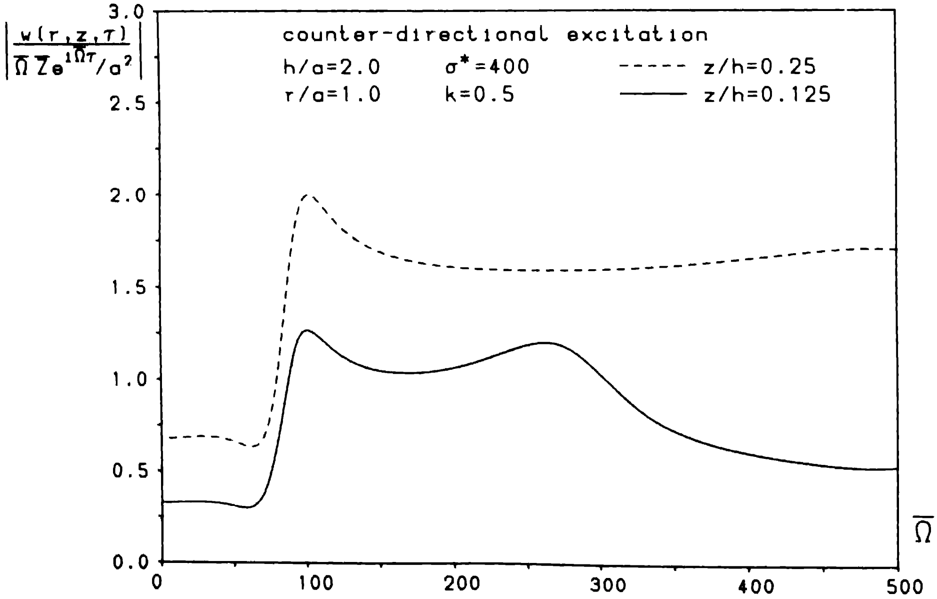
$\left|\frac{w(r,z,\tau)}{\bar{\Omega}\bar{Z}e^{i\bar{\Omega}\tau}/a^2}\right|$
counter-directional excitation
h/a=2.0
r/a=1.0
σ*=400
k=0.5
z/h=0.25
z/h=0.125
$\bar{\Omega}$
0.0
0.5
1.0
1.5
2.0
2.5
3.0
0
100
200
300
400
500

(*b*)

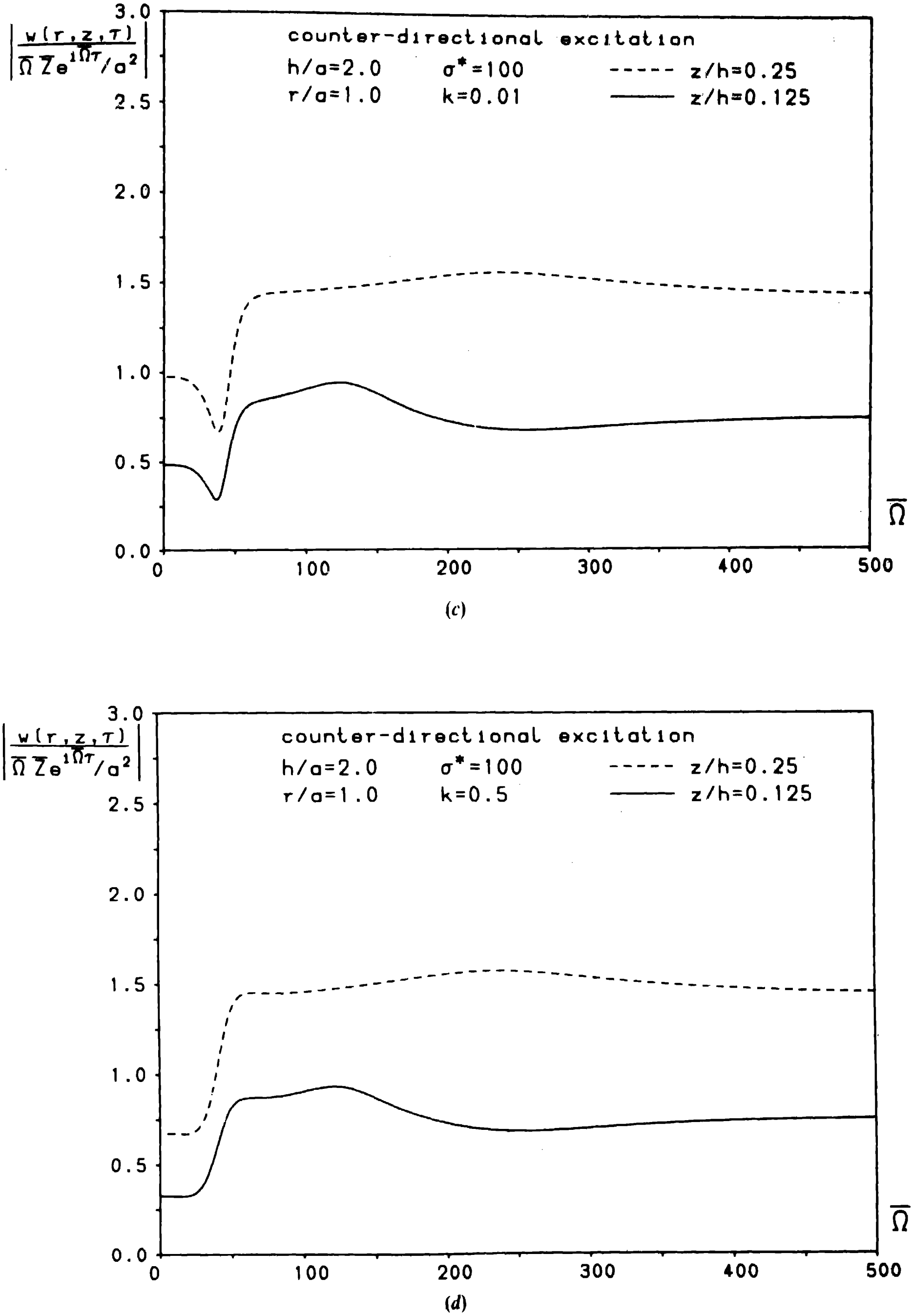

(*c*)

(*d*)

Fig. 3. Response of axial velocity distribution for counter-excited excitation.

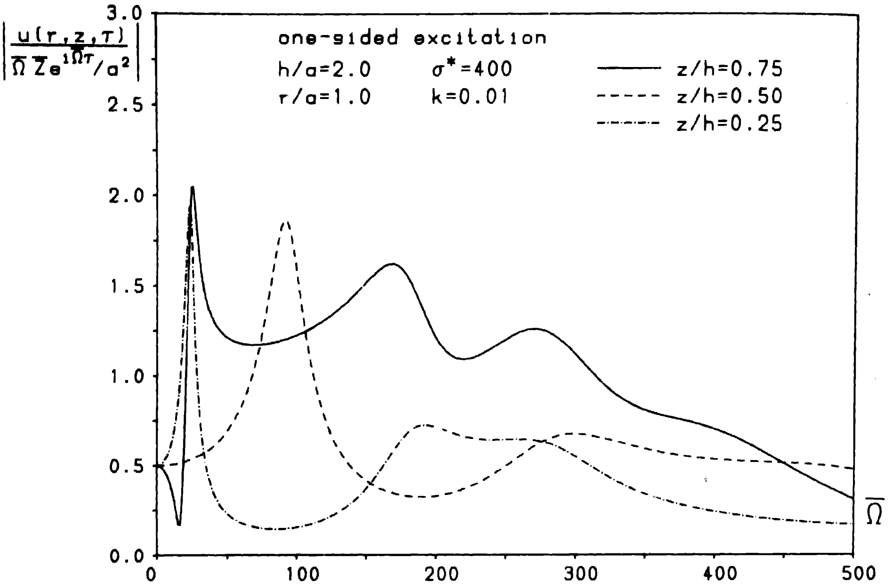
3.0
2.5
2.0
1.5
1.0
0.5
0.0
$\left|\frac{u(r,z,\tau)}{\bar{\Omega}\bar{Z}e^{i\bar{\Omega}\tau}/a^2}\right|$
one-sided excitation
h/a=2.0
r/a=1.0
σ*=400
k=0.01
z/h=0.75
z/h=0.50
z/h=0.25
0
100
200
300
400
500
$\bar{\Omega}$

(*a*)

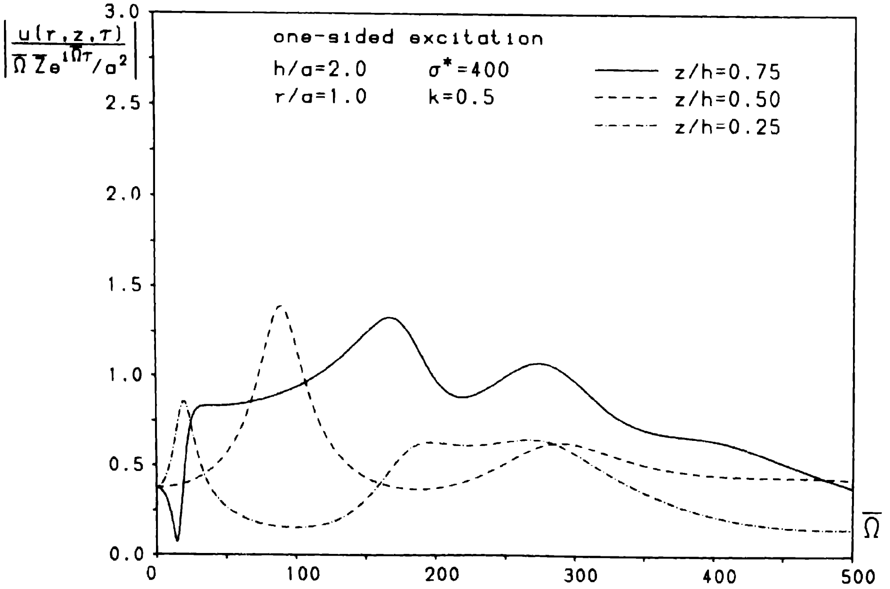
3.0
2.5
2.0
1.5
1.0
0.5
0.0
$\left|\frac{u(r,z,\tau)}{\bar{\Omega}\bar{Z}e^{i\bar{\Omega}\tau}/a^2}\right|$
one-sided excitation
h/a=2.0
r/a=1.0
σ*=400
k=0.5
z/h=0.75
z/h=0.50
z/h=0.25
0
100
200
300
400
500
$\bar{\Omega}$

(*b*)

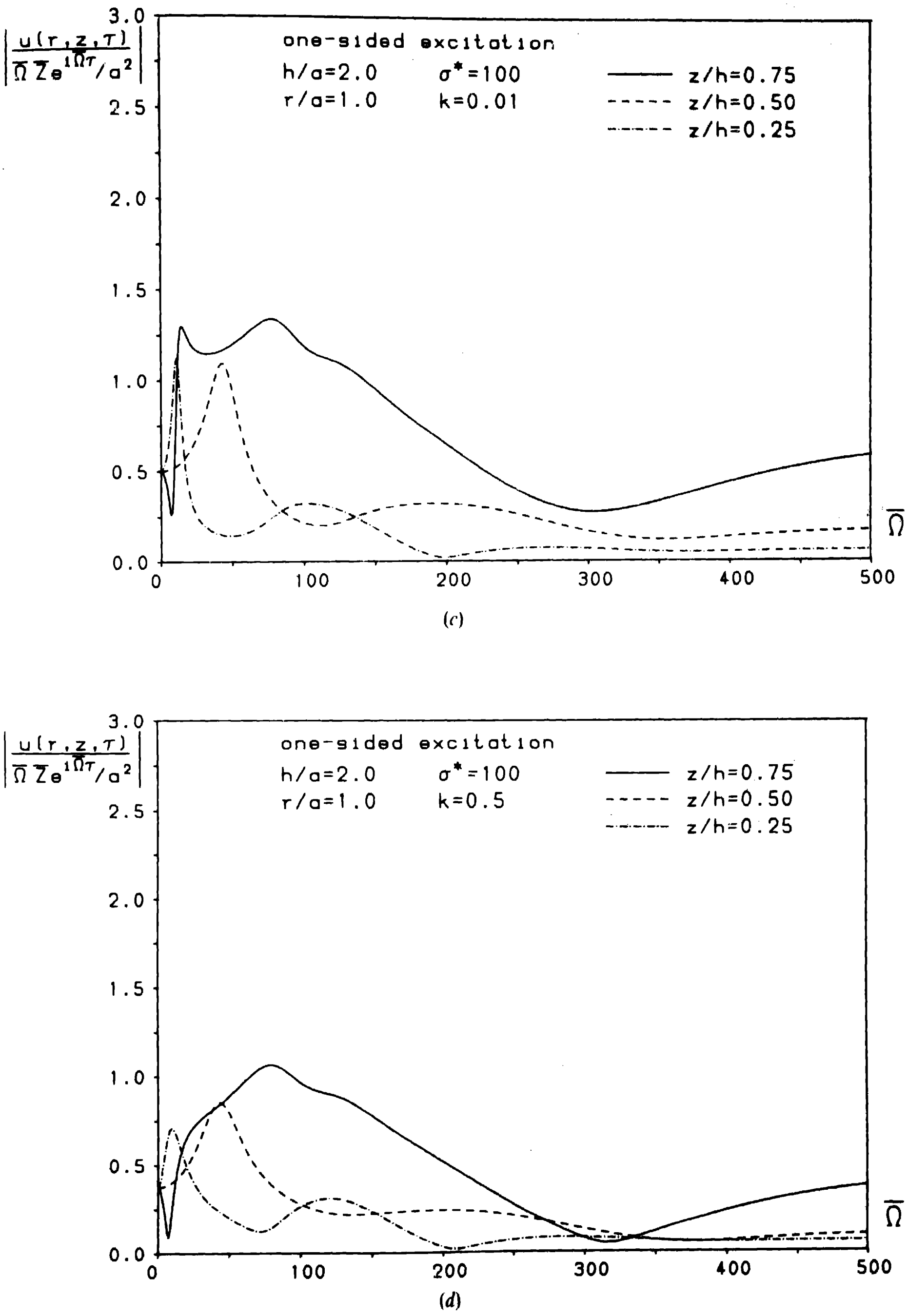

Fig. 4. Response of radial velocity distribution for one-sided excitation.

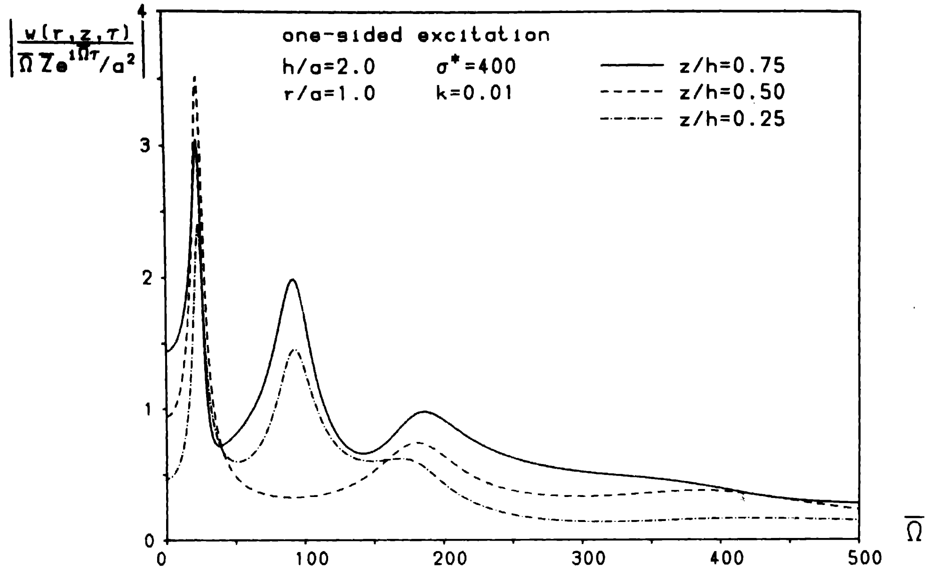
$\left|\frac{w(r,z,\tau)}{\bar{\Omega}\bar{Z}e^{i\bar{\Omega}\tau}/a^2}\right|$
one-sided excitation
h/a=2.0
σ* =400
r/a=1.0
k=0.01
z/h=0.75
z/h=0.50
z/h=0.25
0
1
2
3
4
0
100
200
300
400
500
$\bar{\Omega}$

(a)

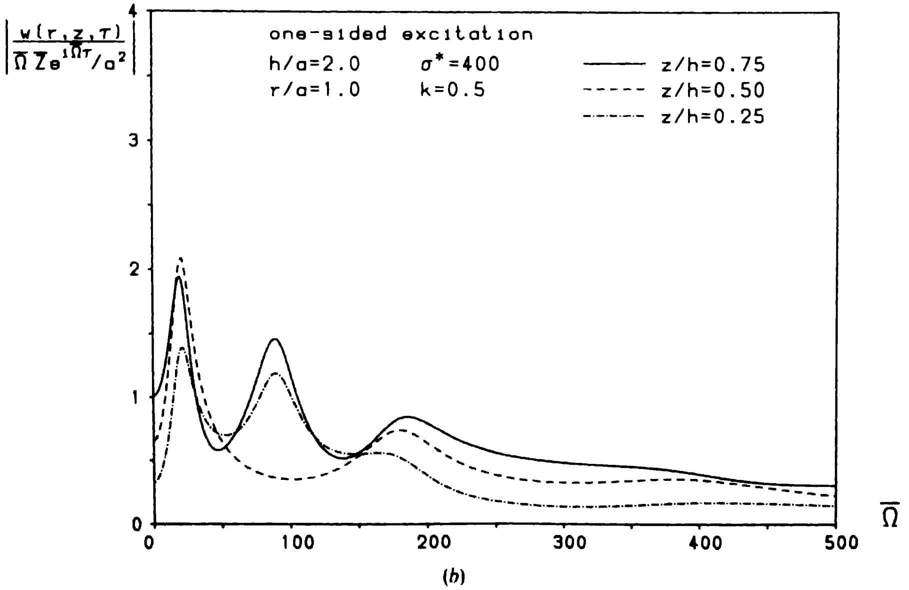
$\left|\frac{w(r,z,\tau)}{\bar{\Omega}\bar{Z}e^{i\bar{\Omega}\tau}/a^2}\right|$
one-sided excitation
h/a=2.0
σ* =400
r/a=1.0
k=0.5
z/h=0.75
z/h=0.50
z/h=0.25
0
1
2
3
4
0
100
200
300
400
500
$\bar{\Omega}$

(b)

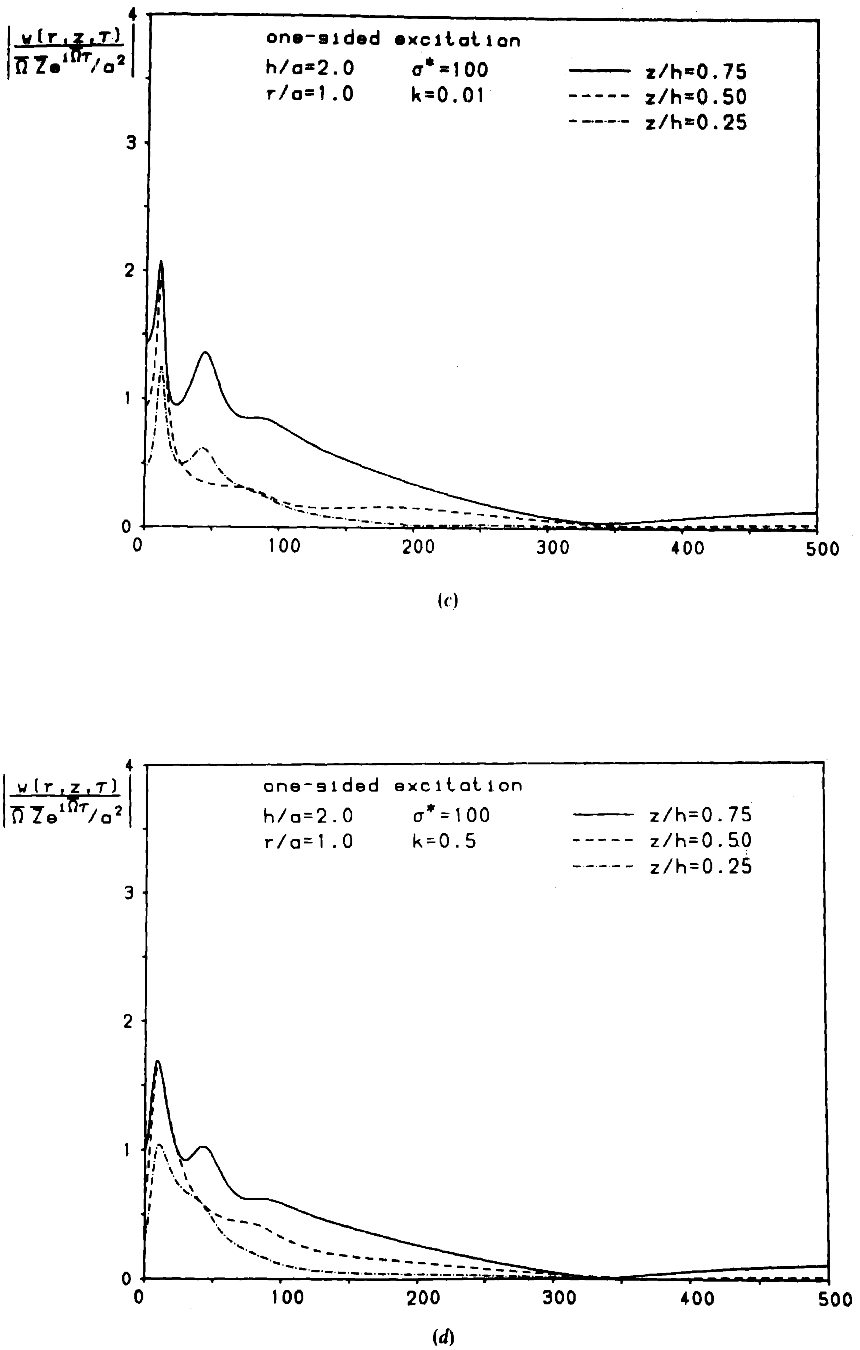

(*c*)

(*d*)

Fig. 5. Response of axial velocity distribution for one-sided excitation.

4.2. *Response due to one-sided excitation*

The response of the radial velocity distribution at the location $r = a$ and $z/h = 0.25$, 0.5 and 0.75 is shown for the same parameters. $\sigma^* = 400$, 100 and $k = 0.01$ and 0.5 in Figs 4*a* to 4*d*. Since all natural frequencies appear, we have to expect more resonance peaks, which are located closer to each other. According to the location z, at which the response has been determined, some resonance peaks may disappear, since a nodal plane may be present at such a location. With the decrease of the thickness of the layer the response becomes smaller, as may be seen in Figs 4*a* and 4*b*. For decreased surface tension parameter $\sigma^* = 100$ the response is further decreased and the resonance peaks become less pronounced (Figs 4*c* and 4*d*).

The trend is similar as in the previous case, where a further decrease of the response magnitude and the resonance peaks may be observed. The response in axial direction shows a velocity distribution as exhibited in Figs 5*a* to 5*d*. The higher the surface tension parameter $\sigma a/\rho\nu^2$ the larger the response and resonance peaks, which decrease also with the decrease of the thickness of the layer (see Figs 5*a* and 5*b*). For $\sigma^* = 100$ the response is shown in Figs 5*c* and 5*d*. The response of the free surface displacement for one-sided excitation may again be obtained from the radial velocity. For more graphical information one may consult [19].

References

1. Rayleigh, Lord, On the Capillary Phenomena of Jets. *Proc. Roy. Soc.* 89 (1879) 71–97.
2. Rayleigh, Lord, On the instability of cylindrical fluid surfaces. *Phil. Mag.* 34 (1892) 177–180.
3. Lamb, H., *Hydrodynamics*. New York: Dover (1045) pp. 471–473.
4. Bauer, H.F., Natural damped frequencies of an infinitely long column of immiscible viscous liquid. *Z. Angw. Math. u. Mech.* 64 (1984) 11, 475–490.
5. Bauer, H.F., Free surface and interface oscillations of an infinitely long visco-elastic liquid column. *Acta Astronautica* 13 (1986) 9–22.
6. Bauer, H.F., Bei Fabrikationsprozessen in zylindrischen Flüssigkeitsbrücken unter Mikrogravitation auftretende Störeffekte. *Ing. Arch.* 55 (1985) 242–257.
7. Meseguer, J., The breaking of axisymmetric slender bridges. *J. Fluid Mech.* 130 (1983) 123–151.
8. Rivas, D. and Mesequer, J., One-dimensional self-similar solution of the dynamics of axisymmetric slenders liquid bridges. *J. Fluid Mech.* 188 (1984) 417–429.
9. Lee, H.C., Drop formation in a liquid jet. *IBM J. Res. Develop.* 18 (1974) 364–369.
10. Bauer, H.F., Vibrational behavior of a viscous column with a free liquid surface. *Z. Flugwiss. Weltraumforsch.* 13 (1989) 248–253.
11. Bauer, H.F., Axial response and transient behavior of a cylindrical liquid column in zero gravity. *Z. Flugwiss. Weltraumforsch.* 14 (1990) 174–182.
12. Bauer, H.F., Response of a liquid column to one-sided axial excitation in zero-gravity. *Forsch. Ing. Wes.* 56 (1990) 14–21.
13. Bauer, H.F., Response of a liquid column to counter-directional excitation under zero-gravity. *J. Spacecraft and Rockets* 27, No. 6 (1990), 675–680.
14. Bauer, H.F., Response of a liquid column to unequal counterdirectional excitation under zero-gravity. *Microgravity Sci. Technol.* III (1990) 1, 34–40.
15. Bauer, H.F., Response of a viscous liquid column to axial excitation in zero-gravity. *ZAMM* 70 (1990) 9, 359–369.

16. Bauer, H.F., Response of a viscous liquid column to pitching and roll excitation. *ZAMM* 71, (1991) 12, 479–491.
17. Bauer, H.F., Response of differently axially excited viscous liquid bridges in zero-gravity. Forschungsbericht der Universität der Bundeswehr München. LRT-WE-9-FB-14 (1989).
18. Bauer, H.F., Vibrational behavior of a viscous cylindrical liquid layer with a free liquid surface. Forschungsbericht der Universität der Bundeswehr München. LRT-WE-9-FB-4 (1990).
19. Bauer, H.F., Response of an annular cylindrical liquid column to various axial excitations in zero-gravity. *Forsch. Ing. Wes.* 56(6) (1990) 183–188.
20. Bauer, H.F., Response of a differently axially excited viscous liquid layer in zero-gravity. Forschungsbericht der Universität der Bundeswehr München. LRT-WE-9-FB-12 (1990).

Applied Scientific Research **49**: 307–334, 1992.
© 1992 *Kluwer Academic Publishers. Printed in the Netherlands.*

On the stability of multi-layered fluids. Part I: analysis

H. KNOESTER[1] & J. VAN DER ZANDEN*

*Delft University of Technology, Department of Mechanical Engineering and Marine Technology, Research Group for Fluid Dynamics, Rotterdamseweg 145, 2628 AL Delft, The Netherlands (*author for correspondence); [1]present address: AKZO Research Laboratory, Arnhem, The Netherlands*

Received 29 September 1989; accepted in revised form 4 November 1990

Key words: stability, linear-stability analysis, multi-layered flow, Orr-Sommerfeld equations, interfacial conditions, generalized eigenvalue problem, air-water flow

Abstract. The linear stability of the Poiseuille flow of multi-layered different fluids, described mathematically by a system of Orr-Somerfeld differential equations, is investigated. A spectral method is used to rewrite this system into a generalized eigenvalue problem, which can be solved with the *QZ*-algorithm. Special attention is paid to the tractibility of the interfacial conditions of the stability problem. Since we will limit ourselves to a linear stability analysis, the analytical treatment of the interfacial conditions is simplified. Some results related to simple flow configurations are presented. The origin of certain regions of interfacial instability is explained by simple analytical reasoning.

1. Introduction

Instability of a laminar single-phase (quasi-) parallel flow, without inflexion points in its velocity profile, generally results in turbulence, which is termed Tollmien-Schlichting instability. In order to investigate the stability it is sufficient to consider only two dimensionless groups: the dimensionless wave number of the velocity disturbance and the Reynolds number.

In the case of a multi-layered flow, instability is determined by a variety of independent dimensionless quantities. Moreover, instability of a multi-layered flow will not necessarily produce turbulence. At the interface(s) discontinuities in density and viscosity can often be considered as the main source of 'interfacial instability'. Instead of initiating turbulence, this kind of instability will generate finite amplitude disturbances of the interface, or will even lead to the breaking off of pieces of the film.

Experimental studies of multi-layered flow configurations (see Charles & Lilleleht (1965) [2]) show the possibility of complete changes of the flow pattern due to interfacial instability. In the case of a pressure-driven gas flow in the core of a channel or a pipe bounded by a thin layer of liquid along the wall, the liquid can–under certain circumstances–form large-sized slugs of a width comparable to that of the channel/pipe (see Taitel & Dukler (1976) [21]). In order to maintain the gas transport, the pressure drop must be increased drastically.

As far as the transport of a liquid through a pipe is concerned, Koman (1977) [11] points out that the drag can be reduced significantly by the presence of a –stable– thin gas layer along the wall. These observations evidently have large implications for transport phenomena, which emphasizes the desirability of an extensive investigation of the stability of multi-layered flow configurations.

The available literature on the stability of multi-phase flow systems is rapidly growing. Hickox (1971) [6] analyzed the stability of two-layer pipe flows. He found that none of the configurations examined was stable for both non-symmetric and axis-symmetrical velocity disturbances. More recently Hooper and Boyd (1983) [7] demonstrated the pure influence of the presence of an interface by considering flow configurations without fixed walls. Their study proves the significance of the configuration of a flow with respect to its stability. The removal of the walls, by assuming infinitely extending fluids, alters the stability of the flow considerably.

Yih (1967) [26] explored the influence of a discontinuous viscosity at the interface of a two-layer Couette and Poiseuille flow. He found that both kinds of flow can be unstable, no matter how small the value of the Reynolds number is. Than, Rosso & Joseph (1987) [23] have also confined their attention to the destabilizing effects of the discontinuity of viscosity. They investigated three-layer flow configurations and defined lubricating flows and fingering flows, where the more viscous fluid is encapsulated by the less viscous fluid and the reverse. They found that fingering flows are unstable, and that lubicating flows are stable for long-wave perturbations. Their conclusion agrees well with the experimentally observed phenomenon that in a two-layer flow the less viscous fluid tends to encapsulate the more viscous one.

In the above-mentioned papers the attention is confined to extremely low or extremely high values of the frequency of the velocity disturbances. The stability analysis of these extreme situations is simplified by the use of asymptotic techniques.

In this paper a pseudo-spectral method has been used to solve the linear stability problem for the complete wavelength spectrum. This method uses Chebychev expansions; they are suited for ordinary differential equations with variable coefficients, and are numerically very stable. We have been inspired by Koman's (1977) [11] approach (see also Koman and Chesters (1981) [12]), who investigated the stability of two-layer horizontal water-air flow configurations with a pseudo-spectral method and solved the resulting eigenvalue problem with a singular-decomposition method.

The stability of core-annular pipe flow of two immiscible liquids has extensively been investigated by Joseph, Renardy & Renardy (1984) [9] by a Galerkin approach to the pseudo-spectral method, extended by Preziosi, Chen & Joseph (1989) [19] to other situations and with a collocation approach to the pseudo-spectral method, by Hu & Joseph (1989) [8] with a finite element approximation to the pseudo-spectral approximation, and by Chen, Bai & Joseph (1900) [3] the same method as Preziosi et al is used, but now gravity is included (vertical pipes) and some experimental observations are presented.

In this paper we have chosen Koman's analysis as a starting point. The two-layer model has been extended to three layers, where the layer thickness of all three layers can be chosen arbitrarily. We also introduced the effect of the direction of the gravity force by considering the flow in a channel on an inclined plane. The numerical method has been modified. Linear stability analysis leads to a system of equations which has the structure of a generalized eigenvalue problem $Ax = \lambda Bx$, where B is a singular matrix and A an ill-conditioned matrix. The problem cannot simply be reduced to an ordinary eigenvalue problem by inversion of any of the matrices. The system can be treated more adequately by the QZ algorithm (see Moler & Stewart (1973) [15]) than by the method of singular value decomposition that Koman used. The QZ algorithm is analogous to the well-known QR algorithm for ordinary eigenvalue problems. However, before applying the QZ algorithm, we integrated the Orr-Sommerfeld equations for the amplitude of the Fourier modes as many times as the order of differentiation of the equations, which gives a better condition of the matrices of the eigenvalue problem. In fact, whereas accuracy requirements are maintained, the integration enables us to reduce the number of polynomials in the Chebychev expansions. Finally, we present a more detailed treatment of the interfacial conditions.

Results are presented and compared with data from the literature in section 4 of this paper. Furthermore, experiments have been performed to verify our computations of the flow on an inclined plane. The experiments confirm our results and will be published in forthcoming paper [16].

2. The mathematical formulation of the problem

In this section the basic equations, namely the Orr-Sommerfeld equations, and the boundary conditions are formulated.

2.1. The geometry of the flow problem

We examine the stationary laminar flow of two Newtonian fluids between parallel walls as drawn in Fig. 1. Fluid 1 is bounded by two thin layers of fluid 2. The three-layer flow is supposed to be fully developed. The flow direction coincides with the x-direction. The meaning of the parameters in Fig. 1 is:

ϑ	angle between channel and horizontal plane	
ρ_q	density of fluid in qth layer	$q = 1, 2, 3.$
μ_q	dynamic viscosity of the fluid of the qth layer	
l_q	dimensionless thickness of the qth layer	

Note that $\rho_2 = \rho_3$ and $\mu_2 = \mu_3$. The thicknesses have been made dimensionless with the help of half the width of the central part of the channel.

2.2. The Orr-Sommerfeld differential equations

According to the classical approach in hydrodynamic stability, infinitesimal time-dependent and space-dependent perturbations in velocity and pressure are imposed

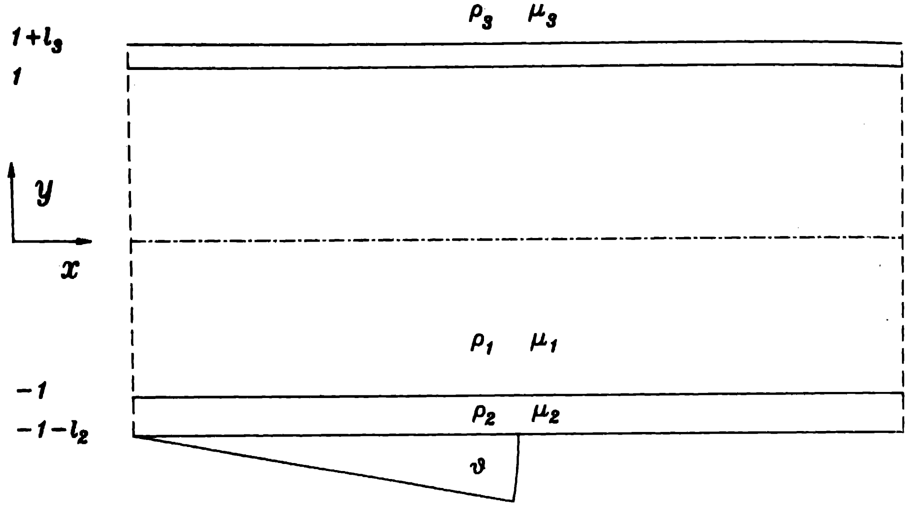

Fig. 1. Geometry of the flow.

on the unperturbed flow. The development of these perturbations in time characterizes the stability of the flow. Suppose $\boldsymbol{U}_q = (U_q(y)\ 0\ 0)^T$ and $P_q(x, y)$ represent the velocity and pressure in the qth layer of the unperturbed flow. The perturbations are denoted by $\boldsymbol{u}_q(x, y, z, t)$ and $p_q(x, y, z, t)$. The perturbed velocity and pressure are now:

$$\begin{cases} \tilde{\boldsymbol{u}}_q = (U_q(y) + u_q(\boldsymbol{x}, t)\ \ v_q(\boldsymbol{x}, t)\ \ w_q(\boldsymbol{x}, t))^T \\ \tilde{p}_q = P_q(x, y) + p_q(\boldsymbol{x}, t),\ \boldsymbol{x} = (x\ y\ z)^T,\ q = 1, 2, 3. \end{cases} \tag{1}$$

Both the unperturbed and the perturbed flow are governed by the Navier-Stokes equations and the incompressibility constraint. The flow is supposed to be isothermal and of constant viscosity. The equations for the perturbed flow are linearized: products of $\boldsymbol{u}_q$ are neglected. Furthermore the equations for the perturbed flow are simplified by the substraction of the corresponding equations for the unperturbed flow. The equations are made dimensionless with a characteristic length scale, velocity scale and density, defined by

$$U = U_1(y = 0),\ L = h/2,\ \rho = \rho_2, \tag{2}$$

where h is the thickness of the layer with fluid 1. In dimensionless form, the resulting equations for the unperturbed case (fully-developed flow) are:

$$\left.\begin{cases} 0 = -\dfrac{\rho_2}{\rho_q}\dfrac{\partial P_q}{\partial x} + R_q^{-1}\dfrac{\mathrm{d}^2 U_q}{\mathrm{d}y^2} - F_R^{-1}\sin\vartheta \\ 0 = -\dfrac{\rho_2}{\rho_q}\dfrac{\partial P_q}{\partial y} - F_R^{-1}\cos\vartheta \end{cases}\right\} q = 1, 2, 3 \tag{3}$$

and for the perturbed case:

$$\begin{cases} \dfrac{\partial u_q}{\partial t} + U_q \dfrac{\partial u_q}{\partial x} + v_q \dfrac{\mathrm{d}U_q}{\mathrm{d}y} = -\dfrac{\rho_2}{\rho_q}\dfrac{\partial p_q}{\partial x} + R_q^{-1}\Delta u_q, \\ \dfrac{\partial v_q}{\partial t} + U_q \dfrac{\partial v_q}{\partial x} = -\dfrac{\rho_2}{\rho_q}\dfrac{\partial p_q}{\partial y} + R_q^{-1}\Delta v_q, \\ \dfrac{\partial w_q}{\partial t} + U_q \dfrac{\partial w_q}{\partial x} = -\dfrac{\rho_2}{\rho_q}\dfrac{\partial p_q}{\partial z} + R_q^{-1}\Delta w_q, \\ \dfrac{\partial u_q}{\partial x} + \dfrac{\partial v_q}{\partial y} + \dfrac{\partial w_q}{\partial z} = 0, \end{cases} \tag{4}$$

with definitions of the Reynolds number of the qth layer and Froude number:

$$R_q = \frac{\rho_q U L}{\mu_q},\ q = 1, 2, 3;\ F_R = \frac{U^2}{gL},$$

where g is the acceleration due to gravity. In stability analysis it is customary (see e.g. Lin (1955) [14]) to specify a particular shape for the infinitesimal perturbations in terms of components of Fourier series:

$$\begin{cases} \mathbf{u}_q = (\hat{u}_q(y)\ \hat{v}_q(y)\ \hat{w}_q(y))^T \mathrm{e}^{j(\beta x + \zeta z - \omega t)}, \\ p_q = \hat{p}_q(y)\mathrm{e}^{j(\beta x + \zeta z - \omega t)}, \end{cases} \tag{5}$$

with positive wave numbers β, ζ in the direction of x and z respectively. The following definitions have been used:

$\omega = \beta\lambda$, $\lambda = \lambda_R + j\lambda_I$, $j^2 = -1$,

$\alpha = (\beta^2 + \zeta^2)^{1/2}$ wavenumber in the propagation direction of the disturbances.

According to Fourier analysis, an arbitrary perturbation can be written as a superposition of the perturbations in equation (5) for various values of β and ζ. The equations are substituted in equation (4). Elimination of $\hat{u}_q$, $\hat{w}_q$, $\hat{p}_q$, $q = 1, 2, 3$ results in an Orr-Sommerfeld equation:

$$\{-(D^2 - \alpha^2)^2 + j\beta R_q[(U_q - \lambda)(D^2 - \alpha^2) - D^2 U_q]\}\hat{v}_q = 0,\ D = \frac{\mathrm{d}}{\mathrm{d}y} \tag{6}$$

for each layer.

2.3. The boundary conditions

The construction of a proper set of boundary conditions for the Orr-Sommerfeld equations (6) will complete the mathematical description of the stability problem. Along the walls we impose the well known 'no-slip' conditions:

$$\left\{\begin{array}{lll} \text{position of the wall} & \text{unperturbed} & \text{perturbed} \\ y = -1 - l_2: & U_2 = 0, & u_2 = v_2 = w_2 = 0, \\ y = 1 + l_3: & U_3 = 0, & u_3 = v_3 = w_3 = 0. \end{array}\right. \tag{7}$$

As a result of the velocity and pressure perturbations, the positions of the interfaces are perturbed too. This complicates the mathematical description of the conditions at the interface considerably. Suppose that the position of the interfaces can be written as (see Fig. 2)

$$y = \eta_2(x, z, t) - 1, \; y = \eta_3(x, z, t) + 1 \tag{8}$$

for the lower and upper interface respectively. For obvious reasons the perturbations η_2, η_3 may be considered as infinitesimally small. We will confine our analysis to the lower interface. Along the interface we impose three kinds of boundary conditions: (1) the kinematic boundary condition, (2) the continuity of velocity, (3) the continuity of stress.

2.3.1. Kinematic boundary condition

The kinematic boundary condition prohibits transport of mass through the interface, which ensures that the fluids remain separated. In practical applications this condition

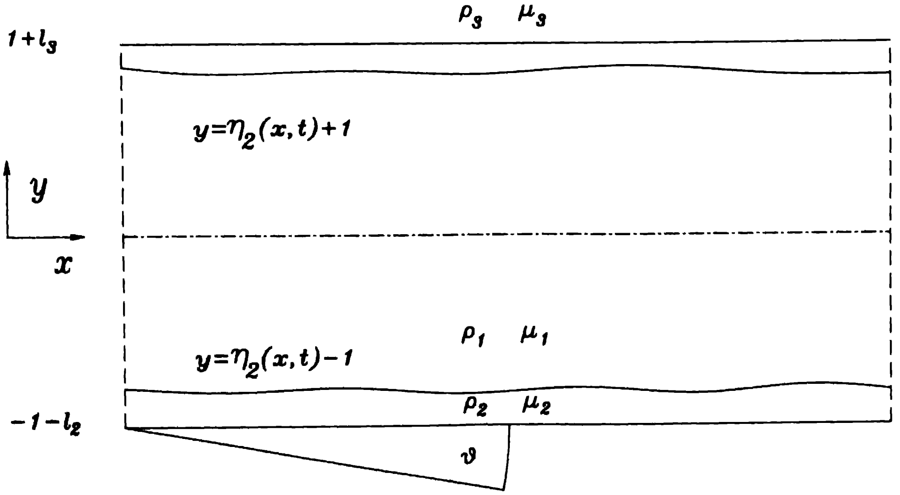

Fig. 2. Perturbed interfaces.

is correct for immiscible fluids. We demand that the velocity of a fluid particle at the interface Q is equal to the time derivative of the position of the interface at Q. Thus all fluid particles at the interface will remain at the interface.

Consider an arbitrary fluid particle at the interface with position vector $\boldsymbol{x}$ and velocity vector $\boldsymbol{v}$:

$$\boldsymbol{x} = (x \quad \eta_2(x,z,t) - 1 \quad z)^T, \ \tilde{\boldsymbol{u}} = \mathrm{d}\boldsymbol{x}/\mathrm{d}t = (\tilde{u}_1 \ \tilde{u}_2 \ \tilde{u}_3)^T \sim (U_1 + u_1 v_1 w_1)^T$$

We need to impose for the velocity in y-direction:

$$\begin{aligned} v_1 &= \frac{\mathrm{d}\eta_2}{\mathrm{d}t} = \frac{\partial\eta_2}{\partial x}\frac{\mathrm{d}x}{\mathrm{d}t} + \frac{\partial\eta_2}{\partial z}\frac{\mathrm{d}z}{\mathrm{d}t} + \frac{\partial\eta_2}{\partial t} \\ &= (U_1 + u_1)\frac{\partial\eta_2}{\partial x} + w_1\frac{\partial\eta_2}{\partial z} + \frac{\partial\eta_2}{\partial t}, \quad y = \eta_2 - 1. \end{aligned} \tag{9}$$

We expand equation (9) in a Taylor series around $y = -1$ and neglect all nonlinear terms. This leads to:

$$v_1 = U_1\frac{\partial\eta_2}{\partial x} + \frac{\partial\eta_2}{\partial t}, \ y = -1. \tag{10}$$

2.3.2. *Continuity of velocity*

Passing through an interface the velocity must remain continuous:

$$\begin{cases} \text{unperturbed, } y = -1; & \text{perturbed, } y = \eta_2 - 1, \\ U_1 = U_2 & U_1 + u_1 = U_2 + u_2, \\ & v_1 = v_2, \\ & w_1 = w_2, \end{cases} \tag{11}$$

and similar expressions for the other interface. Again we expand the expressions of equation (11) in a Taylor series around $y = -1$ and neglect all terms that are quadratic in the perturbations. Furthermore the first equation of equation (11) will be simplified by subtracting from it the first equation of its unperturbed counterpart. This results in:

$$\left\{\left.\begin{aligned} \eta_2\frac{\mathrm{d}U_1}{\mathrm{d}y} + u_1 &= \eta_2\frac{\mathrm{d}U_2}{\mathrm{d}y} + u_2 \\ v_1 &= v_2 \\ w_1 &= w_2 \end{aligned}\right\}\right. \quad y = -1. \tag{12}$$

2.3.3. *Continuity of stress*

At the location of an arbitrary particle I at the interface two vectors $\boldsymbol{c}_1$ and $\boldsymbol{c}_2$ of unit length tangent to the interface are constructed. Suppose that $\boldsymbol{c}_3$ is the unit vector, normal to the interface, pointing in the direction of the upper fluid:

$$\begin{cases} \boldsymbol{c}_1 = \left(1+\left(\dfrac{\partial\eta_2}{\partial x}\right)^2\right)^{-1/2}\left(1\ \dfrac{\partial\eta_2}{\partial x}\ 0\right)^T, \\ \boldsymbol{c}_2 = \left(1+\left(\dfrac{\partial\eta_2}{\partial z}\right)^2\right)^{-1/2}\left(0\ \dfrac{\partial\eta_2}{\partial z}\ 1\right)^T, \\ \boldsymbol{c}_3 = \left(1+\left(\dfrac{\partial\eta_2}{\partial x}\right)^2+\left(\dfrac{\partial\eta_2}{\partial z}\right)^2\right)^{-1/2}\left(-\dfrac{\partial\eta_2}{\partial x}\ 1\ -\dfrac{\partial\eta_2}{\partial z}\right)^T. \end{cases} \tag{13}$$

The surface forces at the fluid particle I are in equilibrium. This balance leads to three dimensionless conditions, provided $\boldsymbol{c}_1$ and $\boldsymbol{c}_2$ are the unit vectors along the principal axes of curvature (see e.g. Batchelor (1967) [1]):

$$\boldsymbol{c}_i\cdot\boldsymbol{\sigma}^{(1)}\cdot\boldsymbol{c}_3-\boldsymbol{c}_i\cdot\boldsymbol{\sigma}^{(2)}\cdot\boldsymbol{c}_3 = \mathrm{We}^{-1}(Ra_1^{-1}+Ra_2^{-1})\boldsymbol{c}_i\cdot\boldsymbol{c}_3,\ i=1,2,3 \tag{14}$$

with

$$\boldsymbol{\sigma}^{(q)} = -\tilde{p}_q\boldsymbol{1}+\frac{\rho_q}{\rho_2}R_q^{-1}(\nabla\tilde{\boldsymbol{u}}_q+(\nabla\tilde{\boldsymbol{u}}_q)^T),\ \nabla\boldsymbol{u}=\frac{\partial u_j}{\partial x_i},\ q=1,2;$$

$$Ra_1^{-1}=\frac{\partial^2\eta_2}{\partial x^2}\left(1+\left(\frac{\partial\eta_2}{\partial x}\right)^2\right)^{-3/2},\ Ra_2^{-1}=\frac{\partial^2\eta_2}{\partial z^2}\left(1+\left(\frac{\partial\eta_2}{\partial z}\right)^2\right)^{-3/2},$$

$$\mathrm{We}=\frac{\rho_2U^2L}{\gamma},\ \gamma = \text{surface tension coefficient.}$$

In the equations above the stress tensor $\boldsymbol{\sigma}$ for a Newtonian fluid, the radii of curvature Ra_1 and Ra_2, and the Weber number We have been defined. Equation (14) expresses balance of tangential forces for $i = 1,2$ and balance of force in normal direction for $i = 3$. For these balances a Taylor series expansion for small departure of the interfacial surface is written down, neglecting quadratic perturbations. The resulting equations are simplified by the substitution of the boundary conditions for the unperturbed case:

$$\mu_1\frac{\mathrm{d}U_1}{\mathrm{d}y}=\mu_2\frac{\mathrm{d}U_2}{\mathrm{d}y};\ P_1=P_2;\ y=-1 \tag{15}$$

so the result for the perturbed case is:

$$\begin{cases} \mu_1\left(\dfrac{\partial u_1}{\partial y}+\eta_2\dfrac{\mathrm{d}^2U_1}{\mathrm{d}y^2}+\dfrac{\partial v_1}{\partial x}\right)=\mu_2\left(\dfrac{\partial u_2}{\partial y}+\eta_2\dfrac{\mathrm{d}^2U_2}{\mathrm{d}y^2}+\dfrac{\partial v_2}{\partial x}\right), \\ \mu_1\left(\dfrac{\partial v_1}{\partial z}+\dfrac{\partial w_1}{\partial y}\right)=\mu_2\left(\dfrac{\partial v_2}{\partial z}+\dfrac{\partial w_2}{\partial y}\right), \\ \rho_2(p_2-p_1)+2R_1^{-1}\rho_1\dfrac{\partial v_1}{\partial y}-2R_2^{-1}\rho_2\dfrac{\partial v_2}{\partial y} \\ =-\rho_2\mathrm{We}^{-1}\left(\dfrac{\partial^2\eta_2}{\partial x^2}+\dfrac{\partial^2\eta_2}{\partial z^2}\right)+\dfrac{\rho_2-\rho_1}{Fr}\eta_2\cos\vartheta. \end{cases} \tag{16}$$

Apart from the perturbations in velocity and pressure, the boundary conditions also contain the perturbations of the positions of the interfaces. Analogous to equation (5), we write for the perturbation η_2 and η_3

$$\eta_q=\hat{\eta}_q e^{j(\beta x+\zeta z-\omega t)},\ q=2,3. \tag{17}$$

We substitute equations (5) and (17) in the boundary conditions for the perturbed flow (7), (10), (12), and (16). An elimination process similar to that of section (2.2) leads to 14 boundary conditions at the solid walls and the interfaces, obtained by substituting the pairs of values ($y_0=-1$, $q=2$) and ($y_0=1$, $q=3$) into the next seven equations:

$$\begin{cases} y=y_0-(-1)^q l_q\colon \hat{v}_q=0\quad D\hat{v}_q=0, \\ y=y_0\colon \hat{v}_1=j\beta\hat{\eta}_q(U_1-\lambda), \\ \hat{v}_1-\hat{v}_q=0, \\ D(\hat{v}_1-\hat{v}_q)=j\beta\hat{\eta}_q(DU_1-DU_q), \\ (D^2+\alpha^2)(\mu_1\hat{v}_1-\mu_q\hat{v}_q)=j\beta\hat{\eta}_q(\mu_1D^2U_1-\mu_qD^2U_q),\ (*) \\ (-D^3+3\alpha^2D)(\mu_1\hat{v}_1-\mu_q\hat{v}_q)+j\beta\{\mu_1R_1((U_1-\lambda)D \\ \qquad -DU_1)\hat{v}_1-\mu_qR_q((U_q-\lambda)D-DU_q)\hat{v}_q\} \\ =\mu_qR_q\alpha^2((-1)^q\alpha^2\mathrm{We}^{-1}+\dfrac{\rho_2-\rho_1}{\rho_2}Fr^{-1}\cos\vartheta)\hat{\eta}_q. \end{cases} \tag{18}$$

These boundary conditions are in agreement with the analysis of Koman, except for the righthand side of (*) of the set, which vanishes identically for horizontal flows and/or for flows with zero density differences ($\rho_2=\rho_1$). Koman investigated the stability of a two-layer horizontal flow.

It should be noted that the mathematical problem, composed of the Orr-Sommerfeld differential equations (see section 2.1) and the above 14 boundary conditions, has the structure of an eigenvalue problem with eigenvalues λ.

3. The generalized eigenvalue problem

In this section the resulting eigenvalue problem and its solution will be discussed in some detail.

3.1. *The application of a spectral method*

Several methods have been developed for solving Orr-Sommerfeld differential equations. Generally we can distinguish between numerical integration methods and matrix methods. Using an integration method, the Orr-Sommerfeld differential equation and the boundary conditions are reformulated into four coupled first order equations with boundary conditions. During integration of this coupled system special techniques are necessary to control the parasytic errors (see Garg (1980) [5]). Besides, integration methods are generally not applicable to a system of two or more differential equations.

Matrix methods are used to rewrite the Orr-Sommerfeld system into an algebraic problem. Koman successfully solved a coupled system of Orr-Sommerfeld differential equations with the help of a spectral method based on Chebychev expansions (see Orszag (1971) [18]). In this paper we present an improvement on the method of Koman, which we will show to be superior to his in section 3.2.

We start with examining the differential equations (6). The eigenfunctions $\hat{v}_q(y)$ will be approximated by finite Chebychev expansions:

$$\hat{v}_q(y) = \sum_{n=0}^{N_q}{}' a_{qn} T_{qn}(y), \quad q = 1, 2, 3 \tag{19}$$

with $T_{qn}(y)$ defined as the nth order Chebychev polynomial on the qth interval and $\Sigma_{i=0}^{N}{}' f_i = f_0/2 + f_1 + f_2 + \cdots + f_N$. In contrast to Koman's procedure, where equation (19) is substituted directly, we first integrate equation (6) four times before substitution is performed. Furthermore, the velocities U_q of the unperturbed equations are written as quadratic expressions

$$U_q = A_q y^2 + B_q y + C_q. \tag{20}$$

We then get

$$\left\{\begin{aligned} \sum_{n=0}^{N_q+6}{}' \gamma_{qn} T_{qn} = {} & \sum_{n=0}^{N_q+6}{}' \big(-a_{qn} + 2\alpha^2 a_{qn}^{(2,0)} - \alpha^4 a_{qn}^{(4,0)} \\ & + j\beta R_q [A_q (a_{qn}^{(2,2)} - 4a_{qn}^{(3,1)} - \alpha^2 a_{qn}^{(4,2)}) \\ & + B_q (a_{qn}^{(2,1)} - 2a_{qn}^{(3,0)} - \alpha^2 a_{qn}^{(4,1)}) \\ & + (C_q - \lambda)(a_{qn}^{(2,0)} - \alpha^2 a_{qn}^{(4,0)})] \big) T_{qn} \\ = {} & \sum_{m=0}^{3}{}' c_{qm} T_{qm} \quad q = 1, 2, 3, \end{aligned}\right. \tag{21}$$

with unknown integration constants c_{qm}. Furthermore

$$a_{qN_q+1} = a_{qN_q+1} = \cdots = 0, \; q = 1, 2, 3$$

and the coefficients $a_{qn}^{(d,e)}$ are defined by

$$\sum_{n=0}^{N_q+6}{}' a_{qn}^{(d,e)} T_{qn} = \int_{(d)} y^e \hat{v}_q (\mathrm{d}y)^d.$$

In the appendix it will be shown that the $a_{qn}^{(d,e)}$ are simple linear functions of the original unknowns

$$\left\{\begin{aligned} a_{qn}^{(d,e)} &= f(a_{qz_1}, a_{qz_1+1}, \ldots, a_{qz_2}), \\ z_1 &= \max\{0, n-d-e\}, \\ z_2 &= \min\{N_q, n+d+e\}, \; d, e \in \mathbb{N}. \end{aligned}\right. \tag{22}$$

Since the Chebychev polynomials are linearly independent, we can extract $(N_1 + N_2 + N_3 + 9)$ linear equations from (21)

$$\begin{aligned} &\gamma_{qn} = 0, \\ &n = 4, 5, \ldots, N_q + 6, \\ &q = 1, 2, 3. \end{aligned} \tag{23}$$

Next we turn to the boundary conditions. First a useful theorem which has been proved by Koman is presented.

Suppose that $v(y) = \Sigma_{n=0}^{N}{}' a_n T_n$ with T_n the nth order Chebychev polynomial on $[a, b]$. Then

$$\left\{\begin{aligned} v(a) &= \sum_{n=0}^{N}{}'(-1)^n a_n, \; v(b) = \sum_{n=0}^{N}{}' a_n, \\ D^M v(a) &= (2V)^{-M} \sum_{n=0}^{N}{}' \prod_{q=0}^{M-1} \left(\frac{n^2 - q^2}{2q+1}\right)(-1)^{n-M} a_n, \\ D^M v(b) &= (2V)^{-M} \sum_{n=0}^{N}{}' \prod_{q=0}^{M-1} \left(\frac{n^2 - q^2}{2q+1}\right) a_n. \end{aligned}\right\} \begin{aligned} &M \geqslant 1 \\ &V = \tfrac{1}{4}(b-a) \end{aligned} \tag{24}$$

We substitute (19) in the set of boundary conditions (18) and the application of the above theorem then leads to 14 linear equations. To visualize these boundary conditions we have to substitute the pairs of values $(y_0 = -1, \; q = 2)$ and

($y_0 = 1, q = 3$) into the next seven equations

$$\left\{\begin{aligned}
&y=y_0-(-1)^q l_q\colon \sideset{}{'}\sum_{n=0}^{N_q}(-1)^{(3-q)n}a_{qn}=0,\ \sideset{}{'}\sum_{n=0}^{N_q}(-1)^{(3-q)(n-1)}n^2a_{qn}=0,\\
&y=y_0\colon \sideset{}{'}\sum_{n=0}^{N_1}(-1)^{(3-q)n}a_{1n}=j\beta\hat{\eta}_q(U_1-\lambda),\\
&\sideset{}{'}\sum_{n=0}^{N_1}(-1)^{(3-q)n}a_{1n}=\sideset{}{'}\sum_{n=0}^{N_q}(-1)^{(q-2)n}a_{qn},\\
&\sideset{}{'}\sum_{n=0}^{N_1}(-1)^{(3-q)(n-1)}a_{1n}=2l_q^{-1}\sideset{}{'}\sum_{n=0}^{N_q}(-1)^{(q-2)(n-1)}n^2a_{qn}+j\beta\hat{\eta}_q(DU_1-DU_q),\\
&\mu_1\sideset{}{'}\sum_{n=0}^{N_1}(-1)^{(3-q)n}\left\{\alpha^2+\frac{1}{3}n^2(n^2-1)\right\}a_{1n}\\
&=\mu_q\sideset{}{'}\sum_{n=0}^{N_q}(-1)^{(q-2)n}\left\{\alpha^2+\frac{4}{3}n^2(n^2-1)l_q^{-2}\right\}a_{qn}+j\beta\hat{\eta}_q(\mu_1D^2U_1-\mu_qD^2U_q),\\
&\mu_1\sideset{}{'}\sum_{n=0}^{N_1}(-1)^{(3-q)(n-1)}\left\{3\alpha^2n^2-\frac{1}{15}n^2(n^2-1)(n^2-4)\right\}a_{1n}\\
&\quad-\mu_q\sideset{}{'}\sum_{n=0}^{N_q}(-1)^{(q-2)(n-1)}\left\{6\alpha^2n^2l_q^{-1}-\frac{8}{15}n^2(n^2-1)(n^2-4)l_q^{-3}\right\}a_{qn}\\
&\quad+j\beta\mu_1R_1(U_1-\lambda)\sideset{}{'}\sum_{n=0}^{N_1}(-1)^{(3-q)(n-1)}n^2a_{1n}\\
&\quad-2j\beta\mu_qR_q(U_q-\lambda)l_q^{-1}\sideset{}{'}\sum_{n=0}^{N_q}(-1)^{(q-2)(n-1)}n^2a_{qn}\\
&\quad-j\beta\mu_1R_1DU_1\sideset{}{'}\sum_{n=0}^{N_1}(-1)^{(3-q)n}a_{1n}+j\beta\mu_qR_qDU_q\sideset{}{'}\sum_{n=0}^{N_q}(-1)^{(q-2)n}a_{qn}\\
&=\mu_qR_q\alpha^2\left\{(-1)^q\alpha^2\,\mathrm{We}^{-1}+\frac{\rho_2-\rho_1}{\rho_2}Fr^{-1}\cos\vartheta\right\}\hat{\eta}^q.
\end{aligned}\right. \tag{25}$$

Thus we have managed to transform the original boundary value problem of the previous section in $\Sigma_{q=1}^{3}(N_q+3)+14$ linear equations for the $\Sigma_{q=1}^{3}(N_q+1)+2$ unknowns a_{qn}, $n=0,1,\ldots,N_q$; $q=1,2,3$, $\hat{\eta}_2$, and $\hat{\eta}_3$. This confronts us with a surplus of 18 equations. After a closer analysis of spectral methods, it turns out to be a normal phenomenon that the number of unknowns is exceeded by the number of the equations. However, this difficulty can be solved quite easily with Lanczos' tau method (1956) [13].

We approximate the 18 equations in (25) by introducing 18 unknown tau variables

$$\left\{\begin{aligned}
&a)\ \gamma_{qn}=0\quad n=4,5,\ldots,N_q,\\
&b)\ \gamma_{qn}=\tau_{qn}\quad n=N_q+1,\ldots,N_q+6,\quad q=1,2,3.
\end{aligned}\right. \tag{26}$$

We construct now a system of linear equations which consists of (25) and (26a). This system can be written as a generalized eigenvalue problem

$$(A + \lambda B)\boldsymbol{x} = \mathbf{0}, \tag{27}$$

where $\boldsymbol{x}$ is the solution vector with components $a_{qn}, \hat{\eta}_2, \hat{\eta}_3$ and A, B are $(\Sigma_{q=1}^{3}(N_q + 1) + 2)^2$ matrices.

3.2. A justification for the choice of the spectral method

In the previous section the Orr-Sommerfeld equations were integrated four times before the spectral method was applied. Some justification of this procedure is needed. In this section we will discuss two methods to solve a differential equation by approximating its solution by a finite series of Chebychev polynomials. In method 1 the approximation is substituted directly in the differential equation. In method 2 the differential equation is first integrated a sufficient number of times before the substitution is performed.

Both methods transform a differential equation into a system of linear equations. Both systems cannot but be equivalent. We will distinguish between three kinds of sets of linear equations, indicated by 'injured', 'perturbed', and 'exact'.

In our problem (previous section) it has already been shown that the number of unknowns is outnumbered by the number of linear equations. This is a general feature of these solution techniques. The surplus of equations in both systems is 'injured' and should be ignored, which actually happens if Lanczos' tau-method is applied. The 'injured' equations are not representative of the original differential equations, since some terms are just differentiated away (method 1) or they are not integrated far enough (method 2).

After the application of Lanczos' tau-method all 'injured' equations are ruled out, and both systems are not equivalent any more (in general). We will now show that system 2 (derived by method 2) is superior to system 1 (derived by method 1).

All remaining equations of system 1 are 'perturbed'. This qualification will be given to all those equations which have to be extended if an arbitrary number of Chebychev polynomials is added to the approximation of the solution. If the nth order Chebychev polynomial T_n is differentiated, the result will be a sum of several Chebychev polynomials:

$$\frac{\mathrm{d}T_n}{\mathrm{d}y} = T_n'(y) = \begin{cases} \displaystyle\sum_{p=2}^{n-1}{}^{(2)} a_p T_p + a_0 T_0 \ (n = \text{odd}), \\ \displaystyle\sum_{p=1}^{n-1}{}^{(2)} a_p T_p + a_0 T_0 \ (n = \text{even}). \end{cases}$$

So the addition of two more Chebychev polynomials would have serious consequences for all the equations of the previous set. These would have to be enlarged by one or more of the new unknowns multiplied by rather large coefficients. In other words, all equations of system 1 are approximations of the (infinite) set of equations which would have been generated if the solution had been approximated by infinitely many Chebychev polynomials.

In system 2 the major part of the linear equations is 'exact'. These equations remain unchanged, no matter how many polynomials are added to the original approximation of the solution. They are exact copies of the corresponding equations in the infinitely large system generated by an infinite number of Chebychev polynomials in the approximation. Before method 2 is effective we have to integrate a *m*th order differential equation at least *m* times in order to get rid of all the derivatives. If the *n*th order Chebychev polynomial is integrated, the result will be a sum of only three Chebychev polynomials:

$$\int T_n \mathrm{d}y = a_{n-1} T_{n-1} + a_{n+1} T_{n+1} + a_0 T_0.$$

So the addition of an extra Chebychev polynomial will only have a small impact on the earlier system. Only a few equations have to be modified by addition of the new unknown multiplied by a relatively small coefficient. In fact, most of the equations remain unchanged.

Summarizing we may state that system 2 is the superior one, since it is built up by a majority of 'exact' equations. Furthermore, the errors in the 'perturbed' equations of system 2 are far less severe than those of system 1.

The question remains whether it is profitable to integrate a *n*th order differential equation more than *n* times. The answer is no. An extra integration does not change the total amount of equations, but one 'exact' equation is transformed into a 'perturbed' one.

It should be emphasized that, for obvious reasons, the above arguments do not hold if one of the differential equations can be represented exactly by a finite series of Chebychev polynomials. In general however, the considerations in this section justify the use of method 2 in this paper.

3.3. The QZ-algorithm

We proceed by analyzing the generalized eigenvalue problem

$$(A + \lambda B)\mathbf{x} = \mathbf{0}. \tag{28}$$

Once the set ν of eigenvalues has been derived, the particular eigenvalue $\lambda' = \lambda'_R + j\lambda'_I$ is selected which satisfies:

$$\lambda'_I \geqslant \lambda_I, \quad \forall \lambda = \lambda_R + j\lambda_I \in \nu. \tag{29}$$

The sign of λ'_I characterizes the stability of the flow. Regarding the shape of the perturbations it can easily be deduced that a negative value of λ'_I implies a stable flow, whereas the flow is unstable for a positive value of λ'_I.

The generalized eigenvalue problem (28) cannot be rewritten into an ordinary eigenvalue problem as the matrix B is singular and the matrix A is nearly singular. Koman & Chesters (1977, 1981) [11] [12] reduce the matrices A and B with the Singular Value Decomposition Method (SVD). After reduction, B is non-singular, so that an ordinary eigenvalue problem can be formulated using the inverse of B. However, the SVD-method is quite laborious.

In this paper we use the QZ-algoritm (see e.g. Moler & Stewart (1973) [15]) to solve the generalized eigenvalue problem. In this method, two non-singular matrices Q and Z are constructed iteratively. They have the following properties:

$$\begin{aligned} QAZ &= A' = \{a'_{ij}\} \quad \text{with } a'_{ij} = 0 \quad i > j, \\ QBZ &= B' = \{b'_{ij}\} \quad \text{with } b'_{ij} = 0 \quad i > j. \end{aligned} \tag{30}$$

We formulate a new generalized eigenvalue problem $(QAZ + \lambda QBZ)\mathbf{y} = \mathbf{0}$, which is equivalent to the original eigenvalue problem (28). This implies that both problems have the same solution, i.e. the same set of eigenvalues:

$$\lambda_i = -\frac{a'_{ii}}{b'_{ii}} \quad (b'_{ii} \neq 0) \quad i = 1, 2, \ldots, N. \tag{31}$$

The matrices are calculated by an iterative procedure, which is analogous to the QR-method for ordinary eigenvalue problems. For a more detailed specification of the analogy of the two methods see Knoester (1986) [10].

4. Results and discussion

The characteristics of interfacial stability are determined by the interfacial conditions (18). Examination of these conditions teaches us that there are basically three fluid properties which influence interfacial stability: (1) surface tension, (2) discontinuity of density, (3) discontinuity of viscosity. Some computations meant to investigate the discontinuity of viscosity; these are discussed and compared with the literature in section 4.1. We chose, however, to study the influence of the discontinuity of density on the stability. We therefore performed computations on both horizontal and inclined, two-layer and three-layer flow of fluids with different densities. Results are shown in section 4.2. In section 4.3 some attention is paid to water-air flow configurations, with both a discontinuity in density and viscosity. Finally, a general discussion on linear stability analysis can be found in section 4.4.

Apart from the water-air case, all computations have been performed for three fictitious liquids:

liquid	$\rho[kg\,m^{-3}]$	$\mu[Pa\,s]$	$\gamma[N\,m^{-1}]$
A	10	0.01	$\gamma_{AB} = 0.1$
B	1000	0.01	$\gamma_{BC} = 0.1$
C	1000	0.0001	

For all computations the channel height was taken $H = 0.01\,[m]$, and we have set $l_2 = l_3 = 0.01$ in dimensionless units, unless otherwise stated. Furthermore, we have restricted our stability analysis to transverse perturbations, with $\zeta = 0$. For this kind of perturbations we can simply replace β by α. This restriction is no severe encroach upon the stability analysis, since Yih (1955) [25] has shown that it is sufficient to consider two-dimensional disturbances for all flow configurations as analysed in this paper.

4.1. Discontinuity of viscosity

Both configurations B over C, and C over B were unstable in the very low α regime. Unstable regions occurred for all Reynolds numbers considered, including the very small ones. This result agrees with those of Yih (1967) [26], who concluded that two-layer plane Poiseuille flow of liquids with equal density can be unstable for all Reynolds numbers, however small. The configuration with the largest layer filled with the less viscous liquid (C over B) appears to be more unstable than B over C. The unstable regions of the first mentioned configuration cover a much larger part of the stability diagram (we will explain later what kind of diagrams we made), and the intensity of the instability (represented by the absolute value of λ_I) is very high. The corresponding stability diagrams show chaotic structures instead of clearly separated stable and unstable regions. We could not establish definite neutral stability curves, which is not an uncommon phenomenon when considering unstable behaviour caused by a discontinuity of viscosity (see Tsahalis (1979) [24]). Due to their limited informative nature we have omitted all stability visualizations for flow configurations with fluids B and C.

The differences in stability between the B over C and the C over B configuration require some extra attention. Since gravity has no relevance, we cannot explain these differences by simply taking into account the positions of the liquids relative to each other. With respect to the discontinuity of viscosity the thickness ratio of the layers is probably the most important flow condition. A highly-viscous layer bounded by one or more less viscous layers is much more stable than the other way around. This conclusion is confirmed by Joseph et al. (1984) [9], who studied a two-layer flow in a cylinder. As a consequence the diagram of the C over B over C configuration does not resemble the diagram of the most unstable two-layer configuration (C over B). The large highly-viscous layer in the C over B over C configuration guarantees a relatively stable character and is therefore comparable with the B over C configuration. Joseph et al. have used an energy principle in order to explain the relatively stable behaviour of configurations in which the larger layer is filled with the more viscous liquid.

In Than et al (1987) [23] stable regions have been found for three-layer configurations. We could not spot any stable region in the stability diagram of the C over B over C configuration; it only showed close resemblance to the one belonging to the B over C configuration.

The presence of unstable behaviour for (very) small values of α (long wave disturbances) is a well-known phenomenon (Yih (1967), Than et al. (1987)). To study the stability against long wave disturbances it is probably much more convenient to use asymptotical expansion techniques, introduced by Yih, and further elaborated by Than et al.

The fact that all configurations stabilize for increasing values of α must be ascribed to the influence of surface tension. In fact, Hooper & Boyd (1983) [7] showed that a two-layer flow with a discontinuous viscosity is unstable in the extreme short wave regime on condition that surface tension is assumed to be zero. However, the mechanism of instabilities generated by discontinuity of viscosity remains a confusing and challenging research topic.

An increasing value of α is equivalent to a decreasing wavelength, which consequently increases the magnitude of the surface tension. The surface tension is directed towards the convex side of the interface, so we can expect that the surface tension stabilizes uni-directional flow. This need not be the case for a two-layer flow in a cylindrical geometry (see Hickox (1971) [6]). In this situation the surface tension tends to intensify axisymmetrical disturbances of the interface, because of the varying curvature in the cross section of the flow.

4.2. Discontinuity of density

Relatively little research has been done on the influence of discontinuity of the density on flow stability. This has to do, probably, with the well-known experience that the heavier fluid always tends to move downward, due to gravity. This phenomenon destabilizes every flow where a dense fluid is carried by a less dense one. In the opposite case, if the less heavy fluid is above the denser one, the discontinuity of density has a stabilizing effect. These conclusions are confirmed by Feldman (1957) [4] and Nakaya & Hasegawa (1974) [17]. Our computations are in agreement with this comprehensible phenomenon. Instability caused by a discontinuity in density (Rayleigh-Taylor instability) is easily explained by the influence of gravity. The stability is affected the more pronounced, when the density ratio is the more different from 1 (see Hickox (1971) [6]). Similar rather simple arguments do not apply to the influence of a discontinuity of the viscosity. The stability diagram of the horizontal configuration B over A has been given in Fig. 3. In this figure, and in Figs 4–11, the contour lines of the imaginary part of the eigenvalue, i.e. λ_I, have been plotted. The flow is stable for regions where $\lambda_I < 0$, and the flow is not stable for regions where $\lambda_I > 0$.

The stability diagram of the horizontal configuration B over A, where the denser fluid is above the less heavy one, is subdivided into two regions by an almost straight horizontal neutral stability curve (see Fig. 3). The level of this curve can easily be estimated from the equation for the balance of normal stress (25). Assume that the expression at the left-hand side equals zero, then we find:

$$\alpha_0^2 = (\rho_B - \rho_A)\frac{gL^2\cos\theta}{\gamma_{AB}} \quad \text{or} \quad \alpha_0^2 = \frac{\rho_B - \rho_A}{\rho_A}\frac{\mathrm{We}}{Fr}\cos\theta, \tag{32}$$

where the second equation is in non-dimensional form, and with $L = H/(2 + l_2)$, where H is the channel height. In Fig. 3 we have $\log\alpha_0 \approx 0.19$. For all $\alpha > \alpha_0$ the surface tension stabilizes the flow, whereas the discontinuity of the density generates instability for $\alpha < \alpha_0$. The intensity of the instability does not continue to increase with the decrease of α; on the contrary, it appears that λ_I reaches a maximum just below the neutral stability curve, almost independent of the value of the Reynolds number. The level of this maximum-instability (horizontal) curve can be computed by

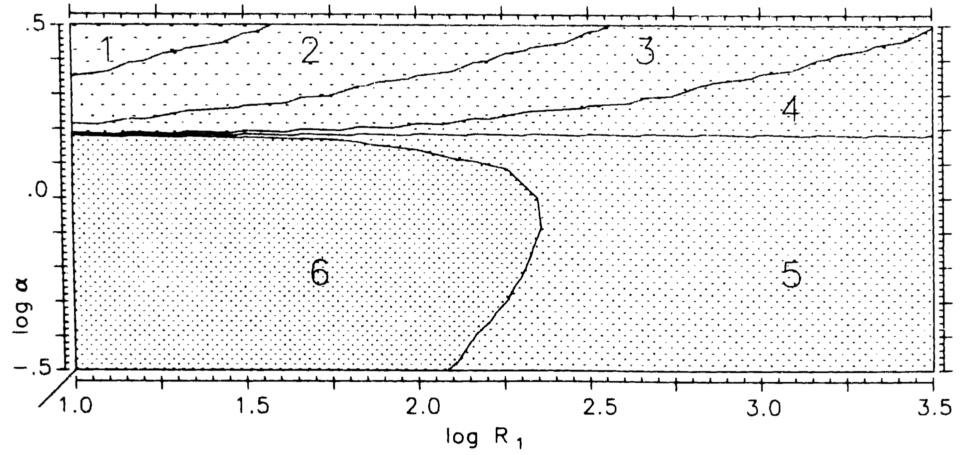

Fig. 3. Stability diagram for flow of B over A; contourlines of λ_I.

region	λ_I	region	λ_I
1	$\lambda_I < -10^{-3}$	2	$-10^{-3} < \lambda_I < -10^{-4}$
3	$-10^{-4} < \lambda_I < -10^{-5}$	4	$-10^{-5} < \lambda_I < 0$
5	$0 < \lambda_I < 10^{-5}$	6	$10^{-5} < \lambda_I < 10^{-4}$

analyzing the right-hand side of the normal-stress balance (25) as a function of α, which reaches a minimum when:

$$\alpha_m^2 = (\rho_B - \rho_A)\frac{gL^2\cos\theta}{2\gamma_{AB}} = \frac{\alpha_0^2}{2} \quad \text{or } \alpha_m^2 = \frac{\rho_B - \rho_A}{\rho_A}\frac{\text{We}}{2Fr}\cos\theta. \tag{33}$$

In our situation we have $\log\alpha_m \approx 0.04$ (see Fig. 3). Another remarkable phenomenon that we want to mention is the magnitude of the propagation speed of the most unstable perturbation (λ'_R), which almost equals the velocity at the interface between both fluids. If the flow is inclined ((see Figs 4 and 5) the level of the neutral stability curve is lowered somewhat, which can analytically be explained by the influence of the $\cos\theta$ term in equation (32). Furthermore, the neutral stability curve is not straight in this case, but declines for increasing value of the Reynolds number. The instabilities for low Reynolds numbers appear to be the most persistent.

The originally stable horizontal A over B configuration gets unstable for low Reynolds numbers on inclined planes (see Figs 6 and 7).

Finally the stability diagram for the three-layer flows A over B over A and the case B over A over B (see Figs 8 and 9) appear to be determined by the most unstable interface B over A, except for some small stable regions which we spotted for small values of α only.

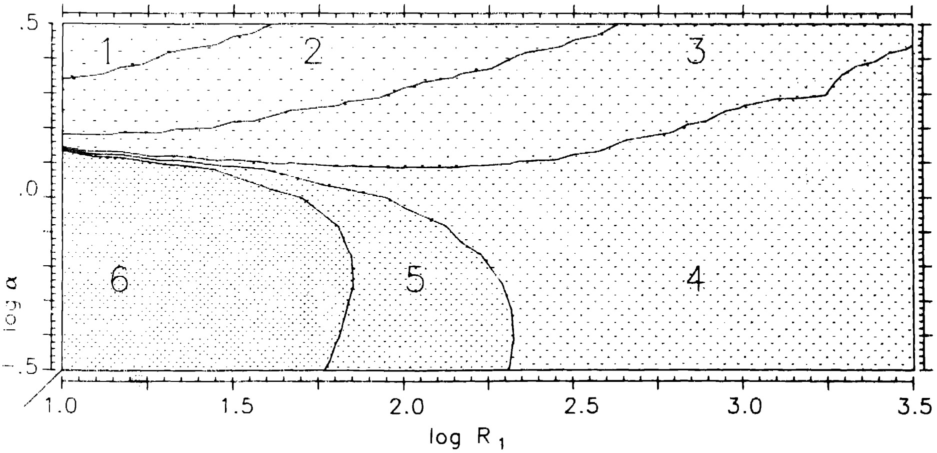

Fig. 4. Stability diagram for flow of B over A, 10°; contourlines of λ_I.

region	λ_I	region	λ_I
1	$\lambda_I < -10^{-3}$	2	$-10^{-3} < \lambda_I < -10^{-4}$
3	$-10^{-4} < \lambda_I < -10^{-5}$	4	$-10^{-5} < \lambda_I < 0$
5	$0 < \lambda_I < 10^{-5}$	6	$10^{-5} < \lambda_I < 10^{-4}$

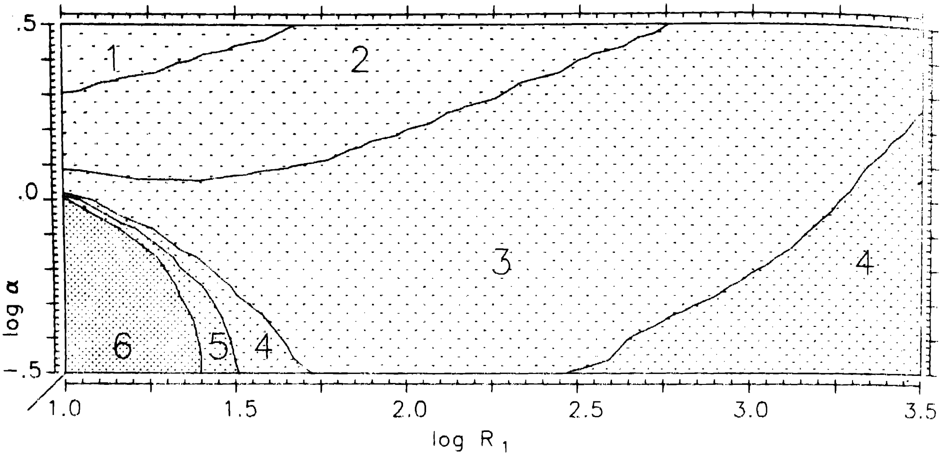

Fig. 5. Stability diagram for flow of B over A, 30°; contourlines of λ_I.

region	λ_I	region	λ_I
1	$\lambda_I < -10^{-3}$	2	$-10^{-3} < \lambda_I < -10^{-4}$
3	$-10^{-4} < \lambda_I < -10^{-5}$	4	$-10^{-5} < \lambda_I < 0$
5	$0 < \lambda_I < 10^{-5}$	6	$10^{-5} < \lambda_I < 10^{-4}$

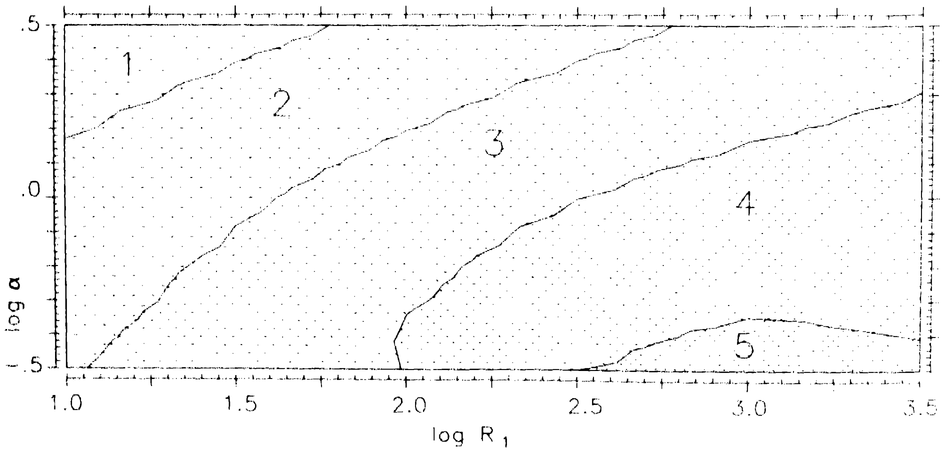

Fig. 6. Stability diagram for flow of A over B, 10°; contourlines of λ_I.

region	λ_I	region	λ_I
1	$\lambda_I < -10^{-5}$	2	$-10^{-5} < \lambda_I < -10^{-6}$
3	$-10^{-6} < \lambda_I < -10^{-7}$	4	$-10^{-7} < \lambda_I < -10^{-8}$
5	$-10^{-8} < \lambda_I < 0$		

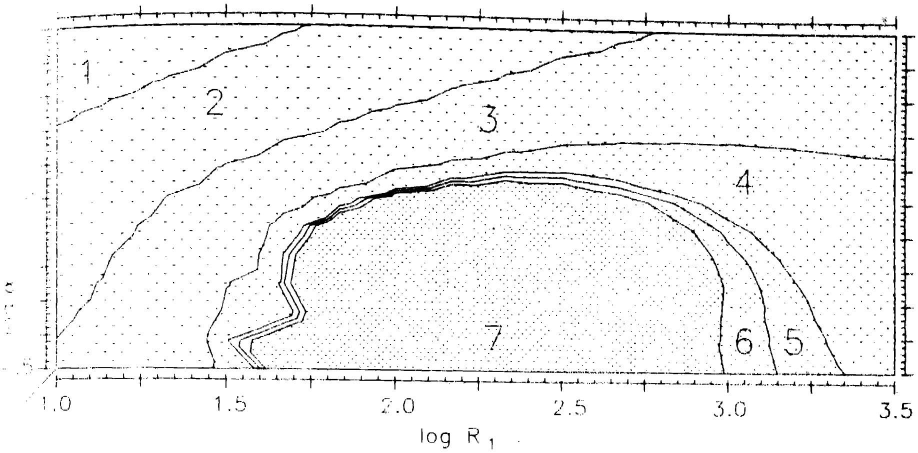

Fig. 7. Stability diagram for flow of A over B, 30°; contourlines of λ_I.

region	λ_I	region	λ_I
1	$\lambda_I < -10^{-5}$	2	$-10^{-5} < \lambda_I < -10^{-6}$
3	$-10^{-6} < \lambda_I < -10^{-7}$	4	$-10^{-7} < \lambda_I < -10^{-8}$
5	$-10^{-8} < \lambda_I < 0$	6	$0 < \lambda_I < 10^{-8}$
7	$10^{-8} < \lambda_I < 10^{-7}$		

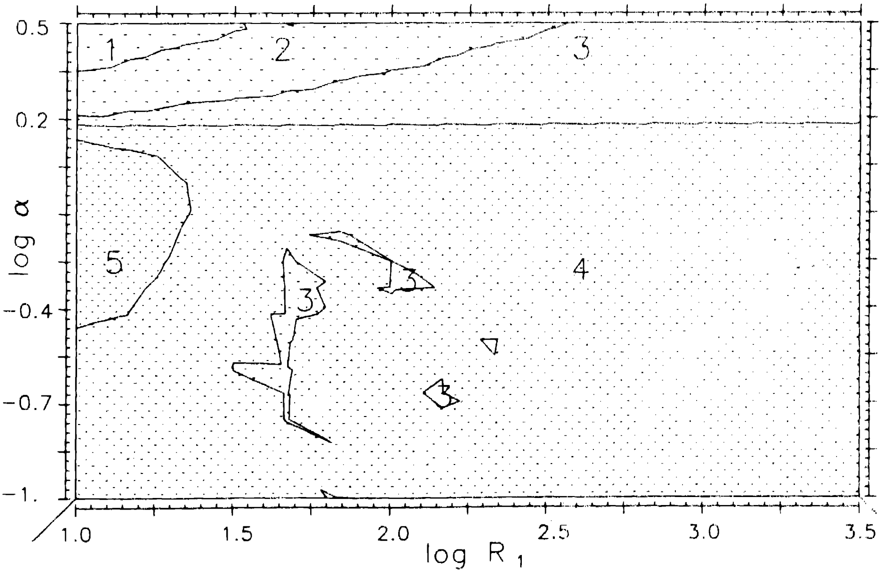

Fig. 8. Stability diagram for flow of A over B over A; contourlines of λ_I.

region	λ_I	region	λ_I
1	$\lambda_I < -10^{-3}$	2	$-10^{-3} < \lambda_I < -10^{-4}$
3	$-10^{-4} < \lambda_I < 0$	4	$0 < \lambda_I < 10^{-4}$
5	$10^{-4} < \lambda_I < 10^{-3}$		

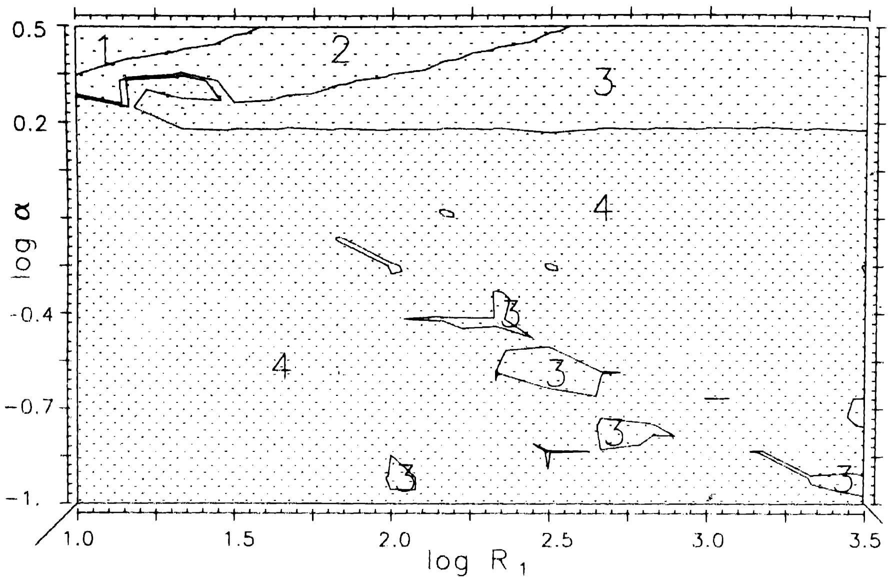

Fig. 9. Stability diagram for flow of B over A over B; contourlines of λ_I.

region	λ_I	region	λ_I
1	$\lambda_I < -10^{-5}$	2	$-10^{-5} < \lambda_I < -10^{-6}$
3	$-10^{-6} < \lambda_I < 0$	4	$0 < \lambda_I < 10^{-5}$

4.3. *Water above air*

The analysis would not be complete without calculations on a multi-layer flow configuration of real fluids. We have chosen for a horizontal water layer above a thin sheet of air ($l_2 = l_0 = 0.01$; $l_3 = 0$), which has been shown in Fig. 10. For low Reynolds numbers we recognize the battle between discontinuity of density and surface tension, resulting in a horizontal asymptote to which all the contour lines seem to converge for $R_1 \downarrow 0$. However, if the Reynolds number increases, then the discontinuity of the density gradually loses its destructive influence, which results in a larger stable region for moderate Reynolds numbers. The influence of the thickness of the air sheet can be investigated by varying the parameter $l_2 = l_0$ while α is kept at a constant value (see Fig. 11). For $\alpha = 1.0$ we cannot expect stability for any Reynolds number if l_0 increases above a certain value, say 0.015 ($\log l_0 > -1.82$).

4.4. *Remarks on linear stability analysis*

Linear stability analysis only predicts stability or the onset of instability, but it cannot foresee how unstable behaviour presents itself. Instabilities in a single-phase flow

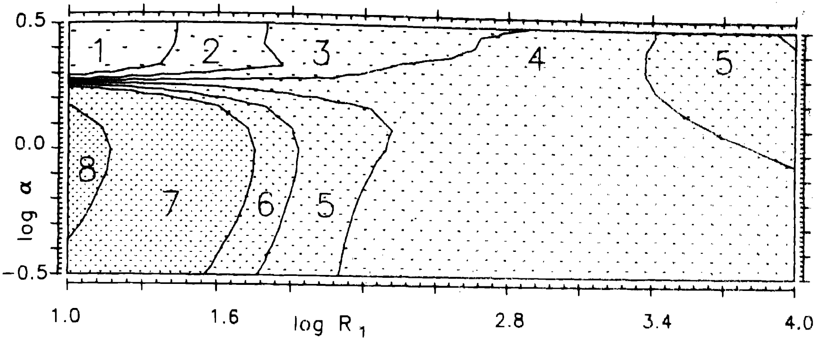

Fig. 10. Stability diagram for water above air; contourlines of λ_I.

region	λ_I	region	λ_I
1	$\lambda_I < -2.10^{-1}$	2	$-2.10^{-1} < \lambda_I < -10^{-1}$
3	$-10^{-1} < \lambda_I < -5.10^{-2}$	4	$-5.10^{-2} < \lambda_I < 0$
5	$0 < \lambda_I < 5.10^{-2}$	6	$5.10^{-2} < \lambda_I < 10^{-1}$
7	$10^{-1} < \lambda_I < 5.10^{-1}$	8	$5.10^{-1} < \lambda_I < 0.75$

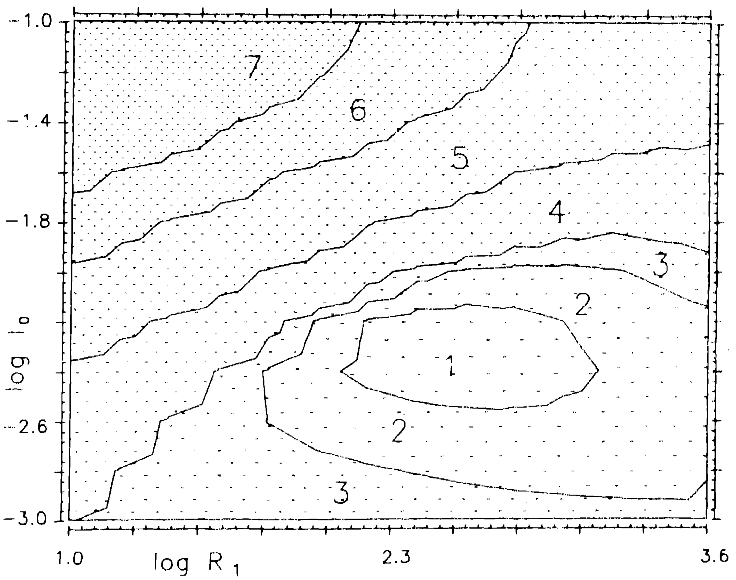

Fig. 11. Stability diagram for water above air for $\alpha = 1.0$; contourlines of λ_I.

region	λ_I	region	λ_I
1	$\lambda_I < -2.10^{-2}$	2	$-2.10^{-2} < \lambda_I < -10^{-2}$
3	$-10^{-2} < \lambda_I < 0$	4	$0 < \lambda_I < 10^{-1}$
5	$10^{-1} < \lambda_I < 1.$	6	$1. < \lambda_I < 5.$
7	$\lambda_I > 5.$		

generate turbulence, which is a well-known fact. Interfacial instabilities do not necessarily result in turbulence. Experimental studies show all kinds of wavy structures along the interface (see Charles & Lilleleht (1965) [2]). Ramshaw (1976) [20] has suggested a mechanism of energy transfer from long waves towards the short-wave disturbances. Ultimately the short wave disturbances are damped by viscous dissipation. This theoretical description of interfacial instability is reminiscent of the cascade model, which is used to explain energy transport in turbulence (see Tennekes & Lumley (1974) [22]).

5. Conclusions

General

The QZ-algorithm has proved to be a useful numerical technique to solve generalized algebraic eigenvalue problems arising from stability analysis with a spectral method.

Both discontinuity of viscosity and discontinuity of density can cause interfacial instability.

Discontinuity of viscosity

Instabilities appeared for perturbations with long wavelengths over the whole domain of Reynolds numbers considered in this paper. Perturbations with small wavelengths are damped by surface tension.

The growth rate of the instabilities is larger if the core region of the channel is filled with the less viscous fluid. Moreover, in this situation perturbations with moderate wavenumbers are unstable too.

In case of three-layer flow the most unstable configuration will be that when the less viscous fluid is encapsulated by the more viscous one.

Discontinuity of density

Instabilities due to a discontinuous density are induced by gravity if a dense fluid is flowing above a less heavy one. Over a large domain of Reynolds numbers there appear to be two critical wavenumbers α_0 and α_m with $\alpha_0 > \alpha_m$ for which the flow is neutrally stable and most unstable respectively. These wavenumbers can be estimated analytically by simple formula manipulation.

In case of three-layer flow, the instability is determined by the most unstable interface.

Due to inclination of the flow the specific wavenumbers α_0 and α_m gradually loose their significance for large Reynolds numbers, where the instabilities disappear for all wavenumbers.

If an originally stable configuration is inclined (the least dense fluid carrying a heavier one) instabilities appear for moderate values of the Reynolds number in the low wavenumber regime.

A. Appendix

Suppose a function $\hat{v}(y)$ can be written as an infinite series of Chebychev polynomials

$$\hat{v} = \sum_{n=0}^{\infty}{}' a_n T_n. \tag{1}$$

T_n is the nth order Chebychev polynomial on the interval $[a, b]$. The coefficients $a_n^{(d,e)}$ are introduced by the following definition:

$$\sum_{n=0}^{\infty}{}' a_n^{(d,e)} T_n = \int_{(d)} y^e \hat{v}(dy)^d. \tag{2}$$

In this appendix it will be shown that the coefficients $a_n^{(d,e)}$ with $d, e \in \mathbb{N}$, $n \geqslant d$ can be expressed as simple linear functions of a finite number of the original unknowns a_m, $m \geqslant 0$.

Part 1 of the proof ($e = 0$)

The Chebychev polynomials can be integrated in a straightforward manner:

$$\begin{cases} \displaystyle\int T_n \,\mathrm{d}y = V\left(\frac{T_{n+1}}{n+1} - \frac{T_{n-1}}{n-1}\right) + c_n T_0 \quad n > 1, \\ \displaystyle\int T_1 \,\mathrm{d}y = V\frac{T_2}{2} + c_1 T_0, \int T_0 \,\mathrm{d}y = 2VT_1 + c_0 T_0, \\ \displaystyle V = \frac{b-a}{4}, \; c_i = \text{constant}, \; i = 0, 1, \ldots. \end{cases} \tag{3}$$

The result of (3) enables us to determine $a_n^{(1,0)}$ for $n \geqslant 1$:

$$\begin{cases} \displaystyle\sum_{n=0}^{\infty}{}' a_n^{(1,0)} T_n = \int \hat{v}\,\mathrm{d}y = \sum_{n=0}^{\infty}{}' a_n \int T_n \,\mathrm{d}y = cT_0 + V\sum_{n=1}^{\infty} \frac{a_{n-1} - a_{n+1}}{n} T_n, \\ \displaystyle a_n^{(1,0)} = V \sum_{r=-1}^{1}{}^{(2)} \frac{j^{r+1} a_{n+r}}{n} \quad n \geqslant 1, \\ \displaystyle \text{with } c = \sum_{n=0}^{\infty}{}' a_n c_n, \; \sum_{r=-1}^{1}{}^{(2)} F(r) = F(-1) + F(1). \end{cases} \tag{4}$$

The application of an analogous form of (4) is used to derive the coefficients $a_n^{(d,0)}$ for $d > 1$:

$$\begin{cases} \sum_{n=0}^{\infty}{}' a_n^{(d,0)} T_n = \sum_{n=0}^{\infty}{}' a_n^{(d-1,0)} \int T_n \,\mathrm{d}y \Rightarrow \\ a_n^{(d,0)} = V \sum_{r=-1}^{1}{}^{(2)} \dfrac{j^{r+1} a_{n+r}^{(d-1,0)}}{n}, d \geqslant 1, n \geqslant d. \end{cases} \tag{5}$$

Part 2 of the proof ($e \neq 0$)

Before we can generalize the preceding results to the situation $e \neq 0$, another important property of Chebychev polynomials has to be highlighted:

$$yT_n = ST_n + VT_{n+1} + VT_{n-1},\ n \geqslant 1,\ yT_0 = ST_0 + 2VT_1,\ S = (a+b)/2. \tag{6}$$

Thus:

$$\text{if } \sum_{n=0}^{\infty}{}' ya_nT_n = \sum_{n=0}^{\infty}{}' c_nT_n \quad \text{then } c_n = a_nS + V \sum_{t=-1}^{1}{}^{(2)} a_{|n+t|},\ n \geqslant 0. \tag{7}$$

The results in (5) and (7) give us sufficient information to determine the remaining coefficients $a_n^{(d,e)}$ with $e \neq 0$:

$$\sum_{n=0}^{\infty}{}' a_n^{(d,e)} T_n = \int_{(d)} \sum_{n=0}^{\infty}{}' y^e a_n T_n (\mathrm{d}y)^d = \int_{(d)} \sum_{n=0}^{\infty}{}' y^{e-1} c_n T_n (\mathrm{d}y)^d = \sum_{n=0}^{\infty}{}' c_n^{(d,e-1)} T_n.$$

So:

$$a_n^{(d,e)} = c_n^{(d,e-1)} = Sa_n^{(d,e-1)} + V \sum_{t=-1}^{1}{}^{(2)} a_{|n+t|}^{(d,e-1)};\ e \geqslant 1,\ d, e \in \mathbb{N},\ n \geqslant d. \tag{8}$$

We conclude that (4) and the recursive formulae (5) and (8) are the tools to express every coefficient $a_n^{(d,e)}$ with $n \geqslant d$ explicitly as a function of $a_m (m \geqslant 0)$. Although the analysis is straightforward, it is very paper-consuming, so we leave this to the interested reader. We limit ourselves to the final result:

$$a_n^{(d,e)} = \sum_{r=0}^{e} \left\{ V^{d+r} S^{e-r} \sum_{t_0=0}^{0} \sum_{t_1=-1}^{1}{}^{(2)} \cdots \sum_{t_{d+r}=-1}^{1} G(n, d, r, t_i) \right\} \quad d, e \in \mathbb{N},\ n \geqslant d \tag{9}$$

with

$$G(n, d, r, t_i) = \frac{j^{d+z(d)} a_{|n+z(d+r)|}}{\prod_{u=0}^{d-1} (n + z(u))},\ z(x) = \sum_{w=0}^{x} t_w,\ \prod_{u=0}^{-1} F(u) = 1.$$

According to (9) the coefficients $a_n^{(d,e)}$ are linear functions of a finite number of the unknowns a_m:

$$\begin{cases} a_n^{(d,e)} = c_{z_1}a_{z_1} + c_{z_1+1}a_{z_1+1} + \cdots + c_{z_2}a_{z_2}, \\ z_1 = \max\{0, n-d-e\},\ z_2 = n+d+e. \end{cases} \quad (n \geqslant d) \tag{10}$$

Furthermore the coefficients c_i, $z_1 \leqslant i \leqslant z_2$ decrease as n increases, if at least one integration is performed (i.e. $d \geqslant 1$). These results support the reasoning in section 3.2.

References

1. Batchelor, G. K., *An introduction to fluid dynamics*. Cambridge: University Press (1967) (various reprints).
2. Charles, M. E. and Lilleleht, L. U., An experimental investigation of stability and interfacial waves in co-current flow of two liquids. *J. Fluid Mech.* 22 (1965) 217.
3. Chen, K., Bai, R. and Joseph, D. D., Lubricated pipelining: stability of core-annular flow. Part 3. *J. Fluid Mech.* 214 (1990) 251.
4. Feldman, S., On the hydrodynamic stability of two viscous incompressible fluids in parallel uniform shearing motion. *J. Fluid Mech.* 2 (1957) 343.
5. Garg, V. K., Improved shooting techniques for linear boundary value problems. *Comp. Meth. Appl. Mech. and Eng.* 22 (1980) 87.
6. Hickox, C. E., Instability due to viscosity and density stratification in axisymmetric pipe flow. *The Physics of Fluids* 14 (1971) 251.
7. Hooper, A. P. and Boyd, W. G. C., Shear flow instability at the interface between two viscous fluids. *J. Fluid Mech.* 128 (1983) 507.
8. Hu, H. H. and Joseph, D. D., Lubricated pipelining: stability of core-annular flow, Part 2. *J. Fluid Mech.* 205 (1989) 359.
9. Joseph, D. D., Renardy, M. and Renardy, Y., Instability of the flow of two immiscible liquids with different viscosities in a pipe. *J. Fluid Mech.* 141 (1984) 319.
10. Knoester, H., Investigation of the stability of two-phase flows, M. Sci. Thesis, Delft, Delft University of Technology, Dept. Mathematics and Informatics, 1986 (in Dutch).
11. Koman, P., Investigation of the instability of a two-layer Poiseuille flow with the aid of Chebychev polynomials, M. Sci. Thesis, Delft, Delft University of Technology, Dept. Mathematics and Informatics, 1977 (in Dutch).
12. Koman, P. and Chesters, A. K., A spectral method for multiphase stratified flow stability problems. In: Hinton, E., Bettes, P. and Lewis, R. W. (eds), *Numerical methods for coupled problems*. Proc. of the Int. Conference, Swansea, University College, 1981.
13. Lanczos, C., *Applied analysis*. Englewood Cliffs: Prentice-Hall (1956).
14. Lin, C. C., *The theory of hydrodynamic stability*. Cambridge: University Press (1955).
15. Moler, C. B. and Stewart, G. W., An algorithm for generalized matrix eigenvalue problems. *SIAM J. Numer. Anal.* 10 (1973) 241.
16. Muiswinkel, J. C. van, Faber, G., Tichelman, H. F. T. and Zanden, J. van der, On the stability of multi-layered fluids, part II experiments, under preparation.
17. Nakaya, C. and Hasegawa, E., Instability of flow of two horizontal fluid layers due to interfacial waves. *J. of the Phys. Soc. Japan* 37 (1974) 214.
18. Orszag, S. A., Accurate solution of the Orr-Sommerfeld stability equation. *J. Fluid Mech.* 50 (1971) 689.
19. Preziosi, L., Chen, K. and Joseph, D. D., Lubricated pipelining: stability of core-annular flow. *J. Fluid Mech.* 201 (1989) 323.
20. Ramshaw, J. D. and Trapp, J. A., Characteristics, stability, and short-wavelength phenomena in two-phase flow equations systems, Aerojet Nuclear Company Report ANCR-1272 (1976).
21. Taitel, Y. and Dukler, A. E., A model for predicting flow regime transition in horizontal and near horizontal gas-liquid flow. *AIChE* 22 (1976) 47.

22. Tennekes, H. and Lumley, J. L., *An introduction to turbulence*. Cambridge (Mass.): The MIT Press, 3rd printing (1974).
23. Than, P. T., Rosso, F. and Joseph, D. D., Instability of Poiseuille flow of two immiscible liquids with different viscosities in a channel. *Int. J. Engng. Sci.* 25 (1987) 189.
24. Tsahalis, D. T., The hydrodynamic stability of two viscous incompressible fluids in parallel uniform shearing motion. *J. Appl. Mech.* 46 (1979) 499.
25. Yih, C.-S., Stability of two-dimensional parallel flows for three-dimensional disturbances. *Quart. Appl. Math.* 12 (1955) 434.
26. Yih, C.-S., Instability due to viscosity stratification. *J. Fluid Mech.* 27 (1967) 337.

Applied Scientific Research **49**: 335–344, 1992
1992 *Kluwer Academic Publishers. Printed in the Netherlands.*

Flow and heat transfer from a continuous surface in a parallel free stream of viscoelastic second-order fluid

I.A. HASSANIEN

Department of Mathematics, Faculty of Science, Assiut University, Assiut, Egypt

Received 24 January 1990; accepted in revised form 7 February 1991

Key words: boundary layer, viscoelastic fluid, second-order fluid, non-Newtonian fluid, Walter's model

Abstract. Boundary layer solutions are presented to investigate the steady flow and heat transfer characteristics from a continuous flat surface moving in a parallel free stream of viscoelastic fluid. Numerical results are presented for the distribution of velocity and temperature profiles within the boundary layer. The effects of the viscoelastic parameter of the fluid on the shear stress at the wall and rate of heat transfer are studied. For the same Reynolds (based on the larger of the free stream and wall velocities) and Prandtl numbers and the same velocity difference $|U_w > U_\infty|$, larger skin-friction and heat transfer coefficient result for $U_w > U_\infty$ than for $U_w < U_\infty$.

Introduction

Boundary-layer behaviour on a moving continuous surface is an important type of flow occurring in a number of engineering processes. Examples of practical applications of a continuous flat surface are, the aerodynamic extrusion of plastic sheets, the cooling of an infinite metallic plate in a cooling bath, the boundary layer along material handling conveyers, the boundary layer along a liquid film in condensation processes and a polymer sheet or filament extruded continuously from a dye, or a long thread travelling between a feed roll and a wind-up roll.

Flow in the boundary layer on a continuous semi-infinite sheet moving steadily through an otherwise quiescent fluid environment was first studied theoretically by Sakiadis [1] and experimentally verified by Tsou et al. [2], who also determined heat transfer rates for certain values of the Prandtl number. Due to the entrainment of ambient fluid, this situation represents a different class of boundary layer problem which has a solution substantially different from that of a boundary layer over a semi-infinite flat plate. Crane [3] considered a moving strip the velocity of which is proportional to the distance from the slit. These types of flow usually occur in drawing of plastic films and artificial fibres. The heat and mass transfer on a stretching sheet with suction or blowing was investigated by Gupta and Gupta [4].

Since the physical properties of the ambient fluid effectively influence the boundary layer characteristics, the study of non-Newtonian fluid flow over a moving sheet has gained considerable importance. Fox et al. [5] have studied the flow of a power-law fluid on a moving surface. The flow of second-order fluid over a stretching sheet without heat transfer has been dealt with by Rajagopal et al. [6]. Bujurke et al. [7] analyzed the momentum and heat transfer in the flow of second-order fluid over a stretching sheet using the momentum integral technique. Siddappa and Abel [8] studied the flow of a viscoelastic fluid obeying Walter's [9] model past a stretching sheet subject to suction.

In the aforementioned studies, the moving surface was placed in an otherwise quiescent surrounding fluid medium, where the free stream velocity was zero. In our study we considered the boundary layer flow of a second-order fluid on a continuous plane sheet which emerges from a slit with a constant surface speed U_w in a parallel free stream U_∞. The continuous moving flat surface sucks the ambient fluid and pumps it again in the downstream direction. Thus, the transverse velocity component in the boundary layer is directed towards the plate when $U_w > U_\infty$. The change in the direction of the transverse velocity component results in quite different characteristics of friction factor and surface heat transfer rates for $U_w > U_\infty$ when compared to $U_w < U_\infty$ for the same velocity difference $|U_w - U_\infty|$. Reynolds and Prandtl numbers.

The velocities referred to in the above are dimensionless. The method of making them dimensionless is discussed in the next section.

Flow analysis

An incompressible second-order fluid has a constitutive equation based on the postulate of gradually fading memory given by Coleman and Noll [10] as

$$T = -pI + \mu A_1 + \alpha_1 A_2 + \alpha_2 A_1^2, \tag{1}$$

where T is the stress tensor, μ, α_1, α_2 are the material constants with $\alpha_1 < 0$, $-pI$ denotes the indeterminate part of the stress due to the constraint of incompressibility and A_1 and A_2 are the kinematic tensors defined as [10]

$$A_1 = \text{grad } V + (\text{grad } V)^T,$$

$$A_2 = \frac{\mathrm{d}A_1}{\mathrm{d}t} + A_1(\text{grad } V) + (\text{grad } V)^T A_1, \tag{2}$$

where V denotes the velocity, and d/dt the material time derivative. The model (1) has been the object of detailed study in recent years and can be considered as a second order approximation of a simple fluid in the sense of retardation (cf. Coleman and Noll), since relation (1) is properly invariant it has also been employed as an exact model for some fluids. This model is applicable to some dilute polymer solutions and is valid at low rates of shear.

We consider a steady, two-dimensional, incompressible flow of a fluid obeying

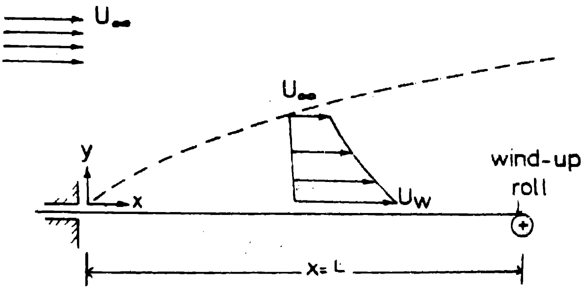

Fig. 1. Schematic representation of the boundary layer on a continuous moving surface.

model (1) past a continuous moving flat plate with a constant velocity U_w in viscoelastic fluid medium whose free stream velocity is U_∞. The plate and the fluid are assumed to move in the same direction. Figure 1 shows the coordinate system (x, y) fixed in space and the flow model for the boundary layer on a continuous moving surface. The origin of coordinates is placed at the location where the plate is drawn into the fluid medium and the y-axis is measured normal to the plate. Distances are normalized by the characteristic length, $\bar{L}$, between the slit and the wind up roll or the portion of this length along which the flow is laminar (the overbars indicate dimensional quantities). Velocities are normalized by the largest velocity in the problem as a reference velocity $\bar{U}_r$:

$$\bar{U}_r = \begin{cases} \bar{U}_w & \text{if } \bar{U}_w > \bar{U}_\infty \\ \bar{U}_\infty & \text{if } \bar{U}_w < \bar{U}_\infty. \end{cases} \tag{3}$$

The velocity components corresponding to the x and y directions are respectively denoted by u and v. Defining the Reynolds number as:

$$\mathrm{Re} = \bar{U}_r \bar{L}/\bar{\nu} = O(\varepsilon^2), \quad \varepsilon \ll 1, \tag{4}$$

and introducing the dimensionless variables:

$$\begin{aligned} &x = \bar{x}/L = O(1), \qquad y = \bar{y}/\bar{L} = O(\varepsilon), \qquad u = \bar{u}/\bar{U}_r = O(1) \\ &v = \bar{v}/\bar{U}_r = O(\varepsilon), \qquad T = (\bar{T} - \bar{T}_\infty)/(\bar{T}_w - \bar{T}_\infty) = O(1), \end{aligned} \tag{5}$$

result in the dimensionless boundary layer equations:

Mass:

$$\frac{\partial u}{\partial x} + \frac{\partial v}{\partial y} = 0 \tag{6}$$

Momentum:

$$u\frac{\partial u}{\partial x}+v\frac{\partial u}{\partial y}$$

$$=\frac{1}{\mathrm{Re}}\frac{\partial^2 u}{\partial y^2}-\alpha^*\left(u\frac{\partial^3 u}{\partial x\partial v^2}+v\frac{\partial^3 u}{\partial y^3}+\frac{\partial u}{\partial x}\frac{\partial^2 u}{\partial y^2}-\frac{\partial u}{\partial y}\frac{\partial^2 u}{\partial x\partial y}\right). \tag{7}$$

Energy:

$$\left(u\frac{\partial T}{\partial x}+v\frac{\partial T}{\partial y}\right)=\frac{1}{\mathrm{Pr}\,\mathrm{Re}}\frac{\partial^2 T}{\partial y^2}, \tag{8}$$

where $\alpha^*=\alpha_1/\rho L^2$, $\nu=\mu/\rho$, $\mathrm{Pr}=\mu c_p/k_f$, the Prandtl number, c_p and k_f being the specific heat and thermal conductivity of the fluid respectively.

The boundary conditions are given by:

$$y=0: u=U_w/U_r,\quad v=0,\quad T=1,$$

$$y\to\infty: u\to U_\infty/U_r,\quad T\to 0. \tag{9}$$

In deriving equation (7) it was assumed that in addition to usual boundary layer approximations the conditions due to the normal stress is of the same order of magnitude as that due to shear stress. Thus both ν and α^*, are $O(\delta^2)$, where δ is the boundary layer thickness (see [11]).

Introducing a dimensionless stream function ψ defined by:

$$\psi(x,y)=\bar{\psi}/(\bar{U}_r\bar{L})=O(\varepsilon),\qquad u=\partial\psi/\partial y,\qquad v=-\partial\psi/\partial x. \tag{10}$$

It may be verified that the continuity equation is automatically satisfied. We define the following transformations:

$$\eta(x,y)=(\mathrm{Re}/x)^{1/2}y,$$

$$\psi(x,y)=(\mathrm{Re}/x)^{-1/2}f(\eta), \tag{11}$$

$$\Theta(\eta)=T(x,y).$$

Substituting the expression (11) into (7) and (8) we have:

$$f'''+\frac{1}{2}ff''=\frac{K}{2}(f''^2-2f'f''-ff^{iv}), \tag{12}$$

$$\theta''+\frac{1}{2}\mathrm{Pr}\,f\theta'=0, \tag{13}$$

where the prime denotes differentiation with respect to η and $K=(\alpha^*U_r/\nu x$ being elastic parameter.

The corresponding boundary conditions are

$$f(0) = 0, \qquad f'(0) = (U_w/U_r), \qquad \theta(0) = 1,$$
$$f'(\infty) = (U_\infty/U_r), \qquad \theta(\infty) = 0. \tag{14}$$

Assuming that $K \ll 1$, we replace the sought functions f with power series in the parameter K. This will result in a fourth-order equation (12) with three boundary conditions. Retaining only the first two terms of the series expansion, thus

$$f = f_0 + Kf_1. \tag{15}$$

Inserting equation (15) into equations (12) and (14), and equating the corresponding coefficients of K up to the first order we obtain the set of relations

$$f_0''' + \frac{1}{2} f_0 f_0'' = 0, \tag{16}$$

$$f_1''' + \frac{1}{2}(f_1 f_0'' + f_1 f_0'') = \frac{1}{2}(f_0''^2 - 2f_0' f_0'' - f_0 f_0^{iv}). \tag{17}$$

The appropriate boundary conditions are

$$f_0(0) = 0, \qquad f_0'(0) = U_w/U_r,$$
$$f_1(0) = 0, \qquad f_1'(0) = 0,$$
$$f_0'(\infty) = U_\infty/U_r, \qquad f_1'(\infty) = 0. \tag{18}$$

Equation (16) is immediately recognizable as the Blasius equation but with the boundary conditions (18) which reduce to those of the classical Blasius problem for the case when $U_w = 0$, $U_\infty = 1$ and reduce to those of Sakiadis [1] for the case when $U_w = 1$, $U_\infty = 0$. Sakiadis obtained a skin friction coefficient $C_f = \bar{\tau}_w/(\bar{\rho}\bar{U}_r^2) = 0.444/\mathrm{Re}_x^{1/2}$ as it has been presented in Fig. 4, higher than that of Blasius $C_f = \bar{\tau}_w/(\bar{\rho}\bar{U}_r^2) = 0.332/\mathrm{Re}_x^{1/2}$ for the classical flat plate problem. The wall shear stress $\bar{\tau}_w$ may be represented by a dimensionless skin-friction coefficient as:

$$C_f = \bar{\tau}_w/\bar{\rho}\bar{U}_r^2 = -f''(0)/(x\,\mathrm{Re})^{1/2}. \tag{19}$$

The local heat flux may be written by Fourier's law as

$$\begin{aligned} q_w(x) &= -k_f\left(\frac{\partial T}{\partial y}\right)_{y=0} \\ &= -(k/\bar{L}_f)(\bar{T}_w - \bar{T}_\infty)(\mathrm{Re}/x)^{1/2}\theta'(0). \end{aligned} \tag{20}$$

The local heat transfer coefficient is given by

$$\bar{h}(x) = \frac{q_w(x)}{(\bar{T}_w - \bar{T}_\infty)}. \tag{21}$$

The local heat transfer coefficient along the wall $\bar{h}(x)$, may be expressed in a dimensionless form in terms of the Nusselt number Nu_x defined as follows:

$$\mathrm{Nu}_x = \frac{\bar{h}(x)\bar{L}}{k_f} = -\theta'(0)(\mathrm{Re}/x)^{1/2}. \tag{22}$$

Numerical solution and discussion

Equations (16) and (17), subject to the appropriate boundary conditions (18) have been solved numerically using finite difference approximations, by reducing these equations to a first order system, where the derivatives are approximated by centered-difference gradients and averages centered at the midpoints of the net defined by

$$\eta_0 = 0, \qquad \eta_j = \eta_{j-1} + h_j, \quad j = 1, 2, 3, \ldots, J, \eta_j = \eta_\infty. \tag{23}$$

A non-uniform grid h_j is defined through

$$h_j = kh_{j-1}, \tag{24}$$

where k is the ratio of adjacent intervals. A constant k is used for this study. The distance from the surface to the jth station is given by:

$$\eta_j = h_j \frac{k^j - 1}{k - 1}, \quad j = 1, 2, \ldots, J. \tag{25}$$

Linearization is achieved by the method of quasilinearization and the resulting system of algebraic equations are then solved by a block-tridiagonal factorization technique (cf. Na [12]). The method is unconditionally stable and second-order accurate. Subsequently, equation (13) was solved by subjecting it to boundary condition (14) and using the above-mentioned technique.

Figure 2 shows the effect of normalized velocity on the plot of friction factor against wall gradient. The figure only refers to the case when the surface velocity is greater than the free stream-velocity. For a constant value of the wall gradient the friction factor decreases as the ratio of the free stream velocity to the surface velocity increases. Figure 3 shows the temperature distribution within the boundary layer for the case

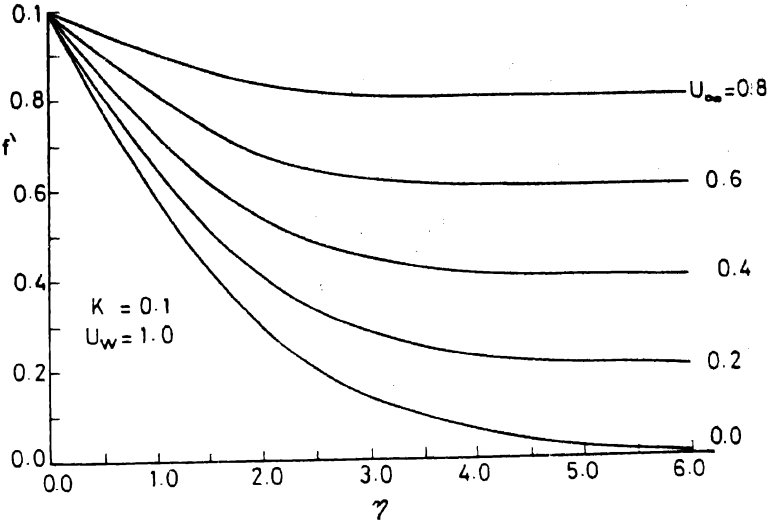

Fig. 2. Velocity distribution.

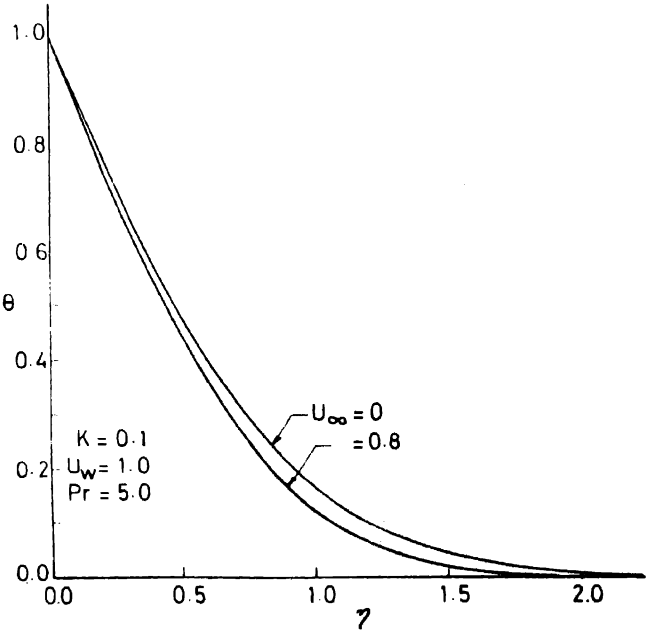

Fig. 3. Temperature distribution.

Table 1. Values of $f''(0)$ and $\theta'(0)$ for $\mathrm{Pr}=5.0$

K	U_w	U_∞	$f''(0)$	$\theta'(0)$	U_w	U_∞	$f''(0)$	$\theta'(0)$
0.0	1.0	0.0	-0.4437^S	-1.15363	0.0	1.0	0.33206^B	-0.57669
		0.2	-0.37781	-1.17284	0.2		0.31336	-0.75607
		0.4	-0.29855	-1.19385	0.4		0.26524	-0.90589
		0.6	-0.20843	-1.21593	0.6		0.19463	-1.03676
		0.8	-0.10864	-1.23859	0.8		0.10539	-1.15421
0.05	1.0	0.0	-0.44587	-1.15339	0.0	1.0	0.32240	-0.57189
		0.2	-0.37754	-1.17296	0.2		0.30540	-0.75317
		0.4	-0.29711	-1.19420	0.4		0.25911	-0.90413
		0.6	-0.20650	-1.21633	0.6		0.19047	-1.03577
		0.8	-0.10712	-1.23888	0.8		0.10329	-1.15379
0.1	1.0	0.0	-0.44718	-1.15314	0.0	1.0	0.31274	-0.56703
		0.2	-0.37728	-1.17308	0.2		0.29778	-0.75025
		0.4	-0.29567	-1.19455	0.4		0.25299	-0.90237
		0.6	-0.20457	-1.21674	0.6		0.18631	-1.03478
		0.8	-0.10561	-1.23917	0.8		0.10118	-1.15336
0.2	1.0	0.0	-0.44981	-1.15265	0.0	1.0	0.29342	-0.55711
		0.2	-0.37675	-1.17333	0.2		0.28153	-0.74433
		0.4	-0.29278	-1.19525	0.4		0.24075	-0.89881
		0.6	-0.20070	-1.21755	0.6		0.17800	-1.03280
		0.8	-0.10255	-1.23975	0.8		0.09698	-1.15251

when $U_w > U_\infty$. The temperature distribution tends to become shallower as the normalized free stream velocity increases.

In several practical applications the surface characteristics such as friction factor and Nusselt number are of considerable importance. Therefore, the values of $f''(0)$ and $\theta'(0)$ are shown in Table 1 for different values of viscoelastic parameter. In general, the effect of increasing the values of the viscoelastic parameter, while keeping the others constant, is to increase the rate of heat transfer at the wall and to reduce the values of $f''(0)$ only for all possible combinations of U_w and U_∞ except the case when $U_w=1.0$ and $U_\infty=0.8$, the opposite trend is observed. In Fig. 4 we have presented the results for the friction factor parameter $f''(0)$ vs. the normalized velocity difference $|U_w-U_\infty|/U_r$. The upper two curves refers to the case where the velocity of the plate is larger than the free stream velocity while the lower two curves show the results for the opposite case. The curves are independent of the magnitudes of velocities whose effect is contained in Re. The points B and S on these curves (and in Table 1) represent the Blasius and Sakiadis solutions respectively for Newtonian fluid, i.e. for $K=0$. The friction factor depends not only on the normalized velocity difference but also on the fact whether the surface or the free stream moves faster. The case corresponding to $U_w > U_\infty$ yields higher friction factors for the same value of the normalized velocity difference than for $U_w < U_\infty$ for both Newtonian and non-Newtonian fluid.

Consider e.g. the two cases:

$$(\bar{U}_w=100\,\mathrm{ms}^{-1},\ \bar{U}_\infty=20\,\mathrm{ms}^{-1})\quad \text{and} \quad (\bar{U}_w=20\,\mathrm{ms}^{-1},\ \bar{U}_\infty=100\,\mathrm{ms}^{-1}).$$

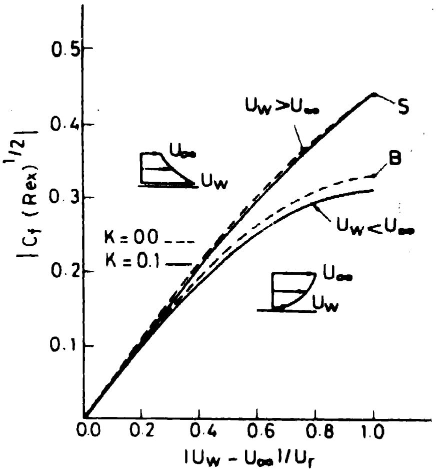

Fig. 4. Friction factor vs. normalized velocity difference.

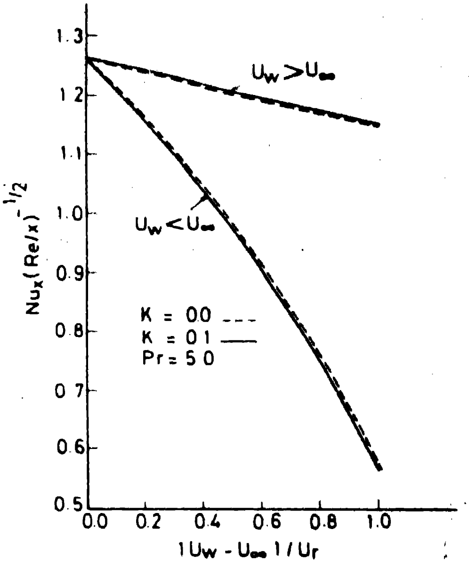

Fig. 5. Nusselt number vs. normalized velocity difference.

The value of Re is the same in both cases and we have the same normalized velocity difference $|U_w - U_\infty| = 0.8$. (Note that, in general, the same magnitude of normalized velocity difference and the same Reynolds number for $U_w > U_\infty$ and $U_w < U_\infty$ implies the same magnitude of dimensional velocity difference). However in the first case we have $U_w > U_\infty$ giving $C_f(x\,\mathrm{Re})^{1/2} = 0.3591$ and 0.3579 for $K = 0.0$ and $K = 0.1$ respectively as seen from the upper two curves in Fig. 5 while for the second case we have $U_w < U_\infty$ giving $C_f(x\,\mathrm{Re})^{1/2} = 0.3037$ and 0.2887 for $K = 0.0$ and $K = 0.1$ respectively as seen from the lower two curves in Fig. 5.

The normalized surface heat transfer rates vs. the normalized velocity difference is displayed in Fig. 5. The upper two curves represent the case when $U_w > U_\infty$ while the lower two curves represent the case when $U_w < U_\infty$. The Nusselt number varies not only as a function of the normalized velocity difference but also on whether $U_w > U_\infty$ or $U_w < U_\infty$. As the normalized velocity difference increases, we see that the surface heat transfer rate falls more rapidly for the case when $U_w < U_\infty$ as compared to the case for which $U_w > U_\infty$. It should be mentioned here that when $U_w = 0$ and $U_\infty = 1$, the results in Fig. 4 and Fig. 5 and also in Table 1 for all values of K are those of Ref. [13]. These results agree very well with the above reference.

Concluding remarks

In this study the flow and heat transfer in a viscoelastic fluid on a continuous moving flat surface in a parallel free stream are presented. Flow of this type represents a new class of boundary-layer problems, with solutions substantially different from those for boundary layer flow on a flat surface of finite length. That is, the solutions of the problems of flow past a flat plate depend on the relative velocity between the flat plate and the free stream, while the solution of the problems of flow past a continuous moving flat surface depend not only on the velocity difference but also on the velocity ratio. Numerical solutions are obtained for the fluid and heat transfer characteristics. The missing wall values of the velocity and temperature functions are tabulated for a range of viscoelastic parameter. For the same values of normalized velocity difference, Reynolds and Prandtl numbers, the case representing $U_w > U_\infty$ yields larger surface friction factor and surface heat transfer rate when compared to the case for which $U_w < U_\infty$.

References

1. Sakiadis, B.C., *AIChE Journal* 7 (1961) 26; 7 (1961) 221.
2. Tsou, F., Sparrow, E. and Goldstein, R., *Int. J. Heat Mass Transfer* 10 (1969) 219.
3. L.J. Crane, *Z. Angew Math. Phys.* (*ZAMP*) 21 (1970) 645.
4. Gupta, P.S. and Gupta, A.S., *Can. J. Them. Engng.* 55 (1977) 744.
5. Fox, V.G., Erickson, L.E. and Fan, L.T., *AIChE Journal* 15 (1969) 327.
6. Rajagopal, K.R., Na, T.Y. and Gupta, A.S., *Rheol. Acta* 23 (1984) 213.
7. Siddappa, B. and Abel, S., *Z. Angew. Math. Phys.* (*ZAMP*) 36 (1985) 890.
8. Bujurke, N.M., Biradar, S.N. and Hiremath, P.S., *Z. Angew Math. Phys.* (*ZAMP*) 38 (1987) 653.
9. Beard, D.W. and Walters, K., *Proc. Camb. Phil. Soc.* 6 (1964) 667.
10. Coleman, B.D. and Noll, W., *Archs ration. Mech. Analysis* 6 (1960) 355.
11. Rajeswari, G. and Rathna, S.L., *Z. Angew. Math. Phys.* (*ZAMP*) 13 (1962) 43.
12. Na, T.Y., *Computational Methods in Engineering: Boundary Value Problems*. New York: Academic Press (1979).

11. Soundalgekar, V.M. and Murti, T.V.R., *Trans. Inzhenerno-Fizicheskii Zhurnal* 40 (1981) 225.

Applied Scientific Research **49**: 345–354, 1992
© 1992 Kluwer Academic Publishers. Printed in the Netherlands.

Analysis of the squeezing flow of dusty fluids

M.H. HAMDAN[1] & R.M. BARRON[2]

[1] *Division of Mecs, University of New Brunswick,*
P.O. Box 5050, Saint John, N.B., Canada, E2L 4L5.
[2] *Department of Mathematics & Statistics, and Fluid Dynamics Research Institute,*
University of Windsor, Windsor, Ontario, Canada N9B 3P4

Received 25 August 1989; accepted in revised form 7 March 1991

Key words: dusty gases, squeezing flow, iterative solution

Abstract. The current investigation deals with the study of the effect of introducing a small fraction of dust, by volume, to the fluid in a squeeze film on the viscous resistance to a steady moving disc. Expressions are obtained for the fluid-phase and the dust-phase velocity distributions and the dust particle number density. Analysis based on an iterative procedure indicates that the resistance to motion experienced by the moving disc increases due to the presence of dust.

Nomenclature

A = arbitrary function of integration
B = bulk concentration
F = resistance to motion experienced by the disc (dusty fluid case)
F_c = resistance to motion experienced by the disc (clean fluid case)
F^* = difference in resistance between the clean fluid and dusty fluid films
f = mass concentration
h = thickness of the squeeze film
K = Stokes coefficient of resistance
m = mass of a single dust particle
μ = fluid viscosity coefficient
N = dust particles number density
N_0 = dust particles number density at $r = R$
n = iteration level
p = fluid pressure in the squeeze film
P = pressure in the surrounding
R = radius of the disc
ρ = fluid density
(r, θ, y) = cylindrical coordinates
t = time
$\mathbf{U}$ = fluid-phase velocity vector
$\mathbf{V}$ = dust-phase velocity vector
$\tilde{U}_1$ = fluid-phase radial velocity component
U_2 = dust-phase radial velocity component

1. Introduction

The theoretical study of squeezing flows was initiated over a century ago by Reynolds [10]. During the past two decades an increasing interest has been witnessed in the study of the squeezing action of thin fluid layers between surfaces due to the importance of such studies in the practical applications of lubrication and adhesion (cf. [2] and references therein). This type of flow is characterized by the dominant viscous forces which offer greater resistive reaction to the motion of the lubricant and thus increase the reaction to externally applied forces on the surfaces lending greater support to loaded bearings.

Attempts have been made by various authors to study the effect of viscous and pressure forces in the thin film on the load carrying capacity in an attempt to provide for more effective bearings design. Although early studies considered the two bounding surfaces to be impermeable, e.g. [8, 9], recent studies have been concerned with the flow between the surfaces when one of the surfaces is permeable and bounds an external porous layer [3, 4, 5, 12, 13]. A slip condition on the porous surface, based on the Beavers and Joseph condition [1], was employed by Sparrow et al. [12] and their results indicate that the effect of the porous wall is to decrease the load-carrying capacity of the film. Some studies have been concerned with the squeezing flow between two surfaces, one of them being a permeable surface bounding a porous layer, in the presence of a magnetic field [3, 4]. Chandrasekhara [3] employed the Beavers and Joseph condition and his results indicate that in the presence of a uniform magnetic field the load-carrying capacity increases.

A theoretical study of squeezing liquid flow generated by the unsteady motion of a disc with respect to a plane surface was conducted by Jackson [9] to illustrate the effect of viscous and inertia forces on the pressure distribution in the squeezed layer. Jackson presented an iterative procedure to obtain a solution to the equations of motion and continuity and his results indicate that the resistance to motion in the film is due to the viscous action and the inertia of the fluid. This iterative procedure is modified in the current investigation to deal with the squeezing flow of a thin layer of fluid containing a small concentration, by volume, of dust particles. Debnath and Ghosh [6, 7] have used Saffman's [11] dusty fluid model to investigate unsteady hydromagnetic flow of a two-phase system when the motion is generated by oscillating parallel plates or by one oscillating and rotating plate. The Saffman model is based on the assumption that the dust particle density is much larger than the fluid density and that the dust particles are sufficiently small so that Stoke's law of resistance between the particles and fluid holds.

In this work, the flow is assumed to be generated by the steady motion of a disc relative to a stationary lower surface. The two-phase flow in the layer is modelled using Saffman's equations [11]. A quasi-static state, common in the literature e.g. [3, 4, 12, 13], has been assumed. This study is undertaken to illustrate the effect of introducing dust to the fluid on the load carrying capacity and the pressure distribution in the squeezed film. Expressions for the fluid-phase and dust-phase velocity distributions, the dust-phase slip velocity distribution at the two surfaces and the particle number density distribution in the fluid layer are derived.

2. Problem formulation

The differential equations governing the steady motion of an imcompressible, viscous dusty fluid can be expressed as [11] *for fluid-phase*

Continuity equation: $\nabla \cdot \mathbf{U} = 0.$ (1)

Conservation of linear momentum:

$$\rho(\mathbf{U} \cdot \nabla)\mathbf{U} = -\nabla p + \mu \nabla^2 \mathbf{U} + KN[\mathbf{V} - \mathbf{U}] \tag{2}$$

for dust-phase

Continuity equation: $\nabla \cdot N\mathbf{V} = 0$ (3)

Conservation of linear momentum:

$$(\mathbf{V} \cdot \nabla)\mathbf{V} = \frac{K}{m}[\mathbf{U} - \mathbf{V}], \tag{4}$$

where $\mathbf{U}$ is the fluid-phase velocity vector, $\mathbf{V}$ is the dust-phase velocity vector, ρ is the fluid density, p is the fluid pressure, μ is the coefficient of viscosity, N is the dust particle number density, m is the mass of each dust particle and K is Stokes' coefficient of resistance.

In the current study we consider the physical model consisting of a rigid plane surface and a rigid circular disc, of radius R, separated by a narrow gap, h, and containing an incompressible, viscous fluid, as shown in Fig. 1. The fluid between these plates is assumed to contain a small concentration, by volume, of dust particles. The flow is generated by the steady motion of the disc in the direction perpendicular to the plates with velocity $\dot{h} = \mathrm{d}h/\mathrm{d}t$, where t is the time.

In this analysis the cylindrical coordinate system (r, θ, y), and the terminology and assumptions adopted by Jackson [9], are utilized. We consider the fluid-phase and the dust-phase velocity components in the r-direction, namely U_1 and U_2 respectively, to be the dominant components and consequently $R/h \gg 1$. It is also assumed that the fluid pressure and the particle number density are functions of r only, and U_1, U_2 are functions of y and r.

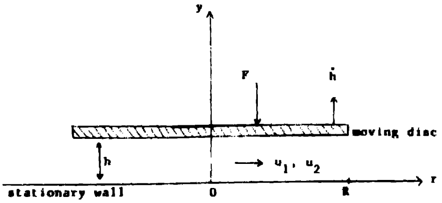

Fig. 1. Representative sketch.

With the above assumptions, our governing equations (1) to (4) reduce to

for fluid-phase

Continuity equation:

$$\frac{1}{r}\frac{\partial rU_1}{\partial r}=0. \tag{5}$$

Momentum equation in the r-direction:

$$\rho U_1\frac{\partial U_1}{\partial r}=-\frac{\partial p}{\partial r}+\mu\left[\frac{\partial^2 U_1}{\partial y^2}+\frac{1}{r}\frac{\partial U_1}{\partial r}-\frac{U_1}{r^2}+\frac{\partial^2 U_1}{\partial r^2}\right]+KN[U_2-U_1] \tag{6}$$

for dust-phase

Continuity equation:

$$\frac{1}{r}\frac{\partial rNU_2}{\partial r}=0 \tag{7}$$

Momentum equation in r-direction:

$$U_2\frac{\partial U_2}{\partial r}=\frac{K}{m}[U_1-U_2]. \tag{8}$$

Equations (5) through (8) represent a system of four equations in the four unknowns U_1, U_2, p and N, with p and N being functions of r only while U_1 and U_2 are functions of r and y.

This system of equations must be solved subject to the no-slip condition for U_1 on the solid surfaces $y=0$ and $y=h$. On the other hand the dust-phase velocity component, U_2, has a non-zero slip value on these solid surfaces due to the deposition of the dust paricles on the solid walls, the reflection of some particles off the walls and the setting into motion of some other particles already present on the walls. The velocity component U_2 is, therefore, a quantity to be determined at the solid walls.

Once $U_2(r,y)$ is known, the number density distribution, $N(r)$, can be determined from the dust-phase conservation of mass equation (7) which implies that

$$rNU_2=A(y), \tag{9}$$

where $A(y)$ is an arbitrary function of y that can be determined from the condition

$N = N_0$ at $r = R$. Equation (9), which is valid for $r > 0$, takes the form

$$N(r) = \frac{RN_0U_2(R, y)}{rU_2(r, y)}. \tag{10}$$

3. Method of solution

The solution to the problem is obtained by an iterative procedure similar to the one given by Jackson [9]. This procedure is modified to suit the current problem and thus equations (8) and (6) are written, respectively, in the following iterative form

$$U_2^{(n+1)} = U_1^{(n)} - \frac{m}{K} U_2^{(n)} \frac{\partial U_2^{(n)}}{\partial r}, \tag{11}$$

$$\begin{aligned} \frac{\partial^2 U_1^{(n+1)}}{\partial y^2} &= \frac{1}{\mu}\left[\rho U_1^{(n)} \frac{\partial U_1^{(n)}}{\partial r} + \frac{\partial p^{(n+1)}}{\partial r} + KN(U_1^{(n)} - U_2^{(n+1)})\right] \\ &\quad + \frac{U_1^{(n)}}{r^2} - \frac{\partial^2 U_1^{(n)}}{\partial r^2} - \frac{1}{r}\frac{\partial U_1^{(n)}}{\partial r}, \end{aligned} \tag{12}$$

where (n) is the previous iteration level and $(n + 1)$ is the current iteration level. In order to accomplish the iterative solution an initial approximation to U_1 and U_2 is required and thus we let [9]

$$U_1^{(1)} = -\frac{r\dot{h}}{2h}. \tag{13}$$

For convenience we take the first approximation to U_2 to be the same as U_1 and thus our solution algorithm takes the following form

1. Using $U_2^{(n)}$ and $U_1^{(n)}$ in (11), find $U_2^{(n+1)}$.
2. Using $U_1^{(n)}$, $U_2^{(n+1)}$ and N in (12), obtain an expression for $\partial^2 U_1^{(n+1)}/\partial y^2$ and integrate it twice with respect to y, noting that $p = p(r)$. Using the no-slip conditions on U_1 at $y = 0$ and $y = h$, obtain an expression for $U_1^{(n+1)}$.
3. Using the expression for $U_1^{(n+1)}$ obtained in step 2, find an expression for $\partial p^{(n+1)}/\partial r$ from the overall fluid-phase continuity equation of the form (cf. [9])

$$-\pi r^2 \dot{h} = \int_0^h 2\pi r U_1^{(n+1)} \mathrm{d}y. \tag{14}$$

4. Using the expression obtained for $\partial p^{(n+1)}/\partial r$ from step 3 in the expression for $U_1^{(n+1)}$ obtained in step 2, obtain an up-to-date expression for U_1.

5. The current $n + 1^{st}$ level of iteration is taken as the nth level in the next iteration and steps 1 through 5 are repeated.

The above procedure was carried out up to $n = 3$, leading to the following expressions for U_1, U_2 and $\partial p/\partial r$:

for n = 1

$$U_1 = -\frac{r\dot{h}}{2h} = U_2, \tag{15}$$

for n = 2

$$U_1 = [y^2 - hy]\,\frac{3r\dot{h}}{h^3}, \tag{16}$$

$$U_2 = -\frac{r\dot{h}}{2h} - \frac{m}{K}\,\frac{r\dot{h}^2}{4h^2}, \tag{17}$$

$$\frac{\partial p}{\partial r} = \frac{6\mu r\dot{h}}{h^3} - \frac{\rho r\dot{h}^2}{4h^2} - \frac{N_0 R^2 m}{r^2}\,\frac{\dot{h}^2}{4h^2}, \tag{18}$$

for n = 3

$$\begin{aligned} U_1 = {} & \frac{y^3 - hy}{2\mu}\left(\frac{6\mu r\dot{h}}{h^3} - \frac{243\rho r\dot{h}^2}{630h^2}\right) \\ & + \frac{9\rho r\dot{h}^2}{2\mu}\left(\frac{y^6}{15h^6} - \frac{y^5}{5h^5} + \frac{y^4}{6h^4} - \frac{y}{30h}\right), \end{aligned} \tag{19}$$

$$U_2 = \frac{3r\dot{h}}{h^3}\,(y^2 - hy) - \frac{mr}{K}\left[\frac{\dot{h}}{2h} + \frac{m}{K}\,\frac{\dot{h}^2}{4h^2}\right]^2, \tag{20}$$

$$\frac{\partial p}{\partial r} = \frac{6\mu r\dot{h}}{h^3} - \frac{243\rho r\dot{h}^2}{630h^2} - \frac{N_0 R^2 m}{r}\left[\frac{\dot{h}}{2h} + \frac{m}{K}\,\frac{\dot{h}^2}{4h^2}\right]^2. \tag{21}$$

Due to rapid convergence the iterative process is terminated after two iterations (cf. [9]). The resistance to motion, F, experienced by the disc is given by

$$F = \int_0^R 2\pi r[P - p]\,\mathrm{d}r, \tag{22}$$

where P is the surrounding pressure such that $p = P$ when $r = R$. The pressure p in equation (22) is found by integrating equation (21) with respect to r. Thus we get, after simplification,

$$F = \frac{\pi R^4}{4}\left(\frac{6\mu \dot{h}}{h^3} - \frac{243\rho \dot{h}^2}{630h^2} - N_0 m\left[\frac{\dot{h}}{2h} + \frac{m}{K}\frac{\dot{h}^2}{4h^2}\right]^2\right). \tag{23}$$

It is interesting to note that equations (17) and (20) imply that $RU_2(r, y) = rU_2(R, y)$ and hence equation (10) reduces to

$$N(r) = N_0 R^2/r^2. \tag{24}$$

For the sake of comparison the corresponding clean fluid problem presented by Jackson [9] was solved when the motion of the disc is steady and the following second approximation, $n = 3$, is obtained:

$$\frac{\partial p}{\partial r} = \frac{6\mu r\dot{h}}{h^3} - \frac{243\rho r\dot{h}^2}{630h^2}, \tag{25}$$

$$\begin{aligned} U_1 &= \frac{y^2 - hy}{2\mu}\left[\frac{6\mu r\dot{h}}{h^3} - \frac{243\rho r\dot{h}^2}{630h^2}\right] \\ &\quad + \frac{9\rho r\dot{h}^2}{2\mu}\left[\frac{y^6}{15h^6} - \frac{y^5}{5h^5} + \frac{y^4}{6h^4} - \frac{y}{30h}\right], \end{aligned} \tag{26}$$

$$F = \frac{\pi R^4}{4}\left[\frac{6\mu\dot{h}}{h^3} - \frac{243\rho\dot{h}^2}{630h^2}\right]. \tag{27}$$

4. Results and discussion

Equation (19) gives the fluid-phase U_1 velocity distribution in the (r, y) plane when the fluid in the squeeze is the dusty fluid. Equation (26) gives the fluid U_1 velocity distribution when the fluid in the squeeze is the clean fluid. These equations indicate that the presence of dust in the squeeze film does not affect the fluid-phase velocity. The presence of dust does, however, influence the fluid pressure distribution as can be seen in equation (21) and therefore it affects the resistance to motion offered by the disc.

Equation (23) gives the resistance to motion, F, that the disc experiences in the case of a dusty fluid film. Equation (27) gives the force F for the case of steady clean fluid

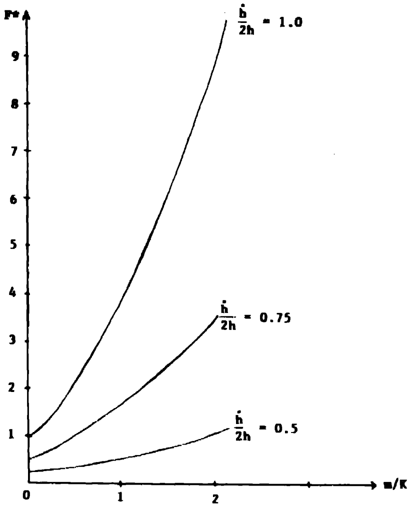

Fig. 2. F^* vs. m/K for various fixed values of $\dot{h}/2h$.

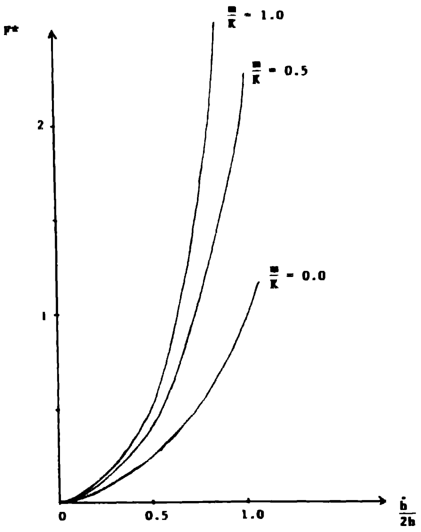

Fig. 3. F^* vs. $\dot{h}/2h$ for various fixed values of m/K.

film. It can be seen from equation (23) that the dust effect on F is characterized by the dust inertial terms. In the last term of equation (23) the quantity in the square brackets is positive and if the loading on the disc is compressive, that is $\dot{h} < 0$, then the inclusion of dust increases the magnitude of the force.

The effect of the dust on the resistance is illustrated as a function of m/K (relaxation time of the particles) for fixed $\dot{h}/2h$ in Fig. 2 and as a function of $\dot{h}/2h$ for various m/K in Fig. 3. F^* refers to the difference in resistance between the clean fluid and dusty fluid films, given by

$$F^* = \frac{F_c - F}{\frac{\pi R^4}{4} N_0 m}, \tag{28}$$

where F_c is the clean fluid result (27).

In the case of clean fluid in the squeeze film the factors producing the resistance to motion are the fluid viscosity and the fluid inertia, as can be seen in equation (27). By contrast, when the squeeze film contains the dusty fluid, the factors producing the resistance to motion are, as can be seen in equation (23), the usual fluid viscosity and inertia in addition to the dust effects which are characterized by the dust inertia. The well-known effect of dust on increasing the viscosity of the fluid, which would be of particular importance in the context of increasing the load-carrying capacity, is not apparent in the current analysis since the dust is seen not to have a direct effect on the viscous term in equation (23). The dust inertia plays a significant role as can be seen in the following analysis.

Substituting equation (24) in (21), equation (21) can be written as

$$\frac{\partial p}{\partial r} = \frac{6\mu r\dot{h}}{h^3} - \frac{243\rho r\dot{h}^2}{630h^2} - Nrm\left[\frac{\dot{h}^2}{2h^2} + \frac{m^2}{K^2}\frac{\dot{h}^4}{16h^4} + \frac{m\dot{h}^3}{4Kh^3}\right]. \tag{29}$$

Dividing the inertia terms by the viscous term, in equation (29), the following expressions are obtained for the fluid-phase and the dust-phase, respectively,

$$\frac{243}{3780}\frac{\rho h\dot{h}}{\mu} \quad \text{and} \quad \frac{mN}{24}\frac{h\dot{h}}{\mu} + \frac{m^2Nh\dot{h}^2}{24K\mu} + \frac{m^3N\dot{h}^3}{96K^2h\mu}.$$

The expression for the fluid-phase results in a type of Reynolds number [9]. The first term of the expression for the dust-phase also results in the above type of Reynolds number as can be easily seen by expressing the dust density, mN, in terms of the fluid density as $mN = \rho f/B$, where B is the bulk concentration and f is the mass concentration [11].

These combined effects of the fluid and dust inertia, therefore, become more significant in cases where the Reynolds number is greater than unity, with the inertial effects in this case being higher than in the case of the clean fluid film and thus they lend greater contribution to the resistance to motion.

5. Conclusion

From the above discussion it can be concluded that the introduction of dust to a fluid squeeze film increases the load-carrying capacity of the squeeze. The main factors contributing to the resistance to motion produced by squeezing a dusty fluid film are the fluid viscosity, the fluid inertia and the dust inertia.

References

1. Beavers, G.S. and Joseph, D.D., Boundary conditions at a naturally permeable wall. *J. Fluid Mech.* 30 (1967) 197–207.
2. Booker, J.F., Squeeze films and bearing dynamics. In: E. R. Booser (ed.), *CRC Handbook of Lubrication (Theory and Practice of Tribology)*, Volume II: Theory and Design. CRC Press (1984) pp. 121–137.
3. Chandrasekhara, B.C., Effect of magnetic field and velocity slip on porous-walled rectangular squeeze films. *Appl. Sci. Res.* 31 (1975) 52–66.
4. Chandrasekhara, B.C., Kantha, R. and Rudraiah, N., Effect of slip on porous-walled squeeze films in the presence of a transverse magnetic field. *Appl. Sci. Res.* 34 (1978) 393–411.
5. Channabasappa, M.N., Umapathy, K.G. and Nayak, I.V., The effect of the thickness of the porous material on the parallel plate channel flow when the walls are provided with non-erodible porous lining. *Appl. Sci. Res.* 32 (1976) 607–617.
6. Debnath, L. and Ghosh, A.K., On unsteady hydromagnetic flows of a dusty fluid between two oscillating plates. *Appl. Sci. Res.* 45 (1988) 353–365.
7. Ghosh, A.K. and Debnath, L., Hydromagnetic Stokes' flow in a rotating fluid with suspended small particles. *Appl. Sci. Res.* 43 (1986) 165–192.
8. Hays, D.F., Squeeze films for rectangular plates. *J. Basic Engg., Trans. ASME*, Series D, 85 (1968) 243–246.
9. Jackson, J.D., A study of squeezing flow. *Appl. Sci. Res.* A-11 (1963) 148–152.
10. Reynolds, O., On the theory of lubrication and its application to Mr. Beauchamp Tower's experiments including an experimental determination of the viscosity of olive oil. *Phil. Trans. Roy. Soc.* 177 (1886) 157–234.
11. Saffman, P.G., On the stability of laminar flow of a dusty gas. *J. Fluid Mech.* 13 (1962) 120–128.
12. Sparrow, E.M., Beavers, G.S. and Hwang, I.T., Effect of velocity slip on porous-walled squeeze films. *J. Lub. Techn., Trans. ASME* 94 (1972) 260–265.
13. Wu, M.N., An analysis of the squeeze film between porous rectangular plates. *J. Lub. Techn., Trans. ASME* 94 (1972) 64–68.

Applied Scientific Research 49: 355–368, 1992
© 1992 Kluwer Academic Publishers. Printed in the Netherlands.

Laminar thermally developing flow inside right-angularly triangular ducts

J.B. APARECIDO[1] & R.M. COTTA*

*Programa de Engenharia Mecânica, COPPE/UFRJ, Cidade Universitária, Cx. Postal 68503, Rio de Janeiro, RJ-21945, Brazil (*author for correspondence)*

[1]*Permanent address: Departamento de Engenharia Mecânica, Av. Brazil 56, Cx. Postal 31, UNESP, Ilha Solteira, SP-15378, Brazil*

Received 20 June 1990; accepted in revised form 6 May 1991

Abstract. An analytical approach based on the generalized integral transform technique is presented, for the solution of laminar forced convection within the thermal entry region of ducts with arbitrarily shaped cross-sections. The analysis is illustrated through consideration of a right triangular duct subjected to constant wall temperature boundary condition. Critical comparisons are made with results available in the literature, from direct numerical approaches. Numerical results for dimensionless average temperature and Nusselt numbers are presented for different apex angles.

Nomenclature

a, b = sides of right triangular duct
A_c = cross-sectional area of duct
c_p = specific heat of fluid
$D_h = \frac{4A_c}{P}$ = hydraulic diameter, with P the wet perimeter
$h(z)$ = heat transfer coefficient at duct wall
k = thermal conductivity
$\mathrm{Pe} = \frac{\rho c_p \bar{u} D_h}{k}$ = Peclet number
$T(x, y, z)$ = temperature distribution
T_0 = inlet temperature
T_w = prescribed wall temperature
$u(x, y)$; $U(X, Y)$ = dimensional and dimensionless velocity profile
$\bar{u}$ = average flow velocity
x; X = dimensional and dimensionless normal coordinate (Fig. 1)
$x_1(y)$; $X_1(Y)$ = dimensional and dimensionless position at irregular boundary (Fig. 1)
y; Y = dimensional and dimensionless normal coordinate (Fig. 1)
z; Z = dimensional and dimensionless axial coordinate

Greek letters

α = side of right triangular duct in X direction (dimensionless)
β = side of right triangular duct in Y direction (dimensionless)
ρ = density of fluid
$\theta(X, Y, Z)$ = dimensionless temperature distribution
θ^* = apex angle of triangular duct (Fig. 1)
θ^{**} = apex angle of triangular duct (Fig. 1)

Introduction

Heat transfer solutions for thermally developing laminar flow inside ducts are of major interest to the establishment of source data for heat exchangers designers, as pointed out in various review articles [1–3]. Most of the available results were compiled in references [1–2] for various duct shapes, and numerical solution procedures briefly discussed. Reliable results within a reasonable range of the thermal entry region, especially for the less usual duct shapes, are still very limited [3], and the development of analytical solutions is desirable, allowing for accurate and cost-effective solutions, as an alternative to purely numerical approaches.

Recently, an analytical approach was advanced for the solution of elliptic diffusion-type problems of irregular domains [4], and applied to the analysis of fully developed laminar flow within ducts of various shapes, such as triangular, trapezoidal, and hexagonal ducts [4–6], by extending the ideas in the so-called generalized integral transform technique [7–12]. Thermally developing laminar flow inside rectangular ducts of finite aspect ratio was also treated analytically [13], again through extension of the generalized integral transform technique, yielding accurate numerical results for quantities of interest such as bulk temperature and Nusselt number, along a wide range of the axial coordinate.

The present work combines the developments in references [4, 13] to provide analytical solutions to thermally developing laminar flow within arbitrarily shaped ducts. The approach is illustrated by considering the case of a right triangular duct, for which the fully developed velocity problem has been previously solved [4], and explicit expressions are now available for the velocity field. Numerical results for the Nusselt number are compared against previously reported results [1, 14], for both the fully developed and thermally developing regions, and additional results are reported for different apex angles of the right triangular duct.

Analysis

We consider laminar forced convection of a Newtonian fluid inside a right triangular duct. Although a more general formulation could be presented, as for general diffusion problems within irregular domains [15], for the sake of clarity a specific duct geometry is analysed and attention focused on the thermally developing flow problem. The decoupled velocity problem for hydrodynamically fully developed flow in a right triangular duct has been previously solved [4], and we now concentrate on solving the energy equation formulated according to the coordinate system and geometry shown in Fig. 1, and given as:

$$\rho c_p u(x, y) \frac{\partial T(x, y, z)}{\partial z} = k \left\{ \frac{\partial^2 T(x, y, z)}{\partial x^2} + \frac{\partial^2 T(x, y, z)}{\partial y^2} \right\},$$

$$\text{in } 0 < y < b, \quad 0 < x < x_1(y), \quad z > 0 \tag{1,a}$$

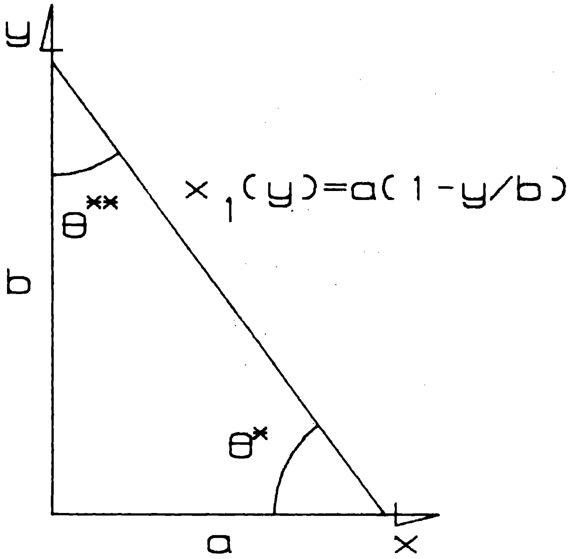

Fig. 1. Geometry and coordinate system for right triangular duct.

subjected to prescribed uniform temperature at the walls

$$T(0, y, z) = T_w, \qquad T[x_1(y), y, z] = T_w, \quad z > 0, \tag{1,b,c}$$

$$T(x, 0, z) = T_w, \qquad T(x, b, z) = T_w, \quad z > 0 \tag{1,d,e}$$

and the inlet condition

$$T(x, y, 0) = T_0, \qquad 0 \leqslant y \leqslant b, \quad 0 \leqslant x \leqslant x_1(y). \tag{1,f}$$

The following dimensionless parameters are defined:

$$X = \frac{x}{D_h}; \quad Y = \frac{y}{D_h}; \quad Z = \frac{z/D_h}{\mathrm{Pe}};$$

$$\mathrm{Pe} = \mathrm{Re}\,\mathrm{Pr} = \frac{\rho c_p \bar{u} D_h}{k}; \qquad \alpha = \frac{a}{D_h}; \qquad \beta = \frac{b}{D_h};$$

$$U(X, Y) = \frac{u(x, y)}{\bar{u}}; \qquad \theta(X, Y, Z) = \frac{T(x, y, z) - T_w}{T_0 - T_w};$$

$$X_1(Y) = \frac{x_1(y)}{D_h} = \alpha\left(1 - \frac{Y}{\beta}\right) \tag{2}$$

and problem (1) is written in dimensionless form as

$$U(X, Y)\frac{\partial \theta(X, Y, Z)}{\partial Z} = \frac{\partial^2 \theta(X, Y, Z)}{\partial X^2} + \frac{\partial^2 \theta(X, Y, Z)}{\partial Y^2},$$

$$0 < Y < \beta, \quad 0 < X < X_1(Y), \quad Z > 0, \qquad (3,a)$$

$$\theta(0, Y, Z) = 0, \qquad \theta[X_1(Y), Y, Z] = 0, \quad Z > 0, \qquad (3,b,c)$$

$$\theta(X, 0, Z) = 0, \qquad \theta(X, \beta, Z) = 0, \quad Z > 0, \qquad (3,d,e)$$

$$\theta(X, Y, 0) = 1, \qquad 0 \leqslant Y \leqslant \beta, \quad 0 \leqslant X \leqslant X_1(Y). \qquad (3,f)$$

Problem (3) above involves two types of difficulties that should prevent it from being analytically solved. One is the non-separable coefficient, $U(X, Y)$, in equation (1) and second is the irregular domain, that does not match the orthogonal coordinate system chosen. For the two reasons, classical approaches could not possibly allow for an analytical solution. However, recently, elliptic diffusion problems of irregular domains [4] were solved by extending the ideas in the so-called generalized integral transform technique [7–12]; besides, a parabolic problem with a non-separable coefficient [13], such as problem (1), but defined within a rectangular domain was again analytically solved by elaborating on this technique. Therefore, by merging the developments in references [4, 13] we seek an analytical solution to the present problem as well, and by following these formalisms we start by considering appropriate auxiliary problems.

$$\frac{d^2\psi(\mu, X)}{dX^2} + \mu^2(Y)\psi(\mu, X) = 0, \quad 0 < X < X_1(Y), \qquad (4,a)$$

$$\psi(\mu, 0) = 0, \qquad \psi(\mu, X_1(y)) = 0, \qquad (4,b,c)$$

and

$$\frac{d^2\phi(\lambda, Y)}{dY^2} + \lambda^2\phi(\lambda, Y) = 0, \quad 0 < Y < \beta, \qquad (5,a)$$

$$\phi(\lambda, 0) = 0, \qquad \phi(\lambda, \beta) = 0, \qquad (5,b,c)$$

where in problem (4) the coordinate Y enters as a parameter, and both problems are solved to yield

$$\psi_i(X, Y) \equiv \psi[\mu_i(Y), X] = \sin\left[\frac{i\pi X}{X_1(Y)}\right], \qquad (6,a)$$

$$\theta_m(Y) \equiv \theta(\lambda_m, Y) = \sin\left(\frac{m\pi Y}{\beta}\right), \qquad (6,b)$$

with eigenvalues obtained from

$$\mu_i(Y) = \frac{i\pi}{X_1(Y)}, \qquad \lambda_m = \frac{m\pi}{\beta}, \quad i, m = 1, 2, \ldots, \tag{6,c,d}$$

and normalization integrals

$$N_i \equiv \int_0^{X_1(Y)} \psi_i^2(X, Y)\,\mathrm{d}X = \frac{X_1(Y)}{2}, \tag{6,e}$$

$$M_m = \int_0^{\beta} \phi_m^2(Y)\,\mathrm{d}Y = \frac{\beta}{2}. \tag{6,f}$$

These auxiliary problems allow the definition of the following integral transform pair:

Transform

$$\bar{\bar{\theta}}_{i,m}(Z) = \int_0^{\beta} \int_0^{X_1(Y)} \mathscr{X}_i(X, Y)\mathscr{Y}_m(Y)\theta(X, Y, Z)\,\mathrm{d}X\,\mathrm{d}Y. \tag{7,a}$$

Inversion

$$\theta(X, Y, Z) = \sum_{m=1}^{\infty} \sum_{i=1}^{\infty} \mathscr{X}_i(X, Y)\mathscr{Y}_m(Y)\bar{\bar{\theta}}_{i,m}(Z), \tag{7,b}$$

where the normalized eigenfunctions are given by

$$\mathscr{X}_i(X, Y) = \left[\frac{2}{X_1(Y)}\right]^{1/2} \sin\left[\frac{i\pi X}{X_1(Y)}\right], \tag{7,c}$$

$$\mathscr{Y}_m(Y) = \left(\frac{2}{\beta}\right)^{1/2} \sin\left(\frac{m\pi Y}{\beta}\right). \tag{7,d}$$

By following the formalism in [13], we now operate on equation (3,*a*) with the operator

$$\int_0^{\beta} \int_0^{X_1(Y)} \mathscr{X}_i(X, Y)\mathscr{Y}_m(Y)\,\mathrm{d}X\,\mathrm{d}Y,$$

making use of the boundary conditions (3,*b*–*e*) and recalling the inversion formula

(7,*b*) to obtain

$$\sum_{j=1}^{\infty}\sum_{n=1}^{\infty} D_{ijmn}\frac{\mathrm{d}\bar{\theta}_{jn}(Z)}{\mathrm{d}Z}+\sum_{j=1}^{\infty}\sum_{n=1}^{\infty} H_{ijmn}\bar{\theta}_{jn}(Z)=0,\quad Z>0, \tag{8,a}$$

where,

$$D_{ijmn}=\int_0^{\beta}\int_0^{X_1(Y)}\mathscr{X}_i(X,\ Y)\mathscr{X}_j(X,\ Y)\mathscr{Y}_m(Y)\mathscr{Y}_n(Y)U(X,\ Y)\,\mathrm{d}X\,\mathrm{d}Y, \tag{8,b}$$

$$H_{ijmn}=E_{iimn}\delta_{ij}-F_{ijmn}-G_{ijmn}+\lambda_m^2\delta_{ij}\delta_{mn}, \tag{8,c}$$

and,

$$E_{iimn}=\int_0^{\beta}\mu_i^2(Y)\mathscr{Y}_m(Y)\mathscr{Y}_n(Y)\,\mathrm{d}Y, \tag{8,d}$$

$$F_{ijmn}=2\int_0^{\beta}\int_0^{X_1(Y)}\mathscr{X}_i(X,\ Y)\frac{\partial\mathscr{X}_j(X,\ Y)}{\partial Y}\mathscr{Y}_m(Y)\frac{\partial\mathscr{Y}_n(Y)}{\partial Y}\,\mathrm{d}X\,\mathrm{d}Y, \tag{8,e}$$

$$G_{ijmn}=\int_0^{\beta}\int_0^{X_1(Y)}\mathscr{X}_i(X,\ Y)\frac{\partial^2\mathscr{X}_j(X,\ Y)}{\partial Y^2}\mathscr{Y}_m(Y)\mathscr{Y}_n(Y)\,\mathrm{d}X\,\mathrm{d}Y, \tag{8,f}$$

while the inlet condition (3,*f*) is operated on with the same operator to yield the transformed inlet condition below

$$\bar{\theta}_{i,m}(0)=\bar{\bar{g}}_{i,m}=\int_0^{\beta}\int_0^{X_1(Y)}\mathscr{X}_i(X,\ Y)\mathscr{Y}_m(Y)\,\mathrm{d}X\,\mathrm{d}Y. \tag{8,g}$$

Equations (8) form a denumerable system of coupled linear first-order ordinary differential equations with constant coefficients. For the purpose of obtaining numerical results from this, a priori, formal solution, the infinite sums in equation (8,*a*) are truncated at the Nth and N^*th elements, respectively, up to any desired accuracy, and equation (8,*a*) is rewritten for the truncated system of $(N.N^*)$ ordinary differential equations as:

$$\sum_{j=1}^{N}\sum_{n=1}^{N^*} D_{ijmn}\frac{\mathrm{d}\bar{\theta}_{jn}(Z)}{\mathrm{d}Z}+\sum_{j=1}^{N}\sum_{n=1}^{N^*} H_{ijmn}\bar{\theta}_{jn}(Z)=0,\quad Z>0, \tag{9,a}$$

with transformed inlet condition

$$\bar{\theta}_{i,m}(0)=\bar{\bar{g}}_{i,m},\quad i=1,2,\ldots,N,\ m=1,2,\ldots,N^*. \tag{9,b}$$

In matrix form, equations (9) are given by

$$D\mathbf{y}' + H\mathbf{y}(Z) = 0, \tag{10,a}$$

$$\mathbf{y}(0) = \mathbf{g}, \tag{10,b}$$

or

$$\mathbf{y}'(Z) + A\mathbf{y}(Z) = 0, \tag{11,a}$$

with,

$$A = D^{-1}H, \tag{11,b}$$

where the various vectors and matrices are obtained from

$$\mathbf{y}(Z) = \{\bar{\bar{\theta}}_{1,1}(Z), \bar{\bar{\theta}}_{1,2}(Z), \ldots, \bar{\bar{\theta}}_{1,N^*}(Z), \ldots, \bar{\bar{\theta}}_{N,1}(Z), \bar{\bar{\theta}}_{N,2}(Z), \ldots, \bar{\bar{\theta}}_{N,N^*}(Z)\}^T, \tag{12,a}$$

$$\mathbf{g} = \{\bar{\bar{g}}_{1,1}, \bar{\bar{g}}_{1,2}, \ldots, \bar{\bar{g}}_{1,N^*}, \ldots, \bar{\bar{g}}_{N,1}, \bar{\bar{g}}_{N,2}, \ldots, \bar{\bar{g}}_{N,N^*}\}^T,$$

$$D = \{\mathrm{d}_{k,l}\}, \quad k, l = 1, 2, \ldots, N.N^*, \tag{12,c}$$

where,

$$\mathrm{d}_{k,l} = D_{ijmn}, \quad i = \mathrm{int}[(k-1)/N^*] + 1, j = \mathrm{int}[(l-1)/N^*] + 1,$$
$$m = k-(i-1)N^*, \; n = l-(j-1)N^*, \tag{12,d}$$

and,

$$H = \{h_{k,l}\}, \quad k, l = 1, 2, \ldots, N.M^*, \tag{12,e}$$

where,

$$h_{k,l} = H_{ijmn}, \tag{12,f}$$

with i, j, m, and n defined as above.

System (10) is then assembled by making use of equations (12); then, matrix D is inverted and equation (11,a) obtained, which is solved analytically once eigenvalues and eigenvectors of the $(N.N^*)\times(N.N^*)$ matrix A are determined by solving the problem below for the eigenvalues, γ's, and eigenvectors, $\boldsymbol{\zeta}$'s:

$$(A - \gamma I)\boldsymbol{\zeta} = 0. \tag{13}$$

The solution of equation (11,*a*) is then given by

$$\mathbf{y}(Z) = \sum_{i=1}^{N.N^*} c_i \mathrm{e}^{-\gamma_i Z} \boldsymbol{\zeta}^{(i)}, \tag{14,a}$$

where the constants c_i's are determined so as to satisfy the transformed inlet condition, equation (10,*b*), from the solution of the following algebraic problem

$$\sum_{i=1}^{N.N^*} c_i \boldsymbol{\zeta}^{(i)} = \mathbf{g}. \tag{14,b}$$

Equations (13) and (14,*b*) can be solved by making use of well-established subroutines packages, such as in the IMSL library [16]. Once the vector of transformed potentials is determined from equation (14,*a*), the inversion formula (7,*b*) is invoked to construct the desired complete potential, $\theta(X, Y, Z)$, here obtained as:

$$\theta(X, Y, Z) = \frac{2}{[\beta X_1(Y)]^{1/2}} \sum_{i=1}^{N} \sum_{m=1}^{N^*} \sin\left[\frac{i\pi X}{X_1(Y)}\right] \sin\left[\frac{m\pi Y}{\beta}\right] \bar{\bar{\theta}}_{i,m}(Z), \tag{15}$$

Quantities of interest can be determined from the temperature profile, equation (15), such as the dimensionless bulk temperature along the duct

$$\theta_{av}(Z) = \frac{1}{A_c} \int_{A_c} U(X, Y)\theta(X, Y, Z)\,\mathrm{d}A, \tag{16,a}$$

which becomes

$$\theta_{av}(Z) = \frac{2}{\alpha} \cdot \left(\frac{2}{\beta}\right)^{1/2} \sum_{i=1}^{N} \sum_{m=1}^{N^*} Q_{i,m} \bar{\bar{\theta}}_{i,m}(Z) \tag{16,b}$$

with,

$$Q_{i,m} = (-1)^{m+1} \int_0^1 \bar{U}_i(\eta) \sin(m\pi\eta)\,\mathrm{d}\eta, \tag{16,c}$$

where the explicit velocity profile obtained in [4] was here recalled in the form

$$U(X, Y) = \sum_{k=1}^{M} \mathscr{X}_k(X, Y) \bar{U}_k(Y), \tag{16,d}$$

and the reader is referred to reference [4] for the details on finding the expressions for the transformed dimensionless velocity, $\bar{U}_k(Y)$, again through the generalized integral transform technique.

The local Nusselt number along the duct length can be evaluated either from application of Fourier law at the duct wall

$$\mathrm{Nu}_1(Z)=\frac{h(Z)D_h}{k}=-\frac{1}{P^*\theta_{av}(Z)}\left\{-\int_0^\beta \left.\frac{\partial\theta(X,Y,Z)}{\partial X}\right|_{X=0}\mathrm{d}Y\right.$$
$$+\int_0^\beta \left.\frac{\partial\theta(X,Y,Z)}{\partial X}\right|_{X=X_1(Y)}\mathrm{d}Y-\int_0^\alpha \left.\frac{\partial\theta(X,Y,Z)}{\partial Y}\right|_{Y=0}\mathrm{d}X$$
$$\left.+\int_0^\beta \left.\frac{\partial\theta(X,Y,Z)}{\partial Y}\right|_{X=X_1(Y)}\mathrm{d}Y\right\}, \tag{17,a}$$

where,

$$P^*=\alpha+\beta+(\alpha^2+\beta^2)^{1/2}, \tag{17,b}$$

or from the heat balance expression obtained by integrating the original energy equation

$$\mathrm{Nu}_2(Z)=\frac{h(Z)D_h}{k}=-\frac{1}{4\theta_{av}(Z)}\frac{\mathrm{d}\theta_{av}(Z)}{\mathrm{d}Z}. \tag{17,c}$$

After substitution of equations (15) and (16,*b*), the following working expressions are obtained for the Nusselt number

$$\mathrm{Nu}_1(Z)=\frac{\alpha}{2P^*}\left(\frac{\beta}{2}\right)^{1/2}\cdot\frac{\sum_{i=1}^{N}\sum_{m=1}^{N^*}J_{i,m}\bar{\bar{\theta}}_{i,m}(Z)}{\sum_{i=1}^{N}\sum_{m=1}^{N^*}Q_{i,m}\bar{\bar{\theta}}_{i,m}(Z)}, \tag{18,a}$$

$$\mathrm{Nu}_2(Z)=-\frac{1}{4}\frac{\sum_{i=1}^{N}\sum_{m=1}^{N^*}Q_{i,m}\dfrac{\mathrm{d}\bar{\bar{\theta}}_{i,m}(Z)}{\mathrm{d}Z}}{\sum_{i=1}^{N}\sum_{m=1}^{N^*}Q_{i,m}\bar{\bar{\theta}}_{i,m}(Z)}, \tag{18,b}$$

where,

$$J_{i,m}=\frac{2}{\beta}\left(\frac{\alpha}{\beta}\right)^{1/2}[1+(-1)^{i+1}]\left(\frac{m}{i}\right)+\left\{\frac{1}{\alpha}\left(\frac{\beta}{\alpha}\right)^{1/2}[1+(-1)^{i+1}]\right.$$
$$\left.+\frac{1}{\beta}\left(\frac{\alpha}{\beta}\right)^{1/2}(-1)^{i+1}\right\}2\pi i I_m, \tag{18,c}$$

$$I_m=\int_0^1\eta^{-3/2}\sin(m\pi\eta)\,\mathrm{d}\eta. \tag{18,d}$$

The average Nusselt number is then evaluated by integrating equation (18,*a*) or (18,*b*) along Z

$$\mathrm{Nu}_{av}(Z) = \frac{1}{Z}\int_0^Z \mathrm{Nu}(Z)\,\mathrm{d}Z, \tag{19,a}$$

to yield the analytical expression

$$\mathrm{Nu}_{av}(Z) = -\frac{1}{4Z}\ln\theta_{av}(Z). \tag{19,b}$$

Although for fully converged solutions, equations (18) for the Nusselt number provide exactly the same numerical results, the two expressions may exhibit different convergence rates and their comparison during the computations provide an additional accuracy check, especially for decreasing values of the dimensionless axial distance.

Results and discussion

The present problem was solved with $N = N^* \leqslant 20$, which proved to be sufficient for the desired convergence in the range of interest for the dimensionless axial distance, $10^{-4} \leqslant Z \leqslant 10^0$. As Z is decreased, like in any other eigenfunction expansion approach, the number of terms required in the series representations increases. A reasonably good estimate of the number of terms to be retained in the infinite sums, is obtained, a priori, from a simple lowest order solution [11, 18] of system (8), which results from neglecting non-diagonal elements in the coefficients matrix. Then, evaluation of the inversion formula from this approximate solution at the smallest Z value of interest, gives an indication of the required values of N and N^*.

The algebraic problems (13) and (14,*b*) are handled by automatic and reliable subroutines in the IMSL library [16]. A typical run of the computer program for the above conditions takes about 400 sec of CPU time on an IBM 4341 computer, under double-precision mode. Alternatively, an initial value problem solver from the IMSL package (subroutine DIVPAG) was employed, with excellent results, to solve equation (11,*a*). The velocity profile is computed from equation (16,*d*) with $M \leqslant 25$ for fully converged results, following [4].

The analysis advanced here is first critically compared with previously reported numerical results, mainly from references [1, 2, 14]. Figure 2 shows fully developed Nusselt numbers from this work and reference [14], where an excellent agreement was obtained for the full range of apex angles, $0 \leqslant \theta^{**} \leqslant 45°$. In Fig. 3 we present results for the local Nusselt number along the thermal entry region, from the present work and from references [1, 14]. The numerical results presented in [1, 2] cover a small

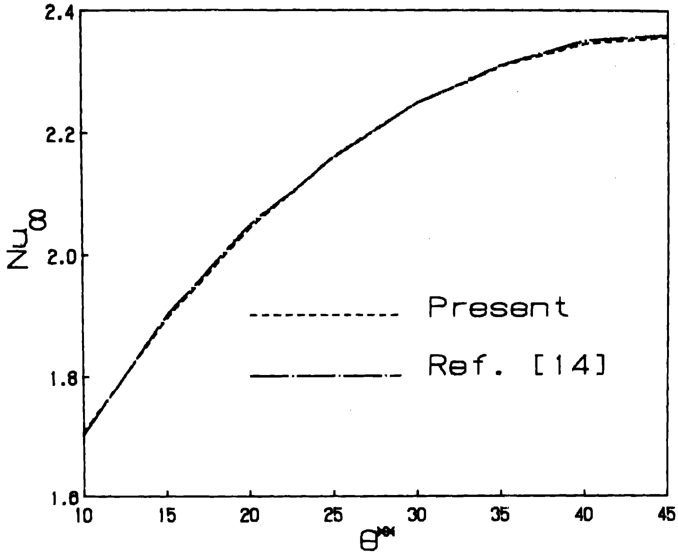

Fig. 2. Comparison of fully developed Nusselt numbers with literature results for various apex angles, θ^{**}

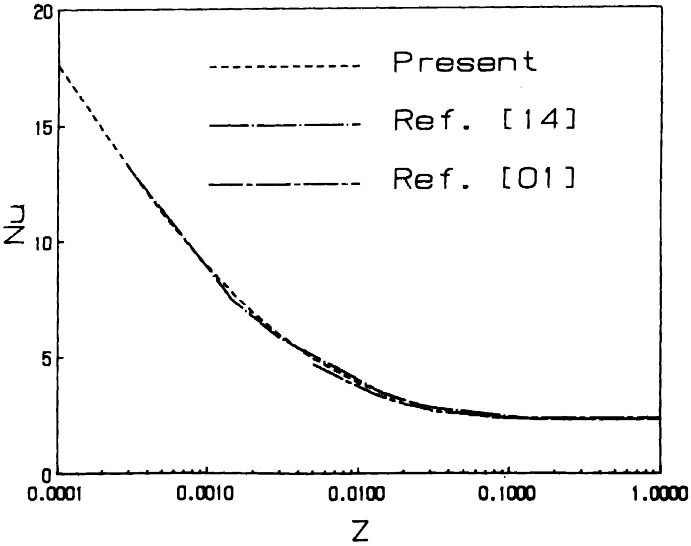

Fig. 3. Comparison of local Nusselt numbers along thermal entry region of a right triangular isosceles duct ($\theta^* = \theta^{**} = 45°$).

range of the dimensionless axial coordinate, $10^{-2} \leqslant Z \leqslant 10^0$, while the results from [14] extend from $Z \geqslant 10^{-4}$, with an expected increase in error for decreasing Z. Therefore, within the applicable ranges, the results are again in excellent agreement, for the most critical situation of $\theta^* = \theta^{**} = 45°$.

Figures 4 to 6 present the axial variations of, respectively, dimensionless bulk temperature, local Nusselt number and average Nusselt number, for the apex angles, $\theta^* = 45°$, $60°$, and $80°$, within the wide range $10^{-4} \leqslant Z \leqslant 10^0$. The Nusselt number curves for different apex angles cross each other at differential axial locations within the thermal entry region, and then tend to their corresponding fully developed values for increasing values of Z, represented in Fig. 2. The evaluation of local Nusselt number from equation (18,*b*) should be recommended, due to the improved convergence behavior relative to equation (18,*a*). These results are interesting for benchmark purposes, since a very limited number of results are presently available for the thermal entry region [3], especially for such a wide range of Z.

The application of the present approach to the different duct geometries in references [1, 2] shall follow, proving reliable source data for heat exchangers designers, which is one of the basic research needs in this field, as pointed out in [3]. Also, if associated with the most recent developments in hybrid numerical-analytical solutions of convection-diffusion problems [17, 18], a wide class of nonlinear/irregular domain problems will become readily tractable through these basic ideas.

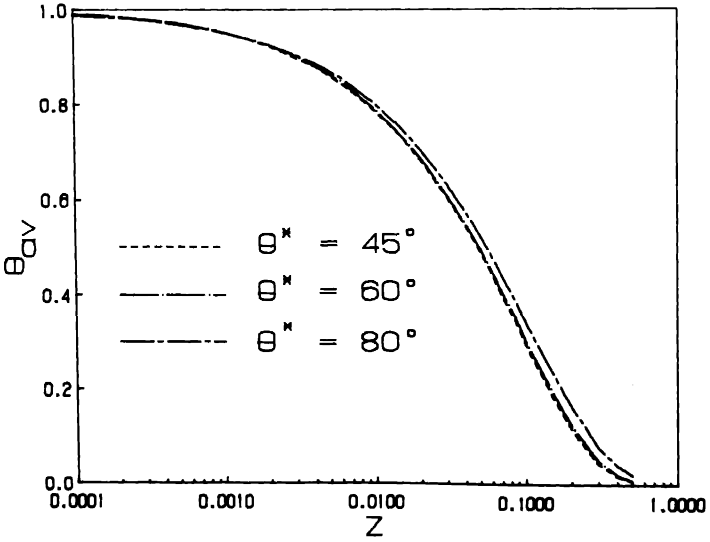

Fig. 4. Dimensionless bulk temperature along thermal entry region of right triangular duct at various apex angles (θ^*).

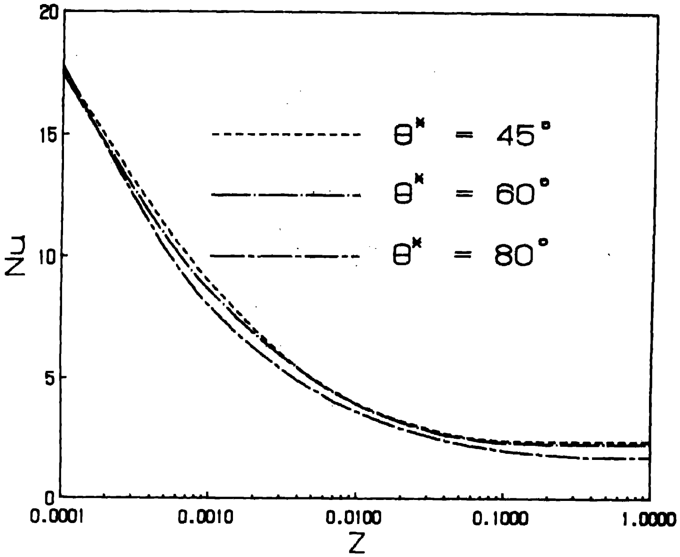

Fig. 5. Local Nusselt number along thermal entry region of right triangular duct at various apex angles (θ*).

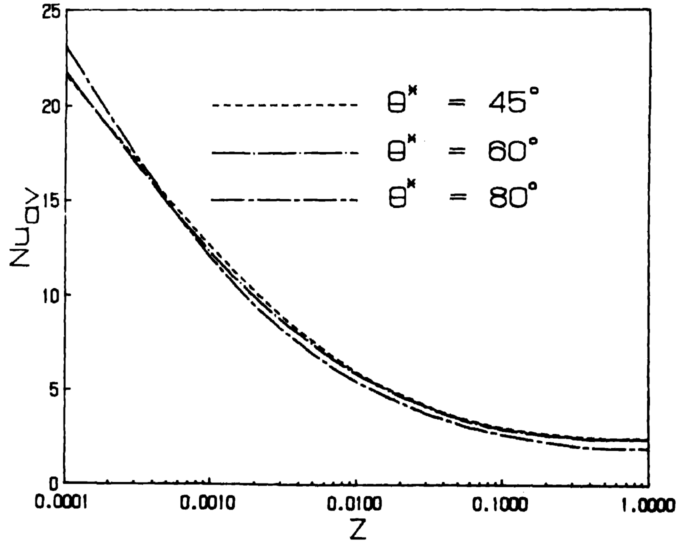

Fig. 6. Average Nusselt number along thermal entry region of right triangular duct at various apex angles (θ*).

Acknowledgements

One of the authors (J.B.A.) wishes to acknowledge the financial support provided by CAPES and UNESP, both from Brazil.

References

1. Shah, R.K. and London, A.L., Laminar flow forced convection in ducts. *Adv. Heat Transfer*, Suppl. 1 (1978).
2. Shah, R.K. and Bhatti, M.S., Laminar convective heat transfer in ducts. In: S. Kakaç, R.K. Shah and W. Aung (eds), *Handbook of Single-Phase Convective Heat Transfer*, Chap. 3. John Wiley (1987) pp. 3.1–3.137.
3. Shah, R.K., Research needs in low Reynolds number flow heat exchangers. In: S. Kakaç, R.K. Shah and A.E. Bergles (eds), *Low Reynolds Number Flow Heat Exchangers*. New York: Hemisphere (1983) pp. 983–1000.
4. Aparecido, J.B., Cotta, R.M., and Özisik, M.N., Analytical solutions to two-dimensional diffusion type problems in irregular geometries. *J. of the Franklin Institute*, V. 326(3) (1989) 421–434.
5. Aparecido, J.B. and Cotta, R.M., Fully developed laminar flow in trapezoidal ducts. *Proc. of the 9th Brazilian Congress of Mechanical Engineering*, IX COBEM, V.1. Florianópolis, SC, December 1987 (1900) pp. 25–28.
6. Aparecido, J.B. and Cotta, R.M., Laminar flow inside hexagonal ducts. *Computational Mechanics* 6 (1990) 93–100.
7. Özisik, M.N. and Murray, R.L., On the solution of linear diffusion problems with variable boundary condition parameters. ASME Paper no. 74-HT-1.
8. Cotta, R.M. and Özisik, M.N., Laminar forced convection in ducts with periodic variation of inlet temperature. *Int. J. Heat & Mass Transfer* 29 (1986) 1495–1501.
9. Cotta, R.M. and Özisik, M.N., Transient forced convection in laminar channel flow with stepwise variations of wall temperature. *Can. J. Chem. Eng.* 64 (1986) 734–742.
10. Cotta, R.M., Steady-state diffusion with space-dependent boundary condition parameters. *Proc. of the 1st National Meeting on Thermal Sciences* – ENCIT 86, Rio de Janeiro, Brazil, December 1986 (1900) pp. 163–166.
11. Cotta, R.M. and Özisik, M.N., Diffusion problems with general time-dependent coefficients. *Braz. J. Mech. Sciences, RBCM* 9 (1987) 269–291.
12. Cotta, R.M., On the solution of periodic multidimensional diffusion problems. *Int. Comm. Heat & Mass Transfer* 16 (1989) 569–579.
13. Aparecido, J.B. and Cotta, R.M., Thermally developing laminar flow inside rectangular ducts. *Int. J. Heat & Mass Transfer* 33 (1990) 341–347.
14. Lakshminarayanan, R. and Haji-Sheik, A., A generalized closed-form solution to laminar thermal entrance problems. In: C.L. Tien, V.P. Carey and J.K. Ferrel (eds), *Proc. of the 8th International Heat Transfer Conference*, San Francisco, USA, July 1986, pp. 871–876.
15. Aparecido, J.B., Generalized integral transform for laminar flow and heat transfer inside straight ducts of arbitrary geometry. D.Sc. Dissertation, ITA, São José dos Campos, Brazil, 1988.
16. IMSL Library, MATH/LIB, Houston, Texas, 1987.
17. Cotta, R.M., Hybrid numerical-analytical approach to nonlinear diffusion problems. *Num. Heat Transfer, part B.* 17 (1990) 217–226.
18. Cotta, R.M., *Diffusion-Convection Problems and the Generalized Integral Transform Technique*, Núcleo de Publicações, COPPE/UFRJ, Rio de Janeiro, 1991.

Applied Scientific Research **49**: 369–375, 1992
© 1992 *Kluwer Academic Publishers. Printed in the Netherlands.*

On the relationship between Lorentz's theorem for viscous flow and Onsager's reciprocal theorem

FLETCHER OSTERLE

Mechanical Engineering Department, Carnegie Mellon University,
Pittsburgh, PA 15213, USA

Received 3 December 1990; accepted in revised form 14 June 1991

Abstract. This paper views the Lorentz reciprocal theorem of slow viscous flow as a thermodynamic theorem and shows that it is a special case of the more general (and powerful) reciprocal theorem of non-equilibrium thermodynamics due to Onsager, applied at the global (as opposed to local) level. The point is illustrated with two simple problems in viscous flow theory.

Nomenclature

a = particle radius
A = area of control surface or cross-sectional area of tube
C = conductance coefficient
e = specific internal energy
F = force on moving plate or particle
h = distance between plates
n = number of particles per unit length
$p, (\hat{p})$ = hydrostatic pressure (modified pressure, Eq. (23))
p_{ij} = stress tensor
P_{ij} = surface traction tensor
$q(Q)$ = local (global) heat flow rate
r_0 = tube radius
R = resistance coefficient
s = specific entropy
$T, (T_0)$ = temperature (reference temperature)
u = fluid velocity
U = velocity of moving plate or particle
u_j = velocity vector
v = Specific volume
V = volume flow rate
W = work rate
α = induction coefficient
λ = fluid thermal conductivity
μ = fluid viscosity
ρ = fluid density
$\theta, (\Theta)$ = Local (global) entropy generation rate

The Lorentz theorem

In 1907, H. A. Lorentz proved a reciprocal theorem for incompressible, isothermal, steady-state, slow (negligible inertia), viscous (Newtonian) flow [6]. The Lorentz theorem and its applications are discussed extensively in references [3] and [5]. The theorem involves the surface tractions (P_{ij}) acting on a control volume in such a flow, and the rate at which these tractions do work (W), where

$$P_{ij} = -p\delta_{ij} + p_{ij}, \tag{1}$$

with p the hydrostatic pressure, p_{ij} the stress tensor, and δ_{ij} the Kronecker delta, and

$$W = \int_A P_{ij} u_j n_i \, \mathrm{d}A, \tag{2}$$

with u_j the fluid velocity, n_i the unit outward normal vector, and A the control surface. Lorentz considered any two such flows (I and II) passing through the same control volume, and proved that the work rate by the tractions of flow I acting on the velocities of flow II is equal to the work rate by the tractions of flow II acting on the velocities of flow I. Since the system is dissipative (non-conservative), Lorentz's theorem is not merely the Maxwell reciprocal theorem of elasticity extended to viscous flow. Nor is it identical to the Helmholtz theorem, which is applicable to the same type of flow (incompressible, isothermal, steady-state, slow), and states that in such flows the correct velocity distribution among all those that satisfy continuity is the one for which the dissipation rate is the least; i.e., the entropy generation rate is a minimum. Since it can be shown that this flow is also the only one that satisfies momentum conservation, the Helmholtz theorem is equivalent to the momentum principle.

The Onsager theorem

Dissipative flows in the laminar regime lie within the domain governed by the macroscopic Onsager reciprocal theorem of non-equilibrium thermodynamics [2], which dates back to 1931. To apply this theorem the appropriate set of conjugate forces and fluxes must be identified, the products of which add up to the dissipation rate in the given steady-state flow process. The theorem, which asserts that the matrix of the coefficients that couple the forces and the fluxes (non-conjugate as well as conjugate) must be symmetric, can be applied *locally* (i.e., at a point in the flow) or *globally* (i.e., to a finite size control volume).

Consider, for example, the type of flow described above, except that the temperature is allowed to vary. At the *local* level, the conservation laws for momentum (neglecting inertia), energy, and entropy can be written as follows:

$$-\frac{\partial p}{\partial x_j} + \frac{\partial p_{ij}}{\partial x_i} = 0, \tag{3}$$

$$-\frac{\partial q_i}{\partial x_i} + p_{ij}\frac{\partial u_j}{\partial x_i} = \rho u_i \frac{\partial e}{\partial x_i}. \tag{4}$$

$$-\frac{\partial}{\partial x_i}\left(\frac{q_i}{T}\right)+\theta=\rho u_i\frac{\partial s}{\partial x_i}, \tag{5}$$

where q_i is the heat flux vector, T the temperature, ρ the density, e the specific internal energy, s the specific entropy, and θ the entropy generation rate. Also applicable is the Gibbs equation, which in Lagrangian form can be written

$$T\,\mathrm{d}s=\mathrm{d}e+p\,\mathrm{d}v \tag{6}$$

with v the specific volume, and in Eulerian form

$$\rho T\left(u_i\frac{\partial s}{\partial x_i}\right)=\rho\left(u_i\frac{\partial e}{\partial x_i}\right)+p\frac{\partial u_i}{\partial x_i}, \tag{7}$$

The last term is zero since the fluid is incompressible. Combining equations (4) and (5) and observing equation (7) we obtain

$$T\theta=p_{ij}\left(\frac{\partial u_j}{\partial x_i}\right)-q_i\left(\frac{1}{T}\frac{\partial T}{\partial x_i}\right) \tag{8}$$

for the local dissipation rate based on the local temperature. In this bi-linear form the first term of each product is the "flux" and the second term the "force". In the first product the force and flux are of second tensorial rank, and in the second product they are of first tensorial rank. Curie's theorem prohibits cross (non-conjugate) coupling between force-flux pairs that differ in tensorial rank by one. Thus the phenomenological equations are the conjugate coupling equations:

$$p_{ij}=\mu\left(\frac{\partial u_i}{\partial x_j}+\frac{\partial u_j}{\partial x_i}\right) \tag{9}$$

which is recognized as Newton's law of viscous friction, and

$$q_i=-\lambda T\left(\frac{1}{T}\frac{\partial T}{\partial x_i}\right) \tag{10}$$

which is recognized as Fourier's law of heat conduction. Of course, μ and λ are the viscosity and thermal conductivity respectively.

This is as far as non-equilibrium thermodynamics can take us when applied locally. However, when applied globally to a specific flow configuration, useful results can be obtained. We will consider two such problems.

The Poiseuille-Couette flow problem

Consider two-dimensional fully developed flow between two horizontal, infinitely wide parallel plates. One plate is fixed and the other moves with a velocity U, and both are maintained at the same temperature (T_0). Substitution of equations (9) and (10) into equation (8) leads to

$$T\theta = \mu\left(\frac{\mathrm{d}u}{\mathrm{d}y}\right)^2 + \frac{\lambda}{T}\left(\frac{\mathrm{d}T}{\mathrm{d}y}\right)^2 \tag{11}$$

and substitution of equations (9) and (10) into equation (4) (noting that the convected energy term is zero for fully developed flow) leads to

$$\lambda\frac{\mathrm{d}^2T}{\mathrm{d}y^2} + \mu\left(\frac{\mathrm{d}u}{\mathrm{d}y}\right)^2 = 0. \tag{12}$$

Eliminating the velocity gradient term between equations (11) and (12) we obtain

$$\theta = -\frac{\mathrm{d}}{\mathrm{d}y}\left(\frac{\lambda}{T}\frac{\mathrm{d}T}{\mathrm{d}y}\right) \tag{13}$$

for the local entropy generation rate. The global entropy generation rate (per unit plate length) defined by

$$\Theta = \int_0^h \theta\,\mathrm{d}y \tag{14}$$

thus becomes

$$\Theta = -\frac{Q}{T_0}, \tag{15}$$

with Q the net heat flow from the plates to the fluid between them (actually a negative value).

Now applying the first law of thermodynamics to this global control volume, we obtain

$$Q - UF = -V\Delta p, \tag{16}$$

where F is the force exerted by the fluid on the moving plate (per unit plate length), V is the volume flow rate of fluid, and Δp is the pressure drop per unit length of plate. Substitution of equation (16) into equation (15) leads to the global dissipation rate

$$T_0\Theta = V\Delta p - UF \tag{17}$$

based on the temperature T_0. Viewing the device as a viscous engine, equation (17) expresses the fact that the dissipation rate is the difference between the maximum power output (power input) and the actual power output. Curie's theorem no longer prohibits cross-coupling, so we expect in the near-equilibrium (laminar) regime

$$F = \alpha\Delta p - RU, \tag{18}$$

$$V = C\Delta p + \alpha U, \tag{19}$$

where the fact that the coefficient of Δp in equation (18) is the same as the coefficient of U in (19) is the result of Onsager's reciprocal theorem [7].

It is easy to show that $\alpha = h/2$, $R = \mu/h$, and $C = h^3/(12\mu)$, where h is the distance between the plates. Equations (18) and (19) imply the following reciprocal relation:

$$\left(\frac{F}{\Delta p}\right)_{U=0} = \left(\frac{V}{U}\right)_{\Delta p=0} \tag{20}$$

We will now show that equation (20), which was derived directly from Onsager's theorem, can also be derived directly from Lorentz's theorem. The Lorentz theorem will be applied to the control volume described above (a unit length of the two-dimensional flow field between the infinite plates, one fixed and the other moving, separated by the distance h). Let the two flows through the control volume necessary to formulate Lorentz's theorem be: (I) Poiseuille flow ($U = 0$), and (II) Couette flow ($\Delta p = 0$). Equation (2) written for the forces of flow I and the velocities of flow II becomes

$$W_{\mathrm{I,II}} = (\Delta p)^{\mathrm{I}}V^{\mathrm{II}} - F^{\mathrm{I}}U^{\mathrm{II}} \tag{21}$$

and for the forces of flow II and the velocities of flow I

$$W_{\mathrm{II,I}} = 0. \tag{22}$$

Equating equations (21) and (22), as required by the Lorentz theorem, we obtain the reciprocal relation of equation (20), previously derived from the Onsager theorem.

The particle-in-a-tube problem

As a further demonstration that for slow viscous flow the Lorentz and Onsager theorems are equivalent, consider the motion of a small spherical particle on the centerline of a vertical round tube containing a flowing viscous liquid. Defining a modified pressure ($\hat{p}$) by

$$\hat{p} = p + \rho g z, \tag{23}$$

where g is the acceleration of gravity, and z the elevation, it is evident that if the fluid is not moving and there are no particles on the tube centerline, $\hat{p}$ is constant with z.

Expressing the global dissipation as the difference between the power input (the net force on the particles times their velocity) and the power output (the volume flow rate times the pressure drop) we can write

$$T_0\Theta = U(nF) - V\Delta\hat{p}, \tag{24}$$

where U is the velocity of the particles, F the net force on a particle (weight less buoyancy), n the number of particles per unit length of tube, V the volume flow rate of fluid, and $\Delta\hat{p}$ the modified pressure rise down the tube per unit length. By Onsager's theorem we expect

$$\Delta\hat{p} = \alpha(nF) - RV, \tag{25}$$

$$U = C(nF) + \alpha V, \tag{26}$$

which implies the following reciprocal relation

$$\left(\frac{\Delta\hat{p}}{nF}\right)_{V=0} = \left(\frac{U}{V}\right)_{F=0}. \tag{27}$$

If we recognize that "no particle on the centerline" is equivalent to $F = 0$ in (25) and (26), it is easy to show that $R = 8\mu/Ar_0^2$, with A the cross-sectional area of the tube and r_0 the tube radius, and that $\alpha = 2/A$. Furthermore, with $V = 0$ in (25) and (26), Stoke's law gives $nC = 1/6\pi a\mu$, with a the radius of the particle ($a \ll r_0$). The fact that

$$(\Delta\hat{p})_{V=0} = \frac{2}{A}(nF) \tag{28}$$

is not easily demonstrated and is presented here as a consequence of Onsager's theorem. Eq. (28) has been confirmed [4] by a detailed (and complicated) analysis of the flow field, and has also been shown to be true by an application of the Lorentz theorem [1, 3].

The reciprocal relation given by equation (27) can be most easily derived from Lorentz's theorem if we let flow I correspond to "no flow in the tube" ($V = 0$), and flow II to "no particle on the centerline" ($F = 0$). Then

$$W_{\mathrm{I,II}} = (nF)^{\mathrm{I}} U^{\mathrm{II}} - (\Delta\hat{p})^{\mathrm{I}} V^{\mathrm{II}} \tag{29}$$

and

$$W_{\mathrm{II,I}} = 0 \tag{30}$$

from which the reciprocal relation of equation (27) follows. Note that from equation (25)

$$\Delta\hat{p} - (\Delta\hat{p})_{F=0} = \alpha n F \tag{31}$$

or

$$\frac{\Delta\hat{p} - (\Delta\hat{p})_{F=0}}{F} = \frac{2n}{A} \tag{32}$$

which, in words, says that the difference in the pressure drop in a tube *without* particles on the centerline and the pressure drop *with* particles on the centerline multiplied by the tube cross-sectional area is equal to *twice* the force on the particles in the tube. In deriving this result from the Lorentz theorem in reference [1], the authors comment that for this problem the Lorentz theorem produces "Onsager-like reciprocal relations", which appears to be as close as anyone has come before to recognizing the connection between the Lorentz and Onsager theorems.

References

1. Bungay, P., and Brenner, H., Pressure drop due to the motion of a sphere near the wall bounding a Poiseuille flow, *J. Fluid Mech.* 60 (1973) 81–96.
2. DeGroot, S.R., and Mazur, P., *Non-equilibrium thermodynamics*, New York, Dover Publications (1984), pp. 35–41.
3. Happel, J. and Brenner, H., *Low Reynolds number hydrodynamics with special applications to particular media*, Norwell MA, Martinus Nijhoff (1983), pp. 90–91.
4. Happel, J. and Byrne, B.J., Motion of a sphere and fluid in a cylindrical tube, *Indust. Engng. Chem.* 46 (1954) 1181–1186.
5. Kim, S., and Karrila, S.J., *Microhydrodynamics: Principles and selected applications*, Boston, Butterworth-Heinemann, (1991).
6. Lorentz, H.A., *Abhandl. Theoret. Phys.* 1 (1907) 23–42.
7. Osterle, J.F., A unified treatment of steady-state energy conversion. *Appl. Sci. Res.* 12 (1964) 425–434.

Applied Scientific Research **49**: 377–378, 1992.

Reviewers of *Applied Scientific Research*, 1991–1992

The essence of ensuring the quality of scientific publications lies in the peer-reviewing system. Such systems can work only when scientists spend some of their valuable time in the scrutinizing of papers of their colleagues. It is satisfying to be able to conclude that the majority of scientists are still willing to do so.

To give tribute to all the scientists who unselfishly have given their time to reviewing papers for *Applied Scientific Research*, and also to draw them somewhat out of the anonymity of their important work, we publish overleaf a list of their names.

F.T.M. NIEUWSTADT
Editor-in-chief

List of reviewers, 1991–1992

R.J. Adrian
A. Alkemade
D. Angirasa
S. Arefi
M. Ayrault
F.B. Barends
G. Bart
J.A. Battjes
K. Bauckhage
J. Bear
W. Bechteler
H. Beer
J. Berghmans
A. Biesheuvel
R.B. Bird
J.P. Boon
H. Bos
B.I.M. ten Bosch
J.F. Brady
G.J. de Bruin
B.H.A.A. van den Brule
S.G. Bryce
P. Buchhave
H. Buggisch
K. Bütefisch
A. Cedenese
A. Chavez
A.K. Chesters
K.S. Choi
R. Clift
G.W. Colenbrander
H. Cornelisse
H.A. Dijkstra
M. Dingemans
T. Dracos
G.B. Eaton
P. Elands
R. Fernandez Luque
A.A.M. Flaman
J.B. Flor
D. Frenkel
C.W.M. van der Geld
J.H.M. Gooden
W.C.M. Gorissen
I. Grant
C. Gray
C.A. Greated
P. Guibert
G.S. Hanumanth
J. Hart
H.J. Hasenack
G.J.F. van Heijst
R.A.W.M. Henkes
A.J. Hermans
H. Hinsch
N. Hirschberg
H.W.M. Hoeymakers
C.J. Hoogendoorn
H.W. Hoogstraten
M. Hulsen
J.C.R. Hunt
J.L. van Ingen
A.I. Isayev
W.M.C. de Jonge
D.D. Joseph
T. Kambe
K.R. Kirchartz
H. Kolkman
J. Kompenhans
G.D.C. Kuiken
H.K. Kuiken
G. Lebon
M.A. Leschziner
L. Lourenco
C.H.M. Machielsen
W. Merzkirch
R. Meynart
C.S. Moraitis
A. Muller
A. Nakayama
H. Nieswaag
K. Oduyemi
R.V.A. Oliemans
G. Ooms
A. Otter
H. Pascal
T.W.J. Peeters
J.M. Perales
R.J. Perkins
J.K. Platten
S.B. Pope
G. Rehbinder
W. Rodi
H. Royer
G. Schouten
H.A. Siller
F.I.P. Smith
A.A. Steenhoven
J. Stefanini
J.A. Steketee
T.L. van Stijn
L. van den Tempel
T. Ueno
R. Uittenbogaard
P. Vasseur
A.E.P. Veldman
A. Verruyt
G.Ph. Vledder
P. Voke
J. Vos
J. van der Vosse
J.P.B. Vreeburg
C.B. Vreugdenhil
C.Y. Wang
B. Weignand
R. van der Welle
J. Westerweel
J.P.P.M. v.d. Zanden
M.M. Zdravkovich

Euromech Meetings in 1993 and 1994

The European Mechanics Council has overall responsibility for Euromech Colloquia and Euromech Conferences. The latter presently comprise the European Solid Mechanics Conference, the European Fluid Mechanics Conference, the European Turbulence Conference and the European Nonlinear Oscillations Conference. General information about Colloquia and Conferences can be obtained from the Secretary of the European Mechanics Council, Prof. B. Lundberg, Department of Mechanical Engineering, Luleå University of Technology, S-951 87 Luleå, Sweden before November 1992, and the Department of Technology, School of Engineering, Uppsala University, Box 534, S-751 21 Uppsala, Sweden.

Euromech Colloquia

These are informal meetings on specialized research topics. Participation is restricted to a small number of European research workers actively engaged in the field of each Colloquium. The organization of each Colloquium, including the selection of participants for invitation, is entrusted to a Chairman. Proceedings are not normally published. Those who are interested in taking part in a Colloquium should write to the appropriate Chairman. Information about **Euromech Colloquia in 1994** will be available in June 1993. Euromech Number, Title, Chairmen, Dates and Location for the **Euromech Colloquia in 1993** are given below.

290. *Mechanics of swelling*
Prof. T. K. Karalis, Democritos University of Thrace, 67100 Xanthi, Greece
Prof. A. Silberberg, Rehovot, and Prof. D. Barthes-Biesel, Compiègne
23–27 August 1993, Rhodos, Greece

299. *Impact damage in composites*
Dr C. Ruiz, UTC for Solid Mechanics, Department of Engineering Science, Oxford University, Parks Road, Oxford OX1 3PJ, England
Dr J. Harding, Oxford
24–26 March 1993, Oxford, England

300. *Interaction between vorticity fields and boundaries*
Prof. C. R. Kaykayoglu, Istanbul Technical University, Faculty of Aeronautics and Astronautics, Maslak 80626, Istanbul, Turkey
Prof. J. M. R. Graham, London
27–30 September 1993, Istanbul, Turkey

301. *Rheology of complex fluids: Food processing and similar applications*
Prof. M. Lebouché, LEMTA - Université de Nancy I, BP 160, F-54504 Vandoeuvre-lès-Nancy Cédex, France
25–27 May 1993, Nancy, France

302. *Spectral analysis of complex structures*
Prof. E. Sanchez-Palencia, Laboratoire de Modelisation en Mécanique, Université Pierre et Marie Curie, Tour 66 - Case 162, F-75252 Paris Cédex 05, France
12–14 May 1993, Paris, France

303. *Influence of microstructure on the constitutive equations of solids*
Prof. O. B. Naimark, Institute of the Mechanics of Continuous Media of the Russian Academy of Sciences, 1 Akad. Korolev Str., 614061 Perm, Russia
Prof. K. P. Herrmann, Paderborn
1–5 June 1993, Perm (on ship on the Kama and Volga rivers), Russia

304. *Mechanics of microstructured materials*
Dr W. J. Stronge, Department of Engineering, University of Cambridge, Trumpington Street, Cambridge CB2 1PZ, England
28–30 June 1993, Cambridge, England

305. *The dynamics and geometry of vortical structures*
P. Orlandi, Dipartimento di Meccanica e Aeronautica, Via Eudossiana 16, I-00184 Rome, Italy
Prof. E. J. Hopfinger, Grenoble
28 June - 4 July 1993, Cortona, Italy

306. *Mechanics of contact impact*
Dr M. Okrouhlik, Institute of Thermomechanics, Czechoslovak Academy of Sciences, Dolejskova 5, 18200 Prague 8, Czechoslovakia
Dr I. Hunek, Prague
7–9 September 1993, Prague, Czechoslovakia

307. *Walking machines*
Prof. M. Frik, Department of Mechanical Engineering, Institute of Engineering Mechanics, University of Duisburg, Lotharstraße 1, D-4100 Duisburg, Germany
Prof. F. Pfeiffer, Munich
8–10 September 1993, Duisburg, Germany

308. *Chaos and noise in dynamical systems*
Prof. T. Kapitaniak, Division of Control and Dynamics, Technical

University of Lódz, Stefanowskiego 1/15, 90-924 Lódz, Poland
Dr J. Brindley, Leeds
20–25 September 1993, Lódz, Poland

309. *Optical flow diagnostics*
Dr K. A. Bütefisch, DLR Institute for Experimental Fluid Mechanics, Bunsenstraße 10, D-3400 Göttingen, Germany
Dr J. R. Bonnet, Poitiers and Dr W. H. Beck, Göttingen
28 September – 1 October 1993, Göttingen, Germany

310. *Sediment transport mechanisms in coastal environments and rivers*
Prof. M. M. Belorgey, Laboraotoire de Mécanique des Fluides, Université du Havre, Quai Frissard BP 265, F-76055 Le Havre Cédex, France
Dr J. F. A. Sleath, Cambridge
13–17 September 1993, Le Havre, France

311. *Blood-wall interaction*
Prof. K. Affeld, Universitätsklinikum Rudolf Virchow, Spandauer Damm 130, D-1000 Berlin 19, Germany
18–21 October 1993, Berlin, Germany

312. *Turbulence and vortices in hypersonic flows*
Dr F.-R. Grosche, DLR Institute for Experimental Fluid Mechanics, Bunsenstraße 10, D-3400 Göttingen, Germany
5–7 October 1993, Göttingen, Germany

313. *CFD in turbomachinery and experimental validation*
Prof. J. L. Kueny, CREMHyG, BP 95, F-38402 Saint Martin d'Hères, France
Prof. F. Leboeuf, Ecully
9–10 December 1993, Val d'Isére (Rhones Alpes), France

314. *Effectiveness of shell-theory formulations for numerical solutions*
Prof. E. L. Axelrad, Universität der Bundeswehr München, W.-Heisenberg-Weg 39, D-8014 Neubiberg, Germany
Prof. F. A. Emmerling, Neubiberg
14–18 September 1993, Munich-Neubiberg, Germany

Euromech Conferences

These are broad in scientific scope. They are open to all those interested and are expected to have a number of participants between 150 and 600. The general purpose is to provide opportunities for scientists and engineers from all parts of Europe to meet and discuss current research. The responsibility for each series of Conferences is delegated to a Standing Committee. The detailed organizational work is carried out by Local Organizing Committees (LOC). Those who are interested in taking part in one of the Conferences should write to the Chairman or Secretary of the appropriate LOC. Some information about the **Euromech Conferences in 1993 and 1994** is given below.

1st European Nonlinear Oscillations Conference
Prof. E. Kreuzer, Meerestechnik II, Technische Universität Hamburg-Harburg, Eißendorfer Straße 42, D-2100 Hamburg 90, Germany
16–20 August 1993, Hamburg, Germany

5th European Turbulence Conference
Prof. R. Benzi, Rome
Summer 1994, Italy

2nd European Solid Mechanics Conference
Prof. A. del Grosso, Istituto di Scienza delle Construzioni, Università di Genova, Via Montallegro 1, I-16145 Genova, Italy
12–16 September 1994, Genova, Italy

2nd European Fluid Mechanics Conference
Prof. H. Zorski, Institute of Fundamental Technological Research, Polish Academy of Sciences, Sweitokrzyska 21, 00-049 Warsaw, Poland
Prof. J. S. Ostrowski, Institute of Aeronautics and Applied Mechanics, Warsaw University of Technology, Nowowiejska 22/24, 00-665 Warsaw, Poland
19–23 September 1994, Cracow, Poland

The 'KLUWER' LaTeX Style File:

Instructions for Authors

Basic Instructions

A. Author 1 and B. Author 2[*]
The Institute and its Address of
Authors 1 and 2.

and

C. Author 3
Institute of Author 3[†]

Abstract. This document is a printout of the file KAPINS02.TEX and it describes in some detail the use of the **KLUWER** style file (version 1.02) for the preparation of articles to be submitted to journals or edited volumes published by Kluwer Academic Publishers. The **KLUWER** style file is very similar to the **ARTICLE** style sheet of LaTeX.

Key words: LaTeX, KLUWER Style File, Authors' Instructions

1 Introduction

The KLUWER style file is the general style file that should be used when submitting an article in LaTeX format for publication in one of the journals of Wolters Kluwer Academic Publishers. Please note that the layout generated by the KLUWER style file will deviate from the style of the journal in which your article will be published. The article will be formatted in the appropriate journal style by Kluwer in a later stage. In this stage, the copyright information will be added, the running heads will be adapted if necessary and the article will be typeset in the Times New Roman font.

In general, you should use standard LaTeX commands as much as possible. Only create your own macros when absolutely necessary and *always* put them in the preamble.

2 To Start

The KLUWER style file is addressed by using the command:

`\documentstyle{kluwer}`. The file `KLUWER.STY` should be accessible for LaTeX.

---

[*] On leave from his original institute.

[†] Affiliated to WKAP, Dordrecht.

3 The 'Opening' Environment

The title, subtitle, author names and institutes and the date are handled by the **opening** environment in the preamble. Its structure is as follows:

```
\begin{opening}
\title{The Title of the Article}
\subtitle{If There Is Any}
\author{Author's Name}
\institute{Institute and/or its Address}
\date{}
\end{opening} \begin{document}
```

3.1 Title and Subtitle

The title and, if necessary, subtitle should be typed in one of the following styles:

`\title{This is my title}`, one initial capital;
`\title{This Is My Title}`, initial capitals for every main word;
`\title{THIS IS MY TITLE}`, only capitals;

according to the style of the journal in which your article is to be published.

The `\subtitle` command may be omitted. A missing `\title` command generates an error message.

You can split the title and subtitle by putting two backslashes at an appropriate place. However, if you do this for the title, you *must* use the `\runningtitle` command to create the running title. Otherwise you will get an error message. The `\runningtitle` command should be inserted in the preamble, before the `\begin{opening}` command.

```
\title{The 'KLUWER' LaTeX Style File: backslashbackslash Instructions
for Authors}
\subtitle{Basic Instructions}
```

have generated the title and subtitle of these instructions. The running title has been produced by putting

```
\runningtitle{THE KLUWER STYLE FILE}
```

in the preamble.

3.2 Author Names and Institute Addresses

For each author's name the `\author` command should be used:

`\author{A. Author 1}`
`\author{B. Author 2}` etcetera.

The names should be written in Initial Capitals and lowercase. The affiliation of authors is generated by the `\institute` command:

```
\institute{The Institute and its Address}
```

Two backslashes can be used within the `\institute` command to split the affiliation at an appropriate place.

If there is more than one author at the same institute, you should first use the `\author` command for each author and then use the `\institute` command.

A second institute's name to the same author can be handled through the `\thanks` command. For these instructions the following sequence of commands was used:

```
\author{A. Author 1}
\author{B. Author 2\thanks{On leave from his original institute.}}
\institute{The Institute and its Address of \\ Authors 1 and 2.}
\author{C. Author 3}
\institute{Institute of Author 3\thanks{Affiliated to WKAP,
Dordrecht.}}
```

3.3 DATE

The `\date` command gives you the possibility of entering the date (or text) yourself at the beginning of your article. If you do not wish to insert a date, you can enter an 'empty' `\date{}` command. If you omit the `\date` command, LaTeX will generate the current date automatically.

4 Running Heads

If the `\title` of your article is longer than 60 characters, the running head will be omitted in the printout. You can make your own running title by using the `\runningtitle{}` command, where you put the shorter title between the curly braces. The `\runningtitle{}` command should be put in the preamble, before the `\begin{opening}` command.

You can also use the `\runningauthor{}` command. but in general this will not be necessary because this will be added by the publishers in the appropriate style.

5 The Abstract Environment

This environment is standard LaTeX. It prints the abstract in a smaller font than the body text. You need not enter the word 'Abstract'.

5.1 KEYWORDS

Key words are printed at the end of an abstract. The `\keywords` command should be used within the **abstract** environment, but after the text of the abstract. For example,

```
\keywords \LaTeX, KLUWER Style File, Authors' Instructions
```

resulted in the key word line at the beginning of these instructions. Please, use a comma to separate the keywords.

6 Sections, Subsections and Subsubsections

A section starts with the command: `\section{The Title of This Section}`. If the (sub-)section title is too long, you can break it at an appropriate place by using `\protect\\`. (The two \\'s only do not work here).

For the section, (sub)subsection titles you are kindly requested to use either Initial Capitals for every main word (see section headings of this article), or one Initial capital and the rest in lower case, or only capitals, according to the style of the journal in which your article will be published. When in doubt, do *not* use capitals only.

7 Figures and Tables

7.1 FIGURES

The `figure` environment produces space and a figure caption in the text. Th numbering of figures is automatic.

```
\begin{figure}
\vspace{5cm} % Amount of vertical space needed
\caption{Caption Text.}
\end{figure}
```

The **KLUWER** style file puts figures wherever possible on the top of the page. This may not always work, in which case you need to be a little creative and consult the LaTeX manual.

*7.1.1 Labeling of Figures*It may be convenient to label the figures in case you have to insert another figure later. The following can be done:

```
\begin{figure}
\vspace{5cm} % Amount of vertical space needed
\caption{Caption Text.}\label{short name}
\end{figure}
```

In the text you can use the `\ref` or `\pageref` command, e.g.: `...can be seen in Fig.~\ref{short name}.`

7.2 TABLES

Tables can be generated in several environments for which we kindly advise you to refer to the LaTeX manual. An example of the convenient `tabular` environment for simple tables follows.

```
\begin{table}[h]
\caption{Caption text.}
\begin{center}
\begin{tabular}{lll}\hline
Description 1 & Description 2 & Description 3\\
\hline\\
Row 1, Col 1 & Row 1, Col 2 & Row 1, Col 3 \\
Row 2, Col 1 & Row 2, Col 2 & Row 2, Col 3 \\
\hlino \end{tabular}
\end{center}
\end{table}
```

This produces:

TABLE I
Caption text.

Description 1	Description 2	Description 3
Row 1, Col 1	Row 1, Col 2	Row 1, Col 3
Row 2, Col 1	Row 2, Col 2	Row 2, Col 3

We wish to avoid using both vertical rules between columns and horizontal rules between rows. You should, however, always use the following three horizontal rules: a top rule, a middle rule and a bottom rule.

*7.2.1 Positioning of Tables*The position of a table in the text may not always be appropriate. As with figures, the style file tries to put it wherever possible on the top of the page. On some occasions you may wish to put it at one particular spot in the text. The option `[h]` can then be used: `\begin{table}[h]`

It is acknowledged that positioning of figures and tables is by no means straightforward.

8 Acknowledgements

Acknowledgements can be given by using the `\acknowledgements` command. The text for this item can start on the same line as the command.

9 Appendices

An Appendix can be generated by using the `\appendix` command, followed by a `\section` command. This results in a Roman numbered Appendix section.

10 References

Vhen you use BiBTeX for your references, we kindly refer you to Section 10.3 elow.

References are inserted in the `thebibliography` environment. We distinguish wo styles of References lists: alphabetically sorted (explained below in Secion 10.1) and numbered (explained in Section 10.2). You can select one of these tyles by including the appropriate document style option in the `\documentstyle` ommand. If no documentstyle option is included, the references will be sorted lphabetically.

10.1 ALPHABETICALLY SORTED REFERENCES

For alphabetically sorted references one should include the document style option `[namedreferences]` in the command:

```
\documentstyle[namedreferences]{kluwer}.
```

Every `\bibitem` in the `thebibliography` environment should have a `\citeauthoryear` command as an option and a key to be referred to. The `\citeauthoryear` should have two arguments: the author's name(s) and the year. The `\citeauthoryear` should be preceded by a `\protect` and in case of more than two authors the argument with the author's name(s) should contain the first author's name with an *et al.*, e.g.:

```
\bibitem[\protect\citeauthoryear{authorname(s)}{year}]{key}.
```

The first part of your References section could like this:

`\begin{thebibliography}{}` % Note the empty pair of curly braces!

```
\bibitem{[\protect\citeauthoryear{Smith {\it et
al.}}{1992}]}{Smith92}
Smith, I.N., Johnes, R.S. and Hines, W.P.:  1992, 'Title of the
Article', {\it Journal Title in Italics}{\bf Vol. no. X}, pp. 00--00
```

The following `\cite` commands can now be used in your article: `\cite`, `\shortcite`, `\citeauthor` and `\citeyear`. For the sample `\bibitem` above, the four `cite` commands would generate the following reference in your text:

`\cite{Smith92}`	generates: (Smith *et al.*, 1992)
`\shortcite{Smith92}`	generates: (1992)
`\citeauthor{Smith92}`	generates: Smith *et al.*
`\citeyear{Smith92}`	generates: 1992

With these commands or combinations of them you can create any reference in your text according to the references style of the journal in which your article is to be published.

You must do the formatting of the bibitems yourself. For the layout conventions we kindly refer you to the authors instructions of the journal in which your article is to be published.

10.2 NUMBERED REFERENCES

For numbered references one should include the documentstyle option `[numreferences]` in the command:

`\documentstyle[numreferences]{kluwer}`.

You should start the **thebibliography** environment with the command:

`\begin{thebibliography}{99}`

The second pair of curly braces should contain a number that corresponds with the widest number in the reference list below.

You should label every `\bibitem` by putting a key between the curly braces, e.g.: `\bibitem{Smith91}`. In your article you can refer to this `\bibitem` with `\cite{Smith91}`.

The `\cite` command will produce the number of the reference in square brackets, e.g. [2]. The `\shortcite`, `\citeauthor` and `\citeyear` commands as mentioned in Section 10.1 can also be used but they will produce the same output as `\cite`.

You must do the formatting of the bibitems yourself. For the layout conventions we kindly refer you to the authors instructions of the journal in which your article is to be published.

10.3 BIBTEX

You may use BIBTEX. But if you do so, please be sure that you send all the necessary files with the LATEX source file, i.e. the **bbl** file. We kindly refer you to the LATEX manual for its use.

11 Information

The **KLUWER** style file is available from:

KLUWER ACADEMIC PUBLISHERS
P.O. Box 17, 3300 AA Dordrecht, The Netherlands
email: SURF406@KUB.NL (Attn. of Editorial Automation Dept.) / Fax: 31-78 334254

If you encounter problems, or if you have suggestions for improving the **KLUWER** style file or these instructions, we would appreciate hearing from you.

Entropy and Energy Dissipation in Water Resources

edited by **V. P. Singh, M. Fiorentino**

WATER SCIENCE AND TECHNOLOGY LIBRARY 9

This book contains a selection of papers arising from an international conference, held in Maratea (Italy), June 26–28, 1991. It comprises six sections encompassing a range of the major aspects of entropy-based developments in water resources. Each section normally starts with an invited, state-of-the-art paper, followed by contributed papers.

Section 1 presents a discussion on the perspectives of entropy and energy dissipation. The applications of entropy in hydrology are considered in Section 2, water resources in Section 3, and hydraulics in Section 4. Sections 5 and 6 deal with the applications of energy principles in, respectively, hydrology and hydraulics.

This book will interest researchers as well as those engaged in civil engineering, agricultural engineering, environmental engineering, hydrology, water resources, earth resources, forestry, geography and climatology. Graduate students, as well as those wishing to conduct research on entropy or its applications, will find this book to be of particular significance.

Contents

Preface. **Section 1:** Perspectives on Entropy and Energy Dissipation. **Section 2:** Application of Entropy in Hydrology. **Section 3:** Application of Entropy in Water Resources. **Section 4:** Application of Entropy in Hydraulics. **Section 5:** Application of Energy Principles in Hydrology. **Section 6:** Application of Energy Principles in Hydraulics.

1992, 608 pp. ISBN 0–7923–1696–7
Hardbound $172.00/Dfl. 295.00/£99.00

P.O. Box 322, 3300 AH Dordrecht, The Netherlands
P.O. Box 358, Accord Station, Hingham, MA 02018-0358, U.S.A.

New
Publication

**KLUWER
ACADEMIC
PUBLISHERS**

Applied Scientific Research

Author index, Volume 49 (1992)

Adrian, R.J., 191
Al Bedoor, B.O., 101
Andersson, H.I., 117
Angirasa, D., 135
Aparecido, J.B., 355
Barron, R.M., 345
Bauer, H.F., 283
Bessem, J.M., 245
Coene, R., 175
Coker, A.K., 67
Cotta, R.M., 355
Dalziel, S.B., 217
Elkouh, A.F., 147
Fusegi, T., 271
Govindarajulu, T., 83
Gulwadi, S.D., 147
Hamdan, M.H., 345
Hamdan, M.N., 101
Hassanien, I.A., 335
Hoefsloot, H.C.J., 161
Hoogstraten, H.W., 161
Hua, T.Q., 49
Hyun, J.M., 271
Jagannadham, M., 135
Janke, G., 261
Janssen, L.P.B.M., 161
Jeffreys, G.V., 67
Jubran, B.A., 101
Keane, R.D., 191
Knobbe, J.W., 161
Knoester, H., 307
Kuwahara, K., 271
Moon, T.J., 49
Moorthy, M.B.K., 83
Mumford, C.J., 67
Nieuwstadt, F.T.M., 189, 245
Osterle, F., 369
Perkins, R.J., 261
Picologlou, B.F., 49
Rao, V.D., 31
Saibabu, J., 31
Sarma, P.K., 31
Siller, H.A., 261
Stapountzis, H., 217
Subba Reddi, K., 135
Takhar, H.S., 1
Thomas, T.G., 1
Tiseth, K.L., 117
Tupholme, G.E., 91
Van der Zanden, J., 307
Walker, J.S., 49
Westendorp, A., 245
Westerweel, J., 245

Fluid Sealing

edited by **B. Nau**

FLUID MECHANICS AND ITS APPLICATIONS 8

This volume presents the edited Proceedings of the 13th International Conference on Fluid Sealing held in Brugge, 7–9 April, 1992. The overall theme of the contributions is the improvement of sealing reliability and effectiveness.
Emission control is a critical function in plant, equipment, machinery and transportation systems. Increasingly it is becoming the focus of legislation to control environmental contamination. Engineering managers should therefore become fully conversant with the latest technology for ensuring seal reliability. The contributions collated in this volume describe developments and insight into the application of the best available seal technology.
The papers are arranged in the main categories of lip seals, static seals, mechanical seal research, mechanical seal application and performance, mechanical seal qualification, value emissions and clearance seals, materials and thermal science, fluid power and packings.
For mechanical, production, civil and safety engineers.

Contents
Lip Seals. Static Seals. Mechanical Seal Research. Mechanical Seal Application and Performance. Mechanical Seal Qualification. Valve Emissions and Clearance Seals. Materials and Thermal. Fluid Power. Packings. Index.

1992, 675 pp. ISBN 0–7923–1669–X
Hardbound $199.00/Dfl. 335.00/£116.00

P.O. Box 322, 3300 AH Dordrecht, The Netherlands
P.O. Box 358, Accord Station, Hingham, MA 02018-0358, U.S.A.

New
Publication

KLUWER
ACADEMIC
PUBLISHERS